

Room-Temperature Quantum Optomechanics and Free-Electron Quantum Optics

Présentée le 10 mai 2024

Faculté des sciences de base
Laboratoire de photonique et mesures quantiques (STI/SB)
Programme doctoral en physique

pour l'obtention du grade de Docteur ès Sciences

par

Guanhao HUANG

Acceptée sur proposition du jury

Prof. H. Brune, président du jury
Prof. T. Kippenberg, directeur de thèse
Prof. G. Steele, rapporteur
Prof. M. Kociak, rapporteur
Dr C. Galland, rapporteur

The race is not to the swift or the battle to the strong,
nor does food come to the wise or wealth to the brilliant or favor to the learned;
but time and chance happen to them all.
— Ecclesiastes 9:11

To my father, who cultivated my compassion,
And to my mother, who taught me to treat everything with rigor.

Acknowledgements

I would like to express my deepest gratitude to my thesis advisor, Tobias Kippenberg, for his patience over the years with these challenging projects. I also could not have undertaken this journey without Nils Engelsen, whose SNSF Ambizione funding supported me over most of my PhD studies. I have worked directly with more than 20 colleagues on diverse topics during my PhD, and I would like to thank them all if possible. In the early years, whenever I had any question, Liu and Itay would always give me a satisfying answer. My colleagues Nils, Junqiu, Erwan, Arslan, and Grigory also helped me get started in the lab when I first joined the group. When the Covid lockdown happened, I am grateful that Tobias encouraged me to work on the electron project, without which I would never have met our friends from Göttingen, especially Armin, Germaine, Ofer, and Claus, who are never short of patience for my sometimes stupid questions. Thanks should also go to our electron team, Arslan and Yujia. I am also thankful to Amirhassan, who has embraced me with all his friendliness that has continued to this day. Outside our research, I sincerely thank Siyu and Giovanni for a year of collaboration on a distant topic, and Professor Lenka Zdeborová, who trusted me with her course. Without all the support I received from everyone I mentioned, it would not have been possible to gather enough spirit to grind through the MIM project with our team members, Alberto and Nils. This project would not have been successful without the scientific support from outside our group, especially Junxin Chen, who patiently answered most of my questions on the experiment and recommended LPQM during my bachelor's. I am also grateful to Martin and Marta, without whom I would have never fixed our laser for the experiment. I have also enjoyed working with the younger generation of PhD students during my studies, especially Alessio, Amirali, Jiahe, Xinru, Zihan, Zheru, and Junyin. I would also like to thank Nils and Terence for proofreading the thesis. Finally, I want to express my deepest gratitude to our laboratory administrators, Kathleen and Antonella, without whom this group could not function efficiently.

Outside the school, I have to give my special thanks to Jijun He, my best friend for many years, whose overwhelming optimism supported me over the years. I am also thankful to Alice Cont, my flatmate for over three years and my biggest hideaway from physics. Lastly, I would like to mention that during the COVID-19 period, Professor Dian Tan and Jianqi Hu offered me the much-desired human interaction.

Nothing would be possible without the full support of my parents, especially since COVID-19 deters my return home. My life's pursuit comes at the cost of their sacrifice. To that, I am forever in debt.

Lausanne, March 8, 2024

Abstract

Quantum optics studies how photons interact with other forms of matter, the understanding of which was crucial for the development of quantum mechanics as a whole. Starting from the photoelectric effect, the quantum property of light has led to the development of atomic physics, laser science, and nonlinear optics. The interaction between quantized photons and free electrons, as well as macroscopic mechanical objects, has only been experimentally investigated in recent years. The journey toward observing the manifestation of the quantum nature of photons constitutes most of this thesis, in two particular settings: optomechanical interaction and free-electron interaction.

Quantum optomechanics studies the quantum effects when macroscopic mechanical objects couple to an electromagnetic field. First developed for studying gravitational wave detection, it is now a platform for exploring the limits of quantum measurements. To date, most of the quantum effects have been demonstrated only with experiments at cryogenic temperatures. In the first half of this thesis, we discuss our effort to establish an experiment system, using the "membrane-in-the-middle" architecture, to demonstrate quantum optomechanical effects at room temperature, which is beneficial to the accessibility and widespread adoption of optomechanical technology. Specifically, we identify the competing physical processes that emerged at room temperature, which cause linear and nonlinear thermomechanical cavity frequency noise, as well as photothermal mechanical instability. Having understood these effects, we develop techniques, including phononic crystal mirrors, nonlinear noise cancellation, and high power-handling soft-clamped membranes, to resolve these challenges, which lead to the operation of a solid-state optomechanical system in the quantum regime at room temperature for the first time. With the system we developed, we demonstrate optomechanical squeezing, measurement of mechanical motion in the quantum limit, measurement-based feedback cooling close to the quantum ground state, and optomechanical sideband asymmetry.

On the other hand, free-electron quantum optics studies the more fundamental interaction between a flying electron and quantum optical fields. The semi-classical interaction between free electrons and an intense laser field has been well studied, but the quantum nature of light remains elusive. By its energy-conserved nature, coherent cathodoluminescence can reveal the quantum nature of electron-light interaction under the right measurement setting. In the second half of this thesis, we discuss the theoretical investigation of the quantum optical interaction between free electrons and light and the experimental platform we developed using integrated photonic circuits. With a classical laser field, we observe efficient stimulated free-electron interaction with both linear and nonlinear optical fields. When the cavity is in

Abstract

a vacuum state, the quantum nature of electron-photon interaction is revealed in the form of coherent cathodoluminescence for the first time by analyzing the correlations of particle coincidence, thanks to complete control over the input-output ports of the used photonic device, as well as event-based electron detectors.

Keywords: Quantum measurement, cavity optomechanics, dissipative dynamics, integrated photonic circuits, electron microscopy, electron energy loss spectroscopy

Résumé

L'optique quantique étudie l'interaction des photons avec d'autres formes de matière, dont la compréhension a été cruciale pour le développement de la mécanique quantique dans son ensemble. À partir de l'effet photoélectrique, la propriété quantique de la lumière a conduit au développement de la physique atomique, de la science des lasers et de l'optique non linéaire. L'interaction entre les photons quantifiés et les électrons libres, ainsi que les objets mécaniques macroscopiques, n'a été étudiée expérimentalement que ces dernières années. Le voyage vers l'observation de la manifestation de la nature quantique des photons constitue la majeure partie de cette thèse, dans deux contextes particuliers : l'interaction optomécanique et l'interaction entre électrons libres.

L'optomécanique quantique étudie les effets quantiques lorsque des objets mécaniques macroscopiques sont couplés à un champ électromagnétique. D'abord développée pour étudier la détection des ondes gravitationnelles, elle constitue désormais une plateforme pour explorer les limites des mesures quantiques. Jusqu'à présent, la plupart des effets quantiques n'ont été démontrés que par des expériences à des températures cryogéniques. Dans la première moitié de cette thèse, nous discutons de nos efforts pour établir un système expérimental, en utilisant l'architecture "membrane au milieu", pour démontrer les effets optomécaniques quantiques à température ambiante, afin de faciliter l'accès à la technologie optomécanique ainsi que son adoption généralisée. Plus précisément, nous identifions les processus physiques concurrents apparaissant à température ambiante, qui provoquent un bruit de fréquence thermomécanique linéaire et non linéaire de la cavité, ainsi qu'une instabilité mécanique photothermique. Après avoir compris ces effets, nous développons des techniques, notamment des miroirs cristallins phononiques, l'annulation du bruit non linéaire et des membranes à serrage souple à haute puissance, afin de résoudre ces problèmes, nous permettant de faire fonctionner pour la première fois un système optomécanique à l'état solide dans le régime quantique à température ambiante. Avec le système que nous avons développé, nous démontrons la compression optomécanique, la mesure du mouvement mécanique dans la limite quantique, le refroidissement par rétroaction basé sur la mesure à proximité de l'état fondamental quantique et l'asymétrie de la bande latérale optomécanique.

L'optique quantique à électrons libres, quant à elle, étudie l'interaction plus fondamentale entre un électron se propageant et des champs optiques quantiques. Bien que l'interaction semi-classique entre des électrons libres et un champ laser intense ait été bien étudiée, la nature quantique de la lumière reste tout autant énigmatique. La cathodoluminescence cohérente, de par sa propriété à conserver l'énergie, peut révéler la nature quantique de l'in-

Résumé

teraction électron-lumière dans les conditions de mesure appropriées. Dans la seconde moitié de cette thèse, nous discutons de l'étude théorique de l'interaction optique quantique entre les électrons libres et la lumière, ainsi que de la plateforme expérimentale que nous avons développée en utilisant des circuits photoniques intégrés. Avec un champ laser classique, nous observons une interaction stimulée efficace entre les électrons libres et les champs optiques linéaires et non linéaires. Lorsque la cavité est vide, la nature quantique de l'interaction électron-photon est démontrée sous la forme de cathodoluminescence cohérente pour la première fois grâce à l'analyse des corrélations de coïncidence des particules, à un contrôle complet des ports d'entrée-sortie du dispositif photonique utilisé, ainsi qu'à des détecteurs d'électrons activés par événements déclencheurs.

Mots-clés : Mesure quantique, optomécanique de cavité, dynamique dissipative, circuits photoniques intégrés, microscopie électronique, spectroscopie de perte d'énergie des électrons

Publications

- [1] **G Huang***, A Beccari*, NJ. Engelsen, TJ Kippenberg. 2024. Room-temperature quantum optomechanics using an ultra-low noise cavity *Nature* 626(7999), 512–516
- [2] Y Yang*, J-W Henke*, AS. Raja*, EJ Kappert*, **G Huang**, G Arend, Z Qiu, A Feist, RN Wang, A Tusnin, A Tikan, C Ropers, TJ. Kippenberg. 2024. Free electron interaction with nonlinear optical states *Science* 383(6679), 168-173.
- [3] J Zhang, Z Li, J Riemensberger, G Lihachev, **G Huang**, TJ. Kippenberg. 2023. Fundamental charge noise in electro-optic photonic integrated circuits arXiv:2308.15404
- [4] **G Huang**, NJ. Engelsen, O Kfir, C Ropers, TJ. Kippenberg. 2023. Electron-photon quantum state heralding using photonic integrated circuits *PRX Quantum* 4, 020351
- [5] V Snigirev*, A Riedhauser*, G Lihachev, J Riemensberger, RN Wang, C Moehl, M Churaev, A Siddharth, **G Huang**, C Möhl, Y Popoff, U Drechsler, D Caimi, S Hönl, J Liu, P Seidler, TJ. Kippenberg. 2023. Ultrafast tunable lasers using lithium niobate integrated photonics *Nature* 615(7952), 411-417
- [6] W Chen, Y Lu, S Zhang, K Zhang, **G Huang**, M Qiao, Xu Su, J Zhang, J-N Zhang, L Banchi, M. S. Kim, K Kim. 2023. Scalable and Programmable Phononic Network with Trapped Ions *Nature Physics* 1745-2481
- [7] S Chen*, **G Huang***, G Piccioli*, L Zdeborová. 2022. The planted XY model: thermodynamics and inference *Phys. Rev. E* 106, 054115
- [8] A Feist*, **G Huang***, G Arend*, Y Yang*, J-W. Henke, A S. Raja, F J. Kappert, R N Wang, H Lourenço-Martins, Z Qiu, J Liu, O Kfir, TJ. Kippenberg, C Ropers. 2022. Cavity-mediated electron-photon pairs *Science* 377(6607), 777-780
- [9] A Shams-Ansari*, **G Huang***, L He, Z Li, J Holzgrafe, M Jankowski, M Churaev, P Kharel, R Cheng, D Zhu, N Sinclair, B Desiatov, M Zhang, TJ. Kippenberg, M Loncar. 2022. Reduced Material Loss in Thin-film Lithium Niobate Waveguides *APL Photonics* 7, 081301
- [10] M Gao*, QF Yang*, QX Ji*, H Wang, L Wu, B Shen, J Liu, **G Huang**, L Chang, W Xie, S-P Yu, SB. Papp, JE. Bowers, TJ. Kippenberg, KJ. Vahala. 2022. Probing material absorption and optical nonlinearity of integrated photonic materials *Nature Communications* 13 (1), 1-8

* equal contribution

Publications

- [11] MJ Beryhi*, A Arabmoheghi*, A Beccari, SA Fedorov, **G Huang**, TJ. Kippenberg, NJ. Engelsen. 2022. Perimeter Modes of Nanomechanical Resonators Exhibit Quality Factors Exceeding at Room Temperature *Physical Review X* 12 (2), 021036
- [12] L Qiu, **G Huang**, I Shomroni, J Pan, P Seidler, TJ. Kippenberg. 2022. Dissipative Quantum Feedback in Measurements Using a Parametrically Coupled Microcavity *PRX Quantum* 3 (2), 020309
- [13] JW Henke*, AS Raja*, A Feist, **G Huang**, G Arend, Y Yang, F J Kappert, RN Wang, M Möller, J Pan, J Liu, O Kfir, C Ropers, TJ. Kippenberg. 2021. Integrated photonics enables continuous-beam electron phase modulation *Nature* 600 (7890), 653-658
- [14] J Liu, **G Huang**, RN Wang, J He, AS. Raja, T Liu, NJ. Engelsen, TJ. Kippenberg. 2021. High-yield, wafer-scale fabrication of ultralow-loss, dispersion-engineered silicon nitride photonic circuits *Nature communications* 12 (1), 1-9
- [15] **G Huang**, E Lucas, J Liu, AS. Raja, G Lihachev, ML. Gorodetsky, NJ. Engelsen, TJ. Kippenberg. 2019. Thermorefractive noise in silicon-nitride microresonators *Physical Review A* 99 (6), 061801

Contents

Acknowledgements	i
Abstract (English/Français/Deutsch)	iii
Publications	vii
Introduction	1
I Room-temperature quantum optomechanics	5
1 Theoretical foundations of photon-phonon interaction	9
1.1 Quantization of cavity photons	9
1.2 Quantization of macroscopic phonons	11
1.3 Photon-phonon coupling mediated by an optical cavity	13
2 Experimental platform for room-temperature quantum optomechanics	17
2.1 Membrane-in-the-middle optomechanical system	18
2.1.1 Theoretical modeling of the membrane-in-the-middle system	18
2.1.2 Assembly procedure of the membrane-in-the-middle system	22
2.1.3 System parameters & calibration	27
2.2 Membrane designs	30
2.2.1 Designs of the employed devices	30
2.2.2 Dissipation dilution effects of 3D mechanical structures	33
2.2.3 Mechanical simulations of density-modulated PnC membranes	35
2.2.4 Microfabrication of density-modulated PnC membranes	39
2.3 Phononic crystal mirrors	41
2.3.1 Cavity noise budget and suppression techniques	41
2.3.2 Fabrication and simulation of phononic crystal mirrors	44
2.3.3 TiSa laser phase noise characterization	46
2.4 Thermal intermodulation noise	47
2.4.1 Quantum Langevin equation with nonlinear transduction	48
2.4.2 Breakdown of the fast-cavity limit	50
2.4.3 Second-order nonlinear noise cancellation in a homodyne detection	54
2.4.4 Third-order nonlinear noise	59

Contents

2.4.5	Nonlinear mixing of vacuum fluctuations	62
2.4.6	Modified Pound-Drever-Hall lock for the magic detuning	68
2.4.7	Reducing cavity transduction nonlinearity	71
2.4.8	Cancelling second-order noise in a heterodyne detection	75
2.5	Absorption-induced mechanical instability	78
2.5.1	Dissipative coupling	80
2.5.2	Photothermal effect	84
3	Measurement-based quantum control of mechanical motion	89
3.1	Optomechanical squeezing	89
3.1.1	Langevin equations governing optical quadrature measurements	90
3.1.2	Measuring optical squeezing	93
3.2	Quantum measurements of mechanical motions	96
3.2.1	Continuous measurement	96
3.2.2	Retrodiction	108
3.2.3	Conditional state preparation	111
3.3	Measurement-based feedback cooling	120
3.3.1	Quantum Langevin equations of measurement-based feedback cooling	120
3.3.2	Using measurement results to infer mechanical phonon occupancy	125
3.3.3	Cancelling cavity response through measurement-based feedback	127
3.4	Cooling a mechanical oscillator close to the quantum ground state	128
3.4.1	Sideband cooling of mechanical oscillators	128
3.4.2	Sideband asymmetry using a dual-homodyne measurement	130
3.5	Future experiments	136
II	Free-electron quantum optics	139
4	Quantum optical interaction between free electrons and photons	143
4.1	Quantum nature of free electrons and photons	144
4.2	Single-mode electron-photon interaction	144
4.2.1	Electron-photon semi-classical interaction	145
4.2.2	Quantization of the optical field	147
4.2.3	Electron ladder operator eigenstate	154
4.3	Electron-photon interaction in the continuum	159
4.3.1	3D quantization of the electromagnetic field in dispersive dielectric media	160
4.3.2	Equivalence to the semi-classical result	164
4.3.3	Modal decomposition and spatial-temporal modes	165
5	Photon-induced near-field electron microscopy	169
5.1	Continuous-wave driven semi-classical electron-light interaction	170
5.1.1	Photonic chip-integration in an electron microscope	171
5.1.2	Simultaneous optical and electron spectroscopy	171
5.2	Free-electron interaction with optical continuum	177

5.2.1	Free-electron interaction with nonlinear optical fields	179
5.2.2	Generalized electron modulation dependence on field properties	182
5.2.3	Continuous electron-soliton interaction	187
6	Free-electron quantum optical interaction with photonic integrated circuits	193
6.1	Electron-photon interactions with dielectric media	195
6.2	Coupling ideality	198
6.2.1	Finite element method simulation of Green functions	202
6.2.2	Substrate and thin film losses	205
6.2.3	Interaction with optical resonators	207
6.3	Shaping optical states from measurements on electron energy	208
6.3.1	Wave-like regime	209
6.3.2	Particle-like regime	212
6.4	Shaping electron states from optical detection	218
6.4.1	Optical detection in coherent state basis	222
6.4.2	Frequency conversion using resonator structures	225
6.5	Theoretical and experimental limitations	228
7	Cavity-mediated electron-photon pairs	231
7.1	Free-electron interaction with cavity modes	232
7.2	Coherent cathodoluminescence	236
7.3	Electron-photon non-classical correlation	238
7.3.1	Time- and energy-correlated electron-photon pairs	238
7.3.2	Violation of Cauchy-Schwarz inequality	249
7.4	Mode imaging enhanced by correlation	255
7.5	Conditional electron state by photon counting	257
7.5.1	Verifying photon statistics	260
7.6	Future improvements	262
8	Electron energy-dispersion effects	265
8.1	Dispersive propagation	266
8.2	Cavity-mediated optical klystron	268
8.2.1	Coherent field amplification	269
8.2.2	Free-electron superradiance	273
8.3	Free-electron recoil blockade	274
8.3.1	Free-electron Rabi oscillation and JC interaction	275
8.3.2	Physical limitations	276
8.4	Bell test using electron-photon pair states	278
8.4.1	Bell inequality of a general d-dimensional state space	278
8.4.2	Bell violation in a synthetic 2D state space using electron ladder eigenstates	280
9	Epilogue	285

Contents

A	Dissipative dynamics in photonic integrated circuits	289
A.1	Fundamental thermal noises	291
A.1.1	Theoretical treatment of thermorefractive noise	291
A.1.2	Measurement of thermorefractive noise	295
A.1.3	Thermal noise cancellation	298
A.2	Kerr nonlinearity	300
A.2.1	Single-mode Kerr squeezing	300
A.3	Absorption-induced dissipative feedback	304
A.3.1	Absorption enhanced Kerr squeezing	311
A.3.2	Photothermal response simulation	314
A.4	Absorption spectroscopy	316
A.4.1	Silicon nitride microrings	316
A.4.2	Lithium niobate microrings	320
A.5	Unidentified thermal noise in silicon nitride microresonators	328
B	Appendix	337
B.1	Different forms of Langevin equations and interpretations of spectral asymmetry	337
B.1.1	General quantum Langevin equation	337
B.1.2	Quantum Langevin equation within the rotating wave approximation . .	340
B.2	Fabrication process flow of density-modulated PnC membranes	341
B.3	Infinite impulse response filters	344
B.4	Broadband feedback cooling using a digital IIR filter	351
B.5	Classical measurement noise and suppressions in interferometers	352
B.6	Simplified derivation of optomechanical squeezing	362
B.7	Simplified picture of measurement-based feedback cooling	364
B.8	Classical laser noise effects on sideband asymmetry	368
B.9	Theory of dissipative Kerr solitons	370
B.10	Classical noise contributions in the Kerr squeezing experiment	371
B.11	Cavity nonlinearity-induced pump-probe response	377
B.12	Fano and split resonances in ring resonators	380
B.13	Filter cavity assembly for the Kerr squeezing experiment	383
B.14	Purity and fidelity of heralded optical states by measurements of electron energy	394
B.15	Purity of heralded electron states by measurements of optical state	398
B.16	Electron-photon entangled states in the wave-like regime	400
B.17	Second-order correlation functions of photons generated by electrons	401
	Bibliography	444
	Curriculum Vitae	445

Introduction

We never experiment with just one electron or atom or (small) molecule.
In thought-experiments we sometimes assume that we do;
this invariably entails ridiculous consequences.
— Erwin Schrödinger 1952

This thesis is structured into two parts: Part I, Room-temperature quantum optomechanics; and Part II, Free-electron quantum optics. Although they are two seemingly disconnected research topics, they are all under the broader research direction of quantum optics and, to some extent, even share similar physical effects. They also reflect the diverse topics we explore in the Laboratory of Photonics and Quantum Measurements, as well as the collaborative research environment. These two parts are arranged in this order not because of chronological reasons. In fact, they are undertaken in parallel.

I started my PhD working with photonic integrated circuits, aiming to generate squeezed light using optical Kerr nonlinearity based on the low-loss material of Si_3N_4 . It has been a long-standing goal in the field to generate textbook continuous-wave (CW) optical squeezing using only a single cavity mode in microresonators, but it has had no success. During my first year of research, we identified and characterized various noise sources and parasitic processes in our low-loss Si_3N_4 photonic integrated circuit platform. I summarized our findings in Appendix A, Dissipative dynamics in photonic integrated circuits, where the discovery of an

Introduction

unidentified noise source indicates that our platform is not yet feasible for CW-squeezed light generation. However, the techniques we developed and the results obtained along the way have motivated me during the early stages of my PhD. These include the measurement and modeling of the thermorefractive noise [1], the development of the framework of dissipative feedback [2], as well as using photothermal response measurements to anchor material absorption rates [3, 4, 5].

After my PhD candidacy exam, we decided to pass on the Kerr squeezing project. I switched my primary PhD project to developing an experimental platform to achieve room-temperature quantum optomechanics. As I had extensive experience with trapped ion systems [6] during my bachelor study, cavity optomechanics is both intuitive and straightforward, where we replace the ion's electronic resonance with an optical cavity and replace the ion's harmonic motion with the displacement of macroscopic mechanical oscillators. At the same time, I am excited to work on the quantum control of manufactured objects for the first time in my career, instead of a single particle I was used to, where the experimental and theoretical considerations are much more complex and diverse. Right around the same time, Covid happened. During the Covid lockdown period, I also started working on the theoretical formulation of electron-photon interaction at home, using my quantum optics knowledge from research and teaching. Even though free particles are the first thing we studied in quantum mechanics, their properties when interacting with other particles are much less well-known. That really interests me and presents new opportunities. These two research directions, i.e., cavity optomechanics and free-electron quantum optics, have been my parallel focus ever since. In particular, the encouraging results from the electron side [7, 8, 9] have been helping me cope with the numerous technical challenges encountered in the cavity optomechanics experiment [10]. I am glad that, in the end, both research directions were fruitful. I have summarized a brief comparison of the two research directions in Chapter 9.

On the optomechanics side, I took over the project from a former PhD student, Sergey Federov. I managed to develop an experiment platform [10], together with my colleague Alberto Beccari, who helped me tremendously with device fabrication, where we observed most of the quantum optomechanical effects, including optomechanical squeezing, position measurement in the quantum limit, measurement-based feedback cooling close to the quantum ground state, and optomechanical sideband asymmetry, demonstrating the outstanding performance of our system. These results have been summarized in Chapter 3, which would not have been possible if not for the numerous technical advances we made in Chapter 2, which resolved many of the challenges when operating the system at room temperature, including photothermal mechanical instability, thermal intermodulation noise, and cavity mirror noise. I find these advances more precious than the optomechanical effects we observed, which are essentially the same as those investigated almost a decade ago in low-temperature systems. Resolving every one of these technical challenges has been the central theme over the past four years during my PhD, where the resolution of one issue typically leads to another new one. Room-temperature operation has been a long-standing goal in the field of cavity optomechanics since its infancy around two decades ago. During my PhD, many groups in the field have been

actively working on this goal, many of which have given up on the project by the end due to the challenging technical difficulties of dealing with unwanted physical processes that emerge at room temperature. I feel fortunate that, before the end of my thesis study, we identified and understood most aspects of the physical processes in our system and developed the necessary techniques to achieve quantum control of a macroscopic oscillator at room temperature.

On the free-electron quantum optics side, I jumped right into the theoretical side of the electron-photon interaction during Covid, which I found timely when the electron project started rolling. The understanding and formulation of physics, new and old alike, have always been encouraging to me, but it was not possible without our experiment collaborators from Claus Roper's group. I firmly believe that experiment and theory should guide each other, and without either, science cannot be done properly, especially for a young and emerging field. During these years, I have tried my best to be critical of my findings, especially ensuring that my theory closely follows the observation and can guide the experiment. Like any theoretical work, anything I derived can be wrong and mistaken before direct experiment evidence is confirmed. In this thesis, I first summarize all the theory basics in Chapter 4 and proceed with the experimental observation of semi-classical electron-light interactions in Chapter 5 in the form of generalized PINEM [7, 11], which is well-studied in the field. The quantum optical part, which is the most complex and easy to confuse oneself, follows in Chapters 6 and 7, where I start with a detailed theoretical analysis of the experiment system [9] (Chapter 6), and ends with our experiment observation of the quantum optical interaction between free-electrons and optical waveguides [8] (Chapter 7). Even though I spent much time understanding the observations as much as possible, to this day, some of the phenomena in the experiment still puzzle me. Chapter 8 follows with the theoretical findings of our continuing work on free-electron interactions with two-ring devices, where the electron energy-momentum dispersion affects the interaction.

Room-temperature quantum optomechanics

Part I

Observing quantum phenomena requires precise measurement and control of the quantum system. Even for single particles, this is not easy, as when they interact with the outside world, they quickly lose their quantum properties. The fragile nature of quantum systems [12] renders them susceptible to the influence of the thermal environment. This presents a significant challenge in quantum science and technology, especially for solid-state systems strongly coupled to their environment. Nevertheless, over the past decade, quantum control has been extended to solid-state mechanical resonators, both with radiation pressure optomechanical coupling [13] and piezoelectric coupling with superconducting qubits [14, 15].

Cavity optomechanics, where a macroscopic mechanical oscillator dispersively couples to an optical cavity, has enabled numerous advances in controlling and engineering the quantum state of the oscillator and light, including ground state cooling [16, 17], optomechanical squeezing of light [18, 19, 20, 21, 22] and entanglement of separate mechanical oscillators [23, 24, 25]. This architecture has also been extended to quantum transducers [26] and may even allow macroscopic tests of quantum mechanics [27] with massive and more macroscopic objects.

However, all these advances necessitate cryogenic cooling to reduce thermal fluctuations. Room temperature operation, on the other hand, is beneficial to the accessibility and the widespread adoption of technology, as witnessed in different branches of physical science [28, 29, 30]. The development of room-temperature quantum optomechanical systems would imply a drastic reduction of experimental complexity by removing the limitations imposed by cryocoolers, such as poor thermalization, excess acoustic noise, and limited optical access. Room temperature operation would stimulate applications such as coupling to atomic systems [31], force microscopy [32], and variational displacement measurements [22]. From a more fundamental perspective, even though quantum optomechanical phenomena were already demonstrated over a decade ago at cryogenic temperatures, observing similar quantum phenomena should not be taken for granted since other physical processes outside the conventional optomechanics interaction will start to dominate. These additional processes that emerge when conducting experiments at higher temperatures are interesting by themselves from the perspective of understanding new physics.

This part of the thesis describes our journey toward establishing an optomechanical system operating in the quantum regime at room temperature, and contains parts adapted from Ref [10]. We first review the theoretical basis of cavity optomechanics in Chapter 1. Then, in Chapter 2, we discuss in detail how we overcome several challenges in a phononic-engineered “membrane-in-the-middle” system to enter the quantum regime of cavity optomechanics at room temperature. Specifically, we reduce the thermodynamical fluctuations of cavity frequency, using a high-finesse cavity whose mirrors are patterned with phononic crystal structures, by more than 700-fold (Section 2.3). In this ultra-low noise cavity, we introduce a silicon nitride membrane oscillator whose density is modulated by silicon nano-pillars [33], yielding both high thermal conductance and a localized mechanical mode with Q of 1.8×10^8 (Section 2.2). The high thermal conductance of the membrane reduces the photothermal ef-

fect, which would otherwise prevent the operation in the quantum regime. The photothermal effect is examined in theoretical modeling and experimental verification (Section 2.5). We also studied the nonlinear thermomechanical noise in the cavity (Section 2.4) and developed a single-port homodyne detection technique to mitigate this noise in many measurement settings. In Chapter 3, we show that these advances enable the operation of the optomechanical displacement sensor within a factor of 2.5 of the Heisenberg limit, leading to squeezing of the probing laser field by 1.09 dB below the vacuum fluctuations (Section 3.1). Moreover, the long thermal decoherence time of the membrane oscillator (more than 30 vibrational periods) allows us to obtain conditional displaced thermal states of motion with an occupation of 0.97 phonons (Section 3.2). We also observed canonical optomechanical sideband asymmetry when cooling the mechanical oscillator close to the quantum ground state (Section 3.4).

We also summarize some acronyms that we use in this part of the thesis below.

ALD: Atomic layer deposition

DBA: Dynamical backaction

FPGA: Field-programmable gate array

FT: Fourier transform

IIR: Infinite impulse response

MIM: Membrane-in-the-middle

PDH: Pound-Drever-Hall

PECVD: Plasma-enhanced chemical vapor deposition

PnC: Phononic crystal

QBA: Quantum backaction

QED: Quantum electrodynamics

Q: Quality factor

SNR: Signal to noise ratio

SQL: Standard quantum limit

TIN: Thermal intermodulation noise

1 Theoretical foundations of photon-phonon interaction

This chapter aims to set up the most fundamental theoretical basics of the quantization procedure of photons and phonons, whose properties are frequently used in the later chapters, particularly in the part of cavity optomechanics. Since cavity optomechanics is primarily concerned with the interaction between a single optical cavity mode and high-Q mechanical modes, which have well-defined frequencies and field profiles, we only quantize discrete optical modes and mechanical eigenmodes of a finite structure, as well as their Fourier components in the frequency domain. Next, we derive the most canonical cavity optomechanics model, and some basic physical effects, including dynamical backaction and quantum backaction. More complex models and theoretical analyses are developed in later chapters, accompanied by the associated experimental results.

Throughout the thesis, we adopt the notion that $\text{FT} = \int e^{i\omega t} dt$, so that $\text{FT}[\dot{A}(t)] = -i\omega A(\omega)$, unless specified otherwise. We also use the following notation for the power spectral density of quantum observables:

$$S_{\hat{A}\hat{B}}(\omega) \equiv \lim_{T \rightarrow \infty} \frac{1}{T} \langle \hat{A}_T^\dagger(-\omega) \hat{B}_T(\omega) \rangle = \iint_T \langle \hat{A}^\dagger(t+\tau) \hat{B}(t) \rangle e^{i\omega\tau} d\tau = \int \langle \hat{A}^\dagger(\omega) \hat{B}(\omega') \rangle \frac{d\omega'}{2\pi}, \quad (1.1)$$

where T is the integration time window, $\hat{A}(\omega) = \int \hat{A}(t) e^{i\omega t} dt$, and $\hat{A}^\dagger(\omega) = \hat{A}(-\omega)^\dagger$.

1.1 Quantization of cavity photons

The quantization of photons is covered in most quantum optics textbooks, e.g., [34]. Here, we follow the framework of the open quantum system, where a cavity mode is coupled to bath modes of input and output fields. In a finite space with a fully reflective boundary condition, the optical eigenmodes $\mathbf{U}_n(\mathbf{r})$ can be solved from the wave equation

$$\nabla \times \nabla \times \mathbf{U}(\mathbf{r}) - \frac{\omega^2}{c^2} \epsilon(\mathbf{r}, \omega) \mathbf{U}(\mathbf{r}) = 0 \quad (1.2)$$

Chapter 1. Theoretical foundations of photon-phonon interaction

with normalization condition

$$\int d^3\mathbf{r} \epsilon(\mathbf{r}, \omega_m) \mathbf{U}_m(\mathbf{r}) \cdot \mathbf{U}_n^*(\mathbf{r}) = \delta_{m,n}. \quad (1.3)$$

Here, $\epsilon(\mathbf{r}, \omega_m)$ is the optical permittivity as a function of spatial coordinate and optical frequency ω , and c is the speed of light. If the space is filled with only vacuum or lossless media, the modal decomposition method [35] is often used, where the optical vector potential is quantized as

$$\hat{\mathbf{A}}(\mathbf{r}, t) = \sum_n \sqrt{\frac{\hbar}{2\omega_n \epsilon_0}} \mathbf{U}_n(\mathbf{r}) \hat{a}_{\omega_n, n} e^{-i\omega_n t} + h.c. \quad (1.4)$$

such that the Hamiltonian of a single optical mode \hat{a}_m is simply

$$\hat{H}_{\text{ph}} = \hbar\omega_m \hat{a}_m^\dagger \hat{a}_m \quad (1.5)$$

where \hbar is the Planck constant. In this thesis, we use the quantum Langevin equation (with rotating wave approximation) derived in Appendix B.1.2 to describe the dynamics governing the creation and annihilation operators of the cavity mode at frequency Ω_0 ,

$$\dot{\hat{a}} = (-i\Omega_0 - \kappa/2) \hat{a} + \sqrt{\kappa} \hat{a}_{\text{in}} \quad (1.6)$$

where the input noise operator obeys

$$\langle \hat{a}_{\text{in}}^\dagger(t) \hat{a}_{\text{in}}(t') \rangle = \bar{n}_{\text{th}} \delta(t - t') \quad (1.7)$$

$$\langle \hat{a}_{\text{in}}(t) \hat{a}_{\text{in}}^\dagger(t') \rangle = (\bar{n}_{\text{th}} + 1) \delta(t - t') \quad (1.8)$$

where the thermal occupancy $\bar{n}_{\text{th}}(\Omega_0, T) = 1/(\exp(\hbar\Omega_0/k_B T) - 1)$. Note that for our particular case of optical frequencies > 100 THz, we can safely set $\bar{n}_{\text{th}} = 0$ in most scenarios.

In the rotating frame of the laser frequency Ω_{laser} , we use the detuning $\Delta = \Omega_0 - \Omega_{\text{laser}}$ instead,

$$\dot{\hat{a}} = (-i\Delta - \kappa/2) \hat{a} + \sqrt{\kappa} \hat{a}_{\text{in}} \quad (1.9)$$

In the presence of classical laser phase noise $\delta p(t)$ and amplitude noise $\delta q(t)$, we have the following correlations for the laser phase and amplitude quadratures:

$$\hat{q} = \frac{\hat{a}_{\text{in}} e^{-i\theta} + \hat{a}_{\text{in}}^\dagger e^{i\theta}}{\sqrt{2}} \quad (1.10)$$

$$\hat{p} = -i \frac{\hat{a}_{\text{in}} e^{-i\theta} - \hat{a}_{\text{in}}^\dagger e^{i\theta}}{\sqrt{2}} \quad (1.11)$$

$$\begin{pmatrix} \langle \delta \hat{q}(t) \delta \hat{q}(t') \rangle & \langle \delta \hat{q}(t) \delta \hat{p}(t') \rangle \\ \langle \delta \hat{p}(t) \delta \hat{q}(t') \rangle & \langle \delta \hat{p}(t) \delta \hat{p}(t') \rangle \end{pmatrix} = \frac{1}{2} \begin{pmatrix} 1 + 2C_{qq} & i + 2C_{qp} \\ -i + 2C_{qp} & 1 + 2C_{pp} \end{pmatrix} \delta(t - t'), \quad (1.12)$$

1.2 Quantization of macroscopic phonons

with which we obtain the following relations for the input noise operator:

$$\langle \hat{a}_{\text{in}}^\dagger(t) \hat{a}_{\text{in}}(t') \rangle = \left(\bar{n}_{\text{th}} + \frac{C_{qq} + C_{pp}}{2} \right) \delta(t - t') \quad (1.13)$$

$$\langle \hat{a}_{\text{in}}(t) \hat{a}_{\text{in}}^\dagger(t') \rangle = \left(\bar{n}_{\text{th}} + 1 + \frac{C_{qq} + C_{pp}}{2} \right) \delta(t - t') \quad (1.14)$$

$$\langle \hat{a}_{\text{in}}(t) \hat{a}_{\text{in}}(t') \rangle = \left(\frac{e^{2i\theta} C_{qq} - e^{2i\theta} C_{pp}}{2} + i e^{i\theta} C_{pq} \right) \delta(t - t') \quad (1.15)$$

where θ is the mean field phase $\bar{a}_{\text{in}} = |\bar{a}_{\text{in}}| e^{i\theta}$. We can also define the optical susceptibility in the Fourier domain

$$\hat{a}(\omega) = \sqrt{\kappa} \chi_{\text{cav}}(\omega) \hat{a}_{\text{in}}(\omega) \quad (1.16)$$

$$\chi_{\text{cav}}(\omega) = \frac{1}{i(\Delta - \omega) + \kappa/2} \quad (1.17)$$

to simplify many of the calculations in this thesis.

1.2 Quantization of macroscopic phonons

The macroscopic oscillators we treat in this thesis are the vibrational eigenmodes of a solid-state object. Compared to the more natural quantization of elementary particles, the macroscopic nature of these oscillations roots in the thermodynamic limit, where a collection of interacting particles yields a few normal modes with easy-to-access macroscopic observables, e.g., center-of-mass motion, whose quantization can be naturally extended from the microscopic counterpart.

The details of the quantization of phonons are more complicated than that of optical photons. For a book of reference, see Ref. [36]. For optical photons, typically losses κ are far smaller than the optical frequencies ω , so we can always use the perturbative approach by separating the lossless Hamiltonian containing all the eigenmodes and then introduce the bath mode coupling using Langevin equations.

This is not easily the case for mechanical phonons unless the mechanical modes are of high quality factors $Q = \Omega_m / \Gamma_m \gg 1$, where Ω_m is the mechanical frequency and Γ_m is the damping rate. For over-damped oscillators, the perturbative approach cannot be easily justified. In order to define a quantum oscillator, the requirement is more strict because the thermal decoherence rate $\Gamma_{\text{th}} = (n_{\text{th}}(\Omega_m, T) + 1/2)\Gamma_m$ is amplified by the bath temperature T , which is especially important for low-frequency mechanical motions. Therefore, the prerequisite of having a quantum oscillator is that the mechanical eigenmode gives a mechanical frequency Ω_m that is larger than the thermal decoherence rate Γ_{th} defined at Ω_m , such that the perturbative approach of Hamiltonian quantization and Langevin equations are justified.

From here, we assume to have a quantum oscillator with $\Omega_m \gg \Gamma_{\text{th}}(\Omega_m)$, then we quantize

Chapter 1. Theoretical foundations of photon-phonon interaction

the position \hat{q} and momentum \hat{p} operators in the frame of the mechanical frequency as:

$$\hat{q} = x_{\text{zpf}}(\hat{b}^\dagger + \hat{b}) \quad (1.18)$$

$$\hat{p} = i p_{\text{zpf}}(\hat{b}^\dagger - \hat{b}) \quad (1.19)$$

where $x_{\text{zpf}} = \sqrt{\hbar/2m\Omega_m}$ is the zero-point position fluctuation, $p_{\text{zpf}} = \sqrt{\hbar m\Omega_m/2}$ is the zero-point momentum fluctuation, and m is the effective mass of the oscillator. This quantization procedure is only possible when $\Omega_m \gg \Gamma_{\text{th}}(\Omega_m)$, because of the frequency-dependent nature of the zero-point fluctuations over the Fourier bandwidth between $\Omega_m \pm \Gamma_{\text{th}}$.

Throughout the thesis, we will generally work with the dimensionless position \hat{Q} and momentum \hat{P} operators instead, which are defined as:

$$\hat{Q} = \frac{1}{\sqrt{2}} \frac{\hat{q}}{x_{\text{zpf}}} = \frac{1}{\sqrt{2}}(\hat{b}^\dagger + \hat{b}) \quad (1.20)$$

$$\hat{P} = \frac{1}{\sqrt{2}} \frac{\hat{p}}{p_{\text{zpf}}} = \frac{i}{\sqrt{2}}(\hat{b}^\dagger - \hat{b}) \quad (1.21)$$

Using the Boson commutation relation, it is clear that $[\hat{Q}, \hat{P}] = i$. Following this commutation relation, we can find the position-momentum uncertainty principle

$$\sigma(\hat{Q})\sigma(\hat{P}) \leq \frac{1}{2} |\langle [\hat{Q}, \hat{P}] \rangle| = \frac{1}{2} \quad (1.22)$$

and their variance in thermal equilibrium

$$\sigma^2(\hat{Q}) = \sigma^2(\hat{P}) = \bar{n}_{\text{th}} + \frac{1}{2} \quad (1.23)$$

In this thesis, we use the generalized quantum Langevin equation (without rotating wave approximation) derived in Appendix B.1.1 to describe the dynamics governing the position and momentum operators due to the lower $\Omega_m/\Gamma_{\text{th}}$ compared to the optical one:

$$\dot{\hat{Q}} = \Omega_m \hat{P} \quad (1.24)$$

$$\dot{\hat{P}} = -\Omega_m \hat{Q} - \Gamma_m \hat{P} + \sqrt{2\Gamma_m} \hat{P}_{\text{in}} \quad (1.25)$$

with the following input noise density:

$$S_{\hat{P}_{\text{in}}\hat{P}_{\text{in}}}(\omega) = \frac{\omega}{\Omega_m} (\bar{n}_{\text{th}}(\omega) + 1) \quad (1.26)$$

$$S_{\hat{P}_{\text{in}}\hat{P}_{\text{in}}}(-\omega) = \frac{\omega}{\Omega_m} \bar{n}_{\text{th}}(\omega) \quad (1.27)$$

1.3 Photon-phonon coupling mediated by an optical cavity

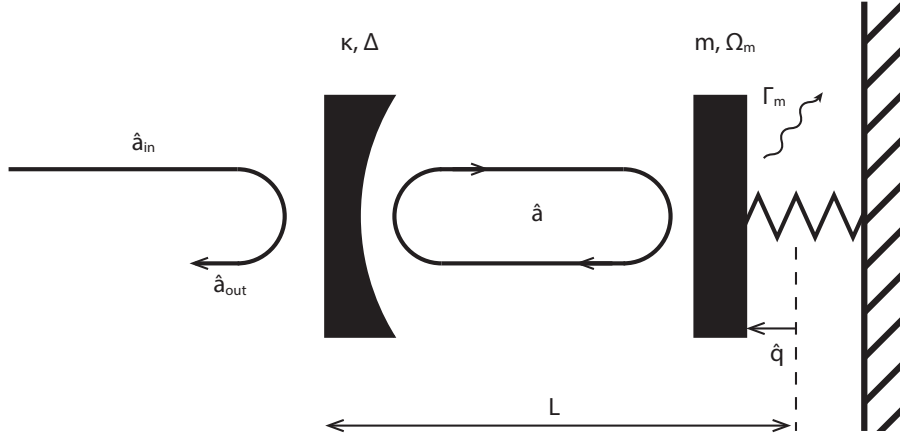


Figure 1.1: Canonical representation of a cavity optomechanical system. One of the end mirrors of the FP cavity is the mechanical oscillator with frequency Ω_m and damping rate Γ_m , whose position operator is \hat{q} . The cavity is at frequency $\Delta = \Omega_0 - \Omega_{\text{laser}}$ detuned from the laser, with a decay rate of κ , whose frequency $\Omega_0(q)$ is determined by the mechanical position \hat{q} .

It is also convenient to define the mechanical susceptibility of

$$\dot{\hat{Q}}(\omega) = \sqrt{2\Gamma_m} \chi_m(\omega) \hat{P}_{\text{in}} \quad (1.28)$$

$$\chi_m(\omega) = \frac{\Omega_m}{\Omega_m^2 - \omega^2 - i\omega\Gamma_m} \quad (1.29)$$

which we will use frequently throughout this part of the thesis.

1.3 Photon-phonon coupling mediated by an optical cavity

A canonical schematic for cavity optomechanics can be found in Fig. 1.1, where the position q of the mechanical resonator changes the resonant frequency $\Omega_0(q)$ of an optical cavity mode. From here, we can write down the semi-classical cavity optomechanics Hamiltonian

$$H = \frac{p^2}{2m} + \frac{m\Omega_m^2}{2} q^2 + \hbar\Omega_0(q) \hat{a}^\dagger \hat{a} \quad (1.30)$$

In the usual case where position fluctuation δq is small and the optomechanical coupling strength $G \equiv \frac{\partial\Omega_0(q)}{\partial q} \neq 0$, we can linearly expand the optical frequency as $\Omega_0(q + \delta q) = \Omega_0(q) + G\delta q$. We can then proceed with the quantization procedure of the phonons discussed in the previous section and set $\delta q \rightarrow \hat{q}$ to arrive at the canonical optomechanical Hamiltonian [13]

$$\hat{H} = \hbar(\Omega_0 + G\hat{q}) \hat{a}^\dagger \hat{a} + \hbar\Omega_m \hat{b}^\dagger \hat{b} \quad (1.31)$$

$$= \hbar\Omega_0 \hat{a}^\dagger \hat{a} + \hbar\Omega_m \hat{b}^\dagger \hat{b} + \hbar g_0 \hat{a}^\dagger \hat{a} (\hat{b}^\dagger + \hat{b}) \quad (1.32)$$

Chapter 1. Theoretical foundations of photon-phonon interaction

where we defined the vacuum optomechanical coupling rate as

$$g_0 = Gx_{zpf} \quad (1.33)$$

Following the Langevin equations derived from earlier sections, we can write out the equation set that is essential to derive most of the dynamics associated with the results obtained in this thesis,

$$\dot{\hat{a}} = -\left[\frac{\kappa}{2} + i(\Delta + \sqrt{2}g_0\hat{Q})\right]\hat{a} + \sqrt{\kappa}\hat{a}_{\text{in}}, \quad (1.34)$$

$$\dot{\hat{Q}} = \Omega_m\hat{P}, \quad (1.35)$$

$$\dot{\hat{P}} = -\Omega_m\hat{Q} + \sqrt{2\Gamma_m}\hat{P}_{\text{in}} - \Gamma_m\hat{P} - \sqrt{2}g_0\hat{a}^\dagger\hat{a}, \quad (1.36)$$

In the case where the cavity is pumped with strong laser fields, such that the intra-cavity photon number $\langle\hat{a}^\dagger\hat{a}\rangle \gg 1$, we can linearize the optical field by working in a frame of the phase space displaced by $\alpha = \langle\hat{a}\rangle$ from the origin. In this thesis, we work in an optical reference frame where the intracavity field $\alpha = |\alpha|$ has zero phase. It is then equivalent to the following transformation:

$$\hat{D}^\dagger(\alpha)\hat{a}^\dagger\hat{a}\hat{D}(\alpha) = \alpha(\hat{a}^\dagger + \hat{a}) + \hat{a}^\dagger\hat{a} \quad (1.37)$$

where $\hat{D}(\alpha) = \exp(\alpha\hat{a}^\dagger - \alpha^*\hat{a})$ is the displacement operator. The second term $\hat{a}^\dagger\hat{a}$ on the right side can be safely ignored in most circumstances because optical vacuum fluctuations are small compared to stimulated fields. However, this might not be the case when the optical fluctuations are dominated by other noise sources, e.g., the thermodynamical noises of the mechanical resonator. In this case, this term exhibits nonlinear effects, which we discuss in Section 2.4 of thermal intermodulation noise.

In the linear regime where photon operator nonlinearity can be safely ignored, it is convenient to define the optomechanical coupling rate $g = g_0\alpha$, with which the frequency-domain Langevin equations are

$$\hat{a}(\omega) = \sqrt{2}ig\chi_{\text{cav}}(\omega)\hat{Q}(\omega) + \sqrt{\kappa}\chi_{\text{cav}}(\omega)\hat{a}_{\text{in}}(\omega) \quad (1.38)$$

$$\hat{Q}(\omega) = \chi_m(\omega)\left(\sqrt{2\Gamma_m}\hat{P}_{\text{in}}(\omega) - 2g\hat{X}(\omega)\right) \quad (1.39)$$

In the presence of an optical drive, the cavity provides a feedback mechanism to modify the

1.3 Photon-phonon coupling mediated by an optical cavity

dynamics of the mechanical oscillator in the following way (dynamical backaction):

$$\hat{Q}(\omega) = \chi'_m(\omega) \left(\sqrt{2\Gamma_m} \hat{P}_{\text{in}}(\omega) - \sqrt{2\kappa} g (\chi_{\text{cav}}(\omega) \hat{a}_{\text{in}}(\omega) + \chi_{\text{cav}}(-\omega)^* \hat{a}_{\text{in}}^\dagger(\omega)) \right) \quad (1.40)$$

$$\chi'_m(\omega) = \frac{1}{\chi_m(\omega)^{-1} + 2ig^2(\chi_{\text{cav}}(-\omega)^* - \chi_{\text{cav}}(\omega))} = \frac{\Omega_m}{\Omega_m'^2 - \omega^2 - i\omega\Gamma_m'} \quad (1.41)$$

$$\Omega_m' = \sqrt{\Omega_m^2 - 2g^2\Omega_m \text{Im}[\chi_{\text{cav}}(-\omega)^* - \chi_{\text{cav}}(\omega)]} \quad (1.42)$$

$$\Gamma_m' = \Gamma_m - 2g^2 \frac{\Omega_m}{\omega} \text{Re}[\chi_{\text{cav}}(-\omega)^* - \chi_{\text{cav}}(\omega)] \quad (1.43)$$

where the mechanical oscillator experiences an optical spring effect $\Omega_m' = \Omega_m + \delta\Omega_m$ and optical damping/amplification $\Gamma_m' = \Gamma_m + \delta\Gamma_m$. Note that optomechanical bistability occurs exactly when $\Omega' \rightarrow 0$. The above expression neglects the frequency-dependent $\Gamma_m(\omega)$, especially when the system is under structural damping instead of viscous damping. This feature is exploited in the case of optically-stiffened cantilevers [21, 37], where a significant optical spring effect leads to a reduction of mechanical loss.

We assume that the mechanical mode is initially thermalized to the environment with occupation \bar{n}_{th} . In our experiment, we mostly work with red detuned laser in the fast cavity limit $\Omega_m \ll \kappa$. The mechanical mode is Doppler-cooled by dynamical backaction damping with the following simplified expressions:

$$\Gamma_m^{\text{dba}} = g^2 \left(\frac{\kappa}{\kappa^2/4 + (\Delta + \Omega_m)^2} - \frac{\kappa}{\kappa^2/4 + (\Delta - \Omega_m)^2} \right) \approx \frac{-4\Omega_m \Delta \kappa g^2}{(\kappa^2/4 + \Delta^2)^2}, \quad (1.44)$$

while at the same time, frequency-shifted by the optical spring effect,

$$\delta\Omega_m^{\text{dba}} = g^2 \left(\frac{\Delta - \Omega_m}{\kappa^2/4 + (\Delta + \Omega_m)^2} + \frac{\Delta + \Omega_m}{\kappa^2/4 + (\Delta - \Omega_m)^2} \right) \approx \frac{2\Delta g^2}{\kappa^2/4 + \Delta^2}. \quad (1.45)$$

One of the critical parameters of the system is the quantum cooperativity $C_q = \frac{4g^2}{\kappa\Gamma_{\text{th}}}$, which characterizes the ratio between the interaction of the oscillator with optical photons vs. that of the environment phonon bath. The dynamical backaction effect can be used to calibrate C_q when the pump is detuned and to calibrate all other effects that contribute to mechanical frequency shift (e.g., thermal expansion due to heating). The optical spring shift can be used to calibrate $C_q \approx \frac{4}{\sqrt{3}} \frac{\delta\Omega_m^{\text{dba}}}{\Gamma_{\text{th}}}$ at the magic detuning $2\Delta_*/\kappa = 1/\sqrt{3}$ discussed in Section 2.4. The same applies to the dynamical back-action damping rate $\Gamma_m^{\text{dba}} \approx \frac{3\sqrt{3}C_q\Gamma_{\text{th}}\Omega_m}{2\kappa}$.

Under laser cooling, the mechanical mode undergoes thermal equilibrium with two baths, one of the thermal environment and one of the laser. The occupation of the mechanical mode is calculated as

$$\bar{n} = \frac{\bar{n}_{\text{th}}\Gamma_m + \bar{n}_m^{\text{dba}}\Gamma_m^{\text{dba}}}{\Gamma_m^{\text{tot}}} \quad (1.46)$$

Chapter 1. Theoretical foundations of photon-phonon interaction

where the equivalent bath occupation of the laser for unresolved sideband cooling is

$$\bar{n}_m^{\text{dba}} = \frac{(\Omega_m + \Delta)^2 + (\kappa/2)^2}{-4\Delta\Omega_m} \quad (1.47)$$

The finite occupation of the laser bath in the unresolved sideband regime comes from quantum backaction (QBA) forces to the mechanics, with an equivalent increase in the mechanical thermal occupation \bar{n}_{qba} . In the resonant setting, $\Delta = 0$, we retrieve $\frac{\bar{n}_{\text{qba}}}{\bar{n}_{\text{th}}} = C_q$. When the laser is detuned, the QBA is reduced to $\frac{\bar{n}_{\text{qba}}}{\bar{n}_{\text{th}}} = \frac{C_q}{1+(2\Delta/\kappa)^2}$.

In the next chapter, we discuss the technical details of establishing an optomechanical system capable of operating in the $C_q > 1$ regime at room temperature, and with quantum-noise-limited imprecision $\bar{S}_{xx}^{\text{imp}}$ and backaction \bar{S}_{FF}^{ba} .

2 Experimental platform for room-temperature quantum optomechanics

To enter the quantum regime of optomechanics, the product between the total force noise $\bar{S}_{FF}^{\text{tot}}$ (including environment thermal force \bar{S}_{FF}^{th} as well as measurement-induced backaction \bar{S}_{FF}^{ba}) and the displacement measurement imprecision $\bar{S}_{xx}^{\text{imp}}$ must approach the limit $\sqrt{\bar{S}_{xx}^{\text{imp}} \bar{S}_{FF}^{\text{tot}}} \geq \hbar/2$ set by the Heisenberg uncertainty principle [13]. A necessary condition imposed by this limit is that the quantum backaction (QBA) rate from the light field $\Gamma_{\text{qba}} = x_{\text{zpf}}^2 \bar{S}_{FF}^{\text{qba}} / \hbar^2$ (x_{zpf} is the oscillator's zero-point displacement fluctuation amplitude) must exceed the thermal decoherence rate $\Gamma_{\text{th}} = x_{\text{zpf}}^2 \bar{S}_{FF}^{\text{th}} / \hbar^2$ of the mechanical oscillator, which is determined by the bath temperature T and by the quality factor Q as $\Gamma_{\text{th}} = k_B T / (\hbar Q)$. In addition, the required measurement imprecision is far below the standard quantum limit (SQL), imposing strict limitations on tolerable cavity frequency noise.

Over the past decade, multiple pioneering approaches have been pursued to reach the ultralow mechanical dissipation required to enter the quantum backaction-dominated regime at room temperature, including levitated nanoparticles [38] and micromechanical objects whose rigidity is controlled by an optical field [37, 39]. These methods enhance the mechanical Q by optical trapping and have resulted in recent observations of quantum backaction [37], optomechanical squeezing of light [21, 40] and ground state cooling [41]—all at room temperature. However, room temperature quantum optomechanical phenomena have not been accessible with engineered ultra-coherent solid-state mechanical resonators because of thermal intermodulation noise [42], vibrations of the cavity mirror substrates [43] and optical heating-induced instability [44]. These thermal effects result in excess imprecision and backaction noise, preventing their product from reaching the Heisenberg limit.

This chapter describes our experimental system and advances to mitigate the abovementioned challenges to achieve operation in the quantum regime of cavity optomechanics. We first start with Section 2.1.1, the design principle of the membrane-in-the-middle (MIM) system, the device assembly procedure, and some parameters of the operating system. Section 2.2.2 discusses the membrane employed in the system, followed by a discussion of phononic crystal mirrors in Section 2.3.1. A detailed discussion of the nonlinear thermomechanical noise is

Chapter 2. Experimental platform for room-temperature quantum optomechanics

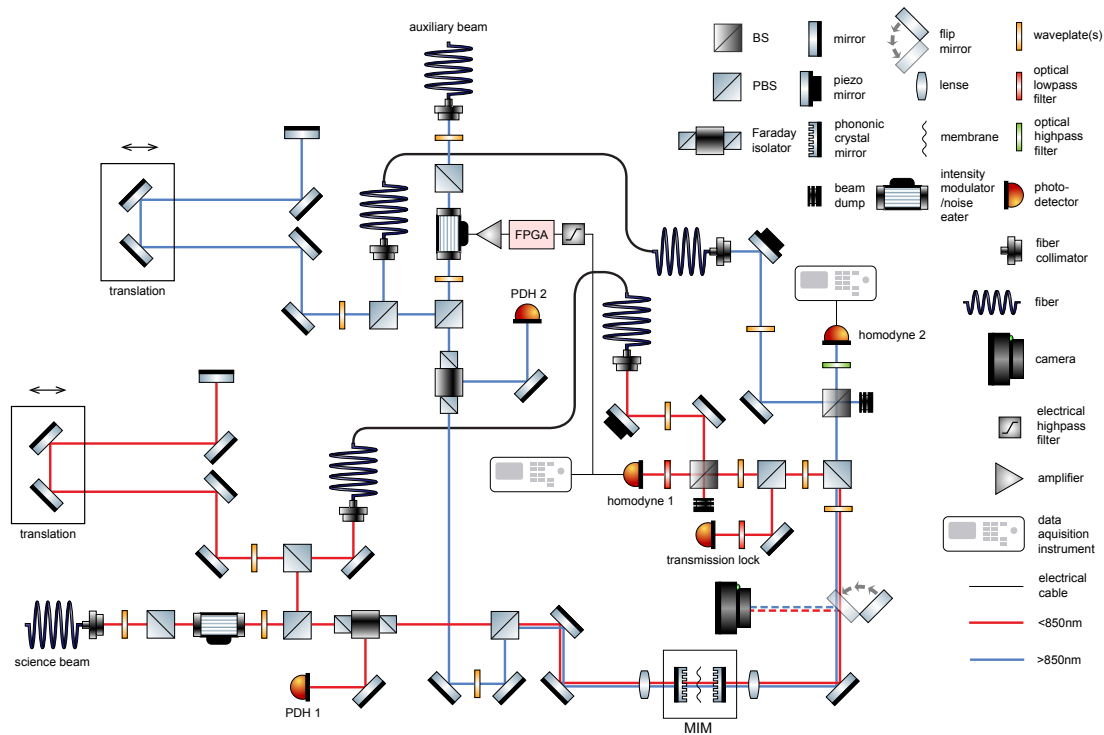


Figure 2.1: Setup schematic of the MIM system in the typical operating configuration used for measurement-based feedback control of the mechanical motion of the membrane. Depending on the specific experiments, some components in the setup are reconfigured.

provided in Section 2.4. Because of the necessity to operate at a specific laser detuning to mitigate the aforementioned nonlinear noise, the photothermal effect arises and induces mechanical instability, which is discussed in Section 2.5. In Section B.3, we discuss the working principle of IIR filters used to implement mode-selective feedback cooling of unstable modes due to the photothermal effect. A setup schematic is also shown in Fig. 2.1, where the IIR filter programmed on an FPGA board is used to implement feedback cooling. The setup is also used for most experiments performed in Chapters 2 and 3, with some components reconfigured when necessary.

2.1 Membrane-in-the-middle optomechanical system

2.1.1 Theoretical modeling of the membrane-in-the-middle system

A significant optical power is required to exert enough radiation shot noise to dominate the thermal force noise experienced by the mechanical oscillator. However, typical lasers exhibit classical noise in both the phase and amplitude of the field, which overwhelms the laser shot noise at high-power operation. Therefore, high-finesse optical cavities are typically used to enhance the radiation pressure force experienced by the mechanical oscillator while keeping

2.1 Membrane-in-the-middle optomechanical system

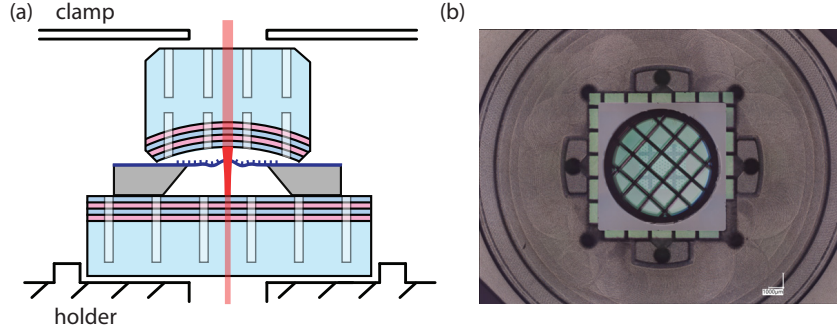


Figure 2.2: **(a)** Schematic of the MIM assembly structure and optical ports. **(b)** Optical microscope image of the MIM assembly from the top, showing the overlapping photonic crystal structures of the top mirror, membrane chip, and bottom mirror.

the optical power low to ensure quantum-noise-limited laser operation.

Furthermore, to access the quantum regime at room temperature for mechanical oscillators, engineered mechanical resonators exploiting the effect of dissipation dilution (discussed in Section 2.2.2) need to be used to achieve enough coherence to qualify as quantum oscillators. These resonators are typically very thin in thickness to achieve high coherence and can not serve well as an end cavity mirror for a high-finesse cavity. Membrane-in-the-middle (MIM) architecture (schematic shown in Fig. 2.2) is one cavity-mechanics configuration that could help to alleviate this inconvenience by placing a thin membrane inside an optical cavity to achieve efficient optomechanical coupling while maintaining high finesse of the cavity.

In the following, we model this configuration in a simplified 1-D analysis using the transfer matrix method [45, 46]. In the transfer matrix method, each optical element, including free-space propagation, can be represented by a 2-by-2 matrix M for the evolution of the optical field vector consisting of the electric and magnetic components E and B ,

$$\begin{pmatrix} E_2 \\ B_2 \end{pmatrix} = M \begin{pmatrix} E_1 \\ B_1 \end{pmatrix} \quad (2.1)$$

For a dielectric membrane of thickness d , the matrix takes the form of

$$M_m = \begin{pmatrix} \cos \phi_m & i n_m^{-1} \sin \phi_m \\ i n_m \sin \phi_m & \cos \phi_m \end{pmatrix} \quad (2.2)$$

where $\phi_m = \frac{2\pi n_m d}{\lambda}$, λ being the optical wavelength and n_m the membrane refractive index. A special case for free-space propagation of length L could be simplified to

$$M_{\text{free}} = \begin{pmatrix} \cos \phi_0 & i \sin \phi_0 \\ i \sin \phi_0 & \cos \phi_0 \end{pmatrix} \quad (2.3)$$

Chapter 2. Experimental platform for room-temperature quantum optomechanics

where $\phi_0 = \frac{2\pi L}{\lambda}$. For dielectric mirrors with finite transmission and loss, the matrix reads

$$M_{\text{mir}} = \begin{pmatrix} 1 & \delta_{\text{loss}}/4 \\ \delta_{\text{loss}}/4 & 1 \end{pmatrix} \begin{pmatrix} 0 & i\sqrt{T_{\text{mir}}}/2 \\ 2i/\sqrt{T_{\text{mir}}} & 0 \end{pmatrix} \quad (2.4)$$

where the light first interacts with the loss matrix and then the transmission matrix. The transfer matrix of an FP cavity could then be calculated as

$$M_{\text{FP}} = \begin{pmatrix} 0 & i\sqrt{T_1}/2 \\ 2i/\sqrt{T_1} & 0 \end{pmatrix} \begin{pmatrix} 1 & \delta_1/4 \\ \delta_1/4 & 1 \end{pmatrix} \begin{pmatrix} \cos\phi_1 & i\sin\phi_1 \\ i\sin\phi_1 & \cos\phi_1 \end{pmatrix} \\ \times \begin{pmatrix} \cos\phi_m & in_m^{-1}\sin\phi_m \\ in_m\sin\phi_m & \cos\phi_m \end{pmatrix} \\ \times \begin{pmatrix} \cos\phi_2 & i\sin\phi_2 \\ i\sin\phi_2 & \cos\phi_2 \end{pmatrix} \begin{pmatrix} 1 & \delta_2/4 \\ \delta_2/4 & 1 \end{pmatrix} \begin{pmatrix} 0 & i\sqrt{T_2}/2 \\ 2i/\sqrt{T_2} & 0 \end{pmatrix} \quad (2.5)$$

With this matrix, we can obtain the field transmission and reflection of the cavity from the following expressions:

$$t = \frac{2}{M_{11} + M_{12} + M_{21} + M_{22}} \quad (2.6)$$

$$r = \frac{M_{11} + M_{12} - M_{21} - M_{22}}{M_{11} + M_{12} + M_{21} + M_{22}} \quad (2.7)$$

We can solve it numerically, as shown in Fig. 2.3. The membrane can experience a similar optomechanical coupling rate compared to the mirrors, depending on the relative position to the cavity mode standing wave and the membrane thickness and refractive index.

One can obtain an analytical solution [45] of the optomechanical coupling strength of the membrane by enforcing the resonance condition $\text{Im}[M_{11} + M_{12} + M_{21} + M_{22}] = 0$,

$$G = \frac{\partial\Omega_0}{\partial z_m} = -\frac{\Omega_0}{L_{\text{cav}}} \frac{2|r_m|\sin(2k_0 z_m)}{\sqrt{1 - |r_m|^2 \cos^2(2k_0 z_m)}} \quad (2.8)$$

where z_m is the position of the membrane, r_m is the membrane reflectivity, k_0 is the optical free-space wave vector, and L_{cav} is the cavity length, used in the transfer matrix. r_m can also be expressed analytically as

$$r_m = \frac{(1 - |n|^2) \sin\phi_m}{(|n|^2 + 1) \sin\phi_m - 2i|n| \cos\phi_m} \quad (2.9)$$

and is approximately 0.2 for a 20-nm thick Si_3N_4 membrane. When comparing G to that of the cavity mirrors, we find that the optomechanical coupling rate of the membrane is penalized by the finite reflectivity of the membrane. In our design, we generally choose to use membranes as thin as possible to achieve sufficiently high quality factors while avoiding higher-order nonlinear thermomechanical noise (discussed in Section 2.4). The relatively lower optomechanical coupling rate can be enhanced by increasing the laser power.

2.1 Membrane-in-the-middle optomechanical system

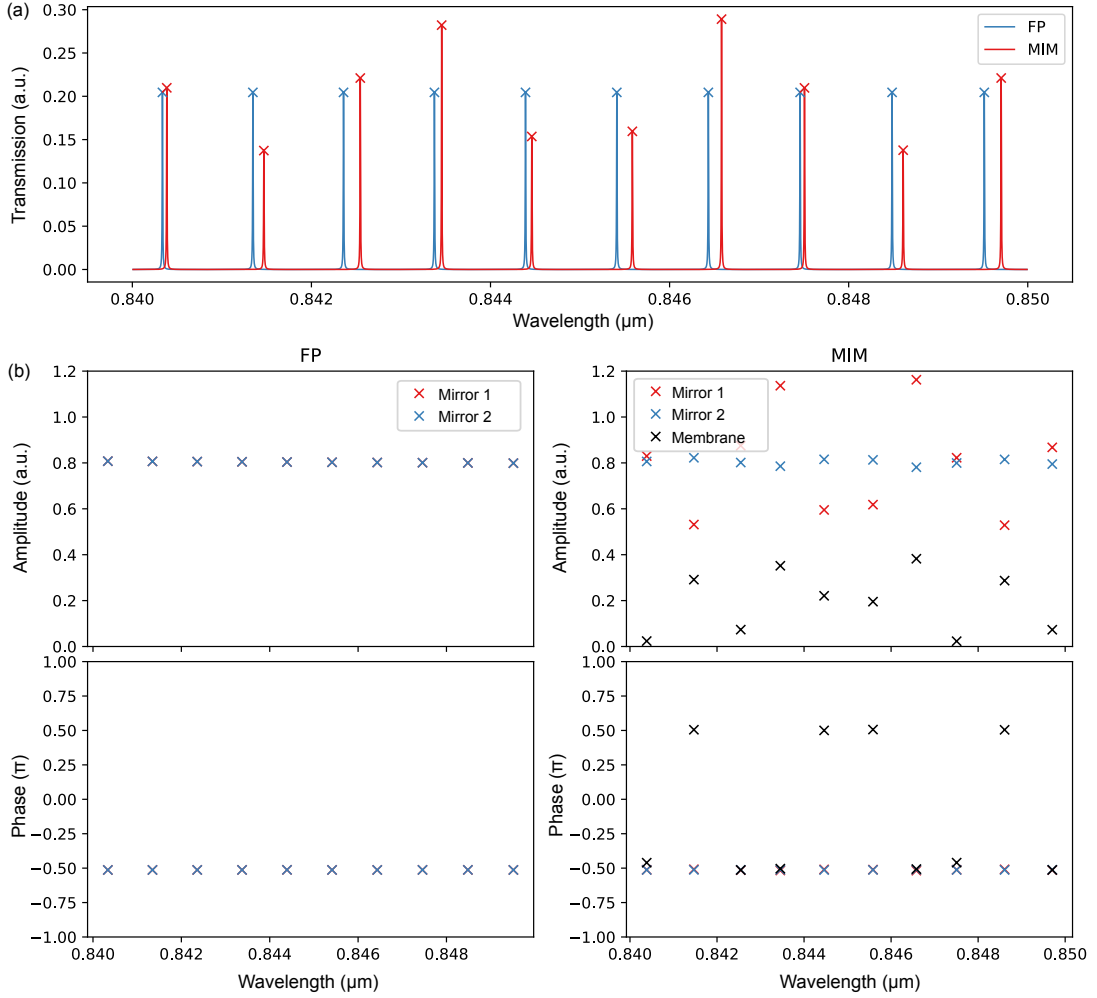


Figure 2.3: Numerical simulation of cavity resonance properties with $T_1 = 2 \times 10^{-3}$, $T_2 = 35 \times 10^{-3}$, $\delta_1 = \delta_2 = 1.5 \times 10^{-3}$, with a cavity length of $350 \mu\text{m}$ and a membrane thickness of 20 nm . The mirror transmission and loss are magnified by a factor of 100 compared to experimental values to help visualize the resonances. **(a)** Comparison between optical resonances in an FP cavity and those a MIM cavity. The membrane insertion modifies both the resonance frequency and the transfer function of the cavity, depending on the membrane's relative position to the cavity's standing waves. **(b)** Comparison between membranes' normalized optomechanical coupling rates and those of the two end mirrors. The membrane experiences a similar magnitude of optomechanical coupling compared to that of the mirrors, and modifies the coupling of the mirrors by redistributing the cavity fields between the two compartments.

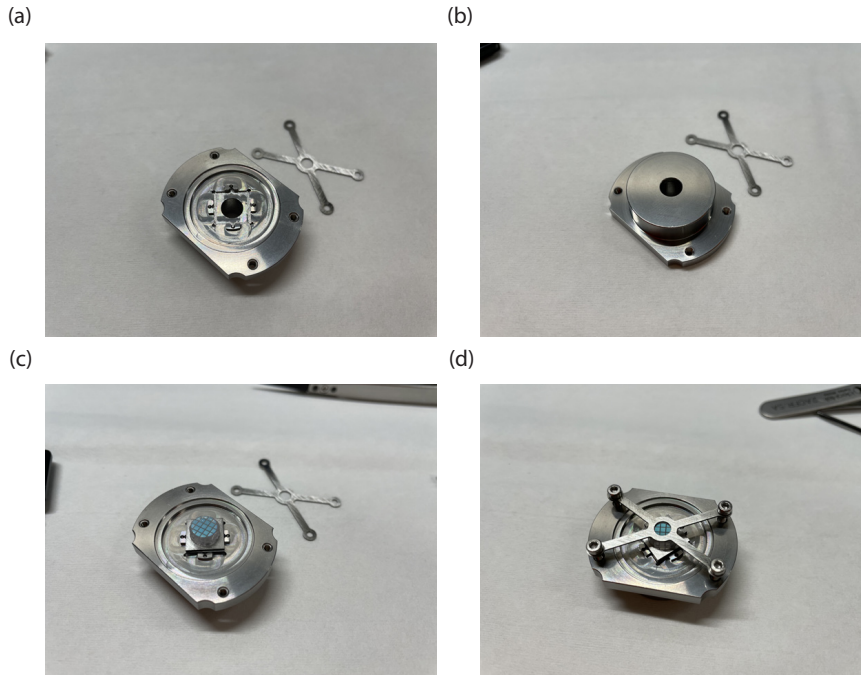


Figure 2.4: Photographs of the MIM assembly holder **(a)** top side and **(b)** bottom side. Photographs of the MIM assembly mounted on top of the holder **(c)** without and **(d)** with the stainless steel clamp.

In the next section, we describe how to assemble a MIM cavity from scratch.

2.1.2 Assembly procedure of the membrane-in-the-middle system

In the following, we first describe the holder that is used to fixate the MIM stack, then the alignment details of the MIM stack, and finally the assembly procedure of the entire device.

MIM holder

The MIM holder is a vacuum-compatible stainless steel block (schematic shown in Fig. 2.2), with a hole in the middle to allow input optical access from the bottom to the MIM device. The MIM device is clamped to the top of the holder using a thin stainless steel clamp (image shown in Fig. 2.4), which also has a hole in the center to allow optical output from the cavity top mirror.

The MIM holder is designed with a heavy cylindrical bulk at the bottom, which can fix the holder inside the vacuum chamber by inserting the cylinder into a complementary metal piece inside the vacuum chamber.

To fixate the MIM device, a square indentation is created centered on the top surface of the

2.1 Membrane-in-the-middle optomechanical system

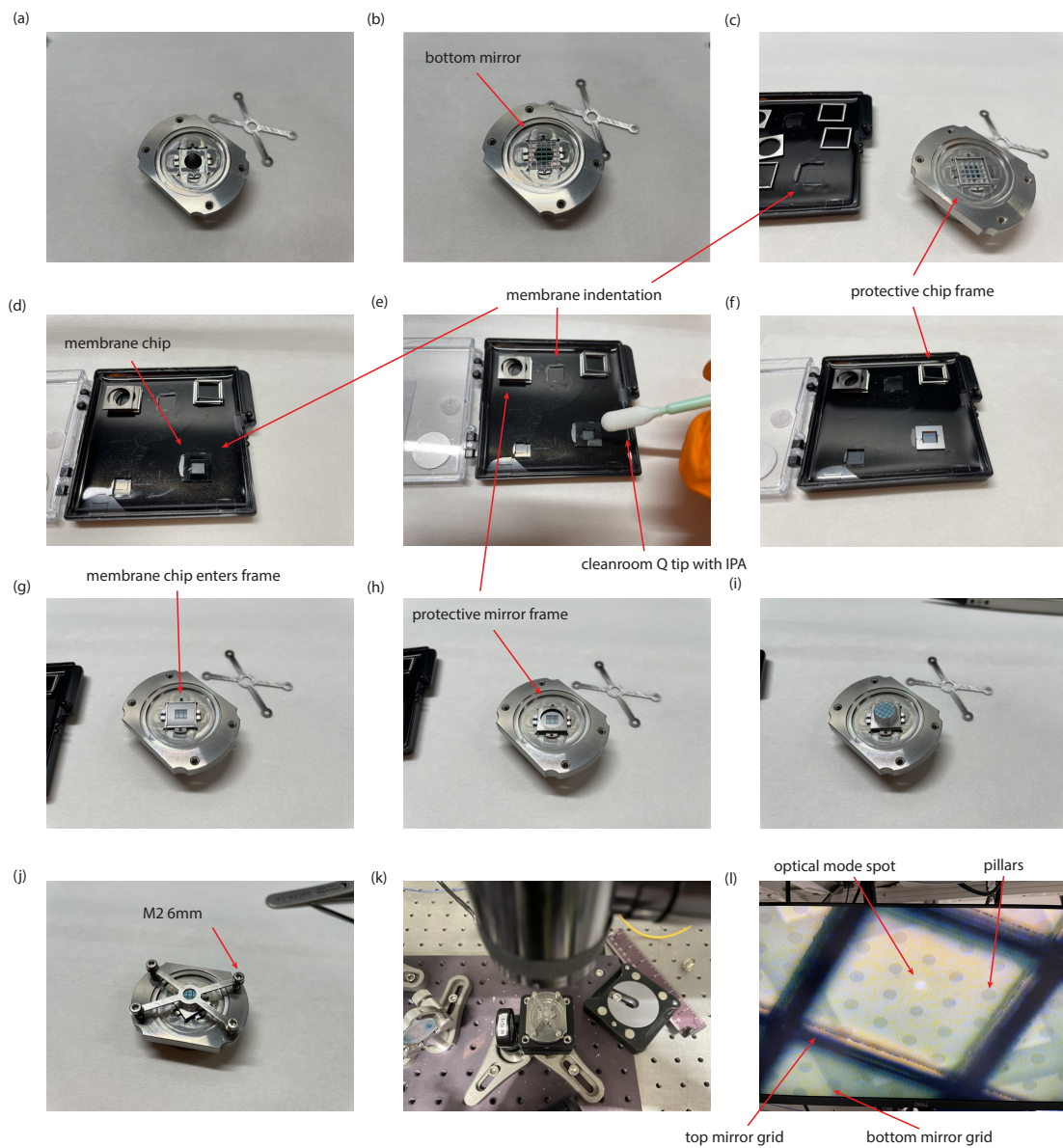


Figure 2.5: **Photographs of the assembly procedures.** (a) Top side of the holder. (b) Bottom mirror inserted into the indentation. (c) Protective chip frame stacked on top of the bottom mirror. (d) Membrane chip flipped upside down, resting on an indentation of the gel box. (e) Cleaning of the membrane chip bottom, using IPA-soaked Q tip. (f) Cleaned the backside surface of the membrane chip. (g) Membrane chip flipped back to the usual orientation (membrane side up) and inserted into the chip frame. (h) Protective mirror frame stacked on top of the chip frame, suspended from the membrane surface. (i) Top mirror stacked on top of the membrane chip, with the help of the mirror frame. (j) Clamping of the MIM stack using metal clamps and screws. (k) Setup for imaging optical modes of the cavity and aligning the mode position to the membrane defect center.

Chapter 2. Experimental platform for room-temperature quantum optomechanics

holder, which is slightly larger than the size of the bottom mirror. The indentation roughly fixes the position of the bottom mirror and allows movement freedom smaller than 1 mm. By stacking the membrane chip and the top mirror (shown in Fig. 2.4) on top of the bottom mirror and then clamping the entire assembly with a metal clamp and screws, sufficient mechanical and optical stability of the MIM cavity can be achieved.

MIM stack

The MIM stack comprises a membrane chip sandwiched between the top and bottom cavity mirrors (shown in Fig. 2.2). The direct contact between them ensures mechanical stability and reduces the cavity length for noise performance reasons (see Section 2.4.7 for nonlinear noise dependence on cavity linewidth). The length does not affect the mirror noise budget for experiments such as ground-state cooling and optomechanical squeezing.

In order to achieve optimal performance of the system, optical alignment is critical in the following three aspects:

- alignment between the membrane plane and the cavity mode wavefront to ensure minimum scattering losses,
- alignment between the cavity mode and the membrane defect center to maximize coupling rate to the defect mechanical mode,
- alignment between the cavity mode and the bottom mirror's unit-cell center to maximize the mirror noise reduction from the mirror modes' symmetry.

In principle, the alignment between the membrane plane and the cavity mode wavefront is only set by the cavity design. For symmetry reasons, the wavefront is completely flat at the bottom mirror surface for the planar-concave cavity configuration. However, the wavefront starts to curve further away from that surface. In order to avoid reflection or coupling to other cavity modes, the membrane surface must match the curvature of the optical wavefront at the membrane position.

The waist size and Rayleigh length of the fundamental cavity mode can be retrieved using

$$\omega_0^2 = \frac{\lambda R}{2\pi} \sqrt{1 - \left(1 - \frac{2L}{R}\right)^2} \quad (2.10)$$

$$z_R = \frac{R}{2} \sqrt{1 - \left(1 - \frac{2L}{R}\right)^2} \quad (2.11)$$

where L is the cavity length, R is the top mirror's curvature radius. For the experimental configuration of $L = 635 \mu\text{m}$, $R = 5 \text{ m}$, we have the waist of the cavity mode at $\omega_0 = 38 \mu\text{m}$, and Rayleigh length at $z_R = 5.6 \text{ mm}$. With these parameters, one can easily calculate the single-trip mode-matching efficiency between the beam reflected from the membrane and the optical

2.1 Membrane-in-the-middle optomechanical system

mode, by comparing the field profile at the bottom mirror

$$u_0(r) = \exp\left\{-\frac{r^2}{\omega_0^2}\right\} \quad (2.12)$$

and the profile reflected by the membrane and back to the bottom mirror (round trip $z = 2d$)

$$u_1(r) = \frac{1}{\sqrt{1 + (2d/z_R)^2}} \exp\left\{i \tan^{-1}\left(\frac{2d}{z_R}\right) - ik\left(2d + \frac{r^2}{2\tilde{R}}\right) - \frac{r^2}{\omega^2}\right\} \quad (2.13)$$

where $\tilde{R}(z) = z + \frac{z_R^2}{z}$ is the radius of the wavefront, and $\omega(z) = \omega_0 \left[1 + \left(\frac{z}{z_R}\right)^2\right]^{1/2}$. The mode matching efficiency at the position of the bottom mirror is

$$\eta = \frac{|\int u_0 u_1^*|^2}{\int |u_0|^2 \int |u_1|^2} = \frac{4(1 + (2d/z_R)^2)}{(2 + (2d/z_R)^2)^2 + \frac{k^2 \omega^4}{4\tilde{R}^2}} \quad (2.14)$$

With experimental parameters $d = 525 \mu\text{m}$ (thickness of the membrane chip), the roundtrip mode-matching efficiency $\eta = 0.9976$, with losses mostly from the wavefront phase mismatch. This is equivalent to a full-reflection finesse of $\mathcal{F} = 2.6 \times 10^3$, which does not limit the current finesse of the cavity $\mathcal{F} \sim 1 \times 10^4$, considering the membrane reflectivity of 4%. A precise number requires the summation of multiple roundtrip losses, but we are satisfied with this order of magnitude estimation. We believe that most of the excess losses we observed in the experiment are attributed to the tilting of the membrane relative to the transverse axes and the surface roughness of the membrane.

Assembly procedure details

The assembly procedure is illustrated in Fig. 2.5. In the following, we discuss the procedure step by step.

- The assembly procedure starts by inserting the bottom mirror into the holder's square indentation.
- Due to the size mismatch between the holder and the membrane chip, a chip frame is first placed on top of the mirror to prevent large movement of the membrane chip, after which the membrane chip is placed in the center. The membrane chip needs to be cleaned before this step, as follows
 - Flip the membrane chip and place it upside-down using an indentation carved out of a gel pad so that the membrane will not touch any surface that could break the membrane.
 - Place a few drops of IPA onto the cleanroom Q tip, shake away excess liquid, and carefully remove the contaminants from the chip backside in the form of white

Chapter 2. Experimental platform for room-temperature quantum optomechanics

dots. It is suspected that these contaminants could result in excess membrane tilting.

- Using the reflection to determine any remaining contaminants and remove them completely.
- Pay attention not to stir particles or droplets onto the membrane during this step.
- After the membrane is placed inside the chip frame, use the Q tip to remove any visible particles on the front side of the membrane. Here, pay attention not to touch the membrane or transfer anything onto it.
- Rest and center the mirror frame on top of the chip frame to help position the top mirror.
- Place the top mirror into the mirror frame. Use the position of the mirror frame to infer the centering of the top mirror. Pay attention not to displace the mirror too far away from the center because the edge of the curved mirror could touch the membrane and break the membrane.
- With the help of the mirror frame, center the top mirror.
- Gently hover the metal clamp on the stack without touching it. Place the four screws in their places before gently releasing the metal clamp so that it falls onto the top mirror.
- Correct any top mirror displacement due to contact with the metal clamp.
- Gently iteratively tighten the screws until the metal clamp is gently fixed (no relative movement with vertical shaking of the holder).
- Transfer the holder to the alignment setup for fine adjustment.
- Use extremely low intensity ($<1\mu\text{W}$) light to locate the center of the cavity modes at a wavelength around 780 nm where the cavity is of low finesse. The low intensity prevents the melting of the silicon pillars from optical absorption.
- Use a screwdriver to gently adjust the position of the chip frame such that the membrane defect center aligns with the center of the bottom mirror unit cell.
- Use the screwdriver to gently adjust the position of the mirror frame such that the center of the optical modes aligns with the center of the bottom mirror unit cell.
- Iteratively tighten the four screws by half rounds and readjust the top mirror alignment.
- Tighten the screws until a gentle push of the top mirror using the screwdriver no longer shifts the center of the optical modes.
- Transfer the holder to the vacuum chamber and pump down the pressure. The experimental test is within reach in about a day!

2.1 Membrane-in-the-middle optomechanical system

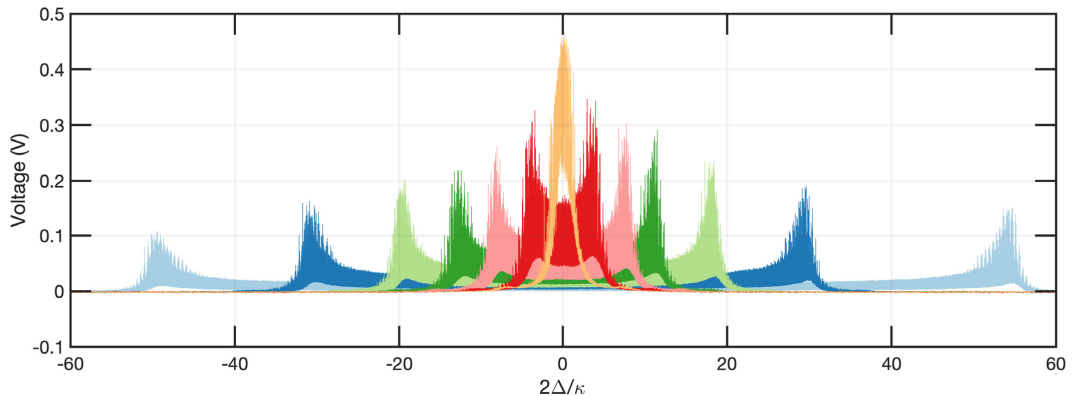


Figure 2.6: Measured optical transmission traces of the cavity mode, with different levels of cavity frequency modulation by mechanical lasing (including no-lasing case). When there is no mechanical lasing, the cavity line shape is still blurred by the high level of thermomechanical cavity frequency noise, causing thermal intermodulation noise (TIN), as discussed in Section 2.4. Once the optical cavity is broadened, it will slowly ring down in a few minutes because of the high-Q nature of the soft-clamped mode. The cavity modulation ring-down is also an indirect measure of the Q of the soft-clamped mode.

2.1.3 System parameters & calibration

We characterize several experimental parameters of the optomechanical cavity before the measurements shown in the thesis and use them as pre-determined parameters for fitting the measured mechanical spectra. We obtained cavity resonance linewidths κ at different optical wavelengths, as shown in Fig. 2(b), by scanning our titanium:sapphire (TiSa) laser frequency at a rate of 300 MHz/s across the optical resonances, with an optical power smaller than $1 \mu\text{W}$ to prevent significant mechanical excitation when the laser frequency crosses to the blue side of the cavity resonance [13]. The laser is phase modulated at 211 MHz with modulation depth ~ 0.1 to generate two small sidebands, which serve as reference points for calibrating the frequency axis. A measured optical transmission trace is shown in Fig. 2.6. A Lorentzian function is fitted to the cavity transmission to extract the optical linewidth. When the optical power is too large, optical amplification of mechanical oscillation, mainly of the soft-clamped mechanical mode, causes mechanical lasing. Mechanical lasing broadens the optical line shape by thousands of orders of overlapping Bessel sidebands, as shown in Fig. 2.6.

The mechanical frequency of the membrane defect mode, Ω_m , is measured from the cavity transmission spectrum at low input optical power, to limit optical spring effects due to dynamical backaction. The mechanical energy decay rate Γ_m is measured with a mechanical ringdown measurement (see Fig. 1(d)). In the ringdown experiment, a pump laser is first tuned to the blue side of an optical cavity mode at 845 nm (high finesse) to excite the membrane defect mode (phonon lasing) strongly. Then, the pump laser is switched off, and a weak probe laser is switched on near the cavity mode at 780 nm (low finesse) to measure the mechanical oscillation amplitude decay through the cavity transmission signal. The exact ringdown

Chapter 2. Experimental platform for room-temperature quantum optomechanics

measurement is repeated at multiple probe laser detuning frequencies, to ensure that no dynamical backaction damping or amplification is present during the ringdown measurement. The extracted damping rate is consistent with a previous measurement of the membrane in an optical interferometer before cavity assembly, indicating that no significant mechanical dissipation is added to the defect mode during the MIM assembly.

To obtain vacuum optomechanical coupling rates, g_0 , we follow the procedure described by [47]. We phase-modulate a weak laser probe with known depth, and compare the mechanical signal to the phase modulation tone transduced on the transmitted light intensity, which is directly detected at the cavity output. The probe laser is stabilized at the magic detuning to avoid heating from the intracavity TIN. We assume that the mechanical mode is initially thermalized to room temperature, and undergoes dynamical backaction cooling by the red-detuned probe laser. The probe power is kept relatively low ($C_q \ll 1$) to avoid quantum backaction heating, such that the thermal occupation of the defect mode can be reliably inferred from the dynamical backaction cooling rate found by fitting the mechanical spectrum. The probe laser is phase modulated at 1.1457 MHz with a depth of 0.1275, and at 1.19 MHz with a depth of 0.152. The two modulation frequencies are selected to be at the edges of the mechanical bandgap, and are symmetric to the defect mode frequency. The geometric average of their transduced signals is calculated to cancel the OMIT frequency response [48] from the defect mode and estimate g_0 . In the experiment, however, the field-enhanced optomechanical coupling rate $g = g_0 \bar{a}$ is the relevant parameter, where \bar{a} is the cavity field amplitude. g is left as a free parameter in all the fittings of the measured mechanical spectra. In the experiments shown in Chapter 3, where $C_q \sim 1$, we have $g/2\pi \sim 500$ kHz approaching the mechanical frequency.

The system parameters are summarized in the table below. They are from our latest generation device employing a density-modulated membrane with phononic crystal cavity mirrors.

System parameter	Value
$\Omega_m/2\pi$	1.167 MHz
$g_0/2\pi$	159.0 Hz
$\kappa/2\pi$	34.2 MHz
$\Gamma_m/2\pi$	6.41 mHz
C_0	0.461

We now discuss the various contributions to the detection efficiency η_d , an essential figure of merit for the state preparation experiment. In the experiments, we retrieve the detection efficiency by spectral fitting of the squeezing/mechanical signal, which depends sensitively on it. In the following, we individually identify and describe the calibration of some inefficiency contributions in the measurement chain:

- The detector electronics noise is measured by blocking the optical beam. The elec-

2.1 Membrane-in-the-middle optomechanical system

tronics noise is flat and broadband, so its inefficiency contribution can be retrieved by comparing it with the laser shot noise.

- The transmission from the optical elements after the cavity output and before the detector is measured with a handheld power meter. This loss term is dominated by a series of polarizing beam splitters, a beam pick-off for generating an error signal for laser locking, several waveplates, and the highly asymmetric beam splitter, which combines the local oscillator with the signal beam.
- The detector quantum efficiency is calculated from the detector responsivity specified by the manufacturer.
- The homodyne efficiency is calculated from the mode matching efficiency of 90% between the local oscillator and signal beam, given the measured interference visibility of 95%. The efficiency is only 75% in contrast to the usual 90% in conventional balanced homodyne detection, because we are using a single detector homodyne scheme to cancel the nonlinear mixing noise. The single detector homodyne has a quadrature angle-dependent efficiency: the efficiency is lower when measuring mechanical motion, and higher for optomechanical squeezing detection. The quadrature angle-dependent homodyne efficiencies are shown in Fig. 2.21(d).
- The cavity output efficiency is hard to infer from the cavity reflection scan due to the unknown optical input mode-matching efficiency, and from the empty cavity characterization due to the redistributed intra-cavity optical power in the presence of the weakly reflective membrane. We assume a perfect cavity out-coupling efficiency of 94.8%, and consider the added cavity inefficiency from membrane scattering and absorption as part of the overall detection inefficiency in the measurement chain. This residual inefficiency is retrieved from the spectral fitting of the mechanical signal.
- The defect-mode conversion to mixing sidebands at other frequencies due to the cavity transduction nonlinearity could also reduce the linear transduction efficiency. It is, in principle, also included in the fitted residual inefficiency. From the measured $\langle \delta \Delta^2 \rangle / \kappa^2 < 10^{-3}$, this contribution is estimated to be less than 2% and thus excluded from the analysis.

The various inefficiency terms degrading the SNR of the mechanical displacement records are shown in the table below.

Inefficiency source	Value
Cavity output (ideal)	94.8 %
Detector electronics noise	86.1 %
Passive optics	66.5 %
Detector quantum efficiency	90 %
Homodyne efficiency	75 %
Fitted additional loss	83.5 %
Total efficiency	30.6 %

2.2 Membrane designs

In this section, we discuss the designs of the employed density-modulated membrane in our latest generation of the MIM device. Then, we quickly summarize the generalized dissipation dilution in a 3D structure, with which we simulated the mechanical properties of the density-modulated membranes and the pillar-induced excess mechanical losses. A summary of the detailed fabrication process flow is at the end of this section.

2.2.1 Designs of the employed devices

A suitable ultracoherent mechanical membrane resonator is vital for operating the MIM system at room temperature. During the thesis study, we first started with soft-clamped trampoline membranes [49], where soft-clamping is employed with a fractal structure. We gave up on this design in the end for two reasons:

- The soft clamping effect is not substantial, and the membrane can barely maintain one quantum coherent oscillation at room temperature.
- The above factor also leads to a substantial degradation of quality factor when the trampoline chip is in direct contact with the cavity mirror. We suspected the degradation to be from the hybridization between the trampoline fundamental mode and the silicon chip modes, due to redistributed stress from hard contact with the mirror. The degradation is also consistent with what other people observed in the field [50, 51].

We then tried the typical perforated soft-clamped membranes-[52], with which ~ 20 quantum coherent oscillations can be maintained at room temperature, and we did not observe any Q degradation due to contact with the cavity mirrors, expected from the substantial soft-clamping effect from phononic crystal shielding structure. However, we observed a significant photothermal-induced mechanical instability, discussed in Section 2.5. This thermal effect is likely due to the finite optical absorption of the membrane, which leads to a considerable dynamical temperature gradient due to perforated patterns on the membranes. We can work with this structure by employing feedback stabilization of the unstable mechanical modes at

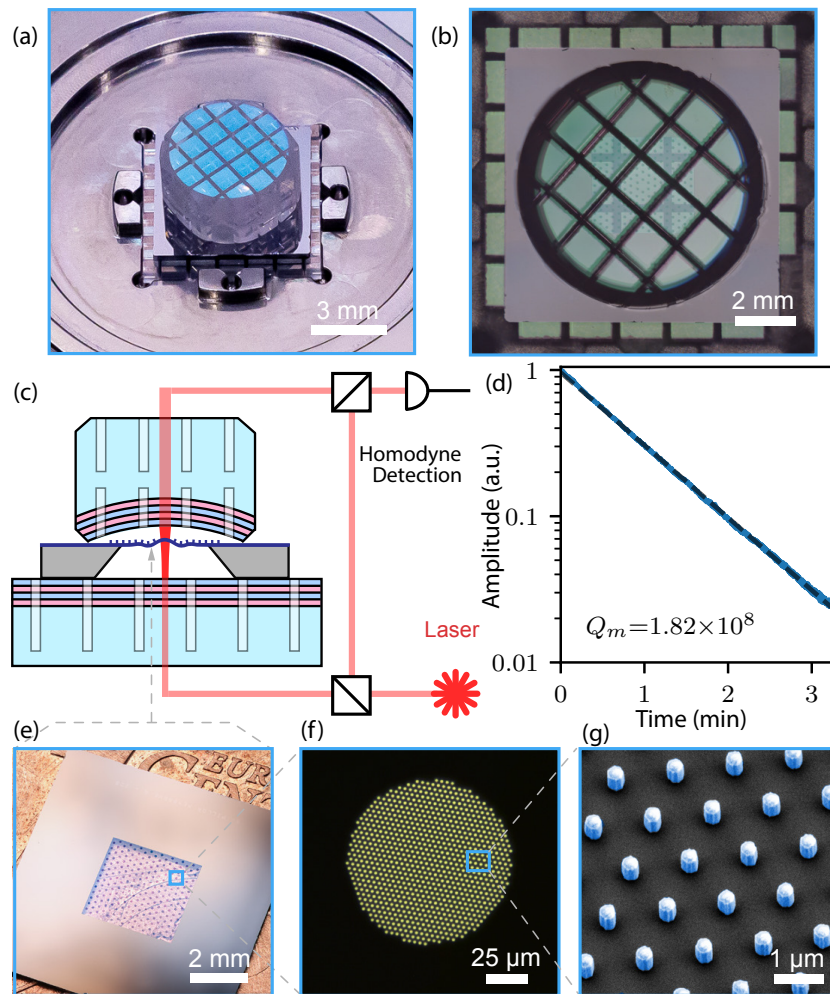


Figure 2.7: Ultra-low noise phononic-engineered membrane cavity. **(a)** Photograph of the membrane-in-the-middle assembly. **(b)** Optical microscope image of the MIM assembly from the top, showing the overlapping square unit cells of the top and bottom phononic crystal mirrors and the density-modulated membrane. **(c)** Setup schematic. **(d)** Mechanical ringdown measurement of the pillar membrane's soft clamped mode quality factor. The ringdown was acquired with the membrane installed in the MIM cavity. **(e, f, g)** Overview image and details of a pillar membrane sample at different length scales.

Chapter 2. Experimental platform for room-temperature quantum optomechanics

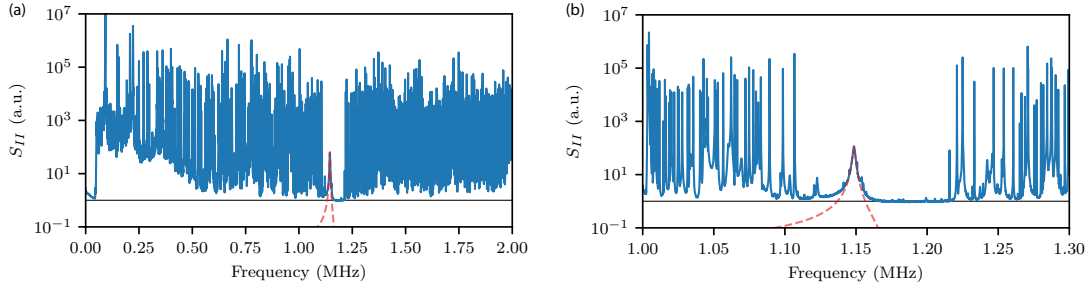


Figure 2.8: Mechanical spectra in **(a)** wideband and **(b)** narrowband frequency spans, measured from the optical direct detection of the cavity transmission beam. The cavity is pumped at the magic detuning on the red side, enacting significant optical damping on all the mechanical modes. The high-Q defect-mode signal after shot noise (indicated by the black line) subtraction is highlighted in a red dashed line, whose asymmetric spectral shape indicates a significant quantum correlation with the measurement shot noise.

high optical power, using another laser to exert feedback optical forces. Using this method, we have improved the C_q from 0.1 to unity, though with poor long-time stability of the system. The instability can be attributed to the spatial symmetry of these modes, due to the choice of designing the defect right at the membrane center. We tried to make some membranes with a defect displaced off the center to break this symmetry, but we never managed to obtain a good sample due to the low yield of the fabrication process.

In the end, we come across the recently demonstrated phononic density-modulated membranes [33] in late 2021. Compared to earlier stress-modulated, perforated, soft-clamped membranes [52], this design maintains higher material stress, enhancing dissipation dilution. Furthermore, the unperforated membrane reduces optical losses due to scattering from Si_3N_4 -vacuum interfaces, and increases heat dissipation, diminishing the thermal effects due to optical absorption. After discussing with my colleague Alberto, we decided to work on this new design instead of the displaced-defect design of the perforated membrane we had failed to fabricate. After reproducing this design, we found, however, that the membrane had high optical absorption, which led to significant cavity bi-stability [53] and mechanical instability [44]. Therefore, we developed a fabrication process that minimizes optical absorption, such that photothermal effects are absent for the optical mode and powers used in this experiment. With this design, we can operate the system beyond the $C_q = 1$ threshold, with some caveat discussed in Section 2.5. However, the thermal stability of the system has improved significantly compared to that of the perforated design.

The final design we employed in the MIM cavity consists of a Si_3N_4 nanomechanical membrane patterned with aSi-HfO₂ nanopillars (700-nm diameter) much smaller than the acoustic wavelength, implementing phononic density modulation [33]. The consideration of this specific material stack is discussed in detail in Section 2.2.4. Microscope images of the device at different length scales are shown in Fig. 2.7(e,f,g). The periodic density modulation creates a mechanical bandgap ~ 100 kHz, shown in Fig. 2.8, that spectrally isolates a 7-ng

high- Q soft-clamped defect mode with a mechanical frequency of $\Omega_m/2\pi = 1.16$ MHz and a damping rate of $\Gamma_m/2\pi = 6.41$ mHz, corresponding to a room temperature thermal occupancy of $\bar{n}_{\text{th}} = 5.3 \times 10^6$ and zero-point fluctuations of $x_{\text{zpf}} = 1.0$ fm. A ringdown measurement of mechanical Q is shown in Fig. 2.7(d), giving $Q = 1.8 \times 10^8$.

2.2.2 Dissipation dilution effects of 3D mechanical structures

For conventional bulk material, mechanical vibrations typically decay with a rate $\Gamma_m = \Omega_m \phi$ determined by the material loss angle ϕ . The intrinsic mechanical quality factor $Q_{\text{int}} = 1/\phi$ are, therefore, mostly limited to the order of thousands at room temperature, depending on the materials and their dominant loss mechanism. For thin film silicon nitride membranes employed in the thesis study, the thin film surface loss contributes the most, and for 20 nm thickness, is measured to be $Q_{\text{int}} \sim 2500$. However, these oscillators have shown quality factors on the order of a billion [49, 52, 54, 55, 56, 57], and achieve quantum coherent oscillations $\Omega_m/\Gamma_m \gg 1$ even at room temperature, by exploiting the effect of dissipation dilution [58].

Intuitively speaking, dissipation dilution of mechanical structures manifests as the dilution of mechanical loss rates by storing energy in some specific way of mechanical displacements that does not involve stretching the material structure. For example, the elongation of a string would involve material loss angle ϕ , but the rotation of an object does not involve any mechanical loss. Therefore, by carefully designing the geometry of a mechanical structure, one can convert most of the mechanical energy into the lossless portion in a stressed material, and achieve dilution of the mechanical loss determined by the intrinsic material loss angle.

In the following, we derive the analytical expression for evaluating the dissipation dilution factor of a given structure. In this section, all the repeating tensor indices are summed below. The time-dependent displacement field of the structure $U_i(x, y, z, t) : i = x, y, z$, which can be retrieved from FEM simulation of a particular structure, determines the Green-Lagrange strain tensor by

$$e_{ij} = \frac{1}{2} \left(\frac{\partial U_i}{\partial x_j} + \frac{\partial U_j}{\partial x_i} + \frac{\partial U_l}{\partial x_i} \frac{\partial U_l}{\partial x_j} \right) \quad (2.15)$$

where the third term on the right is the geometric nonlinearity, which helps achieve lossless potential. The stress tensor is related to the strain tensor by

$$\sigma_{ij} = \frac{E}{1+\nu} \left(e_{ij} + \frac{\nu}{1-2\nu} e_{ll} \delta_{ij} \right) \quad (2.16)$$

where δ_{ij} is the Kronecker delta, E is the Young's modulus, and ν is the Poisson's ratio. Assume that the deformation field $U_i(x, y, z, t)$ can be separated into a static deformation field $\bar{U}_i(x, y, z)$ and a dynamic deformation field $\Delta U_i(x, y, z)$ as

$$U_i(x, y, z, t) = \bar{U}_i(x, y, z) + \text{Re}[\Delta U_i(x, y, z) e^{-i\Omega_m t}] \quad (2.17)$$

Chapter 2. Experimental platform for room-temperature quantum optomechanics

where $\Delta U_i(x, y, z)$ is the complex envelope of an eigenmode, e.g., solved from the COMSOL Multiphysics structural damping module. We can follow the same step and separate the static and dynamic components of the strain and stress tensors as well,

$$e_{ij}(t) = \bar{e}_{ij} + \Delta e_{ij}(t) \quad (2.18)$$

$$\sigma_{ij}(t) = \bar{\sigma}_{ij} + \Delta \sigma_{ij}(t) \quad (2.19)$$

From here, we can calculate the elastic energy as

$$W = \frac{1}{2} \int \sigma_{ij}(t) e_{ij}(t) dV \quad (2.20)$$

and separate it into the lossy energy, as well as the lossless dilution energy,

$$\langle W_{\text{lossy}} \rangle = \frac{1}{2} \int \langle \Delta \sigma_{ij}(t) \Delta e_{ij}(t) \rangle dV \quad (2.21)$$

$$\langle W_{\text{dil}} \rangle = \frac{1}{2} \int \langle \bar{\sigma}_{ij} \Delta e_{ij}(t) + \bar{e}_{ij} \Delta \sigma_{ij}(t) \rangle dV \quad (2.22)$$

where $\langle \dots \rangle$ is averaged over a vibration period. It is further convenient to list the following expressions of averaged strain tensor products using the complex displacement envelope obtained from COMSOL, as

$$\langle \Delta e_{ij}(t) \rangle = \frac{1}{4} \text{Re} \left(\frac{\partial \Delta U_l}{\partial x_i} \frac{\partial \Delta U_l^*}{\partial x_j} \right) \quad (2.23)$$

$$\langle \Delta e_{ij}(t)^2 \rangle = \frac{1}{8} \left| \frac{\partial \Delta U_j}{\partial x_i} + \frac{\partial \Delta U_i}{\partial x_j} + \frac{\partial \bar{U}_l}{\partial x_i} \frac{\partial \Delta U_l}{\partial x_j} + \frac{\partial \bar{U}_l}{\partial x_j} \frac{\partial \Delta U_l}{\partial x_i} \right|^2 \quad (2.24)$$

As one can see, geometric nonlinearity is solely responsible for the dilution energy, while in general it also contributes a little bit to the lossy energy. With Virial theorem

$$\langle W_{\text{kin}} \rangle = \frac{1}{2} \int \Omega_m^2 \rho |\Delta U_l|^2 dV \quad (2.25)$$

one can verify numerically whether $\langle W_{\text{kin}} \rangle = \langle W_{\text{lossy}} \rangle + \langle W_{\text{dil}} \rangle$ for a sanity check of the modeling and formula used for calculating dissipation dilution effects of a given structure.

The dissipation dilution factor $D_Q = Q_m / Q_{\text{int}}$ can then be evaluated as

$$D_Q = 1 + \frac{\langle W_{\text{dil}} \rangle}{\langle W_{\text{lossy}} \rangle} \quad (2.26)$$

with state-of-the-art achieving values on the order of a million.

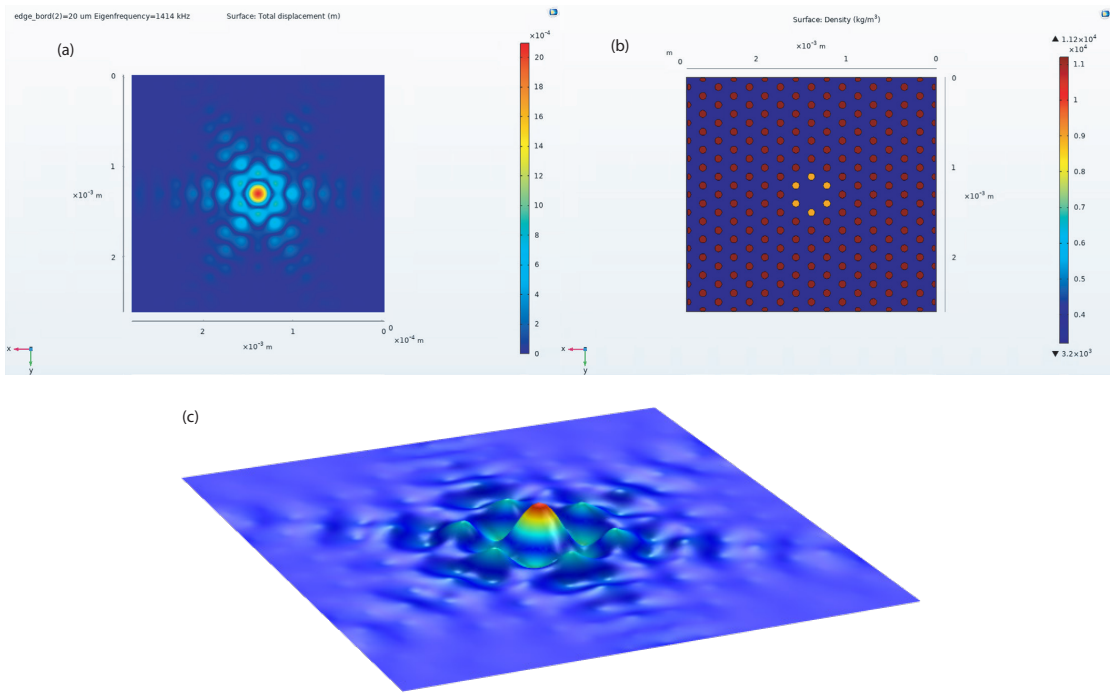


Figure 2.9: **(a)** Displacement profile of the soft-clamped 1.5-MHz mode of the density modulated membrane. **(b)** Effective density modulation pattern of the simulated membrane. **(c)** 3D displacement profile of **(a)**.

2.2.3 Mechanical simulations of density-modulated PnC membranes

Here, we show the design and simulation procedure of a density-modulated membrane using COMSOL Multiphysics. Due to the clear separation of the physical dimensions between the nanopillars ($\sim 1 \mu\text{m}$), and the composite membrane motions ($\sim 1 \text{ mm}$), we can separate the numerical simulation in two separate steps.

First, we analyze the mechanical properties by treating the addition of pillars as an effective density modulation of the membrane without introducing additional losses at the MHz frequency range. In the second step, we will analyze the loss added by the pillars, and how they effectively modify the membrane loss.

The effective density modulation pattern and the simulated soft-clamped mode profile are shown in Fig. 2.9. We perform pre-stressed eigenfrequency analyses in COMSOL Multiphysics to compute dilution factors D_Q , using the “Shell” interface in the structural damping module. This finite elements study is particularly suitable for simulating high aspect ratio nanomechanical objects.

The dilution factor depends strongly on the mode curvature close to the clamping points [59]. For this reason, we refine the mesh for the finite element model close to the membrane’s clamping boundaries (outer edges), using a typical element size around $\lambda L/30$. Here, L is the

Chapter 2. Experimental platform for room-temperature quantum optomechanics

largest lateral dimension of the membrane, $\lambda = \sqrt{Eh^2/(12\sigma L^2)} \ll 1$ is the strain parameter, E is the membrane Young's modulus, σ is the material stress, and h is the membrane thickness. Fixed boundary conditions are imposed at the membrane clamping points, i.e., $\vec{u} = \partial\vec{u}/\partial\vec{n} = 0$ (where $\partial\vec{u}/\partial\vec{n}$ is the displacement field derivative normal to the boundary).

The dilution factors are calculated with the ratio of kinetic and linear elastic energies defined earlier[58], and can be greatly simplified for 2D structures. For out-of-plane bending modes:

$$D_Q = \frac{12\rho\Omega_m^2}{Eh^2} \times \frac{(1-\nu^2) \int w^2 dx dy}{\int (\partial^2 w/\partial x^2 + \partial^2 w/\partial y^2)^2 + 2(1-\nu) \left((\partial^2 w/\partial x\partial y)^2 - \partial^2 w/\partial x^2 \cdot \partial^2 w/\partial y^2 \right) dx dy}, \quad (2.27)$$

where w is the u component in the out-of-plane direction, Ω is the mechanical frequency, ρ is the mass density of the membrane material and ν is Poisson's ratio. A PnC nanomechanical structure can enhance the D_Q of some flexural modes, by localizing the displacement to a defect in the spatial-periodic modulation of the speed of sound $v = \sqrt{\frac{\sigma}{\rho}}$ and suppressing its curvature close to the clamping boundaries. This idea, introduced by Tsaturyan et al. in 2016 [52], was the first incarnation of the "soft clamping" effect. An example of a localized soft-clamped mode is illustrated in Fig. 2.9(a).

In our case, the PnC is realized with a modulation of the resonator's effective mass density, described by $\rho_{\text{eff}}(x, y) = g(x, y)\rho$ [33]. In practice, the density modulation is implemented by patterning nanopillars over the nanomechanical membrane, with a thickness much larger than that of the membrane. Pillars are confined to circular regions of diameter commensurate with the membrane acoustic wavelength (see Fig. 2.7(f) and Fig. 2.9(b)), and are arranged in a triangular pattern.

The second step would be to consider the loss added by the nanopillars. The nanopillars locally mass-load the membrane to realize an effective density modulation, but also introduce additional mechanical dissipation. When a bending wave impinges on the pillar, it induces deformation without a significant geometrically nonlinear contribution [58]. The pillars will thus reduce the dissipation dilution of the Si_3N_4 membrane, by an amount that depends sensitively on the pillars' geometrical dimensions and the frequency of the flexural mode. The lower the frequency and the smaller the pillars, the lower the susceptibility of the pillar deformation, and the lower the added dissipation induced by the individual pillars. The pillar damping contribution can be dominant, or sufficiently low that it is negligible compared to the finite dissipation dilution of the soft clamped mode, depending on the oscillation frequency and the pillars' geometry [33].

A nanopillar unit cell simulation is illustrated in Fig. 2.10, where the stationary stress distribution due to the deposition of the pillars at different conditions is shown, as well as the dissipation energy density when a bending wave impinges on the pillar. We assume that the pillars are arranged in a triangular lattice with a lattice constant a_{pil} (separation between the

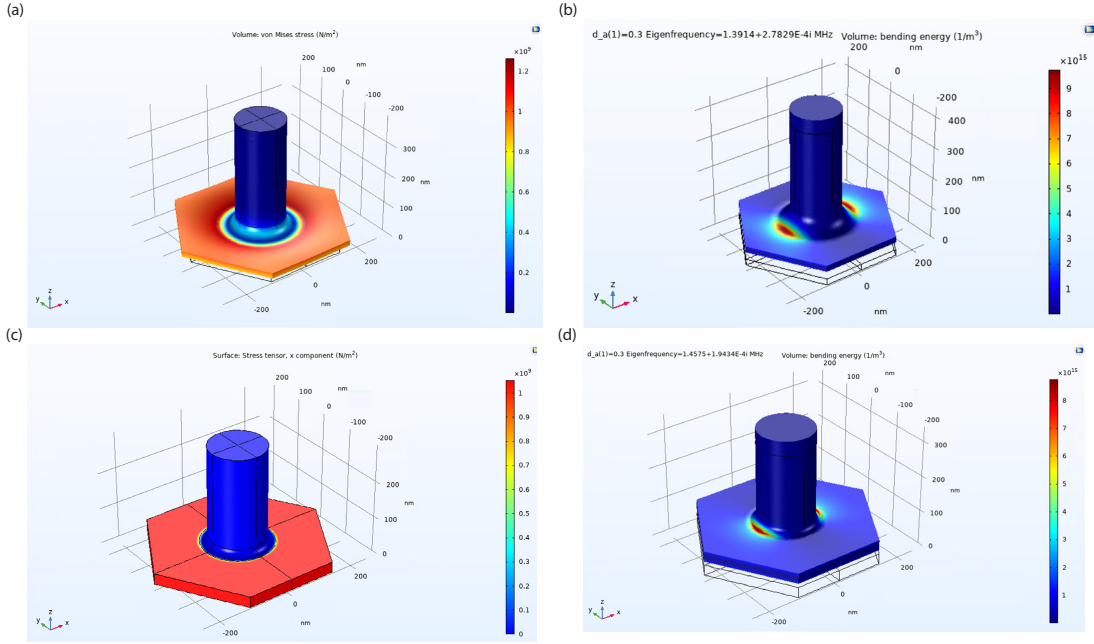


Figure 2.10: Study of pillar losses at 1.5 MHz in an infinite periodic membrane. **(a)(b)** Static stress and mechanical loss distribution of a membrane deposited with LPCVD silicon nitride pillars. **(c)(d)** Static stress and mechanical loss distribution of a membrane deposited with PECVD silicon nitride pillars.

nearest neighbors), and we identify the pillar diameter and height (thickness) with d_{pil} , h_{pil} . Here, we effectively simulate an infinitely repeating membrane with periodically patterned pillars. By subtracting the original membrane losses, we can obtain the effectively added loss from the nanopillars. The effective density in the circular regions patterned with the nanopillars is

$$\rho_{\text{eff}} = \rho \left[1 + \frac{\pi}{2\sqrt{3}} \frac{\rho_{\text{pil}} h_{\text{pil}}}{\rho h} \left(\frac{d_{\text{pil}}}{a_{\text{pil}}} \right)^2 \right], \quad (2.28)$$

where h and ρ are the thickness and density of the membrane film (Si_3N_4). The periodicity of the pillar array is embedded in the simulation by restricting the domain to a hexagon-shaped unit cell (see Fig. 2.12(a)) with Floquet boundary conditions $[\vec{u}(\vec{x} + \vec{R}) = \vec{u}(\vec{x}) e^{-i\vec{k} \cdot \vec{R}}]$ on opposing sides of the hexagon. The magnitude of the elastic wavevector that defines the boundary conditions, k , is chosen in order to produce a flexural eigenmode at the mechanical frequency of interest ($ka_{\text{pil}} \ll 1$)

$$k \approx \Omega \sqrt{\frac{\rho_{\text{eff}}}{\sigma}}, \quad (2.29)$$

where σ is the membrane deposition stress and Ω is the mechanical frequency in angular units. The model is then solved for its first eigenmode, which represents the pillar displacement upon the arrival of the flexural wave.

The dissipation dilution of an infinite pillar lattice is evaluated using the general 3D D_Q

Chapter 2. Experimental platform for room-temperature quantum optomechanics

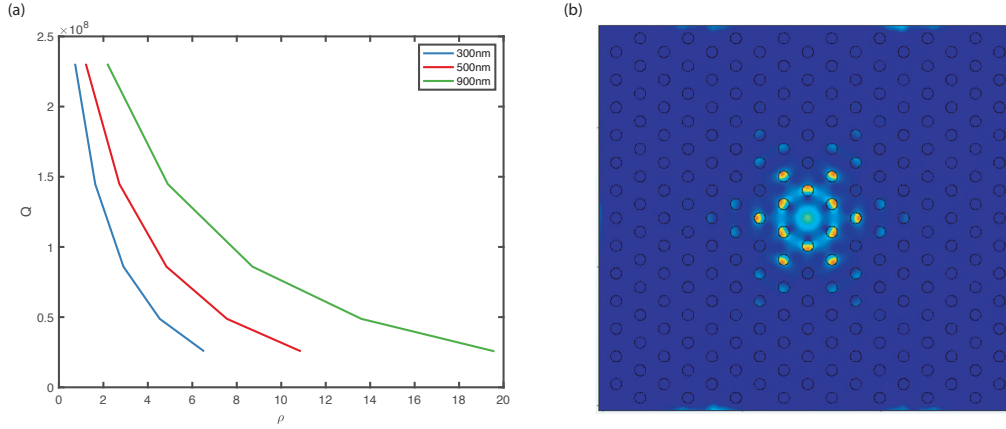


Figure 2.11: **(a)** Effective mechanical quality factors in the pillar regions at 1.5 MHz as a function of effective density and pillar height. **(b)** Bending loss energy participation of the soft-clamped defect mode of the density-modulated membrane.

expression from Section 2.2.2. The results of the infinitely-extended pillar lattice's quality factor computation are shown in Fig. 2.12(a), as a function of different effective density modulations and different pillar heights. Based on the loss of the pillars, we also need to calculate the bending energy participation ratio in the pillar regions of the density-modulated membrane, shown in Fig. 2.12(b). This ratio is typically around 40 % for soft-clamped modes, depending on the size of the pillar regions and the effective density modulation.

After we reproduced the device from [33], we observed severe optical absorption that prevents the usual laser operation in a cavity. The optical absorption-induced heating manifests in cavity bistability and photothermal mechanical instability discussed in Section 2.5. As a result, we developed a new fabrication process involving two ALD layers to shield the membrane from plasma damages during the device fabrication, e.g., PECVD growth of pillars and dry etching of the pillars. However, this procedure results in a potential thin undercut layer at the base of the pillars during the removal of the ALD layers, which could lead to higher pillar-induced loss. In this scenario, the frequency of the first bending mode of the nanopillars is decreased, as shown by the blue dots in Fig. 2.12(c), and the pillar motion can start to hybridize with the soft clamped membrane mode. The undercut induces a significant reduction in the overall quality factor when the undercut covers a significant portion of the pillar base (see the yellow dots in Fig. 2.12(c)). Note that the undercut is not visible in the figure inset, as it is carved in a layer of only 6 nm at the pillar base, similar to the fabricated pillar geometrical parameters. The simulation here is performed for a fixed pillar thickness of $h_{\text{pil}} = 450$ nm and separation $a_{\text{pil}} = 2 \mu\text{m}$, and variable diameters and mechanical frequencies.

Note that for the pillar material, HfO₂-aSi in the final design, the loss angle is an unknown parameter in the FEM simulations. We arbitrarily set it by choosing $Q_{\text{int}} = 10000$. The results in Fig. 2.12(b) do not depend sensitively on $Q_{\text{int,aSi}}$; nevertheless, one should treat them as a rough estimation of the pillar damping contribution.

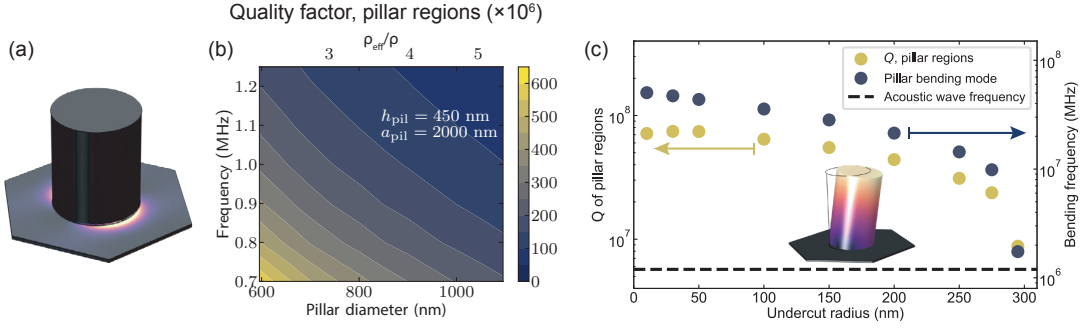


Figure 2.12: Losses induced by bending of nanopillars used to modulate ρ_{eff} . **(a)**, Visualization of the linear elastic energy density, which is associated with mechanical dissipation, close to the nanopillar. The largest contribution to dissipation occurs close to the nanopillar base. **(b)**, Q of a uniform pillar array with infinite extent as a function of the frequency of the acoustic flexural wave and the pillar diameter. The pillar separation a_{pil} and the pillar thickness h_{pil} are kept constant to the specified values. The horizontal axis is expressed in terms of the pillar diameter and of the resulting density modulation $g = \rho_{\text{eff}}/\rho$. **(c)**, Effect of an undercut at the pillar base on the pillar Q . For this simulation, the pillar has a diameter of 600 nm and a thickness of 1000 nm, and the separation between nearest-neighbours pillars is fixed to 1.5 μm . The undercut layer is hardly visible in the illustration, as it is only 6 nm-thick. The membrane's Q (ochre dots) drops significantly when the nanopillar's first flexural resonance frequency (blue dots, the inset illustrates the displacement field) approaches the acoustic excitation frequency, marked by a horizontal dashed line.

For the PnC membrane device employed in these experiments, the macroscopic estimate of the quality factor, neglecting pillar dissipation, is $D_Q \times Q_{\text{int}} \approx 6 \cdot 10^8$, slightly lower than the design value due to a low-density modulation, $g_{\text{max}} \approx 2.9$, an accidental result of fabrication drifts. The dissipation contribution due to the nanopillars was comparable for the measured pillar dimensions: $Q_{\text{pillar bend}} \approx 6 \cdot 10^8$. Overall, the two dissipation contributions combine to estimate the overall intrinsic loss-dominated quality factor $Q \approx 3 \cdot 10^8$, slightly higher than measured with the membrane device. We also cannot exclude a small contribution to the observed dissipation due to collisions with the residual gas molecules in the vacuum chamber where the MIM cavity is located [60].

2.2.4 Microfabrication of density-modulated PnC membranes

The device fabrication was done by my colleague Alberto Beccari. The exact fabrication process is discussed in detail in his thesis [61], as well as in [10] SI. Here, a few key points of the fabrication process are summarized that are worth mentioning when comparing to work [33].

- We implemented etch-stop layers using atomic layer deposition (ALD) to prevent plasma damage of the Si_3N_4 membrane from the pillar dry etching step. Plasma damage causes high optical absorption of the thin film with visible light.

Chapter 2. Experimental platform for room-temperature quantum optomechanics

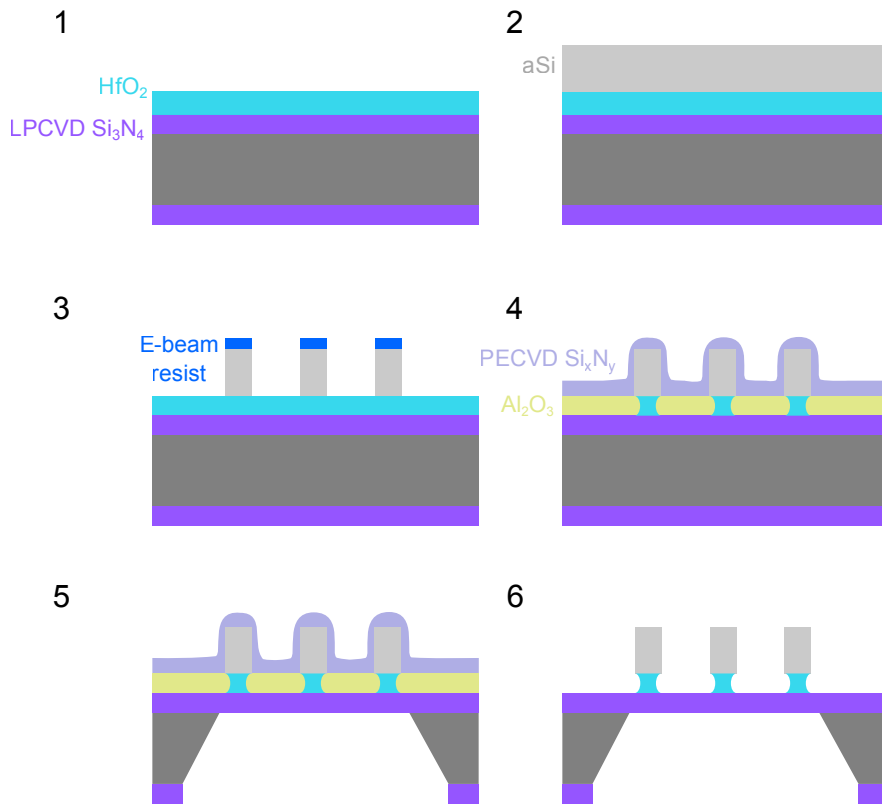


Figure 2.13: Simplified fabrication process for density-modulated membrane resonators [61]. Layer thicknesses and lateral dimensions are not to scale. 1 – Etch stop layer growth. 2 – aSi pillar layer growth. 3 – Electron beam lithography and pillar pattern transfer with RIE. 4 – Growth of PECVD nitride encapsulation layer. 5 – Chip separation and KOH membrane release. 6 – Removal of the encapsulation layer in buffered HF.

- To prevent significant undercut of the pillars during wet etching removal of the ALD layers, we use HfO_2 , which has the best selectivity. Undercut of pillars results in stronger hybridization between the pillar and membrane motions, degrading quality factors of the soft-clamped mode.
- The presence of HfO_2 prevents us from using any high-temperature process as it crystallizes around $500\text{ }^\circ\text{C}$ and becomes hard to remove using wet chemistry.
- PECVD silicon is selected as the pillar material because no high-temperature process can be used.
- ALD layers are always used whenever plasma process is used, e.g., PECVD and dry etching, and are removed using wet etching.

In Appendix B.2, for the sake of completeness of the thesis, the detailed fabrication process in [10] SI is reproduced, as well as in the thesis of my former coworker Alberto Beccari [61].

2.3 Phononic crystal mirrors

2.3.1 Cavity noise budget and suppression techniques

There are typically two requirements to approach Heisenberg-limited operation required for the observation of optomechanical squeezing and the efficient measurement of mechanical motion.

Firstly, the quantum cooperativity C_q must approach or exceed unity. As we discussed in earlier sections, to reach this regime, we adopt a modular approach and employ the membrane-in-the-middle (MIM) architecture [62] using an optical Fabry-Perot cavity [see Fig. 2.7(a,b,c)]. The high-finesse cavity ($\mathcal{F} \sim 10^4$) allows operation at high quantum cooperativity while keeping the optical probe power below 1 mW, where quantum-noise-limited laser operation can be achieved.

Secondly, Heisenberg-limited operation further requires low displacement measurement imprecision, i.e., $\bar{S}_{xx}^{\text{imp}} < x_{\text{zpf}}^2/\Gamma_{\text{th}}$. This level of measurement imprecision is particularly challenging at room temperature, as the required imprecision scales inversely with the temperature of the environment. For our device, we estimate the bound to be $10^{-35} \text{ m}^2/\text{Hz}$. The cavity frequency noise is thus required to be extremely small: the frequency noise $\bar{S}_{\nu\nu}(f) = \bar{S}_{xx}^{\text{imp,cav}}(f) \times g_0^2/(2\pi x_{\text{zpf}})^2$ should satisfy $\bar{S}_{\nu\nu}(f) < (g_0/2\pi)^2/\Gamma_{\text{th}}$ to allow ground state cooling [63] and significant optomechanical squeezing. This bound is well below the typical thermomechanical fluctuations of the cavity mirrors, which also couples to the cavity dispersively, even with state-of-the-art mechanical resonators. In Ref. [43], a phononic shield addressed this problem by producing a phononic bandgap that suppressed the mirror's driven response. In that work, the bottom mirror is fabricated by patterning a silicon wafer with a periodic lattice of holes, and then bonding it with a Pyrex substrate on which the mirror coating is sputtered. Because of the technical difficulty in applying the same procedure for the curved top mirror, a fiber mirror is used instead, which also serves as the high transmission port of the cavity. The use of a fiber mirror resulted in excess broadband cavity frequency fluctuations. Also, the mode mismatch between the fiber and the cavity mode led to a low cavity output efficiency of approximately 4 %.

Due to the absence of an effective way to pattern phononic crystal structures on silica mirror substrates, we have been working on several methods to mitigate mirror noises. From the calibrated cavity frequency noise, we deduced that it is unlikely any of our soft-clamping designs can reach the low thermal decoherence rate required from the mirror noise, so we started working on feed-forward cancellation of mirror noises. The main idea comes from [64], that by measuring the mirror noise from an auxiliary cavity mode, one can use the measurement record to effectively cancel the cavity frequency noise on the science (main) cavity mode by laser frequency modulation. When a homodyne measurement scheme is applied, special care must be taken for the noise suppression on the science detection to work, e.g., proper local oscillator delay length, and position of the phase modulation on the optical path. A detailed

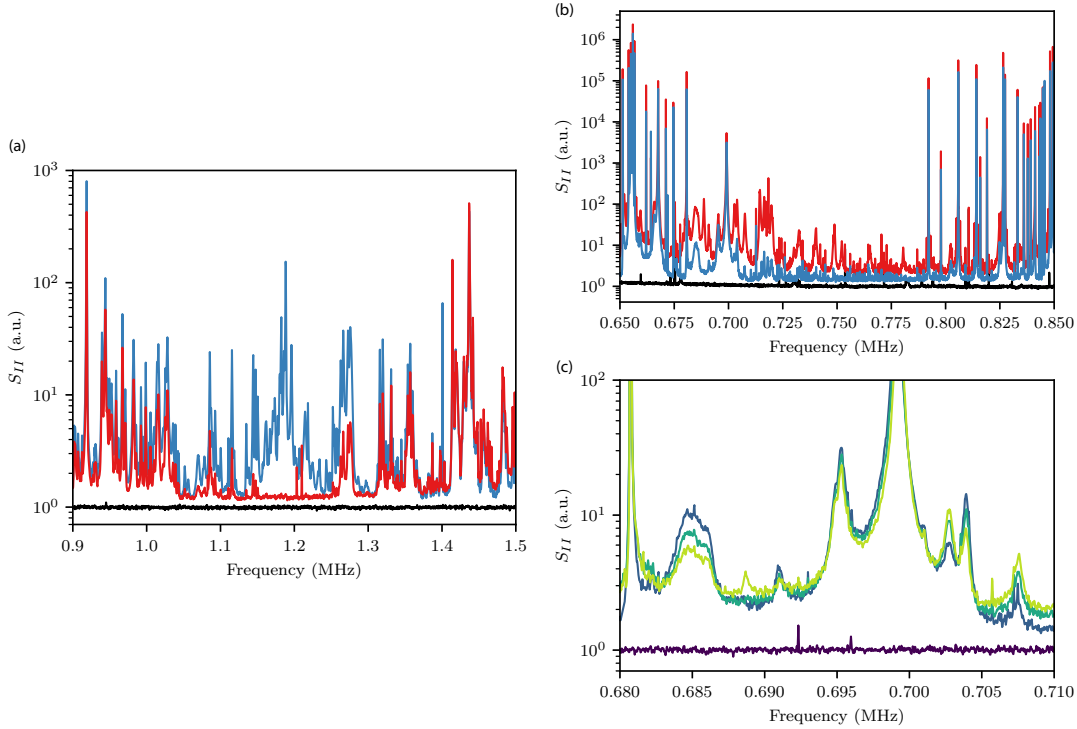


Figure 2.14: **(a)** Feed-forward suppression of empty-cavity frequency noise. The plot shows the science cavity noise with (red) and without (blue) feed-forward suppression. **(b)** Transmission spectrum of auxiliary mode (red) with low g_0 and science mode (blue) with high g_0 . **(c)** Effects of feed-forward of loaded-cavity frequency noise on the science mode. The lighter the color, the higher the gain.

analysis is covered in Section. B.5.

Our first experiment iteration used an empty cavity with a spacer chip instead of the membrane. We measure the cavity noise from the transmission of the auxiliary mode, amplified and fed to a phase modulator (equivalently frequency modulation) of the science laser, and check the noise spectrum at the science cavity transmission. We observed a significant reduction of mirror noise shown in Fig. 2.14(a), with peak suppression around 20 dB, limited by the shot noise impression of the auxiliary laser. One can also identify a finite suppression window due to the phase-frequency relation $-i\omega\theta(\omega) = 2\pi \cdot \nu(\omega)$. The filter response used for this purpose is discussed in Section B.5.

Though without perfect suppression (limited by finite bandwidth and laser shot noise), we proceed to work on a cavity loaded with a membrane chip. To separate the mirror motions from the membrane motions, we choose a cavity mode with the lowest g_0 as the auxiliary mode, and a cavity mode with high g_0 as the science mode, shown in Fig. 2.14(b). The result of the feedback, shown in Fig. 2.14(c), is disappointing, as some of the mirror noise gets suppressed, while the others get amplified. As is discussed in Section. 2.1.1, the presence of

the membrane redistributes the light in both compartments of the cavity, and modifies the way two mirrors couples to the cavity. The mismatched suppression ratio makes the feed-forward scheme unfeasible since perfect noise suppression only happens for a flat gain profile.

Apart from the obstacle mentioned above, the application of the phase modulation also limits the amount of power available for the measurement, since most conventional phase modulators using lithium niobate material have a maximum input power around 25 mW, with typical 3.5 dB insertion loss.

Ultimately, the breakthrough came when we tested our first generation of density-modulated membranes in the MIM assembly. As these pillar membranes have no perforation on the membrane, air gets trapped between the membrane chip and the bottom mirror. Whenever we need to pump down the pressure of the vacuum chamber, the air breaks through the membrane and leaks out from the gap between the top mirror and the membrane chip. To prevent membrane breaking, we used a precision circular diamond saw (usually for dicing silicon chips), to cut a few tranches on the bottom mirror, so that air can go through those tranches instead of the membrane. After cutting, we did not observe any optical degradation of the mirror coating and the surface roughness, as the optical linewidth of the empty cavity remained the same. As the pillar membrane successfully survived the pressure pump down, we also got inspiration for patterning phononic crystal structures on the mirror substrates.

By considering the shape of the cut from the diamond saw, we designed phononic crystal patterns for both the top and bottom mirrors [see Fig. 2.15(d,f)]. We used the precision circular saw to pattern the phononic structure on the glass mirror substrates. The phononic unit cell dimensions are chosen such that mechanical motion in the frequency band of 0.87 MHz to 1.2 MHz is prohibited [see Fig. 2.15(c,e)]. The thermomechanical noise density $\bar{S}_{vv}(f)$ in this frequency band is reduced by a factor of more than 700 as shown in Fig. 2.15(a), where the estimation of the mirror noise suppression is limited by laser noise. This noise reduction drastically relaxes the requirements to observe quantum optomechanical effects at room temperature. Furthermore, we also show linewidth measurements of 23 TE₀₀ cavity resonances with the membrane chip loaded in Fig. 2.15(b). As can be seen from the comparison with the ideal empty cavity linewidth (dashed gray line), the phononic crystal patterning did not result in significant excess optical losses, thereby maintaining high cavity out-coupling efficiency as required for the observation of optomechanical squeezing and measurement-based ground state cooling. The added loss is not observable as long as we do not clamp the cavity too hard, which induces significant degradation of the cavity linewidth even without the membrane loaded. We use the optical mode at 819 nm for most of the experiment, which has an out-coupling efficiency of > 80% with an optical linewidth of $\kappa/2\pi = 34.2$ MHz.

By clamping the density-modulated membrane chip in-between the phononic crystal mirrors, we construct a MIM system with $g_0/2\pi = 160$ Hz and cavity frequency noise satisfying the $\bar{S}_{vv}(f) < 0.11$ Hz²/Hz requirement, which allows high quantum cooperativity operation with quantum-noise-limited measurement imprecision and backaction.

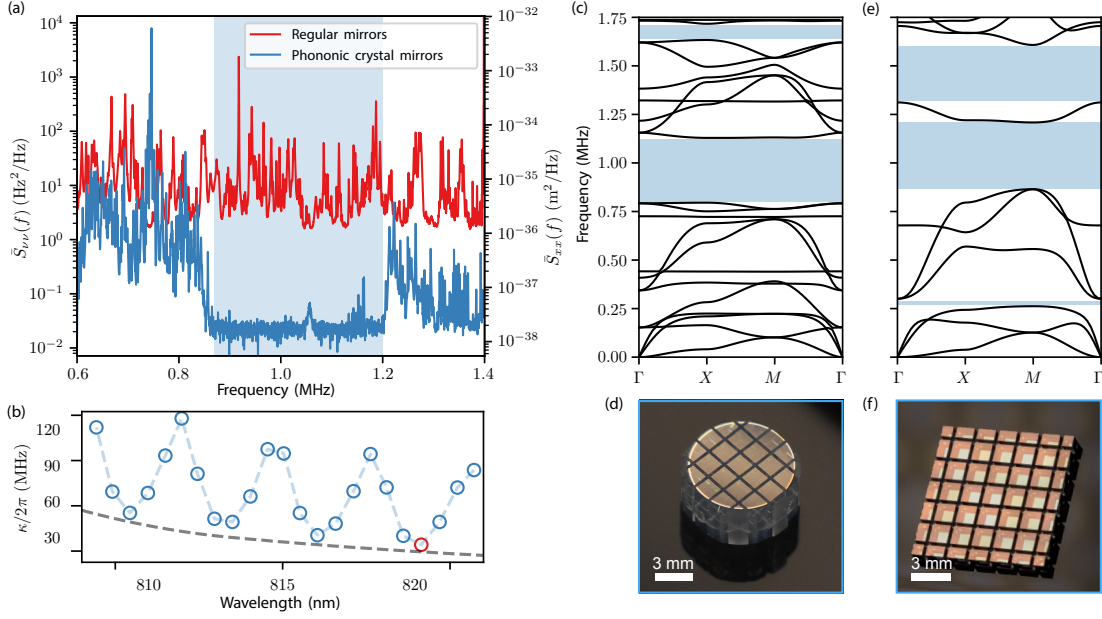


Figure 2.15: **Suppression of cavity frequency noise in the phononic bandgap.** (a) Cavity frequency/displacement noise comparison between regular mirror assembly and phononic crystal mirror assembly, showing a 700-fold total noise reduction within the blue-shaded region. The vertical axis is calibrated in cavity frequency noise units (left) and equivalent mirror mechanical displacement units (right). (b) MIM cavity optical linewidth as a function of wavelength. Blue circles: measured optical cavity linewidths. Red circle: the optical mode used for experiments. The modulation of the cavity linewidth is due to the presence of the membrane in the cavity. Dashed gray line: the ideal empty cavity linewidth based on the measured mirror transmission after deposition of the high-reflectivity coating but before definition of the PnC. (c,d) Band diagram and photograph of the top phononic crystal mirror. (e,f) Band diagram and photograph of the bottom phononic crystal mirror.

2.3.2 Fabrication and simulation of phononic crystal mirrors

In this section, we provide more details on the fabrication and simulation of the phononic crystal mirrors, required to achieve high quantum cooperativity operation with quantum-noise-limited measurement imprecision and backaction.

As mentioned in the previous section, we circumvent these problems by patterning PnC structures on the top and bottom mirrors. The top and bottom mirror substrates are fused silica and borosilicate glass, with a high-reflection coating sputtered on one side and an anti-reflection layer coating on the other. We use a dicing saw for glass machining to dice a regular array of lines into the mirror substrates. The blade is continuously cooled by a pressurized water jet during the dicing process. The maximum cut depth allowed for our blade is 2.5 mm, and we constrain the designed PnC accordingly. We cut the flat bottom mirror only from one side (its thickness is only 1 mm), and the top mirror is diced symmetrically with parallel cuts from both sides, since it is 4-mm thick. The relatively deep cuts in the top mirror need to be

2.3 Phononic crystal mirrors

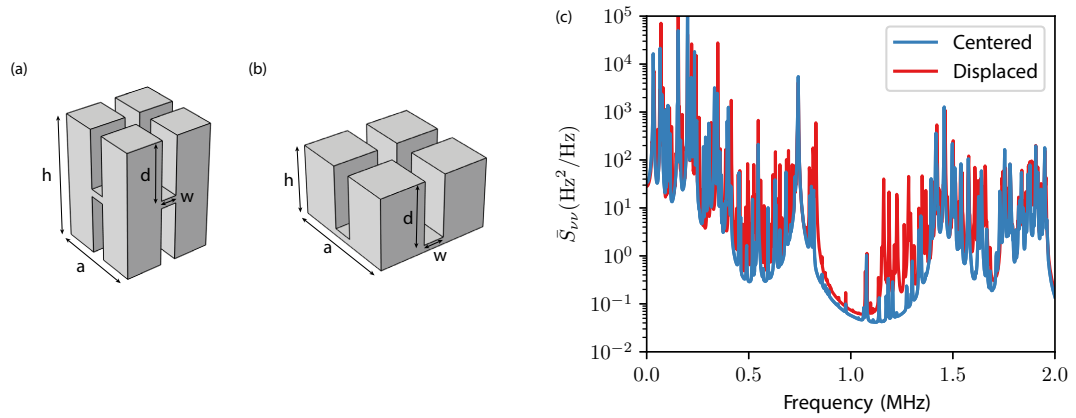


Figure 2.16: **a** Square lattice unit cell of the top mirror. The periodicity is along the horizontal plane. $a=1.4\text{mm}$, $h=4\text{mm}$, $d=1.88\text{mm}$, $w=250\mu\text{m}$. **b** Square lattice unit cell of the bottom mirror. The periodicity is along the horizontal plane. $a=1.6\text{mm}$, $h=1\text{mm}$, $d=900\mu\text{m}$, $w=300\mu\text{m}$. **c** Simulated frequency noise spectra of an empty cavity with PnC top and bottom mirrors. We show both the case of an optical mode perfectly centered on the bottom mirror (blue), and displaced $200\mu\text{m}$ away from the center (red), accounting for a realistic assembly misalignment.

patterned over multiple passes, with gradually increasing depths. After dicing one mirror side, the piece is flipped, and the other side is diced after aligning to the first cuts, visible through the glass substrate. Lines are arranged in a square lattice for simplicity (see Fig. 2.15(d,f)), although more complex patterns can be machined with the dicing saw. We simulate the band diagrams of the unit cells of the top and the bottom mirrors in COMSOL Multiphysics with the Structural Mechanics module. The simulation result is shown in Fig. 2.15. We optimized the lattice constant and cut depths to maximize the bandgap width, while centering the bandgap around 1 MHz and ensuring that the remaining glass thickness is sufficient to maintain a reasonable level of structural stiffness.

Due to the finite size of the mirrors, we expect to observe edge modes within the mechanical bandgap frequency range. These modes' thermal vibrations penetrate the PnC structure with exponentially decaying amplitudes. To account for their noise contributions, we simulated the frequency noise spectrum of the MIM assembly, consisting of the bottom and the top mirrors in contact with a silicon spacer chip, shown in Fig. 2.16. Displacement noise at the location of the cavity optical mode is estimated using the fluctuation-dissipation theorem and the eigenmode parameters obtained from the COMSOL eigenfrequency solver, then converted to frequency noise. From previous measurements of mirror modes, we assume a uniform quality factor of 10^3 for all the modes. The eigenfrequency solution confirmed the existence of edge modes with frequencies within the mechanical bandgap. However, it did not predict any significant contribution to the cavity frequency noise: the PnC is sufficiently large to reduce their contribution at the cavity mode position. The bandgap noise is mainly from the off-resonant tail of the thermomechanical noise from the modes outside the bandgap. We also observe that the noise peaks at the upper edge of the bandgap are sensitive to the

Chapter 2. Experimental platform for room-temperature quantum optomechanics

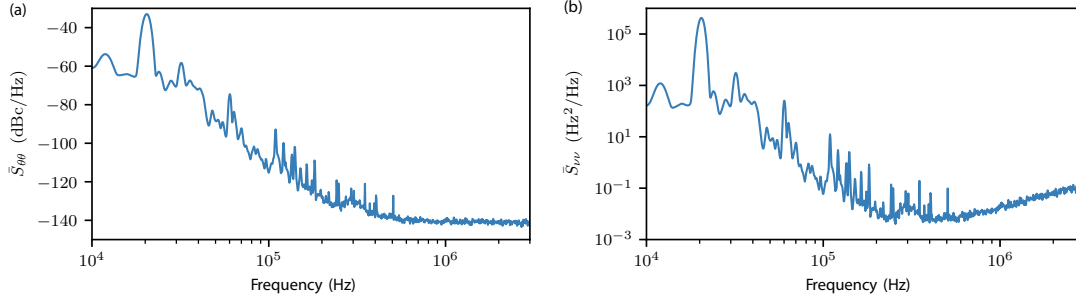


Figure 2.17: Measured noise density of the laser relative **(a)** phase and **(b)** frequency fluctuations of the two TiSa lasers.

relative displacement of the optical mode from the mirror center (see Fig. 2.16). This effect is attributed to the spatial symmetries of these modes.

After patterning the PnC structures on the mirrors, we assembled a cavity with a spacer chip instead of a membrane. We observed that the TE_{00} linewidth with the diced mirrors is identical to that of the original cavity. This indicates that our fabrication process does not cause measurable excess roughness or damage to the mirror surfaces. On the other hand, we noticed that when the assembly was clamped too tightly, excess cavity loss occurred due to significant deformation of the PnC mirrors, with a reduced stiffness. We mitigate this detrimental effect in the experiment by gently clamping the MIM cavity, with a spring tension sufficient to guarantee the structural stability of the assembly. We also ensure that the cavity mode is well-centered on the bottom mirror, to reduce the aforementioned upper band-edge modes' thermal noise contribution. For the MIM experiment, we did not observe any mirror modes within the mechanical bandgap of the membrane chip. We can distinguish membrane modes from mirror modes by exploiting the fact that the coupling rates of membrane modes vary between different cavity resonances, while this is not the case for mirror modes.

2.3.3 TiSa laser phase noise characterization

Since the mirror noise is greatly suppressed using phononic crystal structures on the cavity mirrors, we must understand how much the laser frequency noise limits our experiment. We upper-bound the phase noise of the TiSa laser (Sirah Lasertechnik) used in the experiment by beating it with another TiSa laser (M Squared) with optical power around $100\mu\text{W}$. The frequency difference of the two lasers is passively stable around 9 MHz, and the beating signal is recorded digitally with a sampling rate of 56 MHz. The signal is then demodulated at 9 MHz to retrieve the I/Q data, from which the phase noise is retrieved. The noise densities of the laser phase and frequency are computed and shown in Fig. 2.17. At 1 MHz, where the experiment is conducted, the measured noise density is primarily limited by the detector noise and laser shot noise. Therefore, we upper-bound the laser frequency noise at $\bar{S}_{\nu\nu}(1\text{ MHz}) < 3 \times 10^{-2} \text{ Hz}^2/\text{Hz}$, significantly below the frequency budget of the system.

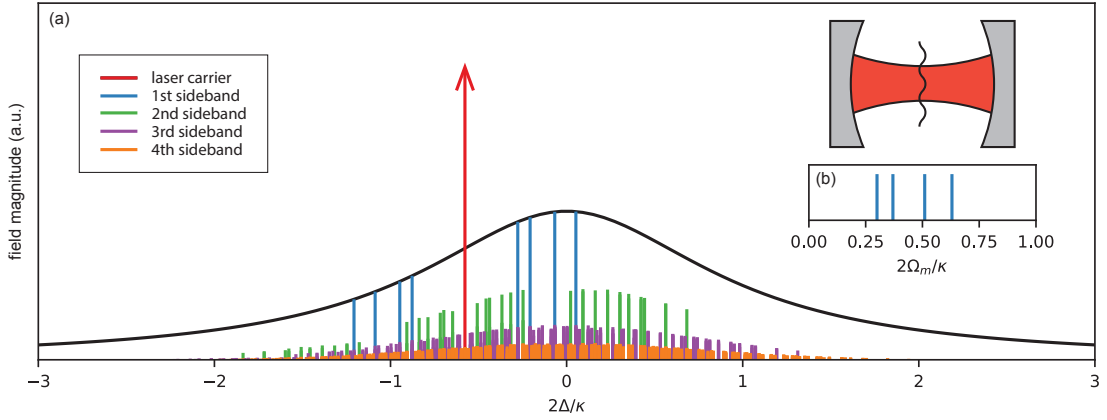


Figure 2.18: **(a)** Simulated optical spectrum as a result of nonlinear optomechanical transduction, showing the laser carrier at the magic detuning Δ_* as well as the generated optical sidebands up to the fourth order. The higher-order sidebands tend to become uniformly distributed within the cavity bandwidth. **(b)** We artificially assume in the simulation that the membrane supports four mechanical modes with equal coupling strengths. In reality, we have thousands of mechanical modes within the optomechanical coupling bandwidth in the experiment.

2.4 Thermal intermodulation noise

Apart from the thermomechanical noise of mirrors, there is one unconventional noise source in the MIM system at room temperature termed thermal intermodulation noise (TIN), first observed by the former PhD student working on this setup [42].

Essentially, the beam spot size of the optical cavity mode determines the cut-off mechanical frequency for efficient optomechanical coupling. Within this cutoff frequency, all the available mechanical modes will contribute to the total thermomechanical noise variance of the membrane. For 2D membranes, the mode density can be extremely high compared to that of a 1D structure and therefore contributes significant cavity frequency noise variance $\langle \Delta^2 \rangle$ contributed from the membrane.

As a high-finesse cavity is employed to achieve quantum-noise-limited laser operation, the cavity mode linewidth κ can approach that of the cavity frequency noise variance $\sqrt{\langle \Delta^2 \rangle}$, even when the cavity mirrors are in direct contact with the membrane chip (cavity length $\sim 635 \mu\text{m}$). In this case, the nonlinearity of the cavity frequency noise transduction manifests, leading to higher-order noise mixing processes in the cavity (shown in Fig. 2.18) and nonlinear noise within the mechanical bandgap of the membrane. This nonlinear transduction process generates optical fields at new frequencies, but how it manifests as noise depends on the system observable of interest. As one will see from the analysis below, this nonlinear noise does not fit into the conventional optical quadrature picture, and must be dealt with with particular attention to the nonlinearity of the photon number operator.

2.4.1 Quantum Langevin equation with nonlinear transduction

We start from the typical quantum Langevin equation (QLE) where mechanical motion is encoded in the cavity detuning $\delta\Delta(t)$ ¹,

$$\dot{a}(t) = [i(\bar{\Delta} + \delta\Delta(t) - \kappa/2)]a(t) + \sqrt{\kappa_p}a_p(t) + \sqrt{\kappa_v}a_v(t) + \dots \quad (2.30)$$

There, the operator \hat{a} is simplified to a . The usual linearization procedure applied on the term $\delta\Delta(t)a(t)$ would be valid if the fluctuation $\delta\Delta(t)$ is small. In the regime where $\delta\Delta(t)$ induces a sufficiently large change in $a(t)$, the linearization becomes invalid, and a more thorough treatment of the equation is required.

Assuming $a_p(t)$ is the pump mode with mean amplitude \bar{a}_p , we can apply FT² to the QLE and get (for simplification we denote $\bar{\Delta}$ as Δ directly, and $\Delta(\omega)$ is the Fourier component of $\delta\Delta(t)$)

$$a(\omega) = \frac{i \int \Delta(\omega - \omega') a(\omega') d\omega' / 2\pi + \sqrt{\kappa_p}(\bar{a}_p 2\pi\delta(\omega) + a_p(\omega)) + \sqrt{\kappa_v}a_v(\omega) + \dots}{i(-\omega - \Delta) + \kappa/2}. \quad (2.31)$$

The above equation is exactly the Fredholm integral equation of the second kind,

$$f(x) = \phi(x) - \lambda \int_a^b K(x, y)\phi(y) dy, \quad (2.32)$$

with the solution usually expressed in the Liouville-Neumann series of multiple orders

$$\phi(x) = \sum_{n=0}^{\infty} \lambda^n \phi_n(x). \quad (2.33)$$

We can easily identify each term in the QLE as

$$\phi(\omega) = a(\omega) \quad (2.34)$$

$$K(\omega, \omega') = \frac{i\Delta(\omega - \omega')/2\pi}{i(-\omega - \Delta) + \kappa/2} \quad (2.35)$$

$$f(\omega) = \frac{\sqrt{\kappa_p}(\bar{a}_p 2\pi\delta(\omega) + a_p(\omega)) + \sqrt{\kappa_v}a_v(\omega) + \dots}{i(-\omega - \Delta) + \kappa/2}. \quad (2.36)$$

Here, for simplicity, we set $\lambda = 1$. The solution can be calculated through the integration of the n th iterated kernel

$$K_n(\omega, \omega') = \iint K(\omega, \omega_1)K(\omega_1, \omega_2) \cdots K(\omega_{n-1}, \omega') d\omega_1 d\omega_2 \cdots d\omega_{n-1}, \quad (2.37)$$

with $K_0(\omega, \omega') = \delta(\omega - \omega')$ and $K_1(\omega, \omega') = K(\omega, \omega')$. The solution can be easily calculated using the following expression

$$\phi_n(\omega) = \int K_n(\omega, \omega') f(\omega') d\omega'. \quad (2.38)$$

¹In this section about TIN, we adopt the notation that $\Delta = \Omega_{\text{laser}} - \Omega_{\text{cavity}}$.

²Here we adopt the notation that FT = $\int e^{i\omega t} dt$ and FT⁻¹ = $\frac{1}{2\pi} \int e^{-i\omega t} d\omega$.

2.4 Thermal intermodulation noise

The 0th order solution is associated with the stationary solution and the vacuum fluctuations:

$$a_0(\omega) = f(\omega) = \frac{\sqrt{\kappa_p}(\bar{a}_p 2\pi\delta(\omega) + a_p(\omega)) + \sqrt{\kappa_v}a_v(\omega) + \dots}{i(-\omega - \Delta) + \kappa/2}, \quad (2.39)$$

while the 1st order solution is the conventional linear cavity transduction

$$a_1(\omega) = \int K(\omega, \omega') f(\omega') d\omega' = \int \frac{i\Delta(\omega - \omega')}{i(-\omega - \Delta) + \kappa/2} \frac{\sqrt{\kappa_p}\bar{a}_p\delta(\omega')}{i(-\omega' - \Delta) + \kappa/2} d\omega' = \bar{a} \frac{i\Delta(\omega)}{i(-\omega - \Delta) + \kappa/2}, \quad (2.40)$$

Starting from the 2nd order solution, we categorize them as TIN

$$\begin{aligned} a_2(\omega) &= \iint K(\omega, \omega_1) K(\omega_1, \omega') f(\omega') d\omega_1 d\omega' \\ &= \frac{1}{2\pi} \iint \frac{i\Delta(\omega - \omega_1)}{i(-\omega - \Delta) + \kappa/2} \frac{i\Delta(\omega_1 - \omega')}{i(-\omega_1 - \Delta) + \kappa/2} \frac{\sqrt{\kappa_p}\bar{a}_p\delta(\omega')}{i(-\omega' - \Delta) + \kappa/2} d\omega_1 d\omega' \\ &= -\bar{a} \int \frac{\Delta(\omega - \omega')}{i(-\omega - \Delta) + \kappa/2} \frac{\Delta(\omega')}{i(-\omega' - \Delta) + \kappa/2} \frac{d\omega'}{2\pi}, \end{aligned} \quad (2.41)$$

and the n th order noise is expressed as

$$a_n(\omega) = \bar{a} \iint \frac{i\Delta(\omega - \omega_1)}{i(-\omega - \Delta) + \kappa/2} \frac{i\Delta(\omega_1 - \omega_2)}{i(-\omega_1 - \Delta) + \kappa/2} \dots \frac{i\Delta(\omega_{n-1})}{i(-\omega_{n-1} - \Delta) + \kappa/2} \frac{d\omega_1}{2\pi} \dots \frac{d\omega_{n-1}}{2\pi}. \quad (2.42)$$

A more complete expression, including vacuum fluctuation contributions to the higher order solutions, can be found at Eq.(2.109-2.111).

In the following, we first analyze the results in the fast cavity limit $\Omega_\Delta \ll \kappa$, where Ω_Δ is the optomechanical coupling cutoff frequency (~ 5 MHz) determined by the optical mode spot size, as it greatly simplifies the result. A more general result is discussed in Section. 2.4.2.

In the fast cavity limit, if we only consider up to the second-order noise, the amplitude quadrature noise measured in a balanced homodyne detection is

$$X(\omega) = \bar{X} \left[\delta(\omega) - \frac{2\Delta/\kappa}{1 + (2\Delta/\kappa)^2} \frac{2\Delta(\omega)}{\kappa} - \frac{(1 - (2\Delta/\kappa)^2)}{[1 + (2\Delta/\kappa)^2]^2} \int \frac{4\Delta(\omega - \omega')\Delta(\omega')}{\kappa^2} \frac{d\omega'}{2\pi} \right]. \quad (2.43)$$

In this expression, one can observe that if a balanced homodyne detection is employed, when the detuning $2\Delta/\kappa = 1$, only linear transduction remains in the detection record. Note that this result is different from [42] in which the detection is done with direct detection. In the conventional quadrature picture, normally, people treat direct detection as equivalent to amplitude quadrature detection. Here, with TIN, the equivalence is broken, as direct detection includes photo-detection nonlinearity, whereas it is canceled out in a balanced homodyne detection. We illustrate the difference in the following.

Chapter 2. Experimental platform for room-temperature quantum optomechanics

In the direct detection, one detects

$$I = |a|^2 = a^\dagger a = |\bar{a}|^2 + \bar{a}(\delta a + \delta a^\dagger) + \delta a^\dagger \delta a \quad (2.44)$$

$$= |\bar{a}|^2 \left[\delta(\omega) - \frac{2\Delta/\kappa}{1 + (2\Delta/\kappa)^2} \frac{2\Delta(\omega)}{\kappa} + \frac{[-1 + 3(2\Delta/\kappa)^2]}{2[1 + (2\Delta/\kappa)^2]^2} \int \frac{4\Delta(\omega - \omega')\Delta(\omega')}{\kappa^2} \frac{d\omega'}{2\pi} \right] \quad (2.45)$$

In the Fourier domain, this would result in

$$I(\omega) = |\bar{a}|^2 \delta(\omega) + \sqrt{2}\bar{a}X(\omega) + \int \delta a^\dagger(\omega - \omega')\delta a(\omega')d\omega'/2\pi. \quad (2.46)$$

we will still observe nonlinear noise in direct detection when $2\Delta/\kappa = 1$, which will now instead cancel out when $2\Delta/\kappa = 1/\sqrt{3}$. In balanced homodyne detection, however, we only observe linear noise as,

$$I = |a + \beta|^2 - |a - \beta|^2 = 2\sqrt{2}|\beta|X_\theta(\omega), \quad (2.47)$$

where the part that involves photo-detection nonlinearity cancels out.

Since they share the same mathematical form, the photo-detection nonlinearity is essentially the photon number nonlinearity. Since the mechanical oscillators experience radiation pressure force in the form of $F = Ga^\dagger a$, in our experiment, we operate at $2\Delta/\kappa = 1/\sqrt{3}$ (magic detuning) to cancel out the nonlinear intra-cavity photon number fluctuation that would otherwise cause excess classical decoherence to the mechanics. For optical detection, only the direct detection of the cavity transmission port is a faithful verification that intra-cavity TIN is completely canceled out.

We must clarify that canceling noise is only possible for some system observables of interest, e.g., the photon number operator in our particular case. The nonlinear optical field generation is always present regardless of how we choose the laser detuning or measure the signal. This fact is evident in Fig. 2.18 that the nonlinear optical sidebands are still generated at the magic detuning Δ_* .

Note that we only consider up to second-order noise mixing processes here. In narrow linewidth optical mode, we also observe third-order mixing noise when the second-order noise is completely canceled out. We discuss it in detail in Section 2.4.4.

2.4.2 Breakdown of the fast-cavity limit

Note that the above perfect cancellation at the magic detuning $2\Delta/\kappa = 1/\sqrt{3}$ only happens in the fast-cavity limit where $\kappa/\Omega_m \rightarrow \infty$. In the actual experiment setting, it is not the case, with the mechanical frequency $\omega \sim \Omega_m \sim 2\pi \cdot 1$ MHz and the cavity linewidth $\kappa \sim 2\pi \cdot 30$ MHz. This effect is also illustrated in Fig. 2.18, that the optical sidebands obtain ω -dependent phases and amplitudes from the cavity susceptibility, propagating down through the cascaded nonlinear process.

To apply a simple correction (though not accurate) to gauge the order of magnitude of the residual noise that can not be canceled at the magic detuning, one can derive an approximation of the limit by ignoring contribution from ω' in all the convolutions, i.e. $i(-\omega' - \Delta) + \kappa/2 \rightarrow -i\Delta + \kappa/2$ in Eq.(2.41). One could argue that it is a minor effect since it is inside the convolution integration of $\Delta(\omega)$, and the thermomechanical spectrum has a cutoff frequency roughly at least one order of magnitude below κ . However, here we show that those two contributions from ω and ω' are similar. One can visualize it through

$$\begin{aligned} & \text{FT} \int \Delta(\omega - \omega') \Delta(\omega') \frac{-i\Delta + \kappa/2}{-i\omega' - i\Delta - \kappa/2} \frac{d\omega'}{2\pi} \\ &= \text{FT} \int \Delta(\omega - \omega') \Delta(\omega') G(\omega') \frac{d\omega'}{2\pi} = \Delta(t) \Delta'(t) \end{aligned} \quad (2.48)$$

$$\Delta'(t) = \int \Delta(t - t') e^{(-\kappa/2 + i\Delta)t'} u(t') (-i\Delta + \kappa/2) dt' = \int \Delta(t - t') G(t') dt', \quad (2.49)$$

where $G(\omega)$ and $G(t)$ are a generalized substitution for frequently occurring expressions like $\frac{-i\Delta + \kappa/2}{-i\omega' - i\Delta - \kappa/2}$ and $e^{(-\kappa/2 + i\Delta)t} u(t) (-i\Delta + \kappa/2)$, which contain the frequency dependence of the convolution, or equivalently the cavity response in either time domain or frequency domain. Note that $u(t)$ is the heavy step function.

If the time scale of the fluctuation of $\Delta(t)$ happens much slower than rate κ , then

$$\Delta'(t) \approx \int \Delta(t - t') \delta(t') dt' = \Delta(t), \quad (2.50)$$

which goes back to the fast-cavity limit result. Here, we keep the expression $\Delta'(t)$ instead and proceed until the calculation of the power spectral density,

$$\text{FT}_\tau \langle \Delta_2^*(t) \Delta_1(t + \tau) \rangle_t = \text{FT}_\tau \left\langle \iint \Delta(t - t'') \Delta(t + \tau - t') \right\rangle_t G_2^*(t'') G_1(t') dt' dt'' \quad (2.51)$$

$$= \int S_{\Delta\Delta}(\omega) e^{i\omega(t' - t'')} G_2^*(t'') G_1(t') dt' dt'' = S_{\Delta\Delta}(\omega) G_2^*(\omega) G_1(\omega), \quad (2.52)$$

which is a simple modification to the spectral density by the cavity response G . The same also happens for the variance,

$$\begin{aligned} \langle \Delta_2(t) \Delta_1(t) \rangle_t &= \left\langle \iint \Delta(t - t'') \Delta(t - t') \right\rangle_t G_2(t'') G_1(t') dt' dt'' \\ &= \iint C(t'' - t') G_2(t'') G_1(t') dt' dt'' = \mathcal{C}. \end{aligned} \quad (2.53)$$

Here, we show a more general result when cavity response can not be factorized,

$$\text{FT}_\omega \int A(\omega - \omega') B(\omega') G(\omega - \omega', \omega') d\omega' = \iint A(t - t_A) B(t - t_B) G(t_A, t_B) dt_A dt_B \quad (2.54)$$

$$G(t, t') = \text{FT}_{\omega, \omega'} G(\omega, \omega') \quad (2.55)$$

Chapter 2. Experimental platform for room-temperature quantum optomechanics

We can then proceed to calculate the power spectral density of the higher order mixing terms like³

$$S_{\Delta^2\Delta^2}(\omega) = \frac{1}{(2\pi)^2} \left\langle \int \Delta(\omega - \omega')^* \Delta(\omega')^* G_{12}(\omega - \omega', \omega')^* d\omega' \right. \\ \left. \int \Delta(\omega - \omega'') \Delta(\omega'') G_{34}(\omega - \omega'', \omega'') d\omega'' \right\rangle \quad (2.56)$$

$$= \left\langle \text{FT}_\tau \left[\iint_w \Delta^*(t - t_1) \Delta^*(t - t_2) \Delta(t + \tau - t_3) \Delta(t + \tau - t_4) \right. \right. \\ \left. \left. G_{12}^*(t_1, t_2) G_{34}(t_3, t_4) dt_1 dt_2 dt_3 dt_4 \right] \right\rangle \quad (2.57)$$

$$= \delta(\omega) \mathcal{C} + \iint \text{FT}_\tau [\langle \Delta^*(t - t_1) \Delta(t + \tau - t_3) \rangle \langle \Delta^*(t - t_2) \Delta(t + \tau - t_4) \rangle + \\ \langle \Delta^*(t - t_1) \Delta(t + \tau - t_4) \rangle \langle \Delta^*(t - t_2) \Delta(t + \tau - t_3) \rangle] \\ G_{12}^*(t_1, t_2) G_{34}(t_3, t_4) dt_1 dt_2 dt_3 dt_4 \quad (2.58)$$

$$= \dots + \iint \text{FT}_\tau [C(t_1 - t_3 + \tau) C(t_2 - t_4 + \tau) + C(t_1 - t_4 + \tau) C(t_2 - t_3 + \tau)] \\ G_{12}^*(t_1, t_2) G_{34}(t_3, t_4) dt_1 dt_2 dt_3 dt_4 \quad (2.59)$$

$$= \dots + \int S_{\Delta\Delta}(\omega - \omega') S_{\Delta\Delta}(\omega') [G_{12}(\omega - \omega', \omega')^* G_{34}(\omega - \omega', \omega') \\ + G_{12}(\omega - \omega', \omega')^* G_{34}(\omega', \omega - \omega')] d\omega' / 2\pi \quad (2.60)$$

If the convolution Kernel G_{12} is separable into $G_1(\omega - \omega') G_2(\omega')$:

$$\text{FT}_\tau \langle \Delta_1^*(t) \Delta_2^*(t) \Delta_3(t + \tau) \Delta_4(t + \tau) \rangle_t \\ = \text{FT}_\tau [\langle \Delta_1^* \Delta_2^* \rangle \langle \Delta_3 \Delta_4 \rangle + \langle \Delta_1^* \Delta_3 \rangle \langle \Delta_2^* \Delta_4 \rangle + \langle \Delta_1^* \Delta_4 \rangle \langle \Delta_2^* \Delta_3 \rangle] \\ = \text{FT} \iint C(t_1 - t_2) C(t_3 - t_4) G_1^*(t_1) G_2^*(t_2) G_3(t_3) G_4(t_4) dt_1 dt_2 dt_3 dt_4 + \\ \int S_{\Delta\Delta}(\omega - \omega') S_{\Delta\Delta}(\omega') G_1^*(\omega - \omega') G_2^*(\omega') [G_3(\omega - \omega') G_4(\omega') + G_4(\omega - \omega') G_3(\omega')] d\omega' / 2\pi \quad (2.61)$$

With the general expression in mind, now let us first examine the simplified method when we assume $\omega' \rightarrow 0$, we can derive the intra-cavity intensity fluctuation to be

$$\delta n(\omega) = \sqrt{2\bar{a}} X(\omega) + \int \delta a^\dagger(\omega - \omega') \delta a(\omega') d\omega' / 2\pi \\ \approx \bar{a}^2 \frac{2i\omega/\kappa + 3(2\Delta/\kappa)^2 - 1}{[(2\Delta/\kappa)^2 + 1]^2} \int \frac{4\Delta(\omega - \omega') \Delta(\omega')}{\kappa^2} \frac{d\omega'}{2\pi}, \quad (2.62)$$

where at the magic detuning $2\Delta/\kappa = 1/\sqrt{3}$ there is still a finite amount of fluctuation remaining at value

$$\delta n_{\text{lim}}(\omega) = \bar{a}^2 \frac{9i\omega}{2\kappa} \int \frac{\Delta(\omega - \omega') \Delta(\omega')}{\kappa^2} \frac{d\omega'}{2\pi}, \quad (2.63)$$

³See Eq.(2.84) for expansion details.

which is a factor of $[\frac{9\Omega_m}{8\kappa}]^{-2} \sim 10^3$ smaller than the zero detuning (max) fluctuation near the high Q mechanical frequency in terms of power spectral density.

Then, we can examine the contribution from ω' by assuming $\omega \rightarrow 0$, using the general expression. For simplicity, we will examine the amplitude quadrature instead (photon number too complicated to compute by hand),

$$S_{XX}(0) = \frac{|\bar{a}|^2}{2} \int S_{\Delta\Delta}(-\omega') S_{\Delta\Delta}(\omega') \frac{|-i\kappa\omega' + 2\kappa^2/4 - 2\Delta^2|^2}{[\Delta^2 + \kappa^2/4]^2 |\Delta^2 + (\kappa/2 - i\omega')|^2} \frac{d\omega'}{2\pi} + \dots \quad (2.64)$$

Again, we have a partial cancellation at the amplitude quadrature magic detuning $|\Delta| = \kappa/2$. To simplify our life, we assume $S_{\Delta\Delta}(\omega')^2$ is flat until a characteristic cutoff frequency $\Omega_\Delta \ll \kappa$ with a very fast roll-off. Then, we can easily compare two scenarios of $\Delta = 0$ vs. $|\Delta| = \kappa/2$, corresponding to maximum intermodulation noise vs. magic detuning cancellation. One can easily find a cancellation factor of $12\kappa^2/\Omega_\Delta^2 \sim 10^3$ assuming $\Omega_\Delta \sim 3\text{MHz}$. Therefore, the effects of ω and ω' are causing comparable effects when the fast-cavity limit breaks down.

With the help of Mathematica, combining Eq.(2.40)(2.41)(2.46), we can find out that the actual intra-cavity noise at magic detuning assuming a similar cutoff Ω_Δ and flat mechanical spectrum,

$$S_{II} = |a|^2 \int S_{\Delta\Delta}(\omega - \omega') S_{\Delta\Delta}(\omega') \frac{32(-12\Delta^2 + \kappa^2)^2}{(4\Delta^2 + \kappa^2)^4} \frac{d\omega'}{2\pi} \\ \approx |a|^2 \frac{32\langle\Delta^2\rangle\bar{S}_{\Delta\Delta}}{\kappa^4} (\Delta=0) \quad (2.65)$$

$$\delta S_{II} \approx |a|^2 \frac{256(3\kappa^2 - 4\Delta^2)\kappa^2\omega^2}{(4\Delta^2 + \kappa^2)^5} \int S_{\Delta\Delta}(\omega - \omega') S_{\Delta\Delta}(\omega') \frac{d\omega'}{2\pi} \\ \approx |a|^2 \frac{256(3\kappa^2 - 4\Delta^2)\kappa^2\omega^2\langle\Delta^2\rangle\bar{S}_{\Delta\Delta}}{(4\Delta^2 + \kappa^2)^5} = |a|^2 \frac{162\langle\Delta^2\rangle\bar{S}_{\Delta\Delta}\omega^2}{\kappa^6} (\Delta=\kappa/\sqrt{3}) \quad (2.66)$$

The actual correct cancellation factor considering all the terms is $\frac{\kappa^2}{10\Omega_m^2} \sim 1 \times 10^2$, a factor of 10 less than assuming $\omega' \rightarrow 0$. Surprisingly, the cancellation factor is almost independent of the thermomechanical noise bandwidth Ω_Δ , as long as $\Omega_\Delta \ll \kappa$. The sensitivity of TIN cancellation to laser detuning is visualized in Fig.2.19.

In the actual experiment, we can observe the noise induced by this limit at low optical power (Section. 2.4.6), with more details shown in Section. 2.4.7 as well as the separation from the third order nonlinear noise. At high optical power, the thermomechanical noises are sufficiently cooled by the laser at magic detuning, and the third-order nonlinear noise is the dominant noise source, which is discussed in detail in Section. 2.4.4

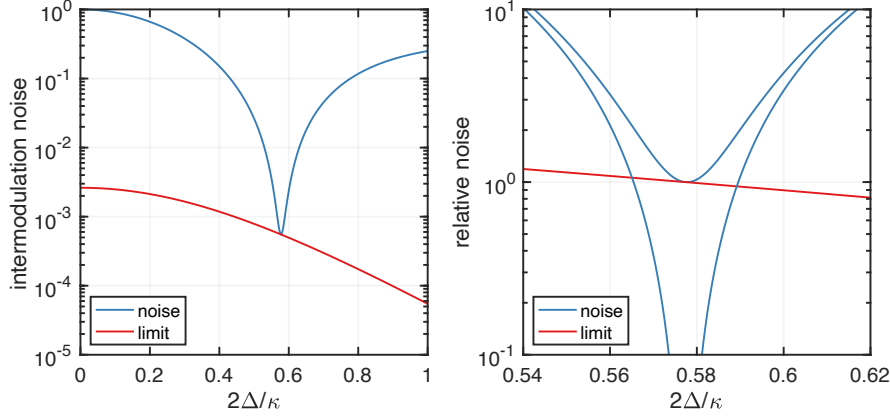


Figure 2.19: Visualization of the thermal intermodulation noise cancellation effect across magic detuning $2\Delta = \kappa/\sqrt{3}$. In the left panel, the intermodulation noise is normalized to the level at $\Delta = 0$. In the right panel, the noise is normalized to the minimum noise level to better illustrate the noise cancellation limit. A system with $\kappa/2\pi = 60$ MHz and $\Omega_m/2\pi = 700$ kHz is assumed.

2.4.3 Second-order nonlinear noise cancellation in a homodyne detection

In the following sections, we consider only the fast-cavity limit unless specified otherwise. Our goal in this section is to find a way to cancel the second-order TIN in the detection with arbitrary optical quadrature angles. Conventional balanced homodyne detection can not satisfy this requirement, as it lacks enough degree of freedom. We draw our inspiration from [21], where a single detector is used to perform high-efficiency quadrature measurement. Single-port configuration provides the photodetection nonlinearity, that allows the extra degrees of freedom provided by the local oscillator power to achieve TIN cancellation at arbitrary quadrature angles. A similar result is also derived later independently by the former student working on this project in a separate manuscript [42]. In the following, we describe our formulation in detail.

The scheme is to mix the local oscillator a_{LO} with the signal a_{sig} through a high transmission ($\eta \rightarrow 1$) beam splitter, such that the signal in the mixed field is mainly contributed from the signal beam δa_{sig} , while the field amplitude and phase is corrected by the local oscillator $\overline{a_{\text{LO}}}$. The mixed field a is directed to the detector, and the photocurrent $a^\dagger a$ is detected. The linearization was done with respect to the phase of the mean fields, such that $a_{\text{sig}} =$

2.4 Thermal intermodulation noise

$(\overline{a_{\text{sig}}} + \delta a_{\text{sig}})e^{-i\theta_{\text{sig}}}$, and we define $\theta = \theta_{\text{LO}} - \theta_{\text{sig}}$.

$$a = \sqrt{\eta}a_{\text{sig}} + i\sqrt{1-\eta}a_{\text{LO}} \quad (2.67)$$

$$I = |a|^2 = \eta n_{\text{sig}} + (1-\eta)n_{\text{LO}} - i\sqrt{\eta(1-\eta)}(a_{\text{sig}}a_{\text{LO}}^\dagger - a_{\text{sig}}^\dagger a_{\text{LO}}) \quad (2.68)$$

$$\begin{aligned} &= \eta \overline{n_{\text{sig}}} + (1-\eta)\overline{n_{\text{LO}}} + 2\sin\theta\sqrt{\eta(1-\eta)}\overline{a_{\text{sig}}a_{\text{LO}}} \\ &\quad + \sqrt{1-\eta}(\sqrt{1-\eta}\overline{a_{\text{LO}}} + i\sqrt{\eta}\overline{a_{\text{sig}}}e^{-i\theta})\delta a_{\text{LO}} + h.c. \\ &\quad + \sqrt{\eta}(\sqrt{\eta}\overline{a_{\text{sig}}} - i\sqrt{1-\eta}\overline{a_{\text{LO}}}e^{i\theta})\delta a_{\text{sig}} + h.c. \\ &\quad + \eta\delta a_{\text{sig}}^\dagger\delta a_{\text{sig}}. \end{aligned} \quad (2.69)$$

Even though θ is the angle between LO and signal, there is an additional $\pi/2$ phase shift when two beams are combined at a beam splitter. Therefore $\theta = 0$ corresponds to the quadrature point of the fringe instead of constructive interference. In the limit where the transmission $\eta \rightarrow 1$, and there is no classical noise injecting from the local oscillator, the photo current can be simplified as

$$I \approx \overline{n_{\text{sig}}} + \overline{n_{\text{LO}}}' + 2\sin\theta\overline{a_{\text{sig}}a_{\text{LO}}}' + [(\overline{a_{\text{sig}}} - i\overline{a_{\text{LO}}}'e^{i\theta})\delta a_{\text{sig}} + h.c.] + \delta a_{\text{sig}}^\dagger\delta a_{\text{sig}}, \quad (2.70)$$

where $\overline{a_{\text{LO}}}' = \sqrt{1-\eta}\overline{a_{\text{LO}}}$.

Due to the presence of intermodulation noise, we can separate $\delta a_{\text{sig}} = \delta a_1 + \delta a_2$ into a linear part

$$\delta a_1(\omega) = \frac{i\overline{a_{\text{sig}}}}{-i\Delta + \kappa/2}\Delta(\omega), \quad (2.71)$$

and a nonlinear part

$$\delta a_2(\omega) = \frac{-\overline{a_{\text{sig}}}}{(-i\Delta + \kappa/2)^2} \int \Delta(\omega')\Delta(\omega - \omega')d\omega' / 2\pi, \quad (2.72)$$

in the fast-cavity limit. If we define the combined field as $a = |a|e^{i\theta'} = \overline{a_{\text{sig}}} + i\overline{a_{\text{LO}}}'e^{-i\theta'}$, the fluctuation in the photo-current (up to the second order) will be

$$\begin{aligned} \delta I(\omega) &= 2|a|\text{Real}[e^{-i\theta'}(\delta a_1(\omega) + \delta a_2(\omega) + \delta a_3(\omega))] \\ &\quad + \int \delta a_1^\dagger(\omega')\delta a_1(\omega - \omega')d\omega' / 2\pi \\ &\quad + 2\text{Real}[\int \delta a_2^\dagger(\omega')\delta a_1(\omega - \omega')d\omega' / 2\pi]. \end{aligned} \quad (2.73)$$

where the nonlinear noises ($\delta a_2(\omega)$ and $\int \delta a_1^\dagger(\omega')\delta a_1(\omega - \omega')d\omega'$) will cancel out at condition

$$\frac{\overline{a_{\text{sig}}}}{|a|} = 2\text{Real}\left[\frac{e^{-i\theta'}}{(-i\Delta + \kappa/2)^2}\right](\Delta^2 + (\kappa/2)^2). \quad (2.74)$$

Therefore, if we wish to observe only the linear thermomechanical signal at quadrature angle

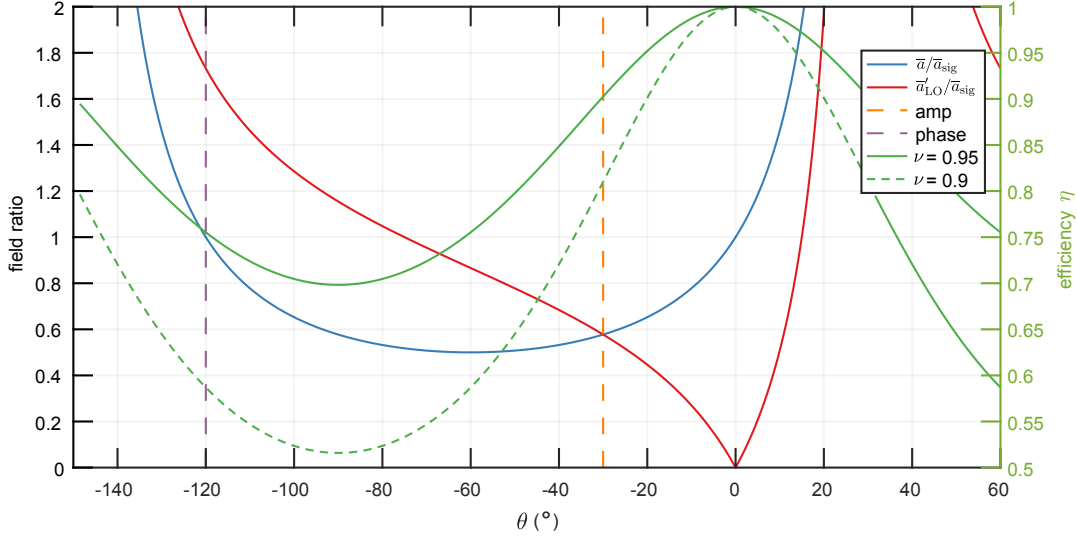


Figure 2.20: The required local oscillator and the combined field ratio for canceling the second order TIN noise in single-port homodyne detection. $\alpha' = \bar{a}$, $\alpha = \bar{a}_{\text{sig}}$, $\beta = \bar{a}_{\text{LO}}'$. Two specific quadrature angles are also plotted in dashed vertical lines for reference. The amplitude quadrature here means the angle that carries minimal information about the mechanical motion. In contrast, the phase quadrature means the angle carrying maximal mechanical motion information. The green curves (axis right) are the calculated homodyne efficiency based on different values of the visibility of the fringes. In our experiment, we achieved a maximum $\nu = 0.95$.

θ' , we need to adjust the combined field $|a|$, done by tuning the correct local oscillator field \bar{a}_{LO}' and the relative phase difference θ . This cancellation condition is illustrated in Fig. 2.20.

It is worth mentioning that even if η does not go to the limit 1, the beam splitter only effectively introduces additional detection loss, and does not change the cancellation relation derived here, which is great for practical reasons.

However, careful readers will notice that when calculating the actual power spectral density, there is also the cross-correlation between terms like $\delta a_1(\omega)$, $\int \delta a_2^\dagger(\omega') \delta a_1(\omega - \omega') d\omega'$ and $\delta a_3(\omega)$ that are not considered yet but will also contribute to the second order mixing noise. They contribute because the cross terms involving them will still be even orders as Gaussian noises $\Delta(t)$, and they are at the same order of magnitude as the auto-correlation of terms like $\delta a_2(\omega)$ and $\int \delta a_1^\dagger(\omega') \delta a_1(\omega - \omega') d\omega'$ which we considered earlier.

We will show below that the noises induced by these correlations can not be canceled but will stay proportional to the linear transduction terms. In other words, they only reduce cavity linear transduction efficiency, as part of the signal is converted to other frequency components from the nonlinear mixing process.

In order to calculate the complete spectra expression, one needs to use some mathematical

tricks from [65]. First, we could recognize that for stochastic variables $x_i(t)$, the relevant spectra that we are concerned with are

$$S_{xy}(\omega) = \int \langle x^*(\omega)y(\omega') \rangle d\omega' / 2\pi = \langle x^*(\omega)y(\omega) \rangle = \left\langle \text{FT}_\tau \left[\int_w x^*(t)y(t+\tau) dt \right] \right\rangle \quad (2.75)$$

$$S_{\Delta\Delta}(\omega) = \langle \Delta^*(\omega)\Delta(\omega) \rangle = \left\langle \text{FT}_\tau \left[\int_w \Delta^*(t)\Delta(t+\tau) dt \right] \right\rangle \quad (2.76)$$

$$S_{\Delta\Delta^2}(\omega) = \frac{1}{2\pi} \left\langle \Delta^*(\omega) \int \Delta(\omega-\omega')\Delta(\omega') d\omega' \right\rangle = \left\langle \text{FT}_\tau \left[\int_w \Delta^*(t)\Delta^2(t+\tau) dt \right] \right\rangle \quad (2.77)$$

$$\begin{aligned} S_{\Delta\Delta^3}(\omega) &= \frac{1}{(2\pi)^2} \left\langle \Delta^*(\omega) \iint \Delta(\omega-\omega')\Delta(\omega'-\omega'')\Delta(\omega'') d\omega'\omega'' \right\rangle \\ &= \left\langle \text{FT}_\tau \left[\int_w \Delta^*(t)\Delta^3(t+\tau) dt \right] \right\rangle \end{aligned} \quad (2.78)$$

$$\begin{aligned} S_{\Delta^2\Delta^2}(\omega) &= \frac{1}{(2\pi)^2} \left\langle \int \Delta^*(\omega-\omega')\Delta^*(\omega') d\omega' \int \Delta(\omega-\omega'')\Delta(\omega'')\omega'' \right\rangle \\ &= \left\langle \text{FT}_\tau \left[\int_w \Delta^{*2}(t)\Delta^2(t+\tau) dt \right] \right\rangle, \end{aligned} \quad (2.79)$$

where $\langle \dots \rangle$ are the average over statistical ensemble. In order to calculate these higher order correlation functions, we could exploit the fact that $\Delta(t)$ at different times is a set of Gaussian random variables, whose higher order cumulants $\langle\langle \Delta(t_1)\Delta(t_2)\dots\Delta(t_n) \rangle\rangle = 0$ for $n > 2$. Furthermore, since we are concerned with fluctuation, we set $\langle \Delta(t) \rangle = 0$. The first few cumulants can be expressed as

$$\langle\langle \Delta_1 \rangle\rangle = \langle \Delta_1 \rangle = 0 \quad (2.80)$$

$$\langle\langle \Delta_1 \Delta_2 \rangle\rangle = \langle \Delta_1 \Delta_2 \rangle - \langle \Delta_1 \rangle \langle \Delta_2 \rangle = \langle \Delta_1 \Delta_2 \rangle \quad (2.81)$$

$$\begin{aligned} \langle\langle \Delta_1 \Delta_2 \Delta_3 \rangle\rangle &= \langle \Delta_1 \Delta_2 \Delta_3 \rangle - \langle \Delta_1 \Delta_2 \rangle \langle \Delta_3 \rangle - \langle \Delta_1 \rangle \langle \Delta_2 \Delta_3 \rangle - \langle \Delta_1 \Delta_3 \rangle \langle \Delta_2 \rangle + 2\langle \Delta_1 \rangle \langle \Delta_2 \rangle \langle \Delta_3 \rangle \\ &= \langle \Delta_1 \Delta_2 \Delta_3 \rangle = 0 \end{aligned} \quad (2.82)$$

$$\begin{aligned} \langle\langle \Delta_1 \Delta_2 \Delta_3 \Delta_4 \rangle\rangle &= \langle \Delta_1 \Delta_2 \Delta_3 \Delta_4 \rangle - \langle \Delta_1 \Delta_2 \rangle \langle \Delta_3 \Delta_4 \rangle - \langle \Delta_1 \Delta_3 \rangle \langle \Delta_2 \Delta_4 \rangle - \langle \Delta_1 \Delta_4 \rangle \langle \Delta_2 \Delta_3 \rangle \\ &= 0 \end{aligned} \quad (2.83)$$

$$\langle\langle \Delta_1 \dots \Delta_n \rangle\rangle = \sum_{\pi} (|\pi| - 1)! (-1)^{|\pi|-1} \prod_{B \in \pi} \left\langle \prod_{i \in B} \Delta_i \right\rangle, \quad (2.84)$$

where π runs through the list of all partitions of $\{1, \dots, n\}$, and $|\pi|$ is the number of parts in the partition. For the fourth cumulants all the terms with $\langle \Delta_i \rangle = 0$ will vanish. We could find that since $\langle \Delta_1 \Delta_2 \Delta_3 \rangle = 0$, we have $\langle \Delta^*(t)\Delta^2(t+\tau) \rangle = 0$ and $S_{\Delta\Delta^2} = 0$. For $\langle \Delta^*(t)\Delta^3(t+\tau) \rangle$ and $\langle \Delta^{*2}(t)\Delta^2(t+\tau) \rangle$, we have the following relations

$$\langle \Delta^*(t)\Delta^3(t+\tau) \rangle = 3\langle \Delta^*(t)\Delta(t+\tau) \rangle \langle \Delta^2 \rangle \quad (2.85)$$

$$\langle \Delta^{*2}(t)\Delta^2(t+\tau) \rangle = |\langle \Delta^2 \rangle|^2 + 2\langle \Delta^*(t)\Delta(t+\tau) \rangle^2, \quad (2.86)$$

Chapter 2. Experimental platform for room-temperature quantum optomechanics

from which we could derive the expressions for their power spectral density (PSD),

$$S_{\Delta\Delta^3}(\omega) = 3\langle\Delta^2\rangle S_{\Delta\Delta}(\omega) \quad (2.87)$$

$$S_{\Delta^2\Delta^2}(\omega) = 2\pi|\langle\Delta^2\rangle|^2\delta(\omega) + 2 \int S_{\Delta\Delta}(\omega')S_{\Delta\Delta}(\omega-\omega')d\omega'/2\pi \quad (2.88)$$

For a single-port homodyne detection discussed earlier, we obtain the following expression

$$\begin{aligned} S_{II}(\omega) &= 4|a|^2|\bar{a}_{\text{sig}}|^2 \text{Real} \left[\frac{ie^{-i\theta'}}{-i\Delta + \kappa/2} \right]^2 S_{\Delta\Delta}(\omega) \\ &+ |\bar{a}_{\text{sig}}|^2 \left[\text{Real} \left[\frac{-2|a|e^{-i\theta'}}{(-i\Delta + \kappa/2)^2} \right] + \frac{|\bar{a}_{\text{sig}}|}{\Delta^2 + \kappa^2/4} \right]^2 \\ &\times \left[2 \int S_{\Delta\Delta}(\omega')S_{\Delta\Delta}(\omega-\omega')d\omega'/2\pi + 2\pi|\langle\Delta^2\rangle|^2\delta(\omega) \right] \\ &- \frac{24|a||\bar{a}_{\text{sig}}|^3\Delta}{(\Delta^2 + \kappa^2/4)^2} \text{Real} \left[\frac{ie^{-i\theta'}}{-i\Delta + \kappa/2} \right] \langle\Delta^2\rangle S_{\Delta\Delta}(\omega) \\ &- 24|a|^2|\bar{a}_{\text{sig}}|^2 \text{Real} \left[\frac{ie^{-i\theta'}}{-i\Delta + \kappa/2} \right] \text{Real} \left[\frac{ie^{-i\theta'}}{(-i\Delta + \kappa/2)^3} \right] \langle\Delta^2\rangle S_{\Delta\Delta}(\omega) \end{aligned} \quad (2.89)$$

So when $\langle\Delta^2\rangle$ approaches the magnitude of κ^2 , the nonlinear mixing process will modify the linear term. Under direct detection, the result can be simplified as

$$S_{II}(\omega) = 4|\bar{a}_{\text{sig}}|^4 \frac{\Delta^2}{(\Delta^2 + \kappa^2/4)^2} \left[1 + 12\langle\Delta^2\rangle \frac{\Delta^2 - \kappa^2/4}{(\Delta^2 + \kappa^2/4)^2} \right] S_{\Delta\Delta}(\omega) \quad (2.90)$$

$$+ |\bar{a}_{\text{sig}}|^4 \left[\frac{3\Delta^2 - \kappa^2/4}{(\Delta^2 + \kappa^2/4)^2} \right]^2 \left[2 \int S_{\Delta\Delta}(\omega')S_{\Delta\Delta}(\omega-\omega')/2\pi + 2\pi|\langle\Delta^2\rangle|^2\delta(\omega) \right]. \quad (2.91)$$

One could see that this leads to a reduction of linear transduction efficiency, as well as slightly lower calibrated g_0 than the actual value by a factor of $1 + 12\langle\Delta^2\rangle \frac{\Delta^2 - \kappa^2/4}{(\Delta^2 + \kappa^2/4)^2}$. This is true when we operate at the magic detuning.

One could also examine the sixth-order correlations associated with the third-order nonlinear noise using the simplified relation

$$\langle\Delta_1 \cdots \Delta_6\rangle = \sum \langle\cdots\rangle\langle\cdots\rangle\langle\cdots\rangle, \quad (2.92)$$

where the summation is over all the non-repetitive arrangements, which is in a total of 15 terms. Therefore, we have the following relations

$$\langle\Delta^3(t)\Delta^3(t+\tau)\rangle = 6\langle\Delta(t)\Delta(t+\tau)\rangle^3 + 9\langle\Delta^2\rangle^2\langle\Delta(t)\Delta(t+\tau)\rangle \quad (2.93)$$

$$\langle\Delta^2(t)\Delta^4(t+\tau)\rangle = 3\langle\Delta^2\rangle^3 + 12\langle\Delta^2\rangle\langle\Delta(t)\Delta(t+\tau)\rangle^2 \quad (2.94)$$

$$\langle\Delta(t)\Delta^5(t+\tau)\rangle = 15\langle\Delta^2\rangle^2\langle\Delta(t)\Delta(t+\tau)\rangle. \quad (2.95)$$

More details on the noise property of the third-order nonlinear noise are in Section 2.4.4.

Experimental observation of TIN in photodetection

In the experiment, to detect a certain quadrature angle while canceling nonlinear noise, we lock the homodyne power at the corresponding combined field intensity I_{hom} . Then, we continuously vary the local oscillator power using a tunable neutral density filter until the noise in the mechanical bandgap is perfectly canceled, as is shown in Fig. 2.21(a). The level of mixing noise is sensitive to the local oscillator power, and therefore, the cancellation point can serve as a good indicator of the measured quadrature angle θ . Knowing the field amplitude ratios between $|\bar{a}_{\text{hom}}|$, $|\bar{a}_{\text{sig}}|$, and that $\bar{\Delta} = -\kappa/(2\sqrt{3})$, we can reconstruct the measured quadrature angles as the ones satisfying the condition in 2.74. The nonlinear noise level in a frequency band inside the mechanical bandgap as a function of local oscillator power is shown in Fig. 2.21(b).

The detection efficiency in this setting differs from the balanced homodyne case, which is given by the square of the interference visibility ν between the signal beam and the LO beam. In our case, the LO and signal beams have comparable optical powers. The added noise comes from the mode-mismatched LO intensity

$$\Delta I_{\text{LO}} = |r\bar{a}_{\text{LO}}|^2(1/\nu^2 - 1), \quad (2.96)$$

which results in the reduced homodyne efficiency of

$$\eta_{\text{hom}} = I_{\text{hom}} / (I_{\text{hom}} + \Delta I_{\text{LO}}). \quad (2.97)$$

Since the local oscillator power is determined by the requirement of nonlinear noise elimination (equation 2.74), the homodyne efficiency acquires a quadrature angle dependence. We plot the efficiency at different quadrature angles in Fig. 2.21(d) given the experimentally characterized visibility $\nu = 95\%$.

2.4.4 Third-order nonlinear noise

Another concern is the third-order nonlinear noise that can not be easily decomposed into the quadrature basis and does not get canceled at the magic detuning Δ_* . For a single-port homodyne, we separate the photocurrent into different orders of the nonlinear mixing

Chapter 2. Experimental platform for room-temperature quantum optomechanics

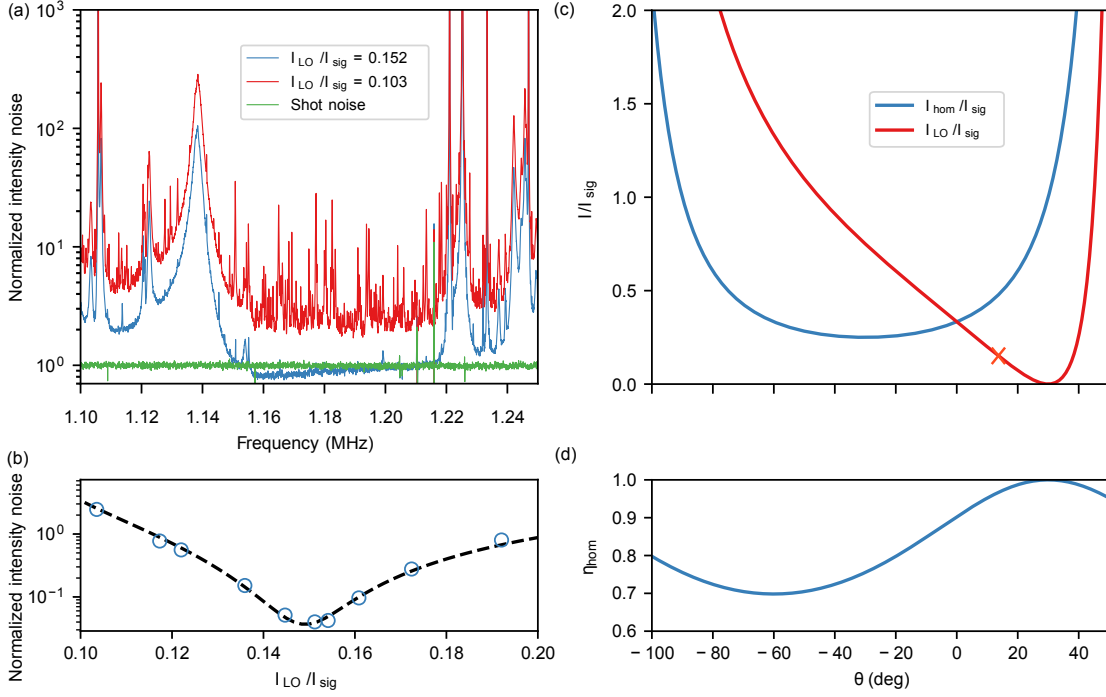


Figure 2.21: **(a)** When the homodyne power is locked to $I_{hom}/I_{sig} = 0.481$, different injected local oscillator intensities I_{LO} result in different optical quadratures being probed, and drastically different nonlinear noise levels in detection. When the appropriate local oscillator intensity is injected, the nonlinear noise can be efficiently canceled (blue). **(b)** The averaged nonlinear noise from 1.16 MHz to 1.18 MHz, normalized to shot noise, is plotted as a function of local oscillator intensity I_{LO} (theory fit in dashed line, including a 4% noise contribution from the third order nonlinear noise). **(c)** Required I_{hom} and I_{LO} for nonlinear noise cancellation at different quadrature angles θ . The angles are displayed after subtracting the cavity-induced angle rotation of -30° at the magic detuning. The red cross marks $I_{LO}/I_{sig} = 0.150$, the noise cancellation condition shown in **(a,b)**. **(d)** Homodyne detection efficiency at different quadrature angles, given the experimentally characterized $\nu = 0.95$.

processes:

$$\begin{aligned}
 I &= \bar{a}^* \bar{a} + 2\text{Re} \left[\bar{a} \sum_k a_k \right] + \left(\sum_k a_k^* \right) \left(\sum_k a_k \right) \\
 &= \bar{a}^* \bar{a} \\
 &+ \bar{a}^* a_1 + \bar{a} a_1^* \\
 &+ \bar{a}^* a_2 + \bar{a} a_2^* + a_1^* a_1 \\
 &+ \bar{a}^* a_3 + \bar{a} a_3^* + a_1^* a_2 + a_2^* a_1 \\
 &+ \bar{a}^* a_4 + \bar{a} a_4^* + a_1^* a_3 + a_2^* a_2 + a_3^* a_1 \\
 &+ \bar{a}^* a_5 + \bar{a} a_5^* + a_1^* a_4 + a_2^* a_3 + a_3^* a_2 + a_4^* a_1 \\
 &+ \dots
 \end{aligned} \tag{2.98}$$

2.4 Thermal intermodulation noise

For the third-order nonlinear noise, we are mostly concerned with the terms above with up to $\Delta(t)^5$. For all possible combination that gives a third-order nonlinear noise, we can apply the following relations to simplify

$$\langle \Delta^3(t)\Delta^3(t+\tau) \rangle = 6\langle \Delta(t)\Delta(t+\tau) \rangle^3 + 9\langle \Delta^2 \rangle^2 \langle \Delta(t)\Delta(t+\tau) \rangle \quad (2.99)$$

$$\langle \Delta^2(t)\Delta^4(t+\tau) \rangle = 3\langle \Delta^2 \rangle^3 + 12\langle \Delta^2 \rangle \langle \Delta(t)\Delta(t+\tau) \rangle^2 \quad (2.100)$$

$$\langle \Delta(t)\Delta^5(t+\tau) \rangle = 15\langle \Delta^2 \rangle^2 \langle \Delta(t)\Delta(t+\tau) \rangle. \quad (2.101)$$

As we are only concerned with the third-order contribution with a substantially different noise property from the second-order and can not be canceled at the magic detuning Δ_* , only the third-order self-correlation terms of the above expressions matter. Other terms manifest as a correction for the first- and second-order noises. Therefore, the third-order noise density is

$$S_{II}^{(3)} = 6|\chi_3|^2 \iint S_{\Delta\Delta}(\omega - \omega') S_{\Delta\Delta}(\omega' - \omega'') S_{\Delta\Delta}(\omega'' - \omega''') d\omega' d\omega'' \quad (2.102)$$

with susceptibility

$$\begin{aligned} \chi_3 &= 2\bar{a}_{\text{sig}} \text{Re} \left[-i|\bar{a}|e^{-i\theta} \chi_{\text{cav}}^3 + i\bar{a}_{\text{sig}} \chi_{\text{cav}} |\chi_{\text{cav}}^3|^2 \right] \\ &= 2\bar{a}_{\text{sig}} |\chi_{\text{cav}}|^3 \left[-\sin(\theta_0)(\bar{a}_{\text{sig}} - |\bar{a}| \cos(2\theta_0 - \theta)) + |\bar{a}| \cos(\theta_0) \sin(2\theta_0 - \theta) \right] \end{aligned} \quad (2.103)$$

where we set the phase reference $\bar{a}_{\text{sig}} = |\bar{a}_{\text{sig}}|$, and other relations $\bar{a} = |\bar{a}|e^{i\theta} = \bar{a}_{\text{sig}} + r\bar{a}_{\text{LO}}$, $\chi_{\text{cav}} = \frac{1}{-i\Delta + \kappa/2} = e^{i\theta_0} / \sqrt{\Delta^2 + (\kappa/2)^2}$.

Since we can only observe the third-order noise when we cancel out completely the second-order noise, we can apply the homodyne cancellation condition for the second-order noise

$$\bar{a}_{\text{sig}} = 2 \cos(2\theta_0 - \theta) |\bar{a}| \quad (2.104)$$

to fix the third-order susceptibility as a function of the homodyne angle

$$\chi_3 = 2|\bar{a}|^2 |\chi_{\text{cav}}|^3 \sin(\theta_0 - \theta). \quad (2.105)$$

Comparing this result with the linear transduction susceptibility,

$$S_{II}^{(1)} = |\chi_1|^2 S_{\Delta\Delta}(\omega) \quad (2.106)$$

$$\chi_1 = -2\bar{a}_{\text{sig}} |\bar{a}| |\chi_{\text{cav}}| \sin(\theta_0 - \theta) \quad (2.107)$$

we can see that due to the homodyne second-order noise cancellation condition, the third-order noise has the same quadrature dependence as the first-order transduction, acting as a phase-quadrature imprecision noise. Note that this is generally not true if we do not apply the cancellation condition for the second-order noise.

As for the third-order intracavity photon number fluctuation, associated with the excess

Chapter 2. Experimental platform for room-temperature quantum optomechanics

classical radiation pressure noise

$$\chi_3^{\text{cav}} = 4\bar{a}_{\text{sig}}^2 |\chi_{\text{cav}}|^3 \sin(\theta_0) \cos(2\theta_0) \quad (2.108)$$

which contributes similarly to a linear frequency noise. In summary, the third-order mixing noise behaves approximately as a cavity frequency noise.

2.4.5 Nonlinear mixing of vacuum fluctuations

Going back to the general solution of the Langevin equation, one will realize that the effect of the vacuum fluctuation in the 0th order term

$$a_0(\omega) = f(\omega) = \frac{\sqrt{\kappa_p}(\bar{a}_p 2\pi\delta(\omega) + a_p(\omega)) + \sqrt{\kappa_v}a_v(\omega) + \dots}{i(-\omega - \Delta) + \kappa/2}, \quad (2.109)$$

is ignored in the higher-order solutions to simplify all the calculations. Here, we investigate the modification of the vacuum fluctuations, i.e., the shot noise level, due to the nonlinear mixing process.

Likewise, the 1st order solution is not only the linear cavity transduction, but also a mixing of detuning noise with the vacuum fluctuation

$$\begin{aligned} a_1(\omega) &= \int K(\omega, \omega') f(\omega') d\omega' = \bar{a} \frac{i\Delta(\omega)}{i(-\omega - \Delta) + \kappa/2} \\ &+ \int \frac{i\Delta(\omega - \omega')}{i(-\omega - \Delta) + \kappa/2} \frac{\sum_v \sqrt{\kappa_v} a_v(\omega')}{i(-\omega' - \Delta) + \kappa/2} \frac{d\omega'}{2\pi}, \end{aligned} \quad (2.110)$$

The same goes for the n th order solution

$$\begin{aligned} a_n(\omega) &= \frac{1}{(2\pi)^{n-1}} \bar{a} \iint \frac{i\Delta(\omega - \omega_1)}{i(-\omega - \Delta) + \kappa/2} \frac{i\Delta(\omega_1 - \omega_2)}{i(-\omega_1 - \Delta) + \kappa/2} \dots \frac{i\Delta(\omega_{n-1})}{i(-\omega_{n-1} - \Delta) + \kappa/2} \\ &\quad \times d\omega_1 \dots d\omega_{n-1} \\ &+ \frac{1}{(2\pi)^n} \iint \frac{i\Delta(\omega - \omega_1)}{i(-\omega - \Delta) + \kappa/2} \dots \frac{i\Delta(\omega_{n-1} - \omega_n)}{i(-\omega_{n-1} - \Delta) + \kappa/2} \frac{\sum_v \sqrt{\kappa_v} a_v(\omega_n)}{i(-\omega_n - \Delta) + \kappa/2} d\omega_1 \dots d\omega_n. \end{aligned} \quad (2.111)$$

If we think hard enough, we will figure out that the first-order correction to the shot noise level is for sure connected to the following type of correlation function

$$\begin{aligned} &\frac{1}{(2\pi)^2} \left\langle a_v^\dagger(\omega) \iint \Delta(\omega - \omega') \Delta(\omega' - \omega'') a_v(\omega'') d\omega' d\omega'' \right\rangle \\ &= \left\langle \text{FT}_\tau \left[\int_w a_v^\dagger(t) a_v(t + \tau) \Delta^2(t + \tau) dt \right] \right\rangle \\ &= \langle \Delta^2 \rangle \left\langle \text{FT}_\tau \left[\int_w a_v^\dagger(t) a_v(t + \tau) dt \right] \right\rangle = \langle \Delta^2 \rangle \langle a_v^\dagger(\omega) a_v(\omega) \rangle, \end{aligned} \quad (2.112)$$

For the other type of correlation function, we might think it only gives a mixing term and can be safely ignored. But do not make the mistake, since the shot noise is delta correlated, the

term also gives a linear correction to the shot noise level,

$$\begin{aligned}
 & \frac{1}{(2\pi)^2} \left\langle \int \Delta(\omega - \omega') a_v^\dagger(\omega') \int \Delta(\omega - \omega'') a_v(\omega'') d\omega' d\omega'' \right\rangle \\
 &= \left\langle \text{FT}_\tau \left[\int_w a_v^\dagger(t) a_v(t + \tau) \Delta(t) \Delta(t + \tau) dt \right] \right\rangle \\
 &= \text{FT}_\tau \left[\int_w \langle \Delta(t) \Delta(t + \tau) \rangle \langle a_v^\dagger(t) a_v(t + \tau) \rangle dt \right] \\
 &= \int S_{\Delta\Delta}(\omega - \omega') \langle a_v^\dagger(\omega') a_v(\omega') \rangle d\omega' / 2\pi = \langle \Delta^2 \rangle \langle a_v^\dagger(\omega) a_v(\omega) \rangle. \tag{2.113}
 \end{aligned}$$

Based on these expressions, we can now check the shot noise contributions in the photocurrent,

$$\begin{aligned}
 \delta I(\omega) &= |a| [e^{-i\theta'} (\delta a_{0,v}(\omega) + \delta a_{1,v}(\omega) + \delta a_{2,v}(\omega))] \\
 &\quad + |a| [e^{i\theta'} (\delta a_{0,v}^\dagger(\omega) + \delta a_{1,v}^\dagger(\omega) + \delta a_{2,v}^\dagger(\omega))] \\
 &+ \sum_{i=0,1} \int \delta a_{i,v}^\dagger(\omega') \delta a_{2-i,\Delta}(\omega - \omega') d\omega' / 2\pi + \sum_{i=1,2} \int \delta a_{i,\Delta}^\dagger(\omega') \delta a_{2-i,v}(\omega - \omega') d\omega' / 2\pi \\
 &\quad + \int \delta a_{0,v}^\dagger(\omega') \delta a_{1,\Delta}(\omega - \omega') d\omega' / 2\pi + \int \delta a_{1,\Delta}^\dagger(\omega') \delta a_{0,v}(\omega - \omega') d\omega' / 2\pi \tag{2.114}
 \end{aligned}$$

from which we could derive the photocurrent PSD,

$$\begin{aligned}
 S_{II}(\omega) &= \langle I(\omega) I(\omega) \rangle \\
 &= \text{Sym} \left[\left\langle |a|^2 \left(\delta a_{0,v}(\omega) \delta a_{0,v}^\dagger(\omega) + \delta a_{1,v}(\omega) \delta a_{1,v}^\dagger(\omega) \right. \right. \right. \\
 &\quad \left. \left. + \delta a_{0,v}(\omega) \delta a_{2,v}^\dagger(\omega) + \delta a_{2,v}(\omega) \delta a_{0,v}^\dagger(\omega) \right) \right. \\
 &\quad \left. + |a| e^{-i\theta'} \left[\delta a_{0,v}(\omega) \left[\sum_{i=0,1} \int \delta a_{i,v}^\dagger(\omega') \delta a_{2-i,\Delta}(\omega - \omega') d\omega' / 2\pi \right] \right. \right. \\
 &\quad \left. \left. + \delta a_{1,v}(\omega) \int \delta a_{0,v}^\dagger(\omega') \delta a_{1,\Delta}(\omega - \omega') d\omega' / 2\pi \right] \right. \\
 &\quad \left. + |a| e^{i\theta'} \left[\left[\sum_{i=1,2} \int \delta a_{i,\Delta}^\dagger(\omega') \delta a_{2-i,v}(\omega - \omega') d\omega' / 2\pi \right] \delta a_{0,v}^\dagger(\omega) \right. \right. \\
 &\quad \left. \left. + \int \delta a_{1,\Delta}^\dagger(\omega') \delta a_{0,v}(\omega - \omega') d\omega' / 2\pi \right] \delta a_{1,v}^\dagger(\omega) \right] \\
 &\quad \left. + \int \delta a_{1,\Delta}^\dagger(\omega') \delta a_{0,v}(\omega - \omega') d\omega' / 2\pi \int \delta a_{0,v}^\dagger(\omega') \delta a_{1,\Delta}(\omega - \omega') d\omega' / 2\pi \right\rangle \tag{2.115}
 \end{aligned}$$

$$\begin{aligned}
 &= |a|^2 \chi_{0,v}(\omega) \chi_{0,v}^*(\omega) + 2|a|^2 \langle \Delta^2 \rangle [\text{Real}[\chi_{0,v}(\omega) \chi_{2,v}^*(\omega)] + |\chi_{1,v}(\omega)|^2] \\
 &\quad + 2|a| \langle \Delta^2 \rangle \text{Real}[e^{-i\theta'} \chi_{0,v}(\omega) \chi_{0,v}^*(\omega) \chi_{2,\Delta}(-\omega) + \chi_{1,v}^*(\omega) \chi_{1,\Delta}(-\omega)] \\
 &+ 2|a| \langle \Delta^2 \rangle \text{Real}[e^{-i\theta'} \chi_{1,v}(\omega) \chi_{0,v}^*(\omega) \chi_{1,\Delta}(-\omega)] + \langle \Delta^2 \rangle |\chi_{0,v}(\omega)|^2 |\chi_{1,\Delta}(-\omega)|^2, \tag{2.116}
 \end{aligned}$$

Chapter 2. Experimental platform for room-temperature quantum optomechanics

where the susceptibilities are defined as

$$\begin{aligned}\chi_{0,v}(\omega) &= \frac{i(-\omega - \Delta) + \kappa/2 - \kappa_v}{i(-\omega - \Delta) + \kappa/2} & \chi_{1,v}(\omega) &= \frac{-i\kappa_v}{[i(-\omega - \Delta) + \kappa/2][-i\Delta + \kappa/2]} \\ \chi_{2,v}(\omega) &= \frac{\kappa_v}{[i(-\omega - \Delta) + \kappa/2][-i\Delta + \kappa/2]^2} \\ \chi_{1,\Delta}(\omega) &= |a_{\text{sig}}| \frac{i}{i(-\omega - \Delta) + \kappa/2} & \chi_{2,\Delta}(\omega) &= |a_{\text{sig}}| \frac{-1}{[i(-\omega - \Delta) + \kappa/2][-i\Delta + \kappa/2]}\end{aligned}\quad (2.117)$$

From these expressions, we can see that the level of modification of the shot noise depends on the quadrature angle. The actual modification of the shot noise also needs to be corrected from the DC field intensity because now the change of quadrature angle changes the photocurrent for a single-port homodyne, and the mixing process also changes the average DC field (stationary cavity output). We examine this particular DC field correction from the noise mixing process in the following.

DC correction from the L-N series

Here, we check whether the shot noise increases or decreases relative to the mean field after mixing. The first thing we check is the modification on the DC field due to the nonlinear effect since the zero-order solution

$$a_0(\omega) = f(\omega) = \frac{\sqrt{\kappa_p} \bar{a}_p 2\pi \delta(\omega)}{i(-\omega - \Delta) + \kappa/2}, \quad (2.118)$$

only contains the trivial mean-field solution independent of the noises in Δ . Here, we ignore the vacuum fluctuations because they contribute negligibly to the total fluctuations. The first order solution does not provide any DC components since $\Delta(\omega = 0) = 0$,

$$\begin{aligned}\frac{1}{\tau} \int_{\tau \rightarrow \infty} \text{FT}_t^{-1}[a_1(\omega)] dt &= \frac{1}{2\pi\tau} \int_{\tau} e^{-i\omega t} a_1(\omega) dt d\omega \\ &= \frac{1}{\tau} \int \delta(\omega) a_1(\omega) d\omega = \frac{a_1(0)}{\tau} = 0.\end{aligned}\quad (2.119)$$

The second-order correction is more interesting as

$$\begin{aligned}\frac{1}{\tau} \int_{\tau \rightarrow \infty} \text{FT}_t^{-1}[a_2(\omega)] dt &= \frac{a_2(0)}{\tau} = - \int \frac{\bar{a}}{[-i\Delta + \kappa/2][-i(\omega + \Delta) + \kappa/2]} \frac{|\Delta(\omega)|^2}{\tau} \frac{d\omega}{2\pi} \\ &= - \frac{\bar{a} \langle \Delta^2 \rangle}{[-i\Delta + \kappa/2]^2}\end{aligned}\quad (2.120)$$

which modifies the field in a DC manner. The photocurrent nonlinear term also contributes in the same way

$$\frac{1}{\tau} \int_{\tau \rightarrow \infty} \text{FT}_t^{-1} \left[\int a_1^\dagger(\omega - \omega') a_1(\omega') d\omega' / 2\pi \right] dt = \frac{\int a_1^\dagger(-\omega') a_1(\omega') d\omega'}{2\pi\tau} = \frac{|\bar{a}|^2 \langle \Delta^2 \rangle}{\Delta^2 + \kappa^2/4}. \quad (2.121)$$

Summing up the contribution from both the field nonlinearity and the photodetection nonlinearity, the total modification to the stationary output current is

$$\delta I = |a_{\text{sig}}| \langle \Delta^2 \rangle \left[-2|a| \text{Real} \left[e^{-i\theta'} \frac{1}{[-i\Delta + \kappa/2]^2} \right] + |a_{\text{sig}}| \frac{1}{\Delta^2 + \kappa^2/4} \right]. \quad (2.122)$$

To my surprise, when the laser is on the magic detuning, and the homodyne is operated with second-order noise canceled out, we find that the output DC does not change ($\delta I = 0$) due to the nonlinear mixing process. In the following, we show a more straightforward derivation of this result using Taylor expansion.

DC correction from Taylor expansion

One can also easily obtain a similar expression of the cavity output flux using Taylor expansion of the stationary solution around $\bar{\Delta}$,

$$a = \frac{\sqrt{\kappa_p}(\bar{a}_p + \delta a_p) + \sqrt{\kappa_v} \delta a_v + \dots}{-i\Delta + i\delta\Delta(t) + \kappa/2} \\ = \frac{\sqrt{\kappa_p}(\bar{a}_p + \delta a_p) + \sqrt{\kappa_v} \delta a_v}{-i\Delta + \kappa/2} \left[1 - \frac{i\delta\Delta}{-i\Delta + \kappa/2} + \left(\frac{i\delta\Delta}{-i\Delta + \kappa/2} \right)^2 - \left(\frac{i\delta\Delta}{-i\Delta + \kappa/2} \right)^3 + \dots \right] \quad (2.123)$$

$$a_{\text{out}} = \delta a_v - \frac{\sqrt{\kappa_v \kappa_p}(\bar{a}_p + \delta a_p) + \kappa_v \delta a_v}{-i\Delta + \kappa/2} \\ \times \left[1 - \frac{i\delta\Delta}{-i\Delta + \kappa/2} + \left(\frac{i\delta\Delta}{-i\Delta + \kappa/2} \right)^2 - \left(\frac{i\delta\Delta}{-i\Delta + \kappa/2} \right)^3 + \dots \right] \quad (2.124)$$

$$I = a_{\text{out}}^\dagger a_{\text{out}} = |a|^2 \left[1 + \frac{\delta\Delta^2}{\Delta^2 + \kappa^2/4} - 2 \text{Real} \left[\frac{\delta\Delta^2}{(-i\Delta + \kappa/2)^2} \right] \right] - 2|a|^2 \text{Real} \left[\frac{i\delta\Delta}{-i\Delta + \kappa/2} \right] \\ + 2|a| \text{Real} \left[\left(\delta a_v - \frac{\sqrt{\kappa_v \kappa_p} \delta a_p + \kappa_v \delta a_v}{-i\Delta + \kappa/2} \left[1 - \frac{i\delta\Delta}{-i\Delta + \kappa/2} + \left(\frac{i\delta\Delta}{-i\Delta + \kappa/2} \right)^2 + \dots \right] \right) \right. \\ \left. \times \left[1 - \frac{i\delta\Delta}{-i\Delta + \kappa/2} + \left(\frac{i\delta\Delta}{-i\Delta + \kappa/2} \right)^2 + \dots \right]^* \right] \quad (2.125)$$

By keeping only the $\delta\Delta^2$ terms, one arrives precisely at the direct detection case of Eq.(2.122).

For the quadrature detection, the local oscillator field is injected into the signal field, and this

Chapter 2. Experimental platform for room-temperature quantum optomechanics

results in a new set of equations for the photocurrent

$$\begin{aligned}
 I = a_{\text{out}}^\dagger a_{\text{out}} = & \left[|a|^2 + |a_{\text{sig}}|^2 \frac{\delta\Delta^2}{\Delta^2 + \kappa^2/4} - 2|a||a_{\text{sig}}| \text{Real} \left[\frac{e^{-i\theta} \delta\Delta^2}{(-i\Delta + \kappa/2)^2} \right] \right] \\
 & - 2|a||a_{\text{sig}}| \text{Real} \left[\frac{ie^{-i\theta} \delta\Delta}{-i\Delta + \kappa/2} \right] \\
 + 2\text{Real} & \left[\left(\delta a_v - \frac{\sqrt{\kappa_v \kappa_p} \delta a_p + \kappa_v \delta a_v}{-i\Delta + \kappa/2} \left[1 - \frac{i\delta\Delta}{-i\Delta + \kappa/2} + \left(\frac{i\delta\Delta}{-i\Delta + \kappa/2} \right)^2 + \dots \right] \right) \right. \\
 & \left. \times \left[|a|e^{i\theta} + |a_{\text{sig}}| \left(-\frac{i\delta\Delta}{-i\Delta + \kappa/2} + \left(\frac{i\delta\Delta}{-i\Delta + \kappa/2} \right)^2 + \dots \right) \right]^* \right] \quad (2.126)
 \end{aligned}$$

By keeping only the $\delta\Delta^2$ terms again, one arrives exactly at Eq.(2.122). With the results derived for the DC modification, we now analyze the vacuum noise modification due to the nonlinear mixing noise.

Vacuum noise modification

Using the expressions derived above, we can analyze how shot noise is modified relative to the DC modification.

It is a tedious job, but we can isolate the terms associated with the output port δa_v ,

$$\begin{aligned}
 & 2|a|^2 \text{Real} \left[\frac{-\kappa_v}{-i\Delta + \kappa/2} \frac{i\Delta + \kappa/2 - \kappa_v}{i\Delta + \kappa/2} \frac{-\delta\Delta^2}{(-i\Delta + \kappa/2)^2} \right] + |a|^2 \left| \frac{-\kappa_v}{-i\Delta + \kappa/2} \right|^2 \frac{\delta\Delta^2}{\Delta^2 + \kappa^2/4} \\
 & + |a_{\text{sig}}|^2 \left| \frac{-i\Delta + \kappa/2 - \kappa_v}{-i\Delta + \kappa/2} \right|^2 \frac{\delta\Delta^2}{\Delta^2 + \kappa^2/4} + 2|a||a_{\text{sig}}| \left| \frac{-i\Delta + \kappa/2 - \kappa_v}{-i\Delta + \kappa/2} \right|^2 \text{Real} \left[\frac{-e^{-i\theta} \delta\Delta^2}{(-i\Delta + \kappa/2)^2} \right] \\
 & + 2|a||a_{\text{sig}}| \text{Real} \left[\frac{-\kappa_v}{i\Delta + \kappa/2} \frac{-i\Delta + \kappa/2 - \kappa_v}{-i\Delta + \kappa/2} \left[\frac{e^{-i\theta} \delta\Delta^2}{|-i\Delta + \kappa/2|^2} + \frac{-e^{i\theta} \delta\Delta^2}{(i\Delta + \kappa/2)^2} \right] \right],
 \end{aligned}$$

as well as the input port δa_p ,

$$\begin{aligned}
 & \frac{\kappa_v \kappa_p}{\Delta^2 + \kappa^2/4} \left[2|a|^2 \text{Real} \left[\frac{-\delta\Delta^2}{(-i\Delta + \kappa/2)^2} \right] + 4|a||a_{\text{sig}}| \text{Real} \left[\frac{-e^{-i\theta} \delta\Delta^2}{(-i\Delta + \kappa/2)^2} \right] \right] \\
 & + \left[|a|e^{-i\theta} + |a_{\text{sig}}| \right]^2 \frac{\delta\Delta^2}{\Delta^2 + \kappa^2/4}
 \end{aligned}$$

We find that the correction terms associated with the shot noise do not generally coincide with the DC correction. For the vacuum port δa_v , because of the interference with the input vacuum field from the input-output relation, it generally does not coincide with the DC correction, no matter the quadrature angle.

In the following, we analyze the modification of the shot noise from numerical simulation using the expressions derived above. At the magic detuning and field ratio (no modification of

2.4 Thermal intermodulation noise

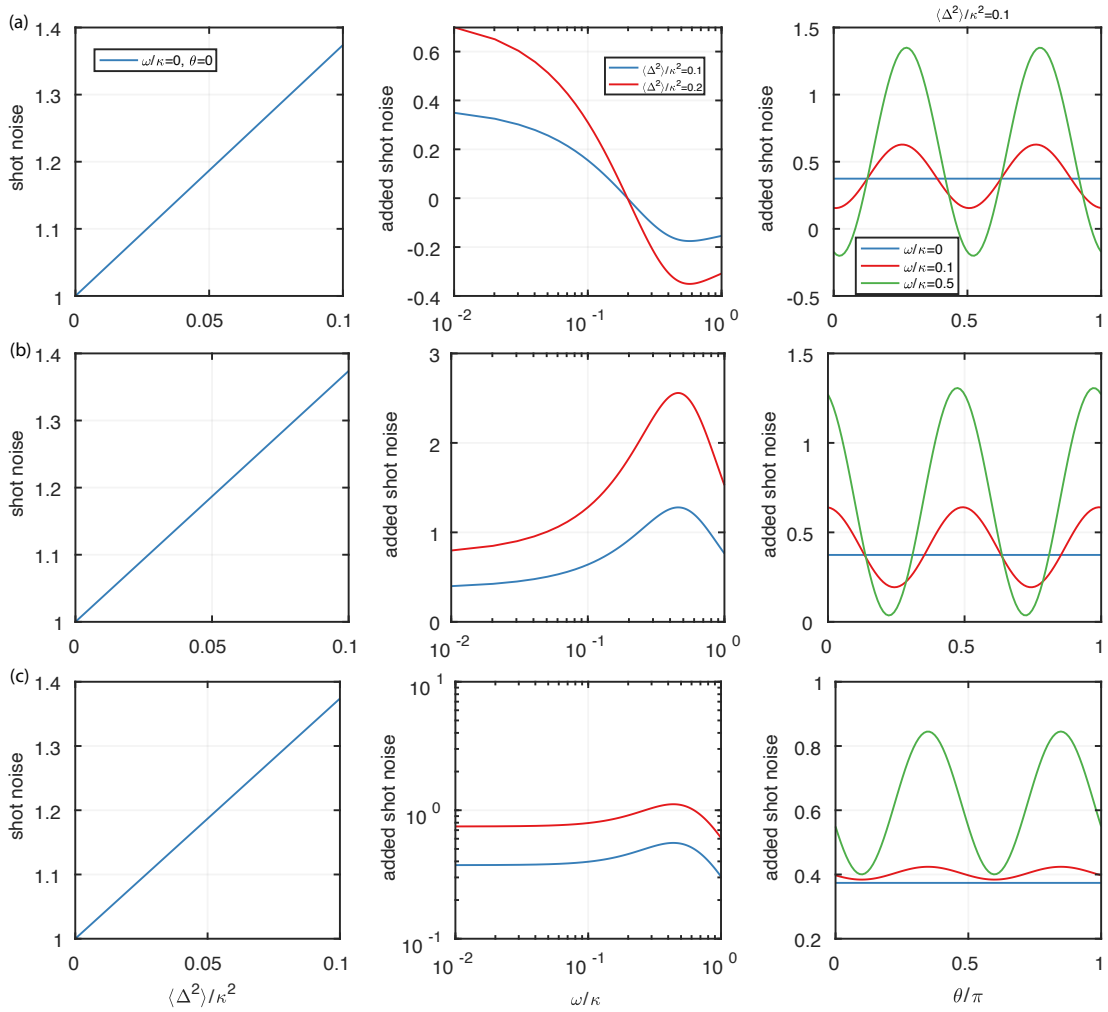


Figure 2.22: Shot noise modification at, left to right: different detuning variance, Fourier frequencies, and detection quadrature angles for **(a)** positive frequency, **(b)** negative frequency, and **(c)** symmetrized spectra. Depending on laser detuning, the noise reduction happens on one side of the Fourier frequency but can be detected neither in homodyne nor heterodyne.

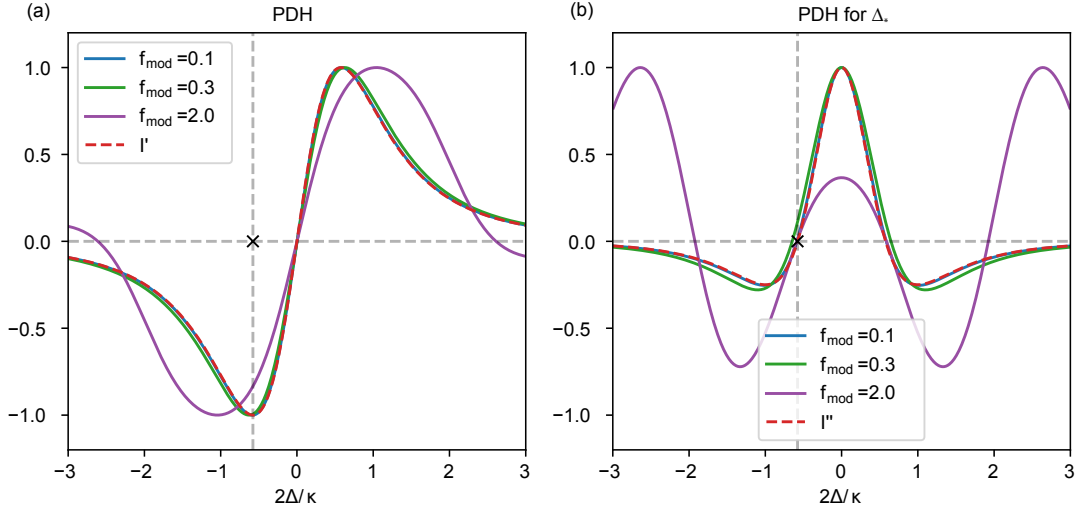


Figure 2.23: Comparison between conventional PDH signal vs. the modified PDH signal for locking at Δ_* . The signal null point at the magic detuning Δ_* is marked by the crossing point of the two dashed lines. **(a)** Comparison of the PDH signal modulated at different frequencies $f_{\text{mod}} = 2\Omega_{\text{mod}}/\kappa$. The red dashed line is the first derivative of cavity transmission $\partial I(\Delta)/\partial\Delta$. **(b)** Comparison of the modified PDH signal modulated at different frequencies f_{mod} . The red dashed line is the second derivative of cavity transmission $\partial^2 I(\Delta)/\partial\Delta^2$.

detection current), we plot out the shot noise modification in Fig.2.22 at different detuning variances $\langle\Delta^2\rangle$, Fourier frequencies ω/κ , and detection quadrature angles θ .

Notice that the spectrum is not symmetric in Fourier frequency, because of the asymmetric nature of the cavity susceptibility. In the experiment, we find $\langle\Delta^2\rangle/\kappa^2$ by locking to the magic detuning and recording the photo-current $I(t)$ on the oscilloscope by direct detection. There is an easy conversion $\langle\Delta^2\rangle/\kappa^2 = 3\langle\delta I^2\rangle/I^2$. $\langle\delta I^2\rangle$ can be read out from the oscilloscope with the correct measurement bandwidth, and for our highest coupling optical mode, at relatively low 100 uW input power, the factor $\langle\Delta^2\rangle/\kappa^2 \sim 6 \times 10^{-3}$, which corresponds to about 3% of shot noise increase by direct detection. The modification is expected to be lower at higher pump power, where the thermomechanical noise is efficiently cooled. One thing to notice is that one can not reduce the shot noise in this particular type of mixing process.

2.4.6 Modified Pound-Drever-Hall lock for the magic detuning

To operate in a quantum-noise-limited way for the MIM experiment at room temperature, we need to lock the laser at the magic detuning on the red side of the cavity mode. Conventional Pound-Drever-Hall (PDH) locking scheme [66] is not convenient for this purpose since the error signal $e(\Delta)$ is roughly the derivative $\partial I(\Delta)/\partial\Delta$ (i.e. the linear transduction function) of the cavity transmission $I(\Delta)$, and the magic detuning $2\Delta_*/\kappa = 1/\sqrt{3}$ is very close to the max/min point of the PDH signal (i.e. turning point $\partial^2 I(\Delta_*)/\partial\Delta^2 = 0$ of the linear transduction

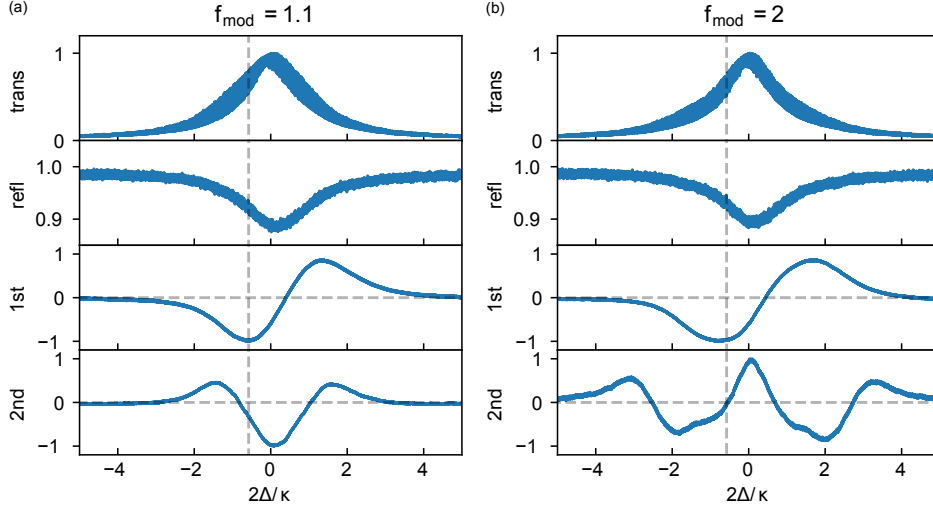


Figure 2.24: Measured signals including cavity transmission, reflection, PDH signal and modified PDH signal for locking at Δ_* . The f_{mod} is set to 1.1 in (a) and 2 in (b). The signal null point at the magic detuning Δ_* is marked by the crossing point of the two dashed lines.

). On the other hand, the PDH locking scheme loses the advantage over the conventional side-of-the-line lock as it is now also sensitive to the amplitude fluctuation of the locking signal, e.g., caused by the optical beam pointing error.

One could directly do a side-of-the-line lock at the cavity transmission port, but it poses an inconvenience during an optical power sweep since the lock is not at a null point of the error signal $I(\Delta_*) \neq 0$. Here, we show a modified PDH lock such that magic detuning is precisely at the null point of the error signal so that a continuous optical power sweep can be done.

The inspiration draws from the fact that the PDH signal is terrible for the lock of magic detuning, which is on the turning point $\partial^2 I(\Delta_*)/\partial\Delta^2 = 0$ of the PDH signal $\partial I(\Delta)/\partial\Delta$. If we take one further derivative of the PDH signal and use it as the error signal, the magic detuning would be precisely on the null point. This point is illustrated in Fig. 2.23. Note that the error signal can be mapped closely to the first derivative $\partial I(\Delta)/\partial\Delta$ only when the PDH modulation frequency $\Omega_{\text{mod}} \ll \kappa$. In most cases, there are deviations from this convenient relation.

To retrieve the second derivative of the cavity transfer function $\partial^2 I(\Delta)/\partial\Delta^2$, for the use as the error signal, we phase modulate the laser at two frequencies Ω_{mod} and $0.65\Omega_{\text{mod}}$. The selection is to prevent overlapping sum/difference frequency sidebands. Then, we demodulate the cavity reflection signal twice, at each modulation frequency, with a specific phase offset. The phase offsets optimize the error signal such that Δ_* is at the null point of $e(\Delta)$, with a decent differential locking gradient. Physically, the error signal here represents the cavity's ability to generate sum/difference frequency sidebands of the two modulation tones, where Δ_* corresponds precisely to the point where the cavity fails to initiate this frequency mixing

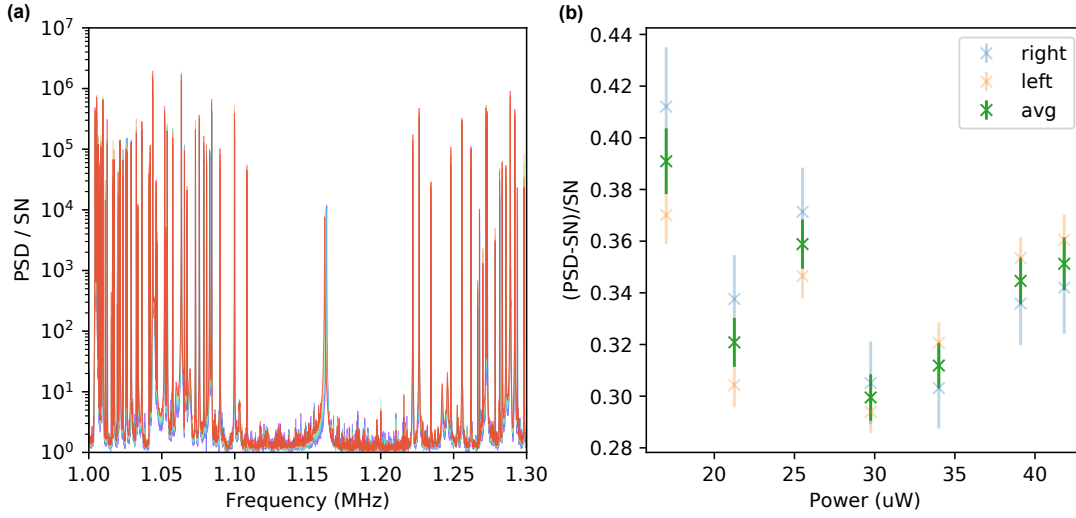


Figure 2.25: Optical power sweep using the modified PDH lock at Δ_* . **(a)** Transmission spectra at different measurement powers. **(b)** The averaged power spectrum density normalized to the shot noise level at different optical powers. The average is taken at the left and right sides of the mechanical bandgap. The power shown here is the measured power at the transmission port of the cavity.

process.

In the experiment, we obtain all the relevant signals, including cavity transmission, reflection, PDH signal, and the modified PDH signal, with the results shown in Fig. 2.24. With $f_{\text{mod}} = 2$, we can lock the laser precisely at Δ_* and is not sensitive to the optical power change. To illustrate these benefits, we conduct a continuous power sweep without any need to adjust the locking offset, with the result shown in Fig. 2.25. From the result, we can observe the dynamical backaction effects on the isolated soft-clamped mode in the center of the mechanical bandgap. We also observe that the residual TIN discussed in Section 2.4.2, manifests as noisy spikes inside the bandgap. In this sweep, we cannot access the high power level used for the quantum optomechanical experiment, due to the limited power budget from the lithium niobate high-speed phase modulator.

Nevertheless, we observe a steady drop of the averaged noise within the bandgap, due to the effective dynamical backaction cooling of the mechanical modes when pumping at Δ_* . This particular power scaling also rules out the noise origin from any linear classical noise process. Ultimately, we resort to a side-of-the-line lock for the MIM experiment, because of the requirement for high-power operation.

2.4.7 Reducing cavity transduction nonlinearity

Electro-optic phase modulators (EOMs) also provide us a way to modify indirectly the cavity transduction response, and thus help reduce the TIN inside the cavity. As discussed in the previous section, the ability to generate the second-order nonlinear noise is critically tied to the second derivative of the cavity transmission $\partial^2 I(\Delta)/\partial\Delta^2$. Using sideband modulations, we can effectively modify the transmission response $I(\Delta)$ to laser detuning, effectively suppressing the nonlinear noise generation associated with the fast-cavity limit. The expression of the transmission in the presence of an EOM drive is

$$I(\Delta) = \sum_{k=-\infty}^{+\infty} J_k(\beta)^2 L(\Delta + k\Omega_{\text{mod}}) \quad (2.127)$$

$$L(\Delta) = \frac{1}{1 + (2\Delta/\kappa)^2} \quad (2.128)$$

where β is the modulation depth, Ω_{mod} the modulation frequency, and $L(\Delta)$ the cavity transfer function. It is assumed that the detector bandwidth and the optomechanical coupling bandwidth are much smaller than the Ω_{mod} , so cross-talk between sidebands can be safely ignored.

However, this method can not help the noise generated due to the breakdown of the fast-cavity limit, as illustrated in the previous section. Therefore, it presents an effective way to observe the residue second-order TIN due to the finite cavity response speed (discussed in Section 2.4.2), by eliminating the third-order TIN noise induced by the fast cavity.

The effect of modification of cavity transfer function by the application of frequency modulation tone $f_{\text{mod}} = 1$ (chosen to avoid sideband cross-talk) at different modulation depths is shown in Fig. 2.26, as well as the sensitivity to the applied modulation frequency and depth. We could see that around depth $\beta = 0.94$, the linear transduction function δI_{li} shows a very flat plateau, where the higher-order transduction δI_{nl} shows orders of magnitude reduction between $2\Delta/\kappa = [-1, -0.75]$. This significantly suppresses not only the second-order transduction $\delta I_{2\text{nd}}$ but also all the higher-order ones, e.g., $\delta I_{3\text{rd}}$. This modulation technique has great benefits for the following reasons:

- The bandwidth of the Δ_* : $|\delta I_{\text{nl}}(\Delta_*)| \ll 1$ is greatly improved, therefore less sensitive to the cavity detuning drift.
- When operating at Δ_* , we are no longer limited by the third-order nonlinear noise, as all the higher-order noises are also efficiently suppressed.

To demonstrate these effects, we conduct experiments at two optical modes with different cavity linewidth ($\kappa/2\pi = 34.2$ MHz at 819 nm and $\kappa/2\pi = 55.3$ MHz at 810 nm). We calibrated the cavity linewidth accurately as we are very sensitive to the modulation frequency ratio $f_{\text{mod}} = 1$. The modulation depth is also calibrated accurately using a heterodyne beat note of the phase-modulated light.

Chapter 2. Experimental platform for room-temperature quantum optomechanics

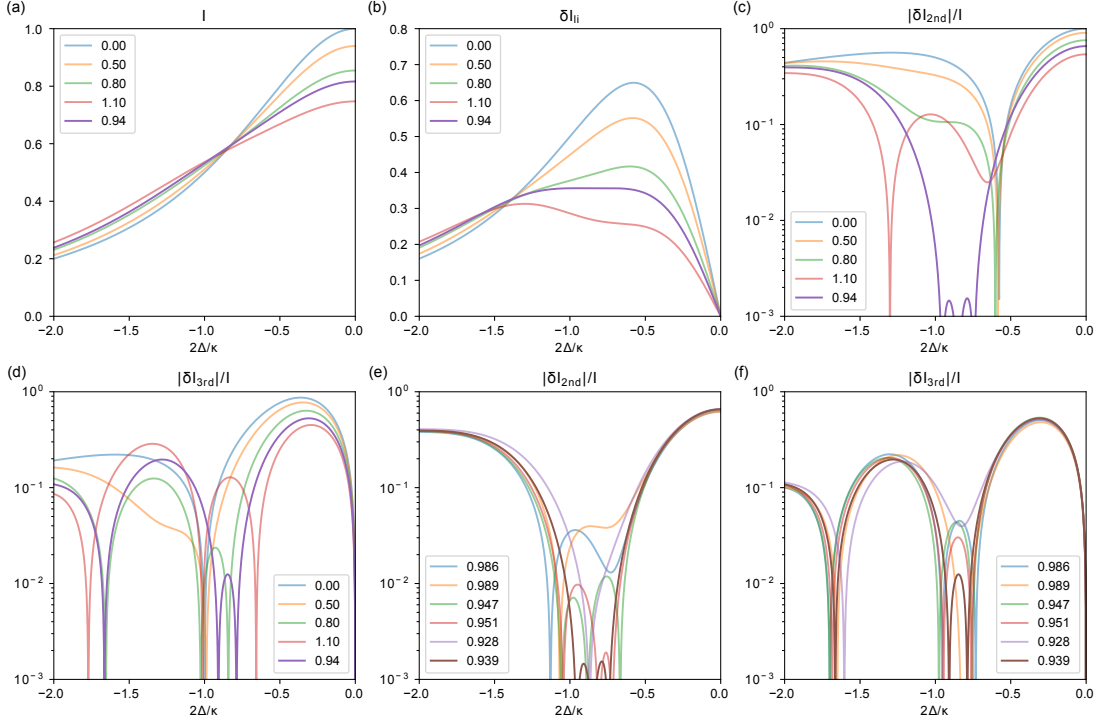


Figure 2.26: Modification of the cavity transfer function $I(\Delta)$ at different modulation depth with modulation frequency $f_{\text{mod}} = 1$. **(a)** Cavity transmission $I(\Delta)$. **(b)** Linear transduction $\delta I_{lj} = \partial I(\Delta)/\partial \Delta$. **(c)** Second-order nonlinear transduction $2\delta I_{2\text{nd}} = \partial^2 I(\Delta)/\partial \Delta^2$. **(d)** Third-order nonlinear transduction $6\delta I_{3\text{rd}} = \partial^3 I(\Delta)/\partial \Delta^3$. **(e,f)** The same quantities as defined above, but with random 5% perturbation on the modulation depth and frequency to visualize the sensitivity to these two parameters.

The experiment results are illustrated in Fig. 2.27 and Fig. 2.28, showing consistent behavior across different optical modes with different optical properties. The theoretical model considers the effect of optical cooling of mechanical modes at different cavity detuning. When no EOM is applied, the second order TIN is shown to correctly cancel exactly and only at $2\Delta_*/\kappa = 1/\sqrt{3}$. The noise floor at the magic detuning does not reach the noise limit predicted by the model accounting for the breakdown of the fast-cavity limit, and is limited by the third-order nonlinear noise. When EOM is applied, the second order TIN is shown to cancel at a different point but within a much larger span $2\Delta/\kappa = [-1, -0.75]$. Since the third-order TIN also cancels out, the noise is shown to be correctly limited by the residue second-order TIN predicted by the model.

Note that in the end, we do not use this method for our high-power experiments, for the following reasons:

- The application of EOM limits the optical power output to the cavity. With 25 mW input limit and 3.5 dB insertion loss, we have around 10 mW power to split for the homodyne.

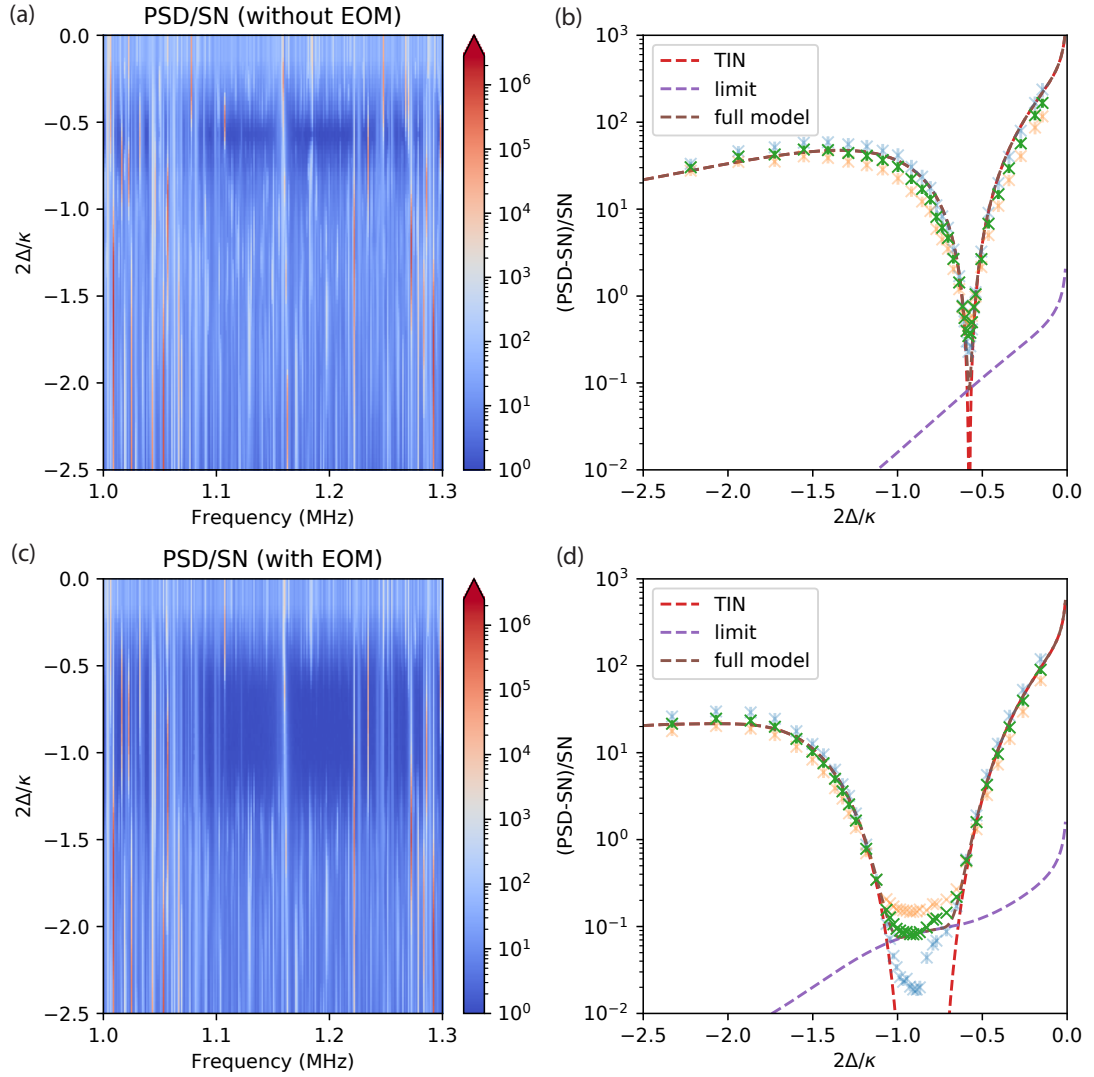


Figure 2.27: Comparison of the nonlinear noise in the mechanical bandgap with and without EOM assisted modification of cavity transduction response. The cavity mode is at 810 nm with $\kappa/2\pi = 55.3$ MHz. For the case without EOM: **(a)** Cavity transmission spectrum at different detuning, showing a small region around the magic detuning $2\Delta_*/\kappa = 1/\sqrt{3}$ where the bandgap is low on spikes. **(b)** Averaged noise density on the left (yellow) and right (blue) of the soft-clamped mechanical mode within the mechanical bandgap. The two's geometric average (green) is also shown to cancel out the effects of the mechanical susceptibility of the soft-clamped mode. The third-order nonlinear noise on the magic detuning limits the noise floor. For the case with EOM: **(c,d)** The detuning span where the nonlinear noise gets efficiently reduced is greatly improved. The third-order nonlinear noise is completely canceled, and the noise is shown to be correctly limited by the residue second-order TIN predicted by the model where the fast-cavity limit breaks down.

Chapter 2. Experimental platform for room-temperature quantum optomechanics

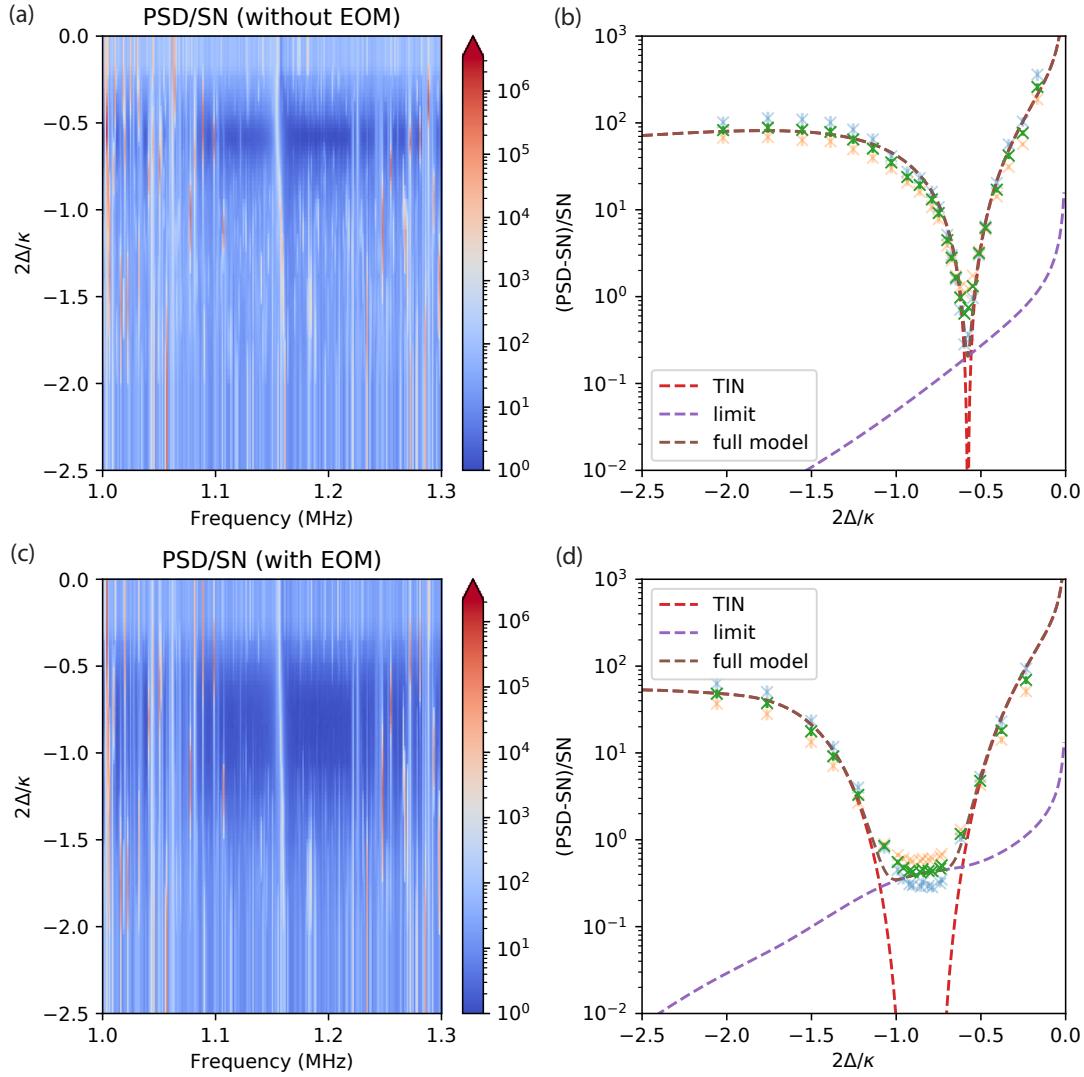


Figure 2.28: The same as the previous figure, but the cavity mode is at 819 nm with $\kappa/2\pi = 34.2$ MHz. For the case without EOM: **(a)** Cavity transmission spectrum. **(b)** Averaged noise density within the mechanical bandgap. On the magic detuning, the noise is also limited by the third-order nonlinear noise. For the case with EOM: **(c,d)** The detuning span where the nonlinear noise gets efficiently reduced is also greatly improved. The third-order nonlinear noise is again completely canceled, and the noise is shown to be correctly limited by the residue second-order TIN as well.

Our experiment needs more power than that to reach $C_q = 1$.

- Due to the presence of multiple frequency sidebands from strong phase modulation, it is hard to shape the frequency components of the local oscillator to match that of the cavity transmission. This effectively leads to mode-mismatch and causes a loss of measurement efficiency.

2.4.8 Cancelling second-order noise in a heterodyne detection

In Section 2.4.3, we discussed a reliable way to cancel second-order TIN in homodyne measurement of arbitrary optical quadrature angles. In conventional optomechanical experiments, homodyne measurement is enough for most experiments, except for the sideband asymmetry of mechanical modes near ground states. Conventional measurement of sideband asymmetry is performed using heterodyne measurement, where positive and negative frequency mechanical sidebands can be efficiently separated. The proposed single-port homodyne detection scheme will not work for heterodyne detection since the relative phase is fast scanning, and we lose that degree of freedom for nonlinear noise cancellation.

We show in Section 3.4.2 a dual homodyne scheme to effectively separate the positive and negative mechanical sidebands in postprocessing, by simultaneously detecting \hat{X} and \hat{Y} optical quadratures, from which the complex field $\hat{a} = (\hat{X} + i\hat{Y})/\sqrt{2}$ can be reconstructed. This section discusses what scheme could enable TIN cancellation directly in heterodyne detection with fast-rotating local oscillator phases.

The homodyne cancellation scheme relies on the photo-detection nonlinearity

$$I(t) \propto \bar{a}_{\text{hom}}^* [a_1(t) + a_2(t)] + h.c. + a_1^\dagger(t) a_1(t) \quad (2.129)$$

where $\bar{a}_{\text{hom}} = \bar{a}_{\text{sig}} + \bar{a}_{\text{LO}}$. Here the $a_2(t) = -\bar{a}_{\text{sig}}(-i\Delta + \kappa/2)^{-2}\delta\Delta^2$ term cancels with the $a_1^\dagger(t) a_1(t) = |\bar{a}_{\text{sig}}|^2 - i\Delta + \kappa/2)^{-2}\delta\Delta^2$ term, given a particular LO amplitude and phase.

In a balanced heterodyne/homodyne, the photocurrent reads

$$I = I_+ - I_- = \frac{1}{2}(a_{\text{sig}}^\dagger - ia_{\text{LO}}^\dagger)(a_{\text{sig}} + ia_{\text{LO}}) - \frac{1}{2}(-ia_{\text{sig}}^\dagger + a_{\text{LO}}^\dagger)(ia_{\text{sig}} + a_{\text{LO}}) \quad (2.130)$$

$$= i(a_{\text{sig}}^\dagger a_{\text{LO}} - a_{\text{sig}} a_{\text{LO}}^\dagger) \quad (2.131)$$

where all the photo-detection nonlinearity terms are canceled. Since heterodyne is averaging over all quadrature angles, there is no way to cancel the $a_2(t)$ terms at all quadrature angles.

In a naive extension of the single-port homodyne scheme, to the case of heterodyne, we still have the same photocurrent expression as Eq.(2.129), except the LO field is now rotating at frequency Ω , as in $\bar{a}_{\text{hom}} = \bar{a}_{\text{sig}} + |\bar{a}_{\text{LO}}|e^{-i(\Omega t + \theta)}$. The rotation converts the $a_2(t)$ terms to frequency Ω , with the photo-detection nonlinearity term $a_1^\dagger(t) a_1(t)$ remaining at DC. Therefore, the components around frequency Ω are identical to the balanced heterodyne scheme as in

Chapter 2. Experimental platform for room-temperature quantum optomechanics

Eq.(2.131), where the nonlinear terms cannot be canceled at all quadrature angles.

Then, the first idea is to up-shift the $a_1^\dagger(t)a_1(t)$ term also to frequency Ω , which can only be done with intensity modulation (instead of phase). For a signal light passing through a balanced Mach-Zehnder interferometer (MZI), the photocurrent is (added vacuum noise terms shortened as vac)

$$I_{\text{MZ}} = \frac{1 + \sin(\beta \cos(\Omega t + \theta_{\text{MZ}}))}{2} a_1^\dagger a + \text{vac} \approx \frac{1 + \beta \cos(\Omega t + \theta_{\text{MZ}})}{2} a_1^\dagger a + \text{vac} \quad (2.132)$$

which imprints the modulation to the $a_1^\dagger(t)a_1(t)$ term. We also obtain the amplitude modulation on the field level,

$$\begin{aligned} a_{\text{MZ}} &= \frac{1}{\sqrt{2}} (\cos(\beta \cos(\Omega t + \theta_{\text{MZ}})/2) + \sin(\beta \cos(\Omega t + \theta_{\text{MZ}})/2)) a + \text{vac} \\ &\approx \frac{1}{\sqrt{2}} (1 + \beta \cos(\Omega t + \theta_{\text{MZ}})/2) a + \text{vac}. \end{aligned} \quad (2.133)$$

Note that here, we neglect the positive second-order sideband (at frequency $+2\Omega$) through the approximation. In reality, MZI also generates higher-order sidebands when the modulation depth β is high. The generation for the second-order sidebands can be efficiently canceled when operating on the quadrature point of the MZI. For the higher-order sidebands, as long as $\beta \ll 1$, they can be efficiently suppressed, or canceled with a structured LO shown later.

Now, if we implement the single-port heterodyne scheme with the MZI operating at the quadrature point, we have

$$\begin{aligned} I(t) &\propto (\bar{a}_{\text{sig}}^* (1 + \beta \cos(\Omega t + \theta_{\text{MZ}})/2) + |\bar{a}_{\text{LO}}| e^{i(\Omega t + \theta)}) \\ &\quad (1 + \beta \cos(\Omega t + \theta_{\text{MZ}})/2) [a_1(t) + a_2(t)] + h.c. \\ &\quad + (1 + \beta \cos(\Omega t + \theta_{\text{MZ}})) a_1^\dagger(t) a_1(t). \end{aligned} \quad (2.134)$$

When we select out the components at $\pm\Omega$, which are relevant to heterodyne detection, we have

$$I(t) \propto (\beta \cos(\Omega t + \theta_{\text{MZ}}) \bar{a}_{\text{sig}}^* + |\bar{a}_{\text{LO}}| e^{i(\Omega t + \theta)}) [a_1(t) + a_2(t)] + h.c. \quad (2.135)$$

$$+ \beta \cos(\Omega t + \theta_{\text{MZ}}) a_1^\dagger(t) a_1(t). \quad (2.136)$$

The result is more or less what we want. However, the term $\beta \cos(\Omega t + \theta_{\text{MZ}}) \bar{a}_{\text{sig}}^*$ leads to non-ideal heterodyne differentiation between the positive and negative sidebands. To illustrate this

2.4 Thermal intermodulation noise

effect, we show below the heterodyne spectra with a small amount of the $\delta e^{-i\Omega t}$ component,

$$I = (e^{i\Omega t} + \delta e^{-i\Omega t})a + h.c. \quad (2.137)$$

$$S_{II}(\omega) = S_{a^\dagger a^\dagger}(\omega - \Omega) + S_{aa}(\omega + \Omega) + |\delta|^2 (S_{a^\dagger a^\dagger}(\omega + \Omega) + S_{aa}(\omega - \Omega)) \\ + 2\delta S_{a^\dagger a}(\omega + \Omega) + 2\delta^* S_{aa^\dagger}(\omega - \Omega) \quad (2.138)$$

$$2\bar{S}_{II}(\omega \rightarrow \Omega) \approx S_{a^\dagger a^\dagger}(\omega - \Omega) + S_{aa}(\Omega - \omega) \\ + |\delta|^2 (S_{a^\dagger a^\dagger}(\Omega - \omega) + S_{aa}(\omega - \Omega)) \\ + 4\text{Re}[\delta S_{a^\dagger a}(\Omega - \omega)] \quad (2.139)$$

where one can see that the presence of a counter-rotating field results in both the averaging of the negative and positive sidebands around frequency Ω , as well as an additional interference term. This is not ideal for heterodyne detection, as our target observation is the asymmetry between the negative and positive frequency sidebands.

To illustrate how we can correct this effect, we go back to the general case where we apply modulation M_1 to the signal field and M_2 to the LO field,

$$a = M_1(\bar{a}_{\text{sig}} + \delta a_{\text{sig}}) + M_2 \bar{a}_{\text{LO}} \quad (2.140)$$

$$\delta I = (|M_1|^2 \bar{a}_{\text{sig}}^* + M_1 M_2^* \bar{a}_{\text{LO}}^*) \delta a_{\text{sig}} + h.c. \\ + |M_1|^2 \delta a_{\text{sig}}^\dagger \delta a_{\text{sig}} \quad (2.141)$$

where we could find that as long as we convert the nonlinear term $\delta a_{\text{sig}}^\dagger \delta a_{\text{sig}}$ to frequency Ω , we will induce a counter rotation term associated with \bar{a}_{sig} . Therefore, M_2 provides the degree of freedom to counter this effect. Assume that with the correct M_2 , we can simplify the expression to

$$\delta I = A^* e^{i\Omega t} \delta a_{\text{sig}} + h.c. \\ + \beta \cos(\Omega t + \theta_{\text{MZ}}) \delta a_{\text{sig}}^\dagger \delta a_{\text{sig}}. \quad (2.142)$$

With this result, we could arrive at the second-order TIN cancellation condition for heterodyne detection

$$A = \bar{a}_{\text{sig}} e^{-i\theta_{\text{MZ}}} \frac{\beta}{2} \frac{i\Delta + \kappa/2}{-i\Delta + \kappa/2} \quad (2.143)$$

from which we could calculate the required modulation M_2 needed for the LO,

$$M_2 \bar{a}_{\text{LO}} = \frac{\beta}{2} \bar{a}_{\text{sig}} \left(\frac{2i\Delta}{-i\Delta + \kappa/2} e^{-i(\Omega t + \theta_{\text{MZ}})} - e^{i(\Omega t + \theta_{\text{MZ}})} \right) \quad (2.144)$$

One can immediately see that the limitation of this scheme is the low detection efficiency, both from the insertion loss of MZI, and finite modulation depth β of the first sideband to keep the higher-order sidebands sufficiently weak. However, the measurement efficiency is

Chapter 2. Experimental platform for room-temperature quantum optomechanics

not of significant concern for sideband asymmetry measurement, as long as the mechanical signal can be reliably distinguished from the background noise floor.

In Section 3.4.2, we show how to directly reconstruct field $\hat{a} = (\hat{X} + i\hat{Y})/\sqrt{2}$, and calculate asymmetric $S_{aa}(\omega)$, with a dual-homodyne scheme in post-processing, which will not be limited by the low detection efficiency required to implement a TIN-cancelled heterodyne detection physically. Our choice is a direct consequence of the fact that it is easy to cancel TIN in homodyne, whereas it is hard in heterodyne.

2.5 Absorption-induced mechanical instability

In the previous Section 2.4, we establish the fact that optical pumping at $2\Delta_*/\kappa = 1/\sqrt{3}$ (magic detuning) is required to achieve quantum-limited radiation pressure force in the cavity (by reducing TIN), as opposed to the conventional resonant pumping in most optomechanics experiments.

In this section, we discuss the emergence of mechanical instability, due to the photothermal effect of optical absorption. This effect directly results from the need to pump at Δ_* at very high power to reach high C_q . We have observed this effect extensively in the previous generation of perforated membranes due to their poor thermal dissipation from thin tethers. The optical absorption of the Si_3N_4 thin film is characterized [67] to be around 0.1-1 dB/cm, or in loss rate unit around 50-500 MHz. Contrary to what has been demonstrated in Si_3N_4 photonic integrated circuits around 0.2 dB/m (~ 1 MHz) that typically require high-temperature annealing over a long period (~ 10 hours) to reduce the impurities, our thin film is not compatible with high-temperature annealing as it loses stress over time, which is the source of the dissipation dilution. We observed that the stress relaxed by around 50% at around 200 °C with beam resonators. Note that these values are for the 20-nm Si_3N_4 thin film in our cavity, and do not describe the cavity absorption rate. The cavity absorption rate should be bounded below 20 kHz by the energy participation ratio. However, this could still result in a significant thermal effect as the thermal capacity of the membrane is also proportional to its thickness. Therefore, the magnitude of the thermal effect does not depend much on the length of the cavity.

The main effect of the mechanical instability is illustrated in Fig. 2.29 and Fig. B.3, where excitation of mechanical modes results in excess nonlinear noise within the mechanical bandgap, and eventually also the stability of the cavity lock. In our experiment, we use an infinite impulse response (IIR) filter implemented on a field-programmable gate array board (discussed in Section B.3) to feedback-damp these unstable modes. From our observation, the instability is always associated with modes that, due to symmetry reasons, always have near-zero dispersive coupling rates, illustrated in Fig. 2.30. The low dispersive coupling rate means that other coupling mechanisms, e.g., the photothermal effect, could start to dominate these modes. Therefore, it is vital to understand these effects for MIM systems, as due to symmetry reasons, many of the mechanical modes will have low dispersive couplings. This is

2.5 Absorption-induced mechanical instability

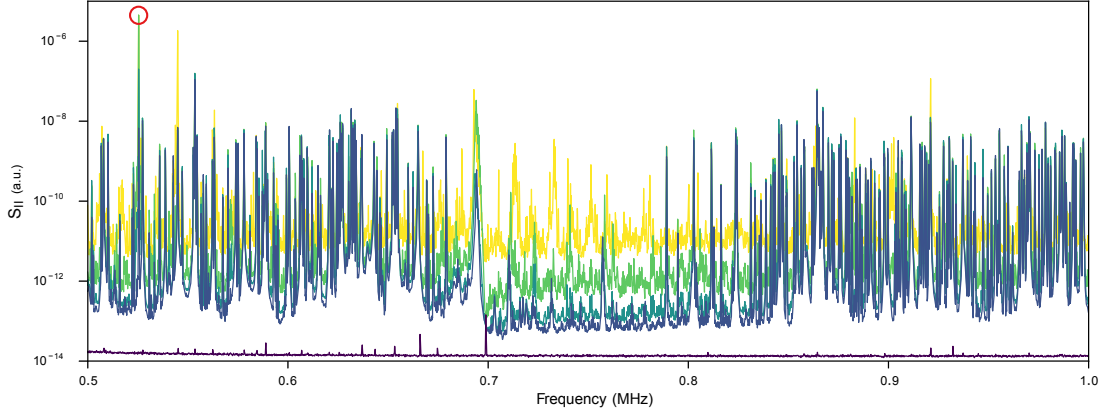


Figure 2.29: Effects of photothermal mechanical instability. The spectra are recorded at few-second intervals, with darker colors indicating earlier spectrum snapshots. We could observe that within the mechanical bandgap [0.7, 0.8]MHz, the nonlinear noise floor keeps rising. The rising noise directly results from the mechanical lasing happening around frequency 0.52 MHz (red circle), where a single mechanical mode experiences parametric gain instead of damping at red detuning. The gain results from the photothermal effect interfering with the dispersive optomechanical coupling.

illustrated in a response measurement shown in Fig. B.9, that more than half of the modes are only weakly coupled to the cavity mode.

From the observation in the experiment, the photothermal instability happens to modes between 100 kHz-500 kHz. We can estimate the spatial scale of the temperature profile associated with these modes, from the simplified 1D heat equation

$$k \frac{\partial^2 T}{\partial x^2} = \rho C \frac{\partial T}{\partial t} \quad (2.145)$$

that when driven with a heat source at frequency Ω_m , one obtains the heat propagation spatial scale at $x(\Omega_m) = \sqrt{\frac{k}{\rho C \Omega_m}} \sim 10 \mu\text{m}$. Compared to the size of the typical wavelength at this range $\sim 100 \mu\text{m}$, the temperature feedback is slow and therefore effectively delayed, and results in either damping or amplification. We modeled this effect, considering the symmetry of these mechanical modes, as well as the unconventional mechanical amplification on the red side of the cavity, using the formalism of dissipative feedback we developed [2] (Section A.3). We found that the inclusion of the photothermal force into our model results in a reversed feedback sign when the laser is detuned across a certain threshold. An illustration of the photothermal effect as a function of optical detuning is shown in Fig. 2.31(a), as well as the theoretical results shown in Fig. 2.31(b). We also observed the particular detuning dependence of the amplification in our experiment, that no matter how much power is coupled to the cavity, as long as the absolute detuning is below a certain threshold (slightly smaller than the magic detuning in our case), the mechanical instability vanishes. This observation allows us to estimate the unstable-mode-specific coupling ratio between these two forces as $|g_{\text{th}}/g_\omega| \sim 0.1$.

Chapter 2. Experimental platform for room-temperature quantum optomechanics

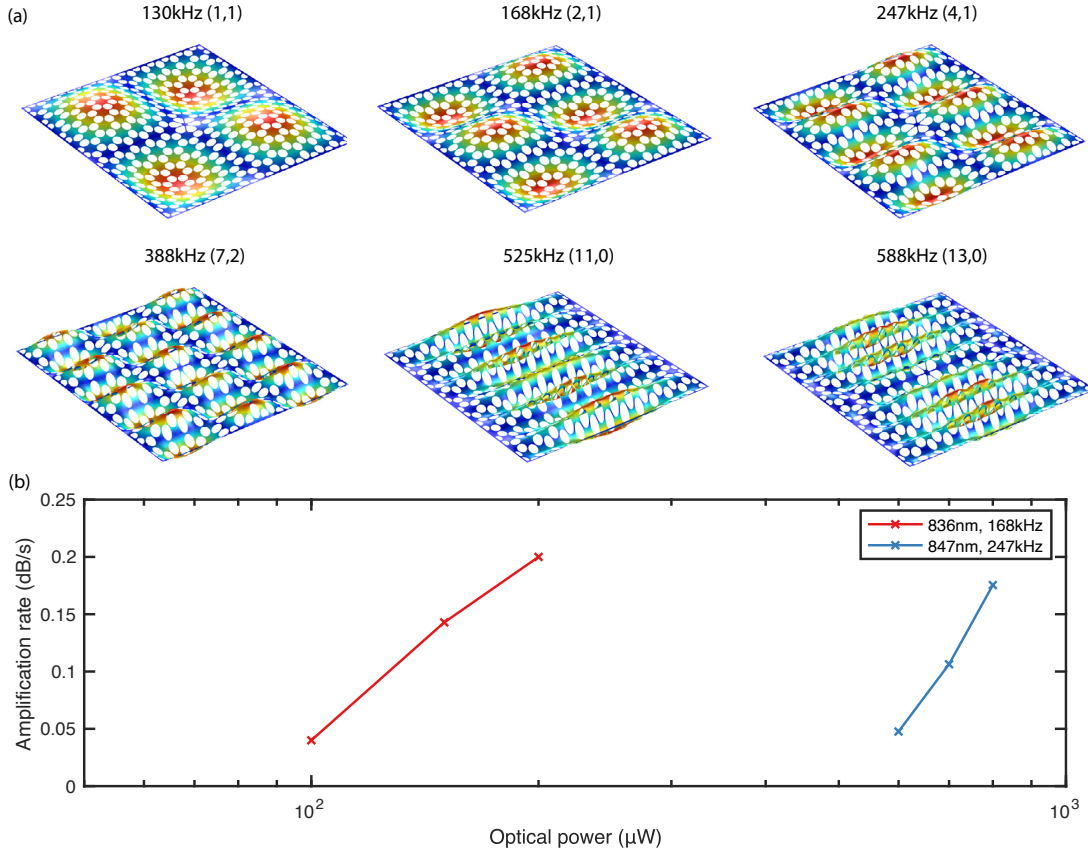


Figure 2.30: **(a)** Mechanical modes that exhibit photothermal instability, from one of the perforated membrane samples used in the experiment. **(b)** Measured ring-up rates of the first unstable mechanical modes at different optical modes. The result shows that the amplification rates are linear to optical power, suggesting unconventional anti-damping when pumping on the red side of the cavity.

In the following sections, we analyze the theoretical modeling of this effect and the experimental verification of the scaling of this effect concerning the membrane-field overlap.

In this section, we use the convention $\Delta = \Omega_0 - \Omega_{\text{laser}}$, such that red detuning is associated with $\Delta > 0$.

2.5.1 Dissipative coupling

First, we need to establish the framework of dissipative coupling, as it involves the optical bath modes as opposed to the conventional treatments of optomechanical dispersive coupling. A detailed derivation is also present in Section A.3.

To derive the dissipative coupling, we need to first go back to the original Hamiltonian with an

2.5 Absorption-induced mechanical instability

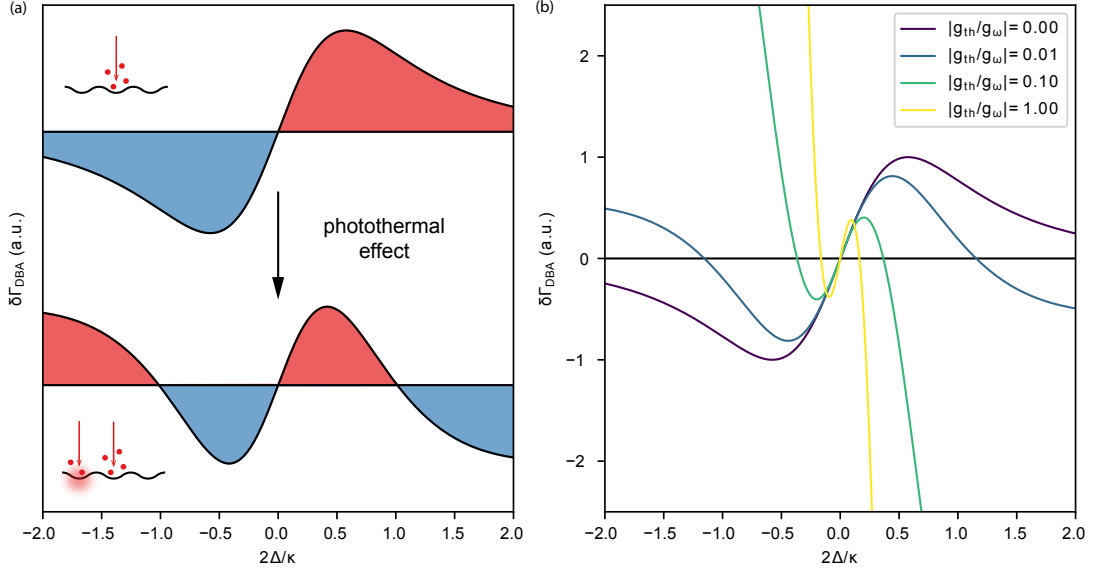


Figure 2.31: **(a)** Illustration of the modification of the dynamical backaction damping rates due to the presence of photothermal feedback force. **(b)** Normalized damping/amplification rates as a function of detuning, with different coupling ratios $|g_{\text{th}}(\Omega_m)/g_\omega|$.

optical cavity mode coupled to a bath,

$$H = \hbar\omega a^\dagger a + \int d\Omega \hbar\Omega b^\dagger(\Omega)b(\Omega) + i\hbar \int d\Omega \rho(\Omega) g(\Omega) [b(\Omega)a^\dagger - b^\dagger(\Omega)a]. \quad (2.146)$$

The optical bath modes have relation $[b(\Omega_1), b^\dagger(\Omega_2)] = \delta(\Omega_1 - \Omega_2)$, and thus we arrive at the following solution for the cavity mode

$$\dot{b}(\Omega) = \frac{i}{\hbar} [H, b(\Omega)] = -i\Omega b(\Omega) - \rho(\Omega) g(\Omega) a \quad (2.147)$$

$$b(t, \Omega) = e^{-i\Omega(t-t_0)} b(0, \Omega) - \rho(\omega) g(\Omega) \int_{t_0}^t e^{-i\Omega(t-t')} a(t') dt' \quad (2.148)$$

$$\begin{aligned} \dot{a} &= \frac{i}{\hbar} [H_{\text{sys}}, a] + \int d\Omega \rho(\Omega) g(\Omega) b(\Omega) \\ &= \frac{i}{\hbar} [H_{\text{sys}}, a] + \int d\Omega \rho(\Omega) g(\Omega) e^{-i\Omega(t-t_0)} b(0, \Omega) \\ &\quad - \int d\Omega \rho(\Omega)^2 g(\Omega)^2 \int_{t_0}^t e^{-i\Omega(t-t')} a(t') dt' \end{aligned} \quad (2.149)$$

defining $\rho(\Omega)^2 g(\Omega)^2 = \kappa/2\pi$, and input field operator $b_{\text{in}}(t) = \frac{1}{\sqrt{2\pi}} \int d\Omega e^{-i\Omega(t-t_0)} b(0, \Omega)$. Note that here, we used a different notation instead of a_{in} to help differentiate the input field a bit more from the cavity field, as it will be treated as a separate loss channel (e.g., absorption) in the following sections.

Chapter 2. Experimental platform for room-temperature quantum optomechanics

In the rotating frame of the laser drive, we have

$$\dot{a} = -\left(\frac{\kappa}{2} + i\Delta\right)a + \sqrt{\kappa}b_{\text{in}} \quad (2.150)$$

$$H_{\text{int}} = i\hbar\sqrt{\kappa}[b_{\text{in}}a^\dagger - b_{\text{in}}^\dagger a]. \quad (2.151)$$

Now we introduce optomechanical coupling to mechanical mode c , through both the dispersive coupling $d\Delta = \frac{\partial\Delta}{\partial x}dx = G_{\omega 0}dx = g_{\omega 0}(c + c^\dagger)$ and the dissipative coupling $d\kappa_0 = \frac{\partial\kappa_0}{\partial x}dx = G_{\kappa 0}dx = g_{\kappa 0}(c + c^\dagger)$, where $x = x_{\text{zpf}}(c + c^\dagger)$ is the mechanical position quadrature, in the displaced frame $a \rightarrow \bar{a} + a$, we have the following set of equations for the optical, mechanical modes, as well as the radiation pressure force,

$$\begin{aligned} \dot{a} = & -\left(\frac{\kappa}{2} + i\Delta\right)a + \sqrt{\kappa_1}a_{\text{in}} + \sqrt{\kappa_0}b_{\text{in}} \\ & + \left[-i\bar{a}g_{\omega 0} + \frac{\bar{b}_{\text{in}}/\sqrt{\kappa_0} - \bar{a}}{2}g_{\kappa 0} \right] (c + c^\dagger) \end{aligned} \quad (2.152)$$

$$\dot{c} = \left(-\frac{\Gamma_m}{2} - i\Omega_m\right)c + \sqrt{\gamma}c_{\text{in}} + \frac{ix_{\text{zpf}}F}{\hbar} \quad (2.153)$$

$$F = -\frac{dH_{\text{int}}}{dx} = \frac{\hbar}{x_{\text{zpf}}} \left[-g_{\omega 0}\bar{a}^*a + i\frac{g_{\kappa 0}}{2\sqrt{\kappa_0}}(\bar{b}_{\text{in}}a^\dagger + \bar{a}^*b_{\text{in}}) + h.c. \right] \quad (2.154)$$

For simplicity, we define $g_\omega = g_{\omega 0}\bar{a}^*$, $g_\kappa = g_{\kappa 0}\bar{a}^*$ and set $\bar{b}_{\text{in}} = 0$ since it is the loss port where vacuum is the only field input. Then, we arrive at the radiation pressure force experienced by the mechanics,

$$F = \frac{\hbar}{x_{\text{zpf}}} \left[-g_\omega a + i\frac{g_\kappa}{2\sqrt{\kappa_0}}b_{\text{in}} + h.c. \right] \quad (2.155)$$

To derive the damping/amplification rate Γ of the mechanical modes, we apply the quantum fluctuation-dissipation theorem [36] that relates force noise density with the damping rate of a quantum harmonic oscillator as a consequence of the detail balance. In the following, we calculate the spectral asymmetry of the open-loop force noise density instead of a closed-loop one. This treatment is only valid when the cavity decay κ is much faster than the rate g at which the mechanical motion modifies the optical force fluctuation. Our system is far from the strong coupling regime $g \sim \kappa$, and the approximation holds well. Note that here, we work in the RWA of the mechanical modes. However, it does not concern us since optical force noise is a consequence of optical susceptibility. We reiterate the power spectral density of quantum observable as

$$S_{AB}(\omega) \equiv \lim_{\tau \rightarrow \infty} \frac{1}{\tau} \langle A_\tau^\dagger(-\omega)B_\tau(\omega) \rangle = \iint_w \langle A^\dagger(t+\tau)B(t) \rangle e^{i\omega\tau} d\tau = \int \langle A^\dagger(\omega)B(\omega') \rangle \frac{d\omega'}{2\pi}, \quad (2.156)$$

2.5 Absorption-induced mechanical instability

where $A(\omega) = \int A(t)e^{i\omega t} dt$, and $A^\dagger(\omega) = A(-\omega)^\dagger$. The correlation of bath operators are

$$\langle a_{\text{in}}^\dagger(t+\tau)a_{\text{in}}(t) \rangle = \bar{n}_{\text{in}}\delta(\tau) \quad (2.157)$$

$$\langle a_{\text{in}}(t+\tau)a_{\text{in}}^\dagger(t) \rangle = (\bar{n}_{\text{in}}+1)\delta(\tau) \quad (2.158)$$

$$\langle a_{\text{in}}^\dagger(\omega)a_{\text{in}}(\omega') \rangle = 2\pi\delta(\omega+\omega')\bar{n}_{\text{in}} \quad (2.159)$$

$$\langle a_{\text{in}}(\omega)a_{\text{in}}^\dagger(\omega') \rangle = 2\pi\delta(\omega+\omega')(\bar{n}_{\text{in}}+1) \quad (2.160)$$

with all the other correlations equal to zero, assuming quantum-limited bath noises.

One could derive the power spectral density of the force operator F (open-loop) as

$$F(\omega) = \frac{\hbar}{x_{\text{zpf}}} \left[\frac{-g_\omega\sqrt{\kappa_1}a_{\text{in}}(\omega) + \left[-g_\omega\sqrt{k_0} + \frac{ig_\kappa}{2\sqrt{\kappa_0}}[i(-\omega+\Delta)+\kappa/2] \right] b_{\text{in}}(\omega)}{i(-\omega+\Delta)+\kappa/2} \right] + h.c. = \frac{\hbar}{x_{\text{zpf}}} [\chi_1(\omega)a_{\text{in}}(\omega) + \chi_2(\omega)b_{\text{in}}(\omega) + h.c.] \quad (2.161)$$

$$S_{FF}(\omega) = \int \langle F^\dagger(\omega)F(\omega') \rangle \frac{d\omega'}{2\pi} = \frac{\hbar^2}{x_{\text{zpf}}^2} [|\chi_1(\omega)|^2(\bar{n}_{\text{in}}+1) + |\chi_1(-\omega)|^2\bar{n}_{\text{in}} + |\chi_2(\omega)|^2] \quad (2.162)$$

where $\chi_1(\omega) = \frac{-g_\omega\sqrt{\kappa_1}}{i(-\omega+\Delta)+\kappa/2}$ and $\chi_2(\omega) = \frac{-g_\omega\sqrt{k_0} + \frac{ig_\kappa}{2\sqrt{\kappa_0}}[i(-\omega+\Delta)+\kappa/2]}{i(-\omega+\Delta)+\kappa/2}$. The damping rate and effective bath temperature for mechanical mode Ω_m is therefore

$$\Gamma = \frac{x_{\text{zpf}}^2}{\hbar^2} (S_{FF}(\Omega_m) - S_{FF}(-\Omega_m)) = |\chi_1(\Omega_m)|^2 - |\chi_1(-\Omega_m)|^2 + |\chi_2(\Omega_m)|^2 - |\chi_2(-\Omega_m)|^2 \quad (2.163)$$

$$\bar{n}_{\text{bath}} = \frac{|\chi_1(-\Omega_m)|^2(\bar{n}_{\text{in}}+1) + |\chi_1(\Omega_m)|^2\bar{n}_{\text{in}} + |\chi_2(-\Omega_m)|^2}{|\chi_1(\Omega_m)|^2 - |\chi_1(-\Omega_m)|^2 + |\chi_2(\Omega_m)|^2 - |\chi_2(-\Omega_m)|^2} \quad (2.164)$$

In the conventional dispersive coupling, where $g_\kappa = 0$ but $g_\omega \neq 0$, the expression for the damping rate can be simplified to

$$\Gamma = \frac{4|g_\omega|^2\kappa\Omega_m\Delta}{[(\Omega_m - \Delta)^2 + \kappa^2/4][(\Omega_m + \Delta)^2 + \kappa^2/4]}. \quad (2.165)$$

With red detuning $\Delta > 0$, the mechanics are effectively damped as expected from dynamical backaction cooling.

In the limit $g_\omega = 0$ but $g_\kappa \neq 0$, the damping rate is $\Gamma = 0$. The null damping rate means that with only dissipative coupling, the mechanics will neither be damped nor amplified [68].

In the circumstances that dissipative coupling and dispersive coupling coexist, the interference

Chapter 2. Experimental platform for room-temperature quantum optomechanics

of these two effects leads to the following expression

$$\Gamma = \frac{4|g_\omega|^2 \kappa \Omega_m \Delta + 2g_\omega^* g_\kappa \Omega_m (\Delta^2 - \Omega_m^2 - \kappa^2/4)}{[(\Omega_m - \Delta)^2 + \kappa^2/4][(\Omega_m + \Delta)^2 + \kappa^2/4]}. \quad (2.166)$$

In the unresolved sideband regime ($\Omega_m \ll \kappa$) we operate in, we have

$$\Gamma \approx \frac{8|g_\omega|^2 \Omega_m (2\Delta/\kappa)}{[(2\Delta/\kappa)^2 + 1]^2} \left[1 + \frac{g_{\kappa 0}}{4g_{\omega 0}} \left(\frac{\kappa}{2\Delta} - \frac{2\Delta}{\kappa} \right) \right]. \quad (2.167)$$

In the case that $\frac{g_{\kappa 0}}{4g_{\omega 0}} \left(\frac{\kappa}{2\Delta} - \frac{2\Delta}{\kappa} \right) < -1$, it is possible to reverse the sign of Γ , e.g. when pumping on the red side, the mechanics could still be amplified.

The evidence of such dissipative coupling effect (given $|\frac{g_{\kappa 0}}{g_{\omega 0}}| \sim 1$) could be verified by comparing the mechanical signal-to-noise ratio (SNR) on the optical phase and amplitude quadratures, for the modes that are unstable under a strong optical pump. When significant dissipative coupling is present, the signal should sit on the amplitude quadrature as mechanical motion modulates the amplitude to the output field.

In the experiment, we swept from the phase to amplitude quadrature. We did not observe significant deviation from the $\sin^2 \theta$ relation of the mechanical signal on the mechanically unstable modes. Here, θ is the optical quadrature angle. Therefore, we could rule out that the dissipative coupling accounts for the observed mechanical instability.

2.5.2 Photothermal effect

Even though the mechanical instability is unlikely from the dissipative coupling widely analyzed by the optomechanics community, we can not rule out the dissipative feedback effects from the non-radiation-pressure cause. E.g., temperature gradient force from optical absorption is a form of dissipative feedback [2], that originates from a dissipation channel. In these types of coupling, the dissipative force can be strong without considerable signal on the amplitude quadrature, as the coupling does not have to modulate the cavity linewidth strongly.

We can model the photothermal effect by simply adding a feedback force

$$F_{\text{th}} = \int g_{\text{th},0}(t' - t) b_{\text{out}}^\dagger(t) b_{\text{out}}(t) dt' \quad (2.168)$$

which in the frequency domain reads

$$\begin{aligned} F_{\text{th}}(\omega) &= g_{\text{th},0}(\omega) \bar{b}_{\text{out}}^* b_{\text{out}}(\omega) + h.c. = g_{\text{th},0}(\omega) \sqrt{\kappa_{\text{th}}} \bar{a}^* b_{\text{out}}(\omega) + h.c. \\ &= g_{\text{th}}(\omega) b_{\text{out}}(\omega) / \sqrt{\kappa_{\text{th}}} + h.c., \end{aligned} \quad (2.169)$$

where $g_{\text{th}}(\omega) = g_{\text{th},0}(\omega) \kappa_{\text{th}} \bar{a}^*$, and κ_{th} is the absorption rate of the cavity induced by the membrane. Here, $g_{\text{th},0}(t)$ and $g_{\text{th},0}(\omega)$ represent the material response relative to the optical

2.5 Absorption-induced mechanical instability

absorption heating. With an estimation of the time scale of the heat propagation, the response should be slow compared to mechanical oscillation frequency, and $g_{\text{th},0}(\omega)$ should be mostly imaginary.

After adding back the dispersive coupling and dissipative coupling terms, the total force now reads

$$\begin{aligned}
 F(\omega) &= \frac{\hbar}{x_{\text{zpf}}} \left[-(g_\omega + g_{\text{th}}(\omega)) a(\omega) + \frac{i g_\kappa + 2 g_{\text{th}}(\omega)}{2\sqrt{\kappa_{\text{th}}}} b_{\text{in}}(\omega) + h.c. \right] \\
 &= \frac{\hbar}{x_{\text{zpf}}} \left[(i(-\omega + \Delta) + \kappa/2)^{-1} \left(-(g_\omega + g_{\text{th}}(\omega)) \sqrt{\kappa_1} a_{\text{in}}(\omega) \right. \right. \\
 &+ \left. \left. \left[-(g_\omega + g_{\text{th}}(\omega)) \sqrt{\kappa_{\text{th}}} + \frac{i g_\kappa + 2 g_{\text{th}}(\omega)}{2\sqrt{\kappa_{\text{th}}}} [i(-\omega + \Delta) + \kappa/2] \right] b_{\text{in}}(\omega) \right) + h.c. \right] \\
 &= \frac{\hbar}{x_{\text{zpf}}} [\chi'_1(\omega) a_{\text{in}}(\omega) + \chi'_2(\omega) b_{\text{in}}(\omega) + h.c.] \tag{2.170}
 \end{aligned}$$

To derive the damping/amplification rate of this process, we can follow the same procedure as the previous section, i.e.

$$\begin{aligned}
 \Gamma &= [(\Omega_m - \Delta)^2 + \kappa^2/4]^{-1} [(\Omega_m + \Delta)^2 + \kappa^2/4]^{-1} (4|g_\omega + g_{\text{th}}(\Omega_m)|^2 \kappa \Omega_m \Delta \\
 &- 2\text{Re} [i(\Delta^2 - \Omega_m^2) \Delta - \kappa \Delta \Omega_m] (g_\omega + g_{\text{th}}(\Omega_m)) (-i g_\kappa^* + g_{\text{th}}^*(\Omega_m))]. \tag{2.171}
 \end{aligned}$$

Again, we can simplify the expression in the unresolved sideband limit ($\Omega_m \ll \kappa$),

$$\Gamma \approx \frac{4|g_\omega + g_{\text{th}}(\Omega_m)|^2 \kappa \Omega_m \Delta - 2\text{Real} [(i\Delta^3 - \kappa \Delta \Omega_m) (g_\omega + g_{\text{th}}(\Omega_m)) (-i g_\kappa^* + 2 g_{\text{th}}^*(\Omega_m))]}{[\Delta^2 + \kappa^2/4]^2}. \tag{2.172}$$

We check the case where the photothermal force dominates the dynamics again, with the dispersive coupling $g_\omega = 0$. We can find $\Gamma = 0$, and the coupling is purely dissipative. The null damping rate is intuitive as the dispersive coupling is the only mechanism to transduce the mechanical motion back into the cavity fields and thus close the feedback loop. From another perspective of force noise density, the photothermal force originates from the optical flux of a bath channel. It always gives a symmetric force spectral density set by the input-output relation. On the other hand, the dispersive force originates from the cavity photon fluctuation, whose positive and negative frequency components can be modified by the cavity susceptibility. Note that the result here is under the open-loop approximation. A more rigorous treatment would involve the photothermal force's closed-loop noise density and arrive at the following result (g_κ ignored)

$$\Gamma(\omega) = -2 \frac{\Omega_m}{\omega} \text{Re} [g_\omega (g_\omega^* + g_{\text{th}}^*(\omega)) (\chi_{\text{cav}}^*(-\omega) - \chi_{\text{cav}}(\omega))]. \tag{2.173}$$

However, the open-loop approximation is sufficient for our discussion here, as $|g_{\text{th}}| \ll \kappa, \Omega_m$.

In the case that we have weak dispersive coupling $g_\omega \sim |g_{\text{th}}(\Omega_m)|$, as is the case from our

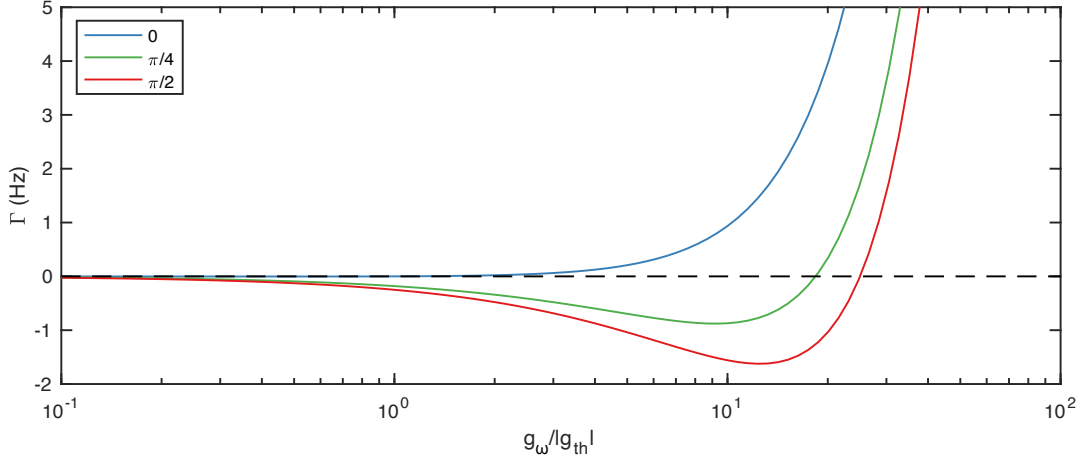


Figure 2.32: Optical backaction damping rates with the photothermal effect. Curves are plotted with different delay phase of the membrane thermal response function $g_{\text{th}}(\Omega_m)$, with realistic system parameters ($\kappa/2\pi = 30$ MHz, $\Omega_m/2\pi = 100$ kHz, $\Delta = \Delta_*$, $|g_{\text{th}}(\Omega_m)|/2\pi = 3$ kHz). The thermal cutoff for the device at mm scale is typically <10 kHz. Therefore, the delay phase is most likely $\pi/2$ for most mechanical modes (mostly imaginary), with lower coupling magnitude at higher frequency. We can observe the switching of feedback signs at different magnitudes of dispersive coupling g_ω .

observation, we could simplify to the following expression,

$$\begin{aligned} \Gamma &\approx \frac{4|g_\omega + g_{\text{th}}(\Omega_m)|^2 \kappa \Omega_m \Delta - 4\Delta^3 \text{Im}[g_\omega g_{\text{th}}^*(\Omega_m)]}{[\Delta^2 + \kappa^2/4]^2} \\ &= \frac{4|g_\omega|^2 \kappa \Omega_m \Delta}{[\Delta^2 + \kappa^2/4]^2} \left[\left| 1 + \frac{g_{\text{th}}(\Omega_m)}{g_\omega} \right|^2 + \frac{\Delta^2}{\kappa \Omega_m} \text{Im} \left[\frac{g_{\text{th}}(\Omega_m)}{g_\omega} \right] \right]. \end{aligned} \quad (2.174)$$

In the case that $-\text{Im} \left[\frac{g_{\text{th}}(\Omega_m)}{g_\omega} \right] > \frac{\kappa \Omega_m}{\Delta^2}$, the effect we observed can happen, i.e. parametric amplification at red detuning. However, this time, the amplitude quadrature has no significant mechanical signal. The detuning dependence of the damping rate is illustrated in Fig. 2.31(b), whereas the photothermal coupling rate dependence exactly on Δ_* is shown in Fig. 2.32.

In the case where $|g_{\text{th}}(\Omega_m)| \gtrsim g_\omega$, we can further simplify the expression in the fast-cavity limit $\Omega_m \ll \kappa$,

$$\Gamma \approx \frac{4\Delta^3}{[\Delta^2 + \kappa^2/4]^2} \text{Im}[g_\omega g_{\text{th}}(\Omega_m)], \quad (2.175)$$

where the dynamics now show a strong dependence on cavity detuning. This effect is verified also in the experiment, that instability quickly disappears when $|2\Delta/\kappa| < 1/\sqrt{3}$. However, as we need to pump at the magic detuning, detuning is not a free parameter to optimize here. Note that the presence of this instability requires a large imaginary component from $g_{\text{th}}(\omega)$, which is easily the case given that the thermal time scale is longer than the mechanical period.

To illustrate the parameter regions where this effect is concerned, we plot the damping rate

2.5 Absorption-induced mechanical instability

of the entire expression, with our system parameters as well as the operation condition, in Fig.2.32 and Fig. 2.31(b), showing the emergence of the amplification when the photothermal coupling rate approaches the dispersive coupling rate.

Scaling verification of photothermal effects

The photothermal effect limits the maximal C_q achievable before the onset of mechanical instability. In the previous generation of devices using perforated membranes, thermal dissipation was particularly poor and was suspected of causing high temperature gradients and large photothermal forces. Ultimately, it limits $C_q < 0.1$ for most of the optical modes we tried. In Section B.3, we discuss how to use the digital feedback to selectively stabilize these mechanical modes in order to approach $C_q \sim 1$.

Our current generation device using density-modulated membranes, with improved heat dissipation, allows us to operate at the quantum backaction dominated regime $C_q > 1$ without the need to apply digital feedback, as no mechanical modes have undergone amplification at optical power of concern. However, in the experiment, only the optical modes showing minimal membrane-field overlap $\eta(z_m)$, i.e., small g_0 and low optical loss rate κ , can achieve this regime. Modes with higher g_0 , which typically come with higher optical loss, still limit $C_q < 1$ when mechanical instability happens. An example of this effect is illustrated in the following table, where three optical resonances are characterized in terms of their maximal C_q :

Wavelength (nm)	$\kappa/2\pi$ (MHz)	$\eta(z_m)$	C_q^{\max}
843.6839	26	high	0.43
843.1020	22	low	0.80
845.8420	17.8	very low	$\gg 1$

In the experiments, we can operate with low g_0 modes to achieve high C_q , while still achieving quantum-limited noise operation using our ultra-low noise cavity with phononic crystal mirrors, as discussed in Section 2.3. The utilization of the ultra-low noise cavity is crucial as the cavity noise budget $\bar{S}_{vv}(f) < (g_0/2\pi)^2/\Gamma_{\text{th}}$ is extremely tight with low g_0 optical modes. During the operation, we also observed a significant increase in the soft-clamped mode temperature, i.e., 15 K increase with a power level of $C_q \sim 1$, obtained through the spectral fitting of the heating-induced mechanical frequency shift, and comparing it to COMSOL simulation.

From the result we derived in this section, we explain this scaling of the photothermal effect with the membrane-field overlap observed in the experiment.

In the regime where $|g_{\text{th}}(\Omega_m)| \gtrsim g_\omega$, as well as the fast-cavity limit $\Omega_m \ll \kappa$, we have the

Chapter 2. Experimental platform for room-temperature quantum optomechanics

simplified expression for the photothermal amplification rate

$$\Gamma \approx \frac{4\Delta^3}{[\Delta^2 + \kappa^2/4]^2} \text{Im} [g_\omega g_{\text{th}}(\Omega_m)] \quad (2.176)$$

$$g_\omega = g_{\omega,0} \bar{a}^* \quad (2.177)$$

$$g_{\omega,0} \sim g_{\omega,0}^{\max} \sin(2k_0 z_m) \quad (2.178)$$

$$g_{\text{th}} = g_{\text{th},0} \bar{a}^* \quad (2.179)$$

$$g_{\text{th},0} \propto \kappa_{\text{th}} \propto \eta(z_m) = \eta_0 \sin(k_0 z_m)^2 \quad (2.180)$$

where $\eta(z_m)$ is the field overlap between the membrane and the cavity mode. With these expressions, we can express again the amplification rate as a function of $C_q = 4g_*^2/\Gamma_{\text{th}}\kappa$,

$$\Gamma \approx C_q \frac{g_{\omega,0}^2}{g_{*,0}^2} \frac{\Gamma_{\text{th}}\Delta^3\kappa}{[\Delta^2 + \kappa^2/4]^2} \text{Im} \left[\frac{g_{\text{th},0}(\Omega_m)}{g_{\omega,0}} \right] \quad (2.181)$$

where g_* is the dispersive coupling rate for the soft-clamped mode.

As the instability threshold is $\Gamma_m + \Gamma = 0$, we obtain the expression of the maximally achievable C_q while the mechanical modes are stable,

$$C_q^{\max} \propto \text{Im} \left[\frac{g_{\text{th},0}(\Omega_m)}{g_{\omega,0}} \right]^{-1} \propto \cot^{-1}(k_0 z_m), \quad (2.182)$$

where high C_q prefers minimal field overlap $\eta(z_m) \rightarrow 0$. This scaling agrees very well with the experiment observation, indicating that the photothermal effect from optical absorption likely induces mechanical instability.

3 Measurement-based quantum control of mechanical motion

After sorting out all the technical details of the experiment platform in Chapter 2, we can finally discuss the measurements of quantum optomechanical effects at room temperature, including optomechanical squeezing (Section 3.1), optimal mechanical state preparation (Section 3.2), feedback control of mechanical motions (Section 3.3), as well as mechanical sideband asymmetry from low phonon occupancy (Section 3.4). Observing quantum effects with a macroscopic object is challenging but also interesting, as it paves the way towards observing the quantum effect directly of macroscopic objects at room temperature. Note that most of the quantum effects we observe here in this chapter can be mostly attributed to the quantum effects of the measurement meter [69]. In other words, we are essentially observing the quantum nature of photons. The quantum nature of macroscopic oscillators requires measurement of non-classical correlations [70] in, e.g., single-photon counting experiments.

Some results shown here have been sorted out in manuscript [10]. Therefore, some texts and figures might be identical to some degree.

3.1 Optomechanical squeezing

One of the most well-known and robust signatures of quantum optomechanical effects is the generation of squeezed light [18, 19, 20, 21, 22] when the mechanical signal is dominated by the motions driven by the quantum backaction of the light [37, 71].

We generate experimentally optomechanical squeezing to demonstrate that our MIM system, using a density-modulated membrane sandwiched by phononic crystal mirrors, operates in the quantum regime at room temperature. To provide more physical intuition of this phenomenon, we explain the physical process enabling squeezed light generation. In the textbook description of cavity optomechanics, when the cavity is driven on-resonance, the vacuum fluctuations of the laser amplitude drive the mechanical oscillator and are imprinted onto the mechanical motion. The linear response of the cavity also transduces the mechanical motion into phase fluctuations of the light field. These two processes result in correlations

Chapter 3. Measurement-based quantum control of mechanical motion

between the amplitude and phase quadratures of the cavity output field, manifesting as a noise reduction below the shot noise level (squeezing).

In this section, we first derive the Langevin equations that lead to the optical squeezing on the measured spectrum, then the experimental realization using the homodyne technique discussed in Section 2.4.3.

3.1.1 Langevin equations governing optical quadrature measurements

Here, we derive the measurement noise spectral density expression from the Quantum Langevin equations (QLE) governing the MIM system. These results are later used for calibrating the system parameters, e.g., measurement efficiency, membrane heating, and C_q , by fitting the experimental data. A simplified derivation of resonant driving is also provided in Appedix B.6, for readers who desire a cleaner physical picture without all the complications from the detuned drive.

Using the quantities defined in Chapter 1, we write down the quantum Langevin equations in the Heisenberg picture,

$$\dot{\hat{a}} = -\left[\frac{\kappa}{2} + i(\Delta + \sqrt{2}g_0\hat{Q})\right]\hat{a} + \sum_{i=a,b,\dots} \sqrt{\kappa_i}\hat{a}_{\text{in},i}, \quad (3.1)$$

for the cavity mode annihilation operator \hat{a} and the input mode operators $\hat{a}_{\text{in},i}$ of different input ports of the MIM cavity, where the detuning is defined as $\Delta = \omega_{\text{cav}} - \omega_{\text{laser}}$. We consider three optical input modes: the low transmission input port $\hat{a}_{\text{in},b}$ where we pump the cavity with the laser, the high transmission output port $\hat{a}_{\text{in},a}$ where the signal is leaked from the cavity, and the cavity internal loss $\hat{a}_{\text{in},c}$ due to absorption or scattering.

Without using the rotating wave approximation, we write down the QLE governing the mechanical mode,

$$\dot{\hat{Q}} = \Omega_m\hat{P} \quad (3.2)$$

$$\dot{\hat{P}} = -\Omega_m\hat{Q} + \sqrt{2\Gamma_m}\hat{P}_{\text{in}} - \Gamma_m\hat{P} - \sqrt{2}g_0\hat{a}^\dagger\hat{a}, \quad (3.3)$$

where we defined the dimensionless mechanical position operator $\hat{Q} = (\hat{b}^\dagger + \hat{b})/\sqrt{2}$ and the momentum operator $\hat{P} = i(\hat{b}^\dagger - \hat{b})/\sqrt{2}$. \hat{b} is the mechanical mode's annihilation operator, and $\hat{P}_{\text{in}}(t) = \frac{i}{\sqrt{2}}(\hat{b}_{\text{in}}^\dagger(t) - \hat{b}_{\text{in}}(t))$ is the input momentum fluctuation. We also define the optical quadrature operators $\hat{X} = (\hat{a}^\dagger + \hat{a})/\sqrt{2}$ and $\hat{Y} = i(\hat{a}^\dagger - \hat{a})/\sqrt{2}$.

Note that these quadrature definitions are only used within this section, as we have to use these symbols for other purposes in later sections. We also define the optomechanical coupling rate $g = g_0\bar{a}$ enhanced by the cavity field.

Combining the equations for the mechanical operators, we obtain the following expressions

both in time and frequency domain,

$$\ddot{\hat{Q}} + \Gamma_m \dot{\hat{Q}} + \Omega_m^2 \hat{Q} = \sqrt{2\Gamma_m} \Omega_m \hat{P}_{\text{in}} - 2g\Omega_m (\hat{X} + X_{\text{nl}}) \quad (3.4)$$

$$\hat{Q}(\omega) = \chi_m(\omega) \left(\sqrt{2\Gamma_m} \hat{P}_{\text{in}}(\omega) - 2g\hat{X}(\omega) \right), \quad (3.5)$$

where we introduced the frequency-domain mechanical susceptibility

$$\chi_m(\omega) \equiv \Omega_m / (\Omega_m^2 - \omega^2 - i\omega\Gamma_m), \quad (3.6)$$

and the nonlinear noise X_{nl} we discussed in Section 2.4, which is canceled at the magic detuning (and set to zero for the following derivations). Note that the dimensionless input momentum fluctuation $\hat{P}_{\text{in}}(t)$ is characterized by the following spectral correlations:

$$S_{\hat{P}_{\text{in}}\hat{P}_{\text{in}}}(\omega) = \frac{\omega}{\Omega_m} (\bar{n}_{\text{th}}(\omega) + 1) \quad (3.7)$$

$$S_{\hat{P}_{\text{in}}\hat{P}_{\text{in}}}(-\omega) = \frac{\omega}{\Omega_m} \bar{n}_{\text{th}}(\omega) \quad (3.8)$$

For simplicity, the mean cavity field \bar{a} is used as the phase reference $\theta = 0$ for all the other fields, such that both \bar{a} and g are real-valued. Considering all optical channels $\hat{a}_{\text{in},i}$, we define the following susceptibilities to help simplify the results,

$$\chi_c(\omega) = 2^{-1/2} (\kappa/2 + i\Delta - i\omega)^{-1} \quad (3.9)$$

$$\chi_c^X(\omega) = i(\chi_c^*(-\omega) - \chi_c(\omega)) \quad (3.10)$$

$$\chi_c^Y(\omega) = -(\chi_c^*(-\omega) + \chi_c(\omega)) \quad (3.11)$$

$$\chi_{mc}^X(\omega) = (1 + 2\sqrt{2}g^2\chi_m(\omega)\chi_c^X(\omega))^{-1} \quad (3.12)$$

$$\chi_{\Delta}^X(\omega) = \bar{a}\chi_c^X(\omega)\chi_{mc}^X(\omega) \quad (3.13)$$

$$\chi_{P_{\text{in}}}^X(\omega) = \sqrt{2}g\chi_m(\omega)\chi_c^X(\omega)\chi_{mc}^X(\omega) \quad (3.14)$$

$$\chi_{a_{\text{in},i}}^X(\omega) = \sqrt{\kappa_i}\chi_c(\omega)\chi_{mc}^X(\omega) \quad (3.15)$$

$$\chi_{a_{\text{in},i}^\dagger}^X(\omega) = \sqrt{\kappa_i}\chi_c^*(-\omega)\chi_{mc}^X(\omega) \quad (3.16)$$

$$\chi_{\Delta}^Y(\omega) = \chi_c^Y(\omega)[\bar{a} - 2\sqrt{2}g^2\chi_m(\omega)\chi_{\Delta}^X(\omega)] \quad (3.17)$$

$$\chi_{P_{\text{in}}}^Y(\omega) = \sqrt{2}g\chi_c^Y(\omega)\chi_m(\omega)(1 - 2g\chi_{P_{\text{in}}}^X(\omega)) \quad (3.18)$$

$$\chi_{a_{\text{in},i}}^Y(\omega) = -i\sqrt{\kappa_i}\chi_c(\omega) - 2\sqrt{2}g^2\chi_c^Y(\omega)\chi_m(\omega)\chi_{a_{\text{in},i}}^X(\omega) \quad (3.19)$$

$$\chi_{a_{\text{in},i}^\dagger}^Y(\omega) = i\sqrt{\kappa_i}\chi_c^*(-\omega) - 2\sqrt{2}g^2\chi_c^Y(\omega)\chi_m(\omega)\chi_{a_{\text{in},i}^\dagger}^X(\omega) \quad (3.20)$$

Using these susceptibilities, we obtain the following frequency-domain equations for the

Chapter 3. Measurement-based quantum control of mechanical motion

optical quadratures:

$$\begin{aligned} \hat{X}(\omega) &= \chi_{\Delta}^X(\omega)\Delta(\omega) + \chi_{P_{\text{in}}}^X(\omega)\sqrt{2\Gamma}\hat{P}_{\text{in}}(\omega) \\ &+ \sum_{i=a,b,\dots} \left(\chi_{a_{\text{in},i}}^X(\omega)\hat{a}_{\text{in},i}(\omega) + \chi_{a_{\text{in},i}^{\dagger}}^X(\omega)\hat{a}_{\text{in},i}^{\dagger}(\omega) \right) \end{aligned} \quad (3.21)$$

$$\begin{aligned} \hat{Y}(\omega) &= \chi_{\Delta}^Y(\omega)\Delta(\omega) + \chi_{P_{\text{in}}}^Y(\omega)\sqrt{2\Gamma}\hat{P}_{\text{in}}(\omega) \\ &+ \sum_{i=a,b,\dots} \left(\chi_{a_{\text{in},i}}^Y(\omega)\hat{a}_{\text{in},i}(\omega) + \chi_{a_{\text{in},i}^{\dagger}}^Y(\omega)\hat{a}_{\text{in},i}^{\dagger}(\omega) \right) \end{aligned} \quad (3.22)$$

We also define quadratures with arbitrary angles $\hat{X}^{\theta} = 2^{-1/2}(\hat{a}e^{-i\theta} + \hat{a}^{\dagger}e^{i\theta}) = \hat{X}\cos\theta + \hat{Y}\sin\theta$. As we discussed earlier, we pick $\hat{a}_{\text{in},a}$ to be the cavity output port, with $\hat{a}_{\text{in},b}$, $\hat{a}_{\text{in},c}$ the input and loss channels. From the input-output formalism, the output quadrature of the cavity output port is,

$$\hat{X}_{\text{out}}^{\theta} = \hat{X}_{\text{in},a}^{\theta} - \sqrt{\kappa_a}\hat{X}^{\theta}. \quad (3.23)$$

With the following susceptibilities ($k = b, c$, Fourier frequency dependence omitted) defined for arbitrary quadrature angles θ ,

$$\chi_{\Delta}^{\theta} = -\sqrt{\kappa_a}(\chi_{\Delta}^X\cos\theta + \chi_{\Delta}^Y\sin\theta) \quad (3.24)$$

$$\chi_{P_{\text{in}}}^{\theta} = -\sqrt{\kappa_a}(\chi_{P_{\text{in}}}^X\cos\theta + \chi_{P_{\text{in}}}^Y\sin\theta) \quad (3.25)$$

$$\chi_{a_{\text{in},a}}^{\theta} = \sqrt{2}^{-1}e^{-i\theta} - \sqrt{\kappa_a}(\chi_{a_{\text{in},a}}^X\cos\theta + \chi_{a_{\text{in},a}}^Y\sin\theta) \quad (3.26)$$

$$\chi_{a_{\text{in},a}^{\dagger}}^{\theta} = \sqrt{2}^{-1}e^{i\theta} - \sqrt{\kappa_a}(\chi_{a_{\text{in},a}^{\dagger}}^X\cos\theta + \chi_{a_{\text{in},a}^{\dagger}}^Y\sin\theta) \quad (3.27)$$

$$\chi_{a_{\text{in},k}}^{\theta} = -\sqrt{\kappa_k}(\chi_{a_{\text{in},k}}^X\cos\theta + \chi_{a_{\text{in},k}}^Y\sin\theta) \quad (3.28)$$

$$\chi_{a_{\text{in},k}^{\dagger}}^{\theta} = -\sqrt{\kappa_k}(\chi_{a_{\text{in},k}^{\dagger}}^X\cos\theta + \chi_{a_{\text{in},k}^{\dagger}}^Y\sin\theta) \quad (3.29)$$

and also taking into account photon collection efficiency η , the detected optical quadrature is expressed as,

$$\begin{aligned} \hat{X}_{\text{det}}^{\theta}(\omega) &= \sqrt{\eta} \left[\chi_{\Delta}^{\theta}\Delta(\omega) + \chi_{P_{\text{in}}}^{\theta}\sqrt{2\Gamma}\hat{P}_{\text{in}}(\omega) + \sum_{i=a,b,c} \left(\chi_{a_{\text{in},i}}^{\theta}\hat{a}_{\text{in},i}(\omega) + \chi_{a_{\text{in},i}^{\dagger}}^{\theta}\hat{a}_{\text{in},i}^{\dagger}(\omega) \right) \right] \\ &+ i\sqrt{1-\eta}\hat{X}_{\text{vac}}(\omega). \end{aligned} \quad (3.30)$$

To calculate the power spectral density of the quadrature observable, we use the following correlation relations for the optical input fields (more general expressions that include classical noises are in Section 2.4),

$$S_{AB}(\omega) = \int \langle A^{\dagger}(\omega)B(\omega') \rangle \frac{d\omega'}{2\pi} \quad (3.31)$$

$$\langle a_{\text{in}}(\omega)a_{\text{in}}^{\dagger}(\omega') \rangle = 2\pi\delta(\omega + \omega') \quad (3.32)$$

$$\langle a_{\text{in}}^{\dagger}(\omega)a_{\text{in}}(\omega') \rangle = 0, \quad (3.33)$$

we can calculate the optical detection spectral densities,

$$S_{\hat{X}_{\text{det}}^\theta \hat{X}_{\text{det}}^\theta}(\omega) = \eta \left[|\chi_\Delta^\theta(\omega)|^2 S_{\Delta\Delta}(\omega) + |\chi_{P_{\text{in}}}^\theta(\omega)|^2 2\Gamma S_{\hat{P}_{\text{in}} \hat{P}_{\text{in}}}(\omega) + \sum_{i=a,b,c} |\chi_{a_{\text{in},i}}^\theta(\omega)|^2 \right] + \frac{1-\eta}{2}, \quad (3.34)$$

Here, due to the large difference in effective mass and quality factors between the soft-clamped mode and the other membrane modes, we only consider the quantization of the soft-clamped mode for the spectral fitting. The other membrane modes and mirror noises are treated as cavity noise in $S_{\Delta\Delta}(\omega)$.

3.1.2 Measuring optical squeezing

In this section, we describe the generation of squeezed light in our MIM system, including the methods to avoid nonlinear force decoherence and to measure at different quadrature angles, as well as the shot noise calibration method used to verify optical squeezing.

Experiment results

As we discussed in Section 2.4, the nonlinear transduction response of the cavity produces nonlinear mixing products of thermomechanical noise, giving rise to excess nonlinear noise beyond vacuum fluctuations in the measurement record that does not naturally fit in the linear framework of optical quadratures. Due to the high number of modes of the membrane and the large Brownian motion at room temperature, the mixing products manifest as broadband noise, termed thermal intermodulation noise (TIN) [42]. TIN results in the generation of new frequency components that have significant power even at frequencies within the mechanical bandgap, thereby degrading the measurement signal-to-noise ratio (SNR), and inducing additional mechanical decoherence [72].

To eliminate TIN intra-cavity photon number fluctuations, which would otherwise lead to access backaction decoherence, we pump the cavity with the laser detuned by $2\Delta_*/\kappa = -1/\sqrt{3}$ (magic detuning), where the quadratic term of the cavity response vanishes. In this way, as discussed in Section 2.4, the second-order TIN can be efficiently eliminated, with only the third-order noise (Section 2.4.4) and the residue second-order noise (Section 2.4.2) remaining.

At high power operation required to reach $C_q \sim 1$, pumping the cavity at Δ_* has the additional effect of optically cooling all the mechanical modes. The optical cooling reduces the amount of residual nonlinear noise well below the laser shot noise (see Fig. 2.21), together with cavity resonances with large linewidth κ . In the experiment, we used the optical resonance at 819 nm ($\kappa/2\pi = 34.2$ MHz), shown in Fig. 2.15. Pumping at this resonance with $C_q \sim 1$ also induces a redshift and cools the defect mode to an occupancy $\bar{n}_{\text{eff}} \approx 20$ phonons, via dynamical backaction cooling [13] (lower effective phonon occupancy of $\bar{n}_{\text{eff}} \approx 5.7$ can be achieved with a narrower-linewidth cavity mode at 862 nm, discussed in later sections).

Chapter 3. Measurement-based quantum control of mechanical motion

Furthermore, to eliminate second-order TIN in the optical detection, we deploy a specialized homodyne detection scheme using only one detector (Section 2.4.3), shown in Fig. 3.1(a). Instead of balanced homodyne detection, a single detector offers the required photodetection nonlinearity to eliminate TIN at arbitrary optical quadrature angles. We achieve this by carefully selecting the local oscillator power for each quadrature angle we detect.

We measure the noise of the cavity output field at optical quadrature angles ranging from -33° to 33° [see Fig. 3.1(c)], where the 0° quadrature is defined as the one with no mechanical displacement information (valid in the fast-cavity limit). Depending on the quadrature angle, we observed optical squeezing (up to 50 kHz bandwidth) on either side of the defect mode, whose extent is limited by the membrane modes at the edge of the bandgap [see Fig. 3.1(b) for a representative spectrum].

For the three frequency bands that are devoid of parasitic modes and nonlinear mixing noise peaks, we compute the average intensity noise over a bandwidth of 5 kHz, as a function of quadrature angle [see Fig. 3.1(d)]. We observe a maximum squeezing of 22.2 % (1.09 dB) below the shot noise level, which matches well with the theory prediction from the spectrum fitting.

To calibrate the shot noise level, we perform a separate measurement where we direct the same amount of optical power onto the same photodetector and measure the laser intensity noise. More details on the shot noise calibration, including an analysis of classical noise and the detector linearity, are described in the next section.

Shot noise calibration

To calibrate the reference shot noise power spectral density for a given signal, in order to retrieve the amount of optical squeezing generated, we use the following procedure:

1. Record the average detector voltage output during data acquisition for each optical power level impinging on the detector,
2. Block the beam from the output of the optical cavity such that only the local oscillator beam hits the detector,
3. Adjust the local oscillator power such that the average detector voltage output is the same as the one recorded during the data acquisition. This can be done with accuracy better than 1 %,
4. Record the noise power spectral density of the detector voltage output through the same electrical signal chain as the data acquisition, which serves as the reference shot noise power spectral density.

Since the detector voltage output is the same, the generated photocurrent flux and the optical noise power should also be the same. However, it must be verified that the local oscillator beam is shot-noise-limited at the Fourier frequency of interest.

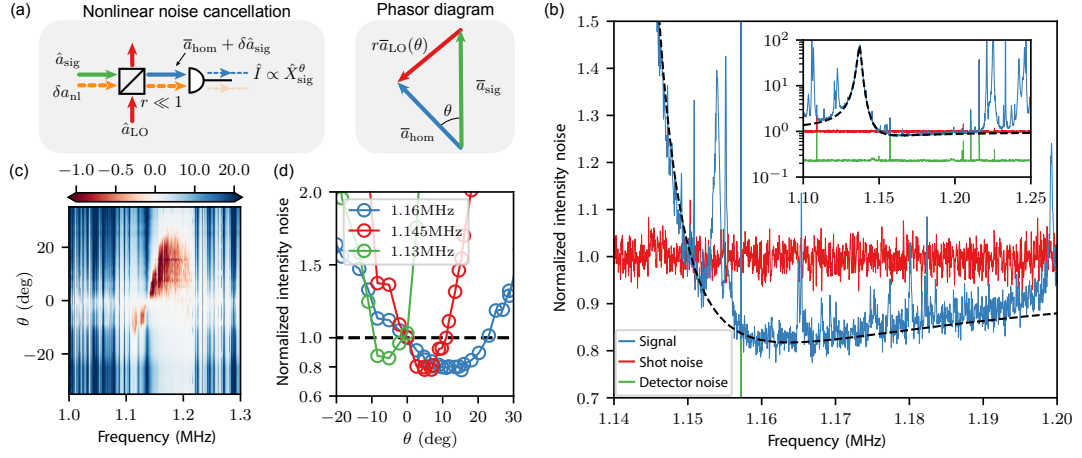


Figure 3.1: **Optomechanical generation of squeezed light.** (a) Homodyne detection scheme that cancels nonlinear mixing noise δa_{nl} from the records of cavity transmission. For each quadrature angle θ , a specific LO amplitude is needed to cancel the nonlinear mixing noise. (b) Detected power spectral density (PSD) at the quadrature angle $\theta = 15.3^\circ$ at frequencies above the mechanical resonance, compared to the measured shot noise (SN) and detector noise. Inset: the same PSD is displayed on broader frequency and power ranges. (c) Collection of homodyne photocurrent spectra of the cavity output field, normalized to the shot noise level, measured at different quadrature angles. The magnitude and bandwidth of squeezing depend on the homodyne quadrature angle. (d) Averaged homodyne PSD within three different frequency bands (5 kHz bandwidth) at different quadrature angles, showing a maximum squeezing depth of 22.2 % (1.09 dB).

The TiSa laser we use is predominantly shot-noise-limited at around 1 MHz under our experimental conditions, as was illustrated in Fig. B.7. We quantify this by recording the photocurrent noise scaling as the optical power varies. The laser shot noise scales linearly with the optical power, proportional to the detector DC voltage output, while any classical noise contribution scales quadratically. We fit the local oscillator noise power integrated over each frequency band as a function of detector DC voltage with a polynomial function consisting of only the 1st-order and the 2nd-order terms, as shown in Fig. 3.2(a). We confirm that within the frequency range of interest and optical powers used in the experiment, the classical noise contribution is less than 1 %, as shown in Fig. 3.2(b). This measurement result is also consistent with what we measured in Fig. B.7. Using the fit results, we correct the measured reference shot noise by subtracting the calibrated classical noise contribution to ensure we do not overstate the amount of squeezing. We also measured the detector DC voltage output linearity with respect to optical power with a reference power meter and found a maximum deviation of less than 0.3 %.

Chapter 3. Measurement-based quantum control of mechanical motion

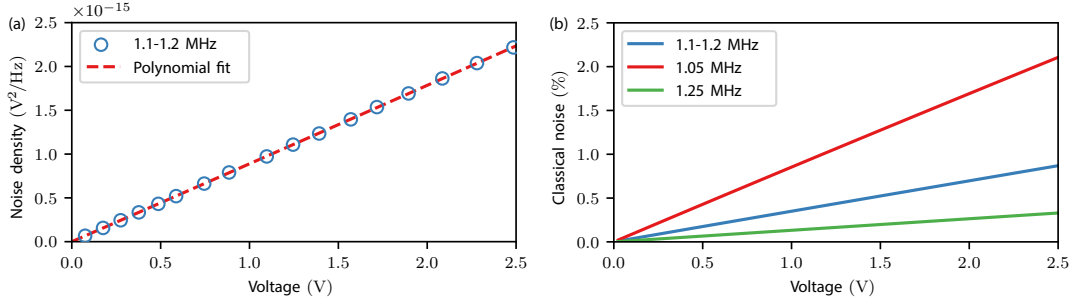


Figure 3.2: **(a)** Laser intensity noise power (detector noise subtracted) averaged over 1.1-1.2 MHz frequency band, as a function of detector output voltage. A polynomial function consisting of linear and quadratic terms is used to fit and extract the contribution of the laser classical noise. **(b)** The laser classical noise fractional contribution to the intensity noise is plotted as a function of detector voltage over three frequency bands. Most classical noise is the high-frequency tail from the laser relaxation oscillation peak around 300 kHz. At the frequency band of interest 1.1-1.2 MHz where the experiment is conducted, the classical noise contribution is less than 1 %.

3.2 Quantum measurements of mechanical motions

In the previous section, we quantified the maximum squeezing of 22 %, which corresponds to the measurement efficiency η_{meas} of the system. This section discusses exploiting the high measurement efficiency to prepare conditional mechanical states with thermal occupancy as low as a single phonon. We establish the basic theory of conditional state preparation from the stochastic quantum master equation, then the more complicated multi-mode model so that all mechanical modes in the frequency span of interest can be faithfully included, and last, the verification of the model as well as the state preparation using the retrodiction method as well as the spectral response.

3.2.1 Continuous measurement

First, we establish the basic theory of continuous quantum measurement of mechanical motions. In this section, we treat only the optical part of the measurement, where the photocurrent of the detector is connected to the mechanical motions and optical noises. The interaction of the optical meter with the mechanical system is modeled in the next section using the quantum master equations.

We work in the fast-cavity limit, so the cavity output field derived in the previous section can

3.2 Quantum measurements of mechanical motions

be greatly simplified as

$$\delta \hat{a}_{\text{out}} = -\frac{-\frac{\kappa}{2} + i\Delta}{\frac{\kappa}{2} + i\Delta} \delta \hat{a}_{\text{in}} + \frac{\sqrt{2}ig_0\bar{a}\sqrt{\kappa}}{\frac{\kappa}{2} + i\Delta} \hat{Q} \quad (3.35)$$

$$\hat{i}_{\text{direct}} = \delta \hat{a}_{\text{out}} + \delta \hat{a}_{\text{out}}^\dagger = e^{i\theta_{\text{in}}} \delta \hat{a}_{\text{in}}^\dagger + e^{-i\theta_{\text{in}}} \delta \hat{a}_{\text{in}} + \frac{2\sqrt{2}\Delta\sqrt{\kappa}g}{(\frac{\kappa}{2})^2 + \Delta^2} \hat{Q} \quad (3.36)$$

$$\hat{i}_{\text{max}} = e^{i\theta_{\text{out}}} \delta \hat{a}_{\text{out}}^\dagger + e^{-i\theta_{\text{out}}} \delta \hat{a}_{\text{out}} = e^{i\theta'_{\text{in}}} \delta \hat{a}_{\text{in}}^\dagger + e^{-i\theta'_{\text{in}}} \delta \hat{a}_{\text{in}} + \frac{2\sqrt{2}\sqrt{\kappa}g}{\sqrt{(\frac{\kappa}{2})^2 + \Delta^2}} \hat{Q} \quad (3.37)$$

In the following, since we are mostly concerned with mechanical states, we only leave the \hat{O} symbol for mechanical operators. After classical detection of the output field current, we obtain the classical measurement record $i(t)$. We rewrite the measurement record $i(t)$ in terms of Wiener increment to simplify our discussion,

$$i(t)dt = dW + \sqrt{8\Gamma_{\text{meas}}}\langle \hat{Q} \rangle dt \quad (3.38)$$

where $\Gamma_{\text{meas}} = \eta\Gamma_{\text{qba}} = \frac{4\eta g^2}{\kappa} \frac{\kappa^2}{\kappa^2 + 4\Delta^2}$ and η is the photon detection efficiency. With detuned direct detection, the efficiency is bounded by $\eta_{\text{direct}} = \frac{\Delta^2}{(\frac{\kappa}{2})^2 + \Delta^2}$. Therefore, only with the most optimal quadrature angle, zero added detection noise, and zero photon loss can we approach $\eta \rightarrow 1$, where the backaction decoherence rate of the oscillator bounds the measurement rate.

Note that the measurement record $i(t)$ is not a quantum operator but rather connected only to the expected trajectory $\langle \hat{Q} \rangle$ of the quantum state. The details of the measurement problem will be discussed in the next section, where we heuristically derive the quantum master equation and connect the measurement result to the state of the oscillator and a classical Wiener increment.

The Wiener increment [73] we use above is defined in terms of an ideal unit Gaussian white noise process,

$$dW(t) \equiv W(t+dt) - W(t) = \xi(t)dt \quad \langle \xi(t)\xi(t') \rangle = \delta(t-t') \quad (3.39)$$

with property $\langle dW(t)dW(t') \rangle = dW(t)dW(t') = \delta_{t,t'}dt$.

To simplify the analysis, we decompose $\hat{Q} = \cos\Omega_m t \hat{X} + \sin\Omega_m t \hat{Y}$ into two slowly varying quadrature observables. Since the measurement rates Γ_{meas} are much smaller than the mechanical frequency Ω_m , our homodyne measurement is equivalent to the heterodyne detection of these two quadratures with symmetric measurement rates.

We perform IQ demodulation at mechanical frequency Ω_m to separate these two quadratures into two independent measurement channels

$$i_X(t)dt = \sqrt{4\Gamma_{\text{meas}}}\langle \hat{X} \rangle dt + dW_X(t) \quad (3.40)$$

$$i_Y(t)dt = \sqrt{4\Gamma_{\text{meas}}}\langle \hat{Y} \rangle dt + dW_Y(t) \quad (3.41)$$

Chapter 3. Measurement-based quantum control of mechanical motion

which is equivalent to detecting both quadratures simultaneously with independent Wiener increment and half the detection efficiencies, similar to heterodyne detection.

Therefore, in our continuous measurement of a mechanical oscillator with rate $\Gamma_{\text{meas}} = \eta\Gamma_{\text{qba}}$ of a system observable $\hat{\mathbf{r}} = (\hat{X}, \hat{Y})$ with Gaussian noise, the output measurement record $\mathbf{i} = (i_X, i_Y)$ can be modeled as a 2-D Wiener process where

$$\mathbf{i}(t)dt = \sqrt{4\Gamma_{\text{meas}}}\langle\hat{\mathbf{r}}\rangle(t)dt + d\mathbf{W}(t) \quad (3.42)$$

Heuristic derivation of stochastic master equation

This section derives the quantum master equations governing the interaction between mechanical oscillators, environment baths, and optical measurement meters.

We establish the continuous measurement formalism in terms of POVMs [74]. For a weak continuous position x measurement, where the state projection is not complete to a specific measurement basis, we measure in the interval time Δt described by the generalized projection operator

$$A(\alpha) = \left(\frac{2\mu\Delta t}{\pi}\right)^{1/4} \int \exp[-\mu\Delta t(x-\alpha)^2] |x\rangle\langle x| dx \quad (3.43)$$

where α is a measurement result in the position continuum. Essentially, the measurement projects the position x state into a Gaussian-weighted vicinity around α . In the case of a strong measurement $\mu \rightarrow +\infty$, the measurement returns to a normal state projection.

For any arbitrary initial state $|\psi\rangle = \int \psi(x)|x\rangle dx$, one can prove that $\langle\alpha\rangle = \langle\hat{x}\rangle_\psi$, with the probability to obtain a measurement record α of

$$P(\alpha) = \text{Tr}[A(\alpha)^\dagger A(\alpha)|\psi\rangle\langle\psi|] \approx \left(\frac{2\mu\Delta t}{\pi}\right)^{1/2} \exp[-\mu\Delta t(\alpha - \langle\hat{x}\rangle_\psi)] \quad (3.44)$$

where the approximation holds accurate in the limit $\Delta t \rightarrow 0$.

From the above probability distribution, it is clear that we can express the measurement result α as a stochastic quantity using Wiener increment,

$$\alpha = \langle\hat{x}\rangle + \frac{\Delta W}{(4\mu)^{1/2}\Delta t}. \quad (3.45)$$

Here, we can identify that in our scenario of continuous measurement of mechanical motion, $\mu = \Gamma_{\text{qba}}$ in the limit of unity efficiency $\eta \rightarrow 1$.

With this result, we can derive the evolution of the quantum state given the measurement

3.2 Quantum measurements of mechanical motions

record α , by following the rules of Ito's calculus,

$$\begin{aligned}
 |\psi(t + \Delta t)\rangle &\propto A(\alpha)|\psi(t)\rangle \\
 &\propto \exp[-\mu\Delta t(\alpha - \hat{x})^2]|\psi(t)\rangle \\
 &\propto \exp[-\mu\Delta t\hat{x}^2 + \hat{x}[2\mu\Delta t\langle\hat{x}\rangle + \sqrt{\mu}\Delta W]]|\psi(t)\rangle \\
 &\propto \left\{1 - \frac{\mu\Delta t}{2}\hat{x}^2 + \hat{x}[2\mu\Delta t\langle\hat{x}\rangle + \sqrt{\mu}\Delta W]\right\}|\psi(t)\rangle.
 \end{aligned} \tag{3.46}$$

After normalizing the update equation using $\sqrt{1 + \delta} = 1 + \frac{1}{2}\delta - \frac{1}{8}\delta^2 + \dots$, we obtained the stochastic Schrodinger equation,

$$d|\psi\rangle = \left\{-\frac{\mu}{2}(\hat{x} - \langle\hat{x}\rangle)^2 dt + \sqrt{\mu}(\hat{x} - \langle\hat{x}\rangle)dW\right\}|\psi(t)\rangle, \tag{3.47}$$

which directly yields the stochastic master equation for the density matrix

$$\begin{aligned}
 d\rho &= (d|\psi\rangle)\langle\psi| + |\psi\rangle(d\langle\psi|) + (d|\psi\rangle)(d\langle\psi|) \\
 &= -\frac{\mu}{2}(\hat{x}^2\rho + \rho\hat{x}^2 - 2\hat{x}\rho\hat{x})dt + \sqrt{\mu}(\hat{x}\rho + \rho\hat{x} - 2\langle\hat{x}\rangle\rho)dW.
 \end{aligned} \tag{3.48}$$

If we generalize a measurement operator $\sqrt{\mu}\hat{x} \rightarrow \hat{c}$, we arrive at one of the most well known expression

$$d\rho = \mathcal{D}[\hat{c}]\rho dt + \mathcal{H}[\hat{c}]\rho dW \tag{3.49}$$

where \mathcal{D} and \mathcal{H} are the Lindblad and measurement superoperators defined by

$$\mathcal{D}[\hat{c}]\rho \equiv \hat{c}\rho\hat{c}^\dagger - \frac{1}{2}(\hat{c}^\dagger\hat{c}\rho + \rho\hat{c}^\dagger\hat{c}) \tag{3.50}$$

$$\mathcal{H}[\hat{c}]\rho \equiv \hat{c}\rho + \rho\hat{c}^\dagger - \langle\hat{c} + \hat{c}^\dagger\rangle\rho \tag{3.51}$$

where \mathcal{D} describes the measurement-induced decoherence of the system, and \mathcal{H} describes the state conditioning effect based on the measurement records α . We can also easily generalize to multiple measurement channels,

$$d\rho = \sum_{\hat{c}} [\mathcal{D}[\hat{c}]\rho dt + \mathcal{H}[\hat{c}]\rho dW_{\hat{c}}]. \tag{3.52}$$

In the case where quantum information loss occurs for some measurement channels, e.g., optical photon loss or interaction with the thermal bath, we can model it with a finite detection efficiency η by setting the loss channel $\langle dW_{\text{lost}}\rangle = 0$, with which we arrive at the expression

$$d\rho = \mathcal{D}[\hat{c}]\rho dt + \sqrt{\eta}\mathcal{H}[\hat{c}]\rho dW. \tag{3.53}$$

Chapter 3. Measurement-based quantum control of mechanical motion

Recall now the Wiener increment is connected to the measurement record as

$$\alpha = \langle \hat{x} \rangle + \frac{\Delta W}{(4\eta\mu)^{1/2} \Delta t}. \quad (3.54)$$

We find the correspondence $\eta\mu = \Gamma_{\text{meas}}$ in our setting.

Evolution of covariance matrix under continuous measurements

The evolution of the density matrix ρ is also covered in [36], where for a measurement observable \hat{c} , the stochastic master equation is

$$d\rho = -\frac{i}{\hbar} [\hat{H}, \rho] + \mathcal{L}_{\text{env}}\rho dt + \mathcal{D}[\hat{c}]\rho dt + \sqrt{\eta}\mathcal{H}[\hat{c}]\rho dW. \quad (3.55)$$

The environmental coupling term $\mathcal{L}_{\text{env}}\rho$ describes the environment bath-coupling induced decoherence dynamics, and under the Markov and rotating wave approximation we find

$$\mathcal{L}_{\text{env}}\rho = \Gamma(\bar{n} + 1)\mathcal{D}[\hat{b}]\rho + \Gamma\bar{n}\mathcal{D}[\hat{b}^\dagger]\rho. \quad (3.56)$$

In the case of a continuous measurement of mechanical motion, the two measurement observables are $\hat{c}_X = \sqrt{\Gamma_{\text{qba}}}\hat{X}$ and $\hat{c}_Y = \sqrt{\Gamma_{\text{qba}}}\hat{Y}$. This results in our single-mode stochastic master equation

$$d\rho = \mathcal{L}_{\text{env}}\rho + \Gamma_{\text{qba}}(\mathcal{D}[\hat{X}] + \mathcal{D}[\hat{Y}])\rho + \sqrt{\Gamma_{\text{meas}}}(\mathcal{H}[\hat{X}]\rho dW_X + \mathcal{H}[\hat{Y}]\rho dW_Y) \quad (3.57)$$

Since the measurement is purely linear, and as the mechanical state starts from a thermal state, the state under continuous measurement will remain a Gaussian state, entirely captured by the first two moments of the orthogonal quadratures.

Evolution of the quadrature expectation values (first moment) and the covariance matrix (second moment) can be derived using the following relations

$$\text{Tr}[\hat{X}\mathcal{D}[\hat{b}]\rho] = -\langle \hat{X} \rangle / 2 \quad \text{Tr}[\hat{X}\mathcal{D}[\hat{b}^\dagger]\rho] = \langle \hat{X} \rangle / 2 \quad (3.58)$$

$$\text{Tr}[\hat{X}\mathcal{D}[\hat{X}]\rho] = \text{Tr}[\hat{Y}\mathcal{D}[\hat{X}]\rho] = 0 \quad (3.59)$$

$$\text{Tr}[\hat{X}\mathcal{H}[\hat{X}]\rho] = 2V_X \quad \text{Tr}[\hat{Y}\mathcal{H}[\hat{X}]\rho] = 2C_{XY} \quad (3.60)$$

where $V_X = \langle \hat{X}^2 \rangle - \langle \hat{X} \rangle^2$ and $C_{XY} = \langle \hat{X}\hat{Y} + \hat{Y}\hat{X} \rangle / 2 - \langle \hat{X} \rangle \langle \hat{Y} \rangle$.

The quadrature expectation values are found to obey the following update equations,

$$d\langle \hat{X} \rangle = -\frac{\Gamma}{2}\langle \hat{X} \rangle dt + \sqrt{4\Gamma_{\text{meas}}}[V_X dW_X + C_{XY} dW_Y] \quad (3.61)$$

$$d\langle \hat{Y} \rangle = -\frac{\Gamma}{2}\langle \hat{Y} \rangle dt + \sqrt{4\Gamma_{\text{meas}}}[V_Y dW_Y + C_{XY} dW_X]. \quad (3.62)$$

3.2 Quantum measurements of mechanical motions

The covariance matrix is slightly harder to compute as

$$dV_X = d\langle \hat{X}^2 \rangle - 2\langle \hat{X} \rangle d\langle \hat{X} \rangle - d\langle \hat{X} \rangle^2 \quad (3.63)$$

$$dC_{XY} = \frac{1}{2} d\langle \hat{X} \hat{Y} + \hat{Y} \hat{X} \rangle - \langle \hat{X} \rangle d\langle \hat{Y} \rangle - \langle \hat{Y} \rangle d\langle \hat{X} \rangle - d\langle \hat{X} \rangle d\langle \hat{Y} \rangle. \quad (3.64)$$

To derive the update equations, we need to use the following relations,

$$\text{Tr}[\hat{X}^2 \mathcal{D}[\hat{b}]\rho] = -\langle \hat{X}^2 \rangle + \frac{1}{2} \quad \text{Tr}[\hat{X}^2 \mathcal{D}[\hat{b}^\dagger]\rho] = \langle \hat{X}^2 \rangle + \frac{1}{2} \quad (3.65)$$

$$\text{Tr}[\hat{X}^2 \mathcal{D}[\hat{Y}]\rho] = \text{Tr}[\hat{Y}^2 \mathcal{D}[\hat{X}]\rho] = 1 \quad (3.66)$$

$$\text{Tr}[\hat{X}^2 \mathcal{H}[\hat{X}]\rho] = 2\langle \hat{X}^3 \rangle - 2\langle \hat{X}^2 \rangle \langle \hat{X} \rangle \quad \text{Tr}[\hat{X}^2 \mathcal{H}[\hat{Y}]\rho] = 2\langle \hat{X} \hat{Y} \hat{X} \rangle - 2\langle \hat{X}^2 \rangle \langle \hat{Y} \rangle. \quad (3.67)$$

To close the equations until the second moment, we need to consider the following moment relations for Gaussian states,

$$\langle \hat{X}^3 \rangle = 3\langle \hat{X} \rangle V_X + \langle \hat{X} \rangle^3 \quad (3.68)$$

$$\langle \hat{X} \hat{Y} \hat{X} \rangle = 2\langle \hat{X} \rangle C_{XY} + \langle \hat{Y} \rangle \langle \hat{X}^2 \rangle, \quad (3.69)$$

which leads to

$$\text{Tr}[\hat{X}^2 \mathcal{H}[\hat{X}]\rho] = 4\langle \hat{X} \rangle V_X \quad \text{Tr}[\hat{X}^2 \mathcal{H}[\hat{Y}]\rho] = 4\langle \hat{X} \rangle C_{XY}, \quad (3.70)$$

as well as the other cross-correlation moments

$$\text{Tr}[[\hat{X}, \hat{Y}]_+ \mathcal{D}[\hat{b}]\rho] = -\text{Tr}[[\hat{X}, \hat{Y}]_+ \mathcal{D}[\hat{b}^\dagger]\rho] = 2C_{XY} + 2\langle \hat{X} \rangle \langle \hat{Y} \rangle \quad (3.71)$$

$$\text{Tr}[[\hat{X}, \hat{Y}]_+ \mathcal{D}[\hat{X}]\rho] = \text{Tr}[[\hat{X}, \hat{Y}]_+ \mathcal{D}[\hat{Y}]\rho] = 0 \quad (3.72)$$

$$\text{Tr}[[\hat{X}, \hat{Y}]_+ \mathcal{H}[\hat{X}]\rho] = 4\langle \hat{X} \rangle C_{XY} + 4\langle \hat{Y} \rangle V_X \quad \text{Tr}[[\hat{X}, \hat{Y}]_+ \mathcal{H}[\hat{Y}]\rho] = 4\langle \hat{Y} \rangle C_{XY} + 4\langle \hat{X} \rangle V_Y. \quad (3.73)$$

With the help of all these relations derived above, we arrive at the covariance matrix update equations

$$\dot{V}_X = -\Gamma V_X + \Gamma \left(\bar{n} + \frac{1}{2} \right) + \Gamma_{\text{qba}} - 4\Gamma_{\text{meas}} (V_X^2 + C_{XY}^2) \quad (3.74)$$

$$\dot{V}_Y = -\Gamma V_Y + \Gamma \left(\bar{n} + \frac{1}{2} \right) + \Gamma_{\text{qba}} - 4\Gamma_{\text{meas}} (V_Y^2 + C_{XY}^2) \quad (3.75)$$

$$\dot{C}_{XY} = -[\Gamma + 4\Gamma_{\text{meas}}(V_X + V_Y)] C_{XY}. \quad (3.76)$$

We notice that in the long time limit, any correlation between the two quadratures will vanish as $C_{XY} \rightarrow 0$. For an initial condition in the thermal state, one can set $C_{XY} = 0$ to simplify the update equations. However, this is not generally the case when multiple oscillators are present.

Chapter 3. Measurement-based quantum control of mechanical motion

State estimation as temporal filtering

Here, we analyze the temporal response of the state estimation and show that this is a one-pole filter response in the frequency domain, corresponding to an exponentially decaying temporal envelope.

The Wiener increments can be expressed using the measurement records and the quadrature expectation values as

$$d\mathbf{W}(t) = \mathbf{i}(t) dt - \sqrt{4\Gamma_{\text{meas}}} \langle \hat{\mathbf{r}} \rangle(t) dt. \quad (3.77)$$

From here, it is fairly straightforward to understand this state estimation procedure as a filtering process as

$$d\langle \hat{X} \rangle = -\left(\frac{\Gamma}{2} + 4\Gamma_{\text{meas}} V_X\right) \langle \hat{X} \rangle dt + \sqrt{4\Gamma_{\text{meas}}} V_X i_X(t) dt \quad (3.78)$$

$$\langle \hat{X} \rangle(\omega) = \frac{\sqrt{4\Gamma_{\text{meas}}} V_X}{\frac{\Gamma}{2} + 4\Gamma_{\text{meas}} V_X - i\omega} i_X(\omega) \quad (3.79)$$

which is a one pole filter response at the mechanical frequency, and with bandwidth $\Gamma_{\text{se}} = \frac{\Gamma}{2} + 4\Gamma_{\text{meas}} V_X$.

Multi-mode quantum master equation

When other mechanical modes are coupled to the light field and measured by the same measurement channel, we must add them to our model. The reason we have to add these modes into our model is that the derivation of the stochastic master equation relies heavily on the Wiener increment property, so we need to make sure that through modeling, the retrieved Wiener increment from the measurement record, by subtracting the position estimations from different modes, is as white as possible.

We assume these other mechanical modes are at frequencies Ω_i . We still perform the demodulation procedure of the photocurrent at the mechanical frequency Ω_m . The demodulated photocurrent vector is

$$\mathbf{i}(t) dt = \sqrt{4\Gamma_{\text{meas}}} \langle \hat{\mathbf{r}} \rangle(t) dt + d\mathbf{W}(t) + \sum_i \sqrt{4\Gamma_{\text{meas}}^i} \mathbf{A}_i(t) \langle \hat{\mathbf{r}}_i \rangle(t) dt, \quad (3.80)$$

with $\mathbf{A}_i(t) = \begin{bmatrix} \cos(\Omega_i - \Omega_m) t & \sin(\Omega_i - \Omega_m) t \\ -\sin(\Omega_i - \Omega_m) t & \cos(\Omega_i - \Omega_m) t \end{bmatrix}$, which is equivalent to measuring multiple observables at one single measurement channel simultaneously.

The measurement observable is, therefore

$$\hat{\mathbf{c}}(t) = \sqrt{\Gamma_{\text{qba}}} \hat{\mathbf{r}} + \sum_i \sqrt{\Gamma_{\text{qba}}^i} \mathbf{A}_i(t) \hat{\mathbf{r}}_i \quad (3.81)$$

3.2 Quantum measurements of mechanical motions

If we write it separately as $\hat{\mathbf{c}}(t) = \sum_i \hat{\mathbf{c}}_i(t)$, and re-define the other mechanical quadratures $\hat{\mathbf{r}}_i \leftarrow \mathbf{A}_i(t)\hat{\mathbf{r}}_i$ (equivalent to a rotating frame transformation at frequency Ω_m), then the \mathcal{D} and \mathcal{H} becomes

$$\begin{aligned} \mathcal{D}[\hat{\mathbf{c}}]\rho &= \sum_i \hat{\mathbf{c}}_i \rho \hat{\mathbf{c}}_i^\dagger - \frac{1}{2} \left(\hat{\mathbf{c}}_i^\dagger \hat{\mathbf{c}}_i \rho + \rho \hat{\mathbf{c}}_i^\dagger \hat{\mathbf{c}}_i \right) + \sum_{ij} \hat{\mathbf{c}}_i \rho \hat{\mathbf{c}}_j^\dagger - \frac{1}{2} \left(\hat{\mathbf{c}}_i^\dagger \hat{\mathbf{c}}_j \rho + \rho \hat{\mathbf{c}}_i^\dagger \hat{\mathbf{c}}_j \right) \\ &= \sum_i \mathcal{D}[\hat{\mathbf{c}}_i]\rho + \sum_{ij} \mathcal{D}_2[\hat{\mathbf{c}}_i, \hat{\mathbf{c}}_j]\rho \end{aligned} \quad (3.82)$$

$$\begin{aligned} \mathcal{H}[\hat{\mathbf{c}}]\rho &= \sum_i \hat{\mathbf{c}}_i \rho + \rho \hat{\mathbf{c}}_i^\dagger - \langle \hat{\mathbf{c}}_i + \hat{\mathbf{c}}_i^\dagger \rangle \rho \\ &= \sum_i \mathcal{H}[\hat{\mathbf{c}}_i]\rho \end{aligned} \quad (3.83)$$

Note that \mathcal{D}_2 describes the common backaction force between two observables and only connects either (X_i, X_j) or (Y_i, Y_j) . Physically, this is due to the common radiation pressure noise impinging on the different mechanical modes, such that their motions are correlated.

For the moments associated with decoherence terms, we have the following relation

$$\text{Tr} \left[Y_i (\mathcal{D}_2[X_i, c_j] + \mathcal{D}_2[c_j, X_i]) \rho \right] = \text{Tr} \left[X_i (\mathcal{D}_2[Y_i, c_j] + \mathcal{D}_2[c_j, Y_i]) \rho \right] = 0 \quad (3.84)$$

$$\text{Tr} \left[Y_i^2 (\mathcal{D}_2[X_i, c_j] + \mathcal{D}_2[c_j, X_i]) \rho \right] = \text{Tr} \left[X_i^2 (\mathcal{D}_2[Y_i, c_j] + \mathcal{D}_2[c_j, Y_i]) \rho \right] = 0 \quad (3.85)$$

$$\text{Tr} \left[X_i Y_i (\mathcal{D}_2[X_i, c_j] + \mathcal{D}_2[c_j, X_i]) \rho \right] = \text{Tr} \left[X_i Y_i (\mathcal{D}_2[Y_i, c_j] + \mathcal{D}_2[c_j, Y_i]) \rho \right] = 0 \quad (3.86)$$

which guarantees that all the terms related to decoherence, except (X_i, X_j) and (Y_i, Y_j) , stay the same.

As we can see, the conditioning effect on the system state \mathcal{H} is perfectly linear on the surface, but different systems can still influence each other through cross-correlations. The moments associated with these terms are

$$\text{Tr} \left[O_i \mathcal{H}[c_j] \rho \right] = 2[\langle O_i c_j \rangle - \langle O_i \rangle \langle c_j \rangle] = 2C_{O_i, c_j} \quad (3.87)$$

Chapter 3. Measurement-based quantum control of mechanical motion

which results in the update equations for the first moments,

$$\begin{aligned}
 d\langle \hat{X}_i \rangle &= \left(-\frac{\Gamma_i}{2} \langle \hat{X}_i \rangle + (\Omega_i - \Omega_m) \langle \hat{Y}_i \rangle \right) dt \\
 &\quad + 2 \left[\sqrt{\Gamma_{\text{meas}}^i} V_{X_i} + \sum_{j \neq i} \sqrt{\Gamma_{\text{meas}}^j} C_{X_i X_j} \right] dW_X \\
 &\quad + 2 \left[\sqrt{\Gamma_{\text{meas}}^i} C_{X_i Y_i} + \sum_{j \neq i} \sqrt{\Gamma_{\text{meas}}^j} C_{X_i Y_j} \right] dW_Y \\
 d\langle \hat{Y}_i \rangle &= \left(-\frac{\Gamma_i}{2} \langle \hat{Y}_i \rangle - (\Omega_i - \Omega_m) \langle \hat{X}_i \rangle \right) dt \\
 &\quad + 2 \left[\sqrt{\Gamma_{\text{meas}}^i} V_{Y_i} + \sum_{j \neq i} \sqrt{\Gamma_{\text{meas}}^j} C_{Y_i Y_j} \right] dW_Y \\
 &\quad + 2 \left[\sqrt{\Gamma_{\text{meas}}^i} C_{Y_i X_i} + \sum_{j \neq i} \sqrt{\Gamma_{\text{meas}}^j} C_{Y_i X_j} \right] dW_X
 \end{aligned}$$

and for the covariance matrix

$$\begin{aligned}
 \dot{V}_{X_i} &= -\Gamma_i V_{X_i} + 2(\Omega_i - \Omega_m) C_{X_i Y_i} + \Gamma_i \left(\bar{n} + \frac{1}{2} \right) + \Gamma_{\text{qba}}^i \\
 &\quad - 4 \left(\left[\sqrt{\Gamma_{\text{meas}}^i} V_{X_i} + \sum_{j \neq i} \sqrt{\Gamma_{\text{meas}}^j} C_{X_i X_j} \right]^2 + \left[\sqrt{\Gamma_{\text{meas}}^i} C_{X_i Y_i} + \sum_{j \neq i} \sqrt{\Gamma_{\text{meas}}^j} C_{X_i Y_j} \right]^2 \right) \\
 \dot{V}_{Y_i} &= -\Gamma_i V_{Y_i} - 2(\Omega_i - \Omega_m) C_{X_i Y_i} + \Gamma_i \left(\bar{n} + \frac{1}{2} \right) + \Gamma_{\text{qba}}^i \\
 &\quad - 4 \left(\left[\sqrt{\Gamma_{\text{meas}}^i} V_{Y_i} + \sum_{j \neq i} \sqrt{\Gamma_{\text{meas}}^j} C_{Y_i Y_j} \right]^2 + \left[\sqrt{\Gamma_{\text{meas}}^i} C_{Y_i X_i} + \sum_{j \neq i} \sqrt{\Gamma_{\text{meas}}^j} C_{Y_i X_j} \right]^2 \right) \\
 \dot{C}_{X_i Y_i} &= (\Omega_i - \Omega_m) (V_{Y_i} - V_{X_i}) - \Gamma_i C_{X_i Y_i} \\
 &\quad - 4 \left[\left(\sqrt{\Gamma_{\text{meas}}^i} V_{X_i} + \sum_{j \neq i} \sqrt{\Gamma_{\text{meas}}^j} C_{X_i X_j} \right) \left(\sqrt{\Gamma_{\text{meas}}^i} C_{X_i Y_i} + \sum_{j \neq i} \sqrt{\Gamma_{\text{meas}}^j} C_{Y_i X_j} \right) \right] \\
 &\quad - 4 \left[\left(\sqrt{\Gamma_{\text{meas}}^i} V_{Y_i} + \sum_{j \neq i} \sqrt{\Gamma_{\text{meas}}^j} C_{Y_i Y_j} \right) \left(\sqrt{\Gamma_{\text{meas}}^i} C_{X_i Y_i} + \sum_{j \neq i} \sqrt{\Gamma_{\text{meas}}^j} C_{X_i Y_j} \right) \right]
 \end{aligned}$$

3.2 Quantum measurements of mechanical motions

with the new cross terms ($i \neq j$)

$$\begin{aligned}
\dot{C}_{X_i Y_j} &= (\Omega_i - \Omega_m) C_{Y_i Y_j} - (\Omega_j - \Omega_m) C_{X_i X_j} - \frac{\Gamma_i + \Gamma_j}{2} C_{X_i Y_j} \\
&\quad - 4 \left[(\sqrt{\Gamma_{\text{meas}}^i} V_{X_i} + \sum_{k \neq i} \sqrt{\Gamma_{\text{meas}}^k} C_{X_i X_k}) (\sqrt{\Gamma_{\text{meas}}^j} C_{Y_j X_j} + \sum_{k \neq j} \sqrt{\Gamma_{\text{meas}}^k} C_{Y_j X_k}) \right] \\
&\quad - 4 \left[(\sqrt{\Gamma_{\text{meas}}^i} C_{X_i Y_i} + \sum_{k \neq i} \sqrt{\Gamma_{\text{meas}}^k} C_{X_i Y_k}) (\sqrt{\Gamma_{\text{meas}}^j} V_{Y_j} + \sum_{k \neq j} \sqrt{\Gamma_{\text{meas}}^k} C_{Y_j Y_k}) \right] \\
\dot{C}_{X_i X_j} &= (\Omega_i - \Omega_m) C_{Y_i X_j} + (\Omega_j - \Omega_m) C_{X_i Y_j} - \frac{\Gamma_i + \Gamma_j}{2} C_{X_i X_j} + \sqrt{\Gamma_{\text{qba}}^i \Gamma_{\text{qba}}^j} \\
&\quad - 4 \left[(\sqrt{\Gamma_{\text{meas}}^i} V_{X_i} + \sum_{k \neq i} \sqrt{\Gamma_{\text{meas}}^k} C_{X_i X_k}) (\sqrt{\Gamma_{\text{meas}}^j} V_{X_j} + \sum_{k \neq j} \sqrt{\Gamma_{\text{meas}}^k} C_{X_j X_k}) \right] \\
&\quad - 4 \left[(\sqrt{\Gamma_{\text{meas}}^i} C_{X_i Y_i} + \sum_{k \neq i} \sqrt{\Gamma_{\text{meas}}^k} C_{X_i Y_k}) (\sqrt{\Gamma_{\text{meas}}^j} C_{X_j Y_j} + \sum_{k \neq j} \sqrt{\Gamma_{\text{meas}}^k} C_{X_j Y_k}) \right]
\end{aligned}$$

derived using the additional moment relations

$$\text{Tr}[X_i X_j (\mathcal{D}_2[Y_i, Y_j] + \mathcal{D}_2[Y_j, Y_i]) \rho] = \text{Tr}[Y_i Y_j (\mathcal{D}_2[X_i, X_j] + \mathcal{D}_2[X_j, X_i]) \rho] = 1. \quad (3.88)$$

These new cross terms are generally non-zero, which means there will be correlations between different observables because they share the same measurement noise and backaction force.

We summarized here the most compact version of the multi-mode quantum master equation,

$$d\langle \hat{\mathbf{r}}_i \rangle = \mathbf{A}_i \langle \hat{\mathbf{r}}_i \rangle dt + 2\mathbf{B}_i d\mathbf{W}(t), \quad (3.89)$$

where

$$\mathbf{A}_i = \begin{bmatrix} -\Gamma_m^i/2 & \Omega_i - \Omega_m \\ \Omega_m - \Omega_i & -\Gamma_m^i/2 \end{bmatrix}$$

and

$$\mathbf{B}_i = \begin{bmatrix} \sum_j \sqrt{\Gamma_{\text{meas}}^j} C_{\hat{X}_i \hat{X}_j} & \sum_j \sqrt{\Gamma_{\text{meas}}^j} C_{\hat{X}_i \hat{Y}_j} \\ \sum_j \sqrt{\Gamma_{\text{meas}}^j} C_{\hat{Y}_i \hat{X}_j} & \sum_j \sqrt{\Gamma_{\text{meas}}^j} C_{\hat{Y}_i \hat{Y}_j} \end{bmatrix}.$$

The covariance matrix elements $C_{\hat{M}\hat{N}} = \langle \hat{M}\hat{N} + \hat{N}\hat{M} \rangle / 2 - \langle \hat{M} \rangle \langle \hat{N} \rangle$ evolve as

$$\begin{aligned}
\dot{C}_{\hat{M}_i \hat{N}_j} &= -\frac{\Gamma_m^i + \Gamma_m^j}{2} C_{\hat{M}_i \hat{N}_j} + \delta_{\hat{M}_i, \hat{N}_j} \Gamma_{\text{th}}^i + \delta_{M, N} \sqrt{\Gamma_{\text{qba}}^i \Gamma_{\text{qba}}^j} \\
&\quad + (-1)^{\delta_{M, Y}} (\Omega_i - \Omega_m) C_{\hat{M}_i \hat{N}_j} + (-1)^{\delta_{N, Y}} (\Omega_j - \Omega_m) C_{\hat{M}_i \hat{N}_j} \\
&\quad - 4 \left(\sum_k \sqrt{\Gamma_{\text{meas}}^k} C_{\hat{M}_i \hat{X}_k} \right) \left(\sum_l \sqrt{\Gamma_{\text{meas}}^l} C_{\hat{N}_j \hat{X}_l} \right) \\
&\quad - 4 \left(\sum_k \sqrt{\Gamma_{\text{meas}}^k} C_{\hat{M}_i \hat{Y}_k} \right) \left(\sum_l \sqrt{\Gamma_{\text{meas}}^l} C_{\hat{N}_j \hat{Y}_l} \right), \quad (3.90)
\end{aligned}$$

Chapter 3. Measurement-based quantum control of mechanical motion

where $\hat{\mathcal{M}}$ and $\hat{\mathcal{N}}$ are the canonical conjugate observables of \hat{M} and \hat{N} .

Physical meaning of different terms

First, notice that in all the covariance updates, no dW is present due to the linearity of the measurement process.

The $[H, \rho]$ term gives rise to the quadrature rotation terms associated with $\Omega_i - \Omega_m$, if the oscillator i is not at frequency Ω_m . The oscillation happens between $\langle \hat{X}_i \rangle$ and $\langle \hat{Y}_i \rangle$. The phase space distribution rotates with this frequency as well, so if $V_{X_i} \neq V_{Y_i}$, the terms V_{X_i} , V_{Y_i} and $C_{X_i Y_i}$ will oscillate at two-times that frequency. For the cross-correlation between different oscillators (i, j), since each quadrature is oscillating at its frequency, the cross-correlation $C_{O_k X_i}$ will oscillate, together with the complimentary part $C_{O_k Y_i}$, with their frequency difference $\Omega_i - \Omega_k$.

$\mathcal{D}[b_i]$ is responsible for the dissipation from the environment coupling. We assume no common bath between oscillators, and the term only manifests as the dissipation associated with the intrinsic loss rate Γ_i . The quadratures decay with half the rate, and the variance decays with the full rate, while also driven by the thermal force $\Gamma_i(\bar{n}_{\text{th}} + 1/2)$. The correlation $C_{X_i Y_i}$ decays with the same rate Γ_i because both quadratures are dissipated with half of it. The same thing reflects in the cross-correlation $C_{X_i Y_j}$ but with an averaged decay rate $(\Gamma_i + \Gamma_j)/2$ of both oscillators.

$\mathcal{D}[X_i]$ is the measurement-induced backaction term that generally causes additional decoherence. It does not steer the quadrature in a particular direction since it is random, so it does not affect the quadrature update equations. However, the variance increases with the QBA rate Γ_{qba}^i . The correlation $C_{X_i Y_i}$ does not depend on it because both quadratures are experiencing independent backaction forces in our model. The cross-correlation $C_{X_i X_j}$, however, can be generated since the two quadratures X_i and X_j are experiencing the same backaction force, which is characterized by the geometric average of their QBA rates $\sqrt{\Gamma_{\text{qba}}^i \Gamma_{\text{qba}}^j}$. Notice that the (X_i, Y_j) term has no common backaction force. Therefore, $C_{X_i Y_j}$ does not depend on QBA.

$\mathcal{H}[X_i]$ gives rise to the measurement-induced steering of the state. The update strength is proportional to the measurement rate $\sqrt{\Gamma_{\text{meas}}^i}$, and also the uncertainty of the state V_{X_i} . This particular scaling can be understood fairly easily by considering a conditional operation with rate μ done on the Gaussian state

$$\exp\left(-\mu\Delta t\left(\langle X \rangle + \frac{\Delta W}{\sqrt{4\mu\Delta t}} - X\right)^2\right) \exp\left(-\frac{(X - \langle X \rangle)^2}{4V_X}\right) \propto \exp\left(-\frac{(X - \langle X \rangle - \frac{2\sqrt{\mu}V_X\Delta W}{1+4\mu\Delta t V_X})^2}{4V_X/(1+4V_X\mu\Delta t)}\right) \quad (3.91)$$

in which we can see that the updated quadrature value is shifted by $2\sqrt{\mu}V_X\Delta W$, and the variance is reduced by $4V_X^2\mu\Delta t$. When observing multiple observables, e.g., X_j , then the update on the observables will influence each other through the covariance matrix $C_{X_i X_j}$, with the

3.2 Quantum measurements of mechanical motions

measurement rate $\sqrt{\Gamma_{\text{meas}}^j}$. This correlation is also a well-known property of the multivariate Gaussian distribution, which is of concern here. The (cross-) correlation $(C_{X_i Y_j}) C_{X_i Y_i}$ is updated each time with the common Wiener increment terms in $(d\langle X_i \rangle d\langle Y_j \rangle) d\langle X_i \rangle d\langle Y_i \rangle$, indirectly through quadrature cross-correlations, i.e. from the first-moment update equations. All the linear terms related to ΔW are canceled due to the linearity of the measurement.

Interestingly, when multiple modes have slightly different frequencies, it seems possible to generate a correlation between (X_i, Y_i) , mediated by quadrature rotation due to the finite frequency offset. The correlations are first generated between (X_i, X_j) and (Y_i, Y_j) because they experience the same backaction force. Then, due to the slight frequency difference, the quadrature (X_i, X_j) will rotate to, e.g., (X_i, Y_j) and contributes to the correlation between (X_i, Y_i) due to the common measurement channels between (Y_i, Y_j) . This effect can also be interpreted from the picture of Bayesian inference, that a measurement on a common variable (c), with which other two variables (a, b) are correlated, will generate a correlation between (a, b) . Here, a nearby mode serves as the common variable c . However, this effect can not induce a correlation between (X_i, Y_i) in our system, as there are two common variables: $c_1 = X_j$ and $c_2 = Y_j$. The symmetry of these two common variables, in terms of measurement rates, forbids the generation of single-mode correlation. This effect is illustrated in Fig. 3.3, that even if C_{X_i, Y_j} can be non-zero, $C_{X_i, Y_i} = 0$ at all times.

Optimal multi-mode filter

Similar to the single-mode state estimation filter, we write down the photocurrent expression in the multi-mode case,

$$\mathbf{i}(t) dt = d\mathbf{W}(t) + \sum_i \sqrt{4\Gamma_{\text{meas}}^i} \langle \hat{\mathbf{x}}_i \rangle(t) dt. \quad (3.92)$$

Then, we can write the quadrature update equations in a vectorized form (notation $C_{X_i X_i} = V_{X_i}$),

$$\begin{aligned} \frac{d}{dt} \begin{pmatrix} X_1 \\ Y_1 \\ X_2 \\ Y_2 \\ \vdots \end{pmatrix} &= \begin{pmatrix} -\frac{\Gamma_1}{2} & \Omega_1 & 0 & 0 & \cdots \\ -\Omega_1 & -\frac{\Gamma_1}{2} & 0 & 0 & \cdots \\ 0 & 0 & -\frac{\Gamma_2}{2} & \Omega_2 & \cdots \\ 0 & 0 & -\Omega_2 & -\frac{\Gamma_2}{2} & \cdots \\ \vdots & \vdots & \vdots & \vdots & \ddots \end{pmatrix} \begin{pmatrix} X_1 \\ Y_1 \\ X_2 \\ Y_2 \\ \vdots \end{pmatrix} \\ &+ \begin{pmatrix} \sum_i \sqrt{\Gamma_{\text{meas}}^i} C_{X_1 X_i} & \sum_i \sqrt{\Gamma_{\text{meas}}^i} C_{X_1 Y_i} \\ \sum_i \sqrt{\Gamma_{\text{meas}}^i} C_{Y_1 X_i} & \sum_i \sqrt{\Gamma_{\text{meas}}^i} C_{Y_1 Y_i} \\ \sum_i \sqrt{\Gamma_{\text{meas}}^i} C_{X_2 X_i} & \sum_i \sqrt{\Gamma_{\text{meas}}^i} C_{X_2 Y_i} \\ \sum_i \sqrt{\Gamma_{\text{meas}}^i} C_{Y_2 X_i} & \sum_i \sqrt{\Gamma_{\text{meas}}^i} C_{Y_2 Y_i} \\ \vdots & \vdots \end{pmatrix} \left(2 \begin{pmatrix} i_X \\ i_Y \end{pmatrix} - 4 \begin{pmatrix} X_1 & X_2 & \cdots \\ Y_1 & Y_2 & \cdots \end{pmatrix} \begin{pmatrix} \sqrt{\Gamma_{\text{meas}}^1} \\ \sqrt{\Gamma_{\text{meas}}^2} \\ \vdots \end{pmatrix} \right) \end{aligned} \quad (3.93)$$

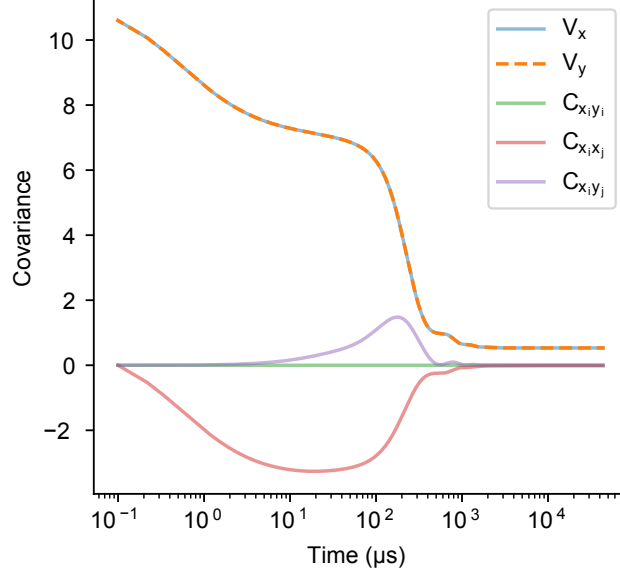


Figure 3.3: Time evolution traces for covariance matrix elements. The system consists of three identical oscillators separated by 10 kHz, at near-zero-temperature, and with measurement rates at 10 kHz. We observe that $C_{x_i x_j}$ first increases due to the common measurement noise. Then, the correlation rotates to $C_{x_i y_j}$ due to finite mechanical frequency difference. Even though at some point $C_{x_i y_j} \neq 0$, there is a pair of anti-symmetric contributions $C_{x_i y_j} = -C_{x_j y_i}$ that both contribute to $C_{x_i y_i}$, cancel with each other. The cancellation leads to a constant $C_{x_i y_i} = 0$ over all the measurement times. This symmetry is induced by the symmetric measurement rate at the two (X,Y) measurement channels, since $\Gamma_{\text{meas}} \ll \Gamma_m$.

We can solve the expression numerically in the frequency domain and get

$$X(\omega) = H_{XX}(\omega) i_X(\omega) + H_{XY}(\omega) i_Y(\omega) \quad (3.94)$$

$$Y(\omega) = -H_{XY}(\omega) i_X(\omega) + H_{XX}(\omega) i_Y(\omega) \quad (3.95)$$

from which we can reconstruct the optimal real-time multi-mode filter

$$Q(\omega) = \frac{1}{\sqrt{2}} (H_{XX}(\omega - \Omega_m) - i H_{XY}(\omega - \Omega_m)) i(\omega) \quad (3.96)$$

by recognizing that $i(\omega^+) = \frac{\sqrt{2}}{2} (i_X(\omega^+ - \Omega_m) + i \cdot i_Y(\omega^+ - \Omega_m))$ and $Q(\omega^+) = \frac{1}{2} (X(\omega^+ - \Omega_m) + i \cdot Y(\omega^+ - \Omega_m))$.

3.2.2 Retrodiction

To verify a state prepared through a conditioning procedure, one usually uses a strong measurement to project the state to some measurement basis. After repeating this step multiple

3.2 Quantum measurements of mechanical motions

times, the population of different basis states can be retrieved, and the state can be verified.

For continuous measurement of mechanical motion, we are not in the regime where the measurement is "strong" on a set of orthogonal basis (quadrature basis). The effective heterodyne measurement of mechanical quadratures effectively projects the state into a non-orthogonal state basis of coherent states [9] by a pair of orthogonal inefficient quadrature projections. Therefore, if we use the "future" record of the measurement as a separate "weak" state projection for comparison with the state prepared using the "past" record, we will not retrieve a population on a set of orthogonal basis, but a phase-space state variance of the prepared state. Since the prepared states are Gaussian states, the phase-space variance holds complete information to describe the property of the mechanical state.

Note that when we prepare the mechanical state using only the "past" record, the best we can do is to prepare coherent states, i.e., phase-space variance the same as the vacuum uncertainty of the quantum ground state, bounded by the Heisenberg uncertainty principle. However, the Heisenberg uncertainty principle only applies to exactly forward prediction. With the combination of backward retrodiction using the "future" record, the state estimation can be much more precise, even beyond the Heisenberg limit. Intuitively, the state at a given time is almost deterministic when we can access the whole measurement record. This technique is frequently used in Wiener filtering, where the prediction uses the causal solution, and the more precise estimation also uses the noncausal part.

In this section, we derive the framework of state retrodiction using the "future" record of the measurement relative to the timing of state preparation. We follow the theory work [75], which established the framework of retrodiction. In that work, the past density matrix is given by

$$\rho_p(t) = \rho(\vec{t})E(\vec{t})/\text{Tr}(\rho(\vec{t})E(\vec{t})) \quad (3.97)$$

where $\rho(\vec{t})$ is the predicted density matrix from the stochastic master equation using the record before t , and $E(\vec{t})$ is the effect matrix evolved backward in time from some final time T in the future following the Hilbert-Schmidt adjoint of the master equation. The trace-preserving version of the backward master equation is

$$dE = i[H, E]dt + \sum_i (\mathcal{D}^\dagger[c_i]E - \langle [c_i, c_i^\dagger] \rangle_E E)dt + \sum_i \sqrt{\eta_i} \mathcal{H}[c_i^\dagger] E dW_i^E(t-dt) \quad (3.98)$$

where $\mathcal{D}^\dagger[c]E = c^\dagger E c - \frac{1}{2}[c^\dagger, c]_+ E$ and $dW_i^E = i_i dt - \sqrt{\eta_i} \langle [c_i^\dagger + c_i] \rangle_E dt$. Note that the effect matrix E is different from a density matrix, and the initial condition $E(t=T) = \mathcal{I}$ is the identity matrix \mathcal{I} .

[76] solved for the case of Gaussian states by casting the action of quadrature operators on the density matrix into Wigner functions,

$$X_j \rho = \left(X_j + \frac{i}{2} \partial_{Y_j} \right) W_\rho(\mathbf{r}), \quad Y_j \rho = \left(Y_j - \frac{i}{2} \partial_{X_j} \right) W_\rho(\mathbf{r}). \quad (3.99)$$

Chapter 3. Measurement-based quantum control of mechanical motion

Then, the master equation can be rewritten into a Fokker-Planck equation for the Wigner function. In this scenario, the Wigner function always maintains a Gaussian form and can be reduced to the evolution of its first and second moments.

Following this approach, we arrive at the update equations for the first and second moments of the forward density matrix ($\langle \mathbf{r} \rangle, \sigma$) and the backward effect matrix ($\langle \mathbf{r} \rangle_E, \gamma$)

$$d\langle \mathbf{r} \rangle = A\langle \mathbf{r} \rangle dt + (\sigma B^\top - N^\top) \sqrt{\boldsymbol{\eta}} d\mathbf{W} \quad (3.100)$$

$$\dot{\sigma} = A\sigma + \sigma A^\top + D - 2(\sigma B^\top - N^\top) \boldsymbol{\eta} (\sigma B^\top - N^\top)^\top \quad (3.101)$$

$$-d\langle \mathbf{r} \rangle_E = \langle \mathbf{r} \rangle_E(t-dt) - \langle \mathbf{r} \rangle_E(t) = -A\langle \mathbf{r} \rangle_E dt + (\gamma B^\top + N^\top) \sqrt{\boldsymbol{\eta}} d\mathbf{W}^E \quad (3.102)$$

$$-\dot{\gamma} = -A\gamma - \gamma A^\top + D - 2(\gamma B^\top + N^\top) \boldsymbol{\eta} (\gamma B^\top + N^\top)^\top \quad (3.103)$$

where σ is the forward covariance matrix, and γ is the backward covariance matrix. In the case where the observables are Hermitian, $N = 0$. Then, the only difference between the forward and backward equations is that the drift terms A are sign-flipped.

In the simple case of tracking one mechanical oscillator, the backward update equations are

$$-d\langle \mathbf{r} \rangle_E = \left(\frac{\Gamma_m}{2} - \begin{pmatrix} 0 & \delta\omega \\ -\delta\omega & 0 \end{pmatrix} \right) \langle \mathbf{r} \rangle_E(t) dt + 2\sqrt{\Gamma_{\text{meas}}} V_E(t) d\mathbf{W}^E \quad (3.104)$$

$$-\dot{V}_E(t) = \Gamma_m V_E(t) + \Gamma_m \left(n_{\text{th}} + \frac{1}{2} \right) + \Gamma_{\text{qba}} - 4\Gamma_{\text{meas}} V_E(t)^2 \quad (3.105)$$

where $d\mathbf{W}_E = \mathbf{i} dt - 2\sqrt{\Gamma_{\text{meas}}} \langle \mathbf{r} \rangle_E(t) dt$. The initial condition, given $E(t=T) = \mathcal{I}$, is calculated to be $\langle \mathbf{r} \rangle_E(t=T) = 0$ and $V_E(t=T) \rightarrow +\infty$.

However, one important thing to pay attention to is that ($\langle \mathbf{r} \rangle_E, \gamma$) are not the moments for the past quantum state ρ_p , but are only related to the effect matrix E . But since everything is Gaussian, we can retrieve the correct moments for the past quantum states as

$$\langle \mathbf{r} \rangle_p = \frac{\langle \mathbf{r} \rangle V_E + \langle \mathbf{r} \rangle_E V}{V + V_E} \quad V_p = \frac{V V_E}{V + V_E} \quad (3.106)$$

If we express the update formula in terms of ($\langle \mathbf{r} \rangle_p, \sigma_p$), by setting initial moments ($\langle \mathbf{r} \rangle = 0, V = V_{\text{bath}} = n_{\text{th}} + \frac{1}{2} + \Gamma_{\text{qba}}/\Gamma_m$) to the default thermal state similar to the forward updates, we have the following backward update equations for the first two moments of the past density matrix ρ_p ,

$$-d\langle \mathbf{r} \rangle_p = \left(-\frac{\Gamma_m}{2} - \begin{pmatrix} 0 & \delta\omega \\ -\delta\omega & 0 \end{pmatrix} \right) \langle \mathbf{r} \rangle_p(t) dt + 2\sqrt{\Gamma_{\text{meas}}} V_p(t) d\mathbf{W}^p \quad (3.107)$$

$$-\dot{V}_p(t) = -\Gamma_m V_p(t) + \Gamma_m \left(n_{\text{th}} + \frac{1}{2} \right) + \Gamma_{\text{qba}} - 4\Gamma_{\text{meas}} V_p(t)^2 \quad (3.108)$$

where $d\mathbf{W}^p = \mathbf{i} dt - 2\sqrt{\Gamma_{\text{meas}}} \langle \mathbf{r} \rangle_p dt$. Note that the backward update equations are the same as the forward equations but backward in time. It is also true in multi-mode cases, where update

equations are symmetric between forward and backward directions. Our result differs from the reference [77] but is consistent with [78] which we believe is correct.

3.2.3 Conditional state preparation

This section describes the experiment procedure of numerically implementing the multi-mode mechanical state preparation and verifying the numerical implementation. Notably, we emphasize the importance of considering the effective modification of the filter response by the finite sampling rate. With a correctly implemented filter, our measurement strongly correlates different mechanical modes, with which collective motions can be defined to help remove their correlations.

Multi-mode state estimation model

In Section 3.2.1, we derive the equations of quadrature evolution used for implementing the multi-mode mechanical state estimation. This section briefly summarizes the results and discusses how to decouple the correlated mechanical modes through symplectic transformations and reconstruct the covariance matrix using the prediction-retrodiction method.

We work in a parameter regime where the measurement rate Γ_{meas} is significantly smaller than the frequency of the mechanical mode Ω_m , such that we can perform IQ demodulation of the mechanical motion at Ω_m to obtain the slowly-varying X, Y quadratures. Their evolution is described by decoupled quantum master equations [36]. In the case where the measurement rate approaches the mechanical frequency, as can be in the case of resonators with a fundamental mode isolated in frequency from the higher order modes, the two equations can be coupled as was in the case in [37, 41], and measurement-induced mechanical squeezing can happen. Since both quadratures are measured with identical measurement rates, only thermal coherent states are prepared through the measurement process.

Since we operate in the fast-cavity limit $\Omega_m \ll \kappa$, the cavity dynamics is simplified in our modeling. Before the IQ demodulation, the normalized photocurrent signal is described by:

$$i(t) = dW(t) + \sum_i \sqrt{8\Gamma_{\text{meas}}^i} \langle \hat{Q}_i \rangle(t),$$

where multiple mechanical modes \hat{Q}_i oscillating at Ω_i are probed with measurement rates Γ_{meas}^i , and the Wiener increment $dW(t) = \xi(t)dt$ is defined in terms of an ideal unit Gaussian white noise process $\langle \xi(t)\xi(t') \rangle = \delta(t - t')$. Since all oscillation frequencies are close to Ω_m , we decompose the mechanical motion into two slowly varying quadrature observables as $\hat{Q}_i = \cos(\Omega_m t) \hat{X}_i + \sin(\Omega_m t) \hat{Y}_i$, and perform IQ demodulation at frequency Ω_m , which leads to the signal in a vector form:

$$\mathbf{i}(t)dt = d\mathbf{W}(t) + \sum_i \sqrt{4\Gamma_{\text{meas}}^i} \langle \hat{\mathbf{r}}_i \rangle(t)dt \quad (3.109)$$

Chapter 3. Measurement-based quantum control of mechanical motion

where $\mathbf{i} = \begin{bmatrix} i_X \\ i_Y \end{bmatrix}$, $\hat{\mathbf{r}}_i = \begin{bmatrix} \hat{X}_i \\ \hat{Y}_i \end{bmatrix}$ and $d\mathbf{W} = \begin{bmatrix} dW_X \\ dW_Y \end{bmatrix}$. Since the measurement is purely linear, the system stays in Gaussian state-space, and the dynamics are completely captured by the expectation values of the quadratures $\langle X_i \rangle$, $\langle Y_i \rangle$, and their covariance matrix \mathbf{C} . To derive the time evolutions of these quantities, we start from the quantum master equation for the system density matrix $\hat{\rho}$ [36]:

$$d\hat{\rho} = -\frac{i}{\hbar} [\hat{H}_0, \hat{\rho}] + \mathcal{L}_{\text{env}}\hat{\rho}dt + \sum_j \mathcal{D}[\hat{c}_j]\hat{\rho}dt + \sqrt{\eta_d} \sum_j \mathcal{H}[\hat{c}_j]\hat{\rho}dW_j,$$

where the index j is summed over X and Y measurement channels, and η_d is the total detection efficiency. The measurement observables are $\hat{\mathbf{c}}(t) = \sum_i \sqrt{\Gamma_{\text{qba}}^i} \hat{\mathbf{r}}_i$. The system Hamiltonian $\hat{H}_0 = \sum_i \hbar(\Omega_i - \Omega_m) b_i^\dagger b_i$ describes the oscillator unitary dynamics in the Ω_m rotating frame. The environmental coupling term $\mathcal{L}_{\text{env}}\hat{\rho}$ describes the bath-induced decoherence dynamics, and with the Markov approximation in the rotating frame, we have:

$$\mathcal{L}_{\text{env}}\hat{\rho} = \sum_i \Gamma_m^i (\bar{n}_i + 1) \mathcal{D}[\hat{b}_i]\hat{\rho} + \Gamma_m^i \bar{n}_i \mathcal{D}[\hat{b}_i^\dagger]\hat{\rho}.$$

From here, we derive the time evolution of the quadrature expectation values as:

$$d\langle \hat{\mathbf{r}}_i \rangle = \mathbf{A}_i \langle \hat{\mathbf{r}}_i \rangle dt + 2\mathbf{B}_i d\mathbf{W}(t), \quad (3.110)$$

where

$$\mathbf{A}_i = \begin{bmatrix} -\Gamma_m^i/2 & \Omega_i - \Omega_m \\ \Omega_m - \Omega_i & -\Gamma_m^i/2 \end{bmatrix}$$

and

$$\mathbf{B}_i = \begin{bmatrix} \sum_j \sqrt{\Gamma_{\text{meas}}^j} C_{\hat{X}_i \hat{X}_j} & \sum_j \sqrt{\Gamma_{\text{meas}}^j} C_{\hat{X}_i \hat{Y}_j} \\ \sum_j \sqrt{\Gamma_{\text{meas}}^j} C_{\hat{Y}_i \hat{X}_j} & \sum_j \sqrt{\Gamma_{\text{meas}}^j} C_{\hat{Y}_i \hat{Y}_j} \end{bmatrix}.$$

The covariance matrix elements $C_{\hat{M}\hat{N}} = \langle \hat{M}\hat{N} + \hat{N}\hat{M} \rangle / 2 - \langle \hat{M} \rangle \langle \hat{N} \rangle$ evolve as:

$$\begin{aligned} \dot{C}_{\hat{M}_i \hat{N}_j} = & -\frac{\Gamma_m^i + \Gamma_m^j}{2} \dot{C}_{\hat{M}_i \hat{N}_j} + \delta_{\hat{M}_i, \hat{N}_j} \Gamma_{\text{th}}^i + \delta_{M, N} \sqrt{\Gamma_{\text{qba}}^i \Gamma_{\text{qba}}^j} \\ & + (-1)^{\delta_{M, Y}} (\Omega_i - \Omega_m) C_{\hat{\mathcal{M}}_i \hat{N}_j} + (-1)^{\delta_{N, Y}} (\Omega_j - \Omega_m) C_{\hat{M}_i \hat{\mathcal{N}}_j} \\ & - 4 \left(\sum_k \sqrt{\Gamma_{\text{meas}}^k} C_{\hat{M}_i \hat{X}_k} \right) \left(\sum_l \sqrt{\Gamma_{\text{meas}}^l} C_{\hat{N}_j \hat{X}_l} \right) \\ & - 4 \left(\sum_k \sqrt{\Gamma_{\text{meas}}^k} C_{\hat{M}_i \hat{Y}_k} \right) \left(\sum_l \sqrt{\Gamma_{\text{meas}}^l} C_{\hat{N}_j \hat{Y}_l} \right), \end{aligned} \quad (3.111)$$

where $\hat{\mathcal{M}}$ and $\hat{\mathcal{N}}$ are the canonical conjugate observables of \hat{M} and \hat{N} .

Eqs. 3.109, 3.89, 3.90 form a closed set of update equations given the measurement record $\mathbf{i}(t)$, and allow quadrature estimations of an arbitrary number of modes and their correlations.

3.2 Quantum measurements of mechanical motions

The thermal occupancy \bar{n}_{cond}^i of a specific mechanical mode is determined by the quadrature phase space variances $V_{\hat{X}_i} = C_{\hat{X}_i \hat{X}_i}$, $V_{\hat{Y}_i} = C_{\hat{Y}_i \hat{Y}_i}$, which are both equal to $\bar{n}_{\text{cond},i} + 1/2$ due to the symmetric measurement rates of the X, Y channels.

In the case of the evolution of a single mechanical mode, the quadrature variance approaches a steady state described by an analytical solution,

$$V_{X,Y} = \frac{-\Gamma'_m + \sqrt{\Gamma'_m{}^2 + 16\Gamma_{\text{meas}}(\Gamma_{\text{th}} + \Gamma_{\text{qba}})}}{8\Gamma_{\text{meas}}}, \quad (3.112)$$

where $\Gamma'_m = \Gamma_m + \Gamma_{\text{opt}}$ takes into account the optical damping rate Γ_{opt} . For a system consisting of multiple mechanical modes that are not sufficiently separated in frequency ($|\Omega_i - \Omega_j|$ not significantly faster than any other rates in the system), cross-correlations between different mechanical modes emerge due to common measurement imprecision noise and common quantum backaction force. This generally leads to higher quadrature variance due to individual modes' effectively reduced measurement efficiency.

To decouple the mechanical oscillators that are correlated due to the spectral overlap and the measurement process, we define a new set of collective modes through a symplectic (canonical) transformation \mathbf{U} of quadrature basis that diagonalizes the steady state covariance matrix $\mathbf{U}^\dagger \mathbf{C} \mathbf{U} = \mathbf{V}$ [79]. Since the covariance matrix is real and symmetric, the elements of \mathbf{U} are always real, which is required for real observables. The transformation can be understood as a normal mode decomposition of the collective Gaussian state that preserves the commutation relations instead of conventional diagonalization using unitary matrices. This is represented by the requirement of the symplectic transformation $\mathbf{U} \Omega \mathbf{U}^\dagger = \Omega$ where $\Omega = \begin{bmatrix} 0 & \mathbf{I}_N \\ -\mathbf{I}_N & 0 \end{bmatrix}$ is the N -mode symplectic form.

For the multimode estimation experiment, we extract the required system parameters of the nearest ten mechanical modes around Ω_m by fitting the measured spectral noise density and feed the time-series signal $\mathbf{i}(t)$ to the closed update equations to retrieve all the 20 quadrature expectations and 210 independent covariance matrix elements at different times. The signal is normalized such that the Wiener increment gives the correct noise level in the frequency domain, and the filtered unconditional defect mode signal has the correct laser-cooled thermal occupancy.

The prediction-retrodiction method is used to reconstruct the covariance matrix \mathbf{C} , which is then used to compute the symplectic transformation needed to define the new collective mode bases. In Section 3.2.2, we derived the retrodiction update equations and found that they are identical to the prediction update equations [76], except with negative mechanical frequencies. As a result, we have the following relations between covariance matrix elements

Chapter 3. Measurement-based quantum control of mechanical motion

estimated by prediction and retrodiction (respectively identified by the superscripts p and r):

$$C_{\hat{X}_i \hat{X}_j}^p = C_{\hat{X}_i \hat{X}_j}^r \quad (3.113)$$

$$C_{\hat{Y}_i \hat{Y}_j}^p = C_{\hat{Y}_i \hat{Y}_j}^r \quad (3.114)$$

$$C_{\hat{X}_i \hat{Y}_j}^p = -C_{\hat{X}_i \hat{Y}_j}^r. \quad (3.115)$$

The reconstruction of the covariance matrix using the prediction-retrodiction method is discussed in the next part of this section.

Experimental implementation of multimode state estimation

The observation of optomechanical squeezing in Section 3.1 demonstrates that we can conduct quantum measurements with high efficiency. In fact, with quantum-limited detection, the maximum squeezing equals the measurement efficiency $\eta_{\text{meas}} = \Gamma_{\text{meas}} / (\Gamma_{\text{th}} + \Gamma_{\text{qba}})$ of the system, with Γ_{meas} being the measurement rate [80], and quantifies how far the measurement is from the Heisenberg uncertainty limit: $\sqrt{\bar{S}_{xx}^{\text{imp}} \bar{S}_{FF}^{\text{tot}}} = \hbar / (2\sqrt{\eta_{\text{meas}}})$. Measurement efficiency is likewise crucial for measurement-based quantum control of mechanical motion [17]: the measurement rate $\Gamma_{\text{meas}} = x_{\text{zpf}}^2 / (4\bar{S}_{xx}^{\text{imp}})$ represents the rate at which information is gained and the decoherence rate $\Gamma_{\text{th}} + \Gamma_{\text{qba}}$ the rate at which information is lost. We prepare conditional mechanical states by measuring the mechanical resonator at a rate close to its decoherence rate. This demonstrates that our system is in a parameter regime where quantum control of mechanical motion is possible at room temperature.

We proceed by locking the laser to the cavity at the magic detuning and adjust the single-detector homodyne to measure the mechanical motion at the quadrature angle $\theta \approx -90^\circ$, maximizing the readout efficiency of mechanical motion. We digitize the measurement signal at a 14 MHz rate over 2 s for state preparation in post-processing and measure a long-time average of the spectrum on a real-time spectrum analyzer for system parameter calibration. By fitting the measured noise spectrum with our model, we extract a total detection efficiency of $\eta_{\text{d}} = 31\%$, and $\mathcal{C}_q = 0.93$. These parameters correspond to a measurement rate of $\Gamma_{\text{meas}} = \eta_{\text{d}} \Gamma_{\text{qba}} = 2\pi \times 11 \text{ kHz}$ (equivalent imprecision noise quanta $n_{\text{imp}} = \Gamma_m / 16\Gamma_{\text{meas}} = 3.6 \times 10^{-8}$), approaching the thermal decoherence rate of $\Gamma_{\text{th}} = 2\pi \times 34 \text{ kHz}$ and resulting in a measurement efficiency of $\eta_{\text{meas}} = 16\%$. This efficiency corresponds to an imprecision-force noise product 2.5 times the Heisenberg uncertainty limit. Compared to the maximum squeezing, the degradation of the measurement efficiency mainly comes from the lower homodyne efficiency at quadrature angle $\theta \approx -90^\circ$, discussed in Section 2.4.3.

We record the voltage output from the photodetector using a UHFLI lock-in amplifier (Zurich Instruments), for a total duration of 2 s, digitizing the signal at 14 MHz sampling rate, and we store the data digitally for post-processing. The noise power spectrum density of the digitized signal is compared to the one simultaneously measured on a real-time spectrum analyzer to rule out SNR degradation from the digitization noise. Two 7th-order Butterworth

3.2 Quantum measurements of mechanical motions

bandpass filters with passband 1.05-1.22 MHz are applied in order to reduce the influence of the mechanical modes outside the bandgap, and around 50 notch filters are applied to these mechanical modes until no mechanical peak is above the shot noise level. After the filtering, only the ten mechanical modes around the defect mode frequency Ω_m need to be kept for the multimode state estimation study.

We conduct state preparation [41, 81] on the digitized and filtered signal based on the quantum master equations of the system. As shown in Fig. 3.5(a), the mechanical mode is initially in a thermal state with phase-space variance determined by both thermal decoherence and QBA decoherence. Based on the continuous measurement result, the state estimation procedure predicts the most probable values of the mechanical quadratures $\mathbf{r}^p = (X^p, Y^p)$, and the corresponding uncertainties in time in a theoretically-optimal fashion. However, as parasitic modes are still near the mode of interest, single-mode state estimation underestimates the conditional occupancy. In the estimation procedure, we prepare a multi-mode state and include the nine nearest modes.

As discussed in the previous section, we demodulate the signal at Ω_m , and implement the discretized version of the update equation Eq. 3.89,

$$\Delta \langle \hat{\mathbf{r}}_i \rangle = \mathbf{A}'_i \langle \hat{\mathbf{r}}_i \rangle \Delta t + 2\mathbf{B}_i \Delta \mathbf{W}(t) \quad (3.116)$$

where $\mathbf{A}'_i = \begin{bmatrix} -\Gamma_m^i/2 & \Omega'_i - \Omega_m \\ \Omega_m - \Omega'_i & -\Gamma_m^i/2 \end{bmatrix}$ contains modified mechanical parameters:

$$\Gamma_m^i = \Gamma_m^i + 2\text{Re} \left[-\frac{1 - \cos((\Omega_i - \Omega_m)\Delta t)}{\Delta t} \right] \quad (3.117)$$

$$\Omega'_i = \Omega_i - \text{Im} \left[i(\Omega_i - \Omega_m) - \frac{e^{i(\Omega_i - \Omega_m)\Delta t} - 1}{\Delta t} \right] \quad (3.118)$$

to compensate for the influence of discretization on the state estimation performance compared to an ideal continuous one. The effect of the naive discretization of the update equations vs. that in the ideal continuous limit is shown in Fig. 3.4(b). Without considering the discretization effect, the filter response deviates from the correct modeling of the system and causes numerical instability in the data processing.

The matrix \mathbf{B}_i evolution can be computed independently from the sampled time-domain data. Therefore, we calculate the evolution following Eq. 3.90, with an update rate of 140 MHz to mitigate the discretization effect, which is then used for the update equation Eq. 3.116 at the sampling rate of 14 MHz. The correct implementation of the state estimation can be checked from the Kalman filter response numerically calculated from the estimated $i(t)$, $Q_i(t)$ and $W(t)$, and is shown in Fig. 3.4(a), as well as the white noise property shown of the spectral density of the retrieved $W(t)$ from the data.

Using this set of equations, we can isolate the mechanical motion of the defect mode and mitigate spectral contamination between different modes. We can then compute the quadrature

Chapter 3. Measurement-based quantum control of mechanical motion

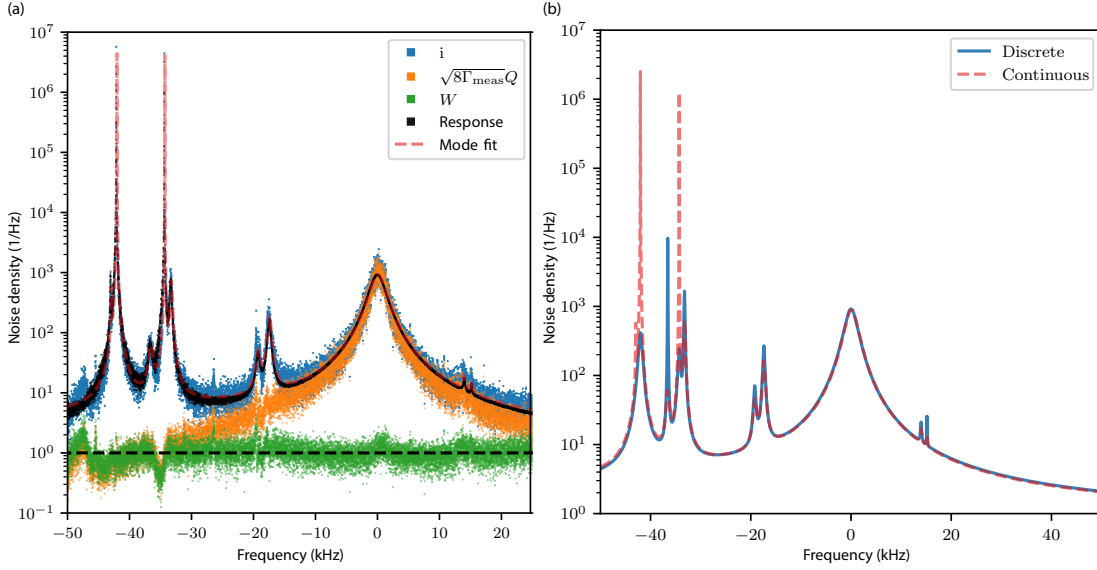


Figure 3.4: **(a)** Multimode state estimation spectral response. The noise density of the photocurrent signal $i(t)$ is shown in blue, together with the fit (dashed red), employed to extract the system parameters for the ten mechanical modes in this frequency band. Those parameters are used to construct the multimode state estimation filter, from which the mechanical mode signals (defect mode shown in orange) and the measurement imprecision (green) are separated. The white noise filter frequency response (gray) is numerically retrieved and identical to the spectral fit, indicating that the multimode state estimation filter is correctly implemented. **(b)** Comparison of the filter responses in the continuous acquisition limit, as well as the naive discretization with the acquisition rate of 14 MHz used in the experiment. By correcting for the effect of discretization on the filter response, we managed to reproduce the ideal continuous-limit filter response in our measurement result shown in **(a)**.

trajectory and the uncertainty of the optimally estimated defect mode [see Fig. 3.5(b)].

To estimate the quadrature variances $V_{X,Y}$, we use the displacement records in the “future” relative to the time of state conditioning as a separate measurement result \mathbf{r}^r , shown in Fig. 3.5(c), to reconstruct the covariance matrix. To experimentally reconstruct the covariance matrix from the estimated quadrature data, for each time trace slice, we calculate the difference between prediction and retrodiction results from $\langle \hat{\mathbf{r}} \rangle_r - \langle \hat{\mathbf{r}} \rangle_p$, and calculate the covariance matrix via

$$\mathbf{C} = \frac{1}{2} \langle \langle (\langle \hat{\mathbf{r}} \rangle_r - \langle \hat{\mathbf{r}} \rangle_p) \cdot (\langle \hat{\mathbf{r}} \rangle_r - \langle \hat{\mathbf{r}} \rangle_p)^\top \rangle \rangle \quad (3.119)$$

where $\langle \langle \dots \rangle \rangle$ is the statistical average over all the time trace slices, and $\hat{\mathbf{r}} = [\dots \hat{X}_i, \hat{Y}_i \dots]^\top$. The variance of the quadrature differences between the prediction and retrodiction results should be exactly $\langle \langle \|\mathbf{r}^r - \mathbf{r}^p\|^2 \rangle \rangle = 4V_{X,Y}$. We retrieved a thermal occupation $\bar{n}_{\text{cond}} = V_{X,Y} - 1/2 = 1.43$ of the prepared single-mode displaced thermal state, with only 3% deviation from the theoretical value. We found that the multi-mode estimation result shows 63% increased

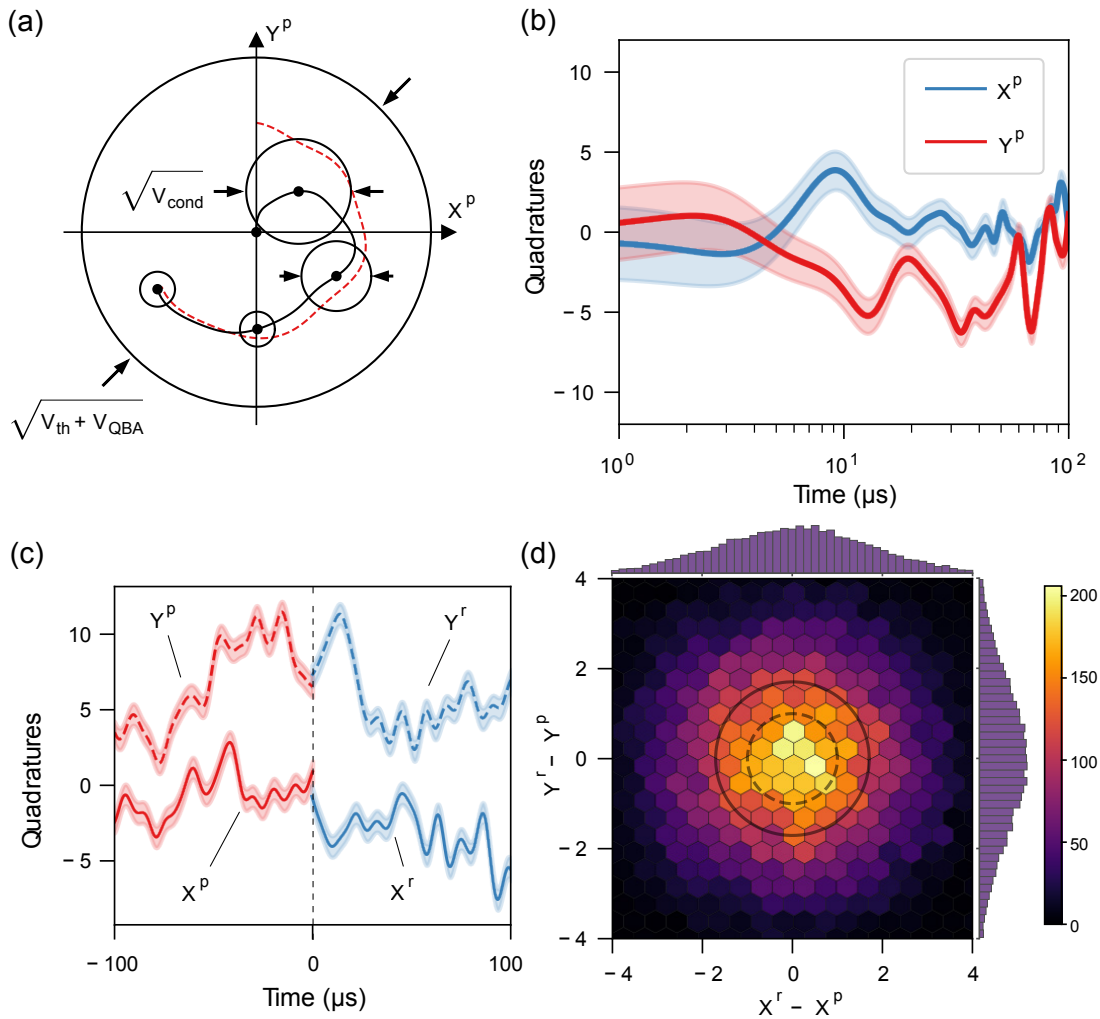


Figure 3.5: **Conditional state preparation and verification.** (a) Schematic of state preparation by continuous displacement measurement. The mechanical mode is initially in a thermal state. Given the measurement record, the state is continuously estimated and purified over time. (b) Exemplary quantum trajectory of the mechanical quadratures $\mathbf{r}^p = (X^p, Y^p)$. The shaded width corresponds to one standard deviation σ of uncertainty in the estimated quadratures. (c) Using state retrodiction $\mathbf{r}^r = (X^r, Y^r)$ (blue), the differences with the prediction result \mathbf{r}^p (red) at $t = 0$ is employed to reconstruct the covariance matrix of the multimode system. (d) Phase space density map of the collective mode of interest, with the solid circle marking the statistical standard deviation and the dashed circle indicating the standard deviation of a pure coherent state as a reference.

Chapter 3. Measurement-based quantum control of mechanical motion

thermal occupancy compared to the idealized single-mode estimation.

The degradation stems from the fact that mechanical modes, although separated in frequency, always have finite spectral overlap and cannot be fully distinguished. This results in strong cross-correlations between mechanical modes, whereby collective modes with enhanced measurement rates can be defined [78]. From the reconstructed multimode covariance matrix \mathbf{C} (definition of the matrix elements $C_{M,N}$ given in the Methods), we can quantify the magnitude of correlations by evaluating $C_{M_i,N_j}/\sqrt{V_{M_i}V_{N_j}}$, where M_i and N_j are arbitrary quadratures of the corresponding modes i and j . The correlation can be as strong as -0.44 depending on the frequency separation and measurement rates. We can define a set of uncorrelated collective modes that diagonalize \mathbf{C} through a symplectic transformation. The covariance matrix is then diagonalized to retrieve the symplectic transformation for the collective modes and the thermal occupations of these modes.

In the collective mode basis, all the modes are uncorrelated and are only weakly modified from the original basis. We conduct a similar prediction-retrodictio procedure using multi-mode filtering and plot the quadrature differences $\mathbf{r}^r - \mathbf{r}^p$ in Fig. 3.5(d). We find a modified defect mode thermal occupancy of $\bar{n}_{\text{cond,col}} = 0.97$ in the new collective mode bases, with a corresponding state purity of 34 %. This value is also very close to the ideal single-mode case, limited by the measurement efficiency. The transformation coefficients for the defect mode \hat{X} are shown in the following table. Note that the contributions from \hat{Y}_i are attributed to statistical uncertainties.

$\Omega_i - \Omega_m$ (kHz)	Coefficients \hat{X}	Coefficients \hat{Y}
0	0.999	5.05×10^{-7}
15.1	1.53×10^{-5}	-2.11×10^{-6}
13.9	-2.54×10^{-7}	-2.33×10^{-6}
-17.4	2.16×10^{-4}	5.06×10^{-6}
-19.3	1.23×10^{-4}	2.11×10^{-6}
-33.3	3.04×10^{-4}	3.14×10^{-6}
-34.4	2.96×10^{-2}	5.27×10^{-4}
-36.6	1.15×10^{-4}	-8.88×10^{-6}
-42.1	4.18×10^{-2}	-2.13×10^{-4}
-43.0	1.50×10^{-4}	3.14×10^{-6}

Measurement preparation of entangled mechanical states

One might ponder, if we can measure the multi-mode system very close to the quantum limit, can we prepare a multi-mode entangled state in our MIM system? In the following, we will present some simple arguments that indicate that it is not possible in our case when $\Gamma_{\text{meas}} \ll \Omega_m$.

Let us assume the most simplified case, where two mechanical oscillators are degenerate

3.2 Quantum measurements of mechanical motions

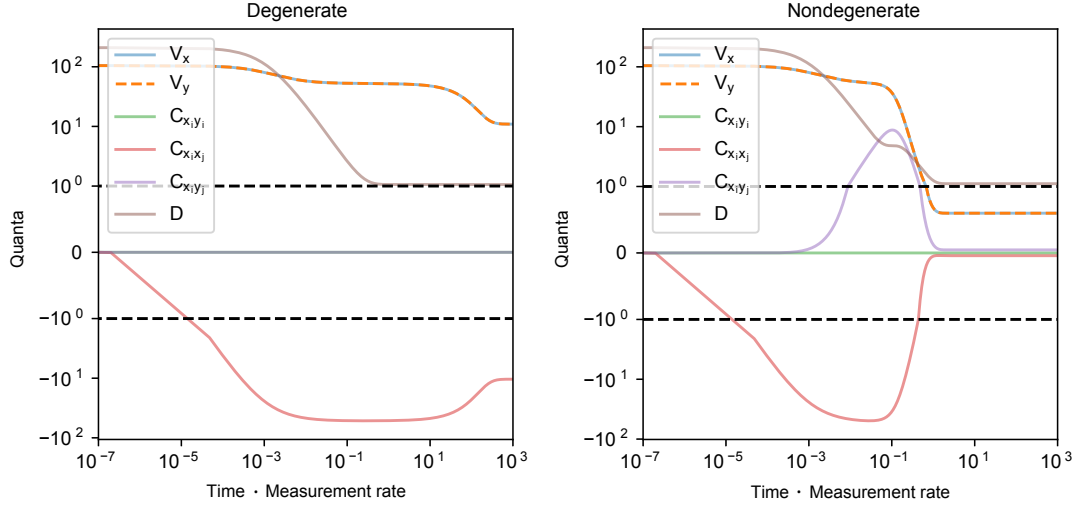


Figure 3.6: Simulation of covariance matrix elements and the Duan criteria D , of continuous measurements of two identical mechanical modes, in either degenerate condition $\delta\Omega_m = 0$ or nondegenerate condition $\delta\Omega_m = 100$ kHz. The measurement efficiency is set to $\eta_{\text{meas}} = 80\%$ with realistic system parameters, with measurement rates $\Gamma_{\text{meas}} = 20$ kHz.

at frequency Ω_m , and have identical mechanical properties, e.g. Γ_{th} . We measure both mechanical oscillators at a rate $\Gamma_{\text{meas}} \gg \Gamma_{\text{th}}$ using a single optical mode. Based on the optical measurement record, prepare conditional two-mode mechanical states, described by the quadrature expectation values and the covariance matrix \mathbf{C} .

Typical criteria for verifying entanglement between two continuous variable modes are the Duan criteria [82], that we can construct collective quadrature variables e.g. $\hat{X}_{\pm} = (\hat{X}_1 \pm \hat{X}_2)/\sqrt{2}$ and $\hat{Y}_{\pm} = (\hat{Y}_1 \pm \hat{Y}_2)/\sqrt{2}$. If the quantum correlation between two original quadratures is strong enough, one could reduce the variance of the collective quadrature below vacuum noise, e.g., $V_{\hat{X}_{\pm}} < 1/2$, entanglement can be achieved, with the criteria $D = V_{\hat{X}_{\pm}} + V_{\hat{Y}_{\pm}} < 1$.

In our system, because $\Gamma_{\text{meas}} \ll \Omega_m$, and also we are using a higher order mechanical mode that is soft-clamped, the measurement channels between \hat{X} and \hat{Y} are independent by the rotating wave approximation. Therefore, a lot of the covariance matrix elements are either zero or symmetric between observables, e.g., $C_{\hat{X}_1 \hat{Y}_2} = 0$ in the long time limit and $C_{\hat{X}_1 \hat{X}_2} = C_{\hat{Y}_1 \hat{Y}_2}$. With the setting we layout, the lowest possible collective quadrature variance is $V_{\hat{X}_{\pm}} = V_{\hat{Y}_{\pm}} = \sqrt{(\Gamma_m V_{\hat{X}_1} + \Gamma_{\text{qba}})/\Gamma_{\text{meas}}}/2 \geq 1/2$, shown in Fig. 3.6, due to the symmetry of the measurement channels mentioned above. Therefore, entanglement is generally impossible, as strong correlation is not quick enough to establish from Γ_{th} before Ω_m rotates the quadrature to the orthogonal one. In the field, people used backaction-evasion measurement with mechanical squeezing interaction [83], or negative mass oscillators [24, 31] to break the quadrature symmetry, and has achieved entanglement in MIM systems [84], though with a spin system. Fast measurement [85] is also a candidate to break the symmetry and induce mechanical squeezing and entanglement.

3.3 Measurement-based feedback cooling

In the previous section, we discuss how to measure mechanical motion as precisely as possible by the restriction from the Heisenberg uncertainty principle. The continuous measurements of mechanical motion predict thermal coherent states of mechanical oscillators at a given time in the measurement record, with which we can control the mechanical states using feedback actuation in real-time of the mechanical mode. This measurement-based feedback control can prepare states like the quantum ground state [17], with the state purity limited by the purity of the mechanical states prepared in the continuous measurement. As shown in the previous section, optimal state preparation can isolate mechanical motions from the nearby parasitic modes, which can also be implemented in real-time with IIR filters discussed in Section B.3.

In this section, even though we primarily discuss experiment results without using an optimal multi-mode filter implemented physically on our FPGAs, our theoretical analysis remains general as we use a generalized feedback filter function $H(\omega)$ in this section. In the experiment, we primarily use a combination of IIR, IQ, and PID filters, which are not yet optimal for the state inference.

3.3.1 Quantum Langevin equations of measurement-based feedback cooling

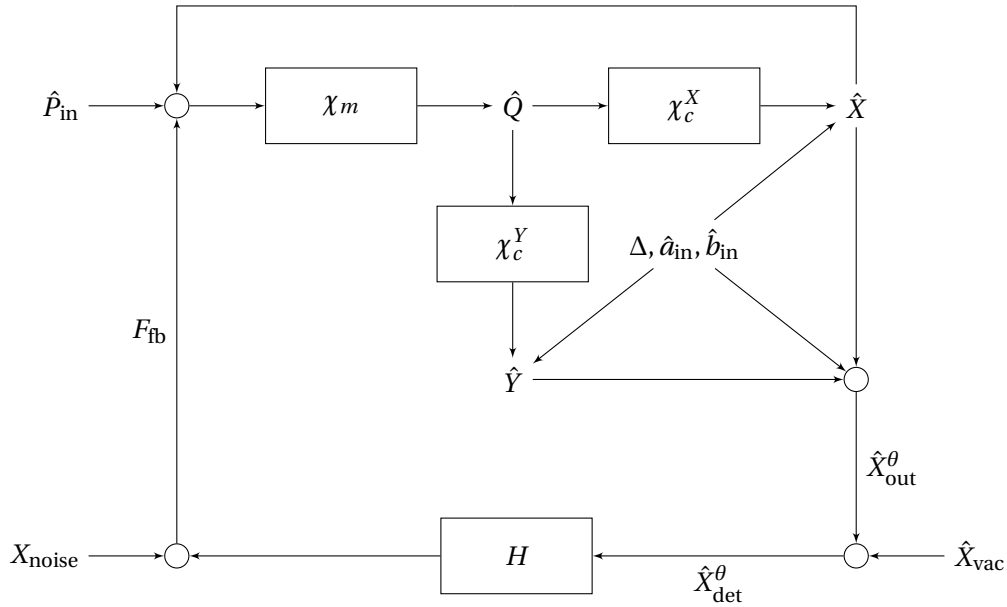


Figure 3.7: System diagram of a mechanical mode undergone feedback damping. Both cavity-assisted dynamical backaction feedback and measurement-based electronic feedback are included. The symbols are defined in Section 3.3.1.

Generally, feedback cooling of the mechanical modes is not as trivial as how we analyzed

above using the resonant pump. The complication arises in the following circumstances:

- When the laser is detuned from cavity resonance (e.g., at Δ_*), the cavity also induces intra-cavity feedback that could cool or heat the mechanical mode in the presence of mirror noise and parasitic membrane modes modeled as cavity detuning noises $\Delta(\omega)$. Optical spring shift also occurs in this setting.
- When the detection is performed at an arbitrary optical quadrature angle θ (e.g., direct detection), the imprecision noise x_{imp} and the measurement-induced backaction force F_{ba} can be correlated and causes interference on the measurement record.

In our analysis, we need to include all these factors that influence the inference results of our feedback cooling. We illustrate a diagram of the closed-loop system in Fig.3.7 to showcase the connections between different parts of the system. In this section, we formally analyze and derive the expressions of the mechanical phonon occupancy in a measurement-based feedback experiment when the laser is detuned from cavity resonance.

In the Heisenberg picture, the Langevin equations are

$$\dot{\hat{a}} = -\left[\frac{\kappa}{2} + i(\Delta + \sqrt{2}g_0\hat{Q})\right]\hat{a} + \sqrt{\kappa}\hat{a}_{\text{in}} \quad (3.120)$$

$$\dot{\hat{Q}} = \Omega_m\hat{P} \quad (3.121)$$

$$\dot{\hat{P}} = -\Omega_m\hat{Q} + \sqrt{2\Gamma}\hat{P}_{\text{in}} - \Gamma\hat{P} - \sqrt{2}g_0\hat{a}^\dagger\hat{a} + F_{\text{fb}} \quad (3.122)$$

where we define the dimensionless mechanical position operator $\hat{Q} = (\hat{b}^\dagger + \hat{b})/\sqrt{2}$ and the momentum operator $\hat{P} = i(\hat{b}^\dagger - \hat{b})/\sqrt{2}$. Similarly, we also define the optical quadrature operators $\hat{X} = (\hat{a}^\dagger + \hat{a})/\sqrt{2}$ and $\hat{Y} = i(\hat{a}^\dagger - \hat{a})/\sqrt{2}$. The detuning here is defined as $\Delta = \nu_{\text{cav}} - \nu_{\text{laser}}$. The feedback force F_{fb} is also included in the equations, whose expression will be derived later. For convenience, we also define the optomechanical coupling rate $g = g_0\bar{a}$.

The mechanical motion obeys the following set of equations in both the time and frequency domain

$$\ddot{\hat{Q}} + \Gamma\dot{\hat{Q}} + \Omega_m^2\hat{Q} = \sqrt{2\Gamma}\Omega_m\hat{P}_{\text{in}} - 2g\Omega_m\hat{X} + \Omega_m F_{\text{fb}} \quad (3.123)$$

$$\hat{Q}(\omega) = \chi_m(\omega) \left(\sqrt{2\Gamma}\hat{P}_{\text{in}}(\omega) - 2g\hat{X}(\omega) + F_{\text{fb}}(\omega) \right), \quad (3.124)$$

where we introduce the mechanical susceptibility $\chi_m(\omega) \equiv \Omega_m/(\Omega_m^2 - \omega^2 - i\omega\Gamma)$, and the dimensionless input momentum fluctuation $\hat{P}_{\text{in}}(t) = \frac{i}{\sqrt{2}}(\hat{b}_{\text{in}}^\dagger(t) - \hat{b}_{\text{in}}(t)) \equiv \frac{x_{\text{zpt}}\hat{F}(t)}{\hbar\sqrt{\Gamma}}$ with correlation

$$S_{\hat{F}\hat{F}}(\omega) = 2m\Gamma(\omega)\hbar\omega(\bar{n}(\omega) + 1) \quad (3.125)$$

$$S_{\hat{F}\hat{F}}(-\omega) = 2m\Gamma(\omega)\hbar\omega\bar{n}(\omega). \quad (3.126)$$

For simplification, the cavity field \bar{a} is set as the $\theta = 0$ reference, such that both \bar{a} and g are

Chapter 3. Measurement-based quantum control of mechanical motion

real-valued. We can then proceed to write down the expressions of the optical quadratures, as well as the mechanical position operator in the Fourier domain,

$$\begin{aligned}\hat{X}(\omega) &= \chi_c^X(\omega)\bar{a}\Delta(\omega) + \chi_c^X(\omega)\sqrt{2}gQ(\omega) \\ &+ \chi_c(\omega)\sqrt{\kappa_a}\hat{a}_{\text{in}}(\omega) + \chi_c^*(-\omega)\sqrt{\kappa_a}\hat{a}_{\text{in}}^\dagger(\omega) + \dots\end{aligned}\quad (3.127)$$

$$\begin{aligned}\hat{Y}(\omega) &= \chi_c^Y(\omega)\bar{a}\Delta(\omega) + \chi_c^Y(\omega)\sqrt{2}gQ(\omega) \\ &- i\chi_c(\omega)\sqrt{\kappa_a}\hat{a}_{\text{in}}(\omega) + i\chi_c^*(-\omega)\sqrt{\kappa_a}\hat{a}_{\text{in}}^\dagger(\omega) + \dots\end{aligned}\quad (3.128)$$

$$\hat{Q}(\omega) = \chi_m(\omega)\left(\sqrt{2\Gamma}\hat{P}_{\text{in}}(\omega) - 2g\hat{X}(\omega) + F_{\text{fb}}(\omega)\right)\quad (3.129)$$

with the cavity susceptibilities defined as

$$\chi_c(\omega) = \sqrt{2}^{-1}(\kappa/2 + i\Delta - i\omega)^{-1}\quad (3.130)$$

$$\chi_c^X(\omega) = i(\chi_c^*(-\omega) - \chi_c(\omega))\quad (3.131)$$

$$\chi_c^Y(\omega) = -(\chi_c^*(-\omega) + \chi_c(\omega))\quad (3.132)$$

After solving the cavity-assisted self-feedback loop, the quadrature expressions are

$$\begin{aligned}\hat{X}(\omega) &= \chi_\Delta^X(\omega)\Delta(\omega) + \chi_{P_{\text{in}}}^X(\omega)(\sqrt{2\Gamma}\hat{P}_{\text{in}}(\omega) + F_{\text{fb}}(\omega)) \\ &+ \chi_{a_{\text{in}}}^X(\omega)\hat{a}_{\text{in}} + \chi_{a_{\text{in}}^\dagger}^X(\omega)\hat{a}_{\text{in}}^\dagger + \dots\end{aligned}\quad (3.133)$$

$$\begin{aligned}\hat{Y}(\omega) &= \chi_\Delta^Y(\omega)\Delta(\omega) + \chi_{P_{\text{in}}}^Y(\omega)(\sqrt{2\Gamma}\hat{P}_{\text{in}}(\omega) + F_{\text{fb}}(\omega)) \\ &+ \chi_{a_{\text{in}}}^Y(\omega)\hat{a}_{\text{in}} + \chi_{a_{\text{in}}^\dagger}^Y(\omega)\hat{a}_{\text{in}}^\dagger + \dots\end{aligned}\quad (3.134)$$

$$\begin{aligned}\hat{Q}(\omega) &= \chi_m(\omega)\left[(1 - 2g\chi_{P_{\text{in}}}^X)(\sqrt{2\Gamma}\hat{P}_{\text{in}}(\omega) + F_{\text{fb}}(\omega))\right. \\ &\left.- 2g(\chi_\Delta^X\Delta + \chi_{a_{\text{in}}}^X\hat{a}_{\text{in}} + \chi_{a_{\text{in}}^\dagger}^X\hat{a}_{\text{in}}^\dagger + \dots)\right]\end{aligned}\quad (3.135)$$

with a new set of susceptibilities originate from the cavity self-feedback loop

$$\chi_{mc}^X(\omega) = (1 + 2\sqrt{2}g^2\chi_m(\omega)\chi_c^X(\omega))^{-1}\quad (3.136)$$

$$\chi_\Delta^X(\omega) = \bar{a}\chi_c^X(\omega)\chi_{mc}^X(\omega)\quad (3.137)$$

$$\chi_{P_{\text{in}}}^X(\omega) = \sqrt{2}g\chi_m(\omega)\chi_c^X(\omega)\chi_{mc}^X(\omega)\quad (3.138)$$

$$\chi_{a_{\text{in}}}^X(\omega) = \sqrt{\kappa_a}\chi_c(\omega)\chi_{mc}^X(\omega)\quad (3.139)$$

$$\chi_{a_{\text{in}}^\dagger}^X(\omega) = \sqrt{\kappa_a}\chi_c^*(-\omega)\chi_{mc}^X(\omega)\quad (3.140)$$

$$\chi_\Delta^Y(\omega) = \chi_c^Y(\omega)[\bar{a} - 2\sqrt{2}g^2\chi_m(\omega)\chi_\Delta^X(\omega)]\quad (3.141)$$

$$\chi_{P_{\text{in}}}^Y(\omega) = \sqrt{2}g\chi_c^Y(\omega)\chi_m(\omega)(1 - 2g\chi_{P_{\text{in}}}^X(\omega))\quad (3.142)$$

$$\chi_{a_{\text{in}}}^Y(\omega) = -i\sqrt{\kappa_a}\chi_c(\omega) - 2\sqrt{2}g^2\chi_c^Y(\omega)\chi_m(\omega)\chi_{a_{\text{in}}}^X(\omega)\quad (3.143)$$

$$\chi_{a_{\text{in}}^\dagger}^Y(\omega) = i\sqrt{\kappa_a}\chi_c^*(-\omega) - 2\sqrt{2}g^2\chi_c^Y(\omega)\chi_m(\omega)\chi_{a_{\text{in}}^\dagger}^X(\omega)\quad (3.144)$$

We proceed to derive the expression of the detected optical quadrature operator at angle θ . We define the quadrature with arbitrary angle $\hat{X}^\theta = \sqrt{2}^{-1}(\hat{a}e^{-i\theta} + \hat{a}^\dagger e^{i\theta}) = \hat{X}\cos\theta + \hat{Y}\sin\theta$. We

3.3 Measurement-based feedback cooling

model the cavity with three coupling ports, i.e., the laser input port \hat{b}_{in} , the transmission port \hat{a}_{in} , and the internal loss port \hat{c}_{in} . We do optical detection on the output mode \hat{a}_{out} , with the output quadrature defined as

$$\hat{X}_{\text{out}}^{\theta} = \hat{X}_{\text{in}}^{\theta} - \sqrt{\kappa_a} \hat{X}^{\theta}. \quad (3.145)$$

We can expand this expression again into different components ((ω) not shown),

$$\hat{X}_{\text{out}}^{\theta}(\omega) = \chi_{\Delta}^{\theta} \Delta + \chi_{P_{\text{in}}}^{\theta} (\sqrt{2\Gamma} \hat{P}_{\text{in}} + F_{\text{fb}}) + \chi_{a_{\text{in}}}^{\theta} \hat{a}_{\text{in}} + \chi_{a_{\text{in}}^{\dagger}}^{\theta} \hat{a}_{\text{in}}^{\dagger} + \sum_{k=b,c} \chi_{k_{\text{in}}}^{\theta} k_{\text{in}} + \chi_{k_{\text{in}}^{\dagger}}^{\theta} k_{\text{in}}^{\dagger} \quad (3.146)$$

with the quadrature-angle-dependent susceptibilities

$$\chi_{\Delta}^{\theta}(\omega) = -\sqrt{\kappa_a} (\chi_{\Delta}^X \cos \theta + \chi_{\Delta}^Y \sin \theta) \quad (3.147)$$

$$\chi_{P_{\text{in}}}^{\theta}(\omega) = -\sqrt{\kappa_a} (\chi_{P_{\text{in}}}^X \cos \theta + \chi_{P_{\text{in}}}^Y \sin \theta) \quad (3.148)$$

$$\chi_{a_{\text{in}}}^{\theta}(\omega) = \sqrt{2}^{-1} e^{-i\theta} - \sqrt{\kappa_a} (\chi_{a_{\text{in}}}^X \cos \theta + \chi_{a_{\text{in}}}^Y \sin \theta) \quad (3.149)$$

$$\chi_{a_{\text{in}}^{\dagger}}^{\theta}(\omega) = \sqrt{2}^{-1} e^{i\theta} - \sqrt{\kappa_a} (\chi_{a_{\text{in}}^{\dagger}}^X \cos \theta + \chi_{a_{\text{in}}^{\dagger}}^Y \sin \theta) \quad (3.150)$$

$$\chi_{k_{\text{in}}}^{\theta}(\omega) = -\sqrt{\kappa_k} (\chi_{k_{\text{in}}}^X \cos \theta + \chi_{k_{\text{in}}}^Y \sin \theta) \quad (3.151)$$

$$\chi_{k_{\text{in}}^{\dagger}}^{\theta}(\omega) = -\sqrt{\kappa_k} (\chi_{k_{\text{in}}^{\dagger}}^X \cos \theta + \chi_{k_{\text{in}}^{\dagger}}^Y \sin \theta). \quad (3.152)$$

At the detector, we model all possible photon losses, e.g., detector quantum efficiency and passive optical losses, into the detection efficiency η . Therefore, we arrive at the expression for the detected optical quadrature as

$$\hat{X}_{\text{det}}^{\theta}(\omega) = \sqrt{\eta} \hat{X}_{\text{out}}^{\theta}(\omega) + i\sqrt{1-\eta} \hat{X}_{\text{vac}}(\omega). \quad (3.153)$$

Given the detection record $\langle \hat{X}_{\text{det}}^{\theta}(\omega) \rangle$, we apply a feedback filter $H(\omega)$ and then use it to actuate the mechanical mode as an optical force F_{fb} . Noises such as electronic noise and optical shot noise are modeled as $X_{\text{noise}}(\omega)$ that adds to the feedback force. Therefore, we can express the feedback force to the mechanical mode as

$$F_{\text{fb}}(\omega) = H(\omega) \hat{X}_{\text{det}}^{\theta}(\omega) + X_{\text{noise}}(\omega) \quad (3.154)$$

with which we close the feedback loop. Note that here, the feedback force is not a quantum observable. Physically, the feedback signal is, at some stage, just electrical current $I(t)$ that we can sample classically. Therefore $F_{\text{fb}}(t)$ commutes with itself at all times, whereas $\hat{X}_{\text{det}}^{\theta}(t)$ does not. Here, we have encountered a common controversial measurement problem of quantum mechanics. Strictly written, we need to enforce the following relation

$$S_{F_{\text{fb}} F_{\text{fb}}}(\omega) = |H(\omega)|^2 \overline{S_{\hat{X}_{\text{det}}^{\theta} \hat{X}_{\text{det}}^{\theta}}}(\omega) + S_{X_{\text{noise}} X_{\text{noise}}}(\omega) \quad (3.155)$$

where the time auto-correlation of $\hat{X}_{\text{det}}^{\theta}(t)$ needs to be symmetrized to become a Hermitian observable before the structuring by the filter $H(\omega)$. For this reason, strictly speaking, Eq. 3.154

Chapter 3. Measurement-based quantum control of mechanical motion

violates some physical laws. However, in our specific case, as the closed-loop auto-correlation requires symmetrization to become a Hermitian observable, the treatment [17, 86] that the feedback force is quantum does not affect the measurement outcome physically. We also discussed this problem in detail in Appendix B.7.

By taking out the variable F_{fb} in the closed-loop equations, we arrive at the closed-loop measurement record

$$\begin{aligned} \hat{X}_{\text{det}}^\theta &= \left(\chi_\Delta^\theta \Delta + \chi_{P_{\text{in}}}^\theta (\sqrt{2\Gamma} \hat{P}_{\text{in}} + X_{\text{noise}}) + \chi_{a_{\text{in}}}^\theta \hat{a}_{\text{in}} + \chi_{a_{\text{in}}^\dagger}^\theta \hat{a}_{\text{in}}^\dagger \right. \\ &+ \left. \sum_{k=b,c} \chi_{k_{\text{in}}}^\theta k_{\text{in}} + \chi_{k_{\text{in}}^\dagger}^\theta k_{\text{in}}^\dagger + i \sqrt{\frac{1-\eta}{\eta}} \hat{X}_{\text{vac}} \right) \left(\sqrt{\eta}^{-1} - \chi_{P_{\text{in}}}^\theta H \right)^{-1} \end{aligned} \quad (3.156)$$

as well as the mechanical position operator

$$\begin{aligned} \hat{Q}(\omega) &= \chi_m(\omega) \left[(\chi_F \chi_H \chi_\Delta^\theta - 2g \chi_\Delta^X) \Delta + [\chi_F (\chi_H \chi_{P_{\text{in}}}^\theta + 1)] (\sqrt{2\Gamma} \hat{P}_{\text{in}} + X_{\text{noise}}) \right. \\ &+ \left. i \chi_F \chi_H \sqrt{\frac{1-\eta}{\eta}} \hat{X}_{\text{vac}} + (\chi_F \chi_H \chi_{a_{\text{in}}}^\theta - 2g \chi_{a_{\text{in}}}^X) a_{\text{in}} + \sum_k \dots \right] \end{aligned} \quad (3.157)$$

in which we define new susceptibilities of χ_F and χ_H associated with the feedback process,

$$\chi_F = (1 - 2g \chi_{P_{\text{in}}}^X) \quad (3.158)$$

$$\chi_H = \frac{H}{\sqrt{\eta}^{-1} - \chi_{P_{\text{in}}}^\theta H}. \quad (3.159)$$

Here, we can easily distinguish the two feedback loops present in the system, i.e., the cavity self-feedback and the measurement-based electronic feedback, as any electronic feedback effect is associated with the electronic filter response $H(\omega)$. With these results, we can calculate the power spectral densities of the in-loop spectral density $S_{\hat{X}_{\text{det}}^\theta \hat{X}_{\text{det}}^\theta}$ and the out-of-loop spectral density $S_{\hat{Q}\hat{Q}}$,

$$\begin{aligned} S_{\hat{X}_{\text{det}}^\theta \hat{X}_{\text{det}}^\theta} &= \left(|\chi_\Delta^\theta|^2 S_{\Delta\Delta} + |\chi_{P_{\text{in}}}^\theta|^2 (2\Gamma S_{\hat{P}_{\text{in}}\hat{P}_{\text{in}}} + S_{\text{noise}}) + \frac{1-\eta}{2\eta} + |\chi_{a_{\text{in}}}^\theta|^2 \bar{n}_{\text{in}} + |\chi_{a_{\text{in}}^\dagger}^\theta|^2 (\bar{n}_{\text{in}} + 1) \right. \\ &+ \left. \sum_k |\chi_{k_{\text{in}}}^\theta|^2 \bar{n}_{\text{in}} + |\chi_{k_{\text{in}}^\dagger}^\theta|^2 (\bar{n}_{\text{in}} + 1) \right) \left| \sqrt{\eta}^{-1} - \chi_{P_{\text{in}}}^\theta H \right|^{-2} \end{aligned} \quad (3.160)$$

and

$$\begin{aligned} S_{\hat{Q}\hat{Q}} &= |\chi_m(\omega)|^2 \left[|(\chi_F \chi_H \chi_\Delta^\theta - 2g \chi_\Delta^X)|^2 S_{\Delta\Delta} + |\chi_F (\chi_H \chi_{P_{\text{in}}}^\theta + 1)|^2 (2\Gamma S_{\hat{P}_{\text{in}}\hat{P}_{\text{in}}} + S_{\text{noise}}) \right. \\ &+ \left. |\chi_F \chi_H|^2 \frac{1-\eta}{2\eta} + |\chi_F \chi_H \chi_{a_{\text{in}}}^\theta - 2g \chi_{a_{\text{in}}}^X|^2 \bar{n}_{\text{in}} + |\chi_F \chi_H \chi_{a_{\text{in}}^\dagger}^\theta - 2g \chi_{a_{\text{in}}^\dagger}^X|^2 (\bar{n}_{\text{in}} + 1) + \sum_k \dots \right] \end{aligned} \quad (3.161)$$

in which the noise correlations defined in Section 1.1 are used.

If there is classical noise in terms of C_{qq} and C_{pp} entering from a specific channel a with a certain susceptibility χ_a , then the spectral density also has these additional terms,

$$\delta S = \frac{C_{qq}|e^{-i\phi}\chi_a + e^{i\phi}\chi_a^\dagger|^2 + C_{pp}|e^{-i\phi}\chi_a - e^{i\phi}\chi_a^\dagger|^2}{2}. \quad (3.162)$$

where ϕ is the mean field phase of the optical input $\bar{a}_{\text{in}} = |\bar{a}_{\text{in}}|e^{i\phi}$. In our experiment, we are not limited by the laser noises, so we can safely set C_{qq} , C_{pp} and \bar{n}_{in} to zero.

3.3.2 Using measurement results to infer mechanical phonon occupancy

In this subsection, we analyze one of the feedback cooling experiments we performed in our previous generation device using conventional cavity mirrors, where mirror noise contaminates the measurement record and heats up the mechanical mode through internal cavity feedback. We also compare the different results using different fitting models, i.e., the simplified approximated model vs. the exact model analyzed in the previous section.

Our previous generation device uses a perforated membrane with a soft-clamped mode at 700 kHz, with the measured spectrum shown in Fig. 3.8(a). We pump the device at the magic detuning Δ_* such that the nonlinear noise disappears. Around the soft-clamped mode, we observe two prominent mechanical noise peaks originating from the thermomechanical motions of the mirror substrates. To circumvent the noise contamination of the mirror motions, we implement a specific IIR feedback filter shown in Fig. 3.9 in combination with an IQ filter, programmed on a Red Pitaya FPGA board, to reduce the feedback force contribution from the mirror noise. Note that the IIR filter used is not theoretically optimal, and a correct implementation in Section 3.2.1 could help better isolate the soft-clamped motion from the mirror motions.

The measured spectrum when the feedback loop is closed is also shown in Fig. 3.8(a), fitting which will yield the mechanical position noise density and the phonon occupancy. We illustrate the differences between the exact model (Eq. 3.160-3.161) derived in this section and the approximated model derived in Appendix B.7, in Fig. 3.8. In the panel *measured*, the exact model captures better the correlation (both classical and quantum) of the imprecision and force noise than the approximated model, especially around the mirror modes. In the panel *inferred*, the exact model captures the mirror-noise-induced heating of the soft-clamped mode due to cavity self-feedback, which results in about 7-10 added phonons in the final mechanical occupancy. The two models also yield different gains of the feedback filter $H(\omega)$, illustrated in the panel *occupancy*.

In summary, the exact model established in this section better captures the measured spectral features from the imprecision-force noise interference, and also indicates that the cavity self-feedback-induced heating from parasitic modes severely limits the final occupation

Chapter 3. Measurement-based quantum control of mechanical motion

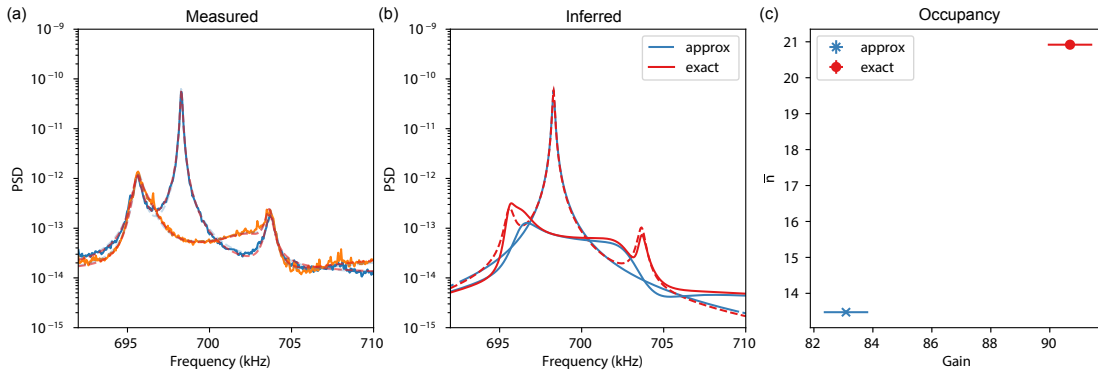


Figure 3.8: Comparison between the approximated model from Appendix B.7 and the exact model in this section by fitting the same measurement record. **(a)** Measured spectral of the optical signal shown in solid lines, with (orange) and without (blue) electronic feedback. The fits using the approximated model (blue) and the exact model (red) are shown in dashed lines. **(b)** Inferred mechanical position spectra using the two fitting models, with (dashed) and without (solid) electronic feedback. **(c)** The calibrated phonon occupancy using the two fitting models as a function of the fitted feedback filter gain.

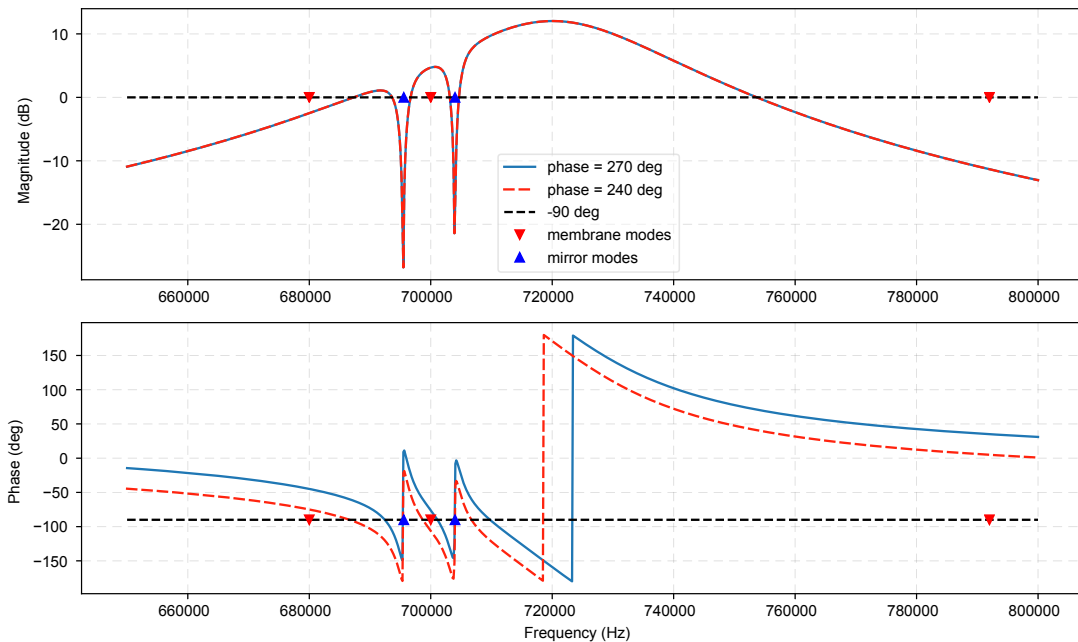


Figure 3.9: Measured response function of the IQ bandpass filter at 720 kHz in series with an IIR filter. The IIR filter consists of two notch filters at the frequencies of the mirror modes.

3.3 Measurement-based feedback cooling

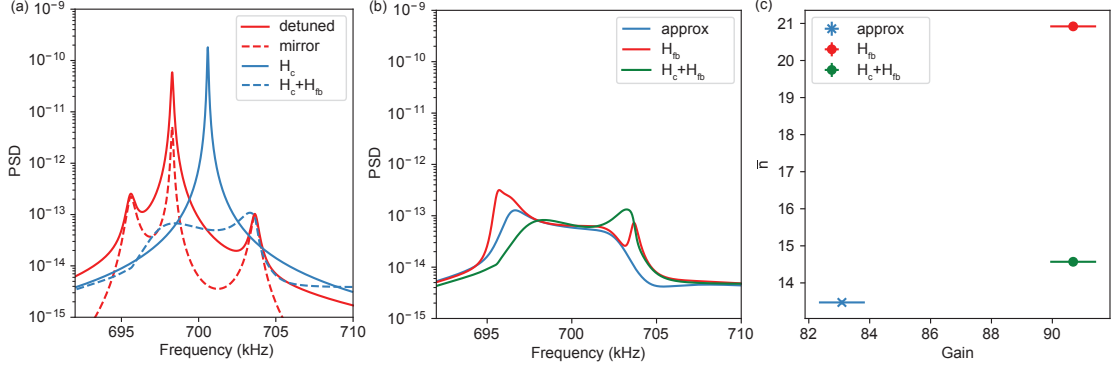


Figure 3.10: **(a)** Comparison of the mechanical position spectra with (blue solid) and without (red solid) the H_c cancellation filter. With the filter is applied, the heating contribution due to the mirror noise (red dashed) are removed. We also show the result when a H_c is applied in parallel with a damping filter H_{fb} . **(b)** Comparison with the cooling result using the parallel filters vs. that of only the feedback filter H_{fb} , as well as the approximate model that does not account for mirror noise heating. **(c)** Calibrated phonon occupancy as a function of fitted feedback filter gain.

achievable from the electronic feedback. The following subsection analyzes the electronic response function required to cancel the cavity self-feedback-induced heating to achieve optimal phonon occupation.

3.3.3 Cancelling cavity response through measurement-based feedback

In the previous section, we observed that when the laser is pumped from the magic detuning Δ_* , the cavity self-feedback drives the soft-clamped mode with the mirror noise. This heating is not preferred for achieving low phonon occupancy but is always present for off-resonant probing.

However, it is possible to cancel the cavity effect using electronic feedback. Given the derived expression of Eq. (3.161) for a general filter response $H(\omega)$, we find that in a special case when $H = -2g/\sqrt{\eta\kappa_a}$, all the effect due to laser detuning is canceled. Under such a feedback condition, the mechanical spectrum is

$$S_{\hat{Q}\hat{Q}}^* = |\chi_m(\omega)|^2 \left[(2\Gamma S_{\hat{p}_{in}\hat{p}_{in}} + S_{\text{noise}}) + \frac{4g^2}{\kappa_a} \left(\frac{1-\eta}{2\eta} + n_{in} + \frac{1}{2} + \sum_k \dots \right) \right] \quad (3.163)$$

where all the dynamical terms are canceled. Instead, the feedback adds only some heating due to added imprecision from detection. Essentially, by feeding back the signal in a specific way to actuate the mechanical mode, the dynamical backaction effect from the cavity can be completely removed, as if the laser is probing the cavity on resonance.

We also numerically investigated this effect, illustrated in Fig. 3.10(a). The result shows the

correct cancellation of both the heating due to mirror modes and the cancellation of the optical spring effect from the cavity. Given this effect, the correct strategy for achieving low phonon occupancy is to apply two filters in parallel $H = H_c + H_{fb}$, where H_c cancels the cavity effect, and the other H_{fb} does the optimal feedback cooling. As we see from Fig. 3.10(a), when the parallel filters are applied, we circumvent the heating due to cavity self-feedback while also achieving significant cooling of the soft-clamped mode.

We compare the result without the cancellation feedback filter H_c in Fig. 3.10(b,c). With the addition of H_c , we can achieve a phonon occupancy as if the mirror heating was never there, which the approximated model assumes. The finite difference is attributed to the canceled optical spring effect that brings the soft-clamped mode closer to the right-side mirror mode and effectively reduces the SNR.

3.4 Cooling a mechanical oscillator close to the quantum ground state

3.4.1 Sideband cooling of mechanical oscillators

This section discusses the results of the optical sideband cooling of mechanical motions using our current generation device, discussed in Chapter 2. Usually, sideband cooling in the fast-cavity limit $\Omega_m \ll \kappa$ is less efficient than measurement-based feedback cooling. In our system, however, we have already achieved a few phonon occupancy with only sideband cooling, which enables the observation of quantum effects such as optomechanical sideband asymmetry that we discuss in the next section.

In our system, due to the reflectivity wavelength dependence of the dielectric coatings of the cavity, we can choose the optical linewidth by tuning the laser to a different optical wavelength. We test the sideband-cooling phonon-occupancy limit of our system with an optical mode at 862.2 nm with optical linewidth $\kappa/2\pi = 13.5$ MHz, the lowest among all the optical modes we characterized. The idealized theoretical cooling limit is:

$$\bar{n}_{\text{ideal}} = \frac{(\Omega_m + \Delta_*)^2 + (\kappa/2)^2}{4\Delta_*\Omega_m} = 2.9, \quad (3.164)$$

evaluated with the laser pump applied at the magic detuning Δ_* . We pump the cavity with 2 mW of input power and measure the output spectrum of the cavity (see Fig. 3.11(a,c)). Using Eq. 3.160 to fit the measured spectrum, we can reliably extract all the system parameters (C_q, η, θ), and also the noise from the nearby spurious mechanical modes $\bar{S}_{\Delta\Delta}(\omega)$. Using the extracted quantities, we can reconstruct the mechanical position noise density $\bar{S}_{QQ}(\omega)$ using Eq. 3.161 (see Fig. 3.11(b,d)) by setting the feedback filter $H = 0$.

We consider two mechanical mode bases for different purposes to estimate the lowest achievable phonon occupancy. In the original mode basis, with the full model described by Eq. 3.160

3.4 Cooling a mechanical oscillator close to the quantum ground state

and Eq. 3.161, the sideband cooling mediates a coupling between mechanical modes. As a result, the correlation between the soft-clamped mode and the spurious modes is non-negligible. It leads to a phonon occupancy of the defect mode larger than the theoretical ideal, as is also analyzed in Section 3.3.1. Under our experimental conditions, the best phonon occupancy with this optical mode was $\bar{n}_{\text{eff}} = 11.7$ at relatively low optical powers ($C_q = 1.0$, see Fig. 3.11(e)), limited by the interaction with nearby mechanical modes.

Next, we analyze the system in the framework of multi-mode optomechanics [87] where the cavity-induced coupling between mechanical modes results in mode hybridization and a new set of decoupled normal mode basis. In the decoupled basis, where the cooling-induced correlations between the mechanical modes are nulled, the decoupled soft-clamped mode achieves a phonon occupancy of $\bar{n}_{\text{eff}} = 5.7$ at $C_q = 1.6$. This phonon occupancy results from the small number of correlation quanta (~ 10) compared to the large phonon occupancy ($\gg 10$) of the spurious modes in the original basis. Such a treatment is similar to those presented in the previous cooling experiments [43, 88], where spurious mechanical modes near the target mode couple to the optomechanical cavity. Essentially, by fitting a Lorentzian to the soft-clamped mode and ignoring nearby spurious modes, we attain the same phonon occupancy as the decoupled mode.

Note that the obtained phonon occupancy in the decoupled basis is also identical to that which would be retrieved by an independent sideband asymmetry measurement [41], shown in the next section. We stress that the phonon occupancy evaluated this way is only associated with the decoupled mode, defined in the cooling pump's presence. In applications requiring the cooling pump's removal, the mechanical modes decouple, and the effective phonon occupancy returns to that of the full model. However, in many applications, removing the cooling pump is not strictly necessary. At the experimental condition of $C_q = 1.6$, the full model would yield an increased phonon occupancy of $\bar{n}_{\text{eff}} = 21.4$ (see Fig. 3.11(e)), still among the lowest phonon occupancy achieved in nanomechanical devices. Generally, the cooling-induced multi-mode hybridization results in higher total phonon occupancy compared to the idealized case, but in some special cases, the decoupled modes can have lower occupancies.

We further stress that the correlated quanta evaluated from the full model do not impose any limit on measurement-based feedback schemes. As discussed in the previous section, in the presence of cavity-mediated optical cooling, the cooling-induced correlations to the spurious modes can be completely canceled in a measurement-based feedback scheme. Therefore, for any measurement-based control scheme that requires a filter $H_1(\omega)$, the constructed filter $H(\omega) = H_0(\omega) + H_1(\omega)$ achieves the desired state with no correlation to spurious modes.

Chapter 3. Measurement-based quantum control of mechanical motion

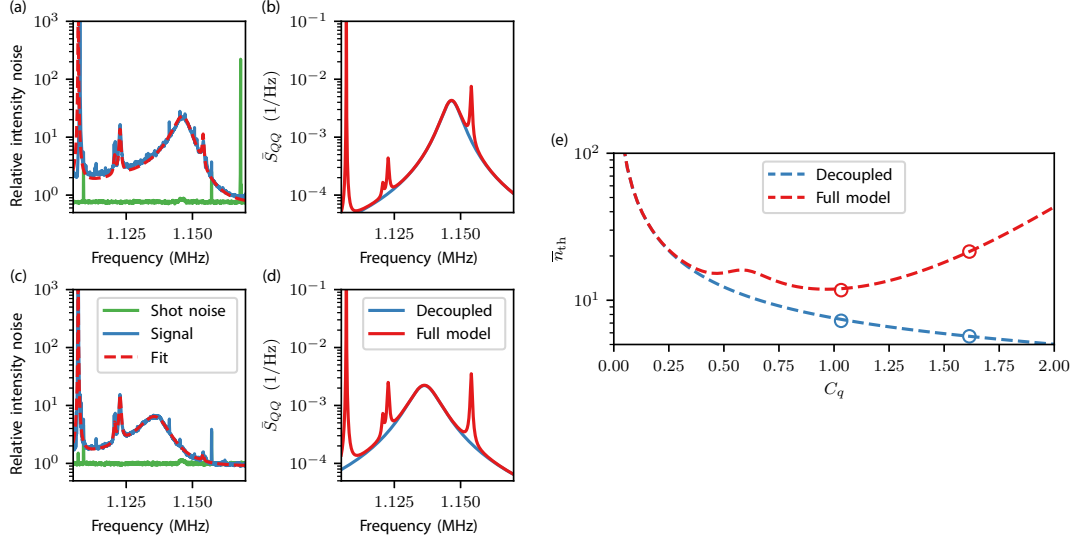


Figure 3.11: Sideband cooling limit study using the 862.2 nm optical mode. **(a)** Measured mechanical spectrum at $C_q = 1.0$, showing spectral overlap between membrane modes. **(b)** From the fit, the position noise density of the defect mode is reconstructed and shows correlations to the nearby auxiliary modes. **(c,d)** Same measurement and analysis but for $C_q = 1.6$. **(e)** Calibrated sideband cooling phonon occupancy at different C_q .

3.4.2 Sideband asymmetry using a dual-homodyne measurement

Dual quadrature scheme

In the previous section, we described that by pumping the cavity at the magic detuning Δ_* , we could efficiently cool the soft-clamped mode optically to an effective phonon occupancy of $\bar{n}_{\text{eff}} \sim 6$. With this level of phonon occupation, the asymmetry in the mechanical force spectral density $S_{F_{\text{tot}}F_{\text{tot}}}(\pm\Omega_m)$ is very pronounced ($\sim 15\%$), which leads to the optomechanical sideband asymmetry of the mechanical position spectral density $S_{QQ} = |\chi'_m|^2 S_{F_{\text{tot}}F_{\text{tot}}}$, where χ'_m is the effective mechanical susceptibility under optical damping. In this section, we observe this mechanical sideband asymmetry using a dual quadrature measurement technique. This specific detection scheme is implemented due to the challenge of canceling TIN in a heterodyne detection (discussed in Section 2.4.8), which is conventionally used to separate positive and negative frequency components.

As established in Section 2.4.3, it is possible to cancel TIN using homodyne detection with a carefully selected local oscillator phase and amplitude. However, asymmetry of the quantum spectrum comes from the fact that the autocorrelation function $C_{QQ}(t) = \langle \hat{Q}(t)\hat{Q}(0) \rangle$ is not a Hermitian observable and therefore can be complex. In physical measurements, only Hermitian operators are observable, e.g., $\bar{C}_{QQ}(t) = \langle \hat{Q}(t)\hat{Q}(0) + \hat{Q}(0)\hat{Q}(t) \rangle / 2$, which leads to a symmetric spectrum $\bar{S}_{QQ}(\omega)$. Therefore, with a single homodyne that directly measures the oscillator's position, we can not effectively separate the negative and positive Fourier

3.4 Cooling a mechanical oscillator close to the quantum ground state

components, which can be done in heterodyne detection. The observation of sideband asymmetry has been controversial and complicated to analyze, as it involves the detailed physical nature of the measurement apparatus. For reference, see [69].

To circumvent this challenge, we implement a measurement setting here to measure two orthogonal optical quadratures simultaneously so that the complex field $a(t)$ can be reconstructed instead of the usual real signal with single quadrature measurement, with which symmetrization of the correlation function has to be enforced. By doing so, the optical fields' negative and positive frequency components relative to the optical carrier can be reliably separated, similar to the heterodyne detection. To reconstruct the complex field, signals of two orthogonal quadratures are required (e.g., amplitude and phase), as in

$$\hat{a}(t) = \frac{\hat{X}(t) + i\hat{Y}(t)}{\sqrt{2}} \quad (3.165)$$

with the penalty of reducing detection efficiencies on both measurement operators, restrained by the Heisenberg uncertainty principle similar to the heterodyne detection. Before we proceed, note here our definition of the optical quadratures of arbitrary quadrature angles

$$\hat{X} = \frac{\hat{a} + \hat{a}^\dagger}{\sqrt{2}} \quad (3.166)$$

$$\hat{Y} = i \frac{\hat{a}^\dagger - \hat{a}}{\sqrt{2}} \quad (3.167)$$

$$\hat{X}_\theta = \frac{\hat{a}e^{-i\theta} + \hat{a}^\dagger e^{i\theta}}{\sqrt{2}} \quad (3.168)$$

In our experiment, we do not wish to detect two orthogonal quadrature angles directly due to the uncertainty in the measured quadrature angles. Instead, we use two measurement settings with well-calibrated quadrature angles such that the complex field $a(t)$ can be faithfully constructed. One of them is done with direct detection ($\theta_{\text{DD}} = \theta_1 = 30 \text{ deg}$, angle rotated due to pumping at the Δ_*), and the other one with a homodyne angle $\theta_{\text{Hom}} = \theta_2 = 0 \text{ deg}$ such that the mechanical signal is minimized on detection. These two detected quadratures hold the following relations for the phase and the amplitude quadratures,

$$\hat{X}_{\text{DD}} = \hat{X}_1 = \sqrt{\eta_1}(\cos(\theta_1)\hat{X} + \sin(\theta_1)\hat{Y}) + \sqrt{1-\eta_1}\hat{X}_{\text{vac},1} \quad (3.169)$$

$$\hat{X}_{\text{Hom}} = \hat{X}_2 = \sqrt{\eta_2}(\cos(\theta_2)\hat{X} + \sin(\theta_2)\hat{Y}) + \sqrt{1-\eta_2}\hat{X}_{\text{vac},2} \quad (3.170)$$

Here, any added noise and optical losses are modeled as the finite detection efficiencies $\eta_{1,2}$, with independently added vacuum noise from the information loss.

In order to reconstruct the amplitude and the phase quadratures of the field, we revert the

Chapter 3. Measurement-based quantum control of mechanical motion

above relations

$$\hat{X} = \frac{1}{\sqrt{\eta_1 \eta_2}} \left(\sqrt{\eta_2} \sin(\theta_2) \hat{X}_1 - \sqrt{\eta_1} \sin(\theta_1) \hat{X}_2 - \sqrt{\eta_2(1-\eta_1)} \sin(\theta_2) \hat{X}_{\text{vac},1} + \sqrt{\eta_1(1-\eta_2)} \sin(\theta_1) \hat{X}_{\text{vac},2} \right) / (\sin(\theta_2) \cos(\theta_1) - \sin(\theta_1) \cos(\theta_2)) \quad (3.171)$$

$$\hat{Y} = \frac{1}{\sqrt{\eta_1 \eta_2}} \left(\sqrt{\eta_2} \cos(\theta_2) \hat{X}_1 - \sqrt{\eta_1} \cos(\theta_1) \hat{X}_2 - \sqrt{\eta_2(1-\eta_1)} \cos(\theta_2) \hat{X}_{\text{vac},1} + \sqrt{\eta_1(1-\eta_2)} \cos(\theta_1) \hat{X}_{\text{vac},2} \right) / (\cos(\theta_2) \sin(\theta_1) - \cos(\theta_1) \sin(\theta_2)) \quad (3.172)$$

In the case of our specific measurement quadrature angles, we obtain the following relations

$$\hat{X} = \frac{\hat{X}_2 - \sqrt{1-\eta_2} \hat{X}_{\text{vac},2}}{\sqrt{\eta_2}} \quad (3.173)$$

$$\hat{Y} = 2 \frac{\hat{X}_1 - \sqrt{1-\eta_1} \hat{X}_{\text{vac},1}}{\sqrt{\eta_1}} - \sqrt{3} \frac{\hat{X}_2 - \sqrt{1-\eta_2} \hat{X}_{\text{vac},2}}{\sqrt{\eta_2}} \quad (3.174)$$

$$\hat{X} + i\hat{Y} = 2i \frac{\hat{X}_1 - \sqrt{1-\eta_1} \hat{X}_{\text{vac},1}}{\sqrt{\eta_1}} + (1 - \sqrt{3}i) \frac{\hat{X}_2 - \sqrt{1-\eta_2} \hat{X}_{\text{vac},2}}{\sqrt{\eta_2}} \quad (3.175)$$

$$2i \frac{\hat{X}_1}{\sqrt{\eta_1}} + (1 - \sqrt{3}i) \frac{\hat{X}_2}{\sqrt{\eta_2}} = \hat{X} + i\hat{Y} + 2i \frac{\sqrt{1-\eta_1} \hat{X}_{\text{vac},1}}{\sqrt{\eta_1}} + (1 - \sqrt{3}i) \frac{\sqrt{1-\eta_2} \hat{X}_{\text{vac},2}}{\sqrt{\eta_2}} \quad (3.176)$$

therefore, by combining signals from the two measurement channels in a specific way, i.e., $\hat{s} = \sqrt{2}i \frac{\hat{X}_1}{\sqrt{\eta_1}} + \frac{1-\sqrt{3}i}{\sqrt{2}} \frac{\hat{X}_2}{\sqrt{\eta_2}}$, we effectively constructed a non-Hermitian observable

$$\hat{s} = \hat{a} + \sqrt{2\left(\frac{1}{\eta_1} + \frac{1}{\eta_2} - 2\right)} \hat{X}_{\text{vac}} \quad (3.177)$$

which yields information on \hat{a} with some added vacuum noise. In our experiment, we can reliably retrieve the measured quadrature angles and the efficiency ratio between the two channels by fitting the noise spectral density ratio $\bar{S}_{\hat{X}_1 \hat{X}_1}(\omega) / \bar{S}_{\hat{X}_2 \hat{X}_2}(\omega)$ between the two channels, a function only determined by the cavity transduction susceptibility which is sensitive to the quadrature angles and the efficiencies.

Here, we need to pay special attention to what we are measuring in the experiment, as classical measurement results at different times commute with each other, whereas the quantum variable does not. Therefore, symmetrization is always required for classical observables. In this case of a non-Hermitian observable, we need to enforce the following symmetrization for the auto-correlation function

$$\begin{aligned} \bar{S}_{\hat{s}\hat{s}}(\omega) &= \frac{1}{2} \text{FT}_{\tau} [\langle \hat{s}^{\dagger}(\tau) \hat{s}(0) + \hat{s}(0) \hat{s}^{\dagger}(\tau) \rangle] \\ &= \frac{S_{\hat{a}\hat{a}}(\omega) + S_{\hat{a}^{\dagger}\hat{a}^{\dagger}}(-\omega)}{2} + 2\left(\frac{1}{\eta_1} + \frac{1}{\eta_2} - 2\right) \bar{S}_{\hat{X}_{\text{vac}} \hat{X}_{\text{vac}}}(\omega) \end{aligned} \quad (3.178)$$

which is the same as what one gets from a heterodyne detection. With this in mind, we omit

3.4 Cooling a mechanical oscillator close to the quantum ground state

the hats on the quantum observables in the following subsection.

Field spectral density of dual homodyne measurement

Here, we derive the spectral density of the reconstructed complex field $a(t)$ and show that it exhibits sideband asymmetry of the force spectral density experienced by the mechanical mode.

First, we start from the standard frequency-domain Langevin equations for mechanics and the cavity mode

$$Q(\omega) = \chi_m(\omega)(\sqrt{2\Gamma_m}P_{\text{in}} - 2gX) \quad (3.179)$$

$$-i\omega a = -\left(\frac{\kappa}{2} + i\bar{\Delta}\right)a - \sqrt{2}igQ(\omega) + \sqrt{k}a_{\text{in}} - i\bar{a}\Delta(\omega) \quad (3.180)$$

$$\chi_m(\omega) = \frac{\Omega_m}{\Omega_m^2 - \omega^2 - i\omega\Gamma_m} \quad (3.181)$$

To simplify the discussion, we also define the cavity susceptibility $\chi_{\text{cav}}^{-1} = \kappa/2 + i(\bar{\Delta} - \omega)$, and its complex conjugate pair $\chi_{\text{cav}}^{*-1} := \chi_{\text{cav}}^{*-1}(-\omega)$.

Since the interaction between the light intensity and the mechanical position couples the conjugate pair of the field operator a , a^\dagger , we need to solve for a from the following coupled equations

$$(\chi_{\text{cav}}^{-1} - 2ig^2\chi_m)a = -2ig\sqrt{\Gamma_m}\chi_m P_{\text{in}} + 2ig^2\chi_m a^\dagger + \sqrt{k}a_{\text{in}} - i\bar{a}\Delta(\omega) \quad (3.182)$$

$$(\chi_{\text{cav}}^{*-1} + 2ig^2\chi_m)a^\dagger = 2ig\sqrt{\Gamma_m}\chi_m P_{\text{in}} - 2ig^2\chi_m a + \sqrt{k}a_{\text{in}}^\dagger + i\bar{a}\Delta(\omega). \quad (3.183)$$

After the cavity-assisted self-feedback, we arrive now at the solution of the cavity field

$$a = \frac{-i\chi_{\text{cav}}(2g\sqrt{\Gamma_m}P_{\text{in}} + \bar{a}\chi_m^{-1}\Delta) + 2ig^2\sqrt{k}\chi_{\text{cav}}\chi_{\text{cav}}^*a_{\text{in}}^\dagger + (\chi_{\text{cav}}\chi_m^{-1} + 2ig^2\chi_{\text{cav}}\chi_{\text{cav}}^*)\sqrt{k}a_{\text{in}}}{\chi_m^{-1} + 2ig^2(\chi_{\text{cav}}^* - \chi_{\text{cav}})} \quad (3.184)$$

and the output field

$$\begin{aligned} a_{\text{out}} &= a_{\text{in}} - \sqrt{k}a \\ &= \left(i\chi_{\text{cav}}\sqrt{k}(2g\sqrt{\Gamma_m}P_{\text{in}} + \bar{a}\chi_m^{-1}\Delta) - 2ig^2\kappa\chi_{\text{cav}}\chi_{\text{cav}}^*a_{\text{in}}^\dagger \right. \\ &\quad \left. + ((1 - \kappa\chi_{\text{cav}})\chi_m^{-1} + 2ig^2(\chi_{\text{cav}}^* - \chi_{\text{cav}} - \kappa\chi_{\text{cav}}\chi_{\text{cav}}^*))a_{\text{in}} \right) / (\chi_m^{-1} + 2ig^2(\chi_{\text{cav}}^* - \chi_{\text{cav}})) \\ &= \chi_m' \left(i\chi_{\text{cav}}\sqrt{k}(2g\sqrt{\Gamma_m}P_{\text{in}} + \bar{a}\chi_m^{-1}\Delta) - 2ig^2\kappa\chi_{\text{cav}}\chi_{\text{cav}}^*a_{\text{in}}^\dagger \right) \\ &\quad + ((1 - \kappa\chi_{\text{cav}}) - \chi_m'2ig^2\kappa\chi_{\text{cav}}\chi_{\text{cav}}^*)a_{\text{in}} \end{aligned} \quad (3.185)$$

Chapter 3. Measurement-based quantum control of mechanical motion

where we define the modified mechanical susceptibility under dynamical backaction cooling

$$\chi'_m(\omega) = \frac{1}{\chi_m^{-1} + 2ig^2(\chi_{\text{cav}}^* - \chi_{\text{cav}})} = \frac{\Omega_m}{\Omega_m'^2 - \omega^2 - i\omega\Gamma'_m} \quad (3.186)$$

$$\Omega'_m = \Omega_m - \frac{2g^2\bar{\Delta}}{(\kappa/2)^2 + \bar{\Delta}^2} \quad (3.187)$$

$$\Gamma'_m = \Gamma_m + \frac{4g^2\Omega_m\bar{\Delta}\kappa}{((\kappa/2)^2 + \bar{\Delta}^2)^2}. \quad (3.188)$$

We can now calculate the power spectral density of the complex field operator, which is (cooperativity $C = \frac{4g^2}{\Gamma_m k}$)

$$\begin{aligned} S_{a_{\text{out}}a_{\text{out}}}(\omega) &= 4g^2\Gamma_m|\chi'_m|^2\kappa|\chi_{\text{cav}}|^2 \left(S_{P_{\text{in}}P_{\text{in}}} + \frac{C}{1 + (2(\bar{\Delta} + \omega)/\kappa)^2} S_{a_{\text{in}}^\dagger a_{\text{in}}^\dagger} + \frac{|\chi_m|^{-2}}{4g_0^2\Gamma_m} S_{\Delta\Delta} \right) \\ &+ \left(1 + 4g^2\Gamma_m|\chi'_m|^2\kappa|\chi_{\text{cav}}|^2 \frac{C}{1 + (2(\bar{\Delta} - \omega)/\kappa)^2} + 2\text{Im} [2g^2\kappa\chi'_m(1 - \kappa\chi_{\text{cav}}^*(\omega))\chi_{\text{cav}}^2] \right) S_{a_{\text{in}}a_{\text{in}}} \\ &+ 2\text{Im} \left[\chi'_m 2g^2\kappa\chi_{\text{cav}}\chi_{\text{cav}}^* ((1 - \kappa\chi_{\text{cav}}) - \chi'_m 2ig^2\kappa\chi_{\text{cav}}\chi_{\text{cav}})^*(\omega) S_{a_{\text{in}}a_{\text{in}}^\dagger} \right] \end{aligned} \quad (3.189)$$

Notice that here there is no vacuum noise in the expression, $S_{a_{\text{in}}a_{\text{in}}} = 0$ for a quantum-limited laser input. However, since $s = a + cX_{\text{vac}}$ is the actual observable, which contains the added vacuum noise from splitting the signal to two homodyne channels. Also, shot noise naturally emerges when calculating $S_{a_{\text{out}}^\dagger a_{\text{out}}^\dagger}$ required for symmetrization. In data processing, we can subtract the vacuum noise out of the record by $S_{a_{\text{out}}a_{\text{out}}} + S_{a_{\text{out}}^\dagger a_{\text{out}}^\dagger} = 2\bar{S}_{ss} - 2|c|^2\bar{S}_{X_{\text{vac}}X_{\text{vac}}}$, to retrieve the field spectrum.

After accounting for the contribution from also the $S_{a_{\text{out}}^\dagger a_{\text{out}}^\dagger}(-\omega)$ term, we arrive at the measured asymmetric (unitless) force spectral density

$$\bar{S}_{F_{\text{tot}}F_{\text{tot}}}(\omega) = \bar{S}_{P_{\text{in}}P_{\text{in}}} + C \left(\frac{1}{1 + (2(\bar{\Delta} + \omega)/\kappa)^2} + \frac{1}{1 + (2(\bar{\Delta} - \omega)/\kappa)^2} \right) S_{a_{\text{in}}^\dagger a_{\text{in}}^\dagger} \quad (3.190)$$

$$- \frac{\omega\Gamma'_m}{2\Omega_m\Gamma_m} S_{a_{\text{in}}^\dagger a_{\text{in}}^\dagger} + \frac{|\chi_m|^{-2}}{4g_0^2\Gamma_m} \bar{S}_{\Delta\Delta} \quad (3.191)$$

which contains four parts. The first term $\bar{S}_{P_{\text{in}}P_{\text{in}}}$ is the symmetrized environment force noise at room temperature. The second term is the symmetrized quantum backaction force noise. The fourth term $\bar{S}_{\Delta\Delta}$ is associated with cavity frequency-noise-induced heating of the mechanical mode and the background frequency noise itself. The third term is the interference between the backaction-driven motion and the imprecision noise from the probe laser, which induces force noise asymmetry. As discussed in [69], the sideband asymmetry in linear quadrature measurements does not come directly from the mechanical sidebands, which are symmetrized in our measurement, but from the backaction and imprecision interference of the optical field. Photon counting of individual sidebands is required to measure the asymmetric mechanical

3.4 Cooling a mechanical oscillator close to the quantum ground state

sidebands directly. However, in the case of optical measurements, both methods always yield the same result, and we regard them as probing the same physics. Therefore, by measuring the asymmetry of the force noise, we have a separate way to verify the phonon occupation calibrated from the conventional homodyne measurement.

Then, we proceed to simplify the result in the case of a quantum-limited laser probe,

$$\bar{S}_{F_{\text{tot}}F_{\text{tot}}}(\omega) = \frac{\Gamma'_m}{\Gamma_m} \left(\frac{\Gamma_{\text{th}} + \Gamma_{\text{qba}}}{\Gamma'_m} - \frac{\omega}{2\Omega_m} + \frac{|\chi_m|^{-2}}{4g_0^2\Gamma'_m} \bar{S}_{\Delta\Delta} \right) \quad (3.192)$$

$$= \frac{\Gamma'_m}{\Gamma_m} \left(\bar{n}_{\text{ideal}} - \frac{\omega}{2\Omega_m} + \frac{|\chi_m|^{-2}}{4g_0^2\Gamma'_m} \bar{S}_{\Delta\Delta} \right) \quad (3.193)$$

with the asymmetry ratio R

$$R = \frac{\bar{n}_{\text{eff}} - \frac{1}{2}}{\bar{n}_{\text{eff}} + \frac{1}{2}} \quad (3.194)$$

where the cavity frequency noise heats the effective phonon occupancy by $\bar{n}_{\text{eff}} = \bar{n}_{\text{ideal}} + \frac{|\chi_m|^{-2}}{4g_0^2\Gamma'_m} \bar{S}_{\Delta\Delta}$. Note that any classical noise sources that do not originate from the measurement meter, in this case, the probe laser, will only manifest as an effective heating of the phonon occupancy, as the required meter-force interference is absent.

Observation of the sideband asymmetry of an oscillator cooled close to the ground state

We pump the cavity at the magic detuning Δ_* and allow optical sideband cooling to stabilize the soft-clamped mode to around $\bar{n}_{\text{eff}} \sim 7$ phonons. Then, we evenly split the cavity output signal into two measurement channels. In the first one, we use the single-port homodyne measurement to cancel the TIN for our quadrature measurement X_{Hom} and optimize the measured quadrature angle to minimize the mechanical signal. In this case, we are sure the correct homodyne angle $\theta = 30$ deg is achieved. The mechanical signal can not be completely removed due to the finite sideband ratio $\Omega_m/\kappa \sim 10$. The cavity susceptibility determines the suppression ratio and can be used to retrieve a precise quadrature angle and measurement efficiency through fitting. In the other measurement channel, we implement direct detection X_{DD} , in which the TIN is canceled directly at the magic detuning.

We use a digitizer to record both signals simultaneously at 14 MHz sampling rate for 2 s, and post-processed the data to reconstruct the non-Hermitian observable $s = \sqrt{2}i \frac{X_{\text{DD}}}{\sqrt{\eta_1}} + \frac{1-\sqrt{3}i}{\sqrt{2}} \frac{X_{\text{Hom}}}{\sqrt{\eta_2}}$. The power spectral densities of the quadrature data and the complex field are illustrated in Fig. 3.12, in which we observed a statistically significant 15 % sideband asymmetry ratio after shot noise removal. As a comparison, all the other mechanical modes visible in the spectrum show less than 2 % statistical variation of the asymmetric ratio. The 15 % sideband asymmetry ratio measured is also consistent with the phonon occupancy fit from the measured quadrature data, showing that our system is in a regime close to the quantum ground state.

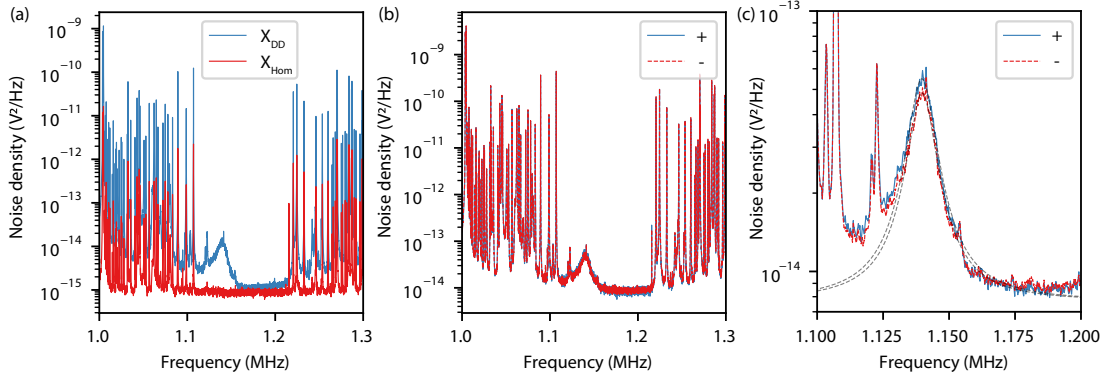


Figure 3.12: **(a)** Calculated spectrum of the two optical quadrature data X_{DD} and X_{Hom} . **(b)** Calculated spectrum of the non-Hermitian observable s , with asymmetric negative and positive frequency noise density. **(c)** Zoomed-in near the soft-clamped mode, with a low-pass filter applied to reduce the noise variance. After shot-noise subtraction, the positive and negative frequency components show statistically significant 15% difference. As a comparison, the nearby mechanical modes show less than 2% of sideband asymmetry.

In Appendix B.8, we analyze the case where the system is contaminated by the laser amplitude and phase noise. This is not the case in our system, as our laser is quantum-limited in both phase and amplitude. Note that the main noise contribution in this experiment is likely the third-order nonlinear noise investigated in Section 2.4.4, due to the narrow cavity linewidth. However, as the modification of sideband asymmetry requires interference between the noise-backaction-driven mechanical motion and the original noise from the measurement meter, the third-order nonlinear noise only contributes to the heating of the mechanical motion and behaves similarly to the cavity-detuning noise. For this reason, the contribution of the nonlinear noise is faithfully accounted for in the measured asymmetry result.

3.5 Future experiments

I worked on this project with my colleague Alberto from late-2019 to mid-2023, and solved multiple technical issues (discussed in Chapter 2), including thermomechanical nonlinear noise, photothermal mechanical instability, and cavity frequency noise, to reach the current stage where quantum control of mechanical motion near the Heisenberg limit is possible at room temperature. Given our device’s current performance, we demonstrated multiple signature phenomena in the quantum regime in this chapter, including optomechanical squeezing, conditional mechanical state preparation, measurement-based feedback cooling, and optomechanical sideband asymmetry. We are currently still working on measurement-based feedback cooling mentioned in section 3.3 with our current generation device to reach phonon occupancy $\bar{n}_{\text{eff}} \ll 1$ in real-time. As cooling to such a low phonon occupancy requires very high feedback gain, to mitigate the anti-damping experienced by nearby mechanical modes during the feedback, we plan to use electrically-gated feedback such that in the long-

time limit, the anti-damped mechanical modes are still stable.

Progressing much further than we have already shown here requires a new generation of Ph.D. students to improve upon what we have already achieved. I summarize a few points here for reference:

- In our current density-modulated membrane, we observe a lot of low-Q membrane modes in the mechanical bandgap that are weakly coupled to the optical modes, with no trace of their existence in the FEM simulation. We suspect these might be the effects of the pillars that we failed to capture in our analysis, but further investigation is required with the testing of more samples.
- In this chapter, we conclude that with symmetric measurement channels of mechanical quadratures, it is impossible to generate squeezed mechanical states, and therefore, mechanical entanglement is not reachable. However, it is possible to use a soft-clamped fundamental mode in other membrane geometries, e.g., [49] that we worked with before, to break the symmetry between these two channels, either using fast measurement [85] or stroboscopic probing [89]. When these symmetries are broken, mechanical squeezing and entanglement are possible even through continuous measurements. However, fundamental modes of mechanical structures generally suffer from Q-degradation when the chip is in contact with the mirrors. A discussion with Jack Sankey and his group members indicates that by using sapphire hemispheres as spacers such that the membrane chip only has point contacts with other components, this Q-degradation issue can be effectively mitigated. However, this would require a new design of the MIM assembly.
- For many years, the field has used silicon nitride as the material for high-Q mechanical resonators. New crystalline materials such as diamond [90] and silicon carbide [91] are promising for the next generation devices, both for their high intrinsic mechanical Q and the possibility of introducing color centers which interact with strain fields of the mechanical modes [92]. With the introduction of the color centers and sufficiently high-Q mechanical modes, integrated trapped-ion-like systems can be effectively fabricated [93], which allows the deterministic generation of non-classical mechanical states at room temperature, and entanglement of distant vacancy qubits mediated by a common vibrational motion.

Free-electron quantum optics **Part II**

The fogs of confusion throughout human history remained unresolved until people saw the facts with their own eyes. Microscopes play an utmost important role in developing our scientific understanding of the world, enabling the discovery of cells and microorganisms [94], driven by our human curiosity to understand things through their finest details.

Light-matter interaction is the first tool we use in microscopes to see the details of objects. When photons at different frequencies are deflected or absorbed by the material, the shape and composition of the object are mapped out. The details that could be visualized were restricted by the size of the photons for three hundred years until the invention of electron microscopes [95] in the mid-twentieth century, which uses electrons that are 10^5 times smaller than the photons. With electron microscopes, viruses [96] and even protein structures [97] can now be visualized. As a much bigger object, photons, the tool that enabled many scientific discoveries, also became the testing subject under the microscope.

In this part of the thesis, we use electrons to examine the properties of light, both in how light oscillates as a wave and behaves as a particle, presenting a new facet of light that is challenging to access through purely optical means. To understand what we see, we first need to understand our tool. Free electrons, being one of the most elementary quantum objects [98], have not been the most well-studied subject in the field of quantum science and technology, where bounded electrons in atomic systems have been the most popular by far. Unlike other quantum systems that couple to photons, free-electron-photon interaction happens on an ultrafast timescale in a non-localized fashion and offers an extra spatial degree of freedom. The ultrafast interaction presents an opportunity for quantum applications but also unique challenges for reliable control [9].

During my PhD, I was involved extensively in our collaboration with the group of Claus Ropers at the Max Planck Institute for Multidisciplinary Sciences, Göttingen, who are experts in ultrafast electron microscopy and have performed numerous pioneering works in the field of electron-photon coupling. We developed a platform [7, 8, 9, 11] capable of strong electron-light interactions using an electron microscope and photonic integrated circuits based on Si_3N_4 . Our setup (Fig. 5.1) allows an electron beam to interact with the co-propagating evanescent field of a microresonator waveguide in the object plane of a transmission electron microscope (TEM). The fiber-coupled microresonator chip features strong electron-light interaction with complete control over the input and output light. This approach establishes a versatile and highly efficient framework for enhanced electron beam control [99, 100, 101, 102, 103, 104, 105, 106]. More fundamentally, we introduce a universal platform for exploring free-electron quantum optics [107, 108, 109, 110], with developments in strong vacuum coupling and electron-photon non-classical correlation, thanks to the tight confinement of the optical field.

In this part of the thesis, we start with Chapter 4, the developed theoretical framework for studying free-electron interaction with semi-classical light, single-mode quantum field (Section 4.2), and multi-mode optical continuum (Section 4.3). In Chapter 5, we proceed with the experimental investigation of the interaction between free electrons with the classical

continuous-wave (CW) field (Section 5.1), and the nonlinear optical field (Section 5.2). In Chapter 6, we analyze the experimental feasibility of free-electron interaction with quantum optical fields of the photonic integrated circuits (Section 6.2), as well as schemes to generate useful photonic and electron quantum states using state heralding (Section 6.3, Section 6.4). This is followed by Chapter 7, the experimental demonstration of the generation of electron-photon pair states, where we observe photon generation, its non-classical correlation, and Poisson statistics. In Chapter 8, we discuss the electron energy-momentum dispersion effect in electron-photon interactions over a long distance of dispersive propagation (Section 8.1), as well as applications enabled by this nonlinearity, including optical klystrons (Section 8.2), Jaynes-Cummings interaction (Section 8.3), and the Bell test of local realism (Section 8.4). Some sections in this part of the thesis are adapted from Refs [7, 8, 9].

We also summarize some acronyms that we use in this part of the thesis below.

CAR: Coincidence to accidental ratio

CL: Cathodoluminescence

DKS: Dissipative Kerr soliton

DLA: Dielectric laser accelerator

EELS: Electron energy-loss spectroscopy

EEGS: Electron energy-gain spectroscopy

EFTEM: Energy-filtered transmission electron microscopy

PINEM: Photon-induced near-field electron microscopy

Q: Quality factor

QED: Quantum electrodynamics

SNR: Signal to noise ratio

SPAD: Single-photon avalanche diode

SPDC: Spontaneous parametric down-conversion

UTEM: Ultrafast transmission electron microscope

TM: Transverse magnetic

ZLP: Zero-loss peak

4 Quantum optical interaction between free electrons and photons

In this chapter, we set up the theoretical foundations of electron-photon interaction. Compared to conventional quantum optics [111] approaches that deal with low-speed particles coupling with a cavity mode, in our physical setting, there are multiple complications. First, the electrons travel near light speed in free space with a de-localized wavefunction and energy-dependent velocity. Therefore, the interaction does not start or end at a specific spatial point or moment in time [112], as different energy components arrive at the photonic structure with a state-dependent delay time, and the energy eigenstates are spatially unbounded. Second, the interaction happens at an ultra-fast time scale and usually only lasts some optical cycles. Therefore, compared to the stationary counterpart in cavity QED, the electron couples to a vast frequency band of optical modes [113], and the frequency selectivity is generally very poor. In this case, multi-mode interaction is natural and usually needs to be accounted for in this type of interaction. Third, the electron couples not only to cavity modes but also generally to all the possible optical modes, guided and non-guided, supported by the optical structure [9]. Therefore, the conventional modal-decomposition method used by the cavity QED community is not convenient for treating these interactions, and other approaches must be adopted [114].

In the following, we derive the theoretical formulation of our system, consisting of high-energy free electrons coupling to our optical structures.

First, the problem will be formulated in the semi-classical picture (Section 4.2.1) where the optical field is not quantized. This type of interaction has been the most well-studied [115] in the field due to the selective single-mode interaction typically driven by a strong optical pump. In this picture, the interaction can be effectively modeled as a phase modulation of the electron wave function imprinted by light.

Then, we quantize a single optical mode (Section 4.2) and in a later Section 7 generalize it to the multi-mode interaction in an experiment realization. Quantization based on modal decomposition is the most conventional quantization procedure in quantum optics. It has been successful for cavity QED systems where interaction time is substantially longer than

Chapter 4. Quantum optical interaction between free electrons and photons

the round trip time of light in a cavity. Due to the ultrafast interaction timescale of the electron-photon interaction, our single-mode treatment is not convenient to apply to actual experiments.

Due to this inconvenience, last, we formulate the free-electron coupling to the optical continuum (Section 4.3) and draw the correspondence to the modal-decomposition method such that all frameworks we developed are self-consistent. These different formalisms are used in later chapters when different types of interactions are concerned.

4.1 Quantum nature of free electrons and photons

Before we begin, we must differentiate the different quantum vs. classical pictures for electrons and photons. They are quite different as electrons are initially classical point particles, and photons are classical electromagnetic waves.

In our quantization, we only quantize the electron until the point of its wave properties and do not deal with the second quantization of the wave function itself. Therefore, when we say the quantum effect of electrons, we are primarily concerned with the wave properties, such that in the time-energy / position-momentum phase space, the electron Wigner function can exhibit negativity [116], which is not possible for a classical point-like particle.

For the photons, we quantize their field operator such that they exhibit particle properties alongside their wave properties. Similarly, if we construct a phase-amplitude phase space for the light, the Wigner function can exhibit negativity [117], which is not possible for a classical wave. The Wigner negativity is also necessary in continuous-variable quantum computing [118] for any quantum speedup to be possible. The particle nature can also be probed by a photon counting correlation measurement [119], where the particle nature of the light exhibits a correlation stronger than it would be possible for classical waves, which is bounded by the Cauchy-Schwarz inequality.

When the two particles are involved simultaneously in an interaction, as is the case we are treating here, the quantum-classical distinction is more delicate. We discuss the non-classical nature of electron-photon interaction in detail in the later section 7.3.

4.2 Single-mode electron-photon interaction

While the length gauge (where the vector potential $\mathbf{A} = 0$) is usually chosen for localized quantum systems in cavity quantum electrodynamics (cQED) [111], the velocity gauge (where the scalar potential $\phi = 0$) is a natural choice for free electrons at finite momentum $\hat{\mathbf{p}}$ in an electromagnetic field with vector potential $\hat{\mathbf{A}}$. In the velocity gauge typically used for traveling particles in electron-magnetic fields, the following Hamiltonian describes the electron-photon

interaction,

$$H = \frac{(\mathbf{p} + e\mathbf{A})^2}{2m} = \frac{\mathbf{p}^2}{2m} + \frac{e}{m}\mathbf{p} \cdot \mathbf{A} + \frac{e^2\mathbf{A}^2}{2m} \quad (4.1)$$

with which we use a perturbation approach where we go to the rotating frame of the original electron energy $H_0 = \frac{\mathbf{p}^2}{2m}$, and treat all the other $H_1 = \frac{e}{m}\mathbf{p} \cdot \mathbf{A}$ and $H_2 = \frac{e^2\mathbf{A}^2}{2m}$ as the interaction terms. Here e is the electron charge, and m is the electron mass. In free space, the electron travels slower than light speed, so the single-photon scattering term $H_1 = \frac{e}{m}\mathbf{p} \cdot \mathbf{A}$ does not contribute to the interaction. Only the two-photon scattering term $H_2 = \frac{e^2\mathbf{A}^2}{2m}$ (Compton scattering) can happen. When a nearby dielectric medium slows the optical field, H_1 interaction can dominate. In our setting, where free electrons interact with the optical field in a phase-matched fashion (electron group velocity matching light phase velocity) mediated by dielectric media, we are mostly concerned with H_1 . Note that we treat the electrons in a non-relativistic form, whereas the actual speed approaches light speed. Theorists found that as long as the relativistic energy-momentum relation $\hat{H}_0|p\rangle\rangle = E(p)|p\rangle\rangle$ is used, the result is compatible with a relativistic treatment of the problem [113].

4.2.1 Electron-photon semi-classical interaction

In this section, we are treating the case where high-energy free-electrons interact with classical optical fields. This semi-classical formulation can also be found in the method section of ref [120]. This picture only quantizes the electron energy \hat{H}_0 and the momentum operator \hat{p} . The vector potential is scalar-valued and is chosen to be $A(z) = F(z) \sin \omega t / \omega$. The electron is analyzed in the plane-wave momentum-state basis $|p\rangle = \int L^{-1/2} e^{ik_p z} |z\rangle dz$, where $L \rightarrow \infty$ is the quantization volume.

In the Schrödinger picture, we can write down the time-dependent Schrödinger equation

$$(\hat{H}_0 - iev_e A(z, t)) \psi(z) = i\hbar \frac{\partial \psi}{\partial t}. \quad (4.2)$$

where v_e is the electron group velocity. We can obtain the generalized solution [121] directly as

$$\psi(z, t) = \psi_0(z, t) e^{-2i\text{Im}[g(z, t)] e^{i\omega(t-z/v_e)}} \quad (4.3)$$

$$g(z, t) = \frac{e}{2\hbar\omega} \int_{-\infty}^z F_z(z') e^{-i\omega z' / v_e} dz'. \quad (4.4)$$

As the optical field effectively modulates the phase of the electron wavefunction (illustrated in Fig. 4.1(a)) with the periodicity of ω^{-1} , the electron energy eigenstates involved in this process are always spaced by $\hbar\omega$ due to the Fourier relation. We choose, therefore, the following state space of the unperturbed Hamiltonian

$$\hat{H}_0|N\rangle = (E_0 + N\hbar\omega)|N\rangle, \quad (4.5)$$

Chapter 4. Quantum optical interaction between free electrons and photons

where the system is assumed to have an initial state $|0\rangle$ with electron energy E_0 , and the final state $|N\rangle$ with final electron energy $E_0 + N\hbar\omega$. Note that $|N\rangle$ here is not the photon Fock state but the label for the electron energy ladder and does not involve the quantization of the photons. The coupling matrix element can be readily calculated as

$$\langle N+1 | \frac{e}{m} \hat{p} A | N \rangle = \frac{2\hbar v_N g}{L} \sin \omega t, \quad (4.6)$$

where we have the unit-less coupling strength defined as

$$g = \frac{e}{2\hbar\omega} \int_{-L/2}^{L/2} F(z) e^{-i\Delta k \cdot z} dz. \quad (4.7)$$

Here, $\Delta k \approx \omega/v_N$ is the momentum change of the electron when the energy is changed by $\hbar\omega$. From here, we can see that a strong electron-light interaction requires a phase-matching condition, i.e., $\Delta k \approx k_l$, where k_l is the wave vector of the light field. The model here is reduced to one dimension where the electron travels, and the electron transverse distribution is assumed to be point-like. The effect of the transverse wavefunction is described in Section 4.3.1.

From here, we can define the electron ladder operators as

$$\hat{b} = \sum_N |N-1\rangle \langle N|, \quad (4.8)$$

so that the coupling term can be written as

$$\frac{e}{m} \hat{p} A = \frac{2\hbar v}{L} (g^* \hat{b} + g \hat{b}^\dagger) \sin \omega t. \quad (4.9)$$

The electron operator \hat{b} defined here has the following properties

$$|N+1\rangle = \hat{b}^\dagger |N\rangle \quad (4.10)$$

$$|N-1\rangle = \hat{b} |N\rangle \quad (4.11)$$

$$\hat{b} \hat{b}^\dagger = \hat{b}^\dagger \hat{b} = 1 \quad (4.12)$$

and is different from the usual bosonic creation and annihilation operators. In the interaction picture Hamiltonian (with rotating wave approximation), we obtain the interaction Hamiltonian

$$\hat{H}_{\text{int}} = \frac{\hbar v}{iL} (g^* \hat{b} - g \hat{b}^\dagger). \quad (4.13)$$

The scattering matrix can then be calculated as

$$\hat{S} = \exp\left(-\frac{i}{\hbar} \int_{-L/2v}^{L/2v} \hat{H}_{\text{int}} dt\right) = \exp(g \hat{b}^\dagger - g^* \hat{b}), \quad (4.14)$$

which can be viewed as a displacement operator for the electron states but with a different property than that of the photons. The transition probabilities from the initial state $|0\rangle$ to the

4.2 Single-mode electron-photon interaction

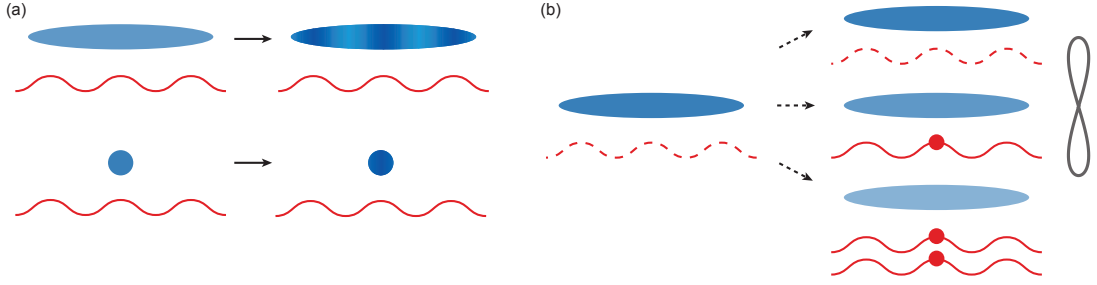


Figure 4.1: **(a)** Free electron interaction with classical light field, whose wave function is phase-modulated, equivalent to the directional acceleration or deacceleration of point electrons at different locations. **(b)** Free electron interaction with quantum optical fields, ending in an electron-photon energy-number entangled state.

final states $|N\rangle$ can be calculated to be

$$P_N = |\langle N|\hat{S}|0\rangle|^2 = J_N(2|g|)^2, \quad (4.15)$$

which oscillates as Bessel functions as a function of the coupling strength g , expected for any phase modulation, and is verified experimentally in ref [116]. Note that here, we are only treating the case that the electron behaves as a wave to begin with, which then manifests the wave properties when phase modulation is applied. When the electron wave function is sub-optical-cycle and behaves more like a point particle, more delicate treatment is required, as discussed in Section 5.2.2.

4.2.2 Quantization of the optical field

In the following, we proceed to derive the case when the electron interacts with a quantum optical field (illustrated in Fig. 4.1(b)). Still, we restrict ourselves first to the one dimension (\hat{z}) where the electron propagates, as $\langle \hat{\mathbf{p}} \cdot \mathbf{e}_z$ is the dominant momentum component for the high-energy electrons. Because the interaction strength scales with $\hat{\mathbf{p}} \cdot \hat{\mathbf{A}}$, the transverse components contribute negligibly to the interaction. In the modal-decomposition method, the vector potential is quantized as

$$\hat{\mathbf{A}} \cdot \mathbf{e}_z = \hat{A}(z) = \sum_m \sqrt{\frac{\hbar}{2\epsilon_0 \omega_m V_m}} (u_m(z) \hat{a}_m + u_m^*(z) \hat{a}_m^\dagger), \quad (4.16)$$

where $u(z)$ is the z projection (along the propagation direction of electron \mathbf{k}_e) of the vector mode function $\mathbf{u}(\mathbf{r})$ which satisfies

$$\int_V \epsilon(\mathbf{r}) \mathbf{u}_m(\mathbf{r}) \mathbf{u}_n^*(\mathbf{r}) d\mathbf{r}^3 = \delta_{m,n} V_m. \quad (4.17)$$

Here, ϵ_0 is the optical permittivity, ω_m the optical frequency of mode m , and V_m is the effective optical mode volume. We first analyze the interaction in the single-mode case ($\hat{a}_m \rightarrow \hat{a}$), where

Chapter 4. Quantum optical interaction between free electrons and photons

all the other modes are neglected. We choose again the electron plane wave states as our analysis basis,

$$|k_e\rangle = \int dz |z\rangle \langle z| |k_e\rangle = \lim_{L \rightarrow \infty} \int_{-L/2}^{L/2} dz L^{-1/2} \exp(ik_e z) |z\rangle \quad (4.18)$$

$$\mathbb{1} = \sum_{k_e} |k_e\rangle \langle k_e| = \lim_{L \rightarrow \infty} \frac{L}{2\pi} \int dk_e |k_e\rangle \langle k_e| \quad (4.19)$$

One-photon scattering

We quantize the coupling term H_1 in a symmetrized fashion, and insert the identity $\mathbb{1}$ above,

$$\begin{aligned} \hat{H}_1 &= \frac{e}{2m} (\hat{p}\hat{A} + \hat{A}\hat{p}) \\ &= \sqrt{\frac{\hbar}{2\epsilon_0\omega V}} \frac{e}{2m} \sum_{k_e} |k_e\rangle \langle k_e| \cdot \hat{p} \cdot \int_{L_c} dz |z\rangle \langle z| (u(z)\hat{a} + u^*(z)\hat{a}^\dagger) \sum_{k'_e} |k'_e\rangle \langle k'_e| + h.c. \\ &= \lim_{L \rightarrow \infty} \sqrt{\frac{\hbar}{2\epsilon_0\omega V}} \frac{e}{mL} \left(\sum_{\Delta k_e} \sum_{k_e} \hbar(k_e - \Delta k_e/2) \int_{L_c} dz e^{-i\Delta k_e \cdot z} u(z) \hat{a} |k_e\rangle \langle k_e - \Delta k_e| + h.c. \right) \\ &= \sqrt{\frac{\hbar}{2\epsilon_0\omega V}} \frac{e\bar{u}k_e^0\hbar}{m} \left(\hat{a} \sum_{k_e} \int_{\Delta k_e} d\Delta k_e \frac{k_e - \Delta k_e/2}{k_e^0} \frac{\Theta(\Delta k_e)}{2\pi} |k_e\rangle \langle k_e - \Delta k_e| + h.c. \right) \\ &= \hbar g_0 \hat{a} \hat{b}^\dagger + \hbar g_0^* \hat{a}^\dagger \hat{b}, \end{aligned} \quad (4.20)$$

with coupling rate

$$g_0 = \sqrt{\frac{1}{2\epsilon_0\hbar\omega V}} \frac{e\bar{u}\hbar k_e^0}{m}, \quad (4.21)$$

and the electron transition operator

$$\hat{b} = \sum_{k_e} \int_{\Delta k_e} d\Delta k_e \frac{k_e - \Delta k_e/2}{k_e^0} \frac{\Theta^*(\Delta k_e)}{2\pi} |k_e - \Delta k_e\rangle \langle k_e|. \quad (4.22)$$

Here, k_e^0 can be chosen arbitrarily, and we choose it to be the wave vector of the initial electron state. $\Theta(\Delta k_e) = \int_{L_c} dz e^{-i\Delta k_e \cdot z} u(z) / \bar{u}$ is the phase matching condition, and can be viewed as an effective interaction length. Again, \bar{u} can be chosen arbitrarily, and we choose it to be the average field amplitude over the optical mode extend. There is no solidly defined interaction rate and length because the electron state basis is infinitely long plane waves. Therefore, we can not define a time or length for this interaction. It is, shown in the following, possible to define an interaction strength g_ω in the case of a single scattering event that lasts for an infinite duration τ , starting from $\tau_i \rightarrow -\infty$ and ending at $\tau_f \rightarrow +\infty$.

4.2 Single-mode electron-photon interaction

In the interaction picture, we derive the scattering matrix as

$$\begin{aligned}
\hat{H}_{\text{int}} &= \hbar g_0 \hat{a} \sum_{k_e} \int_{\Delta k_e} d\Delta k_e \frac{k_e - \Delta k_e / 2}{k_e^0} \frac{\Theta(\Delta k_e)}{2\pi} |k_e\rangle \langle k_e - \Delta k_e| \\
&\quad \times e^{-i\omega t} e^{i[E(k_e) - E(k_e - \Delta k_e)]t/\hbar} + \text{h.c.} \tag{4.23} \\
\hat{S} &= T \exp\left(-\frac{i}{\hbar} \int_{\tau} \hat{H}_{\text{int}} dt\right) \\
&\approx \exp\left(-\int_{\tau} i g_0 \hat{a} \sum_{k_e} \int_{\Delta k_e} d\Delta k_e \frac{k_e - \Delta k_e / 2}{k_e^0} \frac{\Theta(\Delta k_e)}{2\pi} |k_e\rangle \langle k_e - \Delta k_e| \right. \\
&\quad \left. \times e^{i([E(k_e) - E(k_e - \Delta k_e)]/\hbar - \omega)t} dt - \text{h.c.}\right) \\
&= \exp\left(-i g_0 \hat{a} \sum_{k_e} \int_{\Delta k_e} d\Delta k_e \frac{k_e - \Delta k_e / 2}{k_e^0} \Theta(\Delta k_e) |k_e\rangle \langle k_e - \Delta k_e| \right. \\
&\quad \left. \times \delta\left[\frac{E(k_e) - E(k_e - \Delta k_e)}{\hbar} - \omega\right] - \text{h.c.}\right) \\
&= \exp\left(-i g_0 \hat{a} \sum_{k_e} \frac{k_e - \Delta / 2}{k_e^0} \frac{\Theta(\Delta)}{\partial_{p_e} E} |k_e\rangle \langle k_e - \Delta| - \text{h.c.}\right) \\
&\approx \exp\left(-i g_0 \frac{\Theta(\Delta)}{v_e} \hat{a} \sum_{k_e \in [k_e^0 - \epsilon, k_e^0 + \epsilon]} |k_e\rangle \langle k_e - \Delta| - \text{h.c.}\right) \\
&= \exp\left(-i g_0 \tau_{\text{int}} \hat{a} \hat{b}^\dagger - \text{h.c.}\right), \tag{4.24}
\end{aligned}$$

where $\Delta: E(k_e) - E(k_e - \Delta) = \hbar\omega$ is the electron wave-vector change due to the absorption/emission of a photon, and the effective interaction time $\tau_{\text{int}} = \frac{\Theta(\Delta)}{v_e}$ is defined by the effective interaction length $\Theta(\Delta)$ which is set by the phase matching condition. We can now combine g_0 and τ_{int} to eliminate the coefficients we arbitrarily defined earlier and arrive at

$$g_\omega = -i g_0^* \tau_{\text{int}}^* = -i \sqrt{\frac{e^2}{2\epsilon_0 \hbar \omega V}} \int_L dz e^{i\Delta \cdot z} u^*(z), \tag{4.25}$$

such that the scattering matrix can be simplified to $\hat{S} = \exp(g_\omega \hat{a}^\dagger \hat{b} - \text{h.c.})$. The ladder operator is approximated when the levels involved do not experience significant electron energy-momentum dispersion. The complete expression is instead

$$\hat{b} = \sum_{k_e} \frac{k_e - \Delta / 2}{k_e^0} |k_e\rangle \langle k_e + \Delta| \tag{4.26}$$

In the presence of a strong coherent optical drive $|\alpha\rangle$, the scattering matrix reduces to a displacement α operator on the electron state $S \approx \exp(g_\omega \alpha^* \hat{b}^\dagger - \text{h.c.})$. If the initial electron state is a pure momentum state with vector k_e^0 , the probability distribution on the N_{th} sideband

Chapter 4. Quantum optical interaction between free electrons and photons

will be

$$P_N = |\langle k_e^0 + N\Delta | S | k_e^0 \rangle|^2 = J_N(2|g|)^2 \quad (4.27)$$

$$g = \alpha g_\omega^* = i\alpha \sqrt{\frac{e^2}{2\epsilon_0 \hbar \omega V}} \int_L dz e^{-i\Delta \cdot z} u(z). \quad (4.28)$$

As expected, this result is identical to the previous section, where we treat the optical field classically. The substitution $\hat{a} \rightarrow \alpha$ is only correct when $\alpha \ll 1$, i.e., the field approaches the classical limit.

Heuristic derivation of the electron-photon coupling strength

Last, we would like to note that there is an elegant way to heuristically derive the photon emission strength $|g_\omega|^2 = \frac{e^2 L_{\text{cav}}^2}{2\epsilon_0 \hbar \omega V_{\text{eff}}}$. We could picture the optical cavity as a capacitor being charged by a flying electron. The work that is done to the capacitor (initial field seeded by the vacuum fluctuation) is

$$dW = eE(z)dz = \epsilon_0 V_{\text{eff}} E(z) dE(z) \quad (4.29)$$

where the right-hand side is the capacitor energy integrated by the field, which is then parameterized by the flying distance z of the electron. With this expression, we can easily arrive at the coupling strength by quantizing the charged energy into individual photons,

$$W = \int \frac{e^2}{\epsilon_0 V_{\text{eff}}} z dz = \frac{e^2 L_c^2}{2\epsilon_0 V_{\text{eff}}} = \hbar \omega \langle a^\dagger a \rangle \quad (4.30)$$

$$|g_\omega|^2 = \frac{W}{\langle a^\dagger a \rangle} = \frac{e^2 L_{\text{cav}}^2}{2\epsilon_0 \hbar \omega V_{\text{eff}}} \quad (4.31)$$

where we easily retrieve the same expression.

Generalization to the three-dimensional case

In the derivations above, we assumed that the longitudinal (\mathbf{z} direction) momentum transfer dominates the interaction. This assumption is valid primarily for directional high-energy electrons interacting with a co-propagating optical field along the same direction. To derive a generalized expression for the 3D phase matching, we need to use the following identity

$$\mathbb{1} = \sum_{\mathbf{k}_e} |\mathbf{k}_e\rangle \langle \mathbf{k}_e| = \lim_{L^3 \rightarrow \infty} \frac{L^3}{(2\pi)^3} \int d\mathbf{k}_e |\mathbf{k}_e\rangle \langle \mathbf{k}_e| \quad (4.32)$$

4.2 Single-mode electron-photon interaction

during the derivation. The Hamiltonian can be expanded by

$$\begin{aligned}\hat{H}_1 &= \sqrt{\frac{\hbar}{2\epsilon_0\omega V}} \frac{e}{2m} \sum_{\mathbf{k}_e} |\mathbf{k}_e\rangle \langle \mathbf{k}_e| \hat{\mathbf{p}} \cdot \int_{L^3} d\mathbf{r} |\mathbf{r}\rangle \langle \mathbf{r}| (\mathbf{u}(\mathbf{r}) \hat{a} + h.c.) \sum_{\mathbf{k}'_e} |\mathbf{k}'_e\rangle \langle \mathbf{k}'_e| + h.c. \\ &= \sqrt{\frac{\hbar}{2\epsilon_0\omega V}} \frac{e\hbar k_e^0}{m} \left(\hat{a} \sum_{\mathbf{k}_e} \int_{\Delta\mathbf{k}_e} \frac{\int_{L^3} d\mathbf{r} e^{-i\Delta\mathbf{k}_e \cdot \mathbf{r}} \frac{\mathbf{k}_e - \Delta\mathbf{k}_e/2}{k_e^0} \cdot \mathbf{u}(\mathbf{r})}{(2\pi)^3} |\mathbf{k}_e\rangle \langle \mathbf{k}_e - \Delta\mathbf{k}_e| + h.c. \right)\end{aligned}\quad (4.33)$$

with the scattering matrix

$$\begin{aligned}\hat{S} &= \exp \left(-i \sqrt{\frac{\hbar}{2\epsilon_0\omega V}} \frac{ek_e^0}{m} \hat{a} \sum_{\mathbf{k}_e} \int_{\Delta\mathbf{k}_e} \frac{\int_{L^3} d\mathbf{r} e^{-i\Delta\mathbf{k}_e \cdot \mathbf{r}} \frac{\mathbf{k}_e - \Delta\mathbf{k}_e/2}{k_e^0} \cdot \mathbf{u}(\mathbf{r})}{(2\pi)^3} |\mathbf{k}_e\rangle \langle \mathbf{k}_e - \Delta\mathbf{k}_e| \right. \\ &\quad \left. \times \int_{\tau} e^{i([E(\mathbf{k}_e) - E(\mathbf{k}_e - \Delta\mathbf{k}_e)]/\hbar - \omega)t} dt - h.c. \right) \\ &= \exp \left(-i \sqrt{\frac{\hbar}{2\epsilon_0\omega V}} \frac{ek_e^0}{m} \hat{a} \sum_{\mathbf{k}_e} \int_{\Delta\mathbf{k}_e} \int_{L^3} d\mathbf{r} e^{-i\Delta\mathbf{k}_e \cdot \mathbf{r}} \frac{\mathbf{k}_e - \Delta\mathbf{k}_e/2}{(2\pi)^2 k_e^0} \cdot \mathbf{u}(\mathbf{r}) |\mathbf{k}_e\rangle \langle \mathbf{k}_e - \Delta\mathbf{k}_e| \right. \\ &\quad \left. \times \delta \left[\frac{E(\mathbf{k}_e) - E(\mathbf{k}_e - \Delta\mathbf{k}_e)}{\hbar} - \omega \right] - h.c. \right) \\ &\approx \exp \left(-i \sqrt{\frac{\hbar}{2\epsilon_0\omega V}} \frac{ek_e^0}{m} \hat{a} \sum_{\mathbf{k}_e} \int_{\Delta\mathbf{k}_e} \int_{L^3} d\mathbf{r} e^{-i\Delta\mathbf{k}_e \cdot \mathbf{r}} \frac{\mathbf{k}_e - \Delta\mathbf{k}_e/2}{(2\pi)^2 k_e^0} \cdot \mathbf{u}(\mathbf{r}) |\mathbf{k}_e\rangle \langle \mathbf{k}_e - \Delta\mathbf{k}_e| \right. \\ &\quad \left. \times \frac{\delta \left[\Delta_{\parallel} - \frac{\omega}{|\nabla_{\mathbf{p}} E|} \right]}{|\nabla_{\mathbf{p}} E|} - h.c. \right)\end{aligned}\quad (4.34)$$

$$\begin{aligned}&\approx \exp \left(-i \sqrt{\frac{e^2}{2\epsilon_0\hbar\omega V}} \hat{a} \sum_{\mathbf{k}_e} \int_{\Delta_{\perp}} |\mathbf{k}_{\perp}\rangle \langle \mathbf{k}_{\perp} - \Delta_{\perp}| \int_{L^2} d\mathbf{r}_{\perp} (2\pi)^{-2} e^{-i\Delta_{\perp} \cdot \mathbf{r}_{\perp}} \int_L dr_{\parallel} e^{-i\Delta_{\parallel} r_{\parallel}} \right. \\ &\quad \left. \left[\frac{k_{\parallel} - \Delta_{\parallel}/2}{k_e^0} u_{\parallel}(\mathbf{r}) + \frac{\mathbf{k}_{\perp} - \Delta_{\perp}/2}{k_e^0} \cdot \mathbf{u}_{\perp}(\mathbf{r}) \right] |k_{\parallel}\rangle \langle k_{\parallel} - \Delta_{\parallel}| - h.c. \right)\end{aligned}\quad (4.35)$$

where Eq. 4.34 used the limit $\Delta\mathbf{k}_e \ll \mathbf{k}_e$, Eq. 4.35 used the approximation $|\nabla_{\mathbf{p}} E| = v_e$ and the relation $\Delta_{\parallel} = \omega/v_e$. In the limit that the transverse momentum components are much smaller than the longitudinal momentum, i.e., $|\mathbf{k}_{\perp}| \ll k_{\parallel}$, we can ignore the contribution of $\mathbf{k}_{\perp} \cdot \mathbf{u}_{\perp}$. Using the following identity relation

$$\sum_{\mathbf{k}_{\perp}} \int_{\Delta_{\perp}} |\mathbf{k}_{\perp}\rangle \langle \mathbf{k}_{\perp} - \Delta_{\perp}| \int_{L^2} d\mathbf{r}_{\perp} (2\pi)^{-2} e^{-i\Delta_{\perp} \cdot \mathbf{r}_{\perp}} = \int_{L^2} d\mathbf{r}_{\perp} |\mathbf{r}_{\perp}\rangle \langle \mathbf{r}_{\perp}| \quad (4.36)$$

Chapter 4. Quantum optical interaction between free electrons and photons

we arrive at the generalized 3D scattering matrix

$$\begin{aligned}\hat{S} &= \exp \left(-i \sqrt{\frac{e^2}{2\epsilon_0 \hbar \omega V}} \hat{a} \sum_{k_{\parallel}} \int_{L^2} d\mathbf{r}_{\perp} |\mathbf{r}_{\perp}\rangle \langle \mathbf{r}_{\perp}| \right. \\ &\quad \left. \int_L dr_{\parallel} e^{-i\Delta_{\parallel} r_{\parallel}} \left[\frac{k_{\parallel} - \Delta_{\parallel}/2}{k_e^0} u_{\parallel}(\mathbf{r}) \right] |k_{\parallel}\rangle \langle k_{\parallel} - \Delta_{\parallel}| - h.c. \right) \\ &= \exp \left(\int d\mathbf{r}_{\perp} |\mathbf{r}_{\perp}\rangle \langle \mathbf{r}_{\perp}| g_{\omega}(\mathbf{r}_{\perp}) a^{\dagger} b - h.c. \right)\end{aligned}\quad (4.37)$$

where

$$g_{\omega}(\mathbf{r}_{\perp}) = -i \sqrt{\frac{e^2}{2\epsilon_0 \hbar \omega V}} \int_L dr_{\parallel} e^{i\Delta_{\parallel} r_{\parallel}} u_{\parallel}^*(r_{\parallel}, \mathbf{r}_{\perp}) \quad (4.38)$$

$$b = \sum_{k_{\parallel}} \frac{k_{\parallel} - \Delta_{\parallel}/2}{k_e^0} |k_{\parallel}\rangle \langle k_{\parallel} + \Delta_{\parallel}|. \quad (4.39)$$

We observe that now the transverse position state $|\mathbf{r}_{\perp}\rangle$ picks up a position-dependent coupling strength $g_{\omega}(\mathbf{r}_{\perp})$. This point is of particular importance to Section 4.3.1 and Section 7.3.

Two-photon scattering

The term $\hat{H}_2 = \frac{e^2 \hat{\mathbf{A}}^2}{2m}$ that we have yet undiscussed corresponds to the ponderomotive potential and is associated with two-photon scattering due to the quadratic order of $\hat{\mathbf{A}}$. Usually, this term naturally involves interaction with at least two optical modes. For the sake of investigating the physical consequence of this term, here we again restrict ourselves to the single-mode interaction limit. We assume the optical mode is propagating also along the \mathbf{z} direction. We find that \hat{H}_2 results in a (cavity) optical frequency shift, as well as a two-photon generation

4.2 Single-mode electron-photon interaction

process, as

$$\begin{aligned}
\hat{H}_2 &= \frac{e^2 \hat{\mathbf{A}}^2}{2m} \\
&= \hbar \frac{e^2}{4\epsilon_0 \omega m V} \int |z\rangle \langle z| dz (\mathbf{u}(z) \hat{a} + \mathbf{u}^*(z) \hat{a}^\dagger) \cdot (\mathbf{u}(z) \hat{a} + \mathbf{u}^*(z) \hat{a}^\dagger) \\
&= \hbar \frac{e^2}{4\epsilon_0 \omega m V} \sum_{k_e} |k_e\rangle \langle k_e| \int |z\rangle \langle z| dz \sum_{k'_e} |k'_e\rangle \langle k'_e| (\mathbf{u}(z) \hat{a} + \mathbf{u}^*(z) \hat{a}^\dagger)^2 \\
&= \hbar \frac{e^2}{4\epsilon_0 \omega m V} \sum_{k_e, \Delta k_e} |k_e\rangle \langle k_e - \Delta k_e| \frac{1}{L} \int dz e^{-i\Delta k_e \cdot z} (\mathbf{u}(z) \hat{a} + \mathbf{u}^*(z) \hat{a}^\dagger)^2 \\
&= \hbar \frac{e^2}{4\epsilon_0 \omega m V} \sum_{k_e} \int_{\Delta k_e} d\Delta k_e \left(\frac{\Theta_1(\Delta k_e)}{2\pi} \bar{u}^2 \hat{a}^2 |k_e\rangle \langle k_e - \Delta k_e| + h.c. \right) \\
&\quad + \hbar \frac{e^2}{4\epsilon_0 \omega m V} \sum_{k_e} \int_{\Delta k_e} d\Delta k_e \left(\frac{\Theta_2(\Delta k_e)}{2\pi} |\bar{u}|^2 \hat{a} \hat{a}^\dagger |k_e\rangle \langle k_e - \Delta k_e| + h.c. \right) \\
&= \hbar (g_1 \hat{a}^2 \sum_{k_e} \int_{\Delta k_e} d\Delta k_e \frac{\Theta_1(\Delta k_e)}{2\pi} |k_e\rangle \langle k_e - \Delta k_e| + h.c.) \\
&\quad + \hbar (g_2 \hat{a} \hat{a}^\dagger \sum_{k_e} \int_{\Delta k_e} d\Delta k_e \frac{\Theta_2(\Delta k_e)}{2\pi} |k_e\rangle \langle k_e - \Delta k_e| + h.c.), \tag{4.40}
\end{aligned}$$

where the phase-matching functions are

$$\Theta_1(\Delta k_e) = \int_{L_c} dz e^{-i\Delta k_e \cdot z} \mathbf{u}(z) \cdot \mathbf{u}(z) / \bar{u}^2 \tag{4.41}$$

$$\Theta_2(\Delta k_e) = \int_{L_c} dz e^{-i\Delta k_e \cdot z} |\mathbf{u}(z)|^2 / |\bar{u}|^2 \tag{4.42}$$

with the coupling rates $g_1 = \frac{e^2 \bar{u}^2}{4\epsilon_0 \omega m V}$ and $g_2 = \frac{e^2 |\bar{u}|^2}{4\epsilon_0 \omega m V}$.

Note that for interaction with a dielectric cavity, the magnitude of $\frac{H_2}{H_1} \sim \frac{e|\bar{u}|}{\omega} \sqrt{\frac{1}{\epsilon_0 m V}} \sim 10^{-6}$ even for a cavity with mode volume of $\sim 10^{-16} \text{ m}^3$. In our case of interaction with a ring resonator, we believe these two-photon processes can be neglected. This process usually only happens in free-space coupling with two different photons, i.e., the Compton scattering we are all familiar with. Nevertheless, we would like to understand what the effects are if the interaction is in free space.

To simplify the discussion, we examine the limit of very long interaction length where the phase-matching conditions are $\Theta_2(\Delta k_e)/2\pi \rightarrow \delta(\Delta k_e)$. In this limit, we obtain a cavity frequency shift of $\delta\omega = g_2$.

The term associated with g_1 is effectively a two-photon exchange Kapitza-Dirac effect [122] with a phase matching condition Θ_1 . In the following, we proceed to calculate the scattering

matrix for this specific term,

$$\begin{aligned} \hat{H}_{\text{int}} &= \hbar g_1 \sum_{k_e} \int_{\Delta k_e} d\Delta k_e \Theta_1(\Delta k_e) \hat{a}^2 |k_e\rangle \langle k_e - \Delta k_e| \\ &\times e^{-2i\omega t} e^{i[E(k_e) - E(k_e - \Delta k_e)]t/\hbar} + \text{h.c.} \end{aligned} \quad (4.43)$$

$$\begin{aligned} \hat{S} &= T \exp\left(-\frac{i}{\hbar} \int_{\tau} \hat{H}_{\text{int}} dt\right) \\ &= \exp\left(-i g_1 \sum_{k_e} \int_{\Delta k_e} d\Delta k_e \Theta_1(\Delta k_e) \hat{a}^2 |k_e\rangle \langle k_e - \Delta k_e| \right. \\ &\quad \left. \times \delta\left[\frac{E(k_e) - E(k_e - \Delta k_e)}{\hbar} - 2\omega\right] - \text{h.c.}\right) \\ &= \exp\left(-i g_1 \sum_E \frac{\Theta_1(\Delta)}{\partial_{p_e} E} |E\rangle \langle E - 2\hbar\omega| \hat{a}^2 - \text{h.c.}\right) \\ &\approx \exp\left(-i g_1 \frac{\Theta_1(\Delta)}{v_e} \sum_E |E\rangle \langle E - 2\hbar\omega| \hat{a}^2 - \text{h.c.}\right) \\ &= \exp\left(-i g_1 \tau_{\text{int}} \hat{a}^2 \hat{b}^{\dagger 2} - \text{h.c.}\right), \end{aligned} \quad (4.44)$$

which is essentially a two-photon generation process. This process is not the same as optical squeezing, as the optical number states are entangled with the electron energy. The generation of squeezed light is only possible if the initial electron state energy uncertainty $\Delta E \gg \hbar\omega$, such that the optical states are effectively disentangled from the electron energy state space. Generally, to disentangle the electron state space from that of the photon, we need to invoke the eigenstates of the ladder operator that we discuss below.

4.2.3 Electron ladder operator eigenstate

Suppose we like to effectively disentangle the electron state space from the interaction and use it as a classical point particle. In that case, we need to find the eigenstate $|\beta_e\rangle_e$ for the electron ladder operator \hat{b} with the eigenvalue of β_e . Calling it an electron coherent state, we can simplify the scattering matrix by

$$\hat{S} = \exp\left(g_\omega \beta_e \hat{a}^\dagger - g_\omega^* \beta_e^* \hat{a}\right) = \hat{D}(-g_\omega^* \beta_e^*), \quad (4.45)$$

where $\hat{D}(\alpha)$ is the optical displacement operator. This operation is essential when generating phase-coherent light from this interaction; see Section 8.2. If the electron is, e.g., in an energy eigenstate instead, the interaction will only lead to incoherent photon emission, as the photon number is entangled with the electron energy.

We find that the electron eigenstate is structured in the momentum space as, e.g., illustrated in Fig. 4.2, a comb-like density function, where $\beta_e = \sqrt{n_e} e^{i\phi}$ is a complex number containing an amplitude $\sqrt{n_e}$ and a phase ϕ , just like an optical coherent state in the number basis.

4.2 Single-mode electron-photon interaction

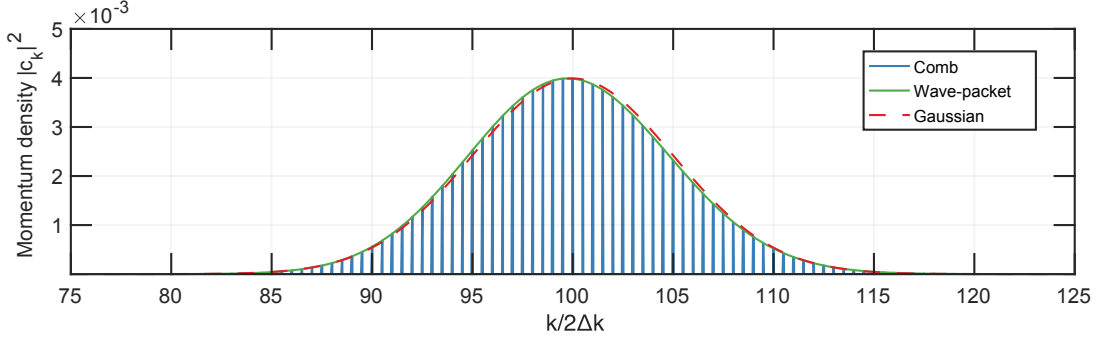


Figure 4.2: Electron momentum density for eigenstates $|\beta\rangle_e$ of the ladder operator \hat{b} , centered around a center momentum $k_e^0 = 200\Delta k$, either in a comb-like shape or a continuum wave-packet. We can see that the distribution almost perfectly overlaps with the Gaussian approximation. The comb-like coherent state here is not normalized to be easier compared to the continuum case.

In the following, we derive the expression of the electron coherent state. We start with an arbitrary state composition $|\psi_e\rangle = \sqrt{\frac{L}{2\pi}} \int c_k |k\rangle dk$, by applying the ladder operator \hat{b} that contains the weak momentum nonlinearity (Eq. 4.26), and mediates interaction with neighboring momentum states spaced by momentum difference $\Delta k = \Delta$,

$$\begin{aligned}
 b|\psi_e\rangle &= \beta|\psi_e\rangle \\
 &= \frac{1}{k_e^0} \int \frac{L}{2\pi} dk_e k_e |k_e\rangle \langle k_e + \Delta k | \sqrt{\frac{L}{2\pi}} \int c_k |k\rangle dk \\
 &= \frac{1}{k_e^0} \sqrt{\frac{L}{2\pi}} \iint c_k dk dk_e k_e |k_e\rangle \delta(k - k_e - \Delta k) \\
 &= \frac{1}{k_e^0} \sqrt{\frac{L}{2\pi}} \int c_k(k - \Delta k) |k - \Delta k\rangle dk = \sqrt{\frac{L}{2\pi}} \int \beta c_k |k\rangle dk, \tag{4.46}
 \end{aligned}$$

One can easily conclude the relation $c_{k+\Delta k}/c_k = \beta k_e^0/k$ for state $|\psi_e\rangle$ to be an eigenstate of b . One can further simplify this relation using the Stirling approximation to

$$\begin{aligned}
 c_{k+\Delta k}/c_{k-\Delta k} &= \frac{\left(\beta \frac{k_e^0}{\Delta k}\right)^{\frac{k}{\Delta k}}}{\frac{k}{\Delta k} \frac{k-\Delta k}{\Delta k} \dots 1} \\
 &\stackrel{\text{Stirling}}{\sim} \sqrt{\frac{\Delta k}{2\pi k}} \left(e\beta \frac{k_e^0}{k}\right)^{\frac{k}{\Delta k}}. \tag{4.47}
 \end{aligned}$$

We can therefore simply assume $c_k = \tilde{c}_k \sqrt{\frac{\Delta k}{2\pi k}} \left(e\beta \frac{k_e^0}{k}\right)^{\frac{k}{\Delta k}}$, where \tilde{c}_k is a periodic function with period Δk .

To derive the expressions for some specific states, we set $|\beta| = 1$ for simplicity so that the

Chapter 4. Quantum optical interaction between free electrons and photons

distribution centers around k_e^0 . We can first assume a uniform distribution $\bar{c}_k = c$, therefore

$$1 = \int dk |c|^2 \frac{\Delta k}{2\pi k} \left(\frac{k}{ek_e^0} \right)^{-\frac{2k}{\Delta k}}. \quad (4.48)$$

This integral does not give a trivial distribution, and the normalization factor $|c|$ could be solved numerically. However, when $k \gg \Delta k$, we can safely approximate this distribution with a normal distribution

$$\begin{aligned} |c_k|^2 &= \text{PDF}_N(k, \mu = k_e^0, 2\sigma^2 = k_e^0 \Delta k) \\ &= \frac{1}{\sqrt{\pi k_e^0 \Delta k}} \exp\left(-\frac{(k - k_e^0)^2}{k_e^0 \Delta k}\right) \end{aligned} \quad (4.49)$$

$$c_k = \frac{1}{(\pi k_e^0 \Delta k)^{1/4}} \exp\left(-\frac{(k - k_e^0)^2}{2k_e^0 \Delta k}\right) e^{i \arg[\beta] \frac{k}{\Delta k}} \quad (4.50)$$

$$\begin{aligned} c_z &= \int \frac{1}{\sqrt{2\pi}} c_k e^{ikz} dk \\ &= \left(\frac{k_e^0 \Delta k}{\pi} \right)^{1/4} \exp\left(-\frac{k_e^0 \Delta k}{2} \left(z - \frac{\arg[\beta]}{\Delta k}\right)^2\right) e^{ik_e^0 \left(z - \frac{\arg[\beta]}{\Delta k}\right)} \end{aligned} \quad (4.51)$$

$$\begin{aligned} |c_z|^2 &= \sqrt{\frac{k_e^0 \Delta k}{\pi}} \exp\left(-k_e^0 \Delta k \left(z - \frac{\arg[\beta]}{\Delta k}\right)^2\right) \\ &= \text{PDF}_N\left(z, \mu = \frac{\arg[\beta]}{\Delta k}, 2\sigma^2 = \frac{1}{k_e^0 \Delta k}\right) \end{aligned} \quad (4.52)$$

which resembles the continuous limit of a Poissonian distribution. Fig. 4.2 features two special examples, the *comb-like* and *the wave-packet-like* coherent states when the momentum distribution is centered around k_e^0 . The statistical properties of these states are very similar to an optical coherent state with a large displacement from the origin.

The time evolution of the electron coherent state $|\beta(t)\rangle$ is also not hard to analyze. We could start first from the Heisenberg picture, as $b(t)|\beta\rangle = e^{-i\omega t} b(0)|\beta\rangle = \beta e^{-i\omega t} |\beta\rangle$. As the eigenvalue is the same both in the Schrodinger picture and the Heisenberg picture, such that $b|\beta(t)\rangle = \beta e^{-i\omega t} |\beta(t)\rangle$. Therefore, the electron coherent state evolves just like an optical coherent state, as $|\beta(t)\rangle = |\beta e^{-i\omega t}\rangle$. From here, we can simply plug $\arg[\beta] = \omega t$ and $|\beta| = 1$ into Eq. 4.51 to obtain a simplified expression

$$\psi_e(z) = \left(\frac{k_e^0 \Delta k}{\pi} \right)^{1/4} \exp\left(-\frac{k_e^0 \Delta k}{2} (z - v_e t)^2\right) e^{ik_e^0 (z - v_e t)}, \quad (4.53)$$

which is simply an electron pulse propagating in the \mathbf{z} direction with a Gaussian density profile of $\sigma = \frac{1}{\sqrt{2k_e^0 \Delta k}}$.

In the following, we illustrate what benefits the electron ladder eigenstate $|\beta_e\rangle$ could bring to our toolbox. If we have a pure momentum state $|k_e^0\rangle$ of the electron, which is typically

4.2 Single-mode electron-photon interaction

accessible in a TEM, and initially the cavity is in its vacuum state $|0\rangle$, the interaction will lead to the energy-number entangled state (electron-photon pair state)

$$|\psi_e, \psi_{\text{ph}}\rangle = \sum_n e^{-|g_\omega|^2/2} \frac{(-g_\omega^* \beta_e^*)^n}{\sqrt{n!}} |k_e^0 - n\Delta k, n\rangle. \quad (4.54)$$

If we trace over the electron state space, we will get the optical state as a mixed state following a Poisson distribution

$$\rho_{\text{ph}} = \sum_n e^{-|g_\omega|^2} \frac{|g_\omega|^2^n}{n!} |n\rangle\langle n|. \quad (4.55)$$

However, with the electron ladder eigenstate $|\beta_e\rangle$, we would instead have

$$|\psi_e, \psi_{\text{ph}}\rangle = |\beta_e\rangle_e \sum_n e^{-|g_\omega|^2/2} \frac{(-g_\omega^* \beta_e^*)^n}{\sqrt{n!}} |n\rangle_{\text{ph}}, \quad (4.56)$$

where an optical coherent state is generated, and the electron state is completely decoupled. Physically, what we have here is an analogy to a classical particle generating a classical optical field, as the electron now has a much smaller spatial extend $(k_e^0 \Delta k)^{-1}$ compared to the optical wavelength, and the coherent state is the closet quantum state to a classical optical wave. There are still two subtle differences: The electron is not a point particle, and the light is not a classical wave. The electron has a well-defined envelope determined by the momentum nonlinearity, whereas the coherent state still has phase and amplitude uncertainty.

The comparison between these two initial electron states is shown in Fig. 4.3 using a low-dimension Qutip simulation. We could see that the generated optical mixed state follows a Poissonian distribution for an initial pure momentum state. However, the process is not quantum coherent as the Wigner function shows that the phase information is lost. However, if the electron is initially structured in a ladder eigenstate state, the generated optical state preserves the phase relation, which is indeed an optical coherent state.

The simulation here is somewhat of an exaggeration as single-mode coupling strength $|g_\omega|^2$ can hardly approach unity. A reasonable photon generation probability when a single electron passes through the evanescent field of a 10-GHz Si_3N_4 microring with an impact distance of 50 nm is shown in Fig. 4.4. Even though the excitation probability for each optical mode is small, the electron-photon phase-matching bandwidth $\Delta\omega$ usually covers at least tens of modes. We can define a spatial-temporal mode (Section 4.3.3) that covers all these frequency components, of which the photon emission probability can approach unity.

Now, one might ask, how exactly can we generate such a ladder eigenstate in the first place? Generally, the initial electron emitted from the emission tip can, in principle, exhibit sub-optical-cycle spatial extend if it is driven by an intense ultrashort optical pulse. However, $(k_e^0 \Delta k)^{-1}$ is typically a hundredth of the optical wavelength, and a more delicate scheme is required to generate such an ultrashort electron pulse. The usual interaction between an electron and a classical optical field (PINEM) can achieve a very broad comb-like structure. However, the energy distribution follows the Bessel functions instead of Gaussian. Also, as

Chapter 4. Quantum optical interaction between free electrons and photons

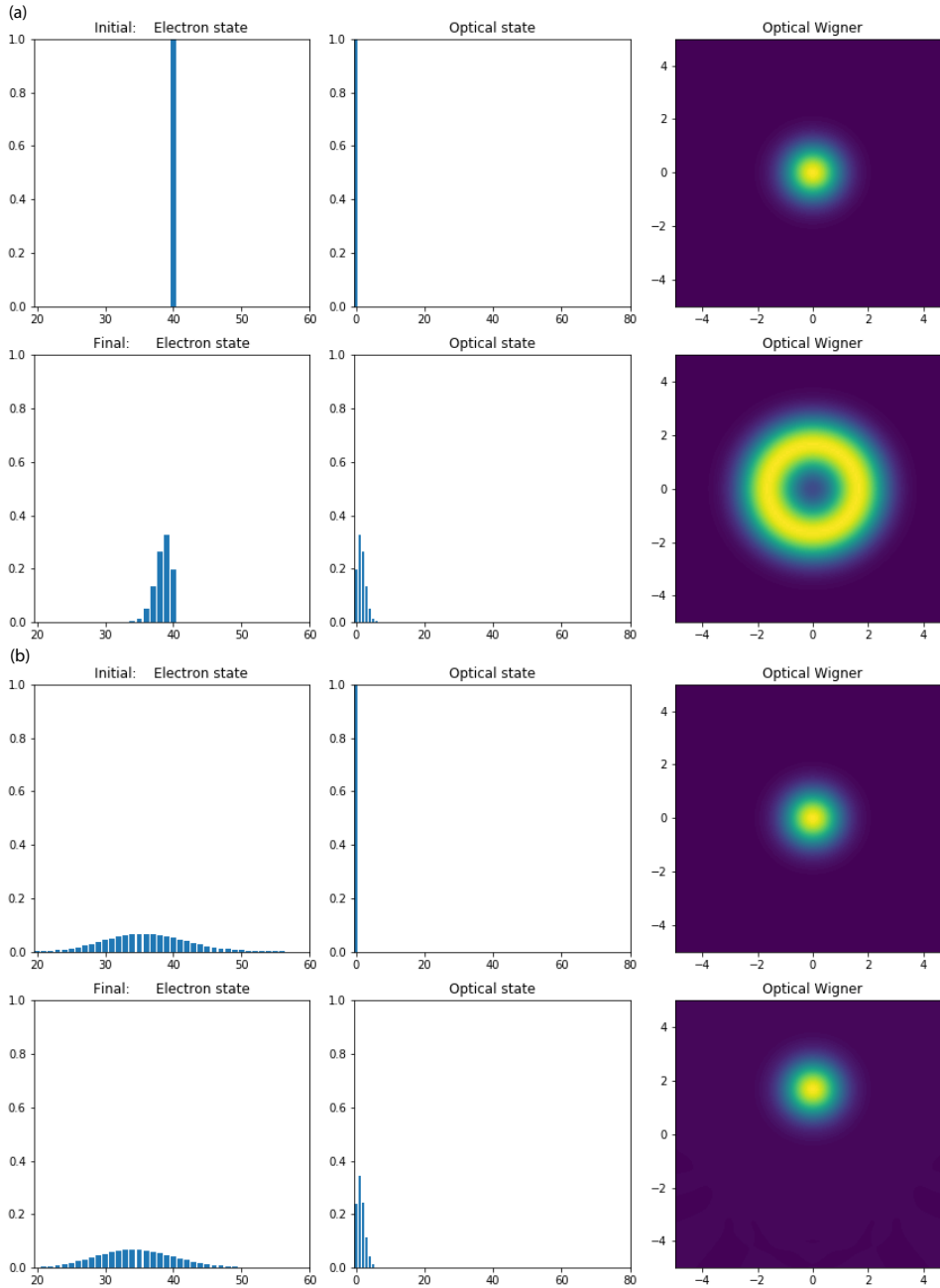


Figure 4.3: Simulation of an electron interacting with a vacuum optical cavity, with the electron being initially in **(a)** a plane-wave momentum state, and **(b)** a ladder eigenstate state. Here, we set $k_e^0 \sim 40\Delta k$ to reduce the computational space. In reality, $k_e^0 \sim 10^5\Delta k$. The x-axis is either in the electron's Δk unit or the cavity field's photon number. We could see that in both cases, the photon number follows a Poisson distribution. However, with the momentum state electron, the light generated is in a mixed state and thus is not phase-coherent. For the ladder eigenstate state electron, the generated light is in a coherent state.

4.3 Electron-photon interaction in the continuum

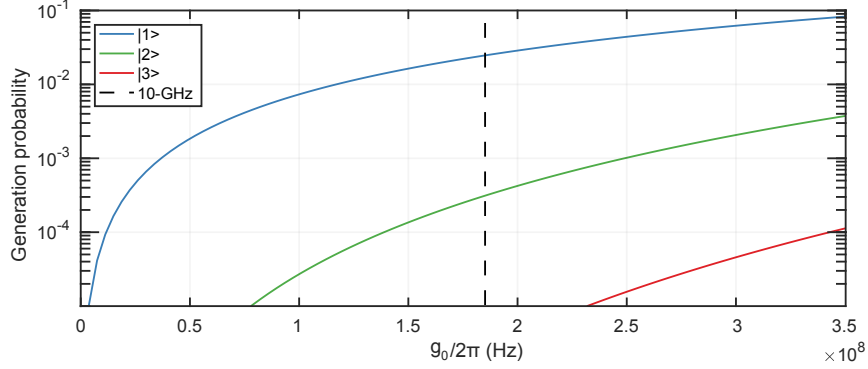


Figure 4.4: Photon generation probability for a single optical mode when each electron passes through the evanescent field of a 10-GHz Si_3N_4 ring resonator, with the impact distance of 50 nm marked in black dashed line.

PINEM effectively only modulates the phase of the electron wavefunction, we do not expect a change in the electron envelope. However, the electron wavefunction can be effectively compressed with dispersive propagation using the electron energy-momentum dispersion. A more detailed discussion of this effect is discussed in Section 8.1. It has been shown in numerical simulation [103] that the combination of multiple modulation and propagation stages can create a decent Gaussian-shaped electron wavefunction that approaches nicely the electron ladder eigenstate by $|\langle b \rangle| = 0.998$.

Note that all the results derived in this section are only valid for interaction between an electron and a single optical mode, which is hardly the case for a realistic physical setting where the interaction time is shorter than an optical round-trip time of the cavity. We formulated the case where an electron interacts with multiple cavity modes of a ring resonator in Section 7.1. In the following section, we derive the multi-mode interaction in a more general case of the optical continuum, considering both the guided and non-guided modes, and draw the connection to the modal-decomposition method discussed in this section.

4.3 Electron-photon interaction in the continuum

In the previous sections, we have treated the particular case where the electron interacts with a single cavity mode that has a well-defined mode function $u(z)$. The interaction is governed by the coupling strength $g_\omega \propto \int dz e^{i\Delta k \cdot z} u^*(z)$, where $\Delta k \approx \omega/v_e$ is the electron wave vector change when it absorbs or emits a photon. This phase-matching condition, in combination with material dispersion, results in a coupling bandwidth $\Delta\omega \sim \Delta v_{\text{FSR}}/|n_g - n_{\text{eff}}|$ of the optical cavity, and typically covers 5-20 azimuthal modes. The electron also couples to numerous higher-order mode families of the cavity. On a different note, the electron could also interact with the non-guided modes traveling in free space or bulk materials, not captured well by the modal decomposition method. In this section, we quantize the electromagnetic fields in

Chapter 4. Quantum optical interaction between free electrons and photons

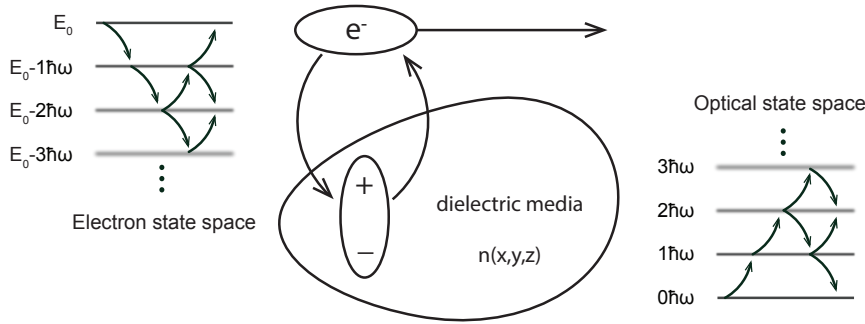


Figure 4.5: Illustration of electron-photon inelastic scattering process mediated by a dielectric media. When an electron flies by a nearby dielectric structure with refractive index distribution $n(x, y)$, the polarized dipoles exert a backaction field (force) on the electron, resulting in electron energy loss and optical field emission at the dielectric material. Here, ω is not the frequency of a cavity mode but one frequency component of the optical continuum. As a result of the coupling bandwidth, the uncertainty of the energy ladder increases as more transitions are made.

the three-dimensional space and derive the optical mode that the electron couples to in the optical continuum.

4.3.1 3D quantization of the electromagnetic field in dispersive dielectric media

The interaction between free electrons and optical modes at a dielectric surface can be understood in a microscopic picture as follows: When an electron passes near the surface of a dielectric structure, the electric field of the flying electron polarizes the dipoles in the structure (see Fig.4.5). As a result, these dipoles generate oscillating electromagnetic fields that cause backaction Coulomb forces on the electron, changing the electron energy. In the conventional quantum optical modal decomposition picture commonly used in the cavity quantum electrodynamics (QED) community, this can be interpreted as the interaction between the free electrons and the optical vacuum fields of the modes supported by the dielectric structure [123].

Here, we no longer restrict ourselves to one spatial dimension and keep everything in the general vector format. We consider an electron beam with a narrow momentum spread around wavevector \mathbf{k}_0 and assume that the photon energies involved in the interaction are much smaller than the electron relativistic energy $E_0 = c\sqrt{c^2 m^2 + \hbar^2 k_0^2}$ (i.e. the no-recoil regime), such that we can linearly expand the electron Hamiltonian in term of electron momentum

4.3 Electron-photon interaction in the continuum

states. In the velocity gauge, the Hamiltonian is described as [124, 125]

$$\hat{H} = \hat{H}_{\text{el}} + \hat{H}_{\text{ph}} + \hat{H}_{\text{int}} \quad (4.57)$$

$$\hat{H}_{\text{el}} = \sum_{\mathbf{k}} [E_0 + \hbar \mathbf{v} \cdot (\mathbf{k} - \mathbf{k}_0)] \hat{c}_{\mathbf{k}}^\dagger \hat{c}_{\mathbf{k}} \quad (4.58)$$

$$\hat{H}_{\text{ph}} = \int d\omega \int d^3 \mathbf{r} \hbar \omega \hat{\mathbf{f}}^\dagger(\mathbf{r}, \omega) \cdot \hat{\mathbf{f}}(\mathbf{r}, \omega) \quad (4.59)$$

$$\hat{H}_{\text{int}} = - \int d^3 \mathbf{r} \hat{\mathbf{j}}(\mathbf{r}) \cdot \hat{\mathbf{A}}(\mathbf{r}) \quad (4.60)$$

where we defined the electron current operator $\hat{\mathbf{j}}(\mathbf{r}) = (-e\mathbf{v}/V) \sum_{\mathbf{k}, \mathbf{q}} e^{i\mathbf{q} \cdot \mathbf{r}} \hat{c}_{\mathbf{k}}^\dagger \hat{c}_{\mathbf{k}+\mathbf{q}}$ using the Fermionic ladder operators $\hat{c}_{\mathbf{k}}$ and the relativistic electron group velocity $\mathbf{v} = \hbar c^2 \mathbf{k}_0 / E_0$, and a linear electron energy dispersion is assumed. The vector potential $\hat{\mathbf{A}}(\mathbf{r}, t) = \int \frac{d\omega}{2\pi} \hat{\mathbf{A}}(\mathbf{r}, \omega) e^{i\omega t} + h.c.$ is associated with the noise current operator $\hat{\mathbf{j}}^{\text{noise}}(\mathbf{r}, \omega)$ through the quantized three-dimensional Maxwell equation [114] and has a formal solution

$$\hat{\mathbf{A}}(\mathbf{r}, \omega) = -4\pi \int d^3 \mathbf{r}' G(\mathbf{r}, \mathbf{r}', \omega) \cdot \hat{\mathbf{j}}^{\text{noise}}(\mathbf{r}', \omega) \quad (4.61)$$

where $G(\mathbf{r}, \mathbf{r}', \omega)$ is the dyadic Green function (Green tensor) of the classical problem satisfying the equation

$$\nabla \times \nabla \times G(\mathbf{r}, \mathbf{r}', \omega) - \frac{\omega^2}{c^2} \epsilon(\mathbf{r}, \omega) G(\mathbf{r}, \mathbf{r}', \omega) = -\mu_0 \delta(\mathbf{r} - \mathbf{r}') \quad (4.62)$$

which describes the field response at \mathbf{r} to a point current excitation at \mathbf{r}' . Since we are dealing with non-magnetic materials, we assume a relative permeability $\mu(\mathbf{r}) = 1$. The noise operator is bosonic and was chosen to be

$$\hat{\mathbf{j}}^{\text{noise}}(\mathbf{r}, \omega) = \omega \sqrt{\hbar \epsilon_0 \text{Im}\{\epsilon(\mathbf{r}, \omega)\}} \hat{\mathbf{f}}(\mathbf{r}, \omega) \quad (4.63)$$

in order to satisfy the fluctuation-dissipation theorem due to material dissipation, with the bosonic ladder operators $\hat{\mathbf{f}}(\mathbf{r}, \omega)$ satisfying commutation relation $[\hat{f}_i(\mathbf{r}, \omega), \hat{f}_i'(\mathbf{r}', \omega')] = \delta_{i,i'} \delta(\mathbf{r} - \mathbf{r}') \delta(\omega - \omega')$. Note that in the limiting case of a dispersive material (assumed in our analysis, characterized by its instantaneous electronic response), $\text{Im}\{\epsilon(\mathbf{r}, \omega)\} \rightarrow 0$. However, this imposes no problem for our formalism here, which is shown to correctly reduce to the mode decomposition method used in the quantized vacuum field [126] due to Kramers-Kronig relations.

When projecting to the direction of the electron trajectory $\hat{\mathbf{z}}$ with transverse coordinate \mathbf{R}_0 , the

Chapter 4. Quantum optical interaction between free electrons and photons

scattering matrix is shown to be

$$\hat{S} = e^{i\hat{\chi}}\hat{U} \quad (4.64)$$

$$\hat{U} = \exp \left\{ \left[\frac{-ie}{2\pi\hbar V^{2/3}} \sum_{\mathbf{k}, \mathbf{q}_\perp} \int d\omega \int d^3\mathbf{r} e^{i\mathbf{q}_\perp \cdot \mathbf{R}} e^{-i\omega z/v_e} \hat{A}_z(\mathbf{r}, \omega) \hat{c}_{\mathbf{k}}^\dagger \hat{c}_{\mathbf{k}+\mathbf{q}_\perp - (\omega/v)\hat{z}} \right] - h.c. \right\} \quad (4.65)$$

where \mathbf{q}_\perp is the transverse component of the exchanged electron wave vector. The phase operator $\hat{\chi}$ is associated with the Aharonov-Bohm effect of the vector potential [127]. We can further simplify the expression by disregarding the phase operator $\hat{\chi}$ and assuming a point-like electron distribution over the transverse direction to obtain

$$\hat{U} = \exp \left[\int d\omega g_\omega \hat{b}_\omega^\dagger \hat{a}_\omega - h.c. \right] \quad (4.66)$$

where the continuum photon and electron operators are introduced

$$\hat{a}_\omega = -\frac{ie}{2\pi\hbar g_\omega} \int dz e^{-i\omega z/v_e} \hat{A}_z(\mathbf{R}_0, z, \omega) \quad (4.67)$$

$$\hat{b}_\omega = \sum_{k_z} \hat{c}_{k_z}^\dagger \hat{c}_{k_z + \omega/v} \quad (4.68)$$

with vacuum coupling strength g_ω associated with the electron energy loss (EELS) probability $\Gamma(\mathbf{R}_0, \omega)$

$$|g_\omega|^2 = \Gamma(\mathbf{R}_0, \omega) = \frac{4e^2}{\hbar} \iint dz dz' \text{Re} \{ i e^{i\omega(z-z')/v} G_{zz}(\mathbf{R}_0, z; \mathbf{R}_0, z'; \omega) \}. \quad (4.69)$$

The operators are defined in this way so that the quantum optical commutation relations are preserved $[\hat{a}_\omega, \hat{a}_{\omega'}^\dagger] = \delta(\omega - \omega')$, and can be easily proven using the identity

$$\sum_{i''} \int d^3\mathbf{r}'' \text{Im} \{ \epsilon(\mathbf{r}'', \omega) \} G_{i, i''}(\mathbf{r}, \mathbf{r}'', \omega) G_{i'', i'}^*(\mathbf{r}', \mathbf{r}'', \omega) = -\frac{1}{\epsilon_0 \omega^2} \text{Im} \{ G_{i, i'}(\mathbf{r}, \mathbf{r}', \omega) \}. \quad (4.70)$$

Note that \hat{a}_ω contains contributions from all the spatial modes at ω , and is not a specific pre-defined spatial mode $\hat{a}_{\omega, m}$ which is frequently used in cavity QED systems.

To find the spatial mode function of \hat{a}_ω , we use the following relations [128] for an arbitrary set of orthogonal basis $\hat{a}_{i, \omega}$

$$\hat{a}_{i, \omega} = \int d^3\mathbf{r} \mathbf{V}_i(\mathbf{r}, \omega) \cdot \hat{\mathbf{f}}(\mathbf{r}, \omega) \quad (4.71)$$

$$\hat{\mathbf{f}}(\mathbf{r}, \omega) = \sum_i \mathbf{V}_i^\dagger(\mathbf{r}, \omega) \hat{a}_{i, \omega} \quad (4.72)$$

4.3 Electron-photon interaction in the continuum

where the weight functions obey the following normalization condition

$$\int d^3\mathbf{r} \mathbf{V}_i(\mathbf{r}, \omega) \cdot \mathbf{V}_j^\dagger(\mathbf{r}, \omega) = \delta_{i,j}. \quad (4.73)$$

From here, we can re-express the field operator in terms of the set of orthogonal bases as

$$\hat{\mathbf{A}}(\mathbf{r}, \omega) = -4\pi\omega \int d^3\mathbf{r}' \sqrt{\hbar\epsilon_0 \text{Im}\{\epsilon(\mathbf{r}', \omega)\}} G(\mathbf{r}, \mathbf{r}', \omega) \cdot \sum_i \mathbf{V}_i^\dagger(\mathbf{r}', \omega) \hat{a}_{i,\omega}. \quad (4.74)$$

By choosing one of the spatial modes $\hat{a}_{i=0,\omega}$ as our mode of interest \hat{a}_ω with the weight function

$$\mathbf{V}_{\hat{a}_\omega}(\mathbf{r}, \omega) = -\frac{2ie\omega}{g_\omega} \sqrt{\frac{\epsilon_0}{\hbar}} \int dz e^{-i\omega z/v_e} \int d^3\mathbf{r}' \sqrt{\text{Im}\{\epsilon(\mathbf{r}', \omega)\}} \hat{\mathbf{z}} \cdot G(\mathbf{R}_0, z; \mathbf{r}', \omega), \quad (4.75)$$

we can find the mode function of our interested optical mode as

$$\hat{\mathbf{A}}_{\hat{a}_\omega}(\mathbf{r}, \omega) = 2\pi \sqrt{\frac{\hbar}{2\omega\epsilon_0}} \mathbf{U}_{\hat{a}_\omega}(\mathbf{r}, \omega) \hat{a}_\omega \quad (4.76)$$

$$\mathbf{U}_{\hat{a}_\omega}(\mathbf{r}) = \frac{-4e}{g_\omega^*} \sqrt{\frac{2\epsilon_0\omega}{\hbar}} \int dz e^{i\omega z/v_e} \text{Im}[G(\mathbf{r}; \mathbf{R}_0, z; \omega) \cdot \hat{\mathbf{z}}], \quad (4.77)$$

which is a mode specifically defined for this interaction. This mode construction corresponds to a linear transformation of the original structure-supported optical spatial modes, such that only one principal optical mode is involved in the interaction. In contrast, all the other transformed modes are dark and invisible to the electron. In this way, it is advantageous to use this formalism to account for the infinite number of spatial modes of the optical structure the electron couples to. This mode function converges to one of the waveguide modes in the limit of unity coupling ideality (defined in Section 6.2). If the electron transverse spread is significant, the EELS probability is shown [129] to be an average over the transverse electron wavefunction

$$\Gamma(\omega) = \int d^2\mathbf{R} |\psi_\perp(\mathbf{R})|^2 \Gamma(\mathbf{R}, \omega). \quad (4.78)$$

However, this type of averaging is not quantum coherent. The coupling coefficients are different at different transverse positions, evident from Eq. 4.37. Therefore, we have to modify the scattering matrix to

$$\hat{S} = \exp \left[\int d\omega d^2\mathbf{R} g_\omega(\mathbf{R}) \hat{b}_\omega^\dagger |\mathbf{R}\rangle \langle \mathbf{R}| \hat{a}_\omega - h.c. \right]. \quad (4.79)$$

Suppose the part of the longitudinal optical field that overlaps with the electron transverse wavefunction has considerable inhomogeneity. In that case, the different transverse position components of the electron will be entangled with different longitudinal electron-photon pair states, characterized by their different coupling strengths. Therefore, information loss occurs when tracing out the transverse degrees of freedom of the electron, leading to state

purity degradation. Since nm-scale electron beam focuses are routinely used in electron microscopes, this is not a significant limitation for near-field coupling to optical waveguides, which have a typical decay length of ~ 100 nm. In our experiment, we observed the state thermalization effect when the electron transverse distribution is significant. We discuss it in detail in Section 7.3.

4.3.2 Equivalence to the semi-classical result

The electron energy loss at a dielectric surface can be interpreted classically (on the optical side) in a microscopic picture [130], see Fig. 6.1(a): if an electron passes near the surface of a dielectric structure, the dipoles in the structures are polarized (equivalently classical current), induced by the electric field from the flying electron, and generates a backaction field $\mathbf{E}(\mathbf{r}_e(t), t)$ to the electron at $\mathbf{r}_e(t)$ that induces electron energy loss. This effect is similar to the analogy we discussed before (charging a capacitor). The total energy loss can be expressed in the time domain and frequency domain as

$$\Delta E = e \int dt \mathbf{v} \cdot \mathbf{E}(\mathbf{r}_e(t), t) = \int \hbar\omega d\omega \Gamma(\omega) \quad (4.80)$$

where the frequency domain energy loss function $\Gamma(\omega)$ is expressed as

$$\Gamma(\omega) = \frac{e}{\pi\hbar\omega} \int dt \text{Re} \left[e^{-i\omega t} \mathbf{v} \cdot \mathbf{E}(\mathbf{r}_e(t), \omega) \right] \quad (4.81)$$

which can be easily verified if one plugs it back into the energy loss expression and the correct time integral is retrieved. Notice that here $\mathbf{E}(\mathbf{r}_e(t), \omega)$ is not the direct Fourier transform of $\mathbf{E}(\mathbf{r}_e(t), t)$. The Fourier transform applies only on the time dependence of the electric field function, not explicitly depending on the electron trajectory function $\mathbf{r}_e(t)$. The frequency domain components depend explicitly on the current induced from a given electron trajectory but do not consider the field's sampling at different positions $\mathbf{r}_e(t)$ at different time t . This treatment ensures that the total energy loss is consistent but renders the formalism non-local. It is consistent with the quantum formalism when the electron is a wave and can be decomposed into perfect momentum states where the wave-packet length is infinite, as one can see from the fact that even though a classical electron only interacts with the structure locally, our resulting energy loss spectrum will show, e.g., discrete mode structure (a non-local property). It is the result of this particular Fourier expansion procedure, given that the electron is a wave instead of a particle. It has been shown [129] that a full quantum treatment also gives the same EELS result.

Using the no-recoil approximation, which assumes that the radiation of electron into the surrounding substrates does not change the trajectory $\mathbf{r}_e(t)$ of the electron significantly, we can directly calculate the induced electric field $\mathbf{E}(\mathbf{r}_e(t), t)$ from the electron current $\mathbf{j}(\mathbf{r}, t)$

4.3 Electron-photon interaction in the continuum

through the Green tensor of the whole dielectric structure,

$$\mathbf{E}(\mathbf{r}, \omega) = -4\pi i\omega \int d^3\mathbf{r}' G(\mathbf{r}, \mathbf{r}', \omega) \cdot \mathbf{j}(\mathbf{r}', \omega) \quad (4.82)$$

where the Green tensor $G(\mathbf{r}, \mathbf{r}', \omega)$ is the elementary solution of the full Maxwell equation

$$\nabla \times \nabla \times G(\mathbf{r}, \mathbf{r}', \omega) - \frac{\omega^2}{c^2} \epsilon(\mathbf{r}, \omega) G(\mathbf{r}, \mathbf{r}', \omega) = -\mu_0 \delta(\mathbf{r} - \mathbf{r}') \quad (4.83)$$

with a point current at position \mathbf{r}' in frequency domain. A flying electron is equivalent to a broadband evanescent source, and here we consider an electron beam at $\hat{\mathbf{z}}$ direction and a transverse coordinate \mathbf{R}_0 , for which the frequency domain electron current density is

$$\mathbf{j}(\mathbf{r}, \omega) = -e\hat{\mathbf{z}}\delta(\mathbf{R} - \mathbf{R}_0)e^{i\omega(z-z_0)/v}. \quad (4.84)$$

From here, we can express the frequency domain loss rate in terms of the Green function as

$$\Gamma(\omega) = \frac{4e^2}{\hbar} \int dz dz' \text{Re}[ie^{i\frac{\omega(z-z')}{v}} G_{zz}(\mathbf{R}_0, z; \mathbf{R}_0, z'; \omega)], \quad (4.85)$$

which coincides with the result of a full QED treatment. We should keep in mind that the Green tensor here has two contributions, one from vacuum G_0 when there is no structure around, and the other component from the backaction field G_{ind} that is induced from the dielectric dipoles. Only the backaction field G_{ind} contributes to electron energy loss because the electron does not emit light in vacuum; the contribution from the vacuum G_0 vanishes in the integral.

4.3.3 Modal decomposition and spatial-temporal modes

The correspondence between the 3D macroscopic quantization method in a dispersive material with the conventional quantum optics quantization procedure using modal decomposition has been demonstrated for the 1D case [126]. Here, we show the correspondence with the quantum optical formalism we derived in earlier sections. To account for all the spatial modes at a given frequency ω , the quantization of the vector potential was chosen as

$$\hat{\mathbf{A}}(\mathbf{r}, \omega) = -4\pi\omega \int d^3\mathbf{r}' \sqrt{\hbar\epsilon_0 \text{Im}\{\epsilon(\mathbf{r}', \omega)\}} G(\mathbf{r}, \mathbf{r}', \omega) \cdot \hat{\mathbf{f}}(\mathbf{r}', \omega) \quad (4.86)$$

to fulfill the canonical field commutation relations. However, in vacuum or lossless media, the modal decomposition method [35] is often used instead, with

$$\hat{\mathbf{A}}(\mathbf{r}, t) = \sum_m \sqrt{\frac{\hbar}{2\omega_m \epsilon_0}} \mathbf{U}_m(\mathbf{r}) \hat{a}_{\omega_m, m} e^{-i\omega_m t} + h.c. \quad (4.87)$$

Chapter 4. Quantum optical interaction between free electrons and photons

where the profile function $\mathbf{U}_m(\mathbf{r})$ of each mode defined in a frequency window $\Delta\omega_m$ satisfies the wave equation

$$\nabla \times \nabla \times \mathbf{U}_m(\mathbf{r}) - \frac{\omega^2}{c^2} \epsilon(\mathbf{r}, \omega_m) \mathbf{U}_m(\mathbf{r}) = 0 \quad (4.88)$$

with the normalization condition

$$\int d^3\mathbf{r} \epsilon(\mathbf{r}, \omega_m) \mathbf{U}_m(\mathbf{r}) \cdot \mathbf{U}_n^*(\mathbf{r}) = \delta_{m,n}. \quad (4.89)$$

From here, we can easily find the correspondence between the spatial mode ladder operators $\hat{a}_{\omega,m}$ and the bosonic ladder operators $\hat{\mathbf{f}}(\mathbf{r}', \omega)$ as

$$\hat{a}_{\omega,m} = -4\pi \int_{\Delta\omega_m} d\omega \iint d^3\mathbf{r} d^3\mathbf{r}' \quad (4.90)$$

$$\sqrt{2\omega^2 \omega_m \text{Im}\{\epsilon(\mathbf{r}', \omega)\}} \epsilon_0 \epsilon(\mathbf{r}, \omega) \mathbf{U}_m^*(\mathbf{r}) \cdot G(\mathbf{r}, \mathbf{r}', \omega) \cdot \hat{\mathbf{f}}(\mathbf{r}', \omega), \quad (4.91)$$

with their vacuum coupling strength to the electron as

$$g_{\omega,m}(\mathbf{R}_0) = -i \sqrt{\frac{e^2}{2\epsilon_0 \hbar \omega_m}} \int dz e^{-i\omega_m z / v_e} U_{m,z}(\mathbf{R}_0, z). \quad (4.92)$$

In this formalism, we can rewrite the scattering matrix in its modal decomposition form

$$\hat{S} = e^{i\hat{\chi}} \exp \left[\int d\omega g_{\omega} \hat{b}_{\omega}^{\dagger} \hat{a}_{\omega} - h.c. \right] = e^{i\hat{\chi}'} \exp \left[\sum_m g_{\omega_m, m} \hat{b}_{\omega_m}^{\dagger} \hat{a}_{\omega_m, m} - h.c. \right] \quad (4.93)$$

where the optical mode operators $\hat{a}_{\omega_m, m}$ are no longer continuum mode operators and now satisfy $[\hat{a}_{\omega_m, m}, \hat{a}_{\omega_n, n}^{\dagger}] = \delta_{m,n}$.

In the case of an optical cavity, the optical modes are well-defined bosonic modes. The treatment is valid as long as the electron energy resolution does not resolve the frequency components of the optical mode, i.e., $\Delta E_{ZLP} > \hbar\kappa$ where κ is the cavity linewidth. For an open waveguide, the modes coupled to the electron are instead traveling modes in a continuum [131]. This is the most general case and can also include the open cavity modes. The vacuum coupling strength of a continuum frequency mode in a spatial mode family is

$$g_{\omega, m}(\mathbf{R}_0) = -i \sqrt{\frac{e^2}{2\epsilon_0 \hbar \omega}} \int dz e^{-i\omega z / v_e} \tilde{U}_{m,z}(\mathbf{R}_0, z, \omega), \quad (4.94)$$

where the profile function $\tilde{\mathbf{U}}_m(\mathbf{r}, \omega)$ satisfies the wave equation as well, but with the normalization condition

$$\int d^3\mathbf{r} \epsilon(\mathbf{r}, \omega) \tilde{\mathbf{U}}_m(\mathbf{r}, \omega) \cdot \tilde{\mathbf{U}}_n^*(\mathbf{r}, \omega') = \delta_{m,n} \delta(\omega, \omega'). \quad (4.95)$$

4.3 Electron-photon interaction in the continuum

Index m represents different spatial mode families. However, when the electron energy resolution does not resolve the frequency structure of the coupling strength to any given mode family, we can still define the corresponding non-continuous operators for different mode families (spatial-temporal modes),

$$\hat{a}_m = \int d\omega \phi_m^*(\omega) \hat{a}_\omega \quad (4.96)$$

$$\hat{a}_\omega = \sum_m \phi_m(\omega) \hat{a}_m \quad (4.97)$$

where $\phi_m(\omega)$ is the Fourier component of the temporal field profile functions [132, 133]

$$\phi_m(\mathbf{r}, t) = i \int d\omega \sqrt{\frac{\hbar\omega}{2\epsilon_0}} \phi_m(\omega) \tilde{\mathbf{U}}_m(\mathbf{r}, \omega) e^{-i\omega t} \quad (4.98)$$

$$\hat{E}(\mathbf{r}, t) = \sum_m \phi_m(\mathbf{r}, t) \hat{a}_m + h.c. \quad (4.99)$$

of the defined mode families. It is a complete orthogonal set of functions on ω ,

$$\int d\omega \phi_m(\omega) \phi_n^*(\omega) = \delta_{m,n} \quad (4.100)$$

$$\sum_m \phi_m(\omega) \phi_m^*(\omega') = \delta(\omega - \omega') \quad (4.101)$$

found through the Gramm-Schmit orthonormalization procedure, such that the commutation relation $[\hat{a}_m, \hat{a}_n^\dagger] = \delta_{m,n}$ is satisfied for these *field operators* in the context of quantum field theory, introduced to avoid using operator-valued distributions. One can, therefore, rewrite the scattering matrix in the new mode-family field-operator basis

$$\hat{S} = e^{i\hat{\chi}} \exp \left[\sum_m g_m \hat{b}_m^\dagger \hat{a}_m - h.c. \right] \quad (4.102)$$

where $g_m = \int d\omega g_\omega \phi_m(\omega)$. The total coupling strength would be

$$|g_m|^2 = \iint d\omega d\omega' g_\omega g_{\omega'}^* \phi_m(\omega) \phi_m^*(\omega'). \quad (4.103)$$

Here, when the frequency bands of different mode families with non-negligible coupling strength g_ω are sufficiently separated, we choose the profile function $\phi_m(\omega) = \mathbb{1}_{\omega \in \Delta\omega_m} g_\omega^* / g_m^*$, where $\Delta\omega_m$ is the frequency window within which we define the field operator for the corresponding mode family, and $|g_m|^2 = \int_{\Delta\omega_m} d\omega |g_\omega|^2$. Note that when the coupling to bulk modes is significant, one can use the coupling strength $g_{\omega,m}$ from the conventional modal decomposition method or directly calculate the mode overlap between $\mathbf{U}_{\hat{a}_\omega}(\mathbf{r})$ and $\mathbf{U}_m(\mathbf{r})$, to quantitatively isolate the coupling to a mode family from background bulk mode contributions.

The cavity mode decomposition is actually the narrow-band approximation of the Gramm-Schmit orthonormalization procedure, where $\phi_m(\omega)$ is strongly peaked around the mode center frequency since all optical modes, though narrow, still have a finite linewidth due to

Chapter 4. Quantum optical interaction between free electrons and photons

the coupling to outside channels (e.g., bus waveguide and cavity losses). The profile function can be found through the input-output formalism [73] of an optical cavity \hat{a}_m , assuming unity coupling efficiency to the bus waveguide mode \hat{a}_{out} with coupling rate κ , which results in a profile function of $\phi_m(\omega) \propto \frac{\sqrt{\kappa}}{-\frac{\kappa}{2} + i(\omega_m - \omega)}$, where the bus waveguide is part of the resonator and forms the continuum modes in the frequency domain.

Until now, we have derived the basic theory of electron-photon interaction. The physical consequences of these interactions will be discussed in later chapters with the associated experimental results.

5 Photon-induced near-field electron microscopy

In recent years, integrated photonics have facilitated extensive control over fundamental light-matter interactions in quantum systems, including neutral atoms [134], trapped ions [135, 136], quantum dots [137], and defect centers [138]. Ultrafast electron microscopy has made free-electron beams also the subject of laser-based quantum manipulation and characterization [113, 139], enabling the observation of free-electron quantum walks [120, 140, 141] and attosecond electron pulses [116, 142, 143, 144]. In this category, integrated photonics [104, 105] promises unique applications in nanoscale quantum control and sensing [145], that remain to be realized in electron microscopy.

However, harnessing coherent electron-light interactions for scientific and technological applications is hampered by its usual limitation to the ultrafast and semi-classical regime. To achieve semi-classical continuous-wave interaction, some studies have implemented IELS [146, 147], a ponderomotive laser phase plate [99] and an attosecond modulator [100] at high optical powers. To date, low coupling efficiencies and material damage have limited the interaction strength. Despite the use of phase matching and resonant amplification in dielectric laser accelerators [104], prism geometries [121, 148] or free-space-coupled whispering-gallery-mode microresonators [149], achieving strong electron-light interactions, both quantum and semi-classical, has remained out of reach for regular electron microscopes.

This chapter shows the experiment results of using a ring resonator inside a TEM to enable efficient electron wavefunction phase modulation. The optical field here is strongly driven by a laser and can be treated classically. Even though we call the process photon-induced near-field electron microscopy (PINEM) due to historical reasons, the optical field here does not exhibit any particle feature in the measurable results. When the field consists of only a single optical frequency, or in other words, continuous wave (CW), the interaction can be reduced to the single-mode semi-classical interaction we derived in Section 4.2.1. When the optical field consists of multiple frequencies, e.g., generated through optical Kerr nonlinearity discussed in Appendix B.9, the interaction effectively becomes multi-mode or nonlinear, and a more delicate treatment is needed. We discuss both of these two cases in the following sections.

5.1 Continuous-wave driven semi-classical electron-light interaction

In this section, we show the experiment result where we use a high-Q integrated photonic silicon nitride resonator in an electron microscope, demonstrating efficient coherent phase modulation of a continuous electron beam. The high-finesse ($\mathcal{F} = 5 \times 10^3$ for a 1-THz ring with $Q_0 \sim 10^6$) cavity enhancement, and a waveguide specifically designed for phase matching at the 120-keV electron energy, lead to efficient electron-light interaction at unprecedentedly low, continuous-wave optical powers. Note that here the cavity optical nonlinearity does not generate new frequency components yet due to its dispersion properties, and further investigation of nonlinear optical states are described in Section 5.2.3.

To state quantitatively how efficient the interaction is, we fully deplete the initial electron energy state component at a cavity-coupled power of only $5.35 \mu\text{W}$, and generate >500 electron-energy sidebands for several milliwatts. Moreover, we probe unidirectional intracavity fields with a record μeV resolution in electron-energy-gain-spectroscopy [150].

Semi-classical electron-photon interaction

The electron-photon interaction at the photonic chip (schematic in Fig. 5.1) is described by the Hamiltonian that we derived in Chapter 4,

$$H_{\text{int}} = \frac{e}{2m} (\hat{p} \cdot \hat{A} + \hat{A} \cdot \hat{p}) = \hbar g_0 \hat{a} \hat{b}^\dagger + \hbar g_0^* \hat{a}^\dagger \hat{b}. \quad (5.1)$$

In this setting, we assume a heuristic interaction time $\tau = L/v_e$, where L is the physical length of the interaction region. The interaction between the optical mode (\hat{a} : annihilation operator) and an electron (\hat{b} : electron-energy ladder operator) is then characterized by the vacuum coupling rate g_0 , determined by the mode distribution and the matching of electron group and optical phase velocities:

$$g_0 = \eta \sqrt{\frac{e^2 v_e^2}{2\epsilon \hbar \omega V}}. \quad (5.2)$$

Here again e is the electron charge, v_e the electron group velocity, ϵ the optical permittivity, ω the optical frequency, and V the effective optical mode volume. The phase matching condition is manifested in the coefficient $\eta = \int dz e^{-i\Delta k \cdot z} u(z) / L$ defined by the optical mode profile function $u(z)$ describing the electric field component along the electron trajectory, linked to the vector potential by $\hat{A} = \hat{A}(z) = \sqrt{\frac{\hbar}{2\epsilon\omega V}} (u(z) \hat{a} + u^*(z) \hat{a}^\dagger)$, and the electron wave vector change $\Delta k = \omega/v_e$ upon photon absorption and emission.

The scattering matrix, summarizing the effect of the interaction on both the electron and the cavity, is given by $S = \exp(-ig_0\tau \hat{a} \hat{b}^\dagger - \text{h.c.})$. Populated by a coherent state $|\alpha(t)\rangle$ from a laser, the free-electron-photon interaction reduces to a dimensionless coupling parameter $g = -i\tau\alpha g_0$, where $|\alpha|^2 = n_c$ is the mean intracavity photon number, and the scattering

5.1 Continuous-wave driven semi-classical electron-light interaction

operator becomes a displacement operator acting on the electron state.

The interaction produces electron energy sidebands separated from the initial energy E_0 by integer multiples of the photon energy $N\hbar\omega$ ($N \in \mathbb{Z}$), with populations following the Bessel functions of the first kind, $P_N = J_N(2|g|)^2$. In a position representation, the interaction imprints a sinusoidal phase modulation onto the electron wavefunction, with which upon dispersive propagation will result in a density modulation of the electron beam [116, 143, 144].

5.1.1 Photonic chip-integration in an electron microscope

To facilitate high interaction strengths, we use photonic chip-based Si_3N_4 microresonators, a platform with many important features including radiation-hardness, high power handling [151], extremely low propagation losses [3] and flexibility to engineer dispersion for phase matching. The chip was fabricated using the photonic Damascene process [3, 152] without top oxide cladding to allow for efficient free-electron-light interaction with the evanescent field. The ring microresonator of $20\ \mu\text{m}$ radius is coupled to a bus waveguide and placed close to a triangular edge of the chip to minimize undesired electron-substrate interactions, see Fig. 5.1(d). For operation in the TEM, the photonic structure is packaged via ultrahigh numerical aperture (UHNA) fibers, see Fig. 5.1(c). The Si_3N_4 microresonators employed here enable phase matching at different electron energies by modifying the waveguide geometry in design, see Fig. 5.1(e), while various established integrated platforms can further extend the phase matching range in electron energy and optical frequency.

In this experiment, we design a ring microresonator (cross-section: $2\ \mu\text{m} \times 650\ \text{nm}$) to provide phase matching at an optical frequency of $\sim 193\ \text{THz}$ ($\lambda \sim 1549\text{-nm}$) for a target electron energy of $115\ \text{keV}$. Fig. 5.1(f) shows a finite-element method (FEM) simulation of the quasi-TM mode profile in terms of its major contributing longitudinal field component E_φ along the electron propagation direction. Owing to the small mode area and considerable evanescent field component, we predict a vacuum coupling rate of $g_0/2\pi \sim 10^{11}\ \text{Hz}$ over an interaction time of $\tau \sim 10^{-13}\ \text{s}$ (interaction length: $L \sim 19\ \mu\text{m}$). The microresonator's high- Q factor enables a unity coupling strength $g \sim 1^1$ at a coupled optical power of $P = n_c \hbar \omega \kappa \sim 1\ \mu\text{W}$, where $\kappa/2\pi = 390\ \text{MHz}$ is the measured cavity decay rate inside of the electron microscope (the intrinsic quality-factor of $Q_0 \sim 0.74 \times 10^6$ is slightly degraded in microscope due to high-energy electron damage of the waveguide material).

5.1.2 Simultaneous optical and electron spectroscopy

In the experiments, the fiber-coupled microresonator is driven by a 1550-nm CW laser via the bus waveguide. It is mounted on a custom-designed sample holder and placed in the object plane of the field-emission TEM, see Fig. 5.1(a). Parallel to the surface, the electron beam passes by the waveguide and interacts with the confined optical mode (Fig. 5.1(a) inset).

¹The coupling constant g is a complex number; for simplicity, in the following, we use g in place of $|g|$.

Chapter 5. Photon-induced near-field electron microscopy

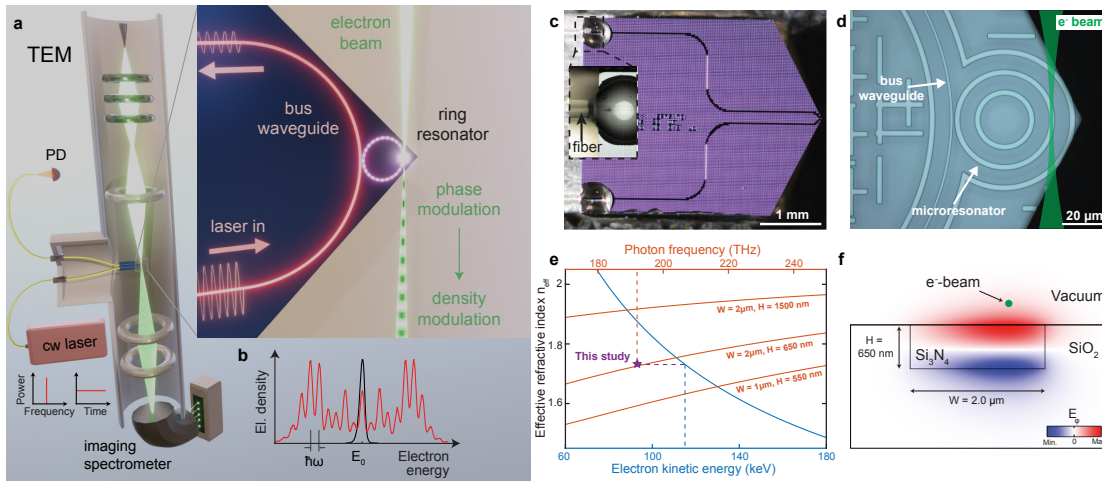


Figure 5.1: Principle of continuous-wave (CW) photonic-chip-based optical phase modulation of free-electron beams. (a) Rendering of the experimental setup including the electron microscope and a fiber-coupled Si_3N_4 photonic chip-based microresonator. (b) After the interaction with the light field, the initially narrow electron spectrum (black) develops discrete sidebands at integer multiples of the photon energy (red). (c) Photograph of the fiber-coupled Si_3N_4 photonic chip mounted on a customized TEM holder. The triangular-shaped chip edge minimizes undesired electron-substrate interactions. (inset: optical fiber glued to the input waveguide). (d) Optical microscope image of the photonic chip showing the bus waveguide and the microresonator. The electron beam (green path, not to scale) traverses the microresonator parallel to the chip surface. (e) Frequency-dependent effective index of the fundamental quasi-TM microresonator mode (red). The integrated on-chip platform allows for achieving phase matching at different electron kinetic energies (blue, 90-145 keV) either by changing the dimensions of the Si_3N_4 waveguide or operating at different optical frequencies. For the waveguide shown in (f), phase matching is achieved between the optical mode at ~ 193.5 THz (corresponding to a wavelength of ~ 1550 nm) and the free electrons at ~ 115 keV. (f) Finite element simulation of the E_φ distribution of the fundamental quasi-TM mode of microresonator (green dot: exemplary electron trajectory pointing into the page).

After traversing the structure, the electron kinetic energy distribution is characterized with an imaging electron spectrometer in two different ways. Specifically, electron energy spectra are recorded using a spectrometer when positioning a sharply focused electron beam in front of the microresonator at a specific location. Alternatively, energy-filtered transmission electron microscopy (EFTEM) using collimated (not sharply focused) TEM-illumination is used to image the interaction uniformly across the entire cavity mode near-field. While the former yields the complete electron spectra for varying experimental parameters (Fig. 5.2), the EFTEM enables imaging of a specific sideband population with high spatial resolution and span. The EFTEM method is briefly discussed in the next section; here, we primarily focus on the first measurement method.

We investigate the strength of the coupling parameter g using a focused electron probe, recording electron spectra while scanning the laser over a resonator resonance. The transmission

5.1 Continuous-wave driven semi-classical electron-light interaction

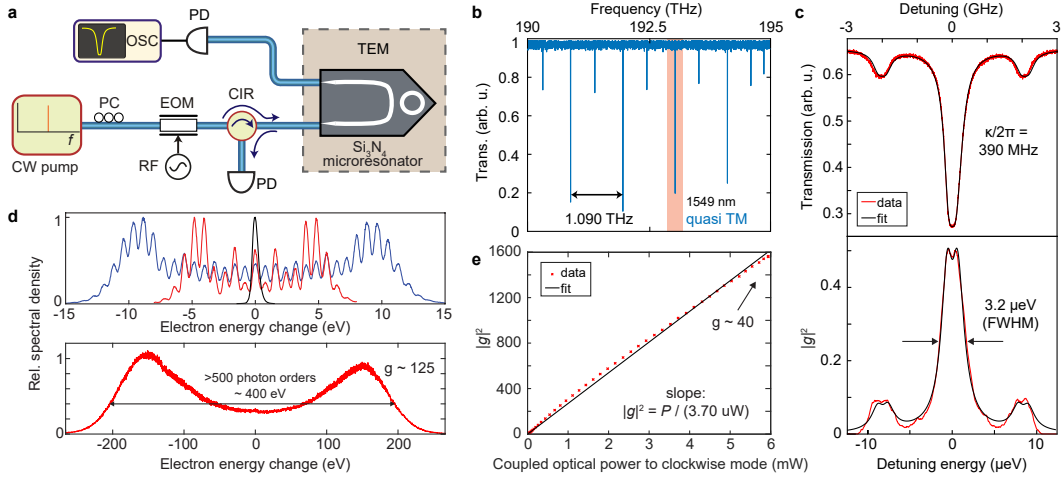


Figure 5.2: Simultaneous optical and electron spectroscopy of a high- Q microresonator mode. (a) A continuous-wave (CW) is used to excite the quasi-TM mode of the Si_3N_4 microresonator by using a polarization controller (PC). The relative optical frequency is calibrated by imparting sidebands ($\pm 2\text{GHz}$) via an electro-optic phase modulator (EOM). The total transmitted and back-reflected light is detected to calibrate the power coupled into the clockwise propagating mode (CIR: circulator, PD: photodiode, OSC: oscilloscope, TEM: transmission electron microscope, RF: radio-frequency synthesizer). (b) Normalized transmission scan of the microresonator quasi-TM mode measured outside of the TEM with a Q -factor of $\sim 0.77 \times 10^6$ ($\kappa_0/2\pi = 112 \text{ MHz}$, $\kappa_{\text{ex}}/2\pi = 139 \text{ MHz}$) and a free spectral range (FSR) of $\sim 1.090 \text{ THz}$. (c) Simultaneously measured optical transmission at the output waveguide (top) and $|g|^2$ retrieved from the electron energy spectra (bottom) during interaction of the electron-beam with the evanescent cavity field. The measured $|g|^2$ trace follows the power coupled to the clockwise mode and a slight splitting is present due to modal coupling. (d) Example electron energy spectra for low (top; $g = 0$ (black), $g \approx 3.5$ (red) and $g \approx 6.7$ (blue)) and high (bottom, $g \approx 125$) optical power. (e) $|g|^2$ varies linearly with optical power coupled to the clockwise mode of the cavity (slope: $|g|^2 = P/3.70 \mu\text{W}$).

spectrum, displayed in Fig. 5.2(b), shows the quasi-TM microresonator modes spaced by a free spectral range (FSR) of 1.090 THz . Figure 5.2(c) shows the laser-excited microresonator mode's simultaneous optical and in-situ electron spectroscopy. An electro-optical modulator (EOM, driven at 2.0 GHz) generates sidebands that can be observed in the transmission spectrum to calibrate the relative optical frequency. The laser is tuned to a single optical mode at $\sim 1549.4 \text{ nm}$ ($\kappa/2\pi = 390 \text{ MHz}$), and the focused electron beam (120-keV beam energy, 25-nm focal spot size, 1-mrad convergence semi-angle, which is a factor of approximately 10 from the position-momentum limit that reduces the transverse spatial coherence, but does not affect our results) is centered just above the surface of the microresonator to record the electron spectra for the stationary e-beam. Harnessing the high-finesse intra-cavity enhancement, we observe populations P_N in multiple photon orders N , reaching a previously inaccessible regime for a continuous laser light source and electron beam, see Fig. 5.2(d). The coupling parameter g is retrieved from the electron spectra. At the same time, the optical power coupled

Chapter 5. Photon-induced near-field electron microscopy

to the clockwise-propagating mode is determined from the recorded optical transmission and reflection data, see Fig. 5.2(e). We observe the expected linear dependence $|g|^2 = P/3.70\mu\text{W}$ of the coupling on the coupled clockwise optical power by calibrating the optical power coupled to the clockwise mode from the measured optical transmission record. From this, we find a value of $5.35\mu\text{W}$ required for suppression of the electron zero energy-loss peak at $g \sim 1.2$ and a value of $g \sim 40$ for an optical power of about 6mW . Note that as the coupling strength g is proportional to the field amplitude, it requires a quadratic increase of optical power to achieve a linear increase in g . For an optical power of $\sim 38\text{mW}$ in the bus waveguide we generate > 500 photon sidebands with $g \sim 125$, see Fig. 5.2(d).

While state-of-the-art dielectric laser accelerators (DLAs) achieve the highest peak acceleration gradients for sub-relativistic electron beams using femtosecond lasers [104, 153], our approach enables continuous acceleration with $330\text{keV}/(\text{m} \cdot \text{mW})$ of micro-bunched electron beams [103, 116]. Regarding the input peak optical power required, this is a 4-orders-of-magnitude improvement in efficiency over free-space coupled dielectric structures [121, 149].

The optical resonance's spectral line shape is analyzed by recording the transmitted optical power and the extracted g for varying laser detuning; see Fig. 5.2(c). The optical transmission trace, formed by the interference of the input light with the light coupled out from the clockwise-propagating resonator mode, exhibits a full-width-half-maximum of 560MHz (total line width $\kappa/2\pi = 390\text{MHz}$). Interestingly, the electron spectra, sensitive only to the intracavity field in the clockwise direction, display a double-peaked structure originating from coupling power to the frequency degenerate counterclockwise mode [154]. The differences in width and shape between the optical and electron spectroscopic measurements are explained by the interference in the optical transmission channel with the input field, and both curves can be fitted consistently in one model as presented below, as well as in Fig. 5.3. These data demonstrate continuous-wave electron energy gain spectroscopy (EEGS) [150, 155] at a spectral feature of only $3.2\mu\text{eV}$ in width (FWHM; $1\mu\text{eV}$ peak separation). In the following, we detail the analysis of the coupling between the clockwise and the counter-clockwise modes and how we calibrate the coupled power to the clockwise mode using the optical transmission trace.

Coupling between clockwise and counter-clockwise resonator modes

The surface Rayleigh or bulk scattering in the microresonator leads to the coupling of clockwise (a_{cw}) and counter-clockwise (a_{ccw}) modes [156]. Assuming both modes have degenerate frequencies ω , due to the time-reversal symmetry, with modal coupling rate γ due to field overlap, the Hamiltonian of the microresonator system reads

$$H = \hbar\omega(a_{\text{cw}}^\dagger a_{\text{cw}} + a_{\text{ccw}}^\dagger a_{\text{ccw}}) + \hbar\gamma(a_{\text{cw}} + a_{\text{cw}}^\dagger)(a_{\text{ccw}} + a_{\text{ccw}}^\dagger). \quad (5.3)$$

5.1 Continuous-wave driven semi-classical electron-light interaction

Going to the laser's frame with frequency $\omega_{\text{laser}} = \omega + \Delta$, under the rotating wave approximation, the Hamiltonian reads

$$H = -\hbar\Delta(a_{\text{cw}}^\dagger a_{\text{cw}} + a_{\text{ccw}}^\dagger a_{\text{ccw}}) + \hbar\gamma(a_{\text{cw}} a_{\text{ccw}}^\dagger + a_{\text{cw}}^\dagger a_{\text{ccw}}). \quad (5.4)$$

After considering coupling to the bus waveguide with rate κ_{ex} and losses to the environment with rate κ_0 , we arrive at the following Langevin equations (ignoring vacuum fluctuation)

$$\dot{a}_{\text{cw}} = (-\kappa/2 + i\Delta)a_{\text{cw}} - i\gamma a_{\text{ccw}} + \sqrt{\eta\kappa} a_{\text{cw},\text{in}} \quad (5.5)$$

$$\dot{a}_{\text{ccw}} = (-\kappa/2 + i\Delta)a_{\text{ccw}} - i\gamma a_{\text{cw}}, \quad (5.6)$$

where $\kappa = \kappa_{\text{ex}} + \kappa_0$ describes the total optical loss rate and $\eta = \kappa_{\text{ex}}/\kappa$ denotes the coupling efficiency. As the laser scan is sufficiently slow, we can use the stationary solution of the intracavity fields, which can be easily obtained as

$$a_{\text{cw}} = \frac{-\sqrt{\eta\kappa} a_{\text{cw},\text{in}}}{-\kappa/2 + i\Delta + \frac{\gamma^2}{-\kappa/2 + i\Delta}} \quad (5.7)$$

$$a_{\text{ccw}} = \frac{-i\gamma a_{\text{cw}}}{-\kappa/2 + i\Delta}. \quad (5.8)$$

The cavity transmission, reflection, and dissipation are then obtained from the input-output formalism $\mathcal{O}_{\text{out}} = \mathcal{O}_{\text{in}} - \sqrt{\kappa_{\text{ex}}}\mathcal{O}$ for any field operator \mathcal{O} ,

$$P_t/\hbar\omega = |a_{\text{cw},\text{out}}|^2 = |a_{\text{cw},\text{in}} - \sqrt{\eta\kappa} a_{\text{cw}}|^2 \quad (5.9)$$

$$P_r/\hbar\omega = |a_{\text{ccw},\text{out}}|^2 = |-\sqrt{\eta\kappa} a_{\text{ccw}}|^2 \quad (5.10)$$

$$P_{\text{diss}}/\hbar\omega = |-\sqrt{(1-\eta)\kappa} a_{\text{cw}}|^2 + |-\sqrt{(1-\eta)\kappa} a_{\text{ccw}}|^2. \quad (5.11)$$

as well as the intracavity photon numbers

$$n_{\text{cw}} = \left| \frac{-\sqrt{\eta\kappa}}{-\kappa/2 + i\Delta + \frac{\gamma^2}{-\kappa/2 + i\Delta}} \right|^2 \dot{n}_{\text{cw},\text{in}} \quad (5.12)$$

$$n_{\text{ccw}} = \left| \frac{-i\gamma}{-\kappa/2 + i\Delta} \right|^2 n_{\text{cw}}. \quad (5.13)$$

Eq.(5.9) and (5.12) are used for fitting the frequency sweep of the optical transmission $P_t(\Delta)$. The frequency sweep fitting was done using the Markov chain Monte Carlo (MCMC) methods [157], with the optical sidebands at $\pm\Omega_{\text{sb}}$ and an absorption-induced cavity frequency shift $\chi_{\text{th}}P_{\text{diss}}(\Delta)$ included in the models. The fitting function is thus $F_{\text{fit}}(\Delta) = \sum_{n=-1,0,1} F_i(\Delta + n\Omega_{\text{sb}} + \chi_{\text{th}}P_{\text{diss}}(\Delta))$, where F_i is either P_t for optical measurement or n_{cw} for the inferred electron-light coupling strength g from the electron spectra. The fitting results are shown in Fig.5.3, and the fitted system parameters show great consistency between the two distinct measurements.

For the power sweep calibration, Eq.(5.9), (5.12) and (5.13) are used for calibrating the clock-

Chapter 5. Photon-induced near-field electron microscopy

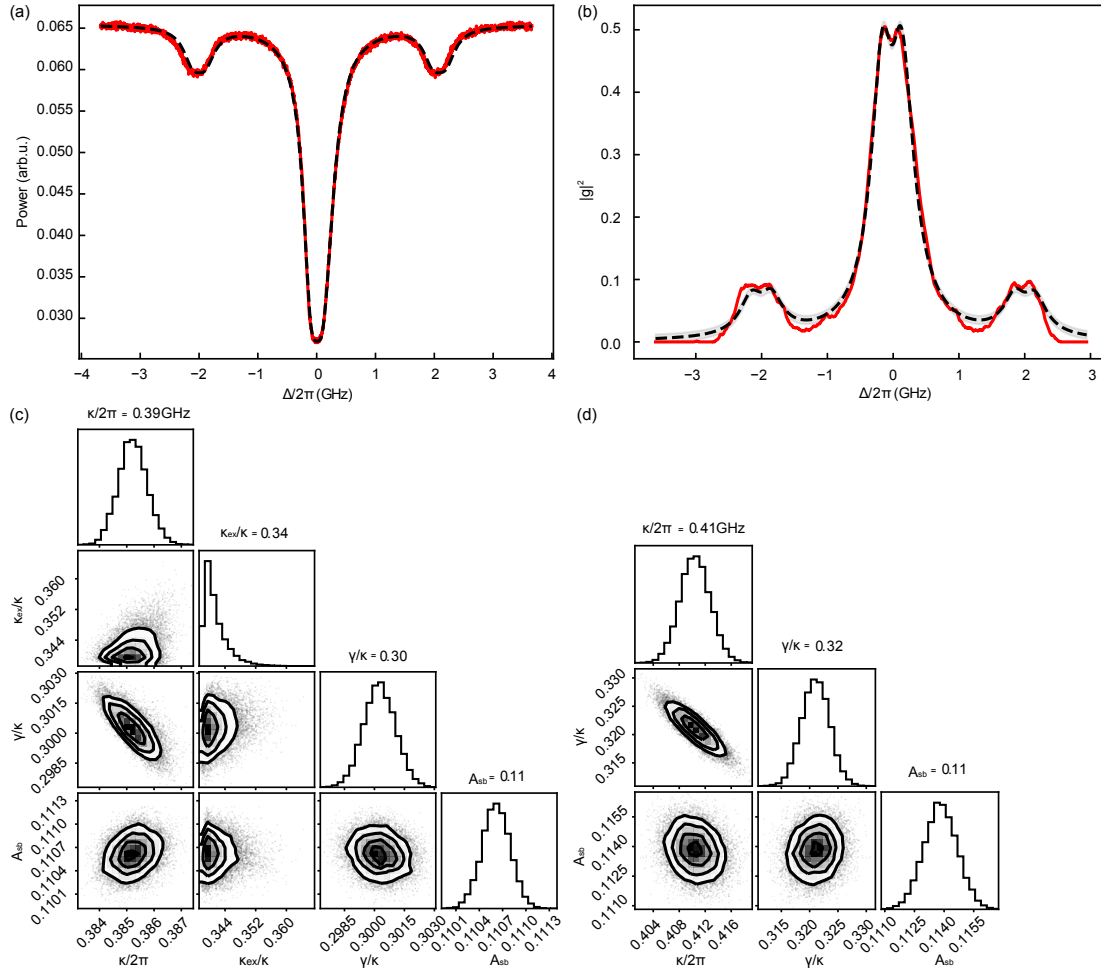


Figure 5.3: **(a)** An optical transmission scan measured at the output of the chip is fitted using Eq. (5.9). The sidebands generated via an electro-optic modulator are used to calibrate the frequency. **(b)** Fitting to the fitted g frequency sweep using Eq. (5.12). Note that the frequency sweep line shape difference near the resonance is due to the coupling to the frequency degenerate counter-clockwise optical mode. **(c,d)** The Markov chain Monte Carlo random walk corner plot of the fitting to the optical data and the fitted g data. The fitted system key parameters (cavity decay rate κ , splitting ratio γ/κ , sideband ratio A_{sb}) of the two frequency sweeps are all within 7% discrepancy, indicating great consistency between the optical and electron spectroscopic measurements. Also, a strong correlation between the fitted γ and κ is observed for both fittings, indicating the necessity of applying the coupled modes model to extract the cavity decay rate correctly.

5.2 Free-electron interaction with optical continuum

wise dissipated power $\tilde{P}_{\text{diss,cw}}(t)$. The detuning $\tilde{\Delta}(t)$ was extracted from the experimentally measured $\tilde{P}_t(t)$ (Fig.5.4(b), suffers the least from background noise and etalon interference) using the fitted resonator parameters (κ, η, γ) from the frequency sweep (Fig.5.4(a)(c)). Then, the clockwise dissipated power $\tilde{P}_{\text{diss,cw}}(t)$ (Fig.5.4(e)) was calibrated from the experimentally measured transmission power $\tilde{P}_t(t)$ and the calibrated $\tilde{\Delta}(t)$ by $\tilde{P}_{\text{diss,cw}}(t) = \frac{P_{\text{diss,cw}}(\tilde{\Delta}(t))}{P_t(\tilde{\Delta}(t))} \tilde{P}_t(t)$. We later calculate the characteristic coupled optical power $P = n_{\text{cw}} \hbar \omega \kappa$ by scaling the dissipated power $P = \frac{\kappa}{\kappa_0} \times \tilde{P}_{\text{diss,cw}}$, and plot it against the fitted coupling constant $|g(t)|^2$ (fig. 5.4(f)), one could find the linear relation to optical power as is expected in theory. The observable oscillations in the linear dependence of $|g|^2$ on the clockwise dissipated power are related to a 50 Hz noise in the beam position, leading to variations in the measured electron-light coupling strength. To eliminate this 50 Hz noise, we binned the retrieved coupling strength in time intervals of 20 ms. Fig. 5.2(e) shows the resulting power dependence. Note that the calibrated cavity response trace is highly oscillatory and unsuitable for calibrating intracavity power. This behavior is because of the background etalon formed by the weak reflection of the chip facets. We detail the physics of this etalon-type split resonance response in Appendix B.12.

Mode imaging and phase matching condition

As I am not heavily involved in the data analysis of the EFTEM for the direct mode and sideband population imaging, this section only briefly discusses the results. Please refer to ref [7] for the more detailed experiment results.

Using a collimated electron beam and an imaging energy filter (800-meV energy passband) to obtain the energy sideband population, spatial maps of the discrete sideband populations P_N can be imaged. One important feature we observed is an oscillatory modulation of g along the chip surface, as the e-beam interacts twice with the ring resonator (geometrical configuration shown in Fig. 5.11 (a)) and results in Ramsey-type constructive or destructive interference that depends on the relative phase of both individual interactions [140]. We also observed varying coupling strength with electron energy, which peaked at the periphery of the ring (tangent line) with the correct phase-matching electron energy of 115 keV. These results are expected and confirmed by the theoretical and numerical simulations. The Ramsey-type inference is particularly useful for studying the spatial amplitude-phase correlation between the nonlinear optical fields at two different spatial points, detailed in our recent result [11].

This section only examined the case when the optical field driving the electron-light interaction is a continuous wave. In the following section, we analyze the case when the optical field is nonlinear and composed of multiple frequency components.

5.2 Free-electron interaction with optical continuum

In the previous chapter, we established the theoretical background of how to treat the free-electron interaction with classical optical fields, single-mode quantized optical mode, and the

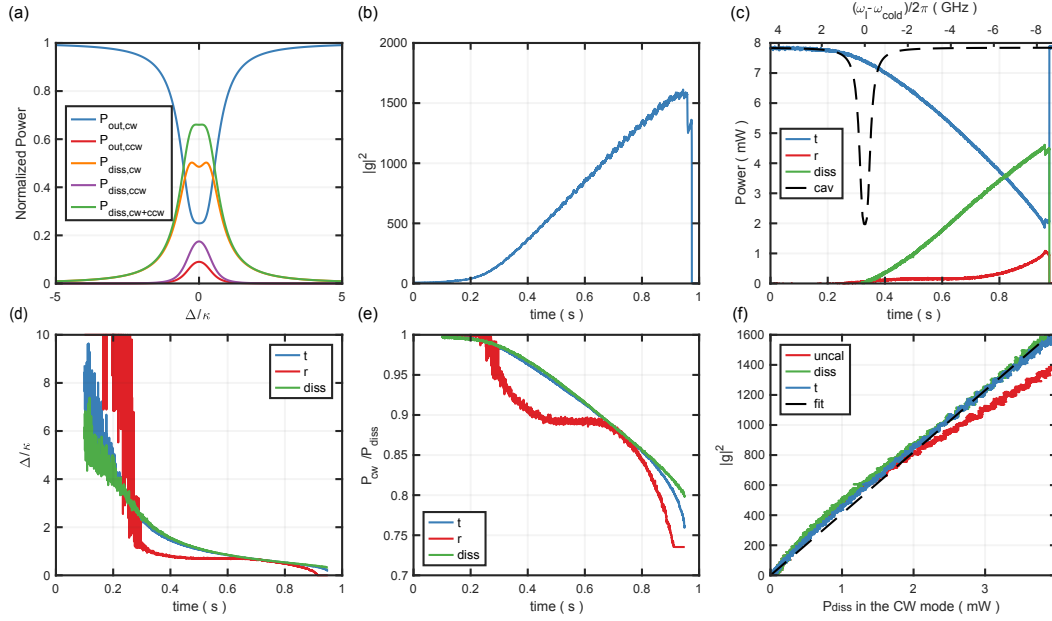


Figure 5.4: **(a)** Simulated power distribution in the optical system when the pump is along the clockwise direction, generated using parameters fitted from the frequency sweep measurement shown in Fig.5.3. **(b)** $|g|^2$ scan where each point is obtained after fitting the electron energy distribution. **(c)** Experimentally measured optical signal of the cavity transmission (blue), reflection (red), and dissipation (green). The resonance-shaped (black dashed) curve shows the inferred cold cavity transmission without thermal absorption and Kerr nonlinearity-induced cavity frequency shift, which is present in the triangular-shaped (blue) curve due to high input power ($\sim > 50\mu W$). **(d)** Calibrated detuning $\Delta(t)$ based on the experimentally measured optical signal in (c). **(e)** Calibrated correction factor $P_{diss,cw}/P_{diss}$ from the detuning plot (d). The reflection calibration is empirically erroneous. This effect can be attributed to the etalon formed by the chip facets, by which the transmission signal is less affected. **(f)** The calibrated dissipated power in the clockwise mode shows a linear relation with $|g|^2$ from different measurement channels (transmission and dissipation).

quantized optical continuum. We also established an experiment platform for free-electron interaction with the near field of a photonic integrated resonator. As discussed in Appendix B.9, these resonators exhibit optical Kerr nonlinearity and generate new frequency components and different families of nonlinear optical states, e.g., dissipative Kerr solitons, at high operating power. Therefore, we would also like to understand electrons' interaction with these nonlinear optical fields.

In this section, we first establish the general theory of free-electron interaction with a general nonlinear optical state. Later, we illustrate some experiment results obtained with free electrons interacting with nonlinear optical fields in our resonator.

5.2.1 Free-electron interaction with nonlinear optical fields

Here, we derive the general result of free electrons interacting with optical fields consisting of multiple frequency components, both in the optical continuum and the discrete mode basis, and show that in either case, we arrive at one consistent result, which is effectively a position-dependent phase modulation of the electron wavefunction.

Interaction with optical continuum

The interaction with the optical continuum is the most general picture. In principle, it also covers the case with optical resonators, which exhibit discrete modes in frequency, since the coupling to the bus waveguide effectively converts the discrete modes into the continuum traveling modes. We start from the scattering matrix derived earlier in Section 4.3.1,

$$\hat{S} = \exp\left(-\int d\omega g_\omega^* \hat{b}_\omega \hat{a}_\omega^\dagger - h.c.\right) \quad (5.14)$$

where

$$g_\omega = \sqrt{\frac{e^2}{2\hbar\omega\epsilon_0}} \int dz e^{-i\frac{\omega}{v}z} U_z(\mathbf{r}, \omega) \quad (5.15)$$

Note that we are concerned with the interaction with an intentionally stimulated field. Therefore, we describe the interaction by only considering a specific waveguide mode family m that we excite with laser inputs. The field function $U_z(\mathbf{r}, \omega) = \mathbf{U}_m(\mathbf{r}, \omega) \cdot \hat{e}_z$ is the z component of the normalized electric field functions $\mathbf{U}_m(\mathbf{r}, \omega)$ which satisfies the wave equation

$$\nabla \times \nabla \times \mathbf{U}_m(\mathbf{r}, \omega) - \frac{\omega^2}{c^2} \epsilon(\mathbf{r}, \omega) \mathbf{U}_m(\mathbf{r}, \omega) = 0 \quad (5.16)$$

and the normalization condition

$$\int d^3\mathbf{r} \epsilon(\mathbf{r}, \omega) \mathbf{U}_m(\mathbf{r}, \omega) \cdot \mathbf{U}_n^*(\mathbf{r}, \omega') = \delta_{m,n} \delta(\omega, \omega'). \quad (5.17)$$

When ignoring the electron energy-momentum dispersion, we can approximate the electron energy ladder operators \hat{b}_ω as $e^{-i\frac{\omega}{v}z}|z\rangle\langle z|$. In the following derivations, $|z\rangle\langle z|$ is hidden for simplicity. When the scattering matrix acts on the electron $|\psi_e\rangle$ and a nonlinear optical state (coherent waves) $\prod_\omega |\alpha_\omega\rangle$, we have

$$\begin{aligned} \hat{S}|\psi_e, \psi_{\text{ph}}\rangle &= \exp\left(-\int d\omega g_\omega^* \hat{b}_\omega \hat{a}_\omega^\dagger - h.c.\right) |\psi_e\rangle \prod_\omega |\alpha_\omega\rangle \\ &\approx \exp\left(-\int d\omega g_\omega^* \alpha_\omega^* e^{-i\frac{\omega}{v}z} - h.c.\right) |\psi_e\rangle \end{aligned} \quad (5.18)$$

Chapter 5. Photon-induced near-field electron microscopy

As the electric field operator in time domain is

$$\hat{\mathbf{E}}(\mathbf{r}, t) = \int d\omega \cdot i \sqrt{\frac{\hbar\omega}{2\epsilon_0}} \mathbf{U}(\mathbf{r}, \omega) e^{-i\omega t} \hat{a}_\omega + h.c. \quad (5.19)$$

$$\hat{\mathbf{A}}(\mathbf{r}, t) = \hat{\mathbf{A}}_-(\mathbf{r}, t) + \hat{\mathbf{A}}_+(\mathbf{r}, t) = \int d\omega \sqrt{\frac{\hbar}{2\omega\epsilon_0}} \mathbf{U}(\mathbf{r}, \omega) e^{-i\omega t} \hat{a}_\omega + h.c., \quad (5.20)$$

we can easily write out the classical counterpart whose time-domain waveform can be retrieved from, e.g., numerical simulation of the LLE,

$$\mathbf{A}_-(\mathbf{r}, t) = \int d\omega \sqrt{\frac{\hbar}{2\omega\epsilon_0}} \mathbf{U}(\mathbf{r}, \omega) e^{-i\omega t} \alpha_\omega. \quad (5.21)$$

With this expression for the optical field $\mathbf{A}(\mathbf{r}, t)$, we can derive the scattering matrix when an electron interacts with a nonlinear optical state as

$$\begin{aligned} \hat{S}|\psi_e, \psi_{\text{ph}}\rangle &\approx \exp\left(-\frac{e}{\hbar} \int dz' A_{+,z}\left(\mathbf{R}_0, z', T = \frac{z' - z}{v}\right) - h.c.\right) |\psi_e\rangle \\ &= \exp\left(-2i \text{Im} \left[\frac{e}{\hbar} \int dz' A_{+,z}\left(\mathbf{R}_0, z', T = \frac{z' - z}{v}\right) \right]\right) |\psi_e\rangle \end{aligned} \quad (5.22)$$

which is essentially a position- z -dependent phase modulation of the electron wavefunction.

Interaction with discrete multi-mode fields

The discrete mode picture is uniquely applied to the case of an optical resonator. The formulation does not change much, as we start with the scattering matrix

$$\hat{S} = \exp\left(-\sum_m g_m^* \hat{b}_m \hat{a}_m^\dagger - h.c.\right) \quad (5.23)$$

where

$$g_m = \sqrt{\frac{e^2}{2\hbar\omega\epsilon_0}} \int dz e^{-i\frac{\omega}{v}z} U_{m,z}(\mathbf{r}) \quad (5.24)$$

and the normalized electric field functions $\mathbf{U}_m(\mathbf{r})$ of mode family m (that we excite) satisfy the wave equation

$$\nabla \times \nabla \times \mathbf{U}_m(\mathbf{r}) - \frac{\omega^2}{c^2} \epsilon(\mathbf{r}, \omega_m) \mathbf{U}_m(\mathbf{r}) = 0 \quad (5.25)$$

with the normalization condition

$$\int d^3\mathbf{r} \epsilon(\mathbf{r}, \omega_m) \mathbf{U}_m(\mathbf{r}) \cdot \mathbf{U}_n^*(\mathbf{r}) = \delta_{m,n}. \quad (5.26)$$

5.2 Free-electron interaction with optical continuum

Again, we can write out the electric field operator in the time domain

$$\hat{\mathbf{A}}(\mathbf{r}, t) = \hat{\mathbf{A}}_-(\mathbf{r}, t) + \hat{\mathbf{A}}_+(\mathbf{r}, t) = \sum_m \sqrt{\frac{\hbar}{2\omega\epsilon_0}} \mathbf{U}_m(\mathbf{r}) e^{-i\omega_m t} \hat{a}_m + h.c. \quad (5.27)$$

Upon substituting g_m with $A_{+,z}$ in the classical limit (large coherent fields), we arrive at the same scattering matrix as we derived earlier,

$$\hat{S}|\psi_e, \psi_{\text{ph}}\rangle = \exp\left(-2i\text{Im}\left[\frac{e}{\hbar} \int dz' A_{+,z}\left(\mathbf{R}_0, z', T = \frac{z' - z}{v}\right)\right]\right)|\psi_e\rangle. \quad (5.28)$$

Electron energy spectrum

From previous subsections, we understand that the interaction with a classical field imprints a phase modulation on the electron wave function. In reality, we can measure quantities like the electron energy change after the interaction in the experiment. Therefore, in this subsection, we aim to understand the effect on the electron energy distribution.

We start with a general initial electron state $|\psi_e\rangle = \int dk \psi(k)|k\rangle$, and $\psi(z) = \int dk \psi(k)e^{ikz}$ in the spatial domain. We can derive the scattered electron energy spectrum as

$$\begin{aligned} P(k) &= |\langle k|\hat{S}|\psi_e, \psi_{\text{ph}}\rangle|^2 \\ &= \left| \iint dz dk' \exp\left(-2i\text{Im}\left[\frac{e}{\hbar} \int dz' A_{+,z}\left(\mathbf{R}_0, z', T = \frac{z' - z}{v}\right)\right]\right) \psi(k') e^{-i(k-k')z} \right|^2 \\ &= \left| \iint dz dk' \exp\left(-2i\text{Im}\left[\frac{e}{\hbar} \int dz' A_{+,z}\left(\mathbf{R}_0, z', T = \frac{z' - z}{v}\right)\right]\right) \psi(z) e^{-ikz} \right|^2 \end{aligned} \quad (5.29)$$

which is essentially the Fourier components of the phase-modulated electron wavefunction $\psi'(z)$ in the spatial domain.

To simplify the result further, we can assume that the optical envelope is time-invariant. The optical time-dependent waveform can be further expanded as

$$A_{+,z}(z, t) = e^{i(\omega t - k_{\text{eff}}(z)z + \phi_1)} \bar{U}(z) \bar{A}(\omega t - k_g z + \phi_2), \quad (5.30)$$

where $\bar{U}(z)$ includes the spatial dependence (e.g., waveguide routing) of the envelope, and $\bar{A}(\omega t - k_g z + \phi_2)$ is the time-invariant optical envelope along the waveguide direction. There k_{eff} and k_g are the optical phase and group wave vectors. Generally, \bar{U} is frequency/time dependent as well due to optical dispersion during the propagation. We restrict ourselves in the case where the dispersion during the propagation can be neglected, especially during the interaction. The dispersion is perfectly balanced in the case of a dissipative Kerr soliton (DKS). We further assume that the electron state is also a plane wave with a time-invariant envelope, $\psi(z) \propto e^{ik_0 z} \bar{\psi}(z)$, during the interaction. With these simplifications, we can further simplify

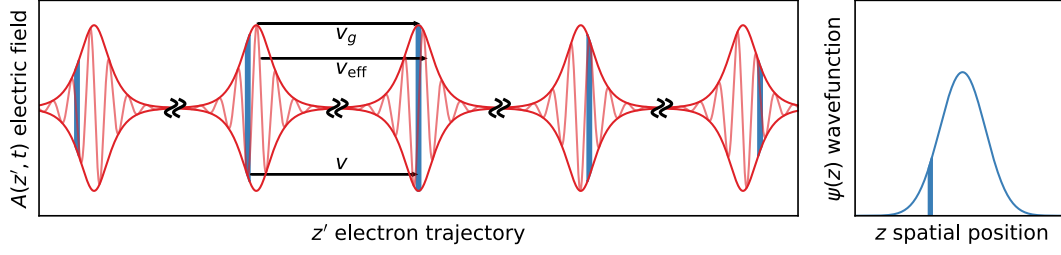


Figure 5.5: Illustration of electron interaction with a nonlinear optical field with a time-invariant envelope. Right: The electron wavefunction is in the rest frame, where the wavefunction is stationary. A blue slice $\psi(z)$ is highlighted, whose phase modulation is to be analyzed in Left: the accumulated electron phase modulation on $\psi(z)$, at different physical coordinates z' near the optical structure, when the electron co-propagates with an optical pulse (five instances in time is shown). When the interaction accumulates over various coordinates z' , the electron experiences the phase-velocity and group-velocity mismatch.

the electron-light interaction as

$$P(K = k - k_0) \propto \left| \text{FT}_{z \rightarrow K} \exp \left(-2i \text{Im} \left[\frac{e}{\hbar} \int dz' e^{i(\frac{\omega}{v} - k_{\text{eff}})z'} \bar{U}(z') \right. \right. \right. \\ \left. \left. \left. \times \bar{A} \left(\left(\frac{\omega}{v} - k_g \right) z' - \frac{\omega}{v} z + \phi_2 \right) e^{-i\frac{\omega}{v} z + i\phi_1} \right] \right) \bar{\psi}(z) \right|^2 \quad (5.31)$$

here, ϕ_1 is one degree of freedom relative between the optical carrier phase and the electron. If the electron and the optical carrier fields are not synchronized, this phase will average out. However, if the electron arrival and the optical phase are synchronized, and when the electron pulse is sub-optical cycle long, different ϕ_1 will lead to directional acceleration or de-acceleration of the electron. ϕ_2 , on the other hand, is related to the arrival timing of the electron relative to the optical pulse envelope and changes the envelope of the phase modulation applied to the electron wave function.

5.2.2 Generalized electron modulation dependence on field properties

To understand the physical picture of this interaction better, we rewrite the electron energy distribution in another way

$$P(K = k - k_0) \propto \left| \text{FT}_{z \rightarrow K} \exp \left(-2i \text{Im} \left[g(z) e^{-i\frac{\omega}{v} z + i\phi_1} \right] \right) \bar{\psi}(z) \right|^2 \quad (5.32)$$

$$g(z) = \frac{e}{\hbar} \int dz' e^{i(\frac{\omega}{v} - k_{\text{eff}})z'} \bar{U}(z') \bar{A} \left(\left(\frac{\omega}{v} - k_g \right) z' - \frac{\omega}{v} z + \phi_2 \right) \quad (5.33)$$

With these expressions, the physical meaning of the interaction is clear, as is illustrated in Fig. 5.5. Since it is the interaction picture, we are looking at the electron's rest frame $\psi(z)$. The interaction adds an effective position- z -dependent spatial phase modulation

$\exp\left(-2i\text{Im}\left[g(z)e^{-i\frac{\omega}{v}z+i\phi_1}\right]\right)$ on the electron wavefunction.

When driven with a CW light source, the optical envelope profile \bar{A} loses time dependence. As a result, $g(z)$ loses z dependence and becomes a constant g . Then, the Bessel sidebands are natural from the Bessel expansion of a sinusoidal phase modulation $\exp(2i|g|\sin(\frac{\omega}{v}z + \phi))$.

Effects of relative pulse width and arrival timing

When the optical envelope co-propagates with the electron, the electron wavefunction $\psi(z)$ experiences a position- z dependent inhomogeneous phase modulation due to light intensity and phase variation. In the energy domain, the sideband distribution also generally deviates from Bessel functions that were for homogeneous phase modulation.

When the group velocity of the light matches that of the electron $k_g = \frac{\omega}{v}$, the relative position of the optical envelope and the electron pulse is synchronized. Therefore, the phase modulation depth is precisely proportional to the optical envelope as in $g(z) \propto \bar{A}(-\frac{\omega}{v}z + \phi_2)$, revealing the intuitive physical picture. We show in Fig. 5.6 the case where the optical group and phase velocities are perfectly matched with the electron velocity (artificial), with varying relative pulse width ratio and relative arrival timing (determined by ϕ_2). As we can see, the more non-uniformity $g(z)$ has relative to $\psi(z)$, the electron spectrum deviates more from the standard Bessel distribution.

Effects of group and phase velocity mismatch

With the group velocity mismatch, the optical field envelope catches an extra term, $\bar{A}((\frac{\omega}{v} - k_g)z' - \frac{\omega}{v}z + \phi_2)$, capturing the effect of relative position slip due to the pulse speed mismatch during the whole interaction length $\int dz'$. As a result, the $g(z)$ integral of z' involves the Fourier components of both the phase velocity mismatch $\frac{\omega}{v} - k_{\text{eff}}$, the group velocity mismatch from $\bar{A}((\frac{\omega}{v} - k_g)z' - \frac{\omega}{v}z + \phi_2)$, as well as the structure spatial dependence $\bar{U}(z')$. For some z they can compensate each other, while for some other z , they reduce the depth of the phase modulation.

We simulate the case where the group and the phase velocities are mismatched with the electron group velocity, shown in Fig. 5.7. As we can see, the group velocity mismatch results in generally broader $g(z)$ due to the effect of the envelope moving average. The broader the $g(z)$, the more *Bessel*-like the electron spectrum is. On the other hand, a phase mismatch introduces oscillatory behavior of $g(z)$ due to the interference mentioned above between different Fourier components.

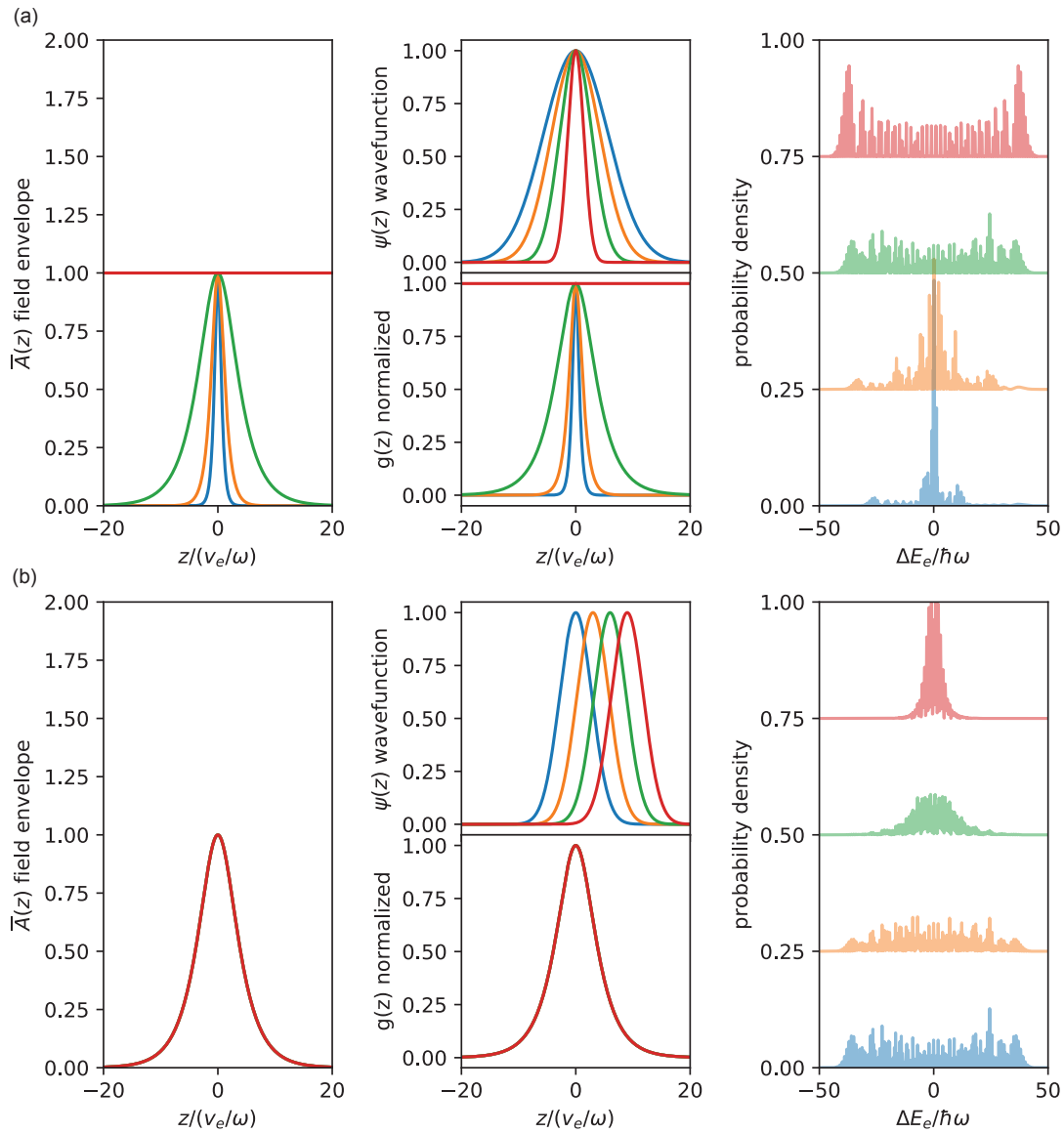


Figure 5.6: Electron energy spectrum after interaction with an optical pulse with perfect phase and group velocity matching. The optical field envelope, the electron wavefunction, and the phase modulation depth $g(z)$ are plotted. **(a)** Changing relative electron-optical pulse width ratio. **(b)** Changing relative arrival timing between electron and optical pulses. Both result in a non-Bessel-shaped electron energy spectrum when the optical waveform is not CW. Note that all the electron spectra are offset by integers of 0.25 for visualization purposes.

5.2 Free-electron interaction with optical continuum

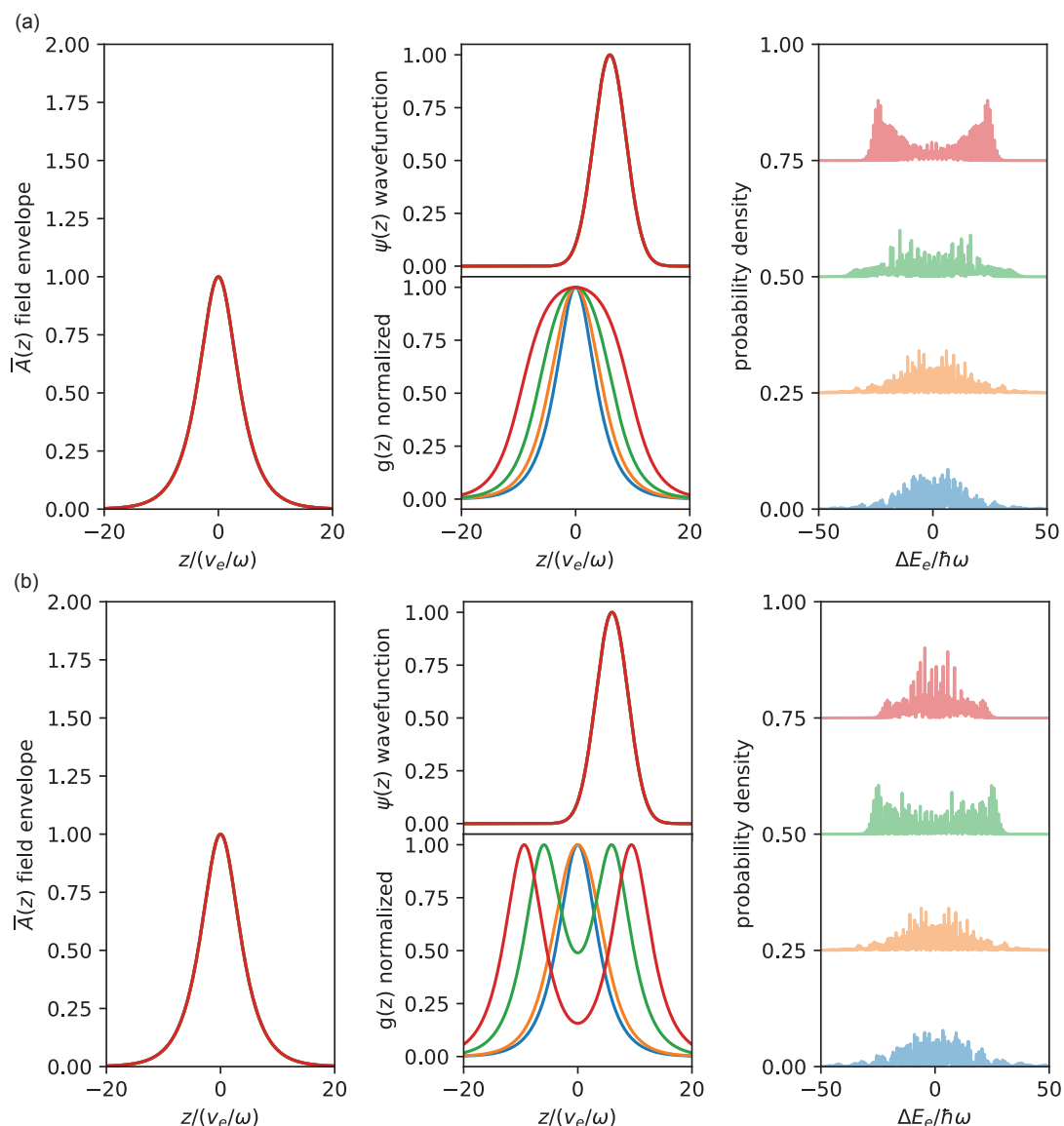


Figure 5.7: Electron energy spectrum after interaction with an optical pulse with phase and group velocity mismatch. The optical field envelope, the electron wavefunction, and the phase modulation depth $g(z)$ are plotted. **(a)** Changing electron group velocity from perfect group-velocity matching (100 keV) to 200 keV. Phase velocity is perfectly matched here to isolate the effect of group-velocity mismatch. We can see that the group-velocity mismatch results in a wider $g(z)$ width due to the moving-average effect. **(b)** Same electron group velocity sweep, but phase velocity is also mismatched here. This results in the oscillatory behavior of $g(z)$. Note that the optical field amplitude is scaled to compensate for the reduced interaction strength due to phase mismatch. All the electron spectra are also offset by integers of 0.25 for visualization purposes.

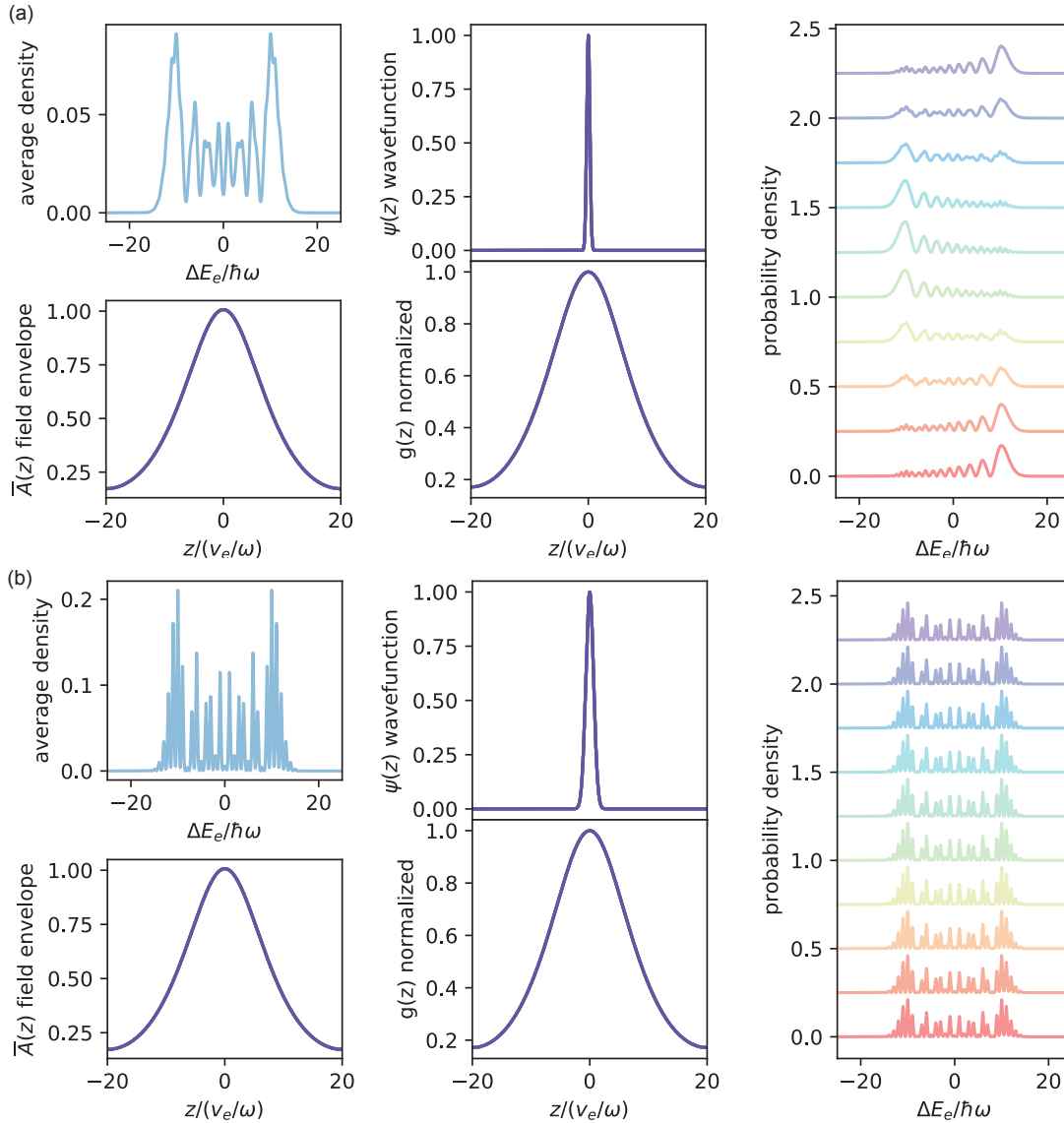


Figure 5.8: Electron energy spectra after interaction with an optical pulse, under perfect phase- and group-velocity matching. Ten electron energy spectra are shown with swept ϕ_1 in a full cycle and the ϕ_1 -averaged energy density. **(a)** Sub-optical-cycle electron pulse, results in ϕ_1 -dependent asymmetric shift of the electron energy. **(b)** Electron pulse spanning multiple optical cycles, results in ϕ_1 -independent symmetric electron spectra. All the electron spectra are offset by integers of 0.25 for visualization purposes.

Effect of the relative phase between optical carrier and electron

As discussed, the relative phase ϕ_1 leads to asymmetric electron energy shift when the electron wavefunction span is sub-optical-cycle. This effect is illustrated in Fig. 5.8. When the electron is more point-like (sub-optical-cycle, energy span larger than $\hbar\omega$), the electron experiences a sub-optical-cycle field, which results in phase-dependent directional energy gain/loss. However, if this relative phase is not synchronized, it will have an averaging effect, leading to a symmetric averaged spectrum. In the experiment, to obtain a stable relative phase ϕ , the electron pulse has to be compressed first by the same (or phase-synchronized) optical field so that the position of the electron pulse is synchronized with the phase of the subsequent optical field, which is used for directional acceleration. When the electron wavefunction is sufficiently large (multiple optical-cycle, energy span smaller than $\hbar\omega$), the spectrum tends to be phase independent, and the electron behaves more wave-like.

Note that any phase averaging, either ϕ_1 or ϕ_2 , in the experiment will lead to the decoherence of the electron state. I.e., the end state of the electron will be a mixed state instead of a coherent one.

Frequency-domain picture

We can also understand the physics from a frequency-domain picture by recasting $g(z)$ into

$$g(z) = \frac{e}{\hbar} \int d\tilde{k} \tilde{U} \left(\left(\frac{\omega}{v} - k_{\text{eff}} \right) - \tilde{k} \right) \tilde{A} \left(\frac{\tilde{k}}{\frac{\omega}{v} - k_g} \right) \exp \left(i \frac{\tilde{k}}{\frac{\omega}{v} - k_g} \left(\frac{\omega}{v} z - \phi_2 \right) \right) \left| \frac{\omega}{v} - k_g \right|^{-1}. \quad (5.34)$$

Here, \tilde{k} is the electron wave-vector offset from the optical carrier k_{eff} , and we are summing up all these optical Fourier components. The three terms here have clear physical meanings. $\tilde{U} \left(\left(\frac{\omega}{v} - k_{\text{eff}} \right) - \tilde{k} \right)$ is the Fourier component contributed by the waveguide routing geometry. $\tilde{A} \left(\frac{\tilde{k}}{\frac{\omega}{v} - k_g} \right)$ is the Fourier component contributed by the moving optical envelope relative to the electron. Furthermore, $\exp \left(i \frac{\tilde{k}}{\frac{\omega}{v} - k_g} \left(\frac{\omega}{v} z - \phi_2 \right) \right)$ is the relative phase accumulation of these Fourier components from the arrival timing of the pulse ϕ_2 .

5.2.3 Continuous electron-soliton interaction

In our experiment, one of the particular nonlinear optical states we generated is the dissipative Kerr soliton (DKS), discussed in Appendix B.9. In most UTEM experiments, a mode-locked laser is used to drive the electron emission process and interact with the electron later with a fixed delay determined by the optical path length. In our experiment, although DKS is an optical pulse, we can not use it to drive the electron emission because of its wavelength. Since our electron field emission process is dominated by one-photon absorption, the photon energy needs to exceed the work function of the tip material. Therefore, first, we must convert the wavelength using third harmonic generation. Second, the soliton pulses' optical power

(20 fJ) is low compared to that of the frequency-doubled mode-locked lasers [158] (10 nJ).

Because of the above reasons, we do not have a synchronization between the optical pulses (DKS) and the electron arrival at the sample. Because of this, the generated electron state is a mixed state, and we have to treat the arrival timing ϕ_2 as a uniformly distributed random variable. Also, our electron intrinsic energy uncertainty $\Delta E < 0.6 \text{ eV} < \hbar\omega$, therefore the specific value of ϕ_1 does not matter as well, and the electron spectrum will be symmetric. Consequently, the measured spectra will be averaged over different relative timing ϕ_2 . Due to the different arrival timing, as well as the relatively narrow DKS timing width, the electron most of the time interacts with the CW background of the laser drive and only interacts with the DKS pulses with small probability, shown in Fig. 5.11 (b). Because of this reason, we need to look at the electron spectrum in log-scale to observe the effect of interaction with the optical pulses.

Another important consideration is that our DKS envelope generated in the experiment (e.g. $\sim 20 \mu\text{m}$) is relatively long compared to the electron spatial extent ($\sim 1 \mu\text{m}$). As a result, the electron wavefunction does not experience significantly the non-uniform phase modulation $g(z)$. Therefore, we hypothesized that for each arrival time ϕ_2 , we can approximate $g(z, \phi_2)$ with a uniform $g(\phi_2)$. Consequently, for each ϕ_2 , the electron spectrum can be approximated with a Bessel distribution. This simplification could greatly reduce the computational time by removing one layer of integral, the Fourier transform that needs to be performed to retrieve the electron spectrum, and replacing it with Bessel functions that can be directly called. Further, when there is no phase- or group-velocity mismatch, evident from Eq. 5.33, we can further approximate $g(\phi_2) \sim \bar{A}(\phi_2)$, removing another layer of numerical integral. In the following, we analyze the physical effects induced by these several approximation steps.

First, we assume perfect phase- and group-velocity matching and analyze the approximation of $g(z, \phi_2) \rightarrow g(\phi_2)$. A comparison between the general and approximated models is shown in Fig. 5.9. As we can see, the two models give visually similar results for each ϕ_2 spectrum and the averaged spectrum.

However, when there is phase- and group-velocity mismatch, which is generally true in our case, the approximation $g(\phi_2) \sim \bar{A}(\phi_2)$ breaks down. As we analyzed in the previous section, these two effects, together with the waveguide routing, will lead to the oscillatory behavior of $g(z)$. As shown in Fig. 5.10, because of this behavior, even though the electron spectrum is still Bessel distributed for each arrival time ϕ_2 , the effective modulation depth is modified significantly. In this case, the full expression of Eq. 5.33 needs to be used.

To avoid significant influence from the group- and phase-velocity mismatch, in our experiment, we choose to minimize the waveguide routing function $\bar{U}(z) \rightarrow \delta(z)$ by positioning the e-beam far away from the peripheral of the ring resonator (small radio distance shown in Fig. 5.11 (a)), and only interact with the optical field close to the center with a large between the propagation directions, such that the interaction length is minimized to the width of the waveguide. In such a condition, we can simplify the phase modulation to $g(\phi_2) \sim \bar{A}(\phi_2)$.

5.2 Free-electron interaction with optical continuum

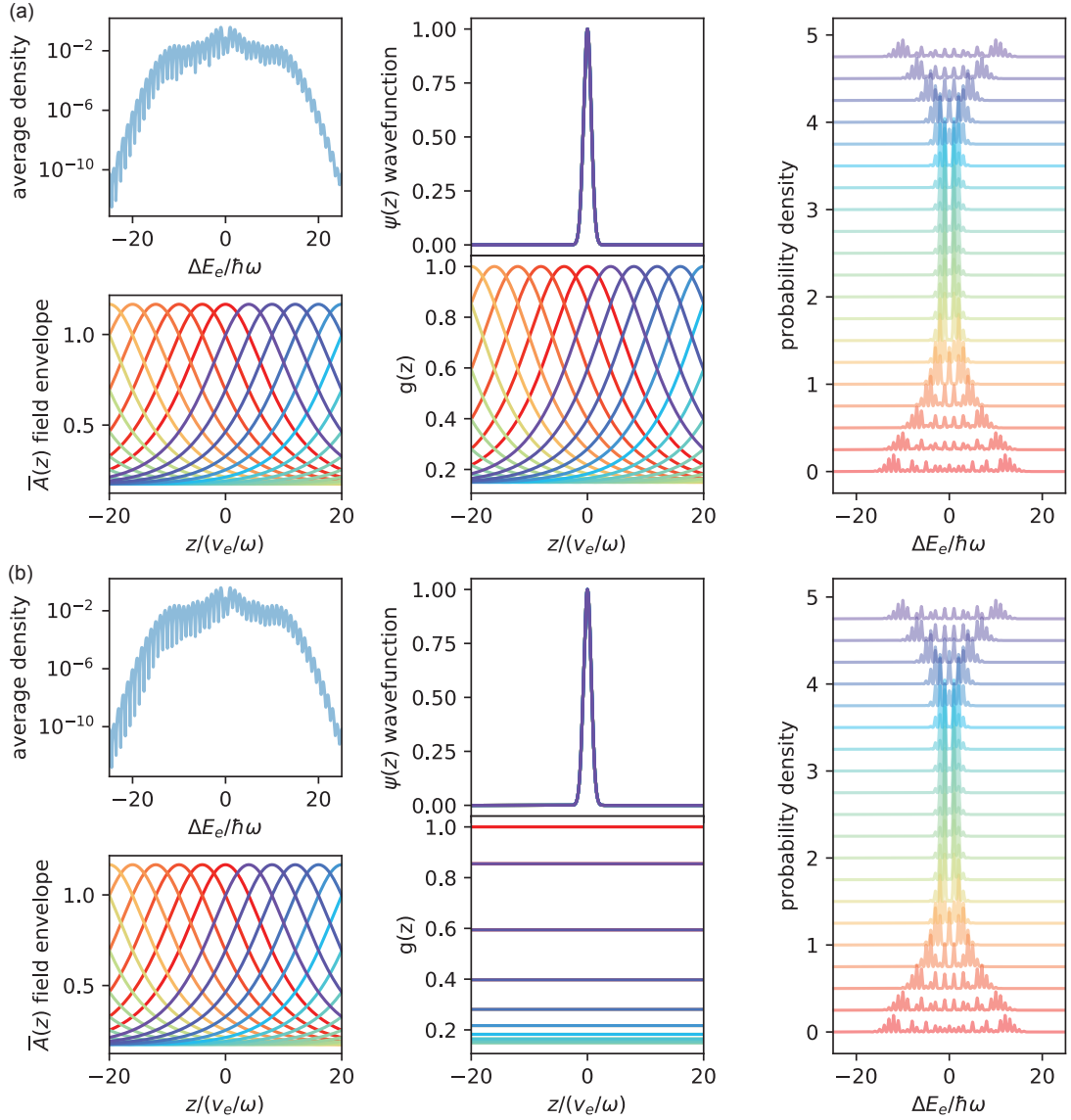


Figure 5.9: ϕ_2 averaged electron spectrum assuming perfect phase- and group-velocity matching. The DKS width is set to $\sim 20 \mu\text{m}$, with a $1/6$ peak amplitude CW background. Electron zero-loss-peak (ZLP) width is 0.5 eV . **(a)** General model considering z -dependent $g(z, \phi_2)$. **(b)** Approximated model with z -independent $g(\phi_2)$. All the electron spectra with different ϕ_2 are offset by integers of 0.25 for visualization. Due to the relatively long optical envelope, little difference is observed in either the ϕ_2 dependent spectra or the averaged one.

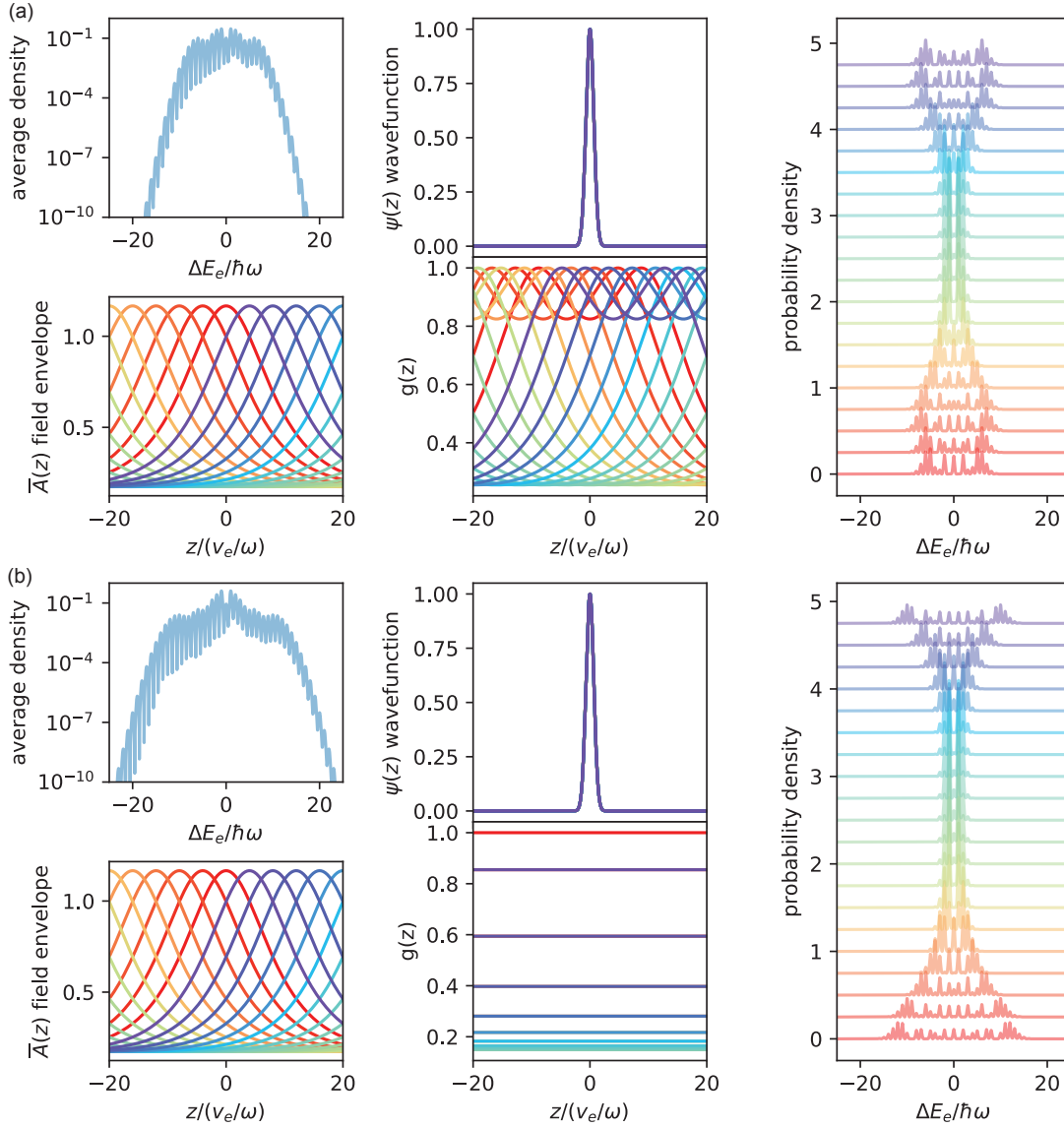


Figure 5.10: ϕ_2 averaged electron spectrum under realistic phase- and group-velocity mismatch. The DKS width is set to $\sim 20 \mu\text{m}$, with a $1/6$ peak amplitude CW background. Electron zero-loss-peak (ZLP) width is 0.5 eV . **(a)** Exact model. **(b)** Approximated model where $g(\phi_2) \sim \bar{A}(\phi_2)$. All the electron spectra with different ϕ_2 are offset by integers of 0.25 for visualization. The characteristic difference in modulation span and amplitude is observed in the averaged spectrum and ϕ_2 -dependent ones, even with broad optical envelopes. This effect is from the effectively broadened $g(z)$ compared to the optical envelope due to group- and phase-velocity mismatch.

5.2 Free-electron interaction with optical continuum

In our visit to the MPI to help them generate DKS in the electron microscope, we used a 200-GHz ring with a cavity loss rate of $\kappa/2\pi = 38.8$ MHz. This level of quality factor is enough for the generation of DKS, as we tested outside the electron microscope. After the e-beam valve is open and the e-beam is positioned next to the waveguide, we observe a slow increase of cavity linewidth and a frequency shift of the resonance in tens of seconds. Afterward, we found that the linewidth of the cavity is broadened to $\kappa/2\pi = 272.6$ MHz due to an increase in optical loss. It is suspected that the high-energy electron beam (200 keV) bombardment on the waveguide induces material damage [159]. Usually, with this level of cavity linewidth, it is impossible to generate DKS due to insufficient optical power. However, as we start pumping the resonator with around 200 mW of on-chip power, we observe that the cavity slowly drifted back to around the original frequency, with a narrower linewidth at $\kappa/2\pi = 39.9$ MHz, with a slightly different mode splitting and line shape. High power pumping is suspected to lead to significant heating at the spots of material damage and recovers from the damage through thermal annealing. With the restored cavity linewidth, we generated DKS inside the electron microscope, with one of the characteristic electron spectra shown in Fig. 5.11 (c), showing a significant deviation from the conventional Bessel distribution. Using our approximated fitting model, we can reliably fit all kinds of electron spectra after interaction with the DKS. Specifically, the electron spectrum would typically consist of a CW component with a narrow span, whereas the DKS component achieves a much broader span due to the much larger peak field of the pulse, though with much lower probability.

One thing to emphasize again is that our experiment does not involve synchronizing the electron arrival time and the DKS pulse. Therefore, these spectra that deviate from the usual Bessel distribution result from the incoherent average of ϕ_2 instead of an actual electron wavefunction that experiences non-uniform phase modulation. Therefore, each single electron effectively interacts only with an almost linear optical field, given our broad optical pulse envelope. The feature of the nonlinear field only appears after averaging different electrons with a random arrival time. Therefore, generating the same averaged electron spectrum is possible using an optical intensity modulator that slowly modulates the intra-cavity field amplitude according to the CW-DKS envelope.

To measure an actual inhomogeneous phase modulation, like the one shown in Ref. [121], synchronization between the optical pulse and the electron arrival time is required. Though technically much harder, it might be possible to phase-synchronize the DKS with the mode-locked laser that drives the electron emission process through pulse pumping the ring resonator [160]. On the other hand, even though no synchronization in our experiment is achieved, we can imagine that the periodic interaction with the soliton pulse can achieve fast periodic modulation of the CW electron beam at hundreds of GHz of repetition rate, which is not typically possible with conventional methods.

After understanding the most general case of free-electron interaction with a classical optical field, we investigate the case when the free electron interacts with quantum optical fields in the next chapter.

Chapter 5. Photon-induced near-field electron microscopy

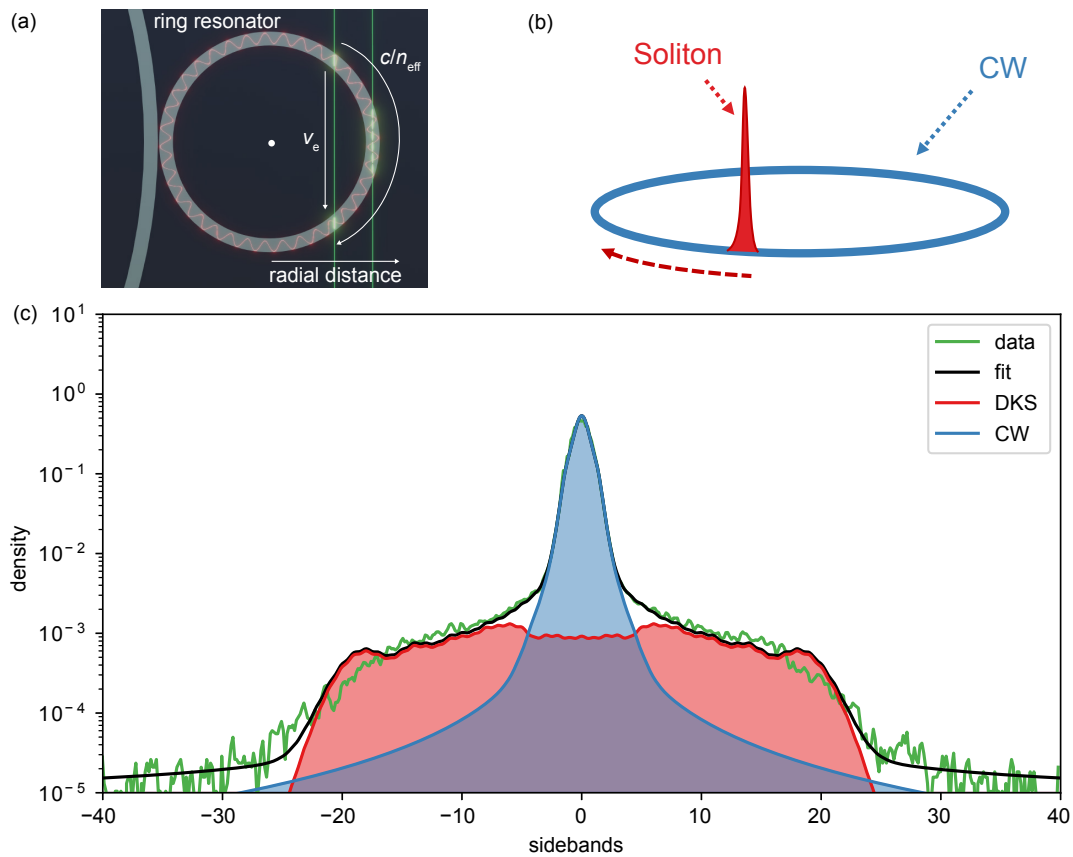


Figure 5.11: **(a)** Geometric configuration of electron-soliton interaction. When interacting with the soliton pulse, we keep the radial distance small. Hence, the electrons only interact with the optical field in a point-like fashion to reduce the effect of group velocity mismatch. **(b)** Cavity field consisting of a CW background and a soliton pulse. **(c)** Electron spectrum fitting using the approximated model, showing the dominant contributions from the CW background and a low probability contribution from the DKS. We define the contribution from the DKS by considering the field around the soliton peak with a maximum distance of 2 times the soliton width. In the fitting, a detector background noise is also assumed.

6 Free-electron quantum optical interaction with photonic integrated circuits

Quantum coherent coupling between distinct physical systems harnesses the advantages and strengths of the different systems to explore new physical phenomena better and potentially develop novel quantum technologies [161, 162]. Optical photons [163] are most commonly used to connect different systems due to the potential for long-range transmission through optical fibers and robustness to decoherence from thermal environments, and have been realized in systems ranging from superconducting qubits [164, 165], solid-state spins [138, 166], ultra coherent mechanics [23, 167], and atomic systems [168, 169, 170, 171, 172], where each offers unique features and advantages to be utilized in a hybrid quantum system. One key aspect of all these systems is the ability to enact high-fidelity quantum control of the interaction with well-defined optical modes in few-photon states.

In the field of electron microscopy, interactions between free electrons and photons have been widely explored in both stimulated [105, 113, 116, 120, 139, 173, 174, 175, 176, 177, 178, 179, 180] and spontaneous processes [113, 145, 181, 182, 183] enhanced by phase-matched interactions and optical resonances [7, 106, 149, 155, 184, 185]. There have also been many proposals that explore the unique quantum properties of electron-photon states [107, 108, 110, 186], assuming the feasibility of coupling electrons to only one optical cavity mode. However, it is still an open question whether high-fidelity quantum control and the strong coupling of this hybrid quantum system can be realized.

High-fidelity quantum control requires high coupling strength between free electrons and optical vacuum fields and low dissipation to keep decoherence at a minimum. The interaction mechanisms and their coupling strengths differ substantially between different physical platforms, which can be categorized into metallic [120] and dielectric structures [7, 105, 121, 148, 149, 175, 176, 178]. For nanophotonic particles, the short attosecond-long interaction time promotes the use of dissipative materials, such as plasmonic structures [187]. The collective electronic response amplifies the interaction while at the same time bringing retardation and dissipation, which is not ideal for quantum-coherent manipulation of electrons with optical states. On the other hand, transparent dielectrics, for which an extended interaction length enhances the coupling, offer a paradigm shift in free-electron quantum optics due to their

Chapter 6. Free-electron quantum optical interaction with photonic integrated circuits

low optical dissipation and practically instant electronic response. Instead of enhancing the interaction by lossy media, optical modes supported by dielectric structures interact with the free electron by a geometric effect through the relativistic field retardation [188], which results in a purely parametric interaction ideally suited for high-fidelity quantum control.

Photonic integrated circuits have only entered the picture very recently [7, 8] in our experiment and have several advantages for free-electron quantum optical experiments. Firstly, integrated photonics enables exquisite control of the optical properties of waveguides [189, 190]. The nearly lossless guided modes [3] and high-efficiency output fiber coupling [191] facilitate coupling to both on-chip [23, 138, 166, 167] and fiber-coupled quantum systems [164, 169, 170, 171, 172]. Additional capabilities are provided by well-established on-chip optical elements such as tunable beam splitters and phase shifters [192], spectral filters [193] and photon counters [194], which offer high-fidelity optical state manipulation and characterization [195]. With the versatile on-chip structures and demonstrated efficient electron phase modulation [7] and electron-photon correlation [8], it is possible to use heralding schemes to shape useful electron and optical states [103, 110, 124, 186] in various application scenarios with photonic integrated circuits.

To transfer the advantages mentioned above to the scenario of generating high-quality quantum states through electron-photon interaction, high-ideality coupling to a single well-defined optical mode is required. However, as we discussed earlier in Section 4.3, due to the complex waveguide structures, parasitic couplings to auxiliary spatial modes cause decoherence of the system, see Fig.6.1(a). In Section 6.2, we first quantitatively investigate this limitation in a realistic experimental scenario and show that with a single-mode waveguide, bigger gap distance, and long interaction length, near-unity coupling ideality and strong coupling [107, 196] can be achieved to the waveguide quasi-TM₀₀ spatial-temporal mode.

Next, we show that even in the limit of single-mode interaction, a state subspace correlation still imposes a fundamental limit to the state fidelity and purity. To address the electron-photon interaction in the conventional quantum optics description, a synthetic ladder state space [103, 107, 108, 110, 116, 186] is usually used (Section 4.2), shown in Fig.6.1(b). This treatment greatly eases the analysis of the interaction between two systems that are actually continuum systems. However, within the subspace of a ladder level, energy conservation enforces a strong correlation between the electron energy loss and the frequency of the photon created. When one neglects the underlying correlation, information loss occurs. This process can be characterized by the state purity \mathcal{P} , which captures both the distance to a pure quantum state and the degree of electron-photon entanglement through the Rényi-2 entropy [197].

Last, in Section 6.3 and Section 6.4, we also propose applications that exploit this underlying correlation to their advantage, e.g., imprinting electron wavefunctions onto optical states, and later examine the state fidelity and purity in quantum state heralding schemes. We find that electrons in particle-like states with high purity are required to generate pure heralded states,

6.1 Electron-photon interactions with dielectric media

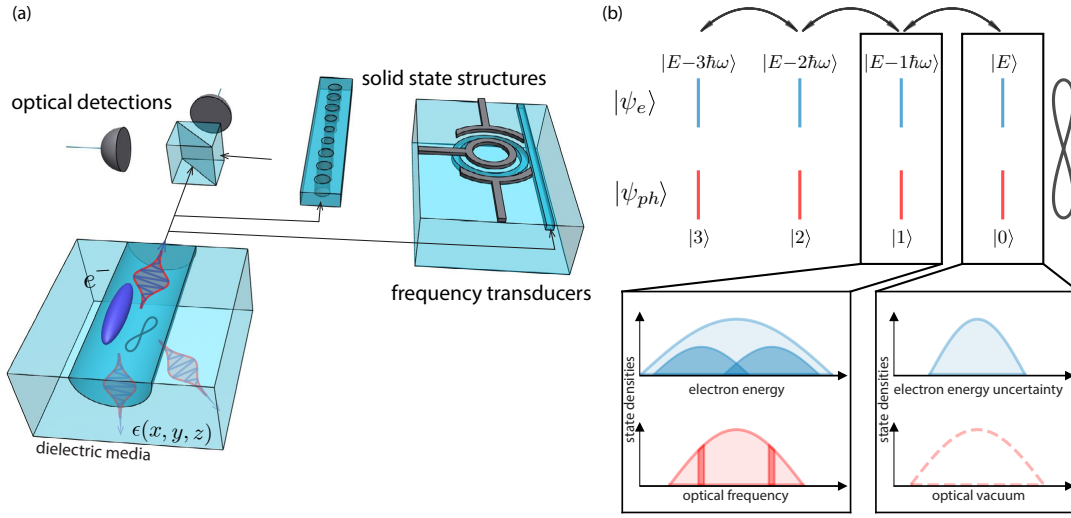


Figure 6.1: **(a)** Illustration of the electron-photon inelastic scattering process mediated by a dielectric waveguide. In an electron microscope, when the high-energy electron passes by a dielectric waveguide structure with a given dielectric permittivity distribution $\epsilon(x, y, z)$, the material dielectric dipoles exert a backaction field (force) on the electron, resulting in correlated electron energy loss and optical emission in both the guided waveguide modes and non-guided bulk modes. High-ideality coupling to a low-loss waveguide mode is required for high-fidelity state preparation and interaction with other quantum systems through optical links. **(b)** Synthetic electron-photon state ladder of the pair state generation through \hat{S}_{e-ph} . Within each ladder state, an underlying subspace still maintains a correlation between electron energy and photon frequencies. For any two optical frequency components (shown in dark red), the correlated electron energy states (shown in dark blue) are only partially degenerate. This correlation can lead to new types of applications but generally leads to degradation of fidelity and purity of the interaction.

and the purity limits are greatly reduced with experimentally feasible interaction length using photonic integrated circuits.

6.1 Electron-photon interactions with dielectric media

In this section, we first recap the theoretical basis we developed in Section 4.3 of free-electron interaction with the optical continuum of a dielectric structure. Here, we formulate the problem as the interaction between propagating free electrons and one single interaction-specific optical spatial mode $\hat{\mathbf{A}}(\mathbf{r}, \omega)$ (see Section 4.3.1 for the field profile) at frequencies ω in the continuum, instead of pre-determined discrete optical modes of the dielectric structure (see Section 4.3.3 for its correspondence to modal decomposition), with the scattering matrix in the interaction picture

$$\hat{S}_{e-ph} = e^{i\hat{\chi}} \exp \left[\int d\omega g_\omega \hat{b}_\omega^\dagger \hat{a}_\omega - h.c. \right], \quad (6.1)$$

Chapter 6. Free-electron quantum optical interaction with photonic integrated circuits

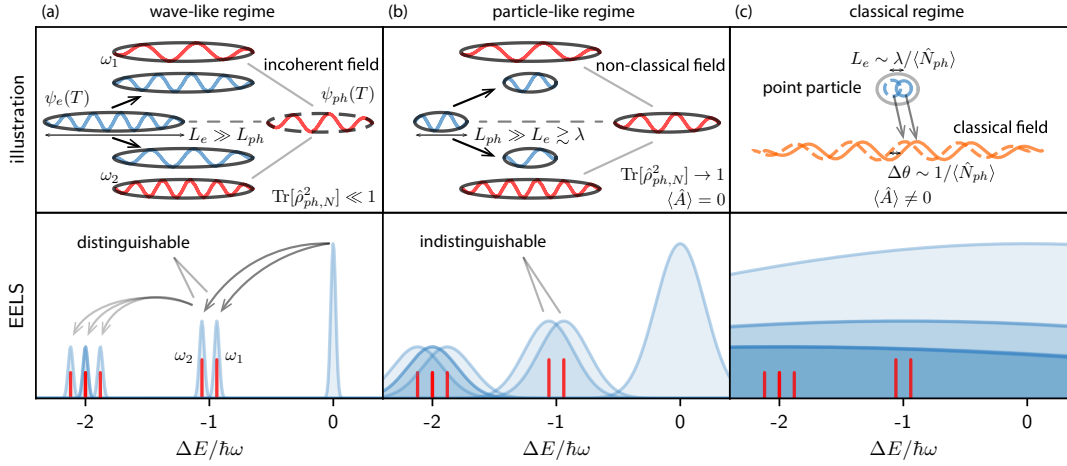


Figure 6.2: Illustration of different parameter regimes of electron-photon interactions. The electron (blue) and photon (red/orange) spatial waveforms as a function of $T = t - z/v_e$, where z is the longitudinal coordinate, are shown in the upper panels, and the corresponding energy (frequency) domain picture is shown in the lower panels. The phase-matching mechanism determines the frequency bandwidth of the generated photon. Two optical frequency components (ω_1 , ω_2) and their correlated electron states are shown in the spatial and energy domain representations to illustrate the qualitative differences between different regimes. The arrows in the panels indicate the direction of the scattering processes. **(a)** Wave-like regime where distinguishable electron states are generated from the emission of photons with the corresponding frequencies. As a result, the optical frequency components can not be coherently combined to form a single-mode field. Therefore, this regime is accompanied by mixed optical ladder states $\rho_{ph,N}$, and incoherent photon emission. **(b)** Particle-like regime where the photon emission at different frequencies generates indistinguishable electron states. The optical state space is sufficiently decoupled from the electron state space and can be described as a single-mode field. This regime has pure optical ladder states $\rho_{ph,N}$, where the synthetic electron-photon state ladder is a valid approximation. **(c)** Classical regime where different photon-sidebands of the electron overlap well, and classical optical field emission with non-zero $\langle \hat{A} \rangle$ is achieved. In the spatial representation, the classical waves are plotted orange to distinguish them from the quantum counterparts in the other regimes.

6.1 Electron-photon interactions with dielectric media

where the phase operator $\hat{\chi}$ acts only on the electron degrees of freedom (ignored in the remaining discussion) and is associated with the Aharonov-Bohm effect of the vector potential [127]. Continuum photon ladder operators \hat{a}_ω and electron operators \hat{b}_ω characterize the energy exchanges between the electron and the optical field at a given optical frequency ω in an energy-conserving manner. The interaction with the vacuum optical fields results in transitions into lower electron energy states with energy differences of $\hbar\omega$. We define the electron-photon coupling strength at a given photon energy $\hbar\omega$ in terms of the vacuum coupling strength g_ω as $\Gamma(\omega) = |g_\omega|^2$. The phase matching condition gives the vacuum coupling strength a finite bandwidth. In the limit where $\Gamma(\omega) \ll 1$, $\Gamma(\omega)$ is equivalent to the electron energy loss probability per unit optical frequency of dielectric media measured in electron energy loss spectroscopy (EELS) and can be derived classically in a simplified picture (See Section 4.3.2). To simplify the discussion here, we also assume a point-like transverse distribution for the electron (see Section 4.3.1 for the discussion on the transverse effect), and the vacuum coupling strength g_ω is derived at a corresponding transverse position \mathbf{R}_0 .

The interaction with the optical continuum, as opposed to the conventional discrete energy-ladder levels illustrated in Fig.6.1 (b), results in a continuum electron-photon pair state

$$|\psi_e, \psi_{\text{ph}}\rangle = \exp\left(-\frac{\int d\omega |g_\omega|^2}{2}\right) \times \left(\sum_N \frac{\left(-\int d\omega g_\omega^* \hat{b}_\omega \hat{a}_\omega^\dagger\right)^N}{N!} \int dE \psi(E) |E\rangle |0\rangle\right), \quad (6.2)$$

where $\psi(E)$ is the electron wavefunction in the energy domain. In this chapter, to simplify the notation, we use zero-loss peak (ZLP) to refer to this quantum coherent energy distribution $\psi(E)$ of the electron, whereas in other chapters, ZLP typically includes also the classical statistical uncertainty of the electron energy. We show in Fig. 6.2 that depending on the size of the electron wave-packet [109, 198, 199], the electron-photon interaction can be categorized into three regimes. The classical regime has been explored [110, 124], and is accessible through laser modulation schemes [103, 116, 143, 200]. Some electron-microscopes equipped with a monochromator fall into the wave-like regime [185, 201], while others with longer interaction length, including our experiment demonstration [8], are in an intermediate wave-particle-like regime. The simplified electron-photon ladder picture is only partially valid in both cases.

In the wave-particle-like regime, the ladder state

$$|\psi_e, \psi_{\text{ph}}\rangle_N \propto \int dE \psi(E) \left(\int d\omega g_\omega^* \hat{b}_\omega \hat{a}_\omega^\dagger\right)^N |E\rangle |0\rangle \quad (6.3)$$

maintains a correlation between electron energies E and photon frequencies ω . To go back to the simplified ladder picture, one traces out the continuum of electron states within each ladder as

$$\hat{\rho}_{\text{ph},N} = \text{Tr}_E [|\psi_e, \psi_{\text{ph}}\rangle_N \langle \psi_e, \psi_{\text{ph}}|_N], \quad (6.4)$$

Chapter 6. Free-electron quantum optical interaction with photonic integrated circuits

which results in a degradation of the optical state purity

$$\mathcal{P} = \text{Tr} \left[\hat{\rho}_{\text{ph},N}^2 \right]. \quad (6.5)$$

A narrower phase-matching bandwidth relative to the electron energy uncertainty is generally required to reduce the degree of correlation and reach the particle-like regime.

In later sections, we show that in photonic integrated circuits, the prolonged interaction length can help reduce the phase-matching bandwidth and lower the energy correlation for a single waveguide mode, pushing the system parameters well into the particle-like regime. However, the complex dielectric environment generally results in multi-mode electron-photon interactions, e.g., parasitic coupling to other optical mode families and other non-guided spatial modes supported by open-ended dielectric substrates. The effective phase-matching bandwidth of the multi-mode coupling is generally large, and a longer interaction length can not suppress the corresponding electron-photon correlation. Therefore, we will first quantitatively analyze how to constrain the interaction to the single-mode case effectively.

Designing and fabricating waveguide structures that achieve 100% spatial overlap between a waveguide mode and the electron optical emission over the whole optical frequency range is generally hard. Therefore, instead of mode-matching, our strategy to achieve single-mode interaction is to exploit a combination of effects resulting from the phase-matching mechanism.

To quantitatively account for the infinite number of interacting spatial optical modes, it is generally impractical to use the conventional modal decomposition method [120]. Instead, as mentioned before, we combine all the possible coupling contributions from different modes into one single interaction-specific spatial mode, following a three-dimensional QED treatment [114]. This formalism, derived using the fluctuation-dissipation theorem, was previously used when analyzing electron energy loss probabilities with dissipative materials [113] that exhibit a delayed material response, the dominant contribution to the main electron energy loss channels. The dielectric materials we study here are transparent in the optical frequency bands of interest. In this sense, we can set $\text{Im}\{\epsilon(\mathbf{r}, \omega)\} \rightarrow 0$, which corresponds to an instantaneous dielectric dipole response and further simplifies the analysis. For materials with sufficiently low absorption, which are used for integrated waveguides designed to guide optical fields, the interaction is purely contributed from the relativistic field retardation effect [188] and prohibits energy and momentum transfer to the material, avoiding loss of coherence. In this sense, the whole process of an electron interacting with a dielectric waveguide is *parametric* in nature.

6.2 Coupling ideality

In this section, we show how to achieve ideal single-mode electron-photon coupling with photonic integrated circuits. As an example, here we quantitatively investigate the electron-photon coupling mediated by an integrated Si_3N_4 waveguide embedded in a silica substrate

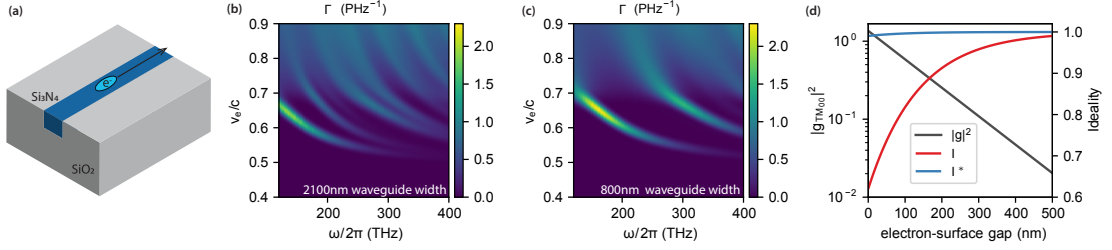


Figure 6.3: **(a)** Illustration of the waveguide structure studied, consisting of a Si_3N_4 waveguide embedded in a silica substrate. The free electron passes by the top surface of the waveguide and generates correlated optical emission. **(b-c)** Electron-photon coupling strength $\Gamma(\omega)$ spectrum for different waveguide geometries and electron positioning. The coupling spectrum is plotted as a function of electron velocity v_e and optical frequency ω . The waveguides have a thickness of 650 nm, and widths of **(b)** 2.1 μm and **(c)** 800 nm. Coupling to different waveguide mode families appears as multiple coupling bands, and their phase-matching bandwidth is kept constant for better visualization. **(d)** Total coupling strength of TM_{00} mode vs. non-conditional and conditional coupling idealities (I and I^* respectively), as a function of gap distance between the electron beam and the waveguide surface, with 800 nm waveguide width, 100 μm interaction length and $v_e/c = 0.65$ electron velocity.

without top cladding (the bottom silicon substrate is not considered), shown in Fig. 6.3(a). This type of structure has been used in our experimental investigations of both stimulated phase-matched interactions [7] and spontaneous inelastic scattering [8] between free electrons and the evanescent field of a photonic-chip-based optical microresonator, and features ultra-low material-limited loss of 0.15 dB/m [3]. We calculate the electron-photon vacuum coupling strength (numerical details in Section 6.2.1) and plot it in Fig. 6.3(b-c) as a function of electron velocity for optical wavelengths ranging from 780 nm to 2.5 μm (where all relevant material properties are well known), which covers most of the frequency bands that are of general interest.

Under the optimal phase-matching condition, the interaction strength of the waveguide transverse modes scales quadratically to the interaction length since they co-propagate with the electron, in contrast to the linear relation of bulk modes. In reality, waveguide-mode phase velocity differs at different optical frequencies. Through the phase-matching mechanism, linear chromatic dispersion limits the coupling bandwidths to scale inversely proportional to the interaction length. With prolonged interaction length, coupling strengths to different waveguide transverse mode families are isolated in optical frequencies and exhibit peak features shown in Fig. 6.3(b-c). Dispersion-free systems are generally feasible in higher dimensions and have been realized in specially structured photonic lattices [202, 203, 204], where the optical modes of interest are generally unguided. In integrated photonics, advances in dispersion engineering have enabled waveguide designs that tailor the modal dispersion [190, 205], promising dispersion-free quadratic coupling enhancement over a broad frequency range. Our study focuses on translation-invariant straight waveguides, which exhibit chromatic dispersion determined by the waveguide materials and geometry.

Chapter 6. Free-electron quantum optical interaction with photonic integrated circuits

The waveguide mode families have finite coupling bandwidths and are well isolated from each other. Therefore, we define discrete spatial-temporal optical modes $\hat{a}_m \propto \int d\omega g_{m,\omega} \hat{a}_\omega$ associated with different waveguide mode families from the optical continuum based on the vacuum coupling strengths $g_{m,\omega}$ of the interaction (details see Section 4.3.3). The coupling strength of a given mode family \hat{a}_m ,

$$|g_m|^2 = \int d\omega |g_{\omega,m}|^2, \quad (6.6)$$

scales linearly with interaction length and inversely with chromatic dispersion. We quantitatively evaluate the coupling strengths $|g_m|^2$ to different spatial-temporal modes \hat{a}_m based on the fitted interaction strength $|g_{m,\omega}|^2$ from the simulation results. As an example, for the quasi-TM₀₀ mode of the 800 nm wide waveguide shown in Fig. 6.3(c), for an electron-waveguide gap of 100 nm, a strong coupling strength [196] of $|g_{\text{TM}_{00}}|^2 \sim 1$ can be achieved with 200 μm of interaction length at an electron velocity of $v_e/c = 0.65$ (a kinetic energy of 160 keV). A 100-nm gap and a 100- μm length of e-beam propagation is experimentally feasible and demonstrated in our experiment [8] with a gradient $d|g_{\text{TM}_{00}}|^2/dz \sim 5 \text{ mm}^{-1}$.

Using the procedure described in the previous paragraph, we quantitatively investigate the influence of competing waveguide modes for a given waveguide configuration and how we can approach unity coupling ideality by properly choosing waveguide geometry and material, as well as electron beam positioning and velocity. Since the lowest order TM₀₀ mode is generally the most strongly coupled and is the most spectrally isolated mode, and can couple efficiently out of the photonic chip using fiber coupling, we target unity coupling ideality, defined by the coupling fraction

$$I \equiv |g_{\text{TM}_{00}}|^2 / \int d\omega |g_\omega|^2, \quad (6.7)$$

to the TM₀₀ mode.

From the numerical result shown in Fig. 6.3(b-c), we find that reduced waveguide cross-section (to single-mode dimension) enhances the mode index contrast and results in more spectrally isolated fundamental modes. With better frequency isolation, the evanescent field of the coupled higher-order modes decays much faster than that of the fundamental mode in the near field due to their higher optical frequencies. Therefore, we can enhance the ideality by increasing the gap distance to the waveguide surface, with $1 - I$ decreasing exponentially with gap distance (details in Section 6.2.1).

In addition to coupling to higher-order waveguide mode families, we can also identify a rising background in the high-velocity region. It can be attributed to strong coupling to the substrate modes in the Cherenkov regime ($v \gtrsim 0.7c$), where the charged particle velocity exceeds the phase velocity of light in dielectric media (here: silica). In Section 6.2.2, we quantify the contribution of the substrate bulk modes. This contribution can be suppressed by either choosing an electron velocity well below the Cherenkov regime of the substrate or by using a

low-index material as the substrate (e.g., by suspending the structure in the vacuum).

Here, we quantitatively analyze the coupling idealities in different application scenarios and show the results in Fig. 6.3(d). First, we consider state heralding applications, e.g., heralded single-photon sources by photon-energy loss selection with EELS. We assume an initial electron state with a fitted 0.6-eV Voigt zero-loss-peak (ZLP) profile, and show that by conditioning on the first energy-loss sideband, one can easily achieve more than 99 % conditional coupling ideality I^* to the TM_{00} mode outside the Cherenkov regime ($v_e \lesssim 0.7c$) with a single-mode waveguide and the electron beam positioned $\gtrsim 100\text{ nm}$ above the surface (details in Section 6.2.1). For a general application that is sensitive to the full optical spectrum, we show that more than 95 % non-conditional coupling ideality I can be achieved with the electron beam placed $\gtrsim 300\text{ nm}$ above the surface, limited by the parasitic coupling to the higher-order waveguide modes. The coupling to the higher-order waveguide modes is not a fundamental limitation, as one can always increase the gap distance from the waveguide surface to achieve higher ideality at the expense of reduced coupling strength. This trade-off is also illustrated in Fig. 6.3(d), where the total coupling strength $|g_{\text{TM}_{00}}|^2$ is plotted against the coupling ideality. However, this effect can generally be compensated with longer interaction length L . As a result, given a fixed waveguide geometry and a target total coupling strength, the deviation from unity is given by $1 - I \propto L^{-1}$.

In the particular case where the waveguide loops and forms a resonator, such as our experiment platform, the result of the open-ended waveguide studied here can equally apply (see Section 6.2.3). In most scenarios, where the electron longitudinal wavefunction is shorter than the cavity round trip length, or in the frequency domain picture where the electron zero-loss-peak (ZLP) width is broader than the cavity free-spectral-range, there is no difference in terms of coupling ideality between a straight waveguide and a resonator. The physical picture is that when the emitted optical pulse does not interact with the electron a second time, the emission is only determined by the local structure around the electron and any non-local emission enhancement, e.g., Purcell effect [206] in atom-cavity systems, is absent. In the case of a resonator, the pulse will circulate multiple times and exit the cavity as a pulse train, and exhibit in the frequency domain as a comb-structure, as was shown in [184, 185] and also our experiment [8] in Section 7.

Note that the experimentally measured ZLP width consists of a coherent energy spread of a single-electron wavefunction, e.g., inherited from the driving laser pulses in the cold field electron emission process, and also an incoherent broadening due to, e.g., the statistical imprecision of the electron acceleration voltage and the measurement instrument. In this thesis, we primarily use ZLP width to refer to the coherent energy width unless otherwise specified.

Generally, residual coupling to the higher-order modes can be further mitigated with heralding schemes. For example, we can place a bandpass spectral filter [193] around the frequency band of the target mode. Upon conditioning on photon-absence events at the dark port of the

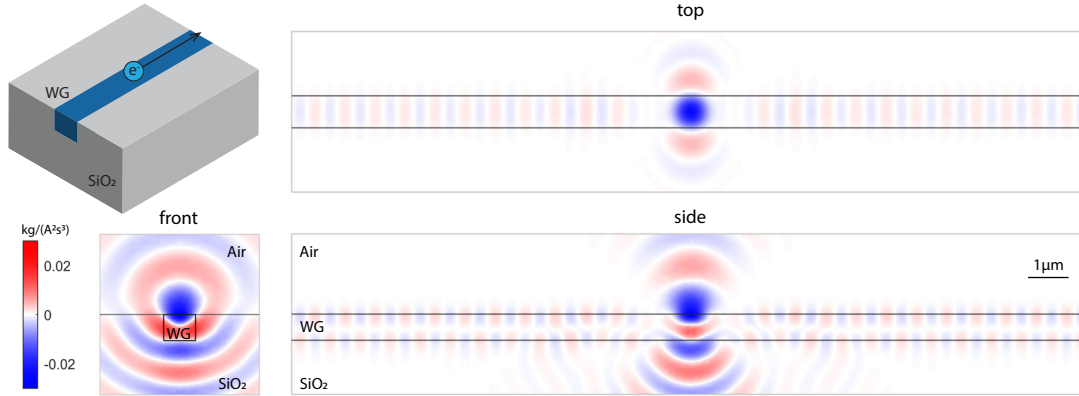


Figure 6.4: Spatial pattern of $\text{Im}[G_{zz}(\mathbf{r}, \mathbf{r}_0, \omega)]$ for the case of a Si_3N_4 waveguide embedded in a silica substrate. In addition to emission into the substrate and free space, some guided modes in the waveguide are also excited by the oscillating electric current dipole and form a beating spatial pattern amongst guided modes along the waveguide direction.

filter, we can further approach unity ideality and eventually be limited by the background bulk contribution. As long as the velocity is far from the Cherenkov regime of the substrate material, we estimate this contribution to be far less than 1%. With near-unity coupling ideality, the fidelity and purity of the interaction will be limited to the correlation between electron energy and the optical frequency components of a single spatial-temporal optical mode within the ladder state space. In Section 6.3 and Section 6.4, we discuss this fundamental limitation in the cases of state heralding schemes.

6.2.1 Finite element method simulation of Green functions

Since all the physical quantities we are interested in can be related to the Green tensor of the classical Maxwell equation given the dielectric structure of interest, we numerically solved the relevant Green tensor component $G_{zz}(\mathbf{r}, \mathbf{r}', \omega)$ of an infinitely long optical waveguide with finite element method (FEM). The spatial map of the imaginary part of the Green function is illustrated in Fig. 6.4. The Green function can be understood intuitively as the Fourier component of the optical field at frequency ω that is excited at position \mathbf{r} by the propagating electron at position \mathbf{r}' . Then, the phase-matching condition determines whether this field constructively or destructively builds up at a given electron velocity.

The Green tensor solution of the Maxwell equation is not directly supported in COMSOL but can be retrieved by Frequency domain study with the radio frequency (RF) module. The waveguide is an air-cladded Si_3N_4 slab embedded in a SiO_2 substrate with different geometries mentioned in the previous section. Perfect matching layers at boundaries are used to prevent boundary reflections and, in turn, allow us to simulate an infinitely long waveguide. In order to solve for the Green function $G(\mathbf{r}, \mathbf{r}', \omega)$, a point oscillating electric current dipole $\mathbf{J}(\omega) = \mathbf{p}(\omega)\delta(\mathbf{r} - \mathbf{r}_0)$ is placed above the waveguide surface at position \mathbf{r}_0 (typically 100 nm or

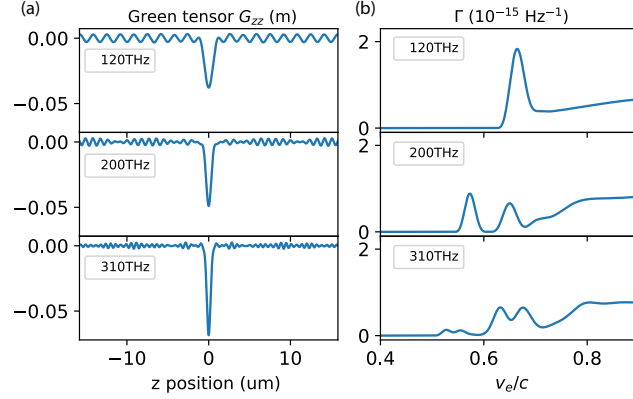


Figure 6.5: **(a)** Examples of the Green function $\text{Im}[G_{zz}(\mathbf{r}, \mathbf{r}_0, \omega)]$ along the trajectory of the electron at different optical frequencies, and **(b)** the corresponding vacuum coupling strength at different electron velocities, for a $50 \mu\text{m}$ interaction length. The spatial beating of many mode families is visible in the Green functions and the coupling strength. The coupling to different mode families is phase-matched at different electron velocities at a given optical frequency. When the electron velocity is in the Cherenkov regime ($v \gtrsim 0.7c$), the energy loss is eventually dominated by the substrate loss.

300 nm). COMSOL solves the electric field, which relates to the Green tensor as

$$\mathbf{E}(\mathbf{r}, \omega) = -4\pi i \omega G(\mathbf{r}, \mathbf{r}_0, \omega) \cdot \mathbf{p}(\omega) \quad (6.8)$$

and thus if one wishes to retrieve G_{zz} component one needs to orient the electric dipole $\mathbf{p} = p\hat{\mathbf{z}}$ along the z direction $\hat{\mathbf{z}}$, and look at the electric field z component E_z , such that

$$G_{zz}(\mathbf{r}, \mathbf{r}', \omega) = \frac{E_z(\mathbf{r}, \omega)}{-4\pi i \omega p(\mathbf{r}', \omega)} \quad (6.9)$$

The results are illustrated in Fig. 6.4. The imaginary part of the Green function can be thought of as the spatial pattern of electron emission in the waveguide (or surrounding substrates) before the application of phase-matching condition. Given the electron velocity, the application of phase-matching

$$\mathbf{U}_{\hat{a}_\omega}(\mathbf{r}) \propto \int dz e^{i\omega z/v_e} \text{Im}[G(\mathbf{r}; \mathbf{R}_0, z; \omega) \cdot \hat{\mathbf{z}}], \quad (6.10)$$

retrieves the field function of the excited optical mode. The Green function along the electron trajectory is shown in Fig. 6.5(a), where one can clearly see the bulk mode contribution near the dipole position and spatial beatings of different waveguide modes under some conditions.

With the optimal phase-matching condition, the coupling strength at a given optical frequency (or a discrete cavity mode) scales quadratically with the interaction length, a unique feature of

Chapter 6. Free-electron quantum optical interaction with photonic integrated circuits

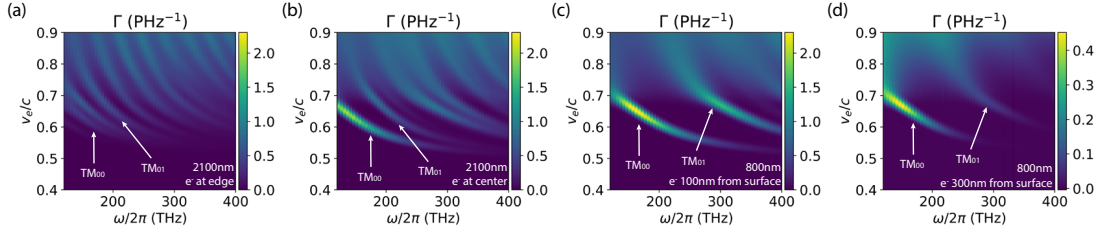


Figure 6.6: Electron-photon coupling spectrum with $50\ \mu\text{m}$ interaction length for different waveguide geometries and electron positioning. The coupling spectrum is plotted as a function of electron velocity v_e and optical frequency ω . The waveguides have a thickness of $650\ \text{nm}$, and widths of **(a-b)** $2.1\ \mu\text{m}$ and **(c-d)** $800\ \text{nm}$, and are embedded in a silica substrate. Coupling to different waveguide mode families appears as multiple coupling bands. Coupling ideality to the target TM_{00} mode is improved by changing the electron beam transverse position from waveguide edge ($100\ \text{nm}$ from surface) **(a)** to waveguide center **(b)**, from multimode waveguide **(b)** to single mode waveguide **(c)**, and moving further away ($300\ \text{nm}$ from surface) **(d)** from the waveguide surface. The waveguide widths and the relative positions of the electron beam are also labeled at the lower right corner of the panels.

guided modes co-propagating with the flying electron. For the spatial modes in the substrate bulk, the excited field is localized around the electron position. Without the benefit of constructive interference from co-propagation with the flying electron, their intensity only scales linearly to the interaction length.

The total coupling strength is related to the Green function through a spatial Fourier transform and shown in Fig. 6.5(b), where one can identify several prominent peaks, mainly contributed from the waveguide modes, and a rising background in the Cherenkov regime ($v \gtrsim 0.7c$) of the silica substrate due to the enhanced bulk mode coupling. The Blackman window is used to eliminate the ripples from the Fourier transform due to finite simulation length and shapes each coupling band to a near-Gaussian shape for easier fitting of the coupling strength with a Gaussian function. The center velocity of the peaks corresponds to the optical mode phase velocity, and the interaction length determines the bandwidth. To improve visualization, we set the interaction length to 30 wavelengths to keep the bandwidths at different optical frequencies uniform. By sweeping the optical frequency in the simulation across the range where we have access to material permittivity, one retrieves the 2D maps shown in Fig. 6.6.

With a multi-mode waveguide, shown in Fig. 6.6(a-b), the effective mode index difference between the fundamental mode and higher-order modes is relatively weak at the same optical frequency, which leads to multi-mode electron-photon interaction within a given frequency band. When the waveguide cross-section is reduced (referred to as *single-mode* waveguide), shown in Fig. 6.6(c), one can enhance the mode index contrast. As a result, the mode frequency spacing is increased, such that the coupled fundamental modes are better isolated from the other mode families. Since most transmission electron microscopes (TEMs) have an energy resolution around $0.5\ \text{eV}$ ($120\ \text{THz}$ in optical frequency), it is crucial to create a large frequency spacing between the phase-matched optical modes so that the interaction with individual

modes can be energy resolved.

The difference between multi-mode and single-mode waveguides in fiber optics is usually quantified by a V-number, a normalized frequency parameter that determines the number of modes of a step-index fiber, as

$$V = \frac{2\pi r}{\lambda} \sqrt{n_1^2 - n_2^2} \quad (6.11)$$

where r is the radial size of the core, n_1 is the core material index, and n_2 is the cladding material index. The single-mode guiding criteria $V < 2.4$ is satisfied by our single-mode waveguide dimension. Such a criterion is crucial for single-mode guiding when used in fiber-optic applications. Here, our design goal is to increase the mode frequency spacing between mode families. Therefore, we only use it as a guiding principle, not a strict criterion.

Due to the higher optical frequency, the evanescent field of the coupled higher-order modes decays faster than that of the coupled fundamental mode. In Fig. 6.6(d), we show that one can further enhance the coupling contrast between the fundamental mode and higher-order modes by placing the electron beam further away (200 nm) from the waveguide surface. In this way, the interaction exponentially favors the fundamental mode at the expense of weaker interaction strength $|g_{\text{TM}_{00}}|^2$, which can be compensated for with a longer interaction length (5 times longer for the shown example).

As discussed in the previous section, the Cherenkov radiation contributes to a rising background in the high-velocity region. In Section 6.2.2, we isolate the contribution of the substrate bulk modes.

We now quantitatively evaluate the coupling ideality to the TM_{00} mode as a function of electron velocity. We fit the coupling spectra with Gaussian functions, illustrated in Fig. 6.7(a), and calculate the conditional and non-conditional idealities as a function of electron velocities, shown in Fig. 6.7(b-c).

6.2.2 Substrate and thin film losses

Though not discussed in the main section, there are different scaling of $\Gamma(\omega)$ for bulk substrate ($\propto L$), thin film ($\propto L \log L$), and guided modes ($\propto L^2$), see Fig. 6.8. We show their coupling spectrum characteristics in Fig. 6.9 with an electron 100 nm above the dielectric surface. It is shown that for a given frequency component ω , the quadratic scaling of a guided mode will dominate the interaction. However, for a waveguide structure with linear dispersion (e.g., the one shown in Fig. 6.9(a)), the phase-matching condition will enforce a linear scaling of the total deposited quanta into one particular waveguide mode. However, due to the relatively weak dispersion of the waveguide modes, the coupling contribution from the waveguide modes dominates over substrate losses, where the latter accounts for far less than 1% of the total coupling strength over a 0.6-eV band with electron velocity $v_e/c \leq 0.6$. For unpatterned thin

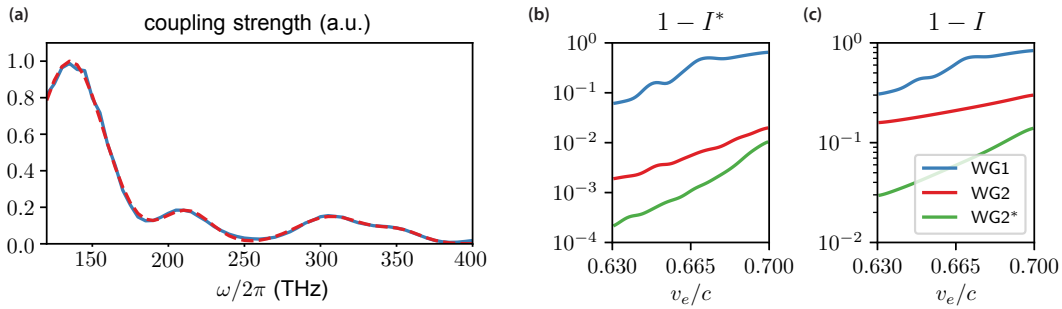


Figure 6.7: **(a)** An example fitting of the coupling spectrum to extract the coupling idealities. Calculated coupling ideality deviations from unity with **(b)** sideband-conditioned ($1 - I^*$) and **(c)** non-conditioned ($1 - I$), shown with different waveguide/electron configurations (WG1:2.1 μm width; WG2:800 nm width; WG2*:electron beam 200 nm further away from the waveguide surface), as a function of electron velocity.

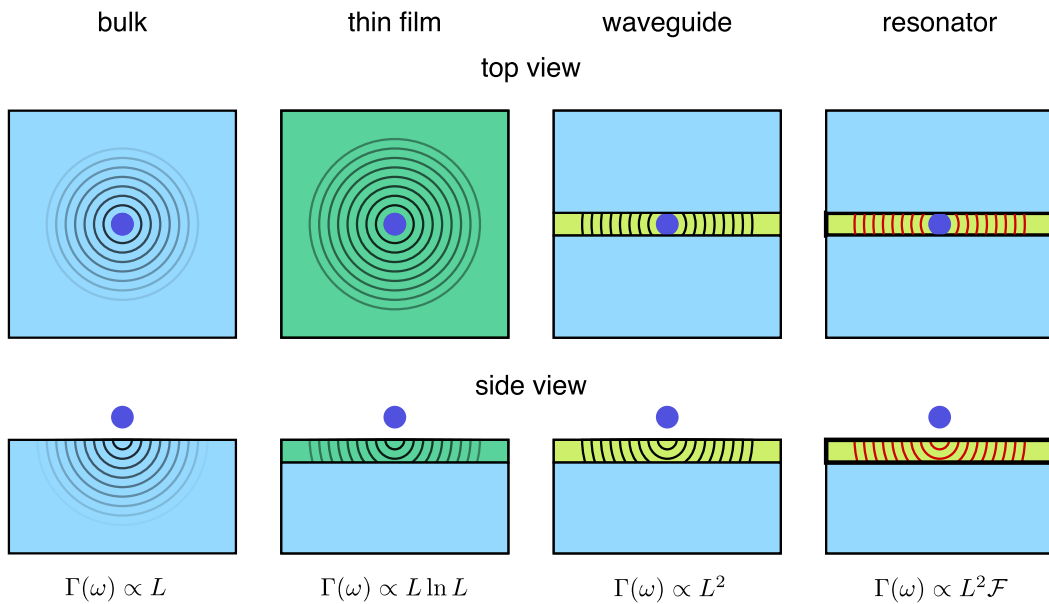


Figure 6.8: Comparison of CL emission patterns at different dielectric environments. In the cases of bulk and thin film dielectric environments, the optical excitation decays over the spatial extent, resulting in a mostly linear scaling of interaction strength to the interaction length. In the cases of waveguide and waveguide resonator, the optical excitation co-propagates with the electron, resulting in a quadratic length dependence of interaction strength (the resonator case is also enhanced by cavity finesse (\mathcal{F}) when on resonance).

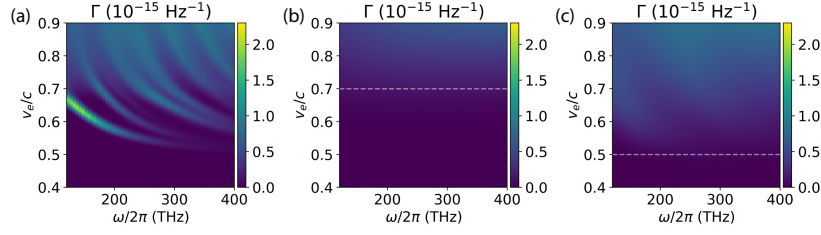


Figure 6.9: Electron energy loss spectrum for a $50 \mu\text{m}$ interaction distance with (a) waveguides, (b) silica substrate, and (c) Si_3N_4 thin film on silica substrate. Notice that for a waveguide, the scaling is quadratic to distance and more structured, whereas for substrate and thin film, the scaling is mostly linear, and the emission is more broadband. The interaction with the waveguide mode will prevail over the substrate and thin film over an interaction length of just a few wavelengths. The dashed gray lines are guides to the eye, showing Cherenkov regime boundaries for silica and Si_3N_4 .

films, the total photon emission is 70% lower than for a waveguide, and the emission is less structured and hard to collect. Note that due to chromatic dispersion, the total coupling strengths of different spatial-temporal optical modes are linearly dependent on distance. Therefore, the ratio of different coupling contributions is distance-independent and depends only on waveguide dispersion, routing, and e-beam positioning.

6.2.3 Interaction with optical resonators

We only discussed results for open-ended waveguides so far. However, most of our current experiments [7, 8] use optical resonators with a discrete set of well-defined frequency modes instead of a continuum of frequency modes in the case of a waveguide. These well-defined modes in state-of-the-art resonators typically have optical line widths of tens of MHz [3], and it is difficult to resolve their Green functions by sweeping the optical frequencies in FEM simulations. Nonetheless, their Green functions can be easily related to the one of open-ended optical waveguides by their optical susceptibility function $\chi(\omega) = \frac{2}{\pi} \frac{F}{1+4(\omega-\omega_0)^2/\kappa^2}$ enforced by the resonator periodic boundary conditions, describing an optical resonance with center frequency ω and Finesse $F = \frac{\Delta\nu_{\text{FSR}}}{\kappa}$, where the cavity free-spectral-range (FSR) is used. We can retrieve the resonator Green function $G(\omega)$ by separating the open waveguide Green function into contributions from different cavity modes (with mode field function $\mathbf{U}_m(\mathbf{r})$, details see Section 4.3.3)

$$G_m(\mathbf{r}, \mathbf{r}', \omega) = \mathbf{U}_m(\mathbf{r}') \int d^3 \mathbf{r}'' \epsilon(\mathbf{r}'', \omega) \mathbf{U}_m^*(\mathbf{r}'') G(\mathbf{r}, \mathbf{r}'', \omega), \quad (6.12)$$

and multiplying the resonance susceptibilities $G(\omega) = \sum_m G_m(\omega) \chi_m(\omega)$. For a closed-loop resonator structure, the corresponding interaction strength $\Gamma(\omega)$ will have a narrow-linewidth comb-like structure (Section 7.2) instead in frequency space, compared to the continuum case of an open-ended waveguide, with the peak intensity enhanced by a factor of $\frac{2F}{\pi}$.

Chapter 6. Free-electron quantum optical interaction with photonic integrated circuits

A comparison between a waveguide and a resonator coupling to free electrons (Γ and Γ_r respectively) is illustrated in Fig. 6.10. The comb-like structure in the electron energy-loss spectrum results from the spectral property of the resonator that is non-local to the interaction region, and is only accessible since the interaction is analyzed in the electron energy basis, whose state is also non-local in nature. However, to access these comb-like features in an EELS experiment, the electron-cavity characteristic interaction time (determined by the measured electron ZLP) has to be longer than the round trip time of the resonator, thus satisfying the energy-time uncertainty principle. Nonetheless, the comb-like structure can always be accessed from the optical side with a measurement time longer than the round trip time, as was shown in Section 7.2.

There is also no difference in the total coupling strength in a given mode family for the open waveguide case and the resonator case, as long as the phase-matching bandwidth $\Delta\nu$ is much larger than $\Delta\nu_{\text{FSR}}$. The resonator structure will considerably alter the total interaction strength $|g_m|^2$ of a mode family when the phase-matching bandwidth $\Delta\nu$ is on the frequency scale of one FSR. The minimum number of modes inside the phase-matching bandwidth can be estimated with $N \sim \frac{1}{|n_g - n_{\text{eff}}|}$ (for common dielectric materials $\sim 5 - 20$), so in order to access the regime where the phase-matching bandwidth is smaller than the FSR, one requires $|n_g - n_{\text{eff}}| > 1$, which is generally very difficult to achieve with structures using only dielectric materials. However, with common dielectric structures and careful mode dispersion engineering, the regime $N = \mathcal{O}(1)$ where the resonance structure has a small impact is accessible.

The motivation for using a resonator instead of an open waveguide is that the optical resonance frequencies are more passively stable, and the wavepackets generated from each resonator mode are generally much longer than the optical pulse length enforced by the phase-matching bandwidth from an open waveguide and have energy density enhanced by the cavity finesse at resonant frequencies. Therefore, resonators have advantages in experiments where optical excitation needs to interfere with a reference local oscillator, and good mode-matching is required. Resonators also provide advantages in experiments where optical frequency filtering is required since the optical density of the excitation is concentrated in frequency. We show a frequency conversion example in Section 6.4.2 to exploit this advantage of optical resonators to convert THz broad optical excitation to MHz broad optical or microwave excitation, useful for bridging interactions with superconducting qubits, mechanical oscillators, and long-life-time optical qubits.

6.3 Shaping optical states from measurements on electron energy

In this section, we consider the case of heralding a general optical state by measuring the electron energy. To simplify the discussion here and capture the main features of the physics considered, we assume coupling to a single spatial-temporal optical mode with $I = 1$ and a coherent electron wavefunction $\psi(E)$ prepared before the interaction. The effect of electron sideband overlaps (with expression shown in Section B.14) is not considered since they can be

6.3 Shaping optical states from measurements on electron energy

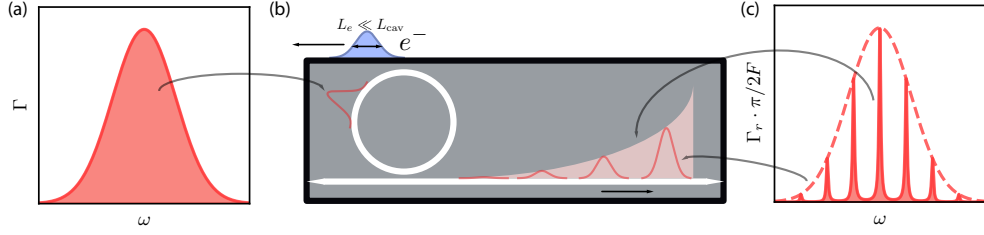


Figure 6.10: Comparison between free electron coupling to waveguides vs. resonators. **(a)** Coupling spectrum for the pulse inside the resonator, indistinguishable from the one generated inside a waveguide with the same geometry. **(b)** Illustration of electron-photon interaction mediated by an optical cavity. An optical pulse is first generated inside the cavity. Then, the pulse circulates inside the cavity and couples out as a pulse train with a repetition rate of FSR and an exponentially decaying envelope. **(c)** Coupling spectrum for the out-coupled pulse trains exhibits a comb-like feature with frequency spacing matching the resonator FSR, peak width matching the pulse train envelope, and comb envelope matching the spectral components of each pulse.

efficiently eliminated experimentally and are thus not a fundamental limitation.

We first investigate the consequences of electron-photon correlation in the state subspace in some general state preparation schemes. We consider a projection $\hat{M} = |E_c\rangle\langle E_c|$ on the electron's first photon sideband (general case in Section B.14). This results in a pure single-photon optical state with frequency components $\phi_\omega \propto g_\omega^* \psi(E_c + \hbar\omega)$, a product between the electron wavefunction and the vacuum coupling strength, reflecting the fact that the electron energy loss is intrinsically correlated with the frequency of the photon created. The strength of the correlation depends on the initial energy uncertainty of the electron, which determines how well measurements of the electron state can distinguish the photon frequency components. In stark contrast, we will see in Section 6.4 that this is not the case for the electron state heralded by photon counting since the frequency of the photon created does not depend on the electron's energy in the no-recoil limit. In this section, we consider two regimes of interest: The wave-like regime that exploits the correlation to its advantage, and the particle-like regime that aims for high-purity state heralding.

6.3.1 Wave-like regime

In the wave-like regime, the electron ZLP width is much narrower than the phase-matching bandwidth, as shown in Fig. 6.11(a), where the electron behaves more wave-like to different optical frequency components. This regime exploits the strong correlation in the subspace between electron energy and optical frequency. This is compatible with the experimentally achieved [201] 4 meV ZLP width using a monochromator [185] combined with the recently demonstrated ~ 100 meV phase-matching bandwidth [8]. In this regime, we show the expres-

Chapter 6. Free-electron quantum optical interaction with photonic integrated circuits

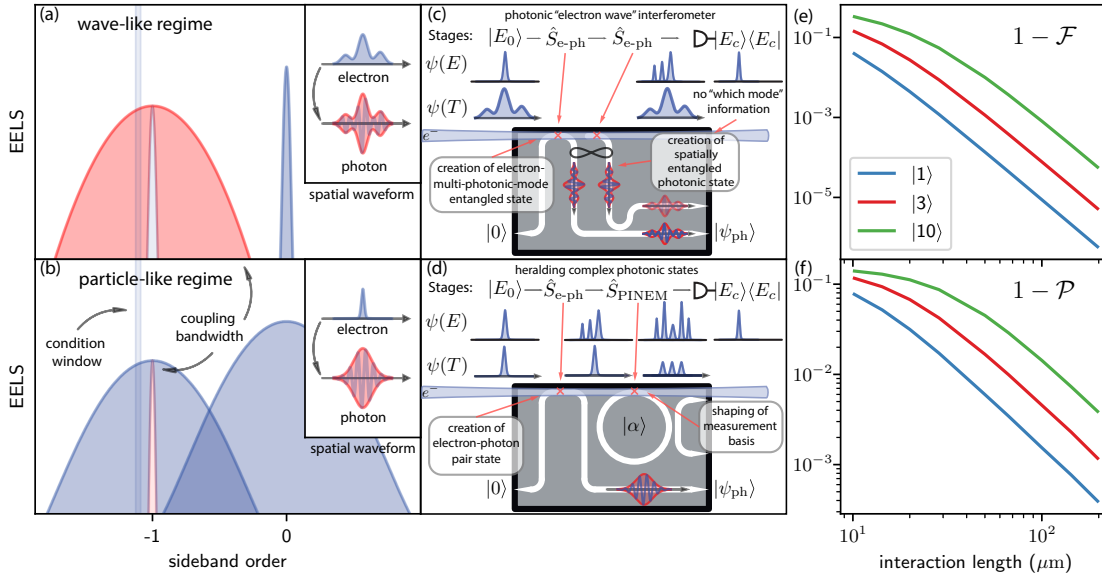


Figure 6.11: **(a-b)** Shaping optical waveforms by measuring electron energy. In the limit of **(a)** strong correlation with narrow zero-loss-peak (ZLP, blue) and broad phase-matching bandwidth (red), heralding results in printing electron wavefunction onto the optical waveform. In the limit of **(b)** weak correlation with broad ZLP and narrow phase-matching bandwidth, the heralded optical waveform is determined by waveguide routing and material dispersion. **(c-d)** Optical state heralding schematics where electron wavefunctions in time ($\psi(T)$) and energy ($\psi(E)$) domains are drawn before and after interaction stages (marked by red crosses). **(c)** Scheme for an electron-mediated self-mode-matched optical interferometer with non-classical states, enables measurement of interferometer imbalance to the order of optical wavelength, and electron wavefunction tomography. **(d)** Scheme for heralding a general optical state by measuring electron energy, consisting of one stage for pair state preparation with \hat{S}_{e-ph} and one stage for measurement basis selection with \hat{S}_{PINEM} . **(e-f)** Investigation of subspace correlation induced degradation of fidelity and purity of different Fock state components as a function of interaction length.

sion for the heralded single-photon Fock state as

$$|\psi_{ph}\rangle \propto \int d\omega \psi(E_c + \hbar\omega) \hat{a}_\omega^\dagger |0\rangle \quad (6.13)$$

In this scenario, ignoring the waveguide dispersion during propagation, as well as electron energy dispersion, we effectively imprint the electron spatial wavefunction $\tilde{\psi}(T = t - z/v_e)$ onto the optical waveform $\phi(T)$ of the generated single-photon Fock state of spatial-temporal mode $\hat{a} \propto \int d\omega \psi^*(E_c + \hbar\omega) \hat{a}_\omega$, with

$$\phi(T) = \tilde{\psi}(T) e^{i\omega_c T} \quad (6.14)$$

and a center frequency $\omega_c = E_c/\hbar$ matching the conditioned electron energy E_c . Therefore, by shaping the electron wavefunction (e.g., pre-compression into THz pulse trains) and

6.3 Shaping optical states from measurements on electron energy

conditioning on a specific sideband energy, one can transfer the arbitrarily shaped electron spatial wavefunction to the optical domain at a desired optical frequency. As for higher-order conditional Fock states $|N\rangle$, they cannot be addressed into the N -photon excitation of a single spatial-temporal mode (see Section B.14) because the optical frequency components are highly correlated. But in any photon counting scheme, the multi-mode optical profile is still shaped as $|\phi(T)|^2$ and contains N photons.

We illustrate in Fig. 6.11(c) an application example in this regime. When an electron passes through two waveguides and is measured at the first photon sideband on the detector (single photon excitation), the measurement does not resolve in which waveguide the photons are created. In this scenario, the measurement creates a spatial entanglement of photon excitation in the two spatially separated waveguides,

$$\hat{S} \propto \int d\omega \psi(E_c + \hbar\omega) \left(\hat{a}_{1,\omega}^\dagger + e^{i\omega\Delta t} \hat{a}_{2,\omega}^\dagger \right) \quad (6.15)$$

with naturally mode-matched waveform $\phi(T)$ and a controlled phase depending on the effective delay Δt from the electron trajectory, essential for generating path entangled NOON states [207]. If we interfere the two entangled modes at a balanced beam splitter, there is coherent quantum inference between the two waveguide excitations (see later discussion). In this way, we effectively constructed an optical interferometer with a non-classical optical state mediated by free electrons, with output differential photon flux

$$f(t) \propto \text{Re} \left[\tilde{\psi}(t) \tilde{\psi}^*(t + \Delta t) e^{i\omega_c \Delta t} \right]. \quad (6.16)$$

Notice that due to the nature of broadband optical coupling, when conditioning on different electron energy E_c , we are effectively scanning the probing optical frequency of the interferometer ω_c , enabling accurate extraction of the time imbalance Δt to the order of only a few optical cycles. When sweeping the optical path length difference to induce mode-mismatch, one can also retrieve electron spectral density based on interference visibility, similar to what was realized in matter interferometers [208]. The electron wavefunction can also be reconstructed through spectral shearing interferometry [209], answering an important question that is both fundamental and practical: how much of the measured electron energy uncertainty is quantum coherent [199]. In the following, we discuss the theoretical details of this path-entangled photon state generation.

Imprinting electron wavefunction onto the optical waveform in an interferometric fashion

In the regime where the electron energy spread is much narrower than the phase-matching bandwidth, the spatial-temporal mode is defined completely by the electron wavefunction, with a phase contribution from the coupling coefficient $g_{\omega_c = -E_c/(N\hbar)}$, where N is the sideband order. Whenever an electron interacts with an optical mode and is measured on the N th electron energy sideband at the energy E_c , it is equivalent to applying an operator $\hat{S} \propto \psi(E_c +$

Chapter 6. Free-electron quantum optical interaction with photonic integrated circuits

$\hbar\omega) \left(e^{i\theta_g} \hat{a}_\omega^\dagger \right)^N$ onto the optical state. When the electron interacts with two waveguides in a sequential manner (identical geometry), the operator is

$$\hat{S} \propto \int d\omega \psi(E + \hbar\omega) \left(e^{i\theta_{g_1}} \hat{a}_{1,\omega}^\dagger + e^{i\theta_{g_2}} \hat{a}_{2,\omega}^\dagger \right)^N \quad (6.17)$$

where a_i is the spatial-temporal mode on waveguide $i = 1, 2$, and the phase is determined by the reference point from both the optical side and the electron side. When the two interaction regimes (positions of waveguides) are separated by a spatial distance that corresponds to an electron propagation time Δt , we have the following phase relation of the coupling coefficients

$$e^{-i\hat{H}_0\Delta t} \hat{S}_{\text{e-ph}}(g_\omega) e^{-i\hat{H}_0\Delta t} = \hat{S}_{\text{e-ph}}(g_\omega e^{i\omega\Delta t}). \quad (6.18)$$

where \hat{H}_0 is the electron free-evolution Hamiltonian. If we assume the optical phase references are set to 0, we can rewrite the scattering as

$$\hat{S} \propto \int d\omega \psi(E + \hbar\omega) \left(\hat{a}_{1,\omega}^\dagger + e^{i\omega\Delta t} \hat{a}_{2,\omega}^\dagger \right)^N. \quad (6.19)$$

As we can see, this interaction projects the optical state into a quantum coherent spatial superposition state of two spatially separated waveguides. In the case that the two waveguides are connected to a 50:50 beam splitter to form an interferometer, the photon flux difference $f(t)$ can be expressed as

$$f(t) \propto \text{Re} \left[\tilde{\psi}(t) \tilde{\psi}^*(t + \Delta t) e^{i\omega_c \Delta t} \right], \quad (6.20)$$

which forms an effective optical interferometer of the time delay the electron experiences between two interaction stages but can also be induced by an external potential. Here, to extract the delay time, one can simply look at the photon counting record at different electron energy records E_c , which determines ω_c . Therefore, compared to conventional optical interferometry, where one has to scan the laser frequency over a vast range to resolve length differences to the order of a few wavelengths, here, we exploit the broad electron emission bandwidth to get an accurate length difference, just by looking at different electron energy records. Note that the imprinted electron wavefunction only provides a profile function with an effective optical delay (convenient for automatic mode matching between the two arms), with its original fast-evolving phase unobservable. Therefore, for a phase object positioned between the two waveguides, the interferometer sensitivity is on the optical wavelength scale, not on the scale of the de Broglie wavelength of the electrons.

6.3.2 Particle-like regime

In the particle-like regime, typically associated with a long interaction length, the phase-matching bandwidth is narrow compared to the electron energy uncertainty, and the coupling strength becomes large, as shown in Fig. 6.11 (b). Without on-chip electron guiding structures

6.3 Shaping optical states from measurements on electron energy

[106, 210], we expect the longest interaction length to be limited to 1 mm with $|g_{\text{TM}_{00}}|^2 \sim 5$ given a beam divergence angle ~ 0.2 mrad [211] with a 100 nm gap. The electron behaves more particle-like in this regime and can hardly distinguish different optical frequency components; therefore, the spatial-temporal optical modes defined in Section 6.2 can be correctly applied. In this limit, the subspace correlation can be greatly suppressed. When conditioning on the N th energy sideband, we can simplify the state to photon excitations of an electron-measurement-independent spatial-temporal mode $\hat{a} \propto \int d\omega g_\omega \hat{a}_\omega$ as

$$|\psi_{\text{ph}}\rangle \propto \left(\int d\omega g_\omega^* \hat{a}_\omega^\dagger \right)^N |0\rangle, \quad (6.21)$$

$$\phi(T) \propto \int dz \tilde{U}_z^*(z, T), \quad (6.22)$$

where the optical waveform $\phi(T)$ is connected to the Fourier transform of the optical mode profile $\tilde{U}_z(z, T) = \text{FT}_\omega [U_z(z, \omega)]$ along the electron propagation trajectory, determined by waveguide routing, and is generally much longer than the spatial extent of the electron wavefunction. For the case that includes propagation dispersion, see the next subsection. Since the electron travels in a straight path, by using a tailor-made waveguide structure with proper dispersion and routing, most types of optical waveforms can be generated. The conditioned electron energy does not determine the center frequency of the optical excitation. However, it can be easily tuned by selecting the appropriate electron velocity, evident in the results shown in Fig. 6.3(b-c).

In the following, we restrict ourselves to the regime of long interaction length since it is most versatile for heralding more complex optical states with higher photon numbers, and the ladder subspace correlation is weaker due to narrow phase-matching bandwidth. Heralding optical states by measuring electron energies has been explored [110, 186], and here we show an example of how to generate highly complex optical states, with the scheme shown in Fig. 6.11(d). The scheme consists of two stages: the first stage entangles the free electron with the waveguide mode, and the second stage selects the effective measurement basis for the electron energy. Specifically, the first stage of the interaction is the same pair-state generation discussed in previous sections. While direct conditioning on the electron energy measurement generates optical Fock states, in order to generate more general optical states, we can select a more general measurement basis by having a second stage to apply a unitary transformation \hat{U} on the electron state before the measurement. Starting from the physical measurement basis $\langle M|$, with the correct unitary transformation \hat{U} , the desired measurement basis $\langle M|\hat{U}$ can be generated. An arbitrary quantum state can be heralded if an arbitrary measurement basis can be constructed. Such a scheme exploits the time-reversal symmetry in quantum mechanics and has been used to demonstrate optical super-resolving phase measurement using only classical lasers [212].

In the illustrated case, shown in Fig. 6.11(d), we apply a standard photon-induced near-field electron-microscopy (PINEM) operation that we demonstrated experimentally in the previous

Chapter 6. Free-electron quantum optical interaction with photonic integrated circuits

chapter,

$$\hat{S}_{\text{PINEM}}(g, \omega) = \exp\left(g \hat{b}_\omega^\dagger - h.c.\right) \quad (6.23)$$

at the same optical frequency (served as the phase reference for any follow-up optical state characterization) before detection, which effectively transforms the measurement basis from $\langle E_c |$ to $\langle E_c | \hat{S}_{\text{PINEM}} = \sum_N c_N \langle E_c + N\hbar\omega |$ with Bessel coefficients c_N . Upon heralding, the generated optical state is

$$|\psi_{\text{ph}}\rangle \propto \sum_N \frac{c_{-(E_c/\hbar\omega+N)} g^N}{\sqrt{N!}} |N\rangle \quad (6.24)$$

with coefficients modified by the selected electron measurement basis. Following this scheme, if at the second stage we select a more general measurement basis by modulating the electron with an optical waveform consisting of multiple harmonics [213] of the base optical frequency $\hat{S} = \prod_n \hat{S}_{\text{PINEM}}(g_n, n\omega)$, one can in principle generate any general optical state e.g. Cat and GKP state [186]. Note that in the no-recoil limit, any operation on the electron wavefunction commutes with the entangling operation $\hat{S}_{\text{e-ph}}$. Therefore, it does not matter whether the operation is applied post-entanglement or pre-entanglement. The commutation will break down when the electron state exhibits dispersion during long-distance propagation, though typically ignored for few photon states.

Until here, we restricted ourselves to state generation in the ideal scenario where electron and photon are completely disentangled in the synthetic electron-photon energy ladder subspace. However, as is discussed in Section 6.1, there are still correlations between electron energy and optical frequency within the subspace. When tracing out the subspace continuum states, this leads to a degradation of state purity $\mathcal{P} = \text{Tr}[\hat{\rho}^2]$ and fidelity $\mathcal{F} = |\langle \psi_{\text{prepared}} | \psi_{\text{target}} \rangle|^2$ of the synthesized quantum state $\hat{\rho}$. We analyze these effects in our state heralding scheme (expressions for \mathcal{P} and \mathcal{F} derived in Appendix B.14, calculated using Monte Carlo sampling due to high dimensionality). We first stress that when conditioning on an electron energy with perfect energy resolution, the purity of the state is always unity, and we define the state fidelity in that limit. However, the relative heralding bandwidth $\gamma = \Delta E / \Delta E_{\text{ZLP}}$ determines the heralding rate and is lower-bounded by the experimental energy resolution. At finite bandwidth, it always results in finite purity of the state. To illustrate the impact of relative heralding bandwidth on state purity, we show the overall scaling of $1 - \mathcal{P} \propto \gamma^2$ in the limit of small heralding bandwidth in Fig. 6.12.

We assume a ZLP width $\Delta E_{\text{ZLP}} = 0.6\text{eV}$ with fitted Voigt lineshape from our experimental data. Given a relative heralding bandwidth $\gamma = 1$, we show in Fig. 6.11(e-f) both the purity \mathcal{P} of the state and the fidelity \mathcal{F} compared to the target state. As the purity is only a function of the occupancy at different Fock state components, we only plot the scheme/state-independent purity at these components. Due to more scrambled correlations between electron energy and photon frequency at higher ladder state subspace $|\psi_e, N\rangle$, their purity is lower, with impurity $1 - \mathcal{P} \propto \sqrt{N}$. We also see that fidelity and purity increase with longer interaction

6.3 Shaping optical states from measurements on electron energy

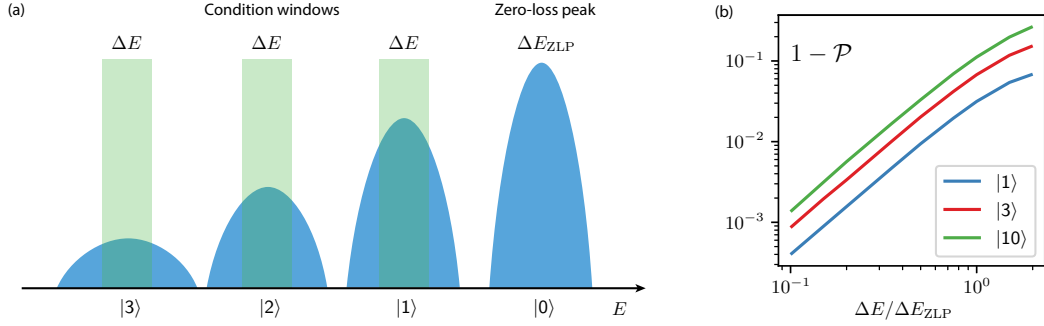


Figure 6.12: **(a)** Illustration of heralding Fock states by selecting a specific electron energy-loss window at different orders of sideband. **(b)** Heralded optical state purity vs relative heralding bandwidth at different Fock state basis. Here we assume $20\ \mu\text{m}$ interaction length.

distance L , with $1 - \mathcal{F} \propto L^{-4}$ and $1 - \mathcal{P} \propto L^{-2}$. This scaling is expected from the narrower phase-matching bandwidth at a longer interaction length and aligns well with the prolonged interaction targeted by the photonic integrated circuits. To help the readers grasp the inverse quadratic scaling to interaction length, we point out that for relatively short interaction length at $10\ \mu\text{m}$ (demonstrated in the previous chapter [7]), the state purity is $< 90\%$ for Fock state components |3> and above, but for an interaction length at $100\ \mu\text{m}$ (demonstrated later in this chapter [8]), the state purity $> 98\%$ even for |10>, with fidelity exceeding 99.9% .

Note that any contribution from the experimental uncertainty of electron energy will lead to the degradation of the electron state purity and increase the relative heralding bandwidth. Therefore, the experimentally measured ZLP width $\sim 0.6\ \text{eV}$ [158] can only serve as the upper bound of the quantum coherent energy uncertainty. Experimentally, the coherent energy uncertainty can be at least lower bounded at $\sim 0.1\ \text{eV}$ by the measured single-electron pulse duration [214], which is in fact still far from the Fourier limit. In the limiting case when the electron energy density matrix is completely incoherent, $\mathcal{P} \rightarrow 0$. Furthermore, as the experimentally measured purity of the heralded optical state through Wigner tomography [215] scales as $1 - \mathcal{P} \propto \Delta E_{\text{coherent}}^{-2}$, the purity characterization can also serve as a probe of the coherence property of the free electron. Even though the coherent electron energy width is hard to determine experimentally, it is fundamentally determined by the electron field-emission mechanism that generates the electron pulse. We can conclude that in order to be quantum coherent, the frequency spread of the heralded optical state must be much smaller than that of the laser pulses used in the electron field emission.

In the following subsections, we discuss the detailed derivations that lead to the result shown in this section.

Optical waveform generated from the electron-photon interaction

In this subsection, we derive the waveform of the conditional optical state when considering the waveguide dispersion. The composite quantum state after the electron-photon interaction is

$$\begin{aligned} |\psi\rangle &= \exp\left(\int d\omega g_\omega \hat{b}_\omega^\dagger \hat{a}_\omega - h.c.\right) |\psi_e\rangle |0\rangle = e^{-\frac{\int d\omega |g_\omega|^2}{2}} e^{-\int d\omega g_\omega^* \hat{b}_\omega \hat{a}_\omega^\dagger} e^{\int d\omega g_\omega \hat{b}_\omega^\dagger \hat{a}_\omega} |\psi_e\rangle |0\rangle \\ &= e^{-\frac{\int d\omega |g_\omega|^2}{2}} e^{-\int d\omega g_\omega^* \hat{b}_\omega \hat{a}_\omega^\dagger} |\psi_e\rangle |0\rangle = e^{-\frac{\int d\omega |g_\omega|^2}{2}} \sum_N \frac{\left(-\int d\omega g_\omega^* \hat{b}_\omega \hat{a}_\omega^\dagger\right)^N}{N!} |\psi_e\rangle |0\rangle \end{aligned} \quad (6.25)$$

when conditioned on the n th energy sideband of the electron state (with electron ZLP much wider than the coupling bandwidth to the optical modes), the heralded optical state is

$$|\psi_{\text{ph}}\rangle \sim \left(-\int d\omega g_\omega^* \hat{a}_\omega^\dagger\right)^N |0\rangle. \quad (6.26)$$

When the interaction is dominated by the coupling to a single optical mode family, we can generate the Fock state of a well-defined spatial-temporal mode as

$$|\psi_{\text{ph}}\rangle \sim \left(\hat{a}_m^\dagger\right)^N |0\rangle \quad (6.27)$$

$$\hat{a}_m = \int_{\Delta\omega_m} d\omega \phi_m(\omega) \hat{a}_\omega \quad (6.28)$$

$$\phi_m(\omega) = \frac{g_{\omega,m}^*}{g_m^*} \quad (6.29)$$

From these results, we can derive this spatial-temporal mode's temporal field profile function, as it may concern experiments that require waveform shaping. Straight from the definition, we get

$$\phi_m(\mathbf{r}, t) \propto \iint dz d\omega e^{i\omega(z/v_e - t)} \tilde{U}_{m,z}^*(\mathbf{R}_0, z, \omega) \tilde{\mathbf{U}}_m(\mathbf{r}, \omega). \quad (6.30)$$

When chromatic dispersion of the frequency modes is ignored, we retrieve the waveform shown in Eq. 6.22. When dispersion is considered, we can further remove the frequency dependence of the mode profile functions by assuming an open waveguide (i.e., no sharp frequency response in the phase-matched region) and up to second-order dispersion β ,

$$\tilde{\mathbf{U}}_m(\mathbf{r}, \omega) \approx \tilde{\mathbf{U}}_m(\mathbf{r}, \omega_m) e^{i(\omega - \omega_m)r_\parallel / v_g} e^{i\beta(\omega - \omega_m)^2 r_\parallel / v_g}, \quad (6.31)$$

where ω_m is the center frequency of the pulse, selected so that the phase velocity at ω_m matches the electron velocity v , $v_g \lesssim v$ is the corresponding group velocity, and r_\parallel is the longitudinal coordinate along the waveguide trajectory. We can then rewrite the expression as

6.3 Shaping optical states from measurements on electron energy

$$\begin{aligned}
\phi_m(\mathbf{r}, t) &\propto \iint dz d\omega e^{i\frac{(\omega-\omega_m)}{v}\left(z-\frac{v}{v_g}(R_{\parallel}(z)-r_{\parallel})-vt\right)} \\
&\times e^{i\beta\frac{(\omega-\omega_m)^2}{v_g}(r_{\parallel}-R_{\parallel}(z))} e^{i\omega_m(z/v_e-t)} \tilde{U}_{m,z}^*(\mathbf{R}_0, z, \omega_m) \tilde{\mathbf{U}}_m(\mathbf{r}, \omega_m) \\
&\propto \int dz e^{i\frac{\left(z-\frac{v}{v_g}(R_{\parallel}(z)-\tilde{r}_{\parallel})\right)^2}{4\beta(r_{\parallel}-R_{\parallel}(z))v^2/v_g}} e^{i\frac{\pi}{4}\text{sgn}(\beta(r_{\parallel}-R_{\parallel}(z)))} \\
&\frac{e^{i\omega_m(z/v_e-t)} \tilde{U}_{m,z}^*(\mathbf{R}_0, z, \omega_m) \tilde{\mathbf{U}}_m(\mathbf{r}, \omega_m)}{\sqrt{|\beta(r_{\parallel}-R_{\parallel}(z))|}} \\
&\propto \int dz K(z, \mathbf{r}, t) \overline{\tilde{U}}_{m,z}^*(\mathbf{R}_0, z, \omega_m) \tilde{\mathbf{U}}_m(\mathbf{r}, \omega_m) e^{-i\omega_m t} \tag{6.32}
\end{aligned}$$

where $\tilde{r}_{\parallel} \equiv r_{\parallel} - v_g t$ is the waveform coordinate in the optical pulse frame with group velocity v_g . $\overline{\tilde{U}}_{m,z}^*(\mathbf{R}_0, z, \omega_m)$ is the mode envelope profile at wave vector ω_m/v . The integral kernel

$$K(z, \mathbf{r}, t) \equiv e^{i\frac{\left(z-\frac{v}{v_g}(R_{\parallel}(z)-\tilde{r}_{\parallel})\right)^2}{4\beta(r_{\parallel}-R_{\parallel}(z))v^2/v_g}} \frac{e^{i\frac{\pi}{4}\text{sgn}(\beta(r_{\parallel}-R_{\parallel}(z)))}}{\sqrt{|\beta(r_{\parallel}-R_{\parallel}(z))|}} \tag{6.33}$$

represents a phase scrambling around the waveform coordinate \tilde{r}_{\parallel} with a bandwidth of $\sim |\beta(r_{\parallel})v^2/v_g|$, due to the presence of second order dispersion. We can get physical intuition of the waveform in the limit of weak dispersion ($\beta \rightarrow 0$), where we can approximate the integral kernel with a Dirac delta function,

$$\begin{aligned}
\phi_m(\mathbf{r}, t) &\propto \int dz \delta\left(z - \frac{v}{v_g}(R_{\parallel}(z) - \tilde{r}_{\parallel})\right) \overline{\tilde{U}}_{m,z}^*(\mathbf{R}_0, z, \omega_m) \tilde{\mathbf{U}}_m(\mathbf{r}, \omega_m) e^{-i\omega_m t} \\
&\propto \sum_i \frac{\overline{\tilde{U}}_{m,z}^*(\mathbf{R}_0, z_i, \omega_m)}{\left|R_{\parallel\partial z}(z_i) - \frac{v_g}{v}\right|} \tilde{\mathbf{U}}_m(\mathbf{r}, \omega_m) e^{-i\omega_m t} \tag{6.34}
\end{aligned}$$

where $z_i(\mathbf{r}, t) : \frac{z_i}{v} - \frac{1}{v_g}(R_{\parallel}(z_i) - \tilde{r}_{\parallel}) = 0$ are the spatial z coordinates where the vacuum field contributes the most through the phase-matching condition to the generated field at \mathbf{r} coordinate at time t . Therefore, the excited optical profile in the time domain is easily connected to the envelope of the optical mode field profile $\tilde{U}_{m,z}(\mathbf{R}_0, z, \omega_m)$ along the electron propagation direction, when the mode dispersion is sufficiently weak. In the exact limit $\beta = 0$, there can be unphysical scenarios when $|R_{\parallel\partial z}(z_i) - \frac{v_g}{v}| = 0$, which corresponds to the infinite phase-matching bandwidth. However, in physical materials, the phase-matching bandwidth is always finite.

The mode dispersion β during pulse propagation will cause pulse shortening or broadening by shifting the phase of different frequency components and leaving the amplitude unchanged. This effect can be easily corrected and is not a fundamental limit to constructing an arbitrary waveform. Therefore, we can structure any desired optical waveform $\phi(\mathbf{r}, t)$ by positioning

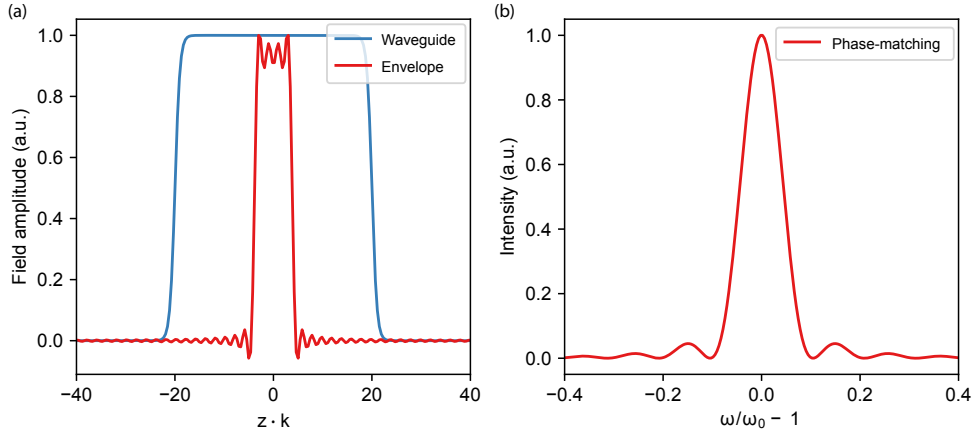


Figure 6.13: **(a)** The carrier envelope and **(b)** the phase-matching bandwidth of the free-electron-coupled spatial-temporal optical modes, with the straight waveguide lengths of $40 \mu\text{m}$. The electron velocity v_e is set to match the optical phase velocity of approximately $v = 0.6c$ at 1550 nm , with an optical group velocity of $v_g = 0.5c$.

the electron beam trajectory on an optical waveguide with a tailor-made waveguide structure. In Fig. 6.13, we show some of the characteristic envelopes of the spatial-temporal optical modes when coupling free electrons to straight waveguides, while neglecting the second-order dispersion β that causes pulse envelope evolution over a long propagation distance.

6.4 Shaping electron states from optical detection

Here, we consider the reciprocal operation of the previous section, which is to generate a complex electron energy superposition state by conditioning on photon counting. This procedure enables the generation of a much broader set of electron states not accessible by conventional PINEM-type phase modulation, e.g., direct amplitude modulation of electron wavefunction. Note that with the no-recoil approximation, here, the heralded spatial-temporal electron wavefunction is not shaped directly by the optical detection and the optical waveform, in sharp contrast to the heralding optical state by measuring electron energy. Therefore, the fidelity \mathcal{F} of the heralded electron wavefunction does not depend on interaction length, but the state purity still does.

In Fig. 6.14(a), we illustrate a similar scheme to that shown in the previous section to generate complex electron states with multiple stages of operations but on the optical side. The principle is the same: a pair-state is generated, then we select an effective measurement basis on the optical side to project the electron state into the desired form. As an example, before the detection, we can use a displacement operation $\hat{D}(\alpha)$, realized by a high-ratio on-chip beam splitter [216], to modify the effective photon number counting [217, 218] measurement basis from $\langle N|$ to $\langle N|\hat{D}(\alpha) = \sum_{N'} c_{N'} \langle N'|$. Based on a photon counting record, a conditional

6.4 Shaping electron states from optical detection

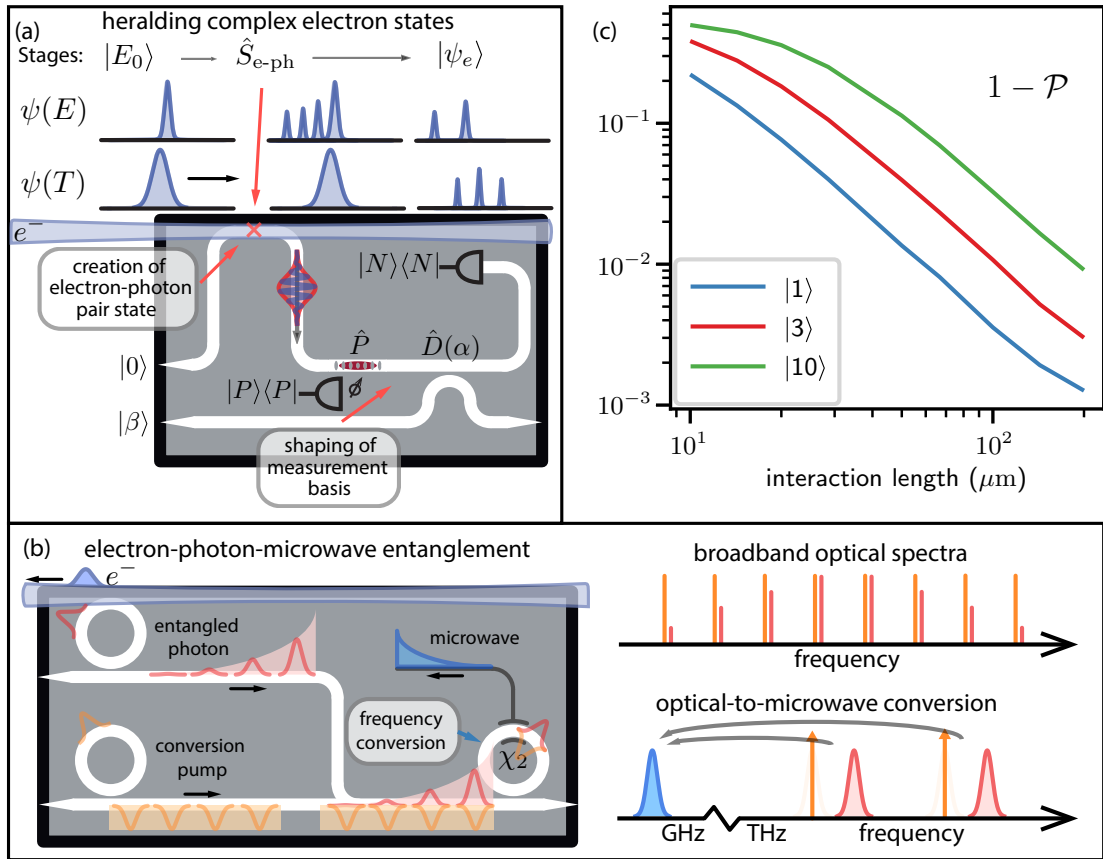


Figure 6.14: **(a)** Scheme for heralding an arbitrary electron state by optical detection, consisting of one stage for pair state preparation with \hat{S}_{e-ph} and one stage for measurement basis selection with on-chip optical operations. **(b)** Scheme to convert the original THz-broad optical excitation to a MHz-broad microwave excitation, with frequency width limited by the linewidth of the optical cavity, using a χ_2 optical-to-microwave transducer. The narrow-linewidth down-converted microwave excitation is useful for interacting with GHz-frequency quantum systems at low temperatures. **(c)** Investigation of subspace correlation induced degradation of purity of different electron ladder state components $|N\rangle$ as a function of interaction length.

Chapter 6. Free-electron quantum optical interaction with photonic integrated circuits

electron state is prepared at

$$|\psi_e\rangle \propto \int dE \psi(E) \sum_N \frac{c_N g^N}{\sqrt{N!}} |E - N\hbar\omega\rangle \quad (6.35)$$

In the special case of the coherent state measurement basis $\langle\alpha|$, which can also be constructed by simultaneously detecting both orthogonal optical quadratures in a homodyne setting (derivation see Section 6.4.1), the heralding operation is equivalent to applying a direct density modulation $\exp(2|g\alpha^*| \cos(\frac{\omega}{v}z + \theta_\alpha))$ on the electron wavefunction. In the limit of large modulation depth $|g\alpha^*| \gg 1$, the width of the electron wavefunction is compressed down to $\Delta z \sim \frac{1.7v}{\omega\sqrt{|g\alpha^*|}}$. The magnitude of pulse compression is similar to what is possible with PINEM-type interaction, but without the required additional dispersive propagation with a modulation-depth-dependent distance [120].

The projection into a sharply density-modulated electron wavefunction by measuring in the basis of optical coherent states can be understood intuitively. Since classical coherent optical excitation can only be generated by point-like electrons, the measurement of coherent states serves as a position measurement of the electrons, projecting them into the possible periodic positions that would give the correct classical phase of the measured optical coherent state. However, since the coherent states are not completely orthogonal to each other, the uncertainty of the projected electron position is determined by the magnitude of the measured field amplitude $|\alpha|$.

We can also prepare an even parity electron energy state to halve the spatial modulation period, useful for generating coherent second harmonic optical emission [124]. This can be achieved by applying conditional optical parity operation $\hat{P}(P)$ using two-level systems [138, 219, 220] or photon-number-resolving counting [221] which modifies the measurement basis to cat states $\langle\text{cat}_\alpha| \propto \langle\alpha| + \langle-\alpha|$. Higher harmonic spatial modulation can be generated by detecting in a higher-order cat state basis. Of course, structuring these measurement bases is much more challenging than the coherent state.

On the optical side, most unitary operations or state characterizations require mode matching to a reference spatial-temporal optical mode, which is difficult to achieve for the emitted THz-broad optical pulses. Here, we discuss two experimentally feasible options. The first option is to reshape the emitted optical spatial-temporal profile through frequency filtering, e.g., using an on-chip photonic crystal filter cavity [138]. When the frequency width is narrow enough to be resolved by the detector, we can choose a continuous wave local oscillator and gate on the detector time sequence [222] synchronized with the electron pulses. To prevent any loss of information that may lead to the degradation of state purity, we need to collect all the optical excitations rejected from the filter and condition on a zero-count event from the dark port. At a single-photon level of optical emission, the relative heralding rate is determined by the filtered optical bandwidth vs. the original optical phase-matching bandwidth. Therefore, such a frequency filtering scheme limits the heralding rate significantly due to the large phase-matching bandwidth (e.g., 1-THz width at 1-cm interaction length). The second option

6.4 Shaping electron states from optical detection

is to directly mode-match with a specifically shaped reference optical pulse. Such pulse shaping with individual control at all the frequency components is generally hard in straight waveguides. Therefore, it requires optical resonators instead of waveguides, as was the case for our experimental demonstration. The reference optical mode can then be generated in an identical resonator [223], e.g., as a dissipative Kerr soliton [224] or an electro-optic frequency comb [225] with control over each frequency component [205, 226]. The time gating resolution required on the optical detection would then be relaxed to the optical cavity lifetime, which can be achieved at the level of 20 ns [3] for materials and structures studied in this thesis. In integrated photonics, cavity life time approaching 1 μ s is also demonstrated [4, 5, 227].

Optical resonators offer the unique advantage of the concentrated optical density of states due to their narrow optical linewidth. We show a frequency conversion example in Fig. 6.14(b) (details of the scheme see Section 6.4.2) to exploit this advantage of optical resonators to convert the THz-broad optical excitation from the electron-photon interaction to a MHz-broad microwave excitation using a χ_2 optical-to-microwave converter [228, 229]. Using a structured local oscillator pump field, the conversion effectively serves as a multi-mode demodulation of the entangled photons. The frequency width of the microwave photon is determined by the linewidth of the optical cavity mediating the electron-photon interaction. Compared to the original THz-broad optical excitation, this frequency conversion is particularly useful to bridge interactions of eV-broad free electrons with quantum systems at GHz frequencies, e.g. superconducting qubits, electron spin qubits and mechanical oscillators. Generally, with the coupling to well-controlled two-level systems in the strong coupling regime, any photon measurement basis can be constructed [230]. As arbitrary quantum state synthesis of microwave photons was experimentally demonstrated in superconducting qubit systems [231], we can construct an arbitrary measurement basis $\langle\psi| = \langle 0|\hat{U}$ by applying the unitary operation \hat{U} on the converted microwave field and then conditioning on the microwave ground state $\langle 0|$ with photon-number resolving measurement [232] using a superconducting qubit, promising arbitrary electron state generation. Optical-to-microwave converters and superconducting qubits mostly require mK temperatures due to their GHz-frequencies and usually operate in a dilution refrigerator. Therefore, optical excitations must be guided out of the electron microscope through optical fibers, stressing the importance of high-efficiency fiber-to-chip couplings [191].

Note that due to multiple stages of operations, the optical measurement event will usually occur after the electron detection due to the high electron velocity. However, a delayed measurement on the optics side does not impair our scheme, as the measurement operators on the two parties commute [233]. Therefore, no real-time action is required.

Here, we show the full bandwidth state purity (expressions derived in Appendix B.15) as a function of interaction length in Fig. 6.14(c). As expected, it follows the same $1 - \mathcal{P} \propto L^{-2}\sqrt{N}$ scaling and favors longer interaction length. We point out again that for a relatively short interaction length at 10 μ m, the electron ladder $|10\rangle$ state purity is 50%, but for an interaction length at 200 μ m, the state purity reaches 99%. Note that the state purity is completely de-

Chapter 6. Free-electron quantum optical interaction with photonic integrated circuits

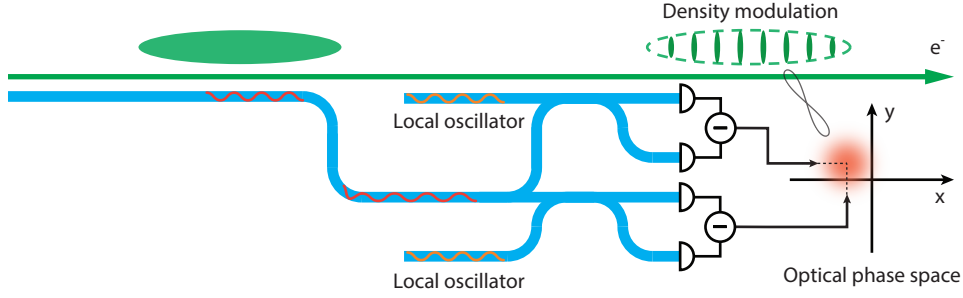


Figure 6.15: Scheme for heralding a density-modulated electron state by optical detection in the coherent state basis using two orthogonal homodyne measurements. This operation is equivalently an electron position measurement.

terminated by the electron-photon interaction and does not depend on specific schemes, e.g., optical-to-microwave conversion.

Here, a lower purity of the initial electron state will also result in purity degradation of the heralded electron wavefunction, similar to the case of the heralded optical state discussed in the previous section. However, effects like heralded density modulation are robust as the electron position projections are always valid given optical measurement records, even with mixed electron states.

In the following subsections, we discuss the detailed derivations that lead to the result shown in this section.

6.4.1 Optical detection in coherent state basis

As we discussed earlier when measuring in a coherent state basis

$$|\alpha\rangle = \sum_N c_N^* |N\rangle = e^{-|\alpha|^2/2} \sum_N \frac{\alpha^N}{\sqrt{N!}} |N\rangle, \quad (6.36)$$

we effectively performed a position measurement on the electron that collapse the electron wavefunction into density waves. We can derive the effective modulation applied to the electron wavefunction as

$$A(z) = \sum_N \frac{c_N g^N}{\sqrt{N!}} e^{iN\frac{\omega}{v}z} \propto \sum_N \frac{(g\alpha^* e^{i\frac{\omega}{v}z})^N}{N!} = e^{g\alpha^* e^{i\frac{\omega}{v}z}} \quad (6.37)$$

which is effectively a direct density modulation of

$$|A(z)|^2 \propto e^{2|g\alpha^*| \cos(\frac{\omega}{v}z + \theta_{g\alpha})} \quad (6.38)$$

The scheme to conduct optical detection in the coherent state basis is illustrated in Fig. 6.15.

6.4 Shaping electron states from optical detection

Somehow, I could not find anything in the past literature that shows a detailed derivation of this scheme, except only a concept figure in ref [212]. We describe it as follows: an arbitrary optical state $|\psi\rangle$ is passed to the input port 1 of a 50:50 beam splitter \hat{U}_{BS} , with two output ports 1 and 2. Each output port is passed to a homodyne detection stage where orthogonal quadratures are measured. This two-quadrature measurement is equivalent to projecting the input state into a coherent state. This projection shares the same physics of projecting a mechanical state into a coherent state by measuring the orthogonal mechanical quadratures with the same rate, as was discussed in Section 3.2. In the following, we first briefly review the quadrature projection in homodyne measurements and then prove this claim.

Projection into quadrature states using homodyne measurement

The homodyne measurement consists of a beam splitter that combines a strong LO field $|\alpha = -A\rangle$ and a signal field $|\psi\rangle = \sum_n \psi_n |n\rangle$. The two output ports are passed to photodetectors, where the photon number at each port is counted. We parameterize the detection result as $|j, m\rangle = |j - m\rangle \otimes |j + m\rangle$, where j is the averaged photon number of both detectors and m is the deviation from the averaged value. We work in experimental settings where the input state is a few-photon state, and the photon number uncertainty of the LO field coherent state is much larger. Because of this, we have the following conditions $m \ll j$, $n \ll \sqrt{j}$.

We can proceed to calculate the projection amplitude of the state as

$$M_m^j = \langle j, m | \hat{U}_{\text{BS}} | -A \rangle | \psi \rangle = e^{-A^2/2} \sum_{n=0}^{2j} \psi_n \frac{(-A)^{2j-n}}{\sqrt{(2j-n)!}} d_{m, j-n}^j \left(\frac{\pi}{2} \right) \quad (6.39)$$

where $d_{m', m}^j(\phi) = \langle j, m' | e^{-\frac{\phi}{2}(\hat{a}_1^\dagger \hat{a}_2 - \hat{a}_2^\dagger \hat{a}_1)} | j, m \rangle$ is the SU(2) Wigner function which has an asymptotic expression

$$d_{m, j-n}^j \left(\frac{\pi}{2} \right) \approx (-1)^n j^{-1/4} u_n(m/\sqrt{j}) \quad (6.40)$$

where $u_n(x) = \langle x | p | n \rangle$ is the n th Hermite Gaussian function, which is also the Fock state projection into the quadrature basis $|x\rangle_p$. In the following, we use the mapping $x = m/\sqrt{j}$ to connect the measurement photon record (j, m) with the measured quadrature value x .

We also use the asymptotic Gaussian expression for the Poisson distribution

$$\frac{(-A)^{2j-n}}{\sqrt{(2j-n)!}} \approx \frac{(-1)^{2j-n}}{(4\pi j)^{1/4}} e^{A^2/2 - (2j-A^2)^2/4A^2} \quad (6.41)$$

Last, we simplify the expression by considering the fact that j mostly peaks around $A^2/2$,

$$M_m^j \approx \frac{e^{-(2j-A^2)^2/4A^2 + 2i\pi j}}{\pi^{1/4} A} \sum_{n=0}^{\infty} u_n(x) \psi_n = \frac{e^{-(2j-A^2)^2/4A^2 + 2i\pi j}}{\pi^{1/4} A} \langle x | p | \psi \rangle \quad (6.42)$$

Chapter 6. Free-electron quantum optical interaction with photonic integrated circuits

with the corresponding measurement POVM defined by $\text{Tr}(\hat{\rho}\hat{\Pi}_m^j) = |M_m^j|^2$

$$\hat{\Pi}_m^j = \frac{e^{-(2j-A^2)^2/2A^2}}{\sqrt{\pi}A^2} |x\rangle_p \langle x|_p \quad (6.43)$$

When the information on j is ignored (since its distribution is highly peaked) and only the differential current m is considered, the measurement POVM is

$$\hat{\Pi}_m = \sum_j \hat{\Pi}_m^j = \frac{\sqrt{2}}{A} |x\rangle_p \langle x|_p \quad (6.44)$$

where the mapping is now $x = \sqrt{2}m/A$. The prefactor $\sqrt{2}/A$ comes from the Jacobian of the mapping, as

$$\sum_m \hat{\Pi}_m = \int dx |x\rangle_p \langle x|_p = 1 \quad (6.45)$$

Equivalence to a conditional coherent state

Homodyne detection is conducted by interfering the signal field with a strong local oscillator field $|A\rangle$ at a balanced beam splitter, and the differential photon number at the two output ports is measured. It has been shown [234] that this type of detection can be simplified as a quadrature state projection, where there is a unique mapping $x = m/\sqrt{2}|A|$ between the differential photon number m and the measured quadrature state $|x\rangle_p$. The mapping requires the photon number variance of the local oscillator field $|A\rangle$ to be much bigger than that of the optical state $|\psi\rangle$.

Therefore, the scheme effectively states that two orthogonal quadrature projections $|x_1\rangle_p \otimes |x_2\rangle_p$ at the two output ports of a beam splitter projects the input state into a coherent state $|\alpha\rangle$. We prove it by expressing a quadrature state as a function of creation operators acting on the vacuum state [235], as in

$$|x\rangle_p = \frac{e^{-x^2/2}}{\pi^{1/4}} e^{-\frac{\hat{a}^{\dagger 2}}{2} + \sqrt{2}x\hat{a}^{\dagger}} |0\rangle. \quad (6.46)$$

We also use the following relations of the actions of the beam splitter

$$\hat{U}_{\text{BS}}^{\dagger} \hat{a}_1^{\dagger} \hat{U}_{\text{BS}} = \frac{\hat{a}_1^{\dagger} + i\hat{a}_2^{\dagger}}{\sqrt{2}}, \quad \hat{U}_{\text{BS}}^{\dagger} \hat{a}_2^{\dagger} \hat{U}_{\text{BS}} = \frac{i\hat{a}_1^{\dagger} + \hat{a}_2^{\dagger}}{\sqrt{2}}. \quad (6.47)$$

Given the measurement results that the output ports are states $|x_1\rangle_p$ and $|x_2\rangle_p$, and a vacuum

6.4 Shaping electron states from optical detection

state $|0_2\rangle$ at the second input port, the conditional state at the first input port will be

$$\begin{aligned}
|\psi_c\rangle &= \langle 0_2 | \hat{U}_{\text{BS}}^\dagger |x_1\rangle_p |x_2\rangle_p = \langle 0_2 | \hat{U}_{\text{BS}}^\dagger \frac{e^{-(x_1+x_2)^2/2}}{\pi^{1/2}} e^{-\frac{\hat{a}_1^{\dagger 2} + \hat{a}_2^{\dagger 2}}{2} + \sqrt{2}(x_1 \hat{a}_1^\dagger + x_2 \hat{a}_2^\dagger)} \hat{U}_{\text{BS}} \hat{U}_{\text{BS}}^\dagger |0_1\rangle |0_2\rangle \\
&= \frac{e^{-(x_1+x_2)^2/2}}{\pi^{1/2}} \langle 0_2 | e^{-i \hat{a}_1^\dagger \hat{a}_2^\dagger + (x_1 + i x_2) \hat{a}_1^\dagger + (i x_1 + x_2) \hat{a}_2^\dagger} |0_1\rangle |0_2\rangle \\
&= \frac{e^{-(x_1+x_2)^2/2}}{\pi^{1/2}} e^{(x_1 + i x_2) \hat{a}_1^\dagger} |0_1\rangle = \pi^{-1/2} \hat{D}(x_1 + i x_2) |0_1\rangle \\
&= \pi^{-1/2} |\alpha_1 = x_1 + i x_2\rangle.
\end{aligned} \tag{6.48}$$

The factor of $\pi^{-1/2}$ comes from the overcompleteness of the coherent state basis, as in

$$\begin{aligned}
1 &= \langle 0_2 | \hat{U}_{\text{BS}}^\dagger \left(\int dx_1 dx_2 |x_1\rangle_p \langle x_1|_p |x_2\rangle_p \langle x_2|_p \right) \hat{U}_{\text{BS}} |0_2\rangle \\
&= \int dx_1 dx_2 \pi^{-1} |\alpha_1 = x_1 + i x_2\rangle \langle \alpha_1 = x_1 + i x_2| = 1.
\end{aligned} \tag{6.49}$$

As we can see, the conditioning of a coherent state comes from the cancellation of the second order term $\hat{a}^{\dagger 2}$ due to the even splitting ratio of the beam splitter and a correct phase relation. If this requirement is not met, it will result in a squeezed coherent state as the conditional state, e.g. for a beam splitter with a transmission of η ,

$$|\psi_c\rangle = \frac{e^{-(x_1+x_2)^2/2}}{\pi^{1/2}} e^{\frac{(2\eta-1)\hat{a}_1^{\dagger 2}}{2} + \sqrt{2}(\sqrt{\eta}x_1 + i\sqrt{1-\eta}x_2)\hat{a}_1^\dagger} |0_1\rangle. \tag{6.50}$$

6.4.2 Frequency conversion using resonator structures

As discussed in Section 6.4, optical resonators provide unique advantages over straight waveguides regarding the concentrated optical density. Here, we show an example scheme to use on-chip ring resonator structures to convert the THz-broad optical excitation from the electron-photon interaction to a MHz-broad optical/electrical excitation, limited by the optical resonator linewidth. Here we define the spatial-temporal mode for the optical excitation of a resonator as $\hat{a}^\dagger = \int d\omega \sum_i \phi_i(\omega) \hat{a}_\omega^\dagger$, where each $\phi_i(\omega)$ is a Lorentzian centered around $\omega_i + \omega_m$ with ω_i the pump center frequency. We also define the microwave excitation as $\hat{c}^\dagger \propto \int d\omega \phi(\omega) \hat{c}_\omega^\dagger$, centered around ω_m . In the ideal case that all the optical azimuthal modes are identical in their frequency components, we have $\phi_i(\omega + \omega_i) = \phi(\omega)$.

Near-unity-efficiency optical to microwave conversion was demonstrated in χ_2 type materials [228, 229]. We assume a ring structure optical resonator (conversion ring) with a strong χ_2 nonlinearity and a relatively high optical quality factor, with identical cavity azimuthal modes of two orthogonal polarizations (e.g., TE and TM fundamental modes) with approximately the same FSR, and a frequency spacing $\sim \omega_m$ between these two mode families that match the microwave mode frequency ω_m . Practically, frequency matching is only required between a few optical resonances since the electron-photon optical excitation from a ring resonator

Chapter 6. Free-electron quantum optical interaction with photonic integrated circuits

can, in principle, only cover about 5-20 azimuthal modes. We use this resonator for frequency down-conversion of the broadband photon excitation \hat{a}^\dagger at frequencies $\omega_i + \omega_m$ from the electron-photon interaction, with a specially structured local oscillator pump at frequencies ω_i . We further assume that two more rings are on the chip, with matched optical frequencies of the modes of interest. We use one of the rings for electron-photon interaction, where the photon excitation is generated on the TM polarization at frequencies $\omega_i + \omega_m$ (signal field). This ring should be designed with the highest quality factor possible since its linewidth determines the microwave linewidth $\phi(\omega)$, and should be narrower than the linewidth of the conversion ring. We use the other ring for generating or filtering a structured continuous wave (CW) optical pump on the TE polarization with frequencies ω_i (LO field). We combine LO and signal field through a polarization beam splitter and send them into the conversion ring for frequency down-conversion.

Theoretically, the signal and LO fields do not have to be orthogonal in polarization to enable efficient and low-noise frequency conversion. The orthogonal polarizations considered here are intended to prevent spectral leakage of the LO field to the signal mode, even though they can be sufficiently separated in frequency.

When the conversion ring is pumped by the LO field with cooperativity $C = 1$ in each pump-field mode pair, the signal frequency component $\phi_i(\omega)$ at the azimuthal mode at frequency $\omega_i + \omega_m$ is converted to a microwave photon at frequency ω_m with frequency component $\phi(\omega)$ and conversion efficiency $\eta = 100\%$. When all the azimuthal modes of the conversion ring convert their signal field components down to the same microwave frequency ω_m with unity efficiencies, the original signal pulse with THz-broad frequency components from the electron-photon interaction will be converted to a single microwave mode excitation at frequency ω_m with frequency width down to MHz with a unity efficiency, and at the same time generate a pump field photon with THz-broad frequency component due to the energy conservation.

Here, we formally analyze this conversion process. We define the scattering matrix of the conversion process with a multi-mode three-wave mixing operator

$$\hat{S}_{\text{TWM}} = e^{\sum_i \int \beta_i(\omega, \omega_i) \hat{a}_{\omega+\omega_i} \hat{c}_\omega^\dagger \hat{d}_{\omega_i}^\dagger - h.c.} \quad (6.51)$$

where ω_i is the frequency of each CW pump comb tooth, and β_i is the coupling constant amplified by the pump field. The coupling constant $\beta_i(\omega, \omega_i)$ contains the conversion frequency response of each pump-signal mode pair, including effects such as phase-matching, cavity responses of the signal and pump field, and microwave cavity response. The operators are the signal field annihilation \hat{a}_ω , the microwave field creation operator \hat{c}_ω^\dagger , and the pump field operator $\hat{d}_{\omega_i}^\dagger = \sum_{N_{\omega_i}} |N_{\omega_i} + 1\rangle \langle N_{\omega_i}|$ which is specially defined high-up in the photon ladder, similar to the electron ladder operator in the no-recoil limit, that represents the addition of a photon to the classical coherent pump field $|\alpha_i\rangle$ with frequency ω_i . In the single-mode conversion case, \hat{d}^\dagger can be ignored. However, in the multi-mode conversion considered here, neglecting \hat{d}^\dagger leads to non-unitary operations. Under such a scattering matrix, the state of the

system changes to

$$\begin{aligned} \hat{S}_{\text{TWM}}|\psi_{\text{ph}}, \psi_m, \psi_{\text{pump}}\rangle &= \hat{S}_{\text{TWM}}F(\hat{a}^\dagger)|0_a, 0_c, \alpha_i\rangle \\ &= F(\hat{S}_{\text{TWM}}\hat{a}^\dagger\hat{S}_{\text{TWM}}^\dagger)\hat{S}_{\text{TWM}}|0_a, 0_c, \alpha_i\rangle = F(\hat{S}_{\text{TWM}}\hat{a}^\dagger\hat{S}_{\text{TWM}}^\dagger)|0_a, 0_c, \alpha_i\rangle \end{aligned} \quad (6.52)$$

$$\begin{aligned} \hat{S}_{\text{TWM}}\hat{a}^\dagger\hat{S}_{\text{TWM}}^\dagger &= \sum_i \phi_i(\omega + \omega_i) \sin(|\beta_i(\omega, \omega_i)|) e^{i\theta_i} \hat{d}_{\omega_i}^\dagger \hat{c}_\omega^\dagger \\ &\quad + \sum_i \phi_i(\omega) \cos(|\beta_i(\omega - \omega_i, \omega_i)|) \hat{a}_\omega^\dagger \end{aligned} \quad (6.53)$$

where $\hat{a}^\dagger = \int d\omega \sum_i \phi_i(\omega) \hat{a}_\omega^\dagger$ is used, $\theta_i = \arg[\beta_i(\omega, \omega_i)]$, and also $|\psi_{\text{ph}}\rangle = F(\hat{a}^\dagger)|0_a\rangle$ is assumed to be a general optical state. In the ideal case where $\phi_i(\omega + \omega_i) = \phi(\omega)G_i$ is separated to the cavity density of states $\phi(\omega)$ and the electron-photon phase-matching coefficient G_i at signal mode i , with unity cooperativity $\beta_i(\omega, \omega_i) = \pi/2$ at every pump-signal mode pair over the frequency components of interest, the state is simplified to

$$|\psi_m, \psi_{\text{pump}}\rangle = F(\hat{c}^\dagger \hat{d}^\dagger)|0_c, \alpha_i\rangle \quad (6.54)$$

where

$$\hat{c}^\dagger = \int d\omega \sqrt{\sum_i |G_i|^2} \phi(\omega) \hat{c}_\omega^\dagger \quad (6.55)$$

$$\hat{d}^\dagger = \sum_i \frac{G_i}{\sqrt{\sum_i |G_i|^2}} e^{i\theta_i} \hat{d}_{\omega_i}^\dagger \quad (6.56)$$

Since the pump field is a strong coherent field and maintains a unity overlap with a photon-added state, we can trace out the pump field state space, and arrive at

$$|\psi_m\rangle = F(\hat{c}^\dagger)|0_c\rangle \quad (6.57)$$

where the state of the signal field $|\psi_{\text{ph}}\rangle = F(\hat{a}^\dagger)|0_a\rangle$ is transferred to the microwave field, with frequency components limited by the signal's cavity mode density-of-states $\propto \phi(\omega)$.

Practically, the amplitude and frequency components of the LO field have to be precisely shaped. However, since the optical excitation from the electron-photon interaction can be limited to only 5-20 optical modes with the maximum interaction length achievable with a racetrack resonator geometry, it is possible to shape a reasonably accurate LO field with a soliton [224] or an electro-optic comb [225] source and a frequency shaper [226] to correct the amplitude and phase of each frequency component.

There are currently two types of main-stream optical-to-microwave converters [163]. One type uses χ_2 optical nonlinearity to directly convert signals from the optical domain to the microwave domain, as is considered here. The other type [236] uses a mechanical oscillator as an intermediate stage to first convert the optical signal to a mechanical signal using optomechanical couplings, and then from the mechanical signal to a microwave signal using electro-mechanical couplings. Both types of systems have shown near-unity conversion

Chapter 6. Free-electron quantum optical interaction with photonic integrated circuits

efficiency and low added noise. However, the mechanical one suffers from the low conversion bandwidth typically at kHz level (not possible to achieve $\beta_i(\omega, \omega_i) \sim \pi/2$ over the cavity bandwidth \sim MHz), limited by the electro-mechanical and optomechanical coupling rates. Therefore, we only consider the χ_2 -type optical-to-microwave converters for our scheme since they offer broadband transductions, essential to convert all the frequency components of the optical excitation to the microwave domain. For a realistic lithium niobate ring resonators with $50 \mu\text{m}$ radius, the microwave frequency at 4 GHz, with optical and microwave cavity linewidths at $\kappa_{\text{ph/m}}/2\pi \sim 10$ MHz, the estimated required pump power to reach $C_i = 1$ is reasonable at $P_i \sim 100 \mu\text{W}$ [237].

Similar schemes can also down-convert the signal to an optical excitation with MHz linewidth. However, a relatively uniform mode spacing over multiple azimuthal modes at the optical frequency scale is generally challenging to design for triply resonant schemes.

6.5 Theoretical and experimental limitations

Until now, we have analyzed the fundamental limits of integrated photonic circuits as a platform for synthesizing high-quality quantum states with free electrons. We show in Section 6.2 that near-unity coupling ideality to the target TM_{00} spatial-temporal waveguide mode can be achieved by suppressing parasitic couplings through the control of electron beam positioning, velocity, and waveguide design. We also investigate the underlying correlation between electron energy and photon frequency in the energy ladder subspace and the induced fundamental limitation as a trade-off between heralding rate and state purity. In Section 6.3, we found that particle-like electrons with coherent energy uncertainty are required to generate pure heralded states, and the purity limit can be greatly relaxed with experimentally feasible interaction length with integrated waveguides. We also show that these correlations can be exploited to shape the optical waveforms, e.g., to map the electron wavefunction to the optical domain and construct an effective optical interferometer mediated by free electrons. However, the spatial sensitivity of such an interferometer remains at the optical-wavelength scale and does not inherit the superior spatial sensitivity of electron waves. It is still an open question whether phase-object-induced electron phases can be transferred to the optical domain, accumulate, and be detected optically, which is relevant for quantum-enhanced phase-object imaging applications [238, 239]. The maximum feasible coupling strength $|g_{\text{TM}_{00}}|^2$ can also be further enhanced through waveguide dispersion engineering [190], with the trade-off of lower state purity due to larger phase-matching bandwidth.

Note that in our discussion, we omit detailed analysis of some experimental limitations, e.g., finite detection efficiencies, primarily on the optical side. The heralded optical state is robust, given the high energy of the electrons. However, the heralded electron state purity is most sensitive to the optical detector efficiencies and other limiting factors, such as optical mode-matching. We discuss the heralded electron state with a finite optical detection efficiency in Section 7.5. We anticipate that there are schemes or parameter regimes that are less prone

to detection inefficiencies. We also restrict our discussion mainly to the interaction picture, except that the electron and optical waveforms are defined in the Schrödinger picture. We remind the reader that in the Schrödinger picture, though not the main focus of the paper, long-distance propagation significantly modifies the electron and optical density profile $|\tilde{\psi}(T)|^2$ and $|\phi(T)|^2$, leading to effects like electron [103, 112, 116, 143, 200] and optical [240] pulse compression. More details on the effect of free-electron dispersive propagation can be found in Chapter 8.

Moreover, in the no-recoil limit, all the electron operations commute with each other. This approximation, though practically valid for few-photon single-chip interactions, limits the controllable degrees of freedom of the heralded optical states to the order of the harmonics of the PINEM field used to shape the electron wavefunction [213]. In the platform of Si_3N_4 microresonators, efficient generation of second [241] and third [242, 243] harmonics are supported with estimated maximum $|g_2| \sim 100$ and $|g_3| \sim 10$, offering a total of 8 degrees of freedom on the heralded optical state. The Si_3N_4 integrated photonics platform also provides an ultra-wide transparency window from 400 nm to 4.5 μm [244], supporting at most ten harmonic components with an externally driven optical source. Beyond the no-recoil limit [112], electron energy transitions significantly modify the velocity due to energy dispersion. When interaction regions are far apart, the recoil effect results in an energy-dependent phase accumulation between different stages (details see Appendix 8.1). The recoil effect can be safely neglected in discussing few-photon single-chip interaction. However, it could be necessary for a broader range of experimental schemes [102, 103, 116, 124, 245], e.g., when multiple chips are involved with significant separation distance.

Furthermore, our analysis is purely in the framework of macroscopic QED [114], where electrons interact with the medium-assisted electromagnetic fields. In optical media like the Si_3N_4 material we discuss here, optical phonons typically exist and result in Raman scattering of optical fields [246]. However, due to their short spatial extent and low energy [247, 248], we do not consider their contribution in long-distance phase-matched interaction with the high-energy free electrons. The same reasoning also excludes higher electron energy loss processes, e.g., valence and inner-shell ionization around 50 eV [249].

Our analysis and results indicate that the photonic integrated circuit platform is ideal for free-electron quantum optics with manageable limitations and promises a pathway to high-fidelity and high-purity quantum state heralding, entanglement of free electrons with other quantum systems, and quantum-enhanced sensing and imaging. In the next section, we discuss our experiment of observing the free-electron interaction with the evanescent quantum optical vacuum fields of a Si_3N_4 microresonator and the electron-photon non-classical correlation generated in this process.

7 Cavity-mediated electron-photon pairs

Optical parametric processes generate quantum correlations of photons without changing the state of the optical medium involved. Entangled photons from parametric down-conversion [250] are an essential resource for heralded single-photon sources, quantum communication, and quantum teleportation [251]. Spatially separated entanglement afforded by such "twin-beam" pairs was extended to various physical contexts, with examples in atomic beams [252], electron spins [253], and photon-phonon correlations in micro-mechanical systems [23].

Free-electron beams are an emerging target for quantum manipulation and sensing, promising quantum-enhanced imaging [238, 254], spectroscopy [108, 255, 256], and excitation [102, 109, 110, 124]. Using the quantum optical measurement techniques, photon statistics are used to reveal single quantum emitters [257] and photon bunching [258, 259]. Recent experiments also studied the electron-induced optical excitation of whispering gallery modes [184, 185] and optical fibers [260]. However, impeded by a lack of mode-specific and sufficiently strong coupling, correlations between single electrons and well-defined photonic states have remained elusive before our work.

In this chapter, within the theoretical framework we developed in the previous chapter, we discuss our first experiment effort [8] to observe free-electron interaction with the evanescent vacuum fields of a high-Q Si_3N_4 200-GHz optical microresonator to generate free-electron cavity-photon pair states. In this platform, we observe single-photon generation (Section 7.2) from the resonator when the free electron passes by the waveguide surface and demonstrate a non-classical electron-photon correlation (Section 7.3), the quantum optical feature that is long sought after. We also demonstrate coincidence imaging (Section 7.4) of the cavity mode with drastic background suppression. Last, we observe the decoherence of the electron state due to interaction with parasitic optical modes and the verification of the Poisson statistics of the generated photons (Section 7.5).

7.1 Free-electron interaction with cavity modes

The interaction of electron beams with cavities and resonant structures represents a universal scheme for generating electromagnetic radiation. In the quantum optical description, the inelastic scattering can be modeled as a coupling of free electrons to optical vacuum fields. Scattering with the evanescent field of the optical microresonator, an electron at energy E generates intracavity photons at frequencies ω in an energy-conserving manner (Fig. 7.1A), described by the scattering matrix $\hat{S} = \exp(g\hat{a}^\dagger\hat{b} - h.c.)$. Here, \hat{a}^\dagger is the creation operator of the cavity spatial-temporal mode, and g is the vacuum coupling strength. The ladder operator \hat{b} reduces the energy of an electron by that of one photon. Here, we measured our phase-matching bandwidth of the optical modes to be 50 meV, much smaller than the ZLP of the electron energy (0.6 eV), and thus sufficiently in the particle-like regime of the interaction discussed in Section 6.3.2.

The interaction induces entanglement between the electron energy and the cavity population and results in the state

$$|\psi_e, \psi_{\text{ph}}\rangle = \sum_{n=0}^{\infty} c_n |E - n\hbar\omega\rangle |n\rangle, \quad (7.1)$$

with the coefficients $c_n = \exp(-\frac{|g|^2}{2}) \frac{g^n}{\sqrt{n!}}$ corresponding to Poissonian scattering probabilities, under the no-recoil approximation. In our experiment, we are still in the regime of a relatively weak vacuum coupling strength $|g|^2 \sim 0.1$, and the state is dominated by the zero- and one-photon contributions:

$$|\psi_e, \psi_{\text{ph}}\rangle \propto |E\rangle |0\rangle + g |E - \hbar\omega\rangle |1\rangle + \mathcal{O}(g^2). \quad (7.2)$$

Our measurements are designed to probe this state by detecting single photons (non-photon-number-resolving) in coincidence with inelastically scattered electrons by one photon energy. In the experiment, the continuous electron beam of a transmission electron microscope (120-keV beam energy, 25-nm focal diameter) passes by a photonic chip-based microresonator (Fig. 7.1C) and interacts with the evanescent vacuum fields to excite the empty cavity modes.

The Si_3N_4 microresonator [152] is designed for low optical loss, efficient fiber coupling, and free-space near-field access. Constrained by electron-photon phase matching, we engineered the resonator cross-section ($2.1 \mu\text{m} \times 650 \text{ nm}$, not single mode) for a maximum photon generation probability per electron, up to 7% around 0.8-eV photon energy (a wavelength of $1.55 \mu\text{m}$).

Cavity photons generated in the clockwise propagating modes (Fig. 7.1A) are coupled out to a bus waveguide and further guided by optical fibers to a single-photon avalanche diode (SPAD). The energy and arrival time of each electron are measured with an event-based detector behind a magnetic prism spectrometer (Fig. 7.1B), allowing for electron-photon coincidence experiments.

7.1 Free-electron interaction with cavity modes

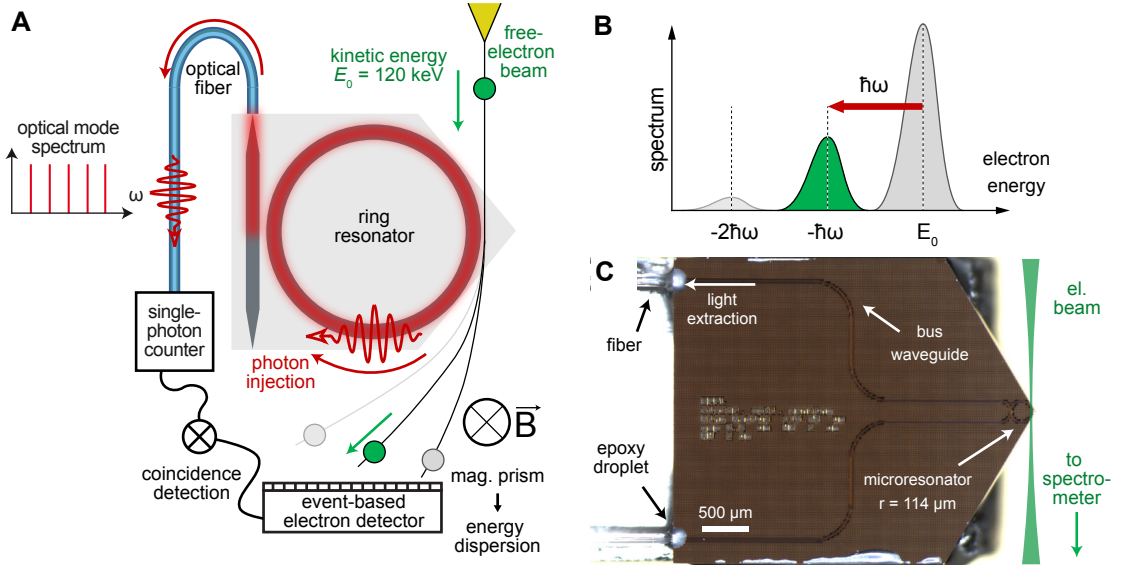


Figure 7.1: **Coincidence detection of electron-photon pairs generated at a photonic chip.** (A) High-energy electrons traverse a fiber-coupled Si_3N_4 microring resonator, generating intracavity photons. Single photons and inelastically scattered electrons are detected in coincidence. (B) Electron spectrum after interaction. (C) Optical microscope image of the photonic chip with a sketch of the passing electron beam.

In the following, we analyze the generated state in detail, starting from the discrete cavity mode basis, and show that the interaction leads to the generation of a single-mode excitation of a well-defined spatial-temporal mode.

Discrete mode description

Here, we present the theoretical description of coupling electrons to multiple cavity modes. We work in the no-recoil approximation regime, where the electron energy dispersion does not affect the interaction. When an electron is interacting with multiple optical modes (indexed by μ), as we are only considering the one-photon interaction $H_1 = \sum_{\mu} H_1^{\mu}$ (two-photon process H_2 neglected), our interaction is linear to the field operator \hat{A}_{μ} . As a consequence, it is easy to generalize the scattering matrix we derived in Eq. 4.24 to

$$S = \exp\left(-\sum_{\mu} g_{\mu}^* \tau a_{\mu} b_{\mu}^{\dagger} - \text{h.c.}\right), \quad (7.3)$$

with the single-mode coupling strength

$$g_{\mu} = \sqrt{\frac{e^2}{2\epsilon_0 \hbar \omega_{\mu} V_{\mu}}} \int_L dz e^{-i\omega_{\mu} z / v_e} u_{\mu}(z), \quad (7.4)$$

where the optical-mode-specific quantities are used.

Electron-cavity interaction in the particle-like regime

The state entanglement between electron-photon interaction has been analyzed in the literature in the presumed single-cavity-mode case [107, 261, 262]. However, electrons are generally coupled to multiple cavity modes. Without the definition of a collective spatial-temporal mode, it is not possible to realize single-mode interaction. Here, we first analyze the case where the electron interacts with multiple cavity modes of the resonator. We derive the interaction in the wave-like regime in Appendix. B.16, as well as a detailed derivation of how to mathematically treat this interaction. In this section, we show that we can simplify it to a single spatial-temporal mode in the particle-like regime.

We start with the electron wavefunction $|\psi_e\rangle = \int dE \psi(E) |E\rangle$ (a factor of $\sqrt{L/2\pi}$ is neglected for simplicity) with an energy (momentum) spread. After the interaction, the final state is

$$|\psi_{e, \{\psi_\mu\}}\rangle = \exp\left(-\frac{1}{2} \sum_\mu |g_\mu|^2\right) \sum_{\{n_\mu\}} \frac{\prod_\mu (-i g_\mu^*)^{n_\mu}}{\sqrt{\prod_\mu n_\mu!}} \int dE \psi(E) |E - \sum_\mu n_\mu \hbar \omega_\mu\rangle \prod_\mu |n_\mu\rangle \quad (7.5)$$

while the reduced electron density matrix becomes

$$\rho_e = \exp\left(-\sum_\mu |g_\mu|^2\right) \sum_{\{n_\mu\}} \frac{\prod_\mu |g_\mu|^{2n_\mu}}{\prod_\mu n_\mu!} \int dE \psi(E) |E - \sum_\mu n_\mu \hbar \omega_\mu\rangle \int dE' \psi^*(E') \langle E' - \sum_\mu n_\mu \hbar \omega_\mu|. \quad (7.6)$$

From this, we can find the redistributed electron energy density function $f(E)$ in terms of the zero-loss-peak density function $f_{ZLP}(E)$ as

$$\begin{aligned} f(E) &= \langle E | \rho_e | E \rangle = \exp\left(-\sum_\mu |g_\mu|^2\right) \sum_{\{n_\mu\}} \frac{\prod_\mu |g_\mu|^{2n_\mu}}{\prod_\mu n_\mu!} |\psi(E + \sum_\mu n_\mu \hbar \omega_\mu)|^2 \\ &= \sum_{\{n_\mu\}} \prod_\mu \exp(-|g_\mu|^2) \frac{|g_\mu|^{2n_\mu}}{n_\mu!} f_{ZLP}(E + \sum_\mu n_\mu \hbar \omega_\mu). \end{aligned} \quad (7.7)$$

In the particle-like regime where optical modes with reasonable g_μ are centered at $\omega = \langle \omega_\mu \rangle$ with phase-matching bandwidth $\Delta\omega \ll (\Delta f_{ZLP}, \omega)$, we can approximate the redistributed electron energy density as

$$f(E) = \sum_n \exp\left(-\sum_\mu |g_\mu|^2\right) \frac{(\sum_\mu |g_\mu|^2)^n}{n!} f_{ZLP}(E + n\hbar\omega) \quad (7.8)$$

which consists of multiple electron energy-loss sidebands at $-n\hbar\omega$ energy with a Poisson distribution at rate $\sum_\mu |g_\mu|^2$. This distribution hints that a spatial-temporal mode can be defined in this regime. We can verify that for our device, we are well within the particle-like regime by considering the parameters of our system and comparing analytical and numerical results (Fig. 7.2) until the fourth sideband order.

7.1 Free-electron interaction with cavity modes

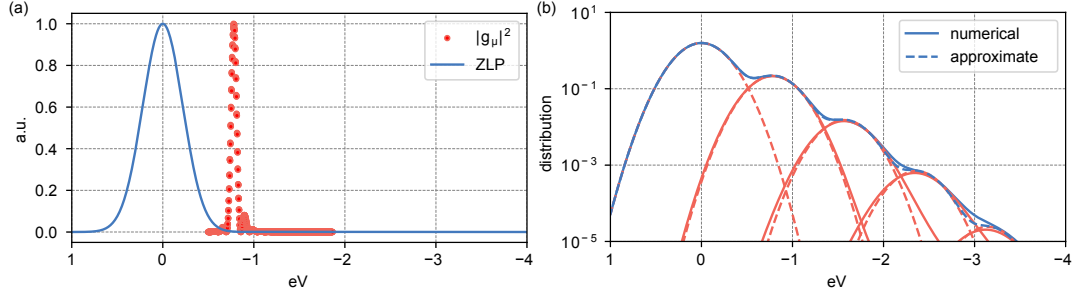


Figure 7.2: **(a)** Electron energy zero-loss-peak distribution and $|g_\mu|^2$ distribution for different optical modes, calculated with parameters of the experiment system. **(b)** Calculated electron energy loss spectrum with exact numerical and approximated analytical results. One can see that the analytical result only starts to deviate at higher order sidebands, hints at the breakdown of the particle-like regime.

We can further calculate the reduced photon density matrix,

$$\begin{aligned} \rho_o = \exp\left(-\sum_{\mu} |g_{\mu}|^2\right) \int_E dE \left(\sum_{\{n_{\mu}\}} \frac{\prod_{\mu} (-i g_{\mu}^*)^{n_{\mu}}}{\sqrt{\prod_{\mu} n_{\mu}!}} \psi(E + \sum_{\mu} n_{\mu} \hbar \omega_{\mu}) \prod_{\mu} |n_{\mu}\rangle \right) \\ \times \left(\sum_{\{n_{\mu}\}} \frac{\prod_{\mu} (i g_{\mu})^{n_{\mu}}}{\sqrt{\prod_{\mu} n_{\mu}!}} \psi^*(E + \sum_{\mu} n_{\mu} \hbar \omega_{\mu}) \prod_{\mu} \langle n_{\mu}| \right), \end{aligned} \quad (7.9)$$

When we only look at the probability of having the $|n_v\rangle$ state in a specific optical mode v ,

$$\begin{aligned} P(n_v) &= \exp\left(-\sum_{\mu} |g_{\mu}|^2\right) \sum_{\{n_{\mu}\}/n_v} \left(\frac{\prod_{\mu} |g_{\mu}|^{2n_{\mu}}}{\prod_{\mu} n_{\mu}!} \int_E dE |\psi(E + \sum_{\mu} n_{\mu} \hbar \omega_{\mu})|^2 \right) \\ &= \exp\left(-\sum_{\mu} |g_{\mu}|^2\right) \sum_{\{n_{\mu}\}/n_v} \frac{\prod_{\mu} |g_{\mu}|^{2n_{\mu}}}{\prod_{\mu} n_{\mu}!} \\ &= \exp(-|g_v|^2) \frac{|g_v|^{2n_v}}{n_v!} \prod_{\mu \neq v} \left(\sum_{n_{\mu}} \exp(-|g_{\mu}|^2) \frac{|g_{\mu}|^{2n_{\mu}}}{n_{\mu}!} \right) \\ &= \exp(-|g_v|^2) \frac{|g_v|^{2n_v}}{n_v!}. \end{aligned} \quad (7.10)$$

Therefore, each optical mode still follows a Poisson distribution, even though the electron couples to many optical modes.

Again, in the limit where the optical modes with reasonable g_{μ} are centered at $\omega = \langle \omega_{\mu} \rangle$ with small phase-matching bandwidth $\Delta\omega$ compared to the zero-loss-peak spread Δf_{ZLP} , we can

Chapter 7. Cavity-mediated electron-photon pairs

approximate the reduced photon density matrix as

$$\rho_o = \exp\left(-\sum_{\mu} |g_{\mu}|^2\right) \int_E dE \left(\sum_n \frac{(-\sum_{\mu} i g_{\mu}^* a_{\mu}^{\dagger})^n}{n!} \psi(E + n\hbar\omega) \prod_{\mu} |0_{\mu}\rangle \right) \times \left(\prod_{\mu} \langle 0_{\mu}| \sum_n \frac{(\sum_{\mu} i g_{\mu} a_{\mu})^n}{n!} \psi^*(E + n\hbar\omega) \right) \quad (7.11)$$

and when the zero-loss peak spread Δf_{ZLP} is much smaller than the sideband energy $\hbar\omega$, the density matrix can be further simplified as,

$$\rho_o = \exp\left(-\sum_{\mu} |g_{\mu}|^2\right) \sum_n \left(\frac{(-\sum_{\mu} i g_{\mu}^* a_{\mu}^{\dagger})^n}{n!} \prod_{\mu} |0_{\mu}\rangle \right) \left(\prod_{\mu} \langle 0_{\mu}| \frac{(\sum_{\mu} i g_{\mu} a_{\mu})^n}{n!} \right) \quad (7.12)$$

where we can define the spatial-temporal mode

$$a = \frac{\sum_{\mu} i g_{\mu} a_{\mu}}{\sqrt{\sum_{\mu} |g_{\mu}|^2}}. \quad (7.13)$$

with the coupling strength $|g|^2 = \sum_{\mu} |g_{\mu}|^2$. Upon conditioning on an electron n th sideband loss event, the optical system collapses to an entangled state between different optical modes a_{μ} , but at the same time, also a Fock state for the cavity spatial-temporal mode a ,

$$|\{\psi_o\}\rangle_c = \frac{(-\sum_{\mu} i g_{\mu}^* a_{\mu}^{\dagger})^n}{\sqrt{n!(\sum_{\mu} |g_{\mu}|^2)^n}} \prod_{\mu} |0_{\mu}\rangle = \frac{(g^* a^{\dagger})^n}{\sqrt{n!|g|^{2n}}} |0\rangle. \quad (7.14)$$

If we do not go to the spatial-temporal mode basis, the original multi-mode state is a large-scale W state [263, 264, 265] with a general interest in quantum information processing. The intuition of generating such a large-scale superposition state is that due to the broad zero-loss peak of the electron state, the detection on n th sideband does not resolve the which-mode information, rendering all the modes in a superposition state.

7.2 Coherent cathodoluminescence

After finding that the electron is expected to interact with a spatial-temporal mode consisting of multiple cavity modes, we seek to observe this effect by first measuring photon excitation from the optical side. First, we spatially and spectrally map the electron-induced cavity excitation by placing the electron beam in the proximity of the resonator (Fig. 7.3A and B). Measured with an optical spectrometer, the overall spectral range of the detected radiation spans from 1520-1620 nm, primarily limited by the bandwidth of electron-light phase matching, and in good agreement with numerical simulations (Fig. 7.3C). The spectrum exhibits a comb-like structure (Fig. 7.3D) due to free-electron coupling to the individual microresonator modes \hat{a}_{μ} . The 1.58-nm spacing of the emission peaks matches the optically characterized quasi-TM

7.2 Coherent cathodoluminescence

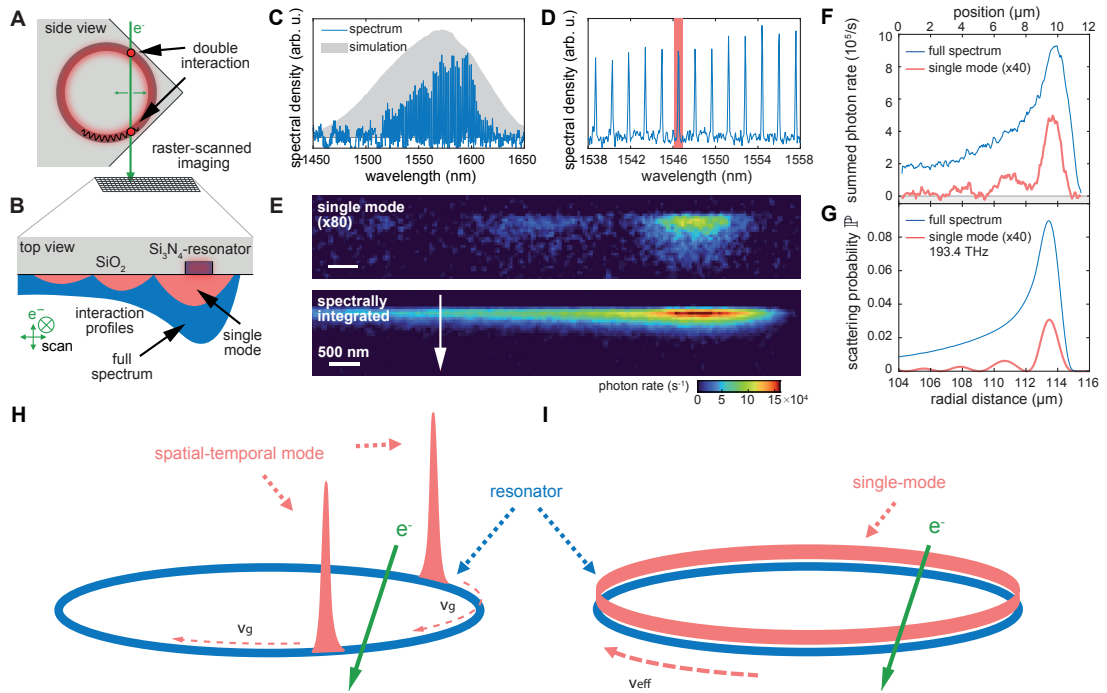


Figure 7.3: **Spatial and spectral mapping of intracavity photon generation.** (A) and (B) Schematic of the measurement geometry. The electron beam (green) passes parallel to the chip surface (grey) and interacts twice (red dots) with the ring resonator (dark red). (C) Optical emission spectrum (electron beam passes resonator tangentially) and simulated spectral envelope (grey). (D) Close-up of the spectral mode comb and a selected single cavity mode (red). (E) Raster-scanned photon-generation maps (saturation-corrected, see Section 7.3) for the selected mode and the full spectrum (intensity patterns illustrated in (A) with red and blue). (F) Signals from panel (E) integrated along the white arrow. (G) Simulation of the position-dependent electron scattering probability (50-nm distance). (H) Full-spectrum / spatial-temporal-mode picture of the double interaction. (I) Single-mode picture of the double interaction.

free-spectral range and confirms the predominant photon extraction from this mode family.

Spatial characterization of the intracavity excitation is obtained by raster-scanning the electron beam (Fig. 7.3A and B) and detecting the emitted light with a SPAD. Fig. 7.3E displays the obtained single-mode (top) and spectrally-integrated (bottom, corresponding to our spatial-temporal mode \hat{a}) photon rates, which decay exponentially with distance from the structure, mapping out the near-field mode profile in this spectral range. The most substantial photon generation is observed for electrons passing the ring resonator tangentially, as expected for the long interaction length.

Fig. 7.3F shows the photon generation rates along the chip surface. The single-mode count rate shows a pronounced oscillation in the radial distance to the center of the ring resonator. The oscillation is caused by the interference between sequential interactions (Fig. 7.3A and I) of an electron with the cavity mode vacuum field [266], proving the conservation of mutual coherence in the scattering process. Similar Ramsey-type interference is also observed in our PINEM experiment.

Integrating the full mode spectrum of the cathodoluminescence averages out the oscillatory pattern, in agreement with numerical simulations (Fig. 7.3G). Intuitively, when the spatial-temporal mode is excited, the spatial extend of the optical pulse ($\sim 10 \mu\text{m}$), as well as the finite group velocity, is much shorter than the spatial separation between the two interaction region, in contrast to the single-mode case where the spatial extend covers the whole ring. Therefore, for the excited spatial-temporal mode, the sequential interaction with the same optical pulse is not possible (see Fig. 7.3H), therefore, showing no interference-induced oscillatory behavior. Here, the total scattering probability of the spatial-temporal mode is $\mathbb{P} = \sum_{\mu} |g_{\mu}|^2$, as the sum of the individual mode contributions g_{μ} , and can be up to 7%.

7.3 Electron-photon non-classical correlation

7.3.1 Time- and energy-correlated electron-photon pairs

The spontaneous creation of photons by single electrons satisfies energy-momentum conservation, lowering the energy of an electron by $\hbar\omega$ and transferring the corresponding momentum to the cavity photon. In this section, we probe the correlation of the electron-photon pair state by coincidence measurements of both particles (Fig. 7.4). The electron beam is held fixed in the near field of the cavity at a $\sim 160\text{-nm}$ distance from the surface. At this position, we detect photons with a probability of 4.6×10^{-5} per electron passing the structure. Considering coupling and detection losses, this corresponds to an intrinsic generation probability of about $\sim 2.5\%$.

The arrival time and kinetic energy of each electron are measured by event-based spectroscopy, using the stream of photon events recorded by the SPAD for time-tagging (Fig. 7.1A). Fig. 7.4A shows the energy- and time-dependent histogram of electron arrivals relative to the photon

7.3 Electron-photon non-classical correlation

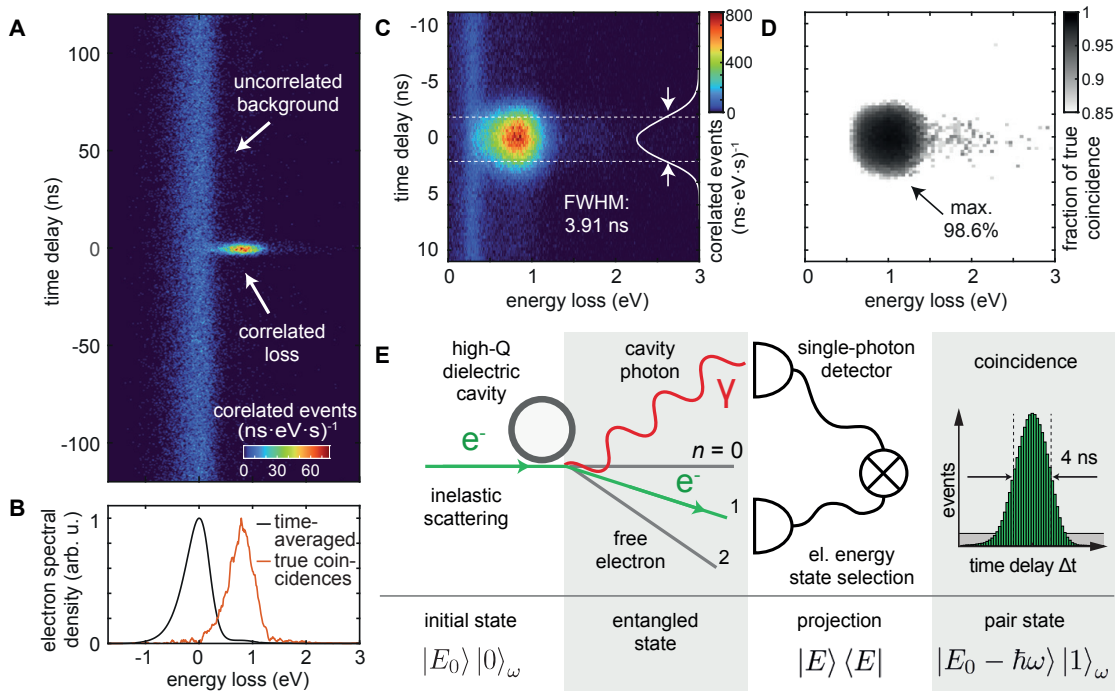


Figure 7.4: **Time- and energy-correlated electron-photon pairs.** (A) Two-dimensional correlation histogram over the electron energy and relative photon timing (30-s integration, 0.65-pA electron current on the detector) showing a strong coincidence peak. (B) Spectral distributions of the uncorrelated and correlated electrons (background subtracted). (C) and (D) Close-up of correlation histogram (ZLP blocked, 60-s integration, 46-pA beam current at sample) with coincidence time trace (white) and fraction of true coincidences. (E) Illustration of cavity-mediated inelastic electron-photon scattering and coincidence measurement.

event closest in time. Two main features observed are a time-independent background of accidental coincidences around zero energy loss, and an anticipated sharp correlation peak around 0.8-eV energy loss and 0-ns time delay. The spectrum of the correlated electrons (Fig. 7.4B, red) is downshifted by one photon energy relative to the zero-loss-peak (ZLP) (black). As a result of the narrow electron-light phase-matching bandwidth of ~ 50 meV, they closely match in broadening and shape (~ 0.5 eV width), as is expected in the particle-like regime. Note that we only observe the most prominent feature in the linear scale of the record. In log-scale, higher order scattering sidebands are present, whose response to the photon counting event is analyzed in detail in Section 7.5.

Next, we insert a mechanical slit in the electron spectrometer (Fig. 7.4C) to reject electrons that were not scattered, allowing for higher total electron flux, and also photon generation rates, without the electron detector saturation. The background-corrected time profile (inset) shows the precise temporal structure of the correlated electron-photon pairs with a width of 3.91 ns. In principle, the temporal correlation trace should reproduce the cavity decay time, but it is not resolved in the present experiments (current device: ~ 0.5 -ns lifetime for a quality factor of $Q \sim 5.5 \times 10^5$). Without significant optical pump power inside the cavity to recover

Chapter 7. Cavity-mediated electron-photon pairs

the high-energy electron-induced material damage, we observe a significant degradation of the optical quality factor as we put the electron beam in the near-field of the waveguide.

We identify correlated events on a single-particle basis by selecting loss-scattered electrons within a specific time window. In contrast to conventional optical spontaneous parametric down-conversion, the measurement of the electron energy for each event presents a direct measure of the energy quanta n deposited in the optical cavity. The single-electron energy detection at the first energy loss sideband represents an optical state projection from the entangled state (Eq. 7.2) onto the (non-classical) single-photon intracavity Fock state of the spatial-temporal mode \hat{a} . This general principle, illustrated in the schematic of Fig. 7.4E, enables inter-particle heralding schemes for either electrons or photons. Notably, interactions with multiple electrons—relevant for studying electron-electron correlations—can be excluded, considering the multi-hit capability of the detector.

Such heralded particle sources are quantified in terms of the measured rates of electrons (R_e), photons (R_p), correlated events (R_{pe}), and the Klyshko heralding efficiencies $\eta_K^i = R_{pe}/R_j$ ($i, j=e, p, i \neq j$) which describe the conditional probability of experimentally detecting a heralded particle. For the data shown in Fig. 7.4C, we measure $\eta_K^p \sim 0.11\%$ and $\eta_K^e \sim 57\%$ for photons and electrons, respectively.

The less efficient heralding of photons follows from considerably higher losses in their output coupling and detection (details see later subsections). Not being a fundamental physical limitation, we expect appreciable improvements in the photon collection efficiency with technical optimizations, including the use of superconducting detectors and strongly over-coupled resonators. Taking into account particle losses in transmission and detection, we estimate intrinsic heralding efficiencies η_1^i of approximately 50% (see detailed estimate of η_1^i in later subsections). As discussed in earlier sections, intrinsic heralding efficiencies can be achieved near unity with an optimal waveguide geometry and e-beam position.

In the following subsections, we detail the analysis processes leading to the results in this section.

Quantitative estimate of heralding efficiencies

Bright sources of single photons [267] and their integration in photonics [268] are essential for future quantum technology. In our approach, inelastic electron scattering at optical fibers can generate light in various geometries [184, 260, 269] and is shown to produce correlated electron-photon pairs. In principle, this scheme enables near-unity intrinsic heralding efficiencies. Accounting for imperfections in the current setup, we quantitatively estimate the various loss channels occurring after photon generation. While the wavelength- and mode-dependent coupling efficiency from the resonator into the bus waveguide can be simulated, other fiber connection losses and backscattering probabilities are estimated by additional measurements. Apart from that, we experienced deviations in the measurement results from the simulations

7.3 Electron-photon non-classical correlation

Photon loss channels	efficiencies
SPAD peak detection efficiency	31(5)%
SPAD CL bandwidth overlap	26(2)%
SPAD saturation	82(2)%
Effective resonator-bus coupling efficiency	originally 27%, degrade to 17(6)%
Directional output efficiency	88(1)%
Holder-fiber coupling efficiency	39(5)%
Fiber propagation/connection transmission	85(4)%
TM mode CL contribution	62(25)%
Electron ZLP accident events	>99%
Electron loss channels	efficiencies
Electron detection efficiency of spectrometer	94(10)%
Detector saturation	96(1)%
Electron propagation loss	unknown
Particle type	predicted chain efficiency
Photon	0.16(13)%
Electron	> 86(10)%
Particle type	measured Klyshko efficiency
Photon	0.11%
Electron	57%

Table 7.1: Efficiency budgets for photon/electron heralding experiments.

due to changes in the resonator properties in the presence of the electron beam, which we also observed in our soliton experiment. We collect all simulated and measured loss channels for photons and electrons in Table 7.1 and give detailed information on selected parts.

Coupling efficiency and optical transmission

To check whether the coupling efficiency from the resonator to the bus waveguide degraded during the experiment, we connected a continuous-wave tunable laser and a photodiode to the chip and analyzed the transmission profile when scanning the laser wavelength through a TM_{00} resonance. A slight increase of around 130 MHz in internal loss rate could be observed after around one hour of exposure to the electron beam. We attribute it to the potential deposition of carbon nanoparticles on the chip surface and electron-beam radiation damage [159]. This results in a degradation of the Q factor and also the coupling efficiency.

Another auxiliary experiment with the electron beam on/off the same resonator chip is shown in Fig. 7.5 to demonstrate this coupling efficiency degradation effect. The transmission signal of the optical resonance from laser wavelength scans allows the quantitative estimation of internal loss rate and coupling efficiency from the resonator to the bus waveguide. We conducted the measurement for one TM_{00} mode at 1548 nm only, estimating the coupling efficiencies of different optical modes during the experiment using the previously measured optical properties.

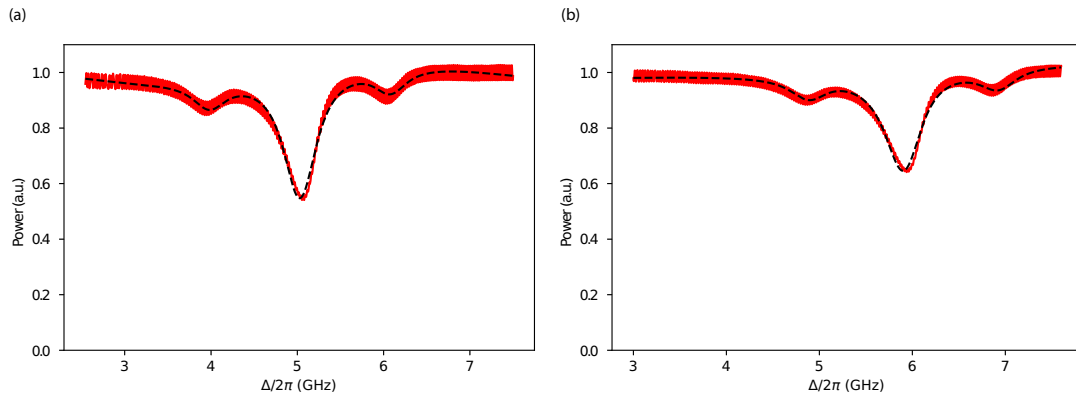


Figure 7.5: Comparison of optical resonance coupling efficiency (visibility) without **(a)** and with **(b)** the electron beam directly on the resonator. One can observe a decrease in resonance visibility, indicating an increase in resonator internal loss (by ~ 50 MHz) with the presence of the electron beam. The observed asymmetry in the mode transmission shape is due to bus waveguide facet reflection and is included in the cavity parameter fitting.

Saturation correction

The single photon detector used in the experiments (IDQ ID230) was operated in the Geiger mode to increase its single photon sensitivity. This leads to the detector's recovery time (dead time) after each detection event, in which it is blind to incoming photons. We changed this dead time for estimating the photon generation rate to reduce the fraction of undetected photons and, at the same time, keep the intrinsic noise of the detector, which increases drastically with shorter dead time, at a minimum. In a simplified model, we assume that the photons have a Poissonian distribution of their arrival time and correct for lost photons by calculating the fraction of events with timing distances shorter than the dead time considering the mean generation rate. Computing this ratio for different mean generation rates, or event rates, (Fig. 7.6) allows us to estimate the initially generated photon number from the number of the experimentally detected photons based on this model.

Photon generation direction

As the photonic chip is inherently symmetric in its geometry and coupling, there are two directions in which the photons can propagate to leave the bus waveguide. Comparing the measured CL signal from both fibers connected to the chip (cf. Fig 7.1C) shows a substantial imbalance in the number of photons. Over $10\times$ more photons are generated in the clockwise direction (cf. Fig 7.1A) than in the counterclockwise one, suggesting that most photons are generated in the direction of the electron beam. The weak signal from the counterclockwise direction would then stem from photons either generated in the opposite direction of the electron beam, which is highly unlikely considering the momentum conservation during photon generation, or scattered inside the microring. This scattering behavior can be observed

7.3 Electron-photon non-classical correlation

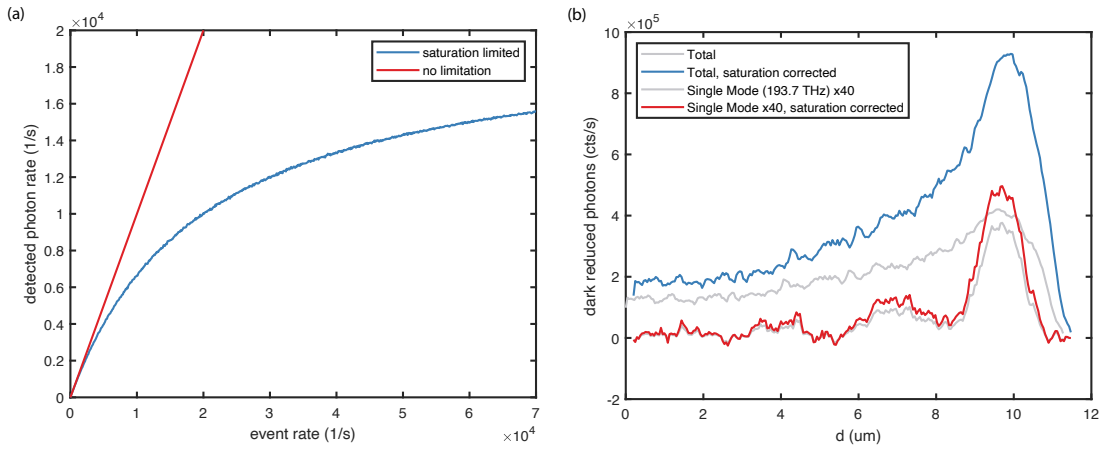


Figure 7.6: **(a)** Detected photon rate as a function of photon rate before the single photon detector (event rate), assuming a Poissonian timing distribution. The saturation limited curve (blue) considers a dead time after detection of 50 us, discarding the events with a smaller delay. Without saturation limit (red), the detected photon rate will stay equivalent to the event rate. **(b)** Comparison between saturation corrected and non-saturation corrected photon rates. Data is the horizontal sum of Fig 7.3C.

as mode splitting in a transmission response measurement and is the most likely explanation.

CL emission center frequency

The overlap efficiency between the CL bandwidth and the SPAD bandwidth strongly depends on the CL emission center wavelength, which has a gradient of about 20 nm/keV to the electron velocity and 7 nm/nm to the waveguide thickness changes. Due to imperfections in the fabrication process, the exact effective mode index of the waveguide is unknown. Therefore, we conclude the emission center frequency from a simplified fitting of the optical emission spectrum shown in Fig. 7.7. The fitting incorporates the fact that the CL emission center frequency can vary due to the uncertainty in the mode index and the possibility that the SPAD cutoff and the spectrometer frequency axis are not synchronized. The inclusion of the synchronization correction is supported by the model preference with a log-scale Bayesian factor (likelihood ratio) of 90 to prevent the possibility of over-fitting. Generally, a factor > 5 is considered decisive evidence for the preferred model. From this fitting, we extract the corrections to the CL emission frequency and the SPAD cutoff, leading to a CL emission frequency shift from our initial expectation by about 70(5)nm towards the higher wavelengths. Given the fitted CL frequency distribution, we estimate a CL-SPAD bandwidth overlap efficiency of 26(2)% (Fig. 7.9).

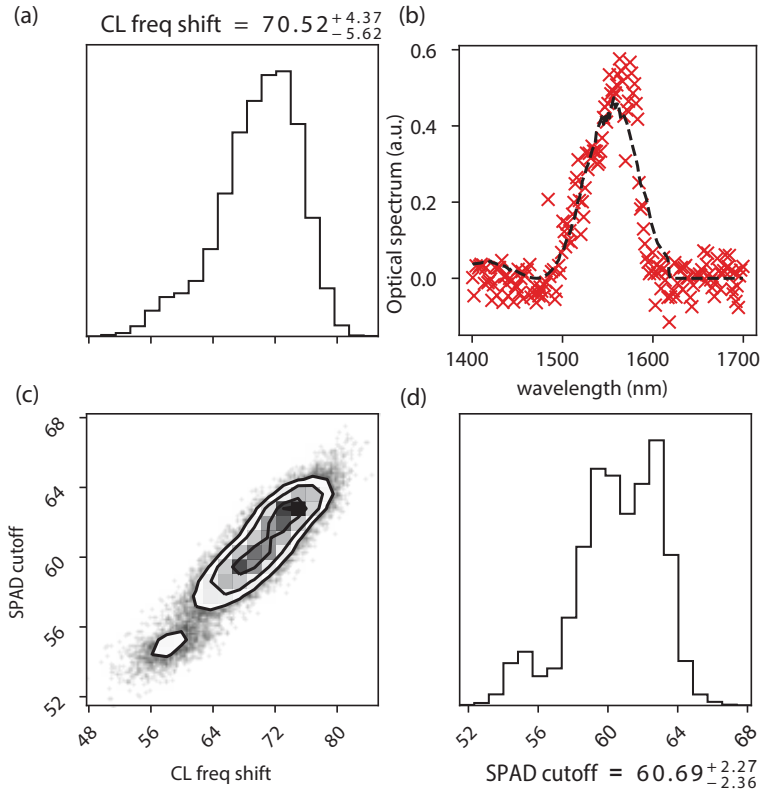


Figure 7.7: **(b)** Optical spectrum of the CL emission (red) and the fit (black). We use the fitting to extract the corrections to the CL emission frequency and the SPAD cutoff. **(a),(d)** The marginal distribution plots of these parameters. **(c)** Their correlation.

TM mode emission efficiency

In principle, the electron emits to an infinite amount of optical modes supported or not supported by the waveguide. In order to calculate the emission efficiency of CL into the TM_{00} mode, which is supported by the waveguide and is coupled out most efficiently, we conducted an electron energy loss simulation of the waveguide structure shown in Section 6.2. Such an approach yields electron-energy loss at different optical frequencies without summing up all the optical modes at that particular frequency. We observe in our simulation that due to the geometry of our waveguide (width of $2.1 \mu\text{m}$), the electron couples to many other waveguide modes in a large frequency band between 780 nm to $2.5 \mu\text{m}$, illustrated in Fig. 6.6.

In our experiment, we obtain electron energy loss spectrum at various impact distances to the waveguide surface, with some examples shown in Fig. 7.8. Even though TM_{00} mode dominates the emission process for the first few sideband orders, we can extract a significant contribution of emission into other optical modes in the form of a distorted ZLP with a semi-exponential tail towards the lower energy direction. Here, the ZLP deviates from the original 0.6-eV Gaussian-shaped peak and exhibits a Voigt-like shape towards the higher energy loss, primarily due to the first-order sideband emission of denser optical modes with exponential-decaying coupling

strength towards higher optical frequency (quicker evanescent field decay), observed in our simulation illustrated in Fig. 6.6. The fitting of the electron spectrum in Fig. 7.8 also takes into account a possible transverse position distribution of the e-beam, which accounts for a non-Poissonian distributed sideband populations even when emission into other modes is taken into account.

When comparing the loss to the energy loss caused by the TM_{00} mode, we extract a CL emission efficiency into the TM_{00} mode of 62%, with the additional loss event contribution from higher order waveguide modes at higher frequencies but could not be distinguished due to the finite electron energy loss resolution. In principle, this is the only efficiency that should limit the intrinsic heralding efficiency, and the emission into the substrate bulk is estimated to be less than 2%. This efficiency can be improved by optimizing over the waveguide geometry, e.g., taking a $0.75\ \mu\text{m}$ waveguide width instead of the $2.1\ \mu\text{m}$ used in the experiment, allowing for a near unity efficiency given our electron energy loss resolution. Further improvement requires a more careful geometric optimization. In the inference of the intrinsic heralding efficiency, the TM mode emission efficiency is set with a uniform distribution, assuming no knowledge due to the uncertainty of e-beam positioning and waveguide geometry from fabrication.

Heralding Efficiency

The Klyshko heralding efficiencies for photons and electrons can be calculated, following Ref. [268], from the detection rates for the coincidence events R_{pe} , the electrons R_e and the photons R_p , using

$$\eta_K^{p(e)} = \frac{R_{pe}}{R_{e(p)}} \quad (7.15)$$

If taking into account the respective detector's detection efficiencies $\eta_d^{p(e)}$ as well as the transmission losses of both particles through their setup $T_{p(e)}$, we arrive at the respective intrinsic heralding efficiency [268]

$$\eta_I^{p(e)} = \frac{\eta_H^{p(e)}}{\eta_d^{p(e)} T_{p(e)}}, \quad (7.16)$$

which indicates the efficiency of the generation process in producing a particle pair. The Klyshko heralding efficiency, on the other hand, is deemed to be very small for the photons due to the multiple loss channels of the setup, as discussed above.

Specifically, from the measurement record, we define coincidence events R_{pe} as the total electron events within the correlation time window and a specific energy window. The photon event rate R_p is taken directly from the SPAD count. The electron event rate R_e detected by the electron detector is limited to the energy window of the coincidence events to reduce the influence of electrons that did not interact with the resonator. The energy window of the coincidence events was chosen to be between 0.5-eV and 1.15-eV electron energy loss for electron heralding efficiency calculation. For the photon heralding efficiency, the energy window of the electrons and coincidence events was reduced to a thin slice around 0.97eV

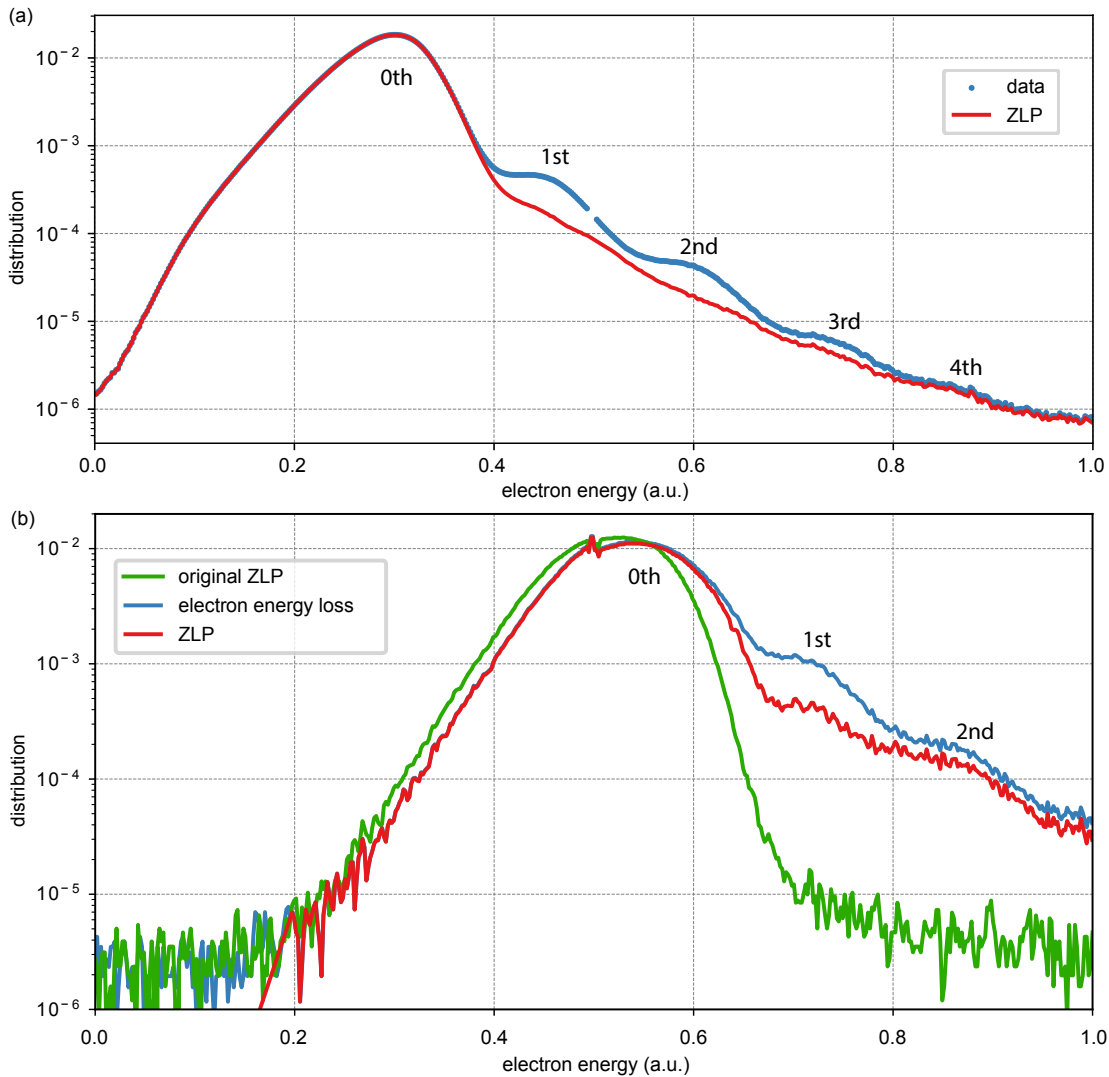


Figure 7.8: Electron energy loss spectra at different impact distances. **(a)** Large impact distance with $\sim 2.5\%$ emission probability into the TM_{00} mode, used in the correlation experiment. We can extract the broadened ZLP (not original) using a fitting algorithm that considers the size of the electron transverse distribution. The broadening is due to the parasitic coupling to higher-order optical modes with exponentially decaying coupling strengths due to their optical frequencies. From this data, we can extract a CL emission efficiency into the TM_{00} mode of 62%. Note that the fitting of the ZLP is highly sensitive to the model and the fitting procedure, which can only be verified when compared to the n -photon-conditional electron energy spectrum (e.g., explained in Fig. 7.16). Therefore, the results presented here can only serve as an order-of-magnitude estimation. **(b)** Electron spectra measured in STEM mode with varying impact distance but with lower number of averaging and sideband orders, with up to $\sim 7\%$ emission probability into the TM_{00} mode. As the coupling ideality of the TM_{00} mode decreases with smaller impact distance, i.e. the electron couples relatively stronger to higher order optical modes, we also observed a broader ZLP shape compared to the original ZLP measured far away from the waveguide, as well as a diminishing feature of the higher order photon sidebands of the TM_{00} mode.

7.3 Electron-photon non-classical correlation

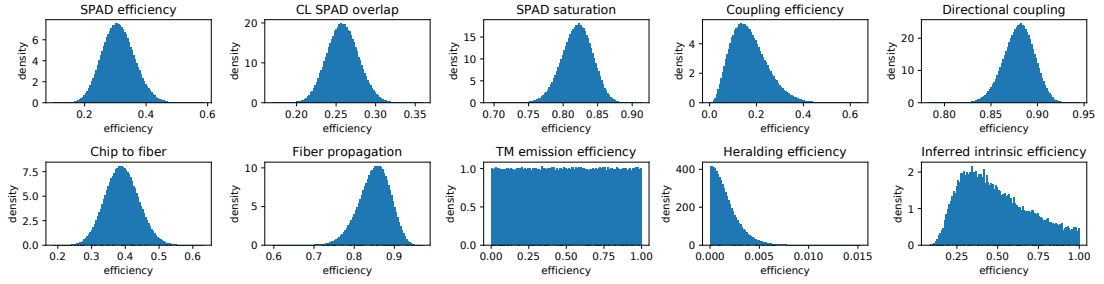


Figure 7.9: Statistical distribution of the sampling results of efficiencies η_i of different loss channels using approximated Beta distribution. A uniform intrinsic heralding efficiency (TM emission efficiency) is assumed here. The total heralding efficiency $\eta_H = \prod_i \eta_i$ is a product (assuming independence of different loss channels) of efficiencies of all the loss channels. By conditioning on a thin slice in the sampled total heralding efficiency based on measurement result 0.11%, the conditioned samples (labeled inferred intrinsic efficiency) are effectively drawn from the target posterior distribution of the intrinsic heralding efficiency.

electron energy loss. This choice maximizes the heralding efficiency, as the contribution from electrons in the ZLP and higher-order transition events are suppressed.

Using the measured data depicted in Fig. 7.4C, we retrieve the Klyshko heralding efficiencies for photons and electrons to be around $\eta_K^p = 0.11\%$ and $\eta_K^e = 57\%$.

Electron losses due to the setup were analyzed for the spectrometer and detector by comparing the electron current at the beginning of the spectrometer with the detected electron number. Further loss channels are still possible between the interaction region on the photonic chip and the spectrometer due to beam-clipping at the chip and apertures and deflection due to charging effects. This is why the calculated intrinsic heralding efficiency for electrons $\eta_I^e = 63(10)\%$ can be seen as a lower limit.

Infering intrinsic photon heralding efficiency

The posterior probability distribution of the intrinsic heralding efficiency (takes into account mode emission efficiency and other unknown factors) can be retrieved from the Bayes theorem,

$$P(\eta_I|\eta_H) = \frac{P(\eta_H|\eta_I)P(\eta_I)}{P(\eta_H)} \propto P(\eta_H, \eta_I) = \prod_i P(\eta_i) \quad (7.17)$$

where the probability distribution of efficiencies of different loss channels (except CL SPAD overlap efficiency and prior intrinsic heralding efficiency) are approximated by independent Beta distribution, which is commonly used to model the distribution of event probabilities. Due to the nature of its high dimensionality, the marginalization over seven variables is hard to perform numerically. Instead, we extract the distribution of intrinsic heralding efficiency through sampling (Fig. 7.9), which scales only linearly with the number of variables. We sample the probability distribution $P(\eta_H, \eta_I)$ from the product of efficiencies $\prod_i \eta_i$ of different

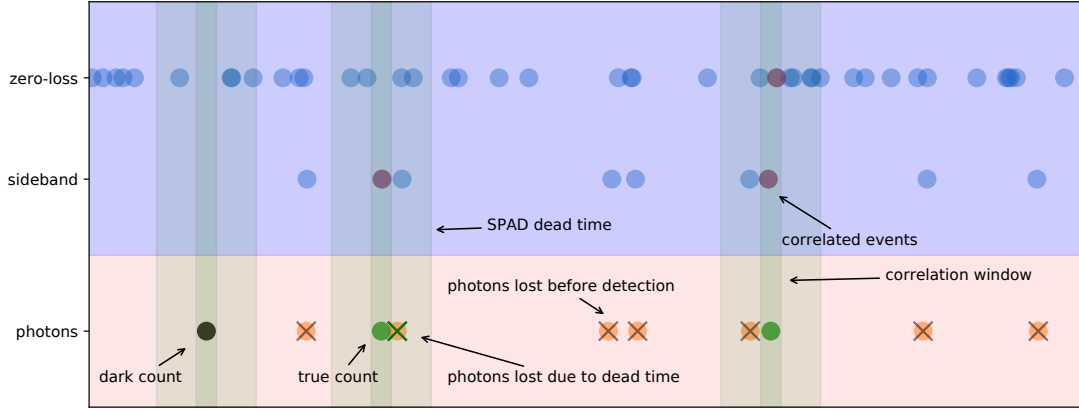


Figure 7.10: Contributions to correlation background: Sketch of electron and photon arrival time and the resulting classification due to photon loss, SPAD dead time, and intrinsic dark counts. The electrons are separated energy-wise in zero-loss (no interaction) and sideband (interaction with cavity) electrons.

loss channels, each drawn from their Beta distributions $P(\eta_i)$. When conditioning on the measured heralding efficiency $\eta_H^p = 0.11\%$ from the correlation experiment, we sample the posterior probability distribution $P(\eta_I^p|\eta_H)$ at $\eta_H = 0.110 \pm 0.005\%$ and obtained the intrinsic photon heralding efficiency with a uniform prior probability distribution $P(\eta_I) = \mathcal{U}_{[0,1]}$ (with no knowledge of intrinsic efficiency),

$$\langle \eta_I^p \rangle_{P(\eta_I^p|\eta_H)} = 49(21)\%. \quad (7.18)$$

When conditioning on the measured heralding efficiency $\eta_H^p = 0.33\%$ from the correlation imaging method, we obtain the intrinsic photon heralding efficiency

$$\langle \eta_I^p \rangle_{P(\eta_I^p|\eta_H)} = 77(16)\%. \quad (7.19)$$

Given our experiment configuration, the calibrated intrinsic efficiency is on the expected order of magnitude. Its precision and value could be further increased by carefully measuring the individual loss channels.

Correlation background-event contributions

Different types of coincidences contribute to the correlation peak's background, which we will now describe in more detail, together with the visualization in Figure 7.10. The figure describes the possible electron (blue) and photon (green) arrivals on the detectors as a random event in time (x-axis). Many generated photons are not detected due to various loss channels, as described in many previous subsections (orange dots with a black cross). Additional losses can occur due to the photon detector's dead time (light green region), which prevents a second photon detection at smaller delay (orange dot with green cross).

The electron arrival time is now analyzed concerning the nearest photon, defining a coincidence as a small time window around the photon arrival time (corrected for fixed delays), in which the electron arrival has to occur (dark green region). The types of false coincidences arising from this analysis are the following:

Electrons that did not scatter inelastically are distributed evenly in their arrival time concerning the next photon and make up most of the background at $\Delta E = 0$ eV. (blue dots in the upper row), as they have not transferred energy to a photon. When arriving near a correlated event, these electrons seemingly increase the number of coincidences (brown dot in the upper row); however, they show the wrong energy. Therefore, they can be filtered out by correct selection of the electron energy.

The second type of coincidence is the electrons that interacted with the optical mode, but the photon was lost in the process. These electrons can be separated from the first type by energy loss (blue dots in the second row). Most of them are measured as uncorrelated events, which reduce the photon heralding efficiency but can be accounted for by correcting the correlated events for these losses (see previous sections).

Thirdly, a false coincidence is possible when electrons correlate with a dark count (cf. Fig 7.10 green region around black dot) or a different photon generated at a similar time. These can not be distinguished from the true coincidences. However, one can reduce its probability by, for example, keeping the number of dark counts far below the number of true photon detections.

7.3.2 Violation of Cauchy-Schwarz inequality

Despite the envisioned utilities of the correlations between electron energies and photon numbers, to prove that the correlation we observe is non-classical, we have to analyze in detail what the classical and non-classical pictures are. For the light, we assume that the classical picture is the classical field theory, where the photoelectric effect produces discrete charges whose probabilities are linked to the stochastic classical field intensities. The non-classical correlation between light fields has been tested decades ago [119] using two-port photon coincidence detection, as classical field correlations are constrained by the Cauchy-Schwarz inequality. Breaking the Cauchy-Schwarz inequality falsified the stochastic classical field theory, and the light field has to be quantized irrespective of the detector model. Spontaneous parametric down-conversion (SPDC) is generally used for these experiments, where two optical beams are generated with correlated photon numbers between them. However, as we have electrons on one of the scattering branches, the situation is more delicate, as electrons are individual particles instead of a classical field. Compared to an SPDC process, the particle number in one frequency of an optical beam can not be mapped to the particle numbers in the electron beam at a given energy, as there is intrinsically only one electron. However, it is possible to map the classical amplitude of the SPDC light field to the electron energy, as the pair states we generated are correlated between photon number and electron energy. Even though electron numbers are classically *quantized*, the classical picture we have in

Chapter 7. Cavity-mediated electron-photon pairs

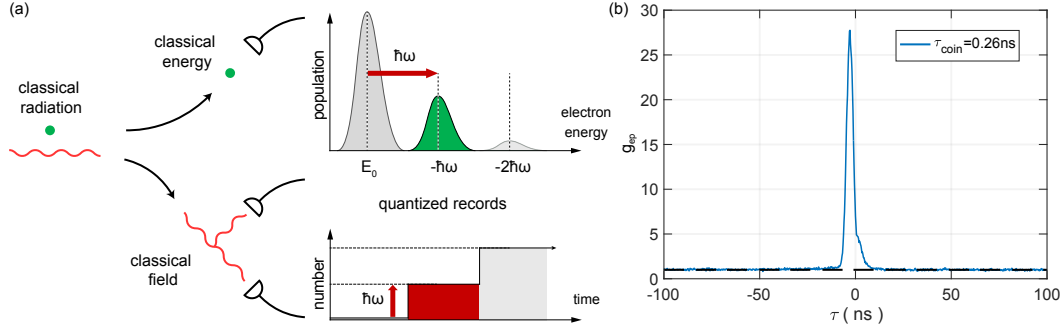


Figure 7.11: **(a)** Classical picture of free-electron radiation of light. Measurement records are quantized based on the classical stochastic electron energy and light amplitude values. The classical correlation generated in this way is bounded by the Cauchy-Schwarz inequality (Eq. 7.28). **(b)** Measured electron-photon correlation function $g_{ep}(\tau)$ as a function of relative delay time τ between the electron and photon detection.

mind is not the particle number, as our measurement observable is actually the continuum-valued electron energy for each electron. Therefore, the picture that each electron has a continuum-valued energy after the scattering event is, in our case, classical. Of course, this picture contradicts our observation that the electron energy change is not single-valued but stochastic and quantized to discrete energy levels. Therefore, we assume that at some stage of the interaction, similar to the optical counterpart, the electron energy and the optical fields are correlated stochastically in a classical way. Finally, we summarize that in the classical picture of electron-light interaction, the classical electron generates a classical light with stochastically correlated energy and fields. This picture is also illustrated in Fig. 7.11(a).

In the classical stochastic field theory [271], given stochastic observables i, j, \dots , we can define the following second-order correlation functions

$$g_{ij}(\tau) = \langle I_i(t+\tau)I_j(t) \rangle / \langle I_i \rangle \langle I_j \rangle \quad (7.20)$$

$$\langle I_i \rangle = \int P(\epsilon_i) I_i(\epsilon_i) d\epsilon_i \quad (7.21)$$

$$\langle I_i I_i \rangle = \int P(\epsilon_i) I_i(\epsilon_i)^2 d\epsilon_i \quad (7.22)$$

$$\langle I_i I_j \rangle = \int P(\epsilon_i, \epsilon_j) I_i(\epsilon_i) I_j(\epsilon_j) d\epsilon_i d\epsilon_j \quad (7.23)$$

where the ϵ_i are fluctuating stochastic complex field amplitudes, and $P(\epsilon_i)$ is a probability distribution in the complex plane. There are a few inequalities that we can derive from this definition. First, as the variance of a random distribution is always positive, we have

$$\langle I_i^2 \rangle - \langle I_i \rangle^2 \geq 0 \quad (7.24)$$

$$g_{ii}(0) \geq 1 \quad (7.25)$$

7.3 Electron-photon non-classical correlation

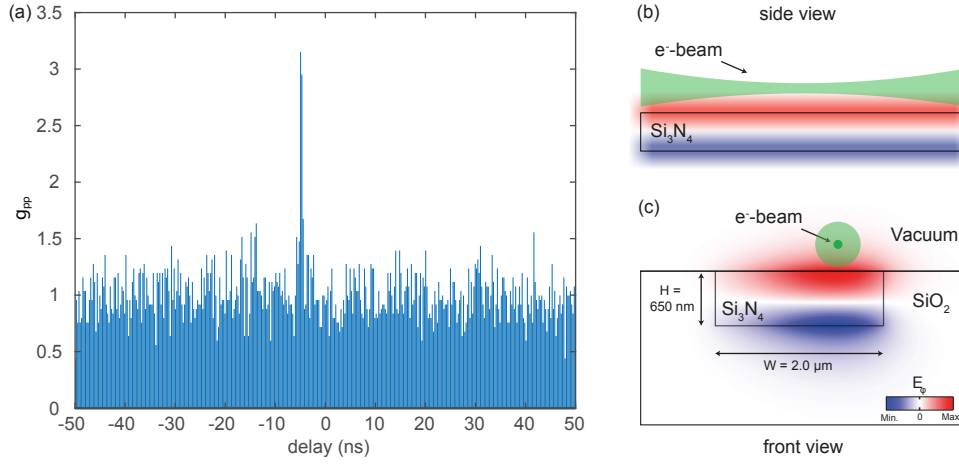


Figure 7.12: **(a)** HBT measurement of photon auto-correlation, showing a prominent peak at zero delay. The photon bunching effect is expected to have originated from the multi-photon generation events of the same electron [260] of coherent cathodoluminescence. **(b,c)** Apart from the contribution from incoherent cathodoluminescence [270], the explicit photon statistics from a single electron can also exhibit a thermal-like distribution due to the incoherent averaging of the electron transverse distribution, equivalent to an intensity modulation of the generated photon flux. We illustrate the electron beam configuration that might cause the substantial g averaging.

Also, we can apply the Cauchy-Schwarz inequality

$$\langle I_i I_j \rangle^2 \leq \langle I_i^2 \rangle \langle I_j^2 \rangle \quad (7.26)$$

$$g_{ij}(0) \leq \sqrt{g_{ii}(0) g_{jj}(0)} \quad (7.27)$$

where the bound is satisfied when ϵ_i and ϵ_j are linearly dependent.

To show that our experiment falsifies this classical picture of the electron-photon interaction, we only need to calculate the second-order correlations of the coincidences and show that it breaks a similar Cauchy-Schwarz inequality, i.e.,

$$\gamma = \frac{g_{ep}(0)}{\sqrt{g_{ee}(0) g_{pp}(0)}} \leq 1 \quad (7.28)$$

where $g_{ep}(\tau) = \langle \hat{E}(t+\tau) \hat{I}(t) \rangle / \langle \hat{E} \rangle \langle \hat{I} \rangle$ is the electron-photon cross-correlation function, whereas $g_{ee}(0) = \langle \hat{E}(t)^2 \rangle / \langle \hat{E} \rangle^2$ and $g_{pp}(\tau) = \langle \hat{I}_1(t+\tau) \hat{I}_2(t) \rangle / \langle \hat{I}_1 \rangle \langle \hat{I}_2 \rangle$ are the auto-correlation functions. $g_{ep}(\tau)$ is already measured in our coincidence experiment, and we illustrate it in Fig. 7.11, showing a maximum $g_{ep}(0) = 28$. To use for the evaluation of the Cauchy-Schwarz inequality, to simplify the calculation, we adjust the time-bin width to 3.6 ns such that in each window on average there is one electron. With the new bin width, we obtain the cross-correlation function $g'_{ep}(0) = 15$.

Chapter 7. Cavity-mediated electron-photon pairs

For optical auto-correlation, historically, people typically equally divide the optical beam into two detectors and measure the correlations between their measured intensities. In the quantum picture, this procedure measures a different observable, and the correlation results differ from that of a single port measurement. However, it measures the same classical second-order correlation function, as the two ports will show identical fluctuations $I_1 = I_2 = I/2$ in the classical theory so that we have the following relations

$$\langle I_1 I_2 \rangle = \frac{1}{2} \int P(\epsilon) I(\epsilon)^2 d\epsilon \quad (7.29)$$

$$\langle I_1 I_2 \rangle / \langle I_1 \rangle \langle I_2 \rangle = \langle I^2 \rangle / \langle I \rangle^2 = g_{pp}(0). \quad (7.30)$$

This is an elegant trick on the optical side as this measurement procedure significantly suppresses the contribution from the single-photon events of $\langle \hat{I}(t)^2 \rangle$, which would otherwise dominate the single port measurement and lead to a much bigger measured $g_{pp}(0) \gg 1$ in the quantum result. We emphasize again that even though the single-port and double-port measurement settings measure the same classical correlation function, they measure drastically different quantum results in the experiment due to the operator ordering, and it is generally preferred to use the two-port schemes to suppress the single-photon events. In fact, if we use single-port detection on both sides, at best with unity detection efficiency, we can saturate the Cauchy-Schwarz bound but not violate it. The two-port detection also makes the measurement result loss-independent. We will see later that the inability to perform a two-port measurement on the electron side results in a $g_{ee}(0) \gg 1$.

We proceed to measure the optical correlation function using two single-photon detectors, shown in Fig. 7.13(a). Contrary to the SPDC process where the signal photons follow a thermal distribution, and therefore $g_{pp} = 2$. In electron-photon interaction, g_{pp} is associated with a Poissonian photon generation/electron energy loss process and is ideally unity. However, this Poissonian generation process is only limited to every single electron during the fs interaction time and the cavity leakage. The two-photon events can also come from different electrons for our measurement setting. In our experiment, our collaborator Germain Arend measured $g_{pp}(0) = 3.2$, shown in Fig. 7.12(a) with a prominent bunching peak with a width on the order of the cavity decay time. We have not yet completely quantified the different contributions leading to this bunching peak.

We found that the background events probability [260] within a time-bin window when $|\tau| \gg \tau_{ph}$, where τ_{ph} is the temporal duration of the optical pulse, is $P_\tau = \eta_1 \eta_2 |g|^4 P_e^2 / 4$ where η_i is the measurement efficiency of a detection channel i , $P_e = 1 - \exp(-\Gamma \Delta t)$ is the probability of finding at least one electron within the time-bin window ($\Delta t \approx 260$ ns bin with 500 ps uncertainty due to the optical pulse length and the detector timing jitter) with electron flux rate $\Gamma \approx 20$ MHz. With these rates, we are looking at the photon statistics with, on average, 0.005 electrons in each time-bin window. Essentially, the background accidental events are dominated by the single-photon events of two different electrons. When $\tau \approx 0$, the contribution also comes from the two-photon events of the same electron, with the probability of $P_0 =$

$\eta_1 \eta_2 \alpha |g|^4 P_e / 4$, where α captures the second-order photon statistics and should be ideally $\alpha = 1$ for a Poisson distributed photon pulse from the same electron. Therefore, the bunching peak ratio should be $g_{pp}(\tau) = 1 + f(\tau)\alpha/P_e$, where $f(\tau)$ is a form factor with property $\int f(\tau)d\tau = 1$ which takes in to account the hardware uncertainty of the detection event timing. A detailed derivation of the correlation function is provided in Appendix B.17. To compensate for the relatively low average electron counts within our time-bin window, such that we are comparing with the same average electron counts as that of the electron-photon correlation results (one electron per window), we need to increase the bin width here to $\Delta t' = 50$ ns, with which we obtain the peak $g'_{pp}(0) = 1.02$ to use for the Cauchy-Schwarz inequality. Note that the HBT-type measurement is not sensitive to optical losses, so we are not concerned with the specific values of the average photon counts.

The photon statistics α can be modified in some scenarios. Apart from a possible contribution from the incoherent cathodoluminescence process [270], we found out that it might also come from the incoherent averaging of the electron transverse position (shown in Fig. 7.12(b)), discussed in Section 4.3.1 Eq. 4.79, which would lead to a thermal-distributed optical state given the Gaussian-distributed beam shape. This is also equivalent to a white-noise intensity modulation of the generated photon flux (insensitive to loss) induced by the drifting of the e-beam position, which yields approximately a biased-thermal state [272] with $g_{pp} \approx 3$ in conventional continuous wave photon flux measurements. In our case, as we do not know precisely the electron flux rate Γ and the time-bin window jittering, we can not reliably retrieve P_e and also the photon statistics α of the generated photons of a single electron in this type of HBT measurement. We could only roughly predict a bunching ratio of $g_{pp}(0) \approx 100$ based on the estimated Δt and Γ in the experiment. The discrepancy between the measured data and theory prediction can be explained by the contributions of incoherent cathodoluminescence [260] by high-energy electrons hitting the waveguide, where the estimated photoemission ratio is $n_{in}/n_{coh} \approx 5$. We verified the Poisson distribution in Section 7.5 in a different way using the electron energy record conditioned on photon counting, such that the results are insensitive to contributions from incoherent cathodoluminescence.

On the electron side, we observe that the electron energy loss does not clearly obey a Poisson distribution, shown in Fig. 7.15 and also Fig. 7.8, but tends towards a thermal-like distribution. We can attribute this effect to two possible factors: first, the broadened ZLP due to the coupling to other optical modes in the structure (discussed in Section 6.2 and verified in Figure. 7.16), and second, the incoherent averaging of the electron transverse position due to the large convergence angle of the e-beam (shown in Fig. 7.12(b)). These experiment complications, however, do not affect the measurement of the electron auto-correlation function, as we only have a single-port measurement of the electron energy. Because the electron is a single particle, we do not have a practical way to divide its energy losses and measure them at two electron detectors, as we did with the optical side. Therefore, the quantum measurement result of the electron auto-correlation function is dominated by the single-photon-loss events, and contributions from the higher-order-loss events are negligible. Because of this, we can derive analytically $g_{ee} \approx |g|^{-2}$, substantially larger than unity. Here, $|g|^2$ is approximately

Chapter 7. Cavity-mediated electron-photon pairs

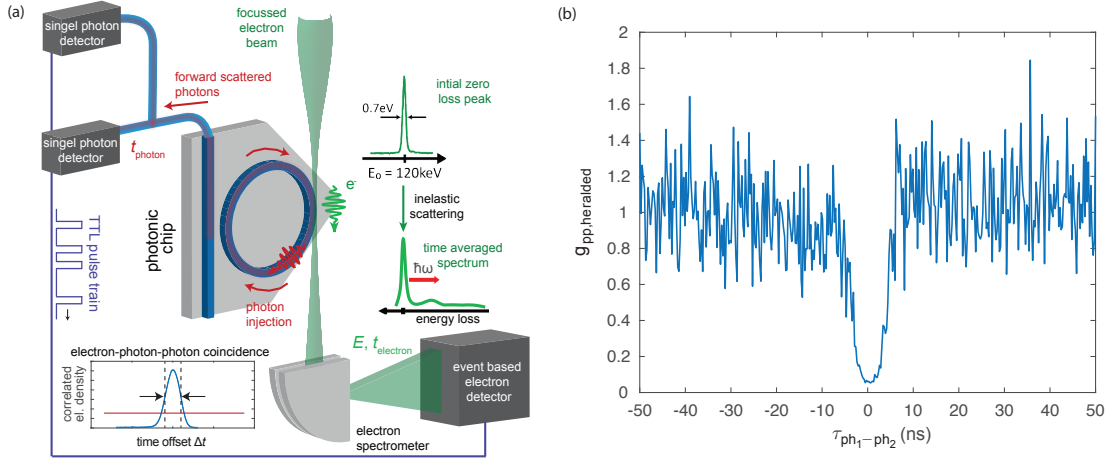


Figure 7.13: **(a)** Hanbury-Brown-Twiss (HBT) measurement of the photon statistics in conjunction with the time-stamped electron energy loss records. **(b)** Preliminary measurement of the auto-correlation function of the heralded single photons.

the probability of a single-photon generation in the electron-photon interaction. Using the measured electron energy-loss spectrum together with $\Gamma \approx 3 \times 10^8$ Hz and $\Delta t \approx 3.5$ ns, we retrieve the auto-correlation function $g_{ee} = 17$, given the measured photon-loss probability of $P_{\Delta t} \approx 1 - \exp(-\Gamma \Delta t (1 - \exp(-P_{\text{loss}}))) = 5.7\%$ in this window.

By combining all the measured correlation results, the Cauchy-Schwarz inequality bound is violated by $\gamma = 3.6 > 1$. The clear violation falsified the classical picture of the electron-light interaction, where the measured correlation has to be non-classical, even with the significant disadvantage of the electron energy measurement. This result is not possible without the strong coupling strength $|g|^2 \sim 0.1$ we achieved in this experiment, and the ability to perform two-port measurement on the optical side.

To prove that electrons and photons are also quantum by themselves, we must measure a less-than-unity auto-correlation function $g_{ii,\text{heralded}}$ using heralding schemes. We expect the $g_{pp,\text{heralded}} = (2g_{ep} - 1 + 1/P_e)/g_{ep}^2$ for the heralded single photons (a detailed derivation of the correlation function is provided in Appendix B.17), which should be as low as 7% given the same experiment setting ($\Gamma \approx 3 \times 10^8$ Hz and $\Delta t \approx 4$ ns). Our collaborator is still currently in the process of measuring the heralded single-photon auto-correlation function using the HBT setup illustrated in Fig. 7.13(a). From a preliminary measurement obtained using a longer straight waveguide as well as superconducting nanowire single-photon detectors, we observed that the achieved $g_{pp,\text{heralded}} \approx 6\% < 1$, shown in Fig. 7.13, proving that the optical field itself is non-classical. The same procedure can also be performed on the electron side, where we measured a $g_{ee,\text{heralded}} = 1.05$ by heralding on photodetection events. Even though it is substantially smaller than the original auto-correlation function g_{ee} , breaking the classical bound on the electron side is generally not possible, restricted by the single-port setting.

7.4 Mode imaging enhanced by correlation

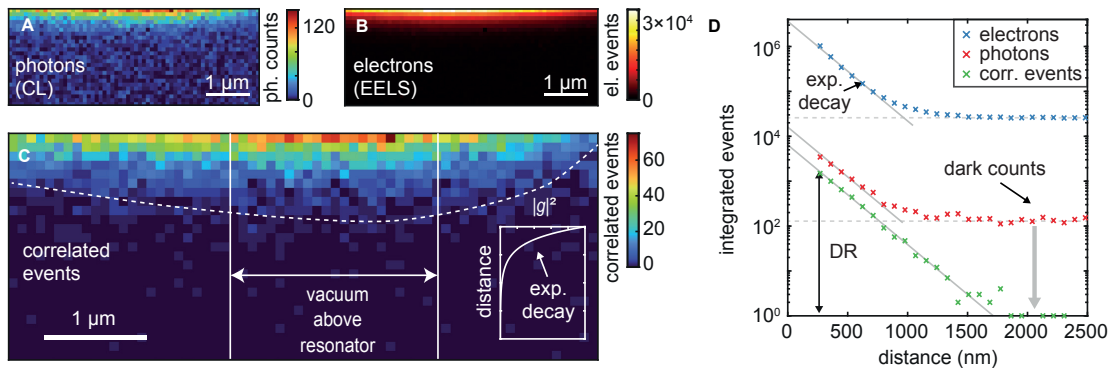


Figure 7.14: **Correlation-enhanced cavity mode imaging.** Spatial distributions of (A) loss-scattered electrons (EELS), (B) photons (CL) and (C) correlated events (30-ms integration per pixel, starting ~ 270 nm above the chip surface; for measurement geometry, see Fig. 7.3). The position of the resonator and the mode envelope (solid/dashed line, guide to the eye) are indicated. Inset: a sketch of the cavity field decay into the vacuum (scattering probability $|g|^2$). The energy windows applied to (B) and (C) are optimized individually. (D) Logarithmic plot comparing the distance-dependent exponential mode decay from (A)-(C) (integrated in the area above the resonator, effectively 1-s acquisition per point). The lowest noise and highest dynamic range (> 3 -orders of magnitude) are observed for the time-correlated imaging.

7.4 Mode imaging enhanced by correlation

Employing both particle channels facilitates correlation-enhanced measurements, isolating physical scattering events from uncorrelated noise such as detector dark counts. As a figure of merit for noise suppression, the fraction of true coincidences $R_{pe}/(R_{pe} - R_{acc})$, with the uncorrelated (accidental) background rate R_{acc} , is defined for selecting a specific time-delay and energy-loss window (Fig. 7.4D), reaching 98.6%, i.e., a coincidence-to-accidental-ratio of $CAR \sim 75$. This demonstrates the high-fidelity generation of correlated electron-photon pairs, promising quantum enhanced imaging.

In the following, we give a proof-of-concept demonstration of coincidence-gated raster mapping of the resonator mode. Specifically, Figs. 7.14A and B show the time-integrated electron and photon signals, respectively, and Fig. 7.14C displays the correlated events only. To quantify the correlation-induced improvement in image contrast, Fig. 7.14D compares the respective count rates for the individual and correlated signals on a logarithmic scale. Both the photon and electron signals trace the exponential decay of the evanescent field away from the structure, leveling off at constant values for larger distances. These background offsets limit the dynamical range of the mode imaging, and are determined by the uncorrelated noise rates, i.e., the photodetector dark counts (130 cts/s) and residual overlap of the ZLP with the energetic gate (1.5×10^4 cts/s), respectively. Rejecting the uncorrelated background, the correlated signal (Fig. 7.14D, yellow curve) resolves the evanescent decay of the cavity field over longer distances. Despite a slightly smaller signal ($\eta_K^e < 1$), we improve the dynamic range (DR) by two orders of magnitude. In the following subsection, we discuss in detail the

Chapter 7. Cavity-mediated electron-photon pairs

improvement of DR concerning the system parameters.

From a broader perspective, harnessing correlations of electrons with radiative emission [273] shows promise for enhancing contrast and resolution, as recently shown in the study of core-level [274] and valence electronic excitations in nanostructured materials [145]. Using post-selection in the electronic and photonic degrees of freedom [110, 255], such schemes can be generalized to trace state-specific scattering cross-sections and create heralded pair states as a function of linear or angular momentum, polarization/spin, or frequency/energy.

Imaging dynamic range improvement using correlated electron-photon pairs

Coincidence detection of electrons and photons enables noise-suppression in X-ray spectroscopy [274, 275] and enhanced imaging of valence electronic excitations in nanomaterials [145], and was recently proposed for mode-specific ghost-imaging of optical excitations [255]. In Fig. 7.14, we compare the photonic mode imaging achieved by employing correlated events using either the electron or photon channel alone.

The background noise contribution of imaging, using only the electron energy sideband, is from the contribution of the ZLP tail at the first-order sideband energy. For convenience, we define $P_{\Delta E} = \int_{\Delta E} dE |\psi_e(E)|^2$ as the ZLP leakage probability to the coincidence energy window. Given N_e the electron flux passing through the sample, with detection efficiency (includes all loss channels) η_e , the accident event rate is therefore $R_{e,acc} = N_e \eta_e P_{\Delta E}$, where ΔE is the first sideband window. The real first sideband event rate is $R_e = N_e \eta_e |g|^2$, giving a signal to noise ratio (SNR) of

$$D_e = \frac{|g|^2}{P_{\Delta E}}. \quad (7.31)$$

For the photon detection imaging method, the noise contribution is mainly from the detector dark count rate R_d . The real signal rate is $R_{ph} = N_e |g|^2 \eta_{ph}$, where η_{ph} is the optical detection efficiency. This gives an SNR of

$$D_{ph} = \frac{N_e |g|^2 \eta_{ph}}{R_d}. \quad (7.32)$$

When the detector saturates at event rate R_{max} , the SNR will reach its theoretical maximum (dynamical range), at $D_{ph} = \frac{R_{max}}{R_d}$.

For imaging using correlated electron-photon pairs, the accident events are still mainly from the electron ZLP. However, they are conditioned on a photon detection dark count and the electron in the correlation time window T_c . Therefore, the accident rate is $R_{e,ph,acc} = N_e T_c \eta_e R_d P_{\Delta E}$. The real correlated signal event rate is $R_{e,ph} = N_e |g|^2 \eta_{ph} \eta_e$. The SNR is therefore

$$D_{e,ph} = \frac{|g|^2 \eta_{ph}}{T_c R_d P_{\Delta E}}. \quad (7.33)$$

In the case of optical detector saturation, one has $D_{e,ph} = \frac{R_{max}}{N_e T_c R_d P_{\Delta E}}$ instead.

7.5 Conditional electron state by photon counting

We are interested in the regime where correlated electron-photon pairs can enhance the imaging dynamical range. When compared to the electron imaging method, the ratio

$$\frac{D_{e,\text{ph}}}{D_e} = \frac{\eta_{\text{ph}}}{T_c R_d} \quad \text{or} \quad \frac{R_{\text{max}}}{N_e |g|^2 T_c R_d}, \quad (7.34)$$

where the correlated method reduces the background noise by a factor of $T_c R_d$ by using the correlation window, but also the maximum signal level by the optical detection efficiency η_{ph} . Given our detector dark count rate of 130 Hz, 10 ns of correlation window, and $\eta_{\text{ph}} \sim 0.1\%$ optical detection efficiency, we estimate a dynamical range enhancement of 10^3 . When compared to the optical imaging method, the ratio

$$\frac{D_{e,\text{ph}}}{D_{\text{ph}}} = \frac{1}{N_e T_c P_{\Delta_E}}, \quad (7.35)$$

where the accident rate is reduced, since the record also conditions on the electron sideband even, by a factor of $N_e T_c \eta_e P_{\Delta_E}$, at the cost of reducing the maximum signal level by the electron detection efficiency η_e . This leads to a dynamical range enhancement of 10^3 , given our electron flux $N_e \sim 10^8$, and ZLP leakage of $P_{\Delta_E} \sim 0.1\%$. In the current experiment, the contrast is also limited by the low event counts shot noise when the electron is far from the resonator surface, which can be improved with a longer integration time.

Note that for Fig. 7.14, the energy windows for the EELS and correlation methods are different and optimized for each method. Therefore, the predicted dynamical range enhancement here does not apply accurately and is about ten times smaller. Given the same energy window, the prediction matches pretty well but is not the optimal case for comparing the best performance of different imaging methods.

Further enhancement can be made with a narrower correlation window T_c , lower electron flux N_e , higher optical detection efficiency η_{ph} , and longer integration time. For a better absolute dynamical range of correlation method, we mainly need to improve optical detection efficiency η_{ph} , where each optical element can be optimized individually and a factor of 10^3 more improvement is likely achievable.

7.5 Conditional electron state by photon counting

Here, we investigate the electron state generated when conditioned on photon counting events, e.g., detecting a single photon. Contrary to a straightforward result of either a perfect 1-photon energy-loss state or a simple removal of the zero-loss-peak with photon-number non-resolving detectors, the state generated is not trivial when we have a finite detection efficiency η . In this section, we first theoretically derive the conditional electron state and the corresponding photon state with a generalized distribution, given that the electron energy distribution we observed in the experiment seemingly deviates substantially from the ideal Poisson distribution. Next, using the result we derived, we test the photon statistics of the

Chapter 7. Cavity-mediated electron-photon pairs

generated photons using the electron energy as QND photon number detectors. We observe that even though the electron energy distribution is highly nontrivial, we can infer that the generated photons follow Poisson statistics by comparing uncorrelated and photon-correlated electron energy spectra.

Detection of one photon

We set up our model in the following way. After the electron-photon interaction, a photonic state is generated with the reduced density matrix

$$\hat{\rho}_1 = c_0|0\rangle_1\langle 0|_1 + c_1|1\rangle_1\langle 1|_1 + c_2|2\rangle_1\langle 2|_1 + \dots = \sum c_k|k\rangle_1\langle k|_1 \quad (7.36)$$

that belongs to optical mode \hat{a}_1 . We aim to derive the conditional optical state $\hat{\rho}$ after detecting one photon, which can be regarded as the same as the conditional electron state due to the energy-conserved nature of this interaction: $|N\rangle_1\langle N|_1 = |N\rangle_{\text{ph}}\langle N|_{\text{ph}}\hat{b}^N\hat{\rho}_e\hat{b}^{\dagger N}$, where ρ_e is the reduced density matrix of the electron after interacting with the other auxiliary optical modes.

We model the optical loss as scattering mode \hat{a}_1 into a different optical mode \hat{a}_2 that we never detect, with an initial density matrix of $\hat{\rho}_2 = |0\rangle_2\langle 0|_2$. The loss mechanism can be modeled as a single beam splitter operator

$$\hat{S} = e^{i\theta(\hat{a}_1^\dagger\hat{a}_2 + \hat{a}_1\hat{a}_2^\dagger)} \quad (7.37)$$

which has the following property

$$\hat{S}\hat{a}_1^\dagger\hat{S}^\dagger = \cos\theta\hat{a}_1^\dagger + i\sin\theta\hat{a}_2^\dagger \quad (7.38)$$

$$\hat{S}^\dagger\hat{a}_1^\dagger\hat{S} = \cos\theta\hat{a}_1^\dagger - i\sin\theta\hat{a}_2^\dagger. \quad (7.39)$$

When the optical loss occurs, and our effective detection of mode \hat{a}_1 is limited to a finite measurement efficiency η , we can rewrite the relation to

$$\hat{S}\hat{a}_1^\dagger\hat{S}^\dagger = \sqrt{\eta}\hat{a}_1^\dagger + i\sqrt{1-\eta}\hat{a}_2^\dagger. \quad (7.40)$$

After scattering into mode \hat{a}_2 , we perform optical detection on mode \hat{a}_1 with unity efficiency.

When we detect the single photon state $|1\rangle_1$, we obtain the new density matrix of mode \hat{a}_2 (photons we did not detect that would contribute to the electron energy loss following the first

photon sideband)

$$\begin{aligned}
 \hat{\rho}'_2 &= \langle 1|_1 \hat{S} \hat{\rho}_1 \hat{\rho}_2 \hat{S}^\dagger |1\rangle_1 \\
 &= \langle 1|_1 \hat{S} \left(c_0 |0\rangle_1 \langle 0|_1 + c_1 \hat{a}_1^\dagger |0\rangle_1 \langle 0|_1 \hat{a}_1 + \frac{c_2}{2!} \hat{a}_1^{\dagger 2} |0\rangle_1 \langle 0|_1 \hat{a}_1^2 + \dots \right) |0\rangle_2 \langle 0|_2 \hat{S}^\dagger |1\rangle_1 \\
 &= \sum_k \frac{c_k}{k!} \langle 0|_1 \hat{a}_1 \hat{S} \hat{a}_1^{\dagger k} \hat{S}^\dagger |0\rangle_1 \langle 0|_1 |0\rangle_2 \langle 0|_2 \hat{S} \hat{a}_1^k \hat{S}^\dagger \hat{a}_1^\dagger |0\rangle_1 \\
 &= \sum_k \frac{c_k}{k!} \langle 0|_1 \hat{a}_1 (\sqrt{\eta} \hat{a}_1^\dagger + i\sqrt{1-\eta} \hat{a}_2^\dagger)^k |0\rangle_1 \langle 0|_1 |0\rangle_2 \langle 0|_2 (\sqrt{\eta} \hat{a}_1 - i\sqrt{1-\eta} \hat{a}_2)^k \hat{a}_1^\dagger |0\rangle_1 \\
 &= \eta \sum_k \frac{k(1-\eta)^{k-1} c_k}{(k-1)!} \hat{a}_2^{\dagger(k-1)} |0\rangle_2 \langle 0|_2 \hat{a}_2^{k-1} \\
 &= \eta \sum_k k(1-\eta)^{k-1} c_k |k-1\rangle_2 \langle k-1|_2
 \end{aligned} \tag{7.41}$$

where $k = 1, 2, \dots$. If we sum up the photons that are in both modes, we have

$$\hat{\rho} = \eta \sum_k k(1-\eta)^{k-1} c_k |k\rangle \langle k| \tag{7.42}$$

Note that this density matrix is not normalized yet and is proportional to the detection probability of a single photon.

We can see that in the limit of unity detection efficiency $\eta \rightarrow 1$, the post-selected state is $\hat{\rho} = c_1 |1\rangle \langle 1|$, which is indeed the single photon state. In the limit of very low detection efficiency $\eta \rightarrow 0$, the post-selected state is $\hat{\rho} = \eta \sum_k k c_k |k\rangle \langle k|$, where the Fock state population is redistributed. Therefore, higher-order photon sidebands are amplified by the number of photons compared to the unconditional state.

Detection of n photon

In a realistic experiment setting, the detection of photons is generally photon-number non-resolving. Therefore, if we label the density matrix generated by counting n photons as $\hat{\rho}_n$, we have the end state

$$\hat{\rho} = \sum_{k=1}^{\infty} \hat{\rho}_k \tag{7.43}$$

upon detection of a single photon in the experiment using a photon-number non-resolving detector.

Chapter 7. Cavity-mediated electron-photon pairs

To derive $\hat{\rho}_n$, we can easily generalize the single-photon result to the n-photon detection, as in

$$\begin{aligned}
\hat{\rho}'_2 &= \langle n|_1 \hat{S} \hat{\rho}_1 \hat{S}^\dagger |n\rangle_1 \\
&= \frac{1}{n!} \sum_k \frac{c_k}{k!} \langle 0|_1 \hat{a}_1^n (\sqrt{\eta} \hat{a}_1^\dagger + i\sqrt{1-\eta} \hat{a}_2^\dagger)^k |0\rangle_1 \langle 0|_1 |0\rangle_2 \langle 0|_2 (\sqrt{\eta} \hat{a}_1 - i\sqrt{1-\eta} \hat{a}_2)^k \hat{a}_1^{\dagger n} |0\rangle_1 \\
&= n! \eta^n \sum_k \frac{C_k^{n2} (1-\eta)^{k-n} c_k}{k!} \hat{a}_2^{\dagger(k-n)} |0\rangle_2 \langle 0|_2 \hat{a}_2^{k-n} \\
&= \eta^n \sum_k C_k^n (1-\eta)^{k-n} c_k |k-n\rangle_2 \langle k-n|_2
\end{aligned} \tag{7.44}$$

where $C_k^n = \frac{k!}{n!(k-n)!}$ is the binomial coefficient of selecting n terms in k total. Here, $k \geq n$. Sum up all the photons again, and we have the total density matrix

$$\hat{\rho} = \eta^n \sum_k C_k^n (1-\eta)^{k-n} c_k |k\rangle \langle k| \tag{7.45}$$

Again, in the limit of unity detection efficiency $\eta \rightarrow 1$, the post-selected state is $\hat{\rho} = c_n |n\rangle \langle n|$, which is indeed the n photon state. In the limit of very low detection efficiency $\eta \rightarrow 0$, the post-selected state is $\hat{\rho} = \eta^n \sum_k C_k^n c_k |k\rangle \langle k|$, where the Fock state population is again redistributed and amplified by C_k^n . However, given our very low detection efficiency $\eta \rightarrow 0$, we will most likely only observe the distribution of the $n = 1$ case in our experiment.

7.5.1 Verifying photon statistics

Here, we investigate the photon statistics using the unconditional and conditional electron energy spectra upon detecting a single photon and two photons. For one of the electron-photon correlation data obtained by our collaborator Germaine Arend from a straight waveguide device (not ring resonator from previous sections), we plot the photon-correlated and the uncorrelated electron spectra in Fig. 7.15.

In the low detection efficiency limit $\eta \rightarrow 0$, one of the consequences of Eq. 7.42 is that, if the photon statistics c_k obeys the Poisson statistics, then the correlated and the uncorrelated electron spectrum should be almost identical, only differ by a $1-\hbar\omega$ energy offset. To prove it, we write out the ratio of adjacent sidebands of a n-photon-conditional electron state

$$\frac{c'_{k+1}}{c'_k} = \frac{C_{k+1}^n}{C_k^n} \frac{c_{k+1}}{c_k} = \frac{k+1}{k+1-n} \frac{c_{k+1}}{c_k}. \tag{7.46}$$

For an initial Poisson distribution, $c_{k+1}/c_k = |g|^2/(k+1)$. This leads to a conditional sideband ratio of $c'_{k+1}/c'_k = |g|^2/(k+1-n)$. If we shift the electron energy spectrum downward by n-photon energy ($k-n \rightarrow k'$), we have a new form $c'_{k'+1}/c'_{k'} = |g|^2/(k'+1)$ that is exactly the ratio for a Poisson distribution. Therefore, the correlated and the uncorrelated electron spectrum should be identical, except with a slight broadening of each sideband due to the convolution with the phase-matching bandwidth (similarly to Fig. 7.2(b)).

7.5 Conditional electron state by photon counting

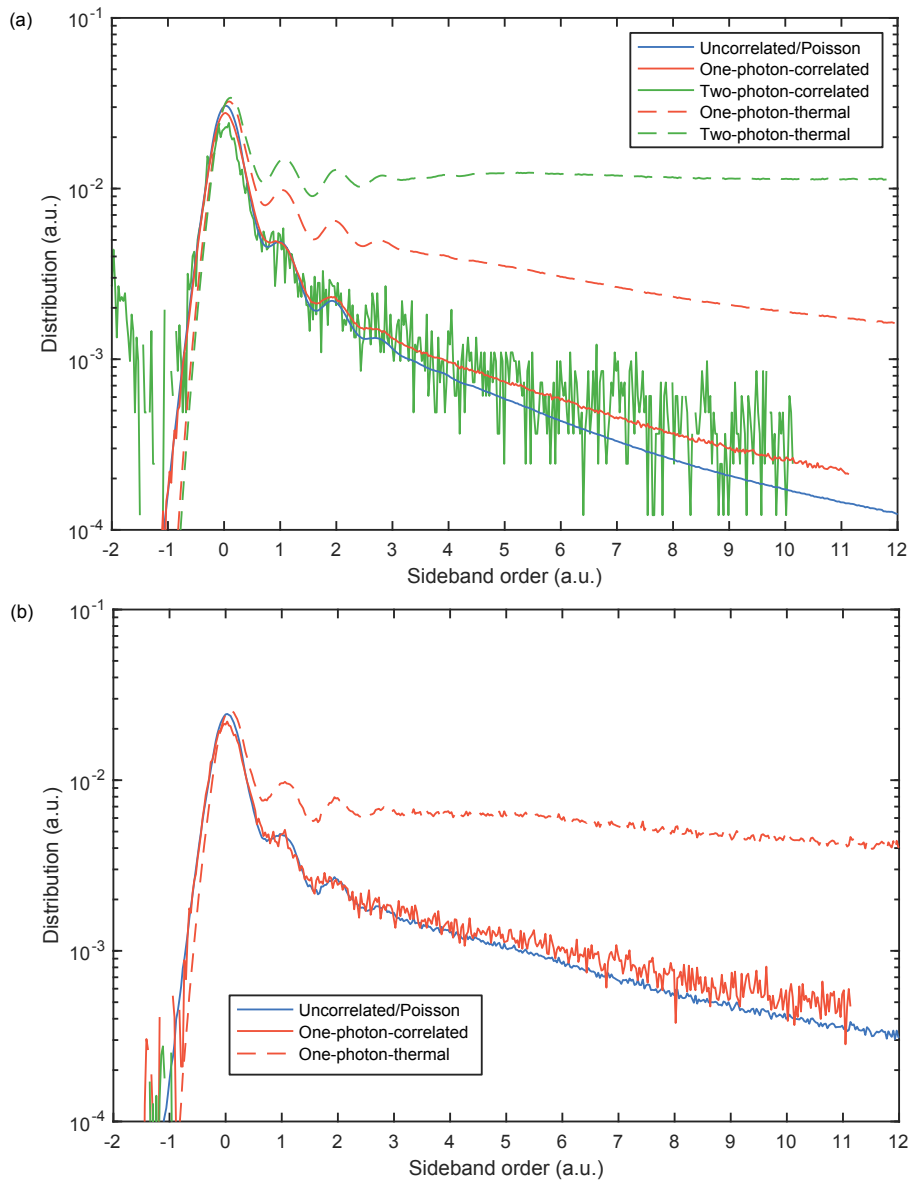


Figure 7.15: **(a)** Electron one-photon-correlated (red, shifted by one quantum), two-photon-correlated (green, shifted by two quanta) and uncorrelated (blue) spectra in solid curves. The predicted correlated spectrum with thermal photon statistics is shown in a dashed curve, while the one with Poisson statistics is the same as the uncorrelated spectrum. The data is integrated over an hour of measurement time, with the correlated spectrum slightly deviating from that of the Poisson statistics. **(b)** Same data but integrated only over one minute, reducing the effect of g averaging (that would lead towards thermal-like distribution), with the correlated spectrum matching closer to that of the Poisson statistics. The two-photon-correlated data is not shown due to insufficient electron counts.

Chapter 7. Cavity-mediated electron-photon pairs

If the photon statistics c_k obey the thermal statistics, these two spectrums should differ significantly. By shifting the one-photon-correlated electron spectrum by one quantum, indeed, we observe that for our system, even though the electron spectrum is very hard to analyze due to the exponential tail as well as the broadening of ZLP, the energy spectrum can approach that of a Poisson statistics instead of a thermal one, demonstrating the Poisson statistics of the generated photons from a straight waveguide. Note that the prediction for the thermal state at the high-order sidebands ($n > 2$) can only serve as an upper bound as we do not know whether the primary contribution is from the tail of the low-order sidebands or the high-order sidebands themselves. For the low-order sidebands ($n \leq 2$), we are confident that the populations are from the sidebands themselves, and the prediction of the thermal distribution should be faithful.

In fact, using the fitted mean photon numbers from the electron's first energy sideband recorded during the experiment, we can even retrieve the zero-loss-peak (ZLP) of the electron due to the interaction with other spatial modes, shown in Fig. 7.16(a). Using the retrieved ZLP and the fitted mean photon numbers, we can predict the one-photon conditional electron spectrum, which shows good agreement with the measured one-photon conditional electron spectrum. From these results, we find that only the first and the second peaks of the electron spectrum are partially due to the coupling to the spatial-temporal mode that we detect. The other energy losses are due to the coupling to other spatial modes or material excitations that we do not detect. E.g., for residue energy loss peaks around 2 eV and 2.5 eV, we suspect them to be from the plasmonic resonances due to gold nanoparticles [276] on our chip surface and edges. For the rising tail from 3 eV of 1-photon data compared to the non-correlated data, it is expected to have occurred due to the excitation of quasiparticles (excitons) in the material as these energy components are larger than the material bandgap. The reason that the 1-photon data has a higher contribution in this energy range could be that some photons are generated during the quasiparticle relaxation, that coupled out through the waveguide and triggered the optical detector.

7.6 Future improvements

We have demonstrated efficient electron-photon pair state generation in an optical ring resonator. However, as expected from our theoretical analysis, we have several limitations to address before moving forward.

We have shown up to $|g^2| \sim 7\%$ photon generation probability for the spatial-temporal mode of the ring cavity, as well as $|g^2| \sim 20\%$ for a long straight waveguide. However, as detailed in Section 6.2, there is a trade-off between the coupling strength and the ideality of the single-mode interaction, even under the ideal waveguide geometry. Non-ideal interaction also involves the entanglement with the higher-order waveguide modes, shown in Fig. 7.8, leading to effective thermalization/decoherence of the composite electron-photon pair state. Because of this effect, high-purity higher-order photon Fock state, as well as a more general

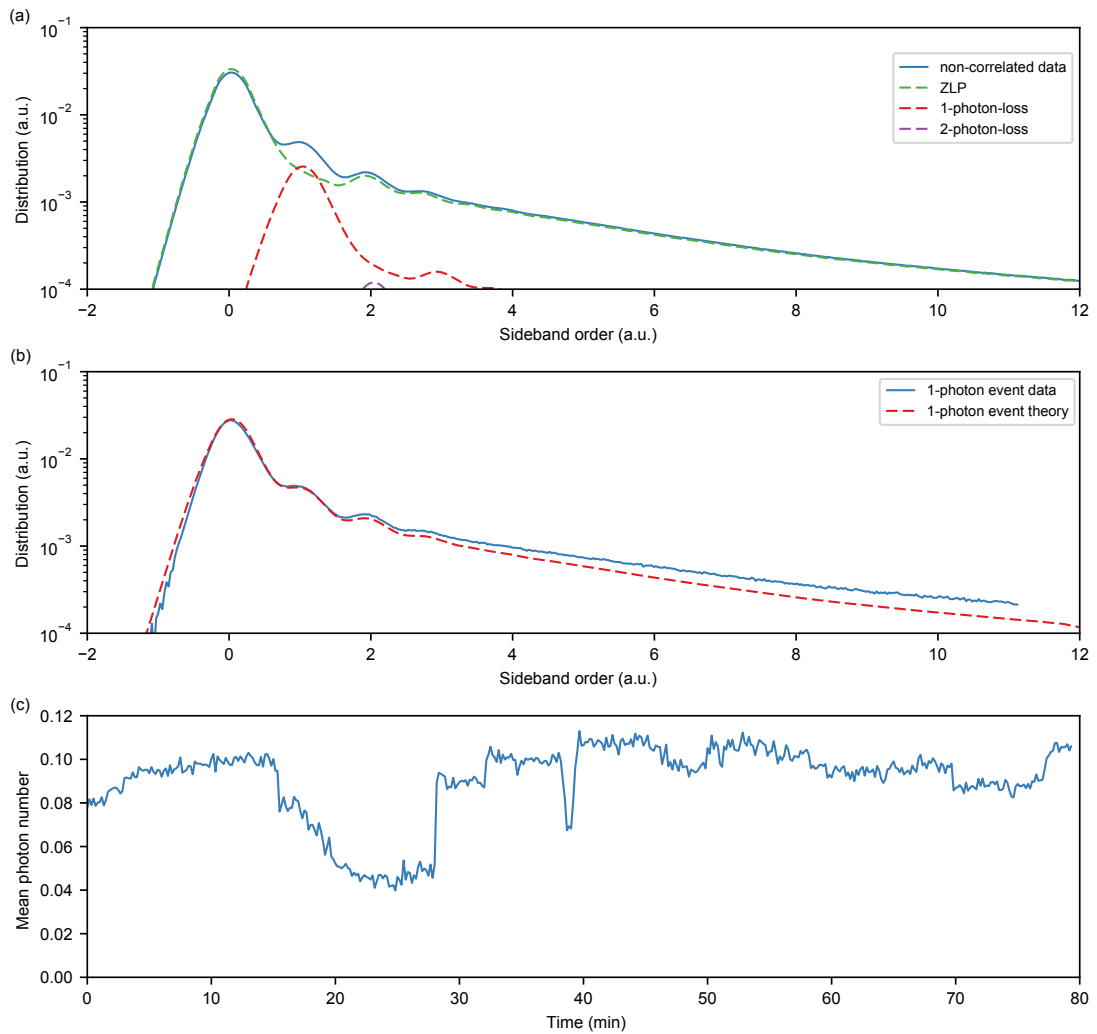


Figure 7.16: **(a)** Non-correlated electron spectrum averaged over 1 hour. Using the mean photon numbers shown in **(c)**, the incoherent averaging of the electron-photon coupling strength is calculated and used to retrieve the zero-loss-peak (ZLP). The theoretical prediction of the 1-photon-loss curve, the 2-photon-loss curve, and the total-loss curve are shown using the retrieved ZLP and the fitted mean photon numbers. **(b)** One-photon conditional electron spectrum down-shifted by one photon energy. The theory prediction using the fitted ZLP from the non-correlated electron spectrum in **(a)** and mean photon numbers in **(c)** shows good agreement with the measurement data. **(c)** Fitted mean photon numbers as a function of time during the experiment.

Chapter 7. Cavity-mediated electron-photon pairs

class of photonic states, are challenging to access in our current data set. On the other hand, much of the observed complexity of our data comes from the fact that our electron energy resolution is only at the level of 0.6 eV, similar to that of the photon energy around 0.8 eV. Many of our questions and doubts might be answered with the possibility of employing a monochromator [185].

To improve the ideality, as well as push towards strong coupling $|g^2| > 1$, we need to utilize the single-mode waveguide (e.g., 800-nm width), keep the e-beam far from the waveguide surface with a small convergence angle, and drastically increase the interaction length. In our current implementation, we have effectively $\sim 40 \mu\text{m}$ of interaction length, but we already observed significant charging of the dielectric substrate that leads to degradation of e-beam quality. For longer interaction lengths up to 1-mm interaction length, we are in the process of trying a new straight waveguide design with a thin layer ($\sim 10 \text{ nm}$) of indium tin oxide (ITO) coating on the waveguide surface. The ITO coating greatly increases the material's electrical conductivity, and thus is expected to reduce the charging effect and drastically increase the feasible interaction length. However, significant optical loss occurs, and resonator designs are no longer favorable. Using a straight waveguide instead (shown in the previous section) circumvents this problem, as the electron couples similarly to a ring or straight waveguide, as the coupled spatial-temporal mode is an ultra-short optical pulse to begin with. With these improvements, we expect to achieve high coupling ideality and thus enable high-purity multi-photon state generation and more sophisticated schemes.

On the application side, we have not yet developed a scheme to achieve a useful enhancement of sensitivity in electron microscopy, exploiting the electron-photon correlation. Apart from the demonstration of Ref. [145], a significant advance in the theoretical research of correlation-enhanced electron microscopy imaging is required, which might lead to a much more significant impact beyond the physical science, e.g., biological imaging using a cryo-electron microscope. In our current study, any form of electron-photon interaction only involves energy/spatial dimension on the scale of optical waves. Therefore, it is not suited for phase-object imaging. The optical heralding of individual electrons is also not useful for phase-object imaging enhancement, as the measurement shot noise comes from the fundamental low scattering probability of the investigated sample. Schemes that can strongly correlate subsequent electrons quantum mechanically on the electron-energy scale remain to be explored in optical systems.

8 Electron energy-dispersion effects

In the previous chapters, we have been investigating electron-photon interaction with the no-recoil approximation, i.e., the electron velocity does not change due to absorption or emission of photons. This approximation leads to the much easier modeling of the interaction and the characteristic Poisson statistics of the electron-photon interaction. The approximation holds when the electron-photon interaction covers only a finite spatial extent, so the recoil effect does not manifest significantly. Note that this threshold distance is highly state-dependent, and for all the experiments we discussed earlier, the recoil effect is only remotely relevant for the PINEM experiment, that for the 10th photon sideband, the relevant distance is around 1 cm. However, when the recoil effect is significant, the electron-photon interaction is modified and can enable a branch of new classical and quantum applications [102, 103, 116, 124, 245].

The velocity change originates from the electron energy-momentum dispersion. As the single-photon energy is considerably smaller than the electron energy, we can usually treat the dispersion using perturbations. The typical effect of the energy second-order dispersion can be described in the Schrodinger picture in terms of the Talbot effect, where the wavefunction of the electron changes its shape periodically over a long distance of propagation [103, 112, 116, 143, 200], with analogy in dispersive propagation of optical waves [240].

This outlook chapter analyzes the case where the electron dispersively propagates between two interaction stages spatially separated by large physical distances, and also serves as a proposal for our future experiments. We start with the derivation of the scattering matrix of the recoil effect in Section 8.1. One thing to pay special attention to in these traveling quantum systems is that the starting time of the interaction at a particular physical location is highly state-dependent. Therefore, the definition of the time of interaction needs to be treated with care. Using this result, we analyze some potential future experiment candidates using the scattering matrix we derived to showcase the recoil effect in later sections.

First, we propose the application of electron-driven optical klystron (Section 8.2), the optical analogy of the microwave klystron that uses free electrons to provide gain and amplify optical fields. Due to the recoil effect, the collective and coherent radiation behavior of many bunched

Chapter 8. Electron energy-dispersion effects

electrons can exhibit superradiance behavior in experimentally accessible parameter regimes.

Next, we exploit the recoil effect as a resource of nonlinearity to induce the free-electron blockade effect. As an analogy to the photon blockade effect, this nonlinearity can bound the dimension of the electron states to a finite space (similar to free-electron qubit [277, 278]) and induce free-electron Rabi oscillation and JC interaction (Section 8.3).

Last, we explore the possibility of using electron-photon pair states for a more fundamental study of quantum mechanics in the case of performing a Bell test (Section 8.4). We find that the typical pair state realized in Section 7 that follows a Poisson distribution does not generate enough entanglement entropy to break the Bell inequality, whereas states accessible through recoil effects can induce Bell violation.

8.1 Dispersive propagation

In the no-recoil limit, the coupling coefficient g_ω is not state-dependent and is generally the case for our experiments performed so far. However, the recoil effect will be significant in multi-stage operations with sufficient spatial separation, where the effect of electron energy-momentum dispersion manifests itself.

To derive the effect of the dispersive propagation, we consider two interaction stages separated by a distance ΔL , each with a point-like interaction length. The coupling coefficient for the first stage is

$$g_{1,\omega} \propto \int dz e^{-i\frac{\omega}{v}z} U_{1,z}(z) \quad (8.1)$$

where $U_{1,z}(z)$ is the optical mode function along the propagation \hat{z} direction. In the first stage, the recoil effect does not play a significant role yet, as the interaction is almost point-like. However, at the second stage that is ΔL away, the electron energy dispersion $\hbar k = \sqrt{E^2/c^2 - m^2c^2}$ changes the phase-matching integral of the off-diagonal element $|E + \hbar\omega\rangle\langle E|$ of the interaction to

$$\begin{aligned} g_{2,\omega}(\Delta E = E - E_0) &\propto \int dz e^{-i\left(\frac{\omega}{v} - 2\pi\left(\frac{2\Delta E}{\hbar\omega} + 1\right)\frac{1}{z_T}\right)z} U_{2,z}(z) \\ &\approx e^{i2\pi\left(\frac{2\Delta E}{\hbar\omega} + 1\right)\frac{\Delta L}{z_T}} \int dz e^{-i\frac{\omega}{v}z} U_{2,z}(z) \end{aligned} \quad (8.2)$$

where now the coupling coefficient accumulates an energy-dependent phase

$$e^{i\theta(\Delta E)} = e^{i2\pi\left(\frac{2\Delta E}{\hbar\omega} + 1\right)\frac{\Delta L}{z_T}}. \quad (8.3)$$

Here $z_T = 4\pi m v^3 \gamma^3 / \hbar\omega^2$ is the Talbot distance [279] and $\gamma = 1/\sqrt{1 - v^2/c^2}$ is the Lorentz factor. ΔE is the energy difference to the reference electron energy E_0 where we choose to do the quadratic expansion of the electron energy-momentum relation. In optical systems, Talbot

distance quantifies specific spatial points where optical waves bunch into periodic pulses due to second-order dispersion. The optical waveform will replicate itself when the two points are spaced exactly by the Talbot distance. Due to the similarity between the electron wave function and optical waves, we also have the bunching of electron pulses after a certain delay.

In our experiment settings, the electron velocity is about $v/c \sim 0.65$, and the optical frequency is about $\omega \sim 2\pi \cdot 2 \times 10^{14}$ Hz. With these values, the Talbot distance is around $z_T \sim 1$ m. Even for the photon order $|N = 10\rangle$, and a typical photonic chip length $\Delta L \sim 5$ mm, the phase accumulation of the sideband state is still only $\theta = 0.1 \cdot 2\pi$, therefore negligible in our most of our discussion in earlier chapters. We anticipate the effect to dominate even for single-photon energy states, e.g., when two photonic chips are involved and with sufficient separation $\Delta L \sim 1$ m. When that is indeed the case, we can still use all the scattering matrices we derived so far with the no-recoil approximation at the sequential stages, but we need to add a propagation matrix

$$\hat{S}_{\text{prop}} = \int dE \exp \left[\frac{-i\Delta L(E - E_0)^2}{2\hbar m v^3 \gamma^3} \right] |E\rangle \langle E| = \int dE \exp \left[\frac{-2\pi i \Delta L(E - E_0)^2}{\hbar^2 \omega^2 z_T} \right] |E\rangle \langle E|, \quad (8.4)$$

in between the stages to account for the recoil-induced phase accumulation of different energy components of the electron during propagation in free space. The phases accumulate differently between different energy components due to their different velocities. Therefore, there is an effective timing difference in their arrival at later stages treated as point interactions with the no-recoil approximation. This approach is consistent with literature that uses Schrödinger equations to solve for the wavefunction evolution between two interaction stages [103] and can also explain effects observed in double-PINEM-type experiment [116].

However, our assumption of the point-like interaction will break down when a single interaction stage is sufficiently long, e.g., $L > 10$ cm, and with transitions involving photon-order $|N > 10\rangle$. Then, a single scattering matrix that includes the recoil effect must account for the dispersive phase accumulation during the interaction. We derive the scattering matrix to be

$$\tilde{\hat{S}}_{\text{e-ph}} = \exp \left[\int d\omega g_\omega \tilde{b}_\omega^\dagger \hat{a}_\omega - h.c. \right] \quad (8.5)$$

where the modified electron energy lowering operator is

$$\tilde{b}_\omega = \int dE |E\rangle \langle E + \hbar\omega| \frac{\int dz e^{i\left(\frac{\omega}{v} - 2\pi\left(\frac{2(E-E_0)}{\hbar\omega} + 1\right)\frac{1}{z_T}\right)z} U_z^*(z)}{\int dz e^{i\frac{\omega}{v}z} U_z^*(z)} \quad (8.6)$$

and the no-recoil coupling coefficient g_ω is used. We observe that the electron transition elements can exhibit oscillatory behavior when the interaction length L approaches z_T , and the interaction becomes highly nonlinear. When using a classical phase-matched optical drive at frequency ω and $L = z_T/4$, all the even-order transition elements can be perfectly canceled in the case of a plane-wave optical envelope, thus enabling applications such as free-electron qubits [277, 278].

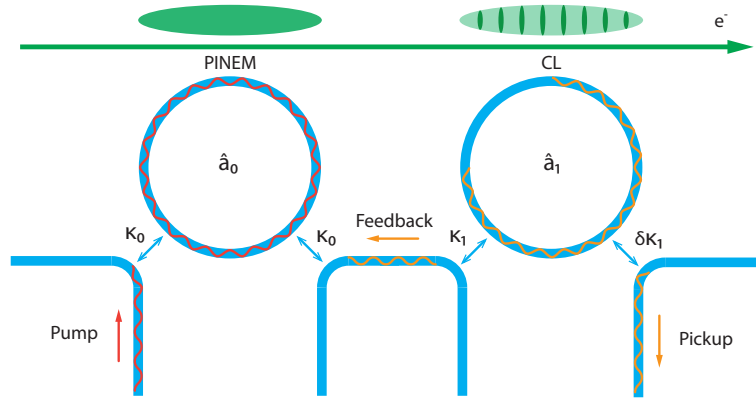


Figure 8.1: The first PINEM cavity \hat{a}_0 is used to modulate the electron wavefunction, forming pulses at the second CL cavity \hat{a}_1 and generating coherent emission. The output field of the second CL cavity is feedback to the first cavity to either dampen or amplify the whole process.

For a non-guided electron beam with a divergence angle around 0.2 mrad and an electron-surface gap 100 nm, the longest propagation on a chip is restricted to about 1 mm to avoid significant e-beam clipping loss. To achieve a long enough distance such that the recoil effect is significant, an on-chip electron guiding structure [106, 210] is required.

In the following sections, we restrict ourselves to the case where each interaction stage can be treated point-like such that the discussions are greatly simplified.

8.2 Cavity-mediated optical klystron

Klystrons are originally invented to amplify radio waves using electron beams. The electron beam first interacts with a cavity and gets phase-modulated. After some propagation, the electron beam bunches into density waves with the same modulation periodicity and emits radio waves with the same frequency into a second cavity. When the signal from the second cavity connects to the first cavity, a feedback loop is formed, and amplification of the first cavity can happen, with gain as high as 60 dB and output up to tens of megawatts.

In Fig. 8.1, we illustrate an optical counterpart of the Klystron that we investigate in this section, with the aim of producing optical gain using the free electrons of a TEM. The system consists of two sequential cavities. The electron interacts with the first cavity (PINEM), which was excited by a weak coherent state $|\beta\rangle$. After dispersive propagation, the electron interacts with the second cavity (CL), which was initially empty. The excitation collected from the second cavity is then guided to the first ring to achieve optical amplification or suppression. Based on the phase relation between the two cavities and the bus waveguide delay, the coherent field in the first ring can be amplified until it reaches a steady state due to intrinsic nonlinearity in the system, a mechanism similar to optical lasing.

Unlike the theoretical basics we covered previously, here we are dealing with not only dispersive propagation of free electrons, but also a large number of sequential electrons and interference between optical fields. In the following, we list some important relations we often use to formulate our model. We assume that the sequential electrons are sufficiently separated from each other so that we can treat their scattering matrix with the optical field \hat{a}_1 independently. For the electron indexed by j , the scattering matrix is

$$\hat{S}_{j,e-ph} = e^{g\hat{b}_j^\dagger \hat{a}_1 - h.c.}. \quad (8.7)$$

Using the Baker-Campbell-Hausdorff (BCH) formula,

$$e^{\hat{B}} \hat{A} e^{-\hat{B}} = \hat{A} + \frac{[\hat{B}, \hat{A}]}{1!} + \frac{[\hat{B}, [\hat{B}, \hat{A}]]}{2!} + \dots, \quad (8.8)$$

we have the following relation for the field operator \hat{a}_1

$$\hat{S}_{j,e-ph}^\dagger \hat{a}_1 \hat{S}_{j,e-ph} = \hat{a}_1 - g^* \hat{b}_j \quad (8.9)$$

where higher-order terms are perfectly canceled in the no-recoil limit. We still consider the recoil effects during the dispersive propagation between the two stages, even though we treat each interaction as point-like. We are interested in the mean fields' evolution and coherence properties.

8.2.1 Coherent field amplification

As we expect to achieve coherent emission at the cavity mode \hat{a}_1 , we proceed to calculate the field operator's first-order moment. The cavity mean field after the interaction with electron j is updated as

$$\begin{aligned} \langle \hat{a}_1 \rangle_j &= \text{Tr}_{\text{ph}} [\hat{\rho}_{j,\text{ph}} \hat{a}_1] = \text{Tr} \left[\hat{\rho}_{j,e} \hat{\rho}_{j-1,\text{ph}} \hat{S}_{j,e-ph}^\dagger \hat{a}_1 \hat{S}_{j,e-ph} \right] \\ &= \text{Tr} \left[\hat{\rho}_{j,e} \hat{\rho}_{j-1,\text{ph}} (\hat{a}_1 - g^* \hat{b}_j) \right] = \langle \hat{a}_1 \rangle_{j-1} - g^* \langle \hat{b} \rangle_{j,e}. \end{aligned} \quad (8.10)$$

where $\hat{\rho}_{j,\text{ph}}$ is the optical density matrix after interacting with the j th electron, and $\hat{\rho}_{j,e}$ is the density matrix of the j th electron before the interaction with the CL cavity. Note that the result can be easily generalized to cases where multiple cavity modes of the CL cavity are excited. However, as we see later that these cavity modes are effectively driven by the electron at the PINEM cavity frequency, we only consider one near-resonant CL cavity mode, as contributions from other modes can be neglected. Furthermore, we assume that our system is still in the weak coupling regime, i.e., $|g| < 1$. We need a constant stream of electrons with flux rate $\Gamma \gg \kappa_1/2\pi$ of the optical cavity to achieve coherent field buildup. We also assume that the CL cavity decay time is much longer than the time to travel to the PINEM ring (such that the change of $\langle \hat{b} \rangle_e$ is adiabatic), which is easily achievable with any high-Q resonators.

We can write out the mean-field equation of the CL cavity and the PINEM cavity, using the

Chapter 8. Electron energy-dispersion effects

QLE of the optical cavities in the rotating frame of the drive laser

$$\langle \dot{\hat{a}}_1 \rangle = (-i\Delta - \frac{\kappa_1}{2}) \langle \hat{a}_1 \rangle - g^* \Gamma \langle \hat{b} \rangle_e \quad (8.11)$$

$$\langle \dot{\hat{a}}_0 \rangle = -\kappa_0 \langle \hat{a}_0 \rangle + \kappa_0 \beta + \sqrt{\kappa_0 \kappa_1} e^{i\theta_{01}} \langle \hat{a}_1 \rangle \quad (8.12)$$

where Δ is the detuning of the CL cavity relative to the laser resonantly driving the PINEM cavity, κ_1 is the coupling rate of the CL cavity to the bus waveguide, and κ_0 is the coupling rate of the PINEM cavity (symmetrically coupled with two ports). The configuration is illustrated in Fig. 8.1, chosen such that pumping the PINEM cavity does not excite the CL cavity. θ_{01} is the phase delay induced by the bus waveguide between the two cavities. Here, in Eq. 8.12, we have no contribution from the electron since we assume the initial electron state $\rho_{0,e}$ before the interaction with the PINEM cavity is a pure momentum state, and has the relation $\text{Tr}[\hat{\rho}_{0,e} \hat{b}] = 0$. The physical picture is very clear. After interacting with the PINEM cavity, the electron bunches at the CL cavity and behaves like a classical particle. Therefore, the electron charges the optical field in the CL cavity in a classical way while de-accelerating.

To calculate $\langle \hat{b} \rangle_e$ (how classical the electron is) that arrives at the CL cavity \hat{a}_1 after a dispersive propagation, we have the following result

$$\langle \hat{b} \rangle_e = \text{Tr}_e [\hat{\rho}_e \hat{b}] = \text{Tr} \left[\hat{\rho}_{0,e} \hat{\rho}_{0,\text{ph}} \hat{S}_{\text{e-ph}}^\dagger \hat{S}_{\text{prop}}^\dagger \hat{b} \hat{S}_{\text{prop}} \hat{S}_{\text{e-ph}} \right] \quad (8.13)$$

$$\hat{S}_{\text{prop}} = \sum_n e^{-in^2\theta} |n\hbar\omega\rangle \langle n\hbar\omega|, \quad \theta = \frac{\hbar\omega^2 \Delta L}{2mv^3\gamma^3} = \frac{2\pi\Delta L}{z_T} \quad (8.14)$$

$$\tilde{\hat{b}} = \hat{S}_{\text{prop}}^\dagger \hat{b} \hat{S}_{\text{prop}} = \sum_n e^{-i(2n-1)\theta} |(n-1)\hbar\omega\rangle \langle n\hbar\omega| \quad (8.15)$$

$$\hat{S}_{\text{e-ph}} = e^{g_0 \hat{b}^\dagger \hat{a}_0 - h.c.} \quad (8.16)$$

Note that $\hat{S}_{\text{e-ph}}$ and \hat{S}_{prop} do not commute with each other, so the correct ordering is required. We further use the BCH formula to continue the derivation,

$$\hat{S}_{\text{e-ph}}^\dagger \tilde{\hat{b}} \hat{S}_{\text{e-ph}} = \tilde{\hat{b}} + [-g_0 \hat{b}^\dagger \hat{a}_0 - h.c., \tilde{\hat{b}}] + \dots \quad (8.17)$$

$$\begin{aligned} [-g_0 \hat{b}^\dagger \hat{a}_0 - h.c., \tilde{\hat{b}}] &= -g_0 (1 - e^{-2i\theta}) \sum_n e^{-i(2n-1)\theta} |n\hbar\omega\rangle \langle n\hbar\omega| \hat{a}_0 \\ &+ g_0^* (1 - e^{2i\theta}) \sum_n e^{-i(2n-1)\theta} |(n-2)\hbar\omega\rangle \langle n\hbar\omega| \hat{a}_0^\dagger \end{aligned} \quad (8.18)$$

⋮

Since the initial electron state is assumed to be a pure energy state $\hat{\rho}_{0,e} = |0\hbar\omega\rangle \langle 0\hbar\omega|$, only the electron transition elements associated with this particular element will contribute to the first moment. We assume the PINEM cavity is initially driven to a coherent state with sufficiently large amplitude so that we can apply the semi-classical approximation $\hat{a}_0 \rightarrow \langle \hat{a}_0 \rangle$, with the

defined $\tilde{g}_0 = g_0 \langle \hat{a}_0 \rangle$, and arrive at

$$\langle \hat{b} \rangle_e = -\tilde{g}_0 e^{i\theta} (1 - e^{-2i\theta}) \left(1 + \frac{-4|\tilde{g}_0|^2 \sin^2 \theta}{1!2!} + \frac{(-4|\tilde{g}_0|^2 \sin^2 \theta)^2}{2!3!} + \dots \right) \quad (8.19)$$

We use the Bessel function expansion and properties of the Gamma function,

$$J_\alpha(x) = \sum_{n=0}^{\infty} \frac{(-1)^n}{n! \Gamma(n + \alpha + 1)} \left(\frac{x}{2} \right)^{2n + \alpha} \quad (8.20)$$

$$\Gamma(n \geq 1) = (n - 1)! \quad (8.21)$$

to simplify the result to

$$\langle \hat{b} \rangle_e = -i e^{i \arg |g_0 \langle \hat{a}_0 \rangle|} J_1(4 |g_0 \langle \hat{a}_0 \rangle| \sin \theta) \quad (8.22)$$

With this result, identical to Ref. [102], we now closed Eq. 8.11, Eq. 8.12 and Eq. 8.22.

There is a natural question: Why does the electron dynamics not have a corresponding decay term in the Langevin equation, like the cavity mode? The answer is that each electron interacts with the optical mode only once at an ultra-fast timescale and, therefore, lacks any feedback mechanism for further damping or amplification. However, when the equations are closed, the coupling between the PINEM mode and the CL mode provides this necessary feedback mechanism that changes $\langle \hat{b} \rangle_e$ for the sequential electrons. Note that the change of $\langle \hat{b} \rangle_e$ over time is not associated with a single electron but rather the averaged value of many sequential electrons.

Another natural question is, when does the approximation $\hat{a}_0 \rightarrow \langle \hat{a}_0 \rangle$ we used in our derivation fail? Even though a coherent state initially populates the PINEM cavity, the input from the CL cavity can significantly modify the photonic states in the PINEM cavity. By assuming $|\langle \hat{a}_0 \rangle| \gg 1$, we can rigorously arrive at the following relation

$$\begin{aligned} \langle \hat{b} \rangle_e &= -g_0 e^{i\theta} (1 - e^{-2i\theta}) \\ &\times \left(\langle \hat{a}_0 \rangle + \frac{-4|\tilde{g}_0|^2 \sin^2 \theta}{1!2!} \langle \hat{a}_0 \hat{a}_0^\dagger \hat{a}_0 \rangle + \frac{(-4|\tilde{g}_0|^2 \sin^2 \theta)^2}{2!3!} \langle \hat{a}_0 \hat{a}_0^\dagger \hat{a}_0 \hat{a}_0^\dagger \hat{a}_0 \rangle + \dots \right) \end{aligned} \quad (8.23)$$

Therefore, we need to consider the values of these higher-order correlation functions and how far they are from the semi-classical limit. Initially, the PINEM cavity is populated by a coherent state $|\beta\rangle$, and later updated by the CL cavity feedback. Using linear expansion (assuming $|g| \ll |\langle b \rangle|$), the higher order correlation functions $\langle f(\hat{a}_1, \hat{a}_1^\dagger) \rangle$ from the CL cavity are updated after each passing electron as

$$\begin{aligned} \langle f(\hat{a}_1, \hat{a}_1^\dagger) \rangle_j &= \text{Tr}_{\text{ph}} \left[\hat{\rho}_{j,\text{ph}} f(\hat{a}_1, \hat{a}_1^\dagger) \right] = \text{Tr} \left[\hat{\rho}_{j,e} \hat{\rho}_{j-1,\text{ph}} \hat{S}_{j,e-\text{ph}}^\dagger f(\hat{a}_1, \hat{a}_1^\dagger) \hat{S}_{j,e-\text{ph}} \right] \\ &= \text{Tr} \left[\hat{\rho}_{j,e} \hat{\rho}_{j-1,\text{ph}} f(\hat{a}_1 - g^* \hat{b}_j, \hat{a}_1^\dagger - g \hat{b}_j^\dagger) \right] \approx \text{Tr}_{\text{ph}} \left[\hat{\rho}_{j-1,\text{ph}} f(\hat{a}_1 - g^* \langle \hat{b}_j \rangle, \hat{a}_1^\dagger - g \langle \hat{b}_j^\dagger \rangle) \right] \\ &= \text{Tr}_{\text{ph}} \left[\hat{D}(-g^* \langle \hat{b}_j \rangle) \hat{\rho}_{j-1,\text{ph}} \hat{D}^\dagger(-g^* \langle \hat{b}_j \rangle) f(\hat{a}_1, \hat{a}_1^\dagger) \right]. \end{aligned} \quad (8.24)$$

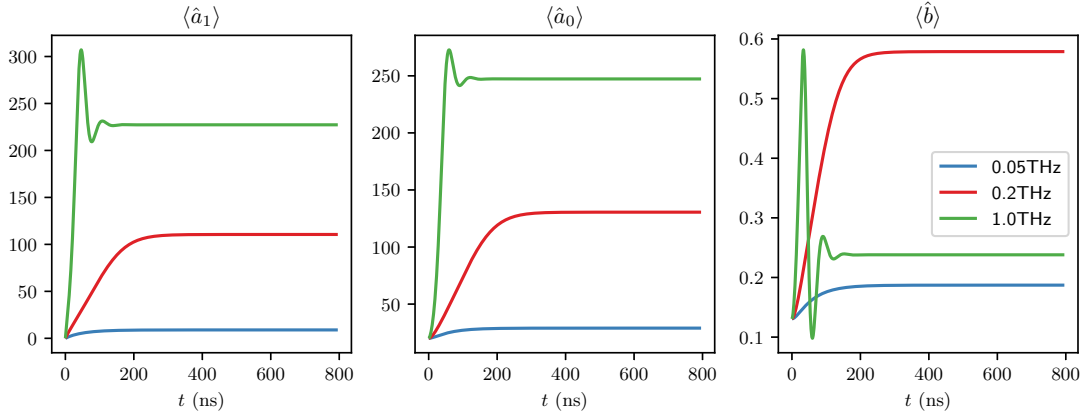


Figure 8.2: Simulation of the first moments' evolution over time for the mean field of both cavities and the first moment of the electron ladder operator. Legend corresponds to different electron flux rates Γ . We set two cavity modes with $\kappa_0 = \kappa_1 = 10 \text{ MHz} \cdot 2\pi$, and the ring spacing at $500 \mu\text{m}$ in the simulation. The optical frequency is set to 780 nm , and the PINEM cavity \hat{a}_0 is initially populated with a coherent state of $|\beta = 20\rangle$.

Therefore, the higher-order correlation functions for both cavities would update as if the optical state is displaced by each electron and follows the statistics of a coherent state in the large electron number limit.

This result means that the closed equations of the first-order moments we derived earlier are exact enough to describe the dynamics of the whole system in the regime $|\langle \hat{a}_0 \rangle| \gg 1$ and $|g| \ll 1$. The approximations will break down when the PINEM cavity is not driven to a strong amplitude, or the CL cavity is strongly coupled to each electron such that $|g| \sim 1$. In our current experimental configuration, we only have $|g| \sim 0.03$ for each cavity mode, so we are well within the regime of $|g| \ll 1$.

We numerically simulate these update equations and plot the real-time first moments in Fig. 8.2 as a function of time at different electron flux rates, as well as the equilibrium first moments as a function of electron flux rate in Fig. 8.3. We observe that when the electron flux rate is relatively low, even though the CL cavity is populated with a coherent field, the PINEM cavity field is not significantly modified. When the flux rate crosses some threshold, we observe amplification of the PINEM cavity field driven by the CL cavity coherent emission, as well as a modification of the coherence property of the electron through $\langle \hat{b} \rangle$. When the flux rate is further increased, we observe a gain saturation and oscillations due to the nonlinear behavior of $\langle \hat{b} \rangle$. Note that a 1-THz rate of electron flux is roughly 160 nA in current, which is challenging to achieve in UTEM due to the trade-off between current and beam quality. On the other hand, a 20-pA of current is possible from some initial testing by our experiment collaborator. In the following, we proceed to analyze the evolution of the second-order moments, showing that the observation of free-electron super-radiance is possible with this current level.

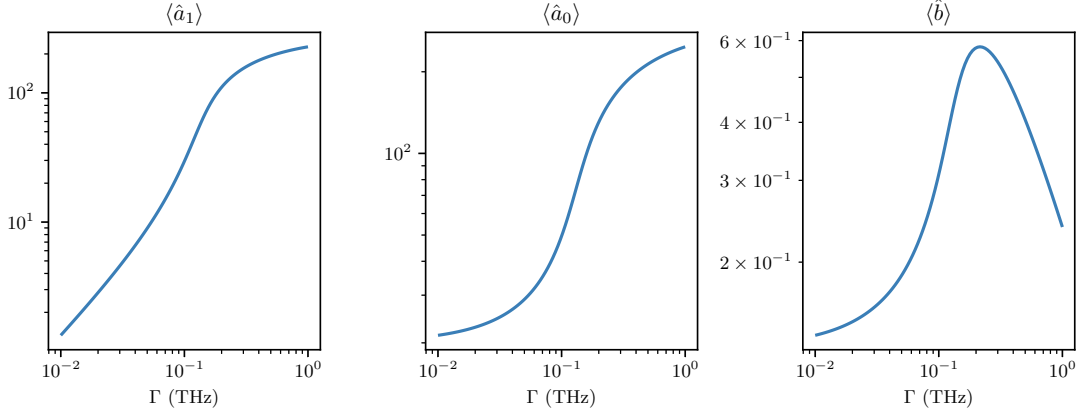


Figure 8.3: Simulation of the steady-state first moments as a function of the electron flux rates Γ . We set two cavity modes with $\kappa_0 = \kappa_1 = 10 \text{ MHz} \cdot 2\pi$, and the ring spacing at $500 \mu\text{m}$ in the simulation. The optical frequency is set to 780 nm , and the PINEM cavity \hat{a}_0 is initially populated with a coherent state of $|\beta = 20\rangle$.

8.2.2 Free-electron superradiance

Using the same method that we used to derive the first-order moments, we can find the following closed equations for all the relevant second-order moments

$$\frac{d}{dt} \langle \hat{a}_1^\dagger \hat{a}_1 \rangle = -\kappa_1 \langle \hat{a}_1^\dagger \hat{a}_1 \rangle - \Gamma (g \langle \hat{b}^\dagger \rangle_e \langle \hat{a}_1 \rangle + g^* \langle \hat{b} \rangle_e \langle \hat{a}_1^\dagger \rangle) + |g|^2 \Gamma (1 - |\langle \hat{b} \rangle_e|^2) \quad (8.25)$$

$$\frac{d}{dt} \langle \hat{a}_0^\dagger \hat{a}_0 \rangle = -2\kappa_0 \langle \hat{a}_0^\dagger \hat{a}_0 \rangle + \kappa_0 (\beta^* \langle \hat{a}_0 \rangle + \beta \langle \hat{a}_0^\dagger \rangle) - \sqrt{k_0 k_1} \langle e^{-i\theta_{01}} \hat{a}_1^\dagger \hat{a}_0 + e^{i\theta_{01}} \hat{a}_0^\dagger \hat{a}_1 \rangle \quad (8.26)$$

$$\frac{d}{dt} \langle \hat{a}_1^\dagger \hat{a}_0 \rangle = (i\Delta - \frac{\kappa_1}{2} - \kappa_0) \langle \hat{a}_1^\dagger \hat{a}_0 \rangle + \kappa_0 \beta \langle \hat{a}_1^\dagger \rangle + \sqrt{k_0 k_1} e^{i\theta_{01}} \langle \hat{a}_1^\dagger \hat{a}_1 \rangle - g\Gamma \langle \hat{b}^\dagger \rangle_e \langle \hat{a}_0 \rangle \quad (8.27)$$

From these equations, one particular term that we need to pay close attention to is the competition between the incoherent photo-emission (photons entangled with the electron states)

$$|g|^2 \Gamma (1 - |\langle \hat{b} \rangle_e|^2), \quad (8.28)$$

and the bunched-electron-driven coherent emission

$$\Gamma (g \langle \hat{b}^\dagger \rangle_e \langle \hat{a}_1 \rangle + g^* \langle \hat{b} \rangle_e \langle \hat{a}_1^\dagger \rangle). \quad (8.29)$$

We can see that the criteria for achieving super-radiance, i.e., the scaling of CL cavity photon number with respect to the electron flux rate is at least quadratic, is $\langle |\langle \hat{b}^\dagger \rangle_e \langle \hat{a}_1 \rangle| \gg |g| (1 - |\langle \hat{b}^\dagger \rangle_e|^2) \sim 0.03$. So it not too challenging to achieve the super-radiance regime as soon as $|\langle \hat{b}^\dagger \rangle_e| > 0.1$ and $|\langle \hat{a}_1 \rangle| > 1$. Intuitively, due to the buildup of the coherent field in the CL cavity, electron-photon pair state generation (entanglement) is efficiently suppressed, and the interaction is dominated by single electron displacing the optical field by a small amount $g^* \langle \hat{b} \rangle_e$. The interaction approaches the semi-classical limit at a high flux rate, where

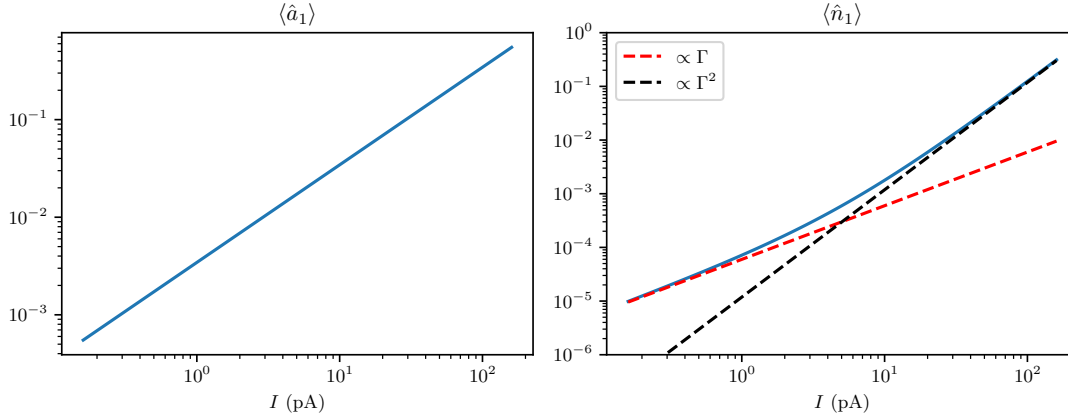


Figure 8.4: Transition into the regime of free-electron super-radiance with a sufficiently high electron current. In the simulation, we set the CL cavity with a $\kappa_1 = 10 \text{ MHz} \cdot 2\pi$, and a ring spacing to the PINEM cavity at $400 \mu\text{m}$. The optical frequency is set to 1550 nm , and the first cavity is initially populated with a coherent state of $|\beta = 3500\rangle$. We observe that around 5 pA of electron current, the CL cavity photon number exhibits a quadratic scaling with respect to the electron flux Γ .

the optical field fully disentangles with the electron state space, approaching a pure coherent state, and can be treated as classical waves. This regime is basically the regime where the microwave klystrons operate.

We numerically simulate the equilibrium values of the second-order moment as a function of different electron flux rates Γ , plotted in Fig. 8.4. The transition into the super-radiance regime can be achieved with a reasonably low electron flux rate $\sim 30 \text{ MHz}$, which corresponds to 5 pA of current. Here, the first ring is pumped by a strong coherent state, and the feedback mechanism between the two cavities is negligible. Note that when the flux is strong enough that the PINEM cavity experiences amplification, the CL cavity photon number can even exceed quadratic scaling with respect to the electron flux rate Γ .

8.3 Free-electron recoil blockade

In this section, we discuss the potential application of using the recoil effect as a source of nonlinearity to form an effective two-level system and thus construct free-electron qubits. We also discuss the physical limitation of using the recoil effect to form the Jaynes-Cummings (JC) model.

8.3.1 Free-electron Rabi oscillation and JC interaction

The electron-photon vacuum coupling coefficient for the off-diagonal element $|E\rangle\langle E - \hbar\omega|\hat{a}^\dagger$ (E : energy difference from the reference energy) is

$$g_\omega(E) \propto \int dz e^{-i(k(E) - k(E - \hbar\omega))z} U_z(z). \quad (8.30)$$

As the electron energy-momentum dispersion $\hbar k = \sqrt{E^2/c^2 - m^2 c^2}$ provides nonlinearity, we can expand it and keep up to the quadratic terms to arrive at

$$g_\omega(E) \propto \int dz e^{2\pi i \left(\frac{2E}{\hbar\omega} - 1\right) \frac{z}{z_T}} e^{-i\frac{\omega}{v}z} U_z(z). \quad (8.31)$$

where $z_T = 4\pi m v^3 \gamma^3 / \hbar\omega^2$ is the Talbot distance. In the case of our experiment condition $v/c \sim 0.65$, when we target optical wavelength 1550 nm, $z_T \sim 1$ m; when we target optical wavelength 780 nm, $z_T \sim 25$ cm.

One interesting case is when the electron interacts with an optical mode over an extended spatial region such that the recoil effect manifests at the single-photon level. We find that this case is also equivalent to interacting with a de-localized optical mode \hat{a} at two far-separated regions (with their separate profile $\mathbf{U}_{i=1,2}$). To simplify the discussion, we focus our analysis on the latter case, where the physical effects of optical dispersion are easier to analyze. We assume the spatial separation $\Delta L \sim z_T \gg$ the interaction length in each region. Thus, we can simplify the coupling coefficient to the following two terms

$$g_\omega(E) = g_{1,\omega} + g_{2,\omega} \times e^{2\pi i \left(\frac{2E}{\hbar\omega} - 1\right) \frac{\Delta L}{z_T}}, \quad (8.32)$$

where $g_{i,\omega} \propto \int dz e^{-i\frac{\omega}{v}z} U_{i,z}(z)$ is the vacuum coupling coefficient in each region calculated using the no-recoil approximation.

The above result can be equally applied to the case of interacting with an optical mode over a prolonged region, where the phases between $g_{i,\omega}$ can be removed by the reference electron energy. We target the relation $g = 2g_{1,\omega} = -2ig_{2,\omega}$ with a specific energy reference, and $\Delta L = z_T/4$, such that we can absorb the energy dependence into the electron operator \hat{b} as in

$$\hat{S}_{\text{e-ph}} = e^{g^* \hat{b} \hat{a}^\dagger - h.c.} \quad (8.33)$$

$$\hat{b} = \sum_{N=0,2,4,\dots} |-(N+1)\hbar\omega\rangle\langle -N\hbar\omega| \quad (8.34)$$

with the following properties

$$\hat{b}\hat{b} = \hat{b}^\dagger\hat{b}^\dagger = 0 \quad (8.35)$$

$$\hat{b}\hat{b}^\dagger + \hat{b}^\dagger\hat{b} = 1. \quad (8.36)$$

Chapter 8. Electron energy-dispersion effects

Due to the missing odd transition elements, if the initial electron energy is in energy state $|0\hbar\omega\rangle$, it can not make transitions except to $|-1\hbar\omega\rangle$.

As an example, the conventional electron-photon pair-state generation will experience blockade on the electron energy,

$$\begin{aligned}
 \hat{S}_{\text{e-ph}}|0\hbar\omega\rangle|0\rangle &= \sum_k \frac{(g^* \hat{b} \hat{a}^\dagger - h.c.)^k}{k!} |0\hbar\omega\rangle|0\rangle \\
 &= \sum_{k=0,2,4,\dots} \frac{|g|^k}{k!} |0\hbar\omega\rangle|0\rangle + e^{-i\arg(g)} \sum_{k=1,3,5,\dots} \frac{|g|^k}{k!} |-\hbar\omega\rangle|1\rangle \\
 &= \cos(|g|)|0\hbar\omega\rangle|0\rangle + e^{-i\arg(g)} \sin(|g|)|-\hbar\omega\rangle|1\rangle
 \end{aligned} \tag{8.37}$$

which is equivalent to a JC model that swaps one photon energy between the optical mode and the effective free-electron qubit.

A similar result goes for the PINEM interaction

$$\begin{aligned}
 \hat{S}_{\text{PINEM}}(\alpha)|0\hbar\omega\rangle &= \sum_k \frac{((\alpha g)^* \hat{b} - h.c.)^k}{k!} |0\hbar\omega\rangle \\
 &= \sum_{k=0,2,4,\dots} \frac{|\alpha g|^k}{k!} |0\hbar\omega\rangle + e^{-i\arg(\alpha g)} \sum_{k=1,3,5,\dots} \frac{|\alpha g|^k}{k!} |-\hbar\omega\rangle \\
 &= \cos(|\alpha g|)|0\hbar\omega\rangle + e^{-i\arg(\alpha g)} \sin(|\alpha g|)|-\hbar\omega\rangle
 \end{aligned} \tag{8.38}$$

which is effectively a Rabi oscillation between the two electron-energy levels. As we have control over the optical phase and amplitude of α , we can access anywhere on the Bloch sphere by using two separated PINEM stages with a delay line between them.

In the following, we analyze if these two hypothetical scenarios can be achieved when considering the phase-matching bandwidth of the optical mode, as the assumption and the free-electron blockade effect break down if the electron interacts with multiple optical modes.

8.3.2 Physical limitations

First, regardless of the achievable coupling coefficient g in the pair-state generation, or αg in PINEM, the cancellation of the odd transitions is sensitive to the energy spread of E in ZLP, as the application is enabled by the energy-momentum nonlinearity on the single-photon energy level. The requirement for a sufficient cancellation of the odd transitions would be $\Delta E \ll \hbar\omega / \max(1, |g| \text{ or } |\alpha g|)$. In electron microscopes with monochromators [185], ZLP as low as 4 meV [201] can in principle be achieved, which compares favorably to a typical photon energy around 1 eV. Therefore, this factor does not impose a hard physical limitation.

The electron state-space isolation requires the electron to interact only with one specific optical mode with tailored properties and a particular physical length. This is intrinsically not

a problem for PINEM-type interaction since the CW-driven mode at high photon occupation dominates the interaction. However, it is challenging to achieve the desired recoil effect for interaction with a vacuum optical mode. This is because the electron generally interacts with many optical modes over a large frequency band, and the optical dispersion of the optical fields is hard to control when multiple modes are involved. When multi-mode interaction happens, leakage to the higher-order energy levels will occur, breaking the electron blockade effect. Even in the limit of unity coupling ideality (discussed in Section 6.2), as the spatial-temporal mode has a finite frequency span, we have a ω -dependent phase accumulation $\delta\phi_g = \delta\omega\Delta L(1/v_g - 1/v)$ on the optical side over a propagation distance of ΔL , as well as that of the electron dispersive phase $\delta\phi_e = -2\pi(\delta\omega/\omega_0)$, where ω_0 is the center optical frequency, v_g is the optical group velocity, and v is the electron group velocity. Due to these relations, we require the following condition

$$\omega_0\Delta L\left(\frac{1}{v_g} - \frac{1}{v}\right) = 1 \quad (8.39)$$

to compensate for the dispersion on both the electron side and the optical side such that the free-electron blockade effect is broadband over ω . This is equivalently

$$\frac{\pi m v^2 \gamma^3}{\hbar \omega_0} \left(\frac{v}{v_g} - 1 \right) = 1 \quad (8.40)$$

which is generally hard as it requires a careful balancing of $\left(\frac{v}{v_g} - 1\right) \sim 10^{-4}$. Assume a ~ 1 mm of interaction length that would result in a typical phase matching bandwidth of 1 THz, the relative coupling-phase oscillation period between two optical frequencies separated by 1 THz is as small as 3 mm, given realistic optical waveguide properties. The intrinsic mismatch between the optical group velocity and the electron group velocity, as phase-matching requires the optical phase velocity to match the electron group velocity, imposes a substantial limitation of achieving single-mode JC interaction between a straight waveguide and free electrons.

The above limitation, however, can potentially be lifted by using two optical cavities connected by a bus waveguide (common bath) in place of a long, straight waveguide (same configuration as in Fig. 8.1). This coupling results in bright- and dark-mode pairs of the cavity. The electron would interact with only the bright modes, in which the bus waveguide defines the relative phase between the optical fields of the two cavities. As the resonant condition significantly reduces the span of frequency components of each cavity mode, even though the electron will still interact with multiple cavity modes (5-20), it is feasible to tailor the frequency ω_i of each resonance pair of the two rings, demonstrated in Ref [205, 226] such that the following condition can be met,

$$(\omega_i - \omega_0)\Delta L\left(\frac{1}{v_g} - \frac{1}{v}\right) \bmod 2\pi = 0 \quad (8.41)$$

or equivalently

$$\frac{\Delta L}{L_{\text{cav}}} \left(\frac{v}{v_g} - 1 \right) \bmod 2\pi = 0 \quad (8.42)$$

With this condition, the effective phase accumulation is correctly canceled for all the bright

cavity modes the electron couples to. As ΔL is generally much larger than the cavity length L_{cav} , fine frequency tuning is generally possible. In this setting, the electron effectively couples to a bright spatial-temporal mode de-localized in two cavities and still maintains the blockade effect because of the phase correction.

Last, UV light and low-velocity electrons can reduce the required spatial separation between the two stages. Assuming wavelength $\lambda = 400$ nm and velocity $0.1c$ (2.5 keV in SEM), we have a extremely short $\Delta L = z_T/4 \sim 130$ μm . UV operation is compatible with, e.g., Si_3N_4 [243], AlN and GaN [280] waveguides.

8.4 Bell test using electron-photon pair states

In this section, we analyze the prospect of using the electron-photon vacuum interaction, as well as post-interaction shaping of the measurement basis, to construct an experiment where the entanglement between the electron and photon state space can be used to test the violation of Bell inequality and local realism.

8.4.1 Bell inequality of a general d-dimensional state space

As the electron-photon state space is generally unbounded, we aim to analyze, in this section, the Bell inequality violation in a high-dimensional state space that covers most of the non-negligible state population.

We first review the general construction of the Bell inequality of a high-dimensional state space. First, we define the probability of a detection event ($A_\alpha = N, B_\beta = n$) given a state as

$$P(A_\alpha = N, B_\beta = n)$$

where $\alpha = 1, 2, \beta = 1, 2$ mark the chosen measurement basis sets, and N, n mark the measurement results. For a d-dimensional state space, we can define a cyclic detection probability

$$P(A_\alpha = B_\beta + i) = \sum_{j=0}^{d-1} P(A_\alpha = j, B_\beta = j + i \pmod{d}) \quad (8.43)$$

with which we can define the Bell inequality [281] to be tested

$$2 \geq I_d = \sum_{i=0}^{\lfloor d/2 \rfloor - 1} \left(1 - \frac{2i}{d-1} \right) \quad (8.44)$$

$$\begin{aligned} & [P(A_1 = B_1 + i) - P(A_1 = B_1 - i - 1) + P(A_2 = B_2 + i) - P(A_2 = B_2 - i - 1) \\ & + P(B_1 = A_2 + i + 1) - P(B_1 = A_2 - i) + P(B_2 = A_1 + i) - P(B_2 = A_1 - i - 1)] \end{aligned}$$

Maximizing the violation

The amount of inequality violation achievable with a quantum state $|\psi\rangle$ and two sets of measurement operators $(A_{\alpha=1,2}, B_{\beta=1,2})$ can be qualitatively understood through the following criteria:

- In both measurement operator sets (A_i, B_i) , the state needs to be close to a maximally entangled state $|\psi\rangle \sim \frac{1}{\sqrt{d}} \sum_k |A_i = k, B_i = k\rangle$ which maximizes the entropy of the entanglement.
- The two measurement sets are almost uncorrelated $|\langle A_1 = i | A_2 = j \rangle|^2 \sim \frac{1}{d}$, i.e., the measurement in one basis gives almost no information on what to expect on the other basis using classical probability theory.

The above criteria give the guiding principle for achieving qualitatively the best contrast between classical and Bell correlation.

Violation in a bounded d-dimensional electron-photon ladder state space

Let us first not restrict ourselves to the types of measurement basis feasible in the experiment and investigate the maximum Bell violation of the electron-photon pair state under an optimal measurement basis. We show that breaking the Bell inequality is impossible in the limit of infinite state dimension, even with optimal measurement basis sets. This result is because the Poisson distributed state is not maximally entangled.

The state we are concerned with is from a plane-wave electron interacting with a vacuum optical mode,

$$|\psi(g)\rangle = \hat{S}_{\text{e-ph}}(g)|N=0, n=0\rangle = \sum_{k=0}^{\infty} e^{-|g|^2/2} \frac{g^k}{\sqrt{k!}} |N=k, n=-k\rangle, \quad (8.45)$$

which is not a maximally entangled state. Therefore, we can expect a lower violation than the optimal violation around $I_d \sim 2.7 - 2.9 > 2$ depending on the system dimension d .

Since the state coefficients $|c_k|^2$ obey Poisson distribution, we initially truncate the state space to a neighboring d-dimension space centered around the mean photon number $|g|^2$. The centering procedure ensures that the truncated state is optimal in terms of achievable entanglement entropy and closer to the maximally entangled state in that space. Note that this operation is artificial and is not supposed to be feasible in the experiment.

The measurement operators we select are within the bounded d-dimensional space, and the

Chapter 8. Electron energy-dispersion effects

quantum Fourier transform of the electron-photon ladder states $|N\rangle, |E_n\rangle$

$$|N'\rangle = \frac{1}{\sqrt{d}} \sum_N \exp\left(i \frac{2\pi}{d} N(N' + \alpha)\right) |N\rangle \quad (8.46)$$

$$|n'\rangle = \frac{1}{\sqrt{d}} \sum_n \exp\left(i \frac{2\pi}{d} n(-n' + \beta)\right) |n\rangle. \quad (8.47)$$

These choices gave optimal Bell violation for a maximally entangled state with some values of α and β . Here, we find the optimal values numerically in different dimensions d , through numerical optimization of α and β . From these definitions, and a coupling strength $|g| = 2$ for the pair state, we find that

- when $d = 2$, the truncated state is almost maximally entangled, and $I_d^{\max} = 2.83$ with $[\alpha_1 = 0, \alpha_2 = 0.5, \beta_1 = -0.25, \beta_2 = 0.25]$, consistent with literature values;
- when $d = 3$, the truncated state does not maximize entanglement entropy and leads to a lower $I_d^{\max} = 2.34$ with $[\alpha_1 = 0, \alpha_2 = 0.4, \beta_1 = -0.2, \beta_2 = 0.2]$;
- when $d \rightarrow \infty$, $I_d^{\max} = 1.96$ with $[\alpha_1 = 0, \alpha_2 = 0.61, \beta_1 = -0.30, \beta_2 = 0.31]$.

Notice that when dimension d is low, where we truncate some state space, the entanglement could lead to the Bell violation. In reality, the accessible operations on the electron and the optical sides are not bounded. Therefore, we need to look at $I_{d \rightarrow \infty}$, which is below the classical bound, even given the optimal measurement sets. This means the state we start with is not entangled enough to break the classical bound. Therefore, we need to construct an electron-photon state space with finite dimension and maximal entanglement, which we discuss below.

8.4.2 Bell violation in a synthetic 2D state space using electron ladder eigenstates

When the initial electron state is in a pure momentum state, the interaction with an optical mode only results in a partially entangled electron-photon pair state. However, achieving a maximum entangled state in a synthetic dimension is possible using the electron ladder operator eigenstate we discussed in Section 4.2.3.

The motivation is that when the electron state exhibits some periodicity $\hat{b}_\omega^d |\psi_e\rangle = |\psi_e\rangle$, the constructed measurement basis on the electron can be bounded in a d -dimension space as $\hat{F}(\hat{b}_\omega) |\psi_e\rangle = \sum_{k=0}^{d-1} c_k \hat{b}_\omega^k |\psi_e\rangle$. These states $|\psi_e\rangle$ are the eigenstates of $\hat{b}_\omega^d \approx \hat{b}_{d \times \omega}$ ladder operators.

As discussed in Section 4.2.3, such an eigenstate can be prepared with multiple stages of PINEM interaction with dispersive propagations, but with the optical pump at the d -harmonics of the target optical frequency ω . Shown in [103], the preparation of the electron eigenstate can achieve sufficiently high fidelity with 3 PINEM stages and $g_{\text{PINEM}} = 20$, with $\langle b_{d \times \omega} \rangle = 0.998$.

8.4 Bell test using electron-photon pair states

In the following, we aim to bound the dimension to $d = 2$ to simplify the discussion. We assume the electron ladder eigenstate is prepared at the second harmonic frequency 2ω before the e-ph entanglement operation, such that $\hat{b}_{2\omega}|\psi_{e,2\omega}\rangle = |\psi_{e,2\omega}\rangle$. With the entanglement operation where the structured electron interacts with the optical mode in a vacuum state at ω , we have the following properties

$$\hat{b}_{\omega}|\psi_{e,2\omega}(\text{even})\rangle = |\psi_{e,2\omega}(\text{odd})\rangle \quad (8.48)$$

$$\hat{b}_{\omega}|\psi_{e,2\omega}(\text{odd})\rangle = |\psi_{e,2\omega}(\text{even})\rangle. \quad (8.49)$$

After the entanglement operation, the ensemble state becomes

$$\begin{aligned} \hat{S}_{\text{e-ph}}(g)|N=0, \psi_{e,2\omega}(\text{even})\rangle &= e^{-|g|^2/2}(|0\rangle + \frac{g^2}{\sqrt{2!}}|2\rangle + \frac{g^4}{\sqrt{4!}}|4\rangle + \dots)|\psi_{e,2\omega}(\text{even})\rangle \\ &\quad + (g|1\rangle + \frac{g^3}{\sqrt{3!}}|3\rangle + \dots)|\psi_{e,2\omega}(\text{odd})\rangle \\ &= \sqrt{\frac{1+e^{-2|g|^2}}{2}}|\text{cat}_{\text{even}}\rangle|\psi_{e,2\omega}(\text{even})\rangle + \sqrt{\frac{1-e^{-2|g|^2}}{2}}|\text{cat}_{\text{odd}}\rangle|\psi_{e,2\omega}(\text{odd})\rangle. \end{aligned} \quad (8.50)$$

This exact way of expressing the state indicates the first type of state measurement basis set we are interested in, as it shows maximal entanglement when $g \gg 1$.

To find the second set of measurement basis, we can add a delay length of $\Delta L = z_T/4$ and a follow-up PINEM operation to rotate the electron states by

$$|\psi_{e,2\omega}(\text{even})\rangle \rightarrow |\psi_{e,2\omega}(\text{even})\rangle + i|\psi_{e,2\omega}(\text{odd})\rangle \quad (8.51)$$

$$|\psi_{e,2\omega}(\text{odd})\rangle \rightarrow -|\psi_{e,2\omega}(\text{even})\rangle + i|\psi_{e,2\omega}(\text{odd})\rangle \quad (8.52)$$

such that the new state is

$$\begin{aligned} &\hat{S}_{\text{e-ph}}(g)|N=0, \psi_{e,2\omega}(\text{even})\rangle \\ &= \left(\frac{\sqrt{1+e^{-2|g|^2}}}{2}|\text{cat}_{\text{even}}\rangle - \frac{\sqrt{1-e^{-2|g|^2}}}{2}|\text{cat}_{\text{odd}}\rangle \right) |\psi_{e,2\omega}(\text{even})\rangle \\ &\quad + i \left(\frac{\sqrt{1+e^{-2|g|^2}}}{2}|\text{cat}_{\text{even}}\rangle + \frac{\sqrt{1-e^{-2|g|^2}}}{2}|\text{cat}_{\text{odd}}\rangle \right) |\psi_{e,2\omega}(\text{odd})\rangle \\ &\sim \frac{1}{\sqrt{2}}|-g\rangle|\psi_{e,2\omega}(\text{even})\rangle + \frac{i}{\sqrt{2}}|g\rangle|\psi_{e,2\omega}(\text{odd})\rangle \end{aligned} \quad (8.53)$$

the operation effectively selects a new set of measurement bases for the electron that yields the least correlation with the first set of measurement bases and, therefore, should maximize the Bell violation. It is also intuitive to understand this state's formation, as illustrated in Fig. 8.5, that depends on the position of the electron pulses (half the period of the optical wavelength), optical coherent states with an electron-position dependent opposite phases are generated. Even though the two optical states (entangled with the electron states) are not orthogonal as

Chapter 8. Electron energy-dispersion effects

they are coherent states, when g is sufficiently large, they are sufficiently separated in phase space and can be reliably distinguished with homodyne detection.

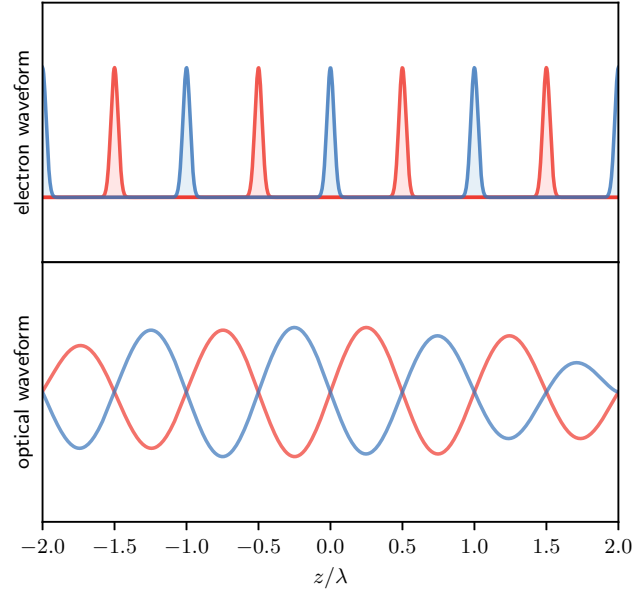


Figure 8.5: Illustration of electron-photon position-phase state generation. Depending on the electron position (red or blue), coherent states with opposite phases are generated, forming the position-phase entangled electron-photon state in a synthetic $d = 2$ dimension space.

On the optical side, we can conduct photon counting to retrieve the parity of the optical state and homodyne measurement to obtain the phase space distribution. On the electron's side, any linear combination of the even and odd bases are accessible through delay and PINEM operations [277].

As for physical limitations, in an optical homodyne measurement, the two opposite coherent states $|\alpha\rangle$ and $|\alpha\rangle$ are not sufficiently separated in phase space, and the measurement results $|\beta\rangle$ will not be completely orthogonal with either state. It is still possible to separate the measurement state space, even though the measured states are not orthogonal to each other, into two halves given the angle $\theta_{\alpha-\beta}$. If the measured result $|\theta| \leq \pi/2$, we group it as state $|A_{\alpha} = 0\rangle$, otherwise, we group it as state $|A_{\alpha} = 1\rangle$. This operation is routinely performed in the dispersive readout of superconducting qubits, where qubit states are entangled with two opposing coherent states.

However, there is a simpler counting method to discriminate between $|\alpha\rangle$ and $|\alpha\rangle$, e.g., by displacing the field by α as

$$D(\alpha)|\alpha\rangle = |2\alpha\rangle \quad (8.54)$$

$$D(\alpha)|-\alpha\rangle = |0\rangle. \quad (8.55)$$

8.4 Bell test using electron-photon pair states

and map the measurement of the $|- \alpha\rangle$ state to a null event for a photon counting measurement. We proceed to define our two sets of measurement bases

$$|A_0 = 0\rangle = |\text{cat}_{\text{even}}\rangle \quad |A_0 = 1\rangle = |\text{cat}_{\text{odd}}\rangle \quad (8.56)$$

$$|A_1 = 0\rangle = \hat{D}(-g)|0\rangle \quad |A_1 = 1\rangle = \hat{D}(-g)\sqrt{1 - e^{-4|g|^2}}(|2g\rangle - |0\rangle) \quad (8.57)$$

with the following relations

$$|A_0 = 0\rangle = \frac{1}{\sqrt{2}} \left(\sqrt{1 + e^{-2|g|^2}} |A_1 = 0\rangle + \sqrt{1 - e^{-2|g|^2}} |A_1 = 1\rangle \right) \quad (8.58)$$

$$|A_0 = 1\rangle = \frac{1}{\sqrt{2}} \left(-\sqrt{1 - e^{-2|g|^2}} |A_1 = 0\rangle + \sqrt{1 + e^{-2|g|^2}} |A_1 = 1\rangle \right) \quad (8.59)$$

$$|A_1 = 0\rangle = \frac{1}{\sqrt{2}} \left(\sqrt{1 + e^{-2|g|^2}} |A_0 = 0\rangle - \sqrt{1 - e^{-2|g|^2}} |A_0 = 1\rangle \right) \quad (8.60)$$

$$|A_1 = 1\rangle = \frac{1}{\sqrt{2}} \left(\sqrt{1 - e^{-2|g|^2}} |A_0 = 0\rangle + \sqrt{1 + e^{-2|g|^2}} |A_0 = 1\rangle \right). \quad (8.61)$$

We can also recast the original state into the new measurement basis,

$$\begin{aligned} & \hat{S}_{\text{e-ph}}(g)|N = 0, \psi_{e,2\omega}(\text{even})\rangle \\ &= \sqrt{\frac{1 + e^{-2|g|^2}}{2}} |A_0 = 0\rangle |\psi_{e,2\omega}(\text{even})\rangle + \sqrt{\frac{1 - e^{-2|g|^2}}{2}} |A_0 = 1\rangle |\psi_{e,2\omega}(\text{odd})\rangle \end{aligned} \quad (8.62)$$

$$\begin{aligned} &= \frac{1}{2} |A_1 = 0\rangle \left[(1 + e^{-2|g|^2}) |\psi_{e,2\omega}(\text{even})\rangle - (1 - e^{-2|g|^2}) |\psi_{e,2\omega}(\text{odd})\rangle \right] \\ &\quad + \frac{\sqrt{1 - e^{-4|g|^2}}}{2} |A_1 = 1\rangle \left[|\psi_{e,2\omega}(\text{even})\rangle + |\psi_{e,2\omega}(\text{odd})\rangle \right] \end{aligned} \quad (8.63)$$

We show in Fig. 8.6 the maximally achievable I_d for different g and optical detection efficiency η , numerically optimized over the electron measurement basis. With unity η , we observe a significant violation of the classical bound even for coupling strength as low as $|g|^2 \sim 0.1$, at the level we already demonstrated experimentally in Section 7.3. Note that different types of measurement inefficiency, especially on the optical side, will degrade the level of measurable $I_d - 2$. Therefore, it is of utmost importance to keep optimizing the optical collection efficiency of the setup. Using straight waveguides and SNSPDs, we expect the achievable detection efficiency to be around 70%, within the budget to observe Bell violation given $|g|^2 = 0.1$.

Chapter 8. Electron energy-dispersion effects

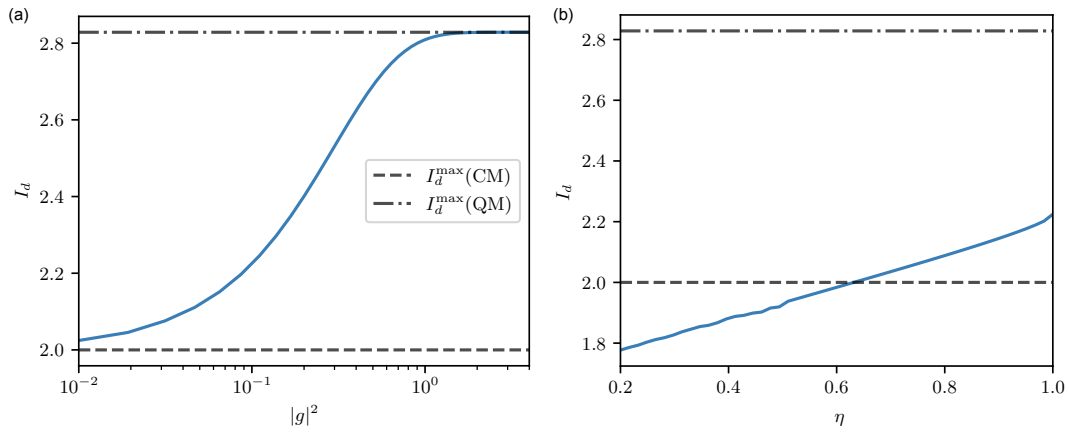


Figure 8.6: **(a)** Maximally achievable I_d with different coupling strength g , compared to the classical bound (CM) and the quantum bound (QM). The optical detection efficiency is set to $\eta = 1$. With $|g|^2 \sim 1$, the electron-photon entangled state can saturate the quantum bound, while it is always above the classical bound even with relatively low coupling strength. **(b)** Maximally achievable I_d with different optical detection efficiency η , compared to the classical bound (CM) and the quantum bound (QM). The coupling strength is set to $|g|^2 = 0.1$.

9 Epilogue

Through this thesis, I have summarized most of my PhD journey, on the topics of establishing a cavity optomechanics platform that operates in the quantum regime at room-temperature environment, and observing quantum optical effects of free-electron-photon interactions mediated by photonic integrated circuits. These two seemingly disconnected research directions are unified under the overall framework of quantum optics, as both quantum optomechanics and free-electron quantum optics involve the quantum nature of photons, i.e. they are discretized particles that can not be further divided. However, we will illustrate below from several perspectives, i.e. coupling bandwidth, decoherence mechanisms, locality of interaction, and difference of their quantum effects, to showcase their rather different regimes for photon interactions.

The coupling dynamics is common in the sense of the generation of quantized photons in optical frequency modes, which are continuum modes in either free space or waveguide. The bandwidths, however, are drastically different, so we need to employ different theoretical frameworks to better describe their dynamics. For a typical value, the bandwidth for optomechanics is on the order of kHz-GHz, determined by the property of the mechanical oscillators, with which the nonlinear interaction only concerns one optical cavity mode that is selectively excited using an optical laser. The bandwidth for electron-photon interaction, even with a very long interaction length of 1 mm, the optical bandwidth is still on the order of THz with ultrafast timescale, as the high-energy electron is intrinsically a broadband radiation source that couples to everything and it is a linear energy exchange process (no selectivity through the external pump in the case of optomechanics). Because of these intrinsic differences, we typically employ the cavity QED framework for optomechanics, where the rate of interaction is very small with pre-defined optical and mechanical modes. In contrast, we employ a more general 3D QED framework for the electron-photon interaction, to find out what is the optical mode in the continuum of frequency and space that the electron is coupling to.

In terms of decoherence mechanisms, both are due to the coupling to auxiliary channels. For optomechanics, it is mostly the coupling of mechanical or optical oscillators to the environment where the information of quantum states gets lost. These are losses that can be

Chapter 9. Epilogue

engineered, especially for the mechanical oscillator where the loss can be diluted by almost a factor of a million with the right geometries and material composition. For the electron-photon interaction, apart from external optical losses (including losses from coupling to unguided modes), there are decoherence channels that are fundamentally tied to the optical response of the material. As the interaction is intrinsically broadband, only optical frequencies in the material transparency window are in principle quantum coherent (parametric), i.e. the interaction is only mediated by the material and no material excitations are produced. For the optical frequencies that go beyond the material bandgap, the optical response of the material will excite a valence electron into the conduction band as a quasiparticle (exciton), after which the relaxation starts and ends into phonon excitations of the lattice and photon excitations at different frequencies. As this is a multi-partite entangled state between electron-photons-phonons at different frequencies, the optical state space is intrinsically incoherent. In the transparency band, the optical photons can in principle co-propagate with the electron and return the energy to the electron, thus reducing the effective optical bandwidth through the phase-matching mechanism. This is not possible for frequency components in the conduction band, as quasiparticles are localized and their excitation energies can not be returned to the electron by the phase-matching mechanism. Therefore the decoherence mechanism can not be effectively modified by the length of the interaction but can be mitigated by how far the electron is to the surface of the material (similarly to the electron-photon coupling ideality concerning higher-order waveguide modes).

In terms of the locality of the interaction, these two systems are also quite different. In our optomechanics model, the mechanical oscillator is a classically bounded acoustic wave, but in terms of its quantum mechanical wave function, it is extremely localized (x_{zpf} about the size of a proton), due to its heavy mass. Therefore, the interaction is modeled between an almost point mass and optical fields that are nonlocalized continuous waves. In other words, it is a stationary object and the interaction with it has a well-defined start-to-end timing defined by the envelope of the optical pump, or the measurement time-window. For free electrons, the wave function is determined by the way the electron emission process is initiated. For either thermal emission or field emission, the coherence length of the free electron is much larger than an optical wavelength, and therefore the electron generally has a delocalized wave function compared to that of the optical wave. Also, when analyzing the interaction naturally in the momentum state basis, the plane wave states are infinite in spatial dimensions. Therefore, the interaction's start-to-end timing is not well defined, especially considering that the electron state's different energy components propagate at different velocities. So, the timings of electron-photon interactions that happen at multiple locations with significant spatial separations are highly state-dependent. In this case, we generally integrate the interaction time from minus infinity to plus infinity, and use a single-pass scattering matrix to describe the interaction.

For both systems, even though the quantum effects can be attributed to the quantized nature of photons, they are of very different physical manifestations. For free electrons, the interaction results in linear energy exchange between the electron and the optical fields, mediated by

the dielectric dipoles inside the material. This results in the generation and absorption of discretized photons each with an extremely broad optical frequency bandwidth ($>$ THz). For optomechanics, the interaction is naturally dispersive (mechanical position couples to the frequency of cavity modes), so effectively when the cavity is in the vacuum state, there is no energy exchange for this type of dispersive coupling. The energy exchange only happens when the cavity is populated with an external optical pump that selectively enhances the interaction between the mechanics and the optical spatial mode being pumped. This breaks the closed system into an open system, where the cavity mode evolution is governed by the CW mode of the laser, and the mechanical mode couples to the nearby frequency modes of the laser excitation. Here, the quantum effects of the photons, e.g., radiation pressure shot noise, are from the highly populated cavity mode. These quantized effects are substantially different from the electron-photon interaction where there are very few photons present that are not associated with any particular cavity modes.

It is not yet clear how to conveniently bridge these two interactions with such drastically different energy or frequency landscapes. One scheme I came up with during my thesis study, which I illustrated in Section 6.4.2, uses nonlinear optical interactions at a frequency transducer to greatly reduce the optical bandwidth of the CL. The nonlinear process essentially demodulates the pulsed CL emissions from optical resonators with an equally broad optical local oscillator to convert the THz-broad optical pulses to MHz-broad microwave pulses. Once the excitation is coherently converted to the microwave domain, further spatial-temporal manipulations are feasible that could lead to the entanglement between mechanical oscillators, which typically come with kHz-MHz bandwidths, and high-energy free electrons through electromechanical interactions.

A Dissipative dynamics in photonic integrated circuits

The distribution of this thesis is mainly through the internet, which involves data communication enabled by the ultralow-loss optical fiber transmission over long distances [282]. Photonic integrated circuits (PICs), which gained traction by the 1980s [283], have been an indispensable component in fiber optic communications due to their miniaturization and portability. In these circuits, photons or light is used to replace applications previously achieved using electronics. The light is detected, generated [284, 285], transported, and processed [286] by the optical waveguiding components on a photonic chip. In recent years, PICs have also received tremendous interest due to their broad range of applications outside optical communications while being compatible with large-scale fabrication using CMOS technologies. These include optical frequency combs [224], laser-based ranging [287], and optical amplifiers [288].

Integrated photonics have also found themselves in quantum optical applications [289], including quantum communication [251], computation [290], and metrology [291], aiming to replicate and boost the utility and widespread usage of the bulk counterparts [292, 293]. Due to the fragile nature of the quantum states, understanding the dissipation dynamics at the microscopic scale, typically more significant than the bulk systems, is crucial for performance-demanding quantum applications. The same can be said for some classical applications, particularly nonlinear optics [224, 294, 295, 296], where loss and nonlinearity play a significant role. In this part of the thesis, in the context of Kerr squeezing [297], we investigate the dissipative dynamics in photonic integrated circuits, including thermodynamic fluctuations [1] and dissipative feedback [2] at the microscopic scale that is particularly strong at room temperature. We also illustrate some exciting interplay and elucidate misunderstandings surrounding the material dissipation-induced and quantum coherent nonlinearities. With the spectroscopy techniques we developed [3, 4, 5], material dissipation can further be categorized and quantified to help guide device optimization. Some sections in this part of the thesis are adapted from Refs [1, 2, 3, 4].

Though not as confined as electrons in modern electronic integrated circuits due to the large size of the photons, the optical field is still shrunk to its minimum size at the wavelength scale. Due to the field enhancement, besides its application in nonlinear optics, photonic integrated

Appendix A. Dissipative dynamics in photonic integrated circuits

circuits allow the scientific study of some of the most fundamental light-matter interactions, facilitate the development of nonlinear photonics [224], cavity optomechanics [13], and coupling to elementary particles [8, 138].

In our research, we use chip-based microresonators to enhance numerous physical phenomena by exploiting the small mode volume of the cavity mode, including nonlinear optics [224], cavity optomechanics [13], and coupling to elementary particles [8, 138].

In particular, most of our research applications utilize integrated photonic circuits based on silicon nitride (Si_3N_4 , image shown in Fig. A.3), which is a radiation-hard [298], CMOS-compatible material [299] with a significant Kerr nonlinearity, an absence of two-photon absorption in the telecommunication window, ultralow losses [152, 300, 301], and a wide transparency window from visible to mid-infrared. These properties have in particular enabled chip-scale frequency combs [189, 224, 302, 303, 304], cavity optomechanics [88], as well as coupling with high-energy free-electrons [7, 8].

Recent advances [300, 305, 306] in fabrication of integrated Si_3N_4 microresonators have enabled optical quality factors $Q > 10^7$, for which many applications are enabled, especially ultra-low-power, robust generation of dissipative Kerr solitons (Section B.9). Squeezed light generation using Kerr nonlinearity on a high-Q integrated chip is also proposed [307] (Section A.2.1). In this Chapter, we primarily focus on the investigation of single-mode Kerr squeezing [307], which is influenced by many parasitic dynamics, including thermal fluctuations and photothermal feedback.

In particular, the thermorefractive noise (TRN) studied in Section A.1 will impose a fundamental limit on the frequency noise of the Si_3N_4 microresonator and can therefore be a limiting factor for Kerr squeezing where the classical noise budget is very tight. It is also considered a limiting factor for classical applications such as microwave generation [294, 295]. Although measurements of the carrier-envelope-offset (CEO) frequency noise of microcombs [296] have already shown clear evidence that thermal noise limits the performance of specific applications, TRN has mostly been directly measured in simple geometries (notably silica microspheres and microtoroids [308, 309]), and has not been systematically studied in photonic integrated microresonators. In this part, we study this noise in both numerical simulation and experimental characterization, and show that this noise plays a vital role in the Kerr squeezing noise budget.

Furthermore, material dissipation, in the form of optical absorption, can lead to competing nonlinear processes along with Kerr nonlinearity. For integrated photonic circuits, the photothermal effect is of the same magnitude as the Kerr effect [3, 4, 5], even for state-of-the-art material purity achieved. However, there is a lack of theoretical and experimental investigation of the consequences of these competing nonlinearities from the perspective of generating squeezed light using Kerr nonlinearity. Some coworkers in the field even suspected that these parasitic nonlinearities, e.g., the photothermal effect, can also squeeze light. In this chapter, we develop a theoretical framework to elucidate the dynamics of cavity dissipation-induced

nonlinearity, and show the intricate interplay between the photothermal and Kerr effect in squeezed light generation. Based on a comprehensive understanding of these dissipative dynamics, measurement techniques (Section A.4) are developed here to help determine these dissipation rates, and thus help guide device performance optimization.

A.1 Fundamental thermal noises

The small mode volume of microresonators enables strong optical nonlinearities, harnessed in emerging technologies such as microcombs [224], and also enhances sensing capabilities used in fundamental research, e.g. cavity quantum optomechanics [13]. However, the small mode volume comes at a cost: limitations on the microresonator's frequency stability arise from thermal fluctuations such as thermo-refractive (TRN) and dimensional fluctuation thermal noise (thermoelastic and elasto-optic [310]). These fluctuations were first theoretically described in the context of laser interferometer gravitational-wave detection [311], and place limits on the frequency stability of an interferometer. The cavity frequency noise we observed and mitigated using phononic crystal structures in the MIM system (Section. 2.3) belongs to the category of thermoelastic noise.

Thermal fluctuations are particularly strong in small mode volume optical resonators and place fundamental limits on applications that require high frequency stability, e.g., optical sensing [312], optomechanical displacement sensing [313], dissipative Kerr soliton microcomb generation [224], electro-optical modulators [314], opto-electronic oscillators [315] and Kerr squeezing [307]. Therefore, different kinds of thermal noises have been extensively studied [309, 311, 316, 317]. However, theoretical analyses show inconsistencies between different platforms [318] and rely on auxiliary measurements of material parameters that are not always well-known. Therefore, experimental characterization is essential to understanding a specific system's limitations. Therefore, refined theoretical and modeling approaches are required to analyze TRN in photonic integrated circuits composed of multiple materials with complex geometry.

Here, in the context of understanding the dissipative dynamics of our system, we present the characterization of TRN in Si_3N_4 microresonators and compare finite element method (FEM) simulations with measurements of TRN using balanced homodyne detection. The results show that TRN is the dominant thermal noise source over frequencies ranging from 10 kHz to 10 MHz. We also simulate the feasibility of using a composite material structure to reduce TRN and discuss the experimental complications.

A.1.1 Theoretical treatment of thermorefractive noise

In an optical resonator, thermo-refractive noise leads to fluctuations of the resonance frequency due to fluctuations of the effective refractive index, n , of the optical mode, caused by the local thermodynamic fluctuations of temperature, δT , whose variance in a given volume

Appendix A. Dissipative dynamics in photonic integrated circuits

V is:

$$\langle \delta T^2 \rangle = \frac{k_B T^2}{\rho C V} \quad (\text{A.1})$$

where T is the temperature of the heat bath, k_B the Boltzmann constant, ρ the density, C the specific heat. Using the material parameters of Si_3N_4 and the optical mode volume of a typical 1 THz free-spectral-range (FSR) microresonator, we can obtain a value of the standard deviation of the heat bath temperature as $\sqrt{\langle \delta T^2 \rangle} \sim 60 \mu\text{K}$. Combined with the measured thermo-optic coefficient, $dn/dT = 2.45 \times 10^{-5} \text{K}^{-1}$, of Si_3N_4 [319], the fractional frequency fluctuation can be estimated as [309] $\sqrt{\langle \delta f^2 \rangle}/f = \frac{\sqrt{\langle \delta T^2 \rangle}}{n} \frac{dn}{dT} \sim 7 \times 10^{-10}$, and the absolute frequency fluctuation $\sqrt{\langle \delta f^2 \rangle}$ is around 150 kHz, which is up to 1% of the cavity linewidth in Si_3N_4 microresonators [306]. Though this is a rough estimate of the noise property, we can see that this magnitude will be of concern for many applications.

The thermo-refractive noise and the thermo-elastic noise, which are both consequences of thermodynamic temperature fluctuations, were previously experimentally observed in silica microspheres [309] and theoretically analyzed (but not observed) in crystalline resonators [316]. In most cases of integrated photonic circuits, where light travels mostly in a solid-state material, thermo-refractive noise is the largest among the thermal noises. For chip-based Si_3N_4 microresonators, TRN is also expected to be the most significant noise source, as the temperature fluctuations, which give rise to dimensional fluctuation thermal noises, are averaged over the entire resonator chip rather than the optical mode volume. However, the different modeling approaches taken in the analysis of the two previously mentioned platforms result in different predictions for the geometric dependency of TRN and its magnitude at low offset frequencies [318].

We now describe the two approaches taken for modeling TRN in microresonators: the first model assumes a homogeneous microresonator in an infinite heat bath, yielding the following expression for the effective temperature fluctuations [318]:

$$S_{\delta T}(\omega) = \frac{k_B T^2}{\sqrt{\pi^3 \kappa \rho C \omega}} \sqrt{\frac{1}{2p+1}} \frac{1}{R \sqrt{d_r^2 - d_z^2}} \frac{1}{(1 + (\omega \tau_d)^{3/4})^2} \quad (\text{A.2})$$

where R is the ring radius of the microcavity (geometry shown in Fig. A.3(a)), d_z and d_r are halfwidths of the fundamental mode for the intensity, with orbital number l , azimuthal number m , meridional mode number $p = l - m$, $\tau_d = \frac{\pi^{1/3}}{4^{1/3}} \frac{\rho C}{\kappa} d_r^2$, and the definitions of the other parameters can be found in Table A.1. The key features are the $\omega^{-1/2}$ dependence at low frequency, the ω^{-2} dependence at high frequency, and the R^{-1} overall scaling. This model gave satisfactory agreements with experimental measurements in microspheres [309].

The second model [316] uses the thermal decomposition method, which does not consider the interaction with the environment. As a consequence, there is a low-frequency cut-off due to the finite dimension of the resonator, which results in the following (single-sided) temperature

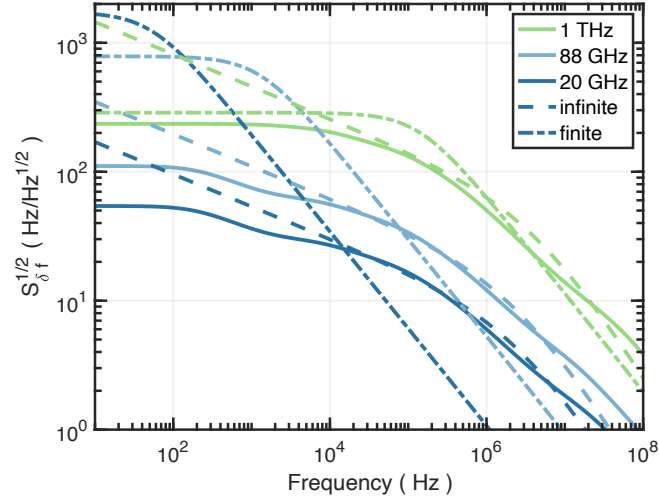


Figure A.1: **Comparison of FEM simulation results of thermo-refractive noise with the theoretical predictions (infinite heat bath and thermal decomposition)**. The graphs show the cavity frequency noise spectral density of a Si_3N_4 microresonator with a free spectral range (FSR) of 1 THz, 99 GHz and 20 GHz. At high frequencies, the simulation curves match better with the infinite heat bath assumption. At low frequencies, the simulation curves experience a cut-off because of the finite size of the modeled chip, which behaves more similarly to the thermal decomposition method.

noise spectral density:

$$S_{\delta T}(\omega) = \frac{k_B T^2 R^2}{12\kappa V_{\text{eff}}} \left(1 + \left(\frac{R^2 \rho C \omega}{3^{5/2} \kappa} \right)^{3/2} + \frac{1}{6} \left(\frac{R^2 \rho C \omega}{8l^{1/3} \kappa} \right)^2 \right)^{-1} \quad (\text{A.3})$$

where V_{eff} is the effective mode volume. Here the expression still has a ω^2 dependence at high frequency but features an overall scaling with R between R^{-3} and R^{-4} depending on how V_{eff} scales with radius (spherical resonator $V_{\text{eff}} \propto R^{11/6}$ or ring resonator $V_{\text{eff}} \propto R$).

The temperature fluctuations can be converted into a frequency noise spectral density through $S_{\delta f} = (f_0 \frac{1}{n_0} \frac{dn}{dT})^2 S_{\delta T}$, where f_0 is the resonance frequency. However, Eq. (A.2) and Eq. (A.3) are both idealized cases assuming homogeneous materials and either the infinite heat bath or isolated model. These assumptions do not match the geometry of integrated Si_3N_4 resonators of complex waveguide structures comprising different materials, invalidating the homogeneity assumption. We therefore performed an FEM simulation based on the fluctuation-dissipation theorem [317, 318], where we simulate the thermo-refractive noise of a Si_3N_4 microresonator embedded in a SiO_2 substrate, using the actual geometry.

The Fluctuation-Dissipation Theorem (FDT) is a valuable tool for studying stationary thermal noises. To simulate thermorefractive noise (TRN), we closely follow the treatment of Ref. [318]¹.

¹The treatment is pedagogically explained in this YouTube video: COMSOL simulation tutorial: Thermal Noise

Appendix A. Dissipative dynamics in photonic integrated circuits

Table A.1: Physical properties used for both the theoretical models and FEM simulations of the thermo-refractive noise of Si₃N₄ microresonators

Physical properties	Values
Density (ρ)	$3.29 \times 10^3 \text{ kg m}^{-3}$
Refractive index (n_0)	1.996
Thermo-optic coefficient (dn/dT)	$2.45 \times 10^{-5} \text{ K}^{-1}$
Thermal expansion coefficient $1/l(dl/dT)$	$3.30 \times 10^{-6} \text{ K}^{-1}$
Thermal conductivity (κ)	$30 \text{ W m}^{-1} \text{ K}^{-1}$
Specific heat capacity (C)	$800 \text{ J kg}^{-1} \text{ K}^{-1}$

Consider a physical quantity that one wants to investigate, $y = \int x(\vec{r}) \times q(\vec{r}) d^3 r$, where x is the generalized coordinate of this given system and is driven by a small, harmonic, generalized probe force $f = F_0 \cos(\omega t) q(\vec{r})$ conjugated with x . Then, the dissipated energy W_{diss} of the system can be calculated over one period of the force oscillation. Last, the fluctuation (one-sided power spectral density) of the observable y can be expressed as

$$S_y(\omega) = 2\hbar \frac{W_{\text{diss}}}{\pi F_0^2} \coth\left(\frac{\hbar\omega}{2k_B T}\right). \quad (\text{A.4})$$

In our case, as we want to simulate the frequency fluctuation of the resonator, we choose our fluctuation observable as $\frac{\delta\omega}{\omega} \approx -\int \delta\Theta(\vec{r}) \epsilon_0 \sqrt{\epsilon_1(\vec{r})} \beta(\vec{r}) |e(\vec{r})|^2$, where the temperature fluctuation $\delta\Theta(\vec{r})$ is chosen as our generalized coordinate. Here, β links the permittivity $\epsilon = \epsilon_0 + \epsilon_1$ to the temperature fluctuation through $\delta\epsilon = 2n\beta\delta\Theta$, and $\vec{e}(\vec{r}) = \vec{E}(\vec{r})/\sqrt{W_{\text{WGM}}}$. The generalized force (which is entropy) is set to $S = F_0 \cos(\omega t) \epsilon_0 \sqrt{\epsilon_1(\vec{r})} \beta(\vec{r}) |e(\vec{r})|^2$. We solve the heat transfer function $i\omega\rho C_V \tilde{\Theta}(\vec{r}, \omega) + \kappa \nabla^2 \tilde{\Theta}(\vec{r}, \omega) = i\omega T \tilde{S}(\vec{r}, \omega)$ of the optical structure in the frequency domain, and calculate the dissipated energy according to $W_{\text{diss}} = \int \frac{\pi\kappa}{\omega T} |\text{grad} \tilde{\Theta}(\vec{r}, \omega)|^2 d^3 r$. The fluctuation density $S_{\delta\omega/\omega}(\omega)$ can thus be calculated by inserting W_{diss} into Eq. A.4.

The simulation was performed using FEM software in the axial symmetry case. We modeled our resonator geometry as a ring waveguide embedded inside the SiO₂ cladding, with air as the top boundary. First, the eigenfrequency problem for the electromagnetic waves in the chosen geometry was solved for different azimuthal numbers to find the eigenfrequencies and their corresponding optical mode profiles. Then, the mode profile of one chosen eigenmode was used as a parameter for the probe force, which is added as a heat source in the heat transfer problem. The frequency of the probe force is scanned, and for each frequency, $S_{\delta\omega/\omega}(\omega)$ is calculated following Eq. A.4 from the dissipated energy of the system solved from the heat transfer problem.

We can now compare the FEM simulation results with the theoretical expressions (see Fig. A.1). Because the thermal properties of Si₃N₄ depend on the material characteristics and the fabrication process, they can exhibit significant variation. We use the median values of the physical properties reported in the literature for both the theoretical predictions and

the FEM simulations (see Table A.1). The optical mode parameters used in Eq. (A.2) and Eq. (A.3) are retrieved from FEM simulations of the Si_3N_4 microresonators. We work with fundamental TE modes of waveguide ring resonators ($l = m$). For the scaling with ring radius, the simulation curves match the infinite heat bath theory Eq. (A.2) well. At the same time, the deviation from the thermal decomposition method becomes more significant as the radius increases. It indicates that, according to FEM simulations, Si_3N_4 microresonators experience thermo-refractive noise more similar to microspheres at high frequency. In contrast, at low frequencies, the noise is reduced due to the cladding region (SiO_2) and the chip geometry. The measurement results, the simulation curves, and the infinite heat bath curves are compared in Fig. A.3.

Due to the R^{-1} scaling and the strong light confinement the Si_3N_4 waveguide offers, the computed spectral density of thermo-refractive frequency noise for resonators with FSR ranging from 20 GHz and 1 THz is sufficiently high to be probed without a highly pure and stable laser. In crystalline microresonators, the much larger mode volume and smaller thermo-optic coefficient (dn/dT) make it much more challenging to measure TRN [320], and correspondingly it is typically not a practical limit.

A.1.2 Measurement of thermorefractive noise

The measurement scheme here (illustrated in Fig. A.2(a)) employs a balanced homodyne setup to measure the phase fluctuations of the transmitted light caused by the cavity frequency noise. The cavity frequency noise is calibrated using a calibration tone. The laser (external cavity diode laser at 1550 nm with a linewidth of ~ 30 kHz) is locked to the cavity resonance via the Pound-Drever-Hall (PDH) locking method [66] with a feedback bandwidth of a few kilohertz. The power level is sufficiently low to avoid unwanted thermal and nonlinear optical effects.

In order to provide an absolute calibration of our measurement, we use a calibration tone generated by phase modulating the RF tone applied to the acousto-optic modulator (AOM). We find that at low modulation frequency < 1 MHz, conventional EOM exhibits residual amplitude modulation. A modulation depth of 1.14 rad is calibrated by sideband fitting using heterodyne detection. The calibration tone induces an extra phase modulation of the light, transduced by the cavity, and results in a narrow peak in the frequency noise spectrum. Because the frequency modulation depth is known for the calibration peak, we can use it to calibrate the absolute magnitude of the corresponding homodyne signal. The same technique (but with EOM at high modulation frequency) is also used to measure the frequency noise of FP cavity in Section 2.3.1. The modulation frequency and the modulation depth are chosen at 50 kHz and 1.14 rad to be outside the PDH locking bandwidth and to keep the frequency modulation depth smaller than the cavity linewidth.

The characterized samples are integrated Si_3N_4 microresonators with radius $R \sim 23 - 1200 \mu\text{m}$, and FSR ranging from 1 THz to 20 GHz. The Q -factors of these microresonators fabricated by

Appendix A. Dissipative dynamics in photonic integrated circuits

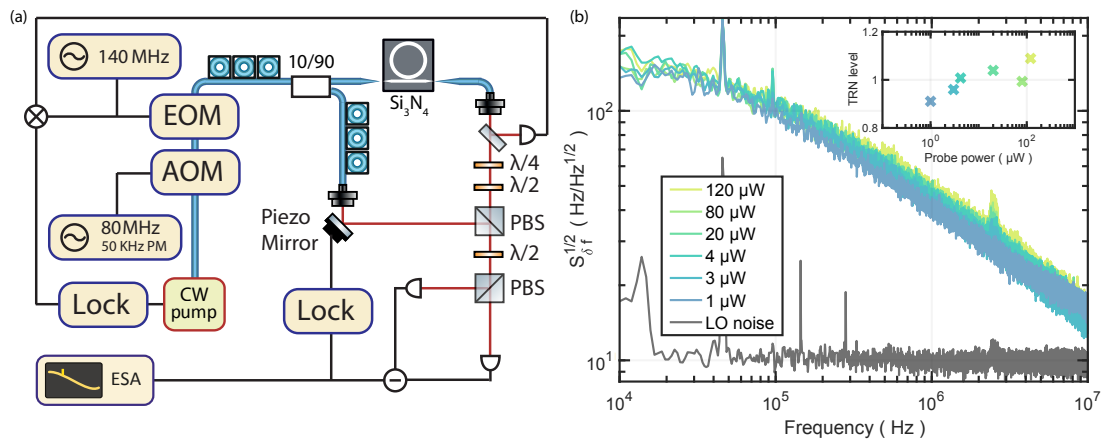


Figure A.2: **(a)** Balanced homodyne setup for measuring thermo-refractive noise of the Si_3N_4 microresonator. The electro-optic modulator (EOM) phase modulates the light at 140 MHz to generate the PDH error signal for locking the laser to the cavity mode. The AOM is modulated with an RF tone with a central frequency of 80 MHz. The RF tone is then phase modulated at 50 kHz with a 1.14 rad modulation depth, which provides an absolute calibration peak for the noise measurements. A piezo mirror is used in the local oscillator path to lock the homodyne at the phase quadrature. The measurement bandwidth is limited by the detector bandwidth of 80 MHz. **(b)** Calibrated thermo-refractive frequency noise spectra measured using different probing power. A Si_3N_4 microresonator with free spectral range of 1 THz was probed with 1 μW to 120 μW of optical power. The bottom line shows the shot noise level with 1 μW of input optical power. The normalized units utilized in the inset figure are obtained by integrating over 200 kHz to 2 MHz and dividing by the average of the integrated values. It indicates that the probe is weak enough to avoid other laser-induced thermal effects (e.g., photothermal noise) and reveals the power-independence expected for thermo-refractive noise.

the photonic Damascene reflow process [305, 306] are typically $Q > 10^7$. The measured noise spectrum is thus filtered by the cavity resonance at high offset frequencies. The resonance linewidth of each microresonator and the response function of the bias tee before the spectrum analyzer are measured and compensated for through data post-processing.

The first thing we did was to verify that the noise we measured was not stimulated by the probe laser, that is indeed fundamental thermal fluctuation of the resonator itself. We verified the power-independent nature of thermo-refractive noise (as expected from Eqs.1-3) by performing an input power sweep (shown in Fig. A.2(b)). The frequency noise level remains the same when varying the laser power of the probe signal by more than two orders of magnitude (from $1\mu\text{W}$ to $120\mu\text{W}$), showing that photothermal noise (frequency noise driven by optical absorption) is not making a significant contribution.

We next investigated the dependence on the optical mode volume. Fig. A.3 (c) presents the measurement results for four different cavity radii, together with the corresponding theoretical curves and FEM simulation curves. The observable background noise sources arise from local oscillator shot noise, several technical spikes, and the calibration peak at 50 kHz. The calibration peaks in the off-resonance noise spectrum and the LO shot noise spectrum result from residual amplitude modulation from the AOM. However, by utilizing phase modulation of the AOM RF tone, a signal-to-noise ratio of 20 dB can be obtained for the calibration peak.

Good agreement of the measured spectra with the simulation curves for both frequency dependence ($\propto \omega^{-1/2}$) and radius dependence ($\propto R^{-1}$) is observed, which also confirms the validity of Eq. (A.2) as a theoretical prediction of TRN (at frequencies above 10 kHz) in the Si_3N_4 microresonator platform. By assuming that the spectrum matches the FEM simulation in the low-frequency range, the total frequency fluctuations due to TRN could be retrieved through integration over the high-frequency experimental data and the low-frequency FEM curves (the latter contributes less than 1% of the total frequency variance), e.g. the 1 THz microresonator has a resonance frequency instability of around 240 kHz, which agrees well with our previous rough estimation of 150 kHz. The agreement further indicates that the heat exchange with the surrounding environment is mainly responsible for generating thermo-refractive noise in this system. However, in the low-frequency range, the approximation of a homogeneous medium in Eq. (A.2) will break down due to heat exchange with the media outside the waveguide, as is indicated by the multiple saturation steps of the FEM simulation curves at low frequency shown in Fig. A.1. Though the heat exchange with the outer layer makes it difficult to derive a simple expression for the thermo-refractive noise in Si_3N_4 microresonators, it offers a possibility to bypass the thermal limit [321], which we will discuss in the next section. The design of such a thermal-noise-reduced photonic microresonator will be more critical when more applications truly reach the thermal limit of their performance, e.g., to realize integrated ultra-narrow linewidth lasers.

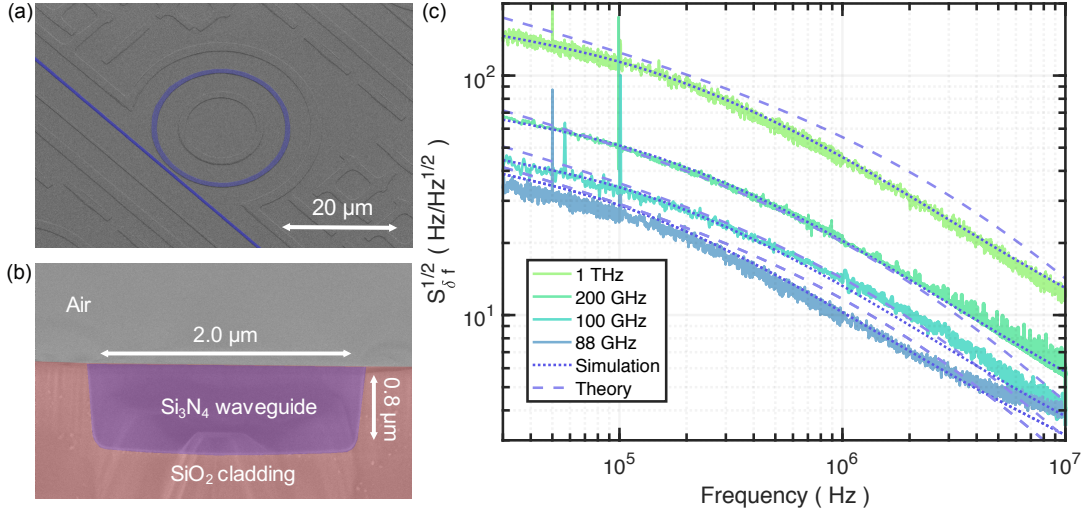


Figure A.3: **Verification of the size dependence of thermo-refractive noise in integrated Si_3N_4 microresonators.** (a) SEM image of a 1 THz-FSR Si_3N_4 microresonator ring (dark blue). (b) SEM image of the waveguide cross-section. The cross-section image is color-shaded to help identify different regions. (c) Thermo-refractive noise measured in integrated Si_3N_4 microresonators with free spectral ranges of 1 THz, 200 GHz, 100 GHz and 88 GHz. The 88 GHz-FSR sample has a bigger width ($2.0\ \mu\text{m}$) compared to other samples ($1.5\ \mu\text{m}$) and there is some run to run variation in sidewall angles. A 30-point moving average was applied to the data. The dotted lines show the FEM simulation results, and the dashed lines show the theoretical predictions from Eq. (A.2). Data below 10 kHz were truncated due to the excess locking noises, and also data above 10 MHz due to the detector's nonlinear response.

A.1.3 Thermal noise cancellation

We have also investigated the possibility of using TiO_2 as a thin cladding layer to reduce the TRN of the waveguide mode. In the literature, TiO_2 exhibits a negative thermo-optic coefficient $dn/dT \sim -10^{-4}\ \text{K}^{-1}$. By counter balancing the positive thermo-optic coefficients of Si_3N_4 ($dn/dT = 2.45 \times 10^{-5}\ \text{K}^{-1}$) and SiO_2 ($dn/dT = 1.29 \times 10^{-5}\ \text{K}^{-1}$), TRN can be suppressed at low frequencies ω ($< 100\ \text{kHz}$) where the thermal wavelength $\lambda \sim \sqrt{\frac{k}{\rho C \omega}} > 10\ \mu\text{m}$ is much larger than the waveguide cross-section dimensions.

We simulated the TRN of a structure with a thin layer of TiO_2 grown directly on top of the Damascene Si_3N_4 waveguide (height 850 nm, width $2\ \mu\text{m}$), shown in Fig. A.4. We find a sweet spot where low-frequency TRN can be efficiently canceled by changing the thickness of the TiO_2 layer. When the frequency/thermal wavelength approaches that of the waveguide cross-section dimension, the TRN can be enhanced due to the more significant heat dissipation due to the temperature gradient at the boundary. Therefore, the TRN behaves like white noise at the perfect cancellation point, with a cutoff frequency when the thermal wavelength is much smaller than the TiO_2 structure.

We fabricated some structure with TiO_2 grown on a Damascene Si_3N_4 wafer to measure

A.1 Fundamental thermal noises

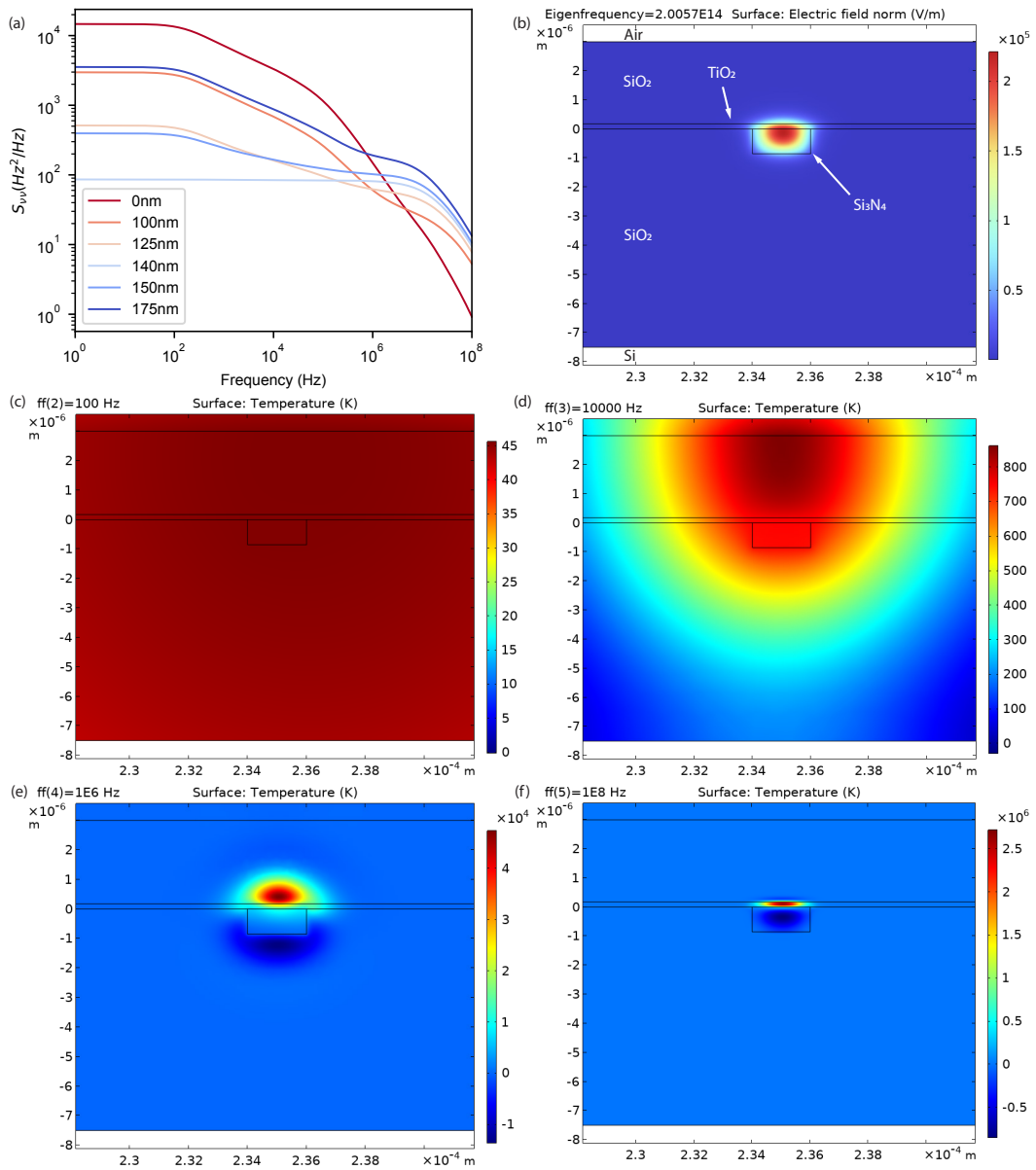


Figure A.4: **FEM simulation results of thermo-refractive noise of varying TiO_2 cladding thickness on top of a 100-GHz FSR Si_3N_4 ring resonator.** (a) TRN spectra of different TiO_2 cladding thickness, showing a reduced low-frequency noise with the correct thickness of TiO_2 , while the high-frequency noise always increases. (b) Mode profile of the fundamental TE mode of the waveguide. (c-f) Frequency-domain temperature distribution given a unity probe entropy force, solved at different drive frequencies.

Appendix A. Dissipative dynamics in photonic integrated circuits

modified TRN. However, the home-grown TiO₂ layer exhibits polycrystalline property and introduces significant optical loss. The quality factor of these resonators is reduced by more than 100-fold, with a typical optical linewidth $\kappa/2\pi \sim 5$ GHz. The added loss prevents us from observing TRN, as the thermal noise is well below the shot noise level of the laser.

In our recent experiment [322], instead of using a heterogeneous structure to cancel TRN, we observed a frequency-independent reduction of the TRN due to the pyroelectric effect in a ferroelectric material lithium niobate (LN). The results were measured on a TE mode of the Z-cut LN ring resonator. Essentially, the pyroelectric effect modifies the material response to a temperature change in the following way,

$$\left. \frac{dn}{dT} \right|_{\text{Pyro}} = \frac{n^3 r_{13} p}{2\epsilon} = -1.74 \times 10^{-5} \text{ K}^{-1} \quad (\text{A.5})$$

where r_{13} is the Pockels coefficient acting on the light field, and $p = -8.3 \times 10^{-5} \text{ CK}^{-1} \text{ m}^{-1}$ is the pyroelectric constant, which is due to the spontaneous polarization generated inside the material when the temperature changes. The benefit of this approach is that the reduction of TRN is frequency-independent, as it effectively modifies the material property. The downside is the emergence of a new form of thermal charge noise [322] and the loss of engineering degrees of freedom.

A.2 Kerr nonlinearity

High-quality-factor microresonators have been widely used for nonlinear optics applications. These nonlinear effects include photothermal nonlinearity, Kerr-nonlinearity, electro-optic effect, and stimulated Raman- and Brillouin-scattering. In the material platform of Si₃N₄, the Kerr nonlinearity has been widely studied, which gives rise to optical parametric oscillations that generate optical frequency combs. Before the onset of parametric oscillation, single-mode nonlinear interaction can also generate squeezed optical states discussed in Section 3.1.

During the thesis study, I worked on both the generation of microcombs for the experiment of electron-photon interaction and the generation of optical squeezing using Kerr nonlinearity. Having understood the fundamental noise limit in our microresonator platform, we continue to discuss the Kerr nonlinearity that could enable on-chip optical squeezers at radio frequency bands. In Appendix B.9, we briefly summarize the theory of generating dissipative Kerr solitons in microresonators. In this section, we discuss in detail the Kerr squeezing dynamics and how different system noises influence the optical squeezing generation.

A.2.1 Single-mode Kerr squeezing

Heisenberg's uncertainty relation sets the lower bound on the electric fields' uncertainty product at orthogonal phases, thus imposing quantum noise on all optical measurements. However, nonlinear optics enables a path to circumvent this limitation by generating squeezed

light, where the quantum uncertainty is redistributed. Not only does squeezed light enhance precision measurements such as LIGO [323], it is also an essential component for continuous variable quantum information and communication protocols [324].

The generation of squeezed light can be realized in various physical systems, from the very first demonstrations with nondegenerate four-wave mixing using Na atomic vapors [325], and optical fibers [326] to the recent demonstration of ponderomotive squeezing using optomechanical interaction [327], all the way to the state of the art squeezed light source in bulk nonlinear crystals [328] using parametric down-conversion. The system complexity of these quantum light sources has been a significant barrier to their application to quantum technologies. In particular, none of those mentioned above proof-of-principle experiments are compatible with lithographically defined photonic integrated circuits, which are orders of magnitude smaller in system size and significantly reduce implementation complexity.

Kerr squeezing relies on self-phase modulation to generate broadband squeezed light. In its essence, the third-order optical nonlinearity imprints the intensity fluctuation of the light to the phase fluctuation, reducing vacuum fluctuation in some quadrature angles (illustrated in Fig. A.5). The physical principle is similar to that of the optomechanical squeezing that we discussed in Section 3.1, except in the Kerr effect, the light drives the electrical dipoles of the material, and in the optomechanical squeezing, the center-of-mass motion of the mechanical object is driven.

Kerr squeezing has been realized in optical fibers [329], where optical pulses enhance the Kerr nonlinear phase shift by reaching extremely high peak intensities. However, operating at a power with quantum-limited noise in the continuous wave regime has been challenging to reach the threshold. Recent advances [306] in the fabrication of integrated Si_3N_4 microresonators have enabled optical quality factors $Q > 10^7$, which means the parametric threshold power is reduced to tens of μW for squeezed light generation [307]. The low threshold power is directly related to the ultra-high optical quality factor and reduces the requirements for laser noise. Further increases in the quality factor would enable squeezed light generation at even lower powers, thereby increasing the prospects for fully on-chip photonic quantum information application.

In this section, we discuss the theoretical consideration of observing Kerr squeezing in Si_3N_4 microresonators, including the nonlinear quantum optical equations that generate squeezing, as well as the classical noise contributions, followed by the next sections on dissipative quantum feedback, as well as a new thermal noise source we identified.

Linearized quantum Langevin equations

We omit the $\hat{\cdot}$ symbols in this section because there are too many quantum operators. The Hamiltonian of the system consisting of a single optical mode exhibiting Kerr nonlinearity is

Appendix A. Dissipative dynamics in photonic integrated circuits

expressed by

$$H = \hbar\omega_0 a^\dagger a + \frac{\hbar g}{2} a^{\dagger 2} a^2, \quad (\text{A.6})$$

where a is the cavity photon annihilation operator. The self phase modulation strength g is given by [307]

$$g = \frac{n_2 c \hbar \omega^2}{2 n^2 V_{\text{mode}}}, \quad (\text{A.7})$$

the same as the one we defined in the previous section. Then, we can write down the Langevin equations

$$\frac{da}{dt} = -\frac{i}{\hbar} [a, H] - \frac{\kappa}{2} a + \sqrt{\kappa_{\text{ex}}} a_{\text{in}} + \sqrt{\kappa_0} b_{\text{in}}. \quad (\text{A.8})$$

where we also include the internal loss channel b_{in} . Going to the rotating frame of the laser frequency ω_{laser} , we get

$$\frac{da}{dt} = -(\kappa/2 + i\Delta) a - i g a^\dagger a^2 + \sqrt{\kappa_{\text{ex}}} a_{\text{in}} + \sqrt{\kappa_0} b_{\text{in}} \quad (\text{A.9})$$

where $\Delta = \omega_0 - \omega_{\text{laser}}$ is the laser detuning to the resonance frequency. We can see here that $g a^\dagger a$ is the Kerr-induced cavity frequency shift.

The mean field solution α could be solved by the steady-state equation

$$\alpha(\kappa/2 + i(\Delta + g|\alpha|^2)) = \sqrt{\kappa_{\text{ex}}} \alpha_{\text{in}}, \quad (\text{A.10})$$

which exhibits bi-stability upon reaching the parametric instability. This section assumes that the laser is feedback-stabilized to the shifted resonance frequency, i.e., $\Delta + g|\alpha|^2 \approx 0$.

Given the mean-field solution α , we can go to the new reference frame in the phase space displaced by α , which essentially linearizes the equation using $a \rightarrow \alpha + \delta a$. By keeping only the first-order fluctuations,

$$\frac{d\mathbf{a}}{dt} = \left[M - \frac{\kappa}{2} I \right] \mathbf{a} + \sqrt{\kappa_{\text{ex}}} \mathbf{a}_{\text{in}} + \sqrt{\kappa_0} \mathbf{b} \quad (\text{A.11})$$

$$M - \frac{\kappa}{2} I = \begin{pmatrix} -\kappa/2 - i(2|\epsilon| + \Delta) & -i\epsilon \\ i\epsilon^* & -\kappa/2 + i(2|\epsilon| + \Delta) \end{pmatrix} \quad (\text{A.12})$$

$$\mathbf{a}_i = \begin{pmatrix} \delta a_i \\ \delta a_i^\dagger \end{pmatrix} \quad (\text{A.13})$$

where we define the effective Kerr shift as $\epsilon = g\alpha^2$. The eigenvalues for this matrix are

$$\lambda_{\pm} = -\kappa/2 \pm \sqrt{|\epsilon|^2 - (\Delta + 2|\epsilon|)^2}. \quad (\text{A.14})$$

The onset of parametric instability occurs when $\text{Re}(\lambda) > 0$, which corresponds to a stability region $|\epsilon| + \frac{2\Delta}{3} \leq \frac{\sqrt{\Delta^2 - 3\kappa^2/4}}{3}$. However, when we lock the laser to the shifted cavity resonance as $\Delta + |\epsilon|$, the eigenvalues become $\lambda_{\pm} = -\kappa/2$, which means the system is always stable.

QLE in the quadrature basis

As optical squeezing manifests as reduced quadrature variances, we proceed with the analysis by casting the QLE in the quadrature basis. We introduce two orthogonal quadrature operators with an arbitrary quadrature angle θ

$$Y_1 = (ae^{-i\theta} + a^\dagger e^{i\theta})/\sqrt{2} \quad (\text{A.15})$$

$$Y_2 = -i(ae^{-i\theta} - a^\dagger e^{i\theta})/\sqrt{2}. \quad (\text{A.16})$$

Here we use the intra-cavity mean field α as the phase reference, such that $\alpha = |\alpha|$ and $\epsilon = |\epsilon|$. The defined quadratures are the amplitude and phase quadratures of the light, with θ being the phase of the mean field $a = |a|e^{i\theta}$.

We define here also the inverse relation between the quadrature operators and field operators,

$$\begin{pmatrix} a \\ a^\dagger \end{pmatrix} = [T] \begin{pmatrix} Y_1 \\ Y_2 \end{pmatrix} = \begin{pmatrix} \frac{e^{i\theta}}{\sqrt{2}} & \frac{ie^{i\theta}}{\sqrt{2}} \\ \frac{e^{-i\theta}}{\sqrt{2}} & \frac{-ie^{-i\theta}}{\sqrt{2}} \end{pmatrix} \begin{pmatrix} Y_1 \\ Y_2 \end{pmatrix}. \quad (\text{A.17})$$

By putting (A.17) into (A.11), and left multiply by $T^{-1} = \begin{pmatrix} \frac{e^{-i\theta}}{\sqrt{2}} & \frac{e^{i\theta}}{\sqrt{2}} \\ \frac{-ie^{-i\theta}}{\sqrt{2}} & \frac{ie^{i\theta}}{\sqrt{2}} \end{pmatrix}$, we have the equation of fluctuation in the quadrature bases

$$\frac{d}{dt} \begin{pmatrix} \delta Y_1 \\ \delta Y_2 \end{pmatrix} = \begin{pmatrix} G_1 & H_1 \\ H_2 & G_2 \end{pmatrix} \begin{pmatrix} \delta Y_1 \\ \delta Y_2 \end{pmatrix} + \begin{pmatrix} J_1 \\ J_2 \end{pmatrix} \quad (\text{A.18})$$

where

$$G_i = -(\kappa/2 \pm i \frac{g}{2} [\alpha^2 e^{-2i\theta} - \alpha^{*2} e^{2i\theta}]) \quad (\text{A.19})$$

$$H_i = \pm(\Delta + 2g|\alpha|^2) - \frac{g}{2} [\alpha^2 e^{-2i\theta} + \alpha^{*2} e^{2i\theta}] \quad (\text{A.20})$$

$$J_i = \sqrt{\kappa_{\text{ex}}}\delta Y_i^{\text{in}} + \sqrt{\kappa_0}\delta Y_i^b. \quad (\text{A.21})$$

From here, we can perform Fourier transformation² on (A.18) and obtain the Fourier-domain solution \tilde{Y}_i ,

$$\tilde{Y}_i = \frac{H_i \tilde{J}_j - \tilde{J}_i (G_j + i\omega)}{(G_i + i\omega)(G_j + i\omega) - H_i H_j}. \quad (\text{A.22})$$

As we are using the same port to couple in and out the signal, according to the input-output relation, we have

$$\begin{aligned} \tilde{Y}_i^{\text{out}} = \tilde{Y}_i^{\text{in}} - \sqrt{\kappa_{\text{ex}}}\tilde{Y}_i = & \left[((G_j + i\omega)(\kappa_{\text{ex}} + G_i + i\omega) - H_i H_j) \tilde{Y}_i^{\text{in}} - H_i (\kappa_{\text{ex}} \tilde{Y}_j^{\text{in}} + \sqrt{\kappa_{\text{ex}}\kappa_0} \tilde{Y}_j^b) \right. \\ & \left. + \sqrt{\kappa_{\text{ex}}\kappa_0} \tilde{Y}_i^b (G_j + i\omega) \right] / ((G_i + i\omega)(G_j + i\omega) - H_i H_j). \end{aligned} \quad (\text{A.23})$$

²Note that here the sign of ω is opposite to the rest of the thesis chapters

Appendix A. Dissipative dynamics in photonic integrated circuits

Here, Y^{out} and Y^{in} do not share the same quadrature angles, as their field phase changes when combined with the cavity mean field. If we define $Y^{\text{out}}(\theta)$ as the e.g. amplitude quadrature, then that for Y^{in} would be $Y^{\text{in}}(\theta - \Delta\theta_{\alpha_{\text{in}}/\alpha_{\text{out}}})$.

Also note that from here, the $S_{XX}(\omega)$ denotes the double-sided spectrum and the $S_X(\omega) = S_X(\omega) + S_X(-\omega)$ denotes the single sided spectrum. The noise spectrum could be obtained by taking a self-correlation of Eq. A.23,

$$S_{Y_i}^{\text{out}}(\omega) = \left(|(G_j + i\omega)(\kappa_{\text{ex}} + G_i + i\omega) - H_i H_j|^2 S_{Y_i}^{\text{in}}(\omega) + \kappa_{\text{ex}}^2 |H_i|^2 S_{Y_j}^{\text{in}}(\omega) \right. \\ \left. + \kappa_{\text{ex}} \kappa_0 (|G_j + i\omega|^2 S_{Y_i}^b + |H_i|^2 S_{Y_j}^b) - 2\kappa_{\text{ex}} H_i (G_j(\kappa_{\text{ex}} + G_i) - H_i H_j - \omega^2) \bar{S}_{Y_i Y_j}^{\text{in}}(\omega) \right) \\ / |(G_i + i\omega)(G_j + i\omega) - H_i H_j|^2. \quad (\text{A.24})$$

assuming $S_{Y_1 Y_2}^{\text{in}} = \frac{i}{2} + \bar{S}_{Y_i Y_j}$ and $S_{Y_2 Y_1}^{\text{in}} = -\frac{i}{2} + \bar{S}_{Y_i Y_j}$. The $\frac{i}{2}$ terms come from the fundamental quantum fluctuation and result in a $\pm \kappa_{\text{ex}} \kappa_0 H_i \omega$ term of the probe field, which cancels each other in symmetrized detection.

One thing to notice is that the vacuum field contribution S_Y^b that comes from cavity internal loss differs from that of the the input field S_Y^{in} . Optical squeezing results from interference between the cavity field and the vacuum input at the cavity coupling port. Therefore, vacuum contribution from the loss channel will not contribute to squeezing due to the absence of field interference.

The quadrature variance at different pump power is plotted in Fig. A.5, when other classical noise sources are not considered.

In Appendix B.10, we discuss in detail how classical noise, including thermorefractive and laser noise, affects the observation of squeezing. We show the simulated spectrum in Fig. A.6, considering all the classical noise sources and the homodyne response, showing that the Kerr nonlinearity with the presence of classical noise sources can still generate squeezing near the cavity bandwidth frequency.

A.3 Absorption-induced dissipative feedback

Having understood how classical system noises influence the generation of optical squeezing, we analyze the dissipative dynamics in the system dominated by the optical absorption-induced dissipative feedback, a nonlinearity that we measured to be as strong as Kerr nonlinearity. The understanding of this mechanism, as well as its interplay with the Kerr nonlinearity, is essential for quantifying the feasibility of observing optical squeezing.

A.3 Absorption-induced dissipative feedback

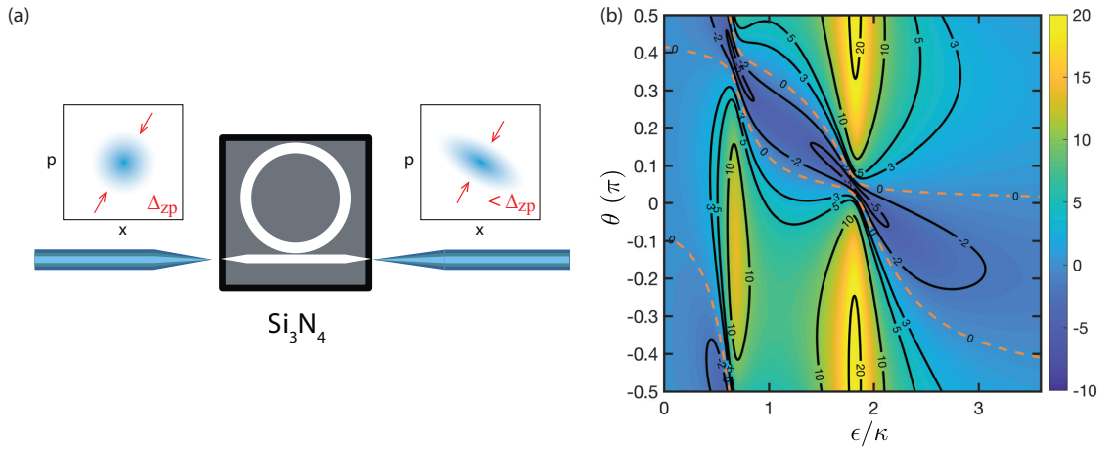


Figure A.5: **(a)** Concept of generating squeezed light using Kerr nonlinearity in chip-based Si₃N₄ ring resonators. **(b)** Simulated quadrature variances in dB scale (shot noise 0dB), as a function of quadrature angles and nonlinear cavity shift $\epsilon = g\alpha^2$. The laser is initially detuned by $\Delta = -2\kappa$.

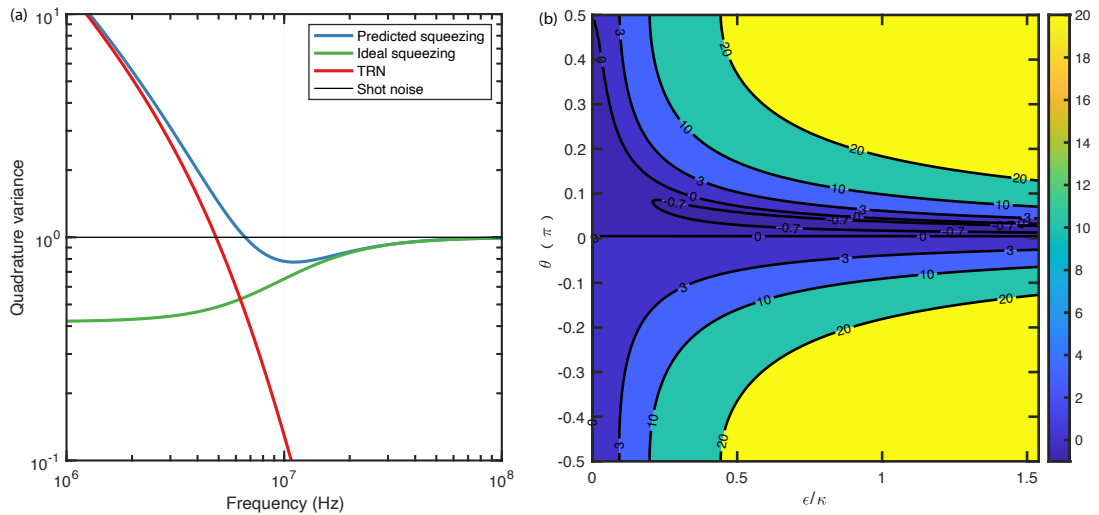


Figure A.6: **(a)** Simulated Kerr squeezing spectrum taking cavity frequency noise (TRN), laser phase and amplitude noise, and homodyne response into account, showing squeezing near the cavity bandwidth edge. The ring resonator has a FSR of 40 GHz, with a quality factor of 27×10^6 , and is pumped at the shifted cavity resonance. **(b)** 2D map of the quadrature variance at 10-MHz Fourier frequency offset.

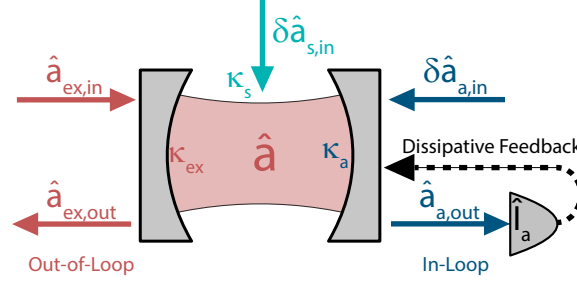


Figure A.7: **Scheme for dissipative feedback in an optical cavity.** The intracavity field \hat{a} is coupled to several different reservoirs, i.e. the laser input \hat{a}_{in} , the vacuum noise from the intrinsic optical loss $\delta \hat{a}_0$ and the dissipative absorption $\delta \hat{a}_a$. The in-loop measurement of absorption field $\delta \hat{a}_a$, results in the absorption flux \hat{I}_a , which is fed back to the optical cavity (black dashed curve). The out-of-loop measurement of \hat{a}_{out} is accessible to observers for coherent and incoherent spectroscopy.

Photothermal cavity frequency shift

When a cavity is pumped by laser light, the optical absorption provides a similar nonlinearity as the Kerr frequency shift and even shares the same scaling to optical power. In most integrated photonics platforms [3, 4, 5], even with state-of-the-art devices, photothermal nonlinearity is on the same order of magnitude as the Kerr nonlinearity and is typically larger. Therefore, it has been speculated that absorption-induced thermal nonlinearity can also serve as a resource in squeezing generation.

Our theoretical analysis shows that thermal nonlinearity alone can not produce optical squeezing, but it could help enhance the Kerr squeezing in some frequency bands when coexisting with Kerr nonlinearity. In this section, we derive the formalism of absorption-induced dissipative feedback to analyze these effects quantitatively.

First, we need to understand the absorption phenomenon conceptually. One could imagine a point defect on the ring resonator, which absorbs a small portion η of light for each round trip. We model it as a beam splitter. If we denote the cavity mode as a , the second input vacuum port mode as b , the absorption field as b' , and the remaining cavity field as a' , then we will have

$$a' = \sqrt{1-\eta}a + i\sqrt{\eta}b \quad (\text{A.25})$$

$$b' = i\sqrt{\eta}a + \sqrt{1-\eta}b. \quad (\text{A.26})$$

Therefore, we can write the update function of the cavity field as

$$\frac{d}{dt}a = \nu_{\text{FSR}} \cdot [(\sqrt{1-\eta} - 1)a + i\sqrt{\eta}b] = -\nu_{\text{FSR}} \cdot \frac{\eta}{2}a + \nu_{\text{FSR}} \cdot i\sqrt{\eta}b. \quad (\text{A.27})$$

With this expression, we can identify that $-\nu_{\text{FSR}} \cdot \frac{\eta}{2} = -\frac{\kappa_{\text{abs}}}{2}$, and $\nu_{\text{FSR}} \cdot i\sqrt{\eta}b = \sqrt{\kappa_{\text{abs}}}b_{\text{in}}$, using

A.3 Absorption-induced dissipative feedback

the following relations: $\eta = \frac{\kappa_{\text{abs}}}{\nu_{\text{FSR}}}$ and $b = -\frac{i}{\sqrt{\nu_{\text{FSR}}}}b_{\text{in}}$. These correspondences can be mapped precisely to a Langevin equation that introduces the absorption as an additional loss channel.

The absorption-induced cavity frequency shift $\Delta_{\text{th}}(t)$ can be expressed as a function of the absorbed light intensity operator $b'^{\dagger}b'$ as

$$\Delta_{\text{th}} = g * \nu_{\text{FSR}} \cdot b'^{\dagger}b' = g * [\kappa_{\text{abs}}a^{\dagger}a + (\nu_{\text{FSR}} - \kappa_{\text{abs}})b^{\dagger}b + i\sqrt{\kappa_{\text{abs}}(\nu_{\text{FSR}} - \kappa_{\text{abs}})}(ab^{\dagger} - a^{\dagger}b)]. \quad (\text{A.28})$$

Here, $*$ represents the convolution operation, and $g(t)$ is the cavity frequency response to a single photon absorption. Note that the cavity frequency detuning is a classical observable, but we treat it as a quantum operator in the equation above. The details of the validity of this treatment are discussed in Appendix B.7. The fluctuation of the cavity frequency shift can be further simplified to

$$\begin{aligned} \delta\Delta_{\text{th}} &= g * [\kappa_{\text{abs}}(\alpha\delta a^{\dagger} + \alpha^* \delta a) + i\sqrt{\kappa_{\text{abs}}(\nu_{\text{FSR}} - \kappa_{\text{abs}})}(\alpha\delta b^{\dagger} - \alpha^* \delta b)] \\ &= g * [\kappa_{\text{abs}}(\alpha\delta a^{\dagger} + \alpha^* \delta a) - \sqrt{\kappa_{\text{abs}}}(\alpha\delta b_{\text{in}}^{\dagger} + \alpha^* \delta b_{\text{in}})] \end{aligned} \quad (\text{A.29})$$

Compared to the Kerr frequency shift $\Delta = g a^{\dagger}a$, we can easily identify an equivalent thermal coefficient $g_{\text{th}} = g\kappa_{\text{abs}}$. With this new definition, we can rewrite the thermal frequency shift as

$$\bar{\Delta}_{\text{th}} = g_{\text{th}}|\alpha|^2 \quad (\text{A.30})$$

$$\delta\Delta_{\text{th}} = g_{\text{th}} * [(\alpha\delta a^{\dagger} + \alpha^* \delta a) - \frac{1}{\sqrt{\kappa_{\text{abs}}}}(\alpha\delta b_{\text{in}}^{\dagger} + \alpha^* \delta b_{\text{in}})]. \quad (\text{A.31})$$

With these results, we can write down the linearized QLE for the cavity field a in the presence of an absorption channel b_{in} ,

$$\begin{aligned} \frac{d}{dt}a &= [-\kappa/2 - i[(2g + g_{\text{th}} + g_{\text{th}}^*)|\alpha|^2 - \Delta]]a - i(g + g_{\text{th}}^*)\alpha^2 a^{\dagger} \\ &+ i\frac{g_{\text{th}}}{\sqrt{\kappa_{\text{abs}}}} * (\alpha^2 \delta b_{\text{in}}^{\dagger} + |\alpha|^2 \delta b_{\text{in}}) + \sqrt{\kappa_c}a_{\text{in}} + \sqrt{\kappa_0}b_0 + \sqrt{\kappa_{\text{abs}}}b_{\text{in}} + i\alpha\delta\Delta_{\text{TRN}}. \end{aligned} \quad (\text{A.32})$$

Here, the $*$ represents the convolution operations again, and we neglect δ of the field fluctuation operator δa .

There is actually an easier way to derive this QLE. We can treat the absorption as another input-output port for the cavity with rate κ_{abs} . The absorption traveling field operator can be easily written as

$$b'_{\text{abs}} = b_{\text{in}} - \sqrt{\kappa_{\text{abs}}}a. \quad (\text{A.33})$$

With this relation, there is no need to introduce mode b as was done in Eq.(A.25).

Back to the thermal response $g_{\text{th}}(t)$ of the cavity, here we discuss a simplified modeling of this function. The general modeling and simulation of this response function are discussed in Section A.3.2. We assume the effective temperature T of the optical mode obeys a first-order

Appendix A. Dissipative dynamics in photonic integrated circuits

diffusion equation with a linear damping with rate γ_{th} ,

$$\Delta \dot{T}(t) = -\gamma_{\text{th}} T(t) + g_1 b'^{\dagger} b' \quad (\text{A.34})$$

$$\Delta T(t) = \int_{-\infty}^t g_1 e^{-\gamma_{\text{th}}(t-s)} b'^{\dagger}(s) b'(s) ds \quad (\text{A.35})$$

$$\delta \Delta_{\text{th}}(t) = g_2 \delta \Delta T(t) = \int_{-\infty}^t g_1 g_2 e^{-\gamma_{\text{th}}(t-s)} (\beta \delta b'^{\dagger}(s) + \beta^* \delta b'(s)) ds \quad (\text{A.36})$$

$$= g_{\text{th}} * [(\alpha \delta a^{\dagger} + \alpha^* \delta a) - \frac{1}{\sqrt{\kappa_{\text{abs}}}} (\alpha \delta b_{\text{in}}^{\dagger} + \alpha^* \delta b_{\text{in}})], \quad (\text{A.37})$$

where $g_{\text{th}}(t) = g_1 g_2 e^{-\gamma_{\text{th}} t}$. Note that here, it is an oversimplification of the cavity response. Using a VNA, we can directly measure this response in the experiment and retrieve $g_{\text{th}}(\omega)$ in the frequency domain. In the following, we assume a general $g_{\text{th}}(\omega)$.

Next, we take the FT of Eq.(A.3) and solve the QLE in the frequency domain,

$$\begin{aligned} a(\omega) &= \left(-i[g + g_{\text{th}}(\omega)]\alpha^2 a^{\dagger} + i \frac{g_{\text{th}}(\omega)}{\sqrt{\kappa_{\text{abs}}}} (\alpha^2 \delta b_{\text{in}}^{\dagger} + |\alpha|^2 \delta b_{\text{in}}) + \sqrt{\kappa_c} a_{\text{in}} + \sqrt{\kappa_0} b_0 + \sqrt{\kappa_{\text{abs}}} b_{\text{in}} \right. \\ &\quad \left. + i\alpha \delta \Delta_{\text{TRN}}(\omega) \right) / (i(\omega + [(2g + g_{\text{th}} + g_{\text{th}}(\omega))|\alpha^2| - \Delta]) + \kappa/2) \\ &= \Theta_a(\omega) a^{\dagger} + \Theta_{b_{\text{in}}^{\dagger}}(\omega) b_{\text{in}}^{\dagger} + \Theta_{b_{\text{in}}}(\omega) b_{\text{in}} + \Theta_{a_{\text{in}}}(\omega) a_{\text{in}} + \Theta_{b_0}(\omega) b_0 + \Theta_{\Delta}(\omega) \delta \Delta_{\text{TRN}} \\ &= \chi_{b_{\text{in}}}(\omega) b_{\text{in}} + \chi_{b_{\text{in}}^{\dagger}}(\omega) b_{\text{in}}^{\dagger} + \chi_{a_{\text{in}}}(\omega) a_{\text{in}} + \chi_{a_{\text{in}}^{\dagger}}(\omega) a_{\text{in}}^{\dagger} \\ &\quad + \chi_{b_0}(\omega) b_0 + \chi_{b_0^{\dagger}}(\omega) b_0^{\dagger} + \chi_{\Delta}(\omega) \delta \Delta_{\text{TRN}} \end{aligned} \quad (\text{A.38})$$

where we defined the following susceptibilities

$$\chi_i(\omega) = \frac{\Theta_i(\omega)}{1 - \Theta_a(\omega) \Theta_a^*(-\omega)}, \quad i = a_{\text{in}}, b_0 \quad (\text{A.39})$$

$$\chi_j(\omega) = \frac{\Theta_a(\omega) \Theta_{j^{\dagger}}^*(-\omega)}{1 - \Theta_a(\omega) \Theta_a^*(-\omega)}, \quad j = a_{\text{in}}^{\dagger}, b_0^{\dagger} \quad (\text{A.40})$$

$$\chi_k(\omega) = \frac{\Theta_k(\omega) + \Theta_a(\omega) \Theta_{k^{\dagger}}^*(-\omega)}{1 - \Theta_a(\omega) \Theta_a^*(-\omega)}, \quad k = b_{\text{in}}, b_{\text{in}}^{\dagger}, \delta \Delta_{\text{TRN}}. \quad (\text{A.41})$$

By a simple examination of Eq. A.38, the introduction of photothermal effect modifies all of the susceptibilities, but especially Θ_a , $\Theta_{b_{\text{in}}^{\dagger}}$, and $\Theta_{b_{\text{in}}}$. It is tough to analyze the final effect of photothermal frequency shift directly; thus, we resort to numerical simulation first. Conceptually, introducing the photothermal effect results in an intra-cavity dissipative feedback loop, illustrated in Fig. A.7, and modifies the noise properties inside the cavity.

However, as our measurement is on the cavity output field, we proceed to calculate both the in-loop absorption field signal and the out-of-loop cavity output field signal by

$$a_{\text{out}} = a_{\text{in}} - \sqrt{\kappa_c} a \quad (\text{A.42})$$

$$b_{\text{out}} = b_{\text{in}} - \sqrt{\kappa_{\text{abs}}} a. \quad (\text{A.43})$$

A.3 Absorption-induced dissipative feedback

Based on which signal s_{out} ($s = a, b$) we want to analyze, we need to update all the previously defined susceptibility by $\chi_i(\omega) \leftarrow \delta_{i, s_{\text{in}}} - \sqrt{\kappa_c / \text{abs}} \chi_i(\omega)$.

When looking at a specific quadrature angle $X_\theta = \frac{s_{\text{out}} e^{-i\theta} + s_{\text{out}}^\dagger e^{i\theta}}{\sqrt{2}}$, we have the following expressions

$$s_{\text{out}}(\omega) = \chi_{b_{\text{in}}}(\omega) b_{\text{in}} + \chi_{b_{\text{in}}^\dagger}(\omega) b_{\text{in}}^\dagger + \chi_{a_{\text{in}}}(\omega) a_{\text{in}} + \chi_{a_{\text{in}}^\dagger}(\omega) a_{\text{in}}^\dagger + \chi_{b_0}(\omega) b_0 + \chi_{b_0^\dagger}(\omega) b_0^\dagger + \chi_\Delta(\omega) \delta \Delta_{\text{TRN}} \quad (\text{A.44})$$

$$\begin{aligned} X_\theta(\omega) &= \frac{1}{2} \sum_{i=a_{\text{in}}, b_{\text{in}}, b_0} \left[(\chi_i(\omega) + \chi_{i^\dagger}(\omega)) e^{-i\theta} + (\chi_{i^\dagger}^*(-\omega) + \chi_i^*(-\omega)) e^{i\theta} \right] q^i \\ &\quad + \frac{i}{2} \sum_{i=a_{\text{in}}, b_{\text{in}}, b_0} \left[(\chi_i(\omega) - \chi_{i^\dagger}(\omega)) e^{-i\theta} + (\chi_{i^\dagger}^*(-\omega) - \chi_i^*(-\omega)) e^{i\theta} \right] p^i \\ &\quad + (\chi_\Delta(\omega) e^{-i\theta} + \chi_\Delta^*(-\omega) e^{i\theta}) \delta \Delta_{\text{TRN}} \quad (\text{A.45}) \\ &= \frac{1}{2} \sum_{i=a_{\text{in}}, b_{\text{in}}, b_0} [\chi_{q^i} q^i + i \chi_{p^i} p^i] + \frac{1}{\sqrt{2}} (\chi_\Delta(\omega) e^{-i\theta} + \chi_\Delta^*(-\omega) e^{i\theta}) \delta \Delta_{\text{TRN}}. \end{aligned}$$

We need to pay special attention again to the definition of quadrature phases when the laser is detuned. It does not impose a problem when the laser is on resonance. We can proceed to calculate the power spectral density as

$$\begin{aligned} S_{X_\theta(\omega)} &= \frac{1}{4} \sum_{i=a_{\text{in}}, b_{\text{in}}, b_0} [|\chi_{q^i}|^2 S_{q^i} + |\chi_{p^i}|^2 S_{p^i} + 2\text{Re} [i \chi_{p^i} \chi_{q^i}^* S_{q^i p^i}]] \\ &\quad + \frac{1}{2} |\chi_\Delta(\omega) e^{-i\theta} + \chi_\Delta^*(-\omega) e^{i\theta}|^2 S_{\text{TRN}}. \quad (\text{A.46}) \end{aligned}$$

If we proceed with the derivation by removing classical laser noises, Kerr nonlinearity, and keeping only the photothermal term and the cavity TRN, with the help of Mathematica, there is a simplified expression for the cavity output field when the laser is on resonance,

$$S_{X_\theta(\omega)} = \frac{1}{2} + \frac{2|\alpha|^2 \kappa_c \sin^2 \theta}{(\omega^2 + \frac{\kappa_c^2}{4})} \left(S_{\text{TRN}} + \frac{|g_{\text{th}}(\omega)|^2 |\alpha|^2}{\kappa_{\text{abs}}} \right). \quad (\text{A.47})$$

which is an incoherent summation of the fundamental thermal noise of the cavity (TRN) and the laser-driven photothermal frequency noise proportional to the laser power.

We plotted the simulated spectrum of the cavity output field and the absorbed field in Fig.A.8(a) with only the photothermal effect, and in Fig.A.8(b) with both the photothermal and Kerr effect. The in-loop absorbed field is efficiently squeezed with the photothermal effect. Squeezing is completely absent for the out-of-loop cavity output field when only the photothermal effect is present. When the Kerr effect is present, the squeezing is present but is limited to the high-frequency band. In the next section, we detail the effect of the coexistence of Kerr and photothermal nonlinearity and how thermal nonlinearity can help improve the Kerr squeezing.

Appendix A. Dissipative dynamics in photonic integrated circuits

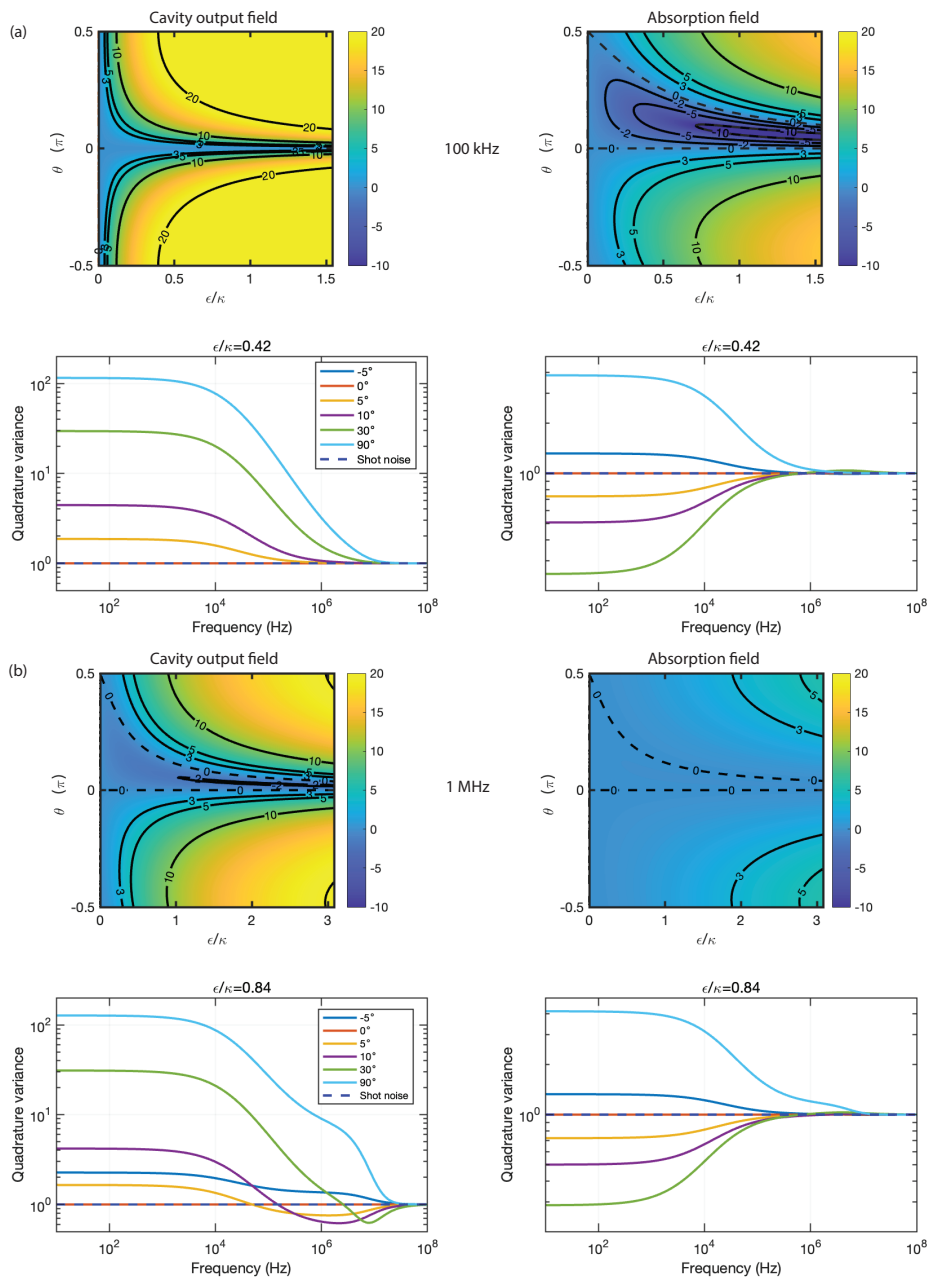


Figure A.8: Spectra of the cavity output field and the absorption field when considering **(a)** only the photothermal effect, and **(b)** both the photothermal and Kerr nonlinearity. The absorption field generally exhibits in-loop squeezing, whereas the cavity output field only shows squeezing with the Kerr effect. The 2D plots are evaluated at Fourier frequency of 100 kHz for **(a)** and 1 MHz for **(b)**.

A.3.1 Absorption enhanced Kerr squeezing

In this section, we consider first only the photothermal effect and later also the Kerr effect. To illustrate the physical effects cleanly, we neglect classical noise sources such as TRN and laser noise. In this simplified setting, we aim to analytically derive the effect of photothermal feedback, showcasing that dissipative feedback can sometimes be useful.

As we discussed in the previous section, we consider again an optical cavity coupled to the input field $\hat{a}_{\text{ex,in}} = (\bar{a}_{\text{in}} + \delta a_{\text{in}})$ at a rate of κ_{ex} , the internal scattering field $\delta \hat{a}_{\text{s,in}}$ at a rate of κ_{s} , and the absorption field $\delta \hat{a}_{\text{a,in}}$ at a rate of κ_{a} . Considering the photon absorption-induced temperature change δT , we have

$$\dot{\hat{a}} = [i(\Delta - \Delta_{\text{th}}) - \frac{\kappa}{2}] \hat{a} + \sqrt{\kappa_{\text{ex}}} \hat{a}_{\text{ex,in}} + \sqrt{\kappa_{\text{s}}} \delta \hat{a}_{\text{s,in}} + \sqrt{\kappa_{\text{a}}} \delta \hat{a}_{\text{a,in}} \quad (\text{A.48})$$

with $\Delta = \omega_L - \omega_c$, and $\Delta_{\text{th}} = g_2 \delta T$ the cavity frequency shift via optical absorption induced temperature change δT with coefficient g_2 .

The input-output relation of the absorption field is,

$$\hat{a}_{\text{a,out}} = \delta \hat{a}_{\text{a,in}} - \sqrt{\kappa_{\text{a}}} \hat{a}, \quad (\text{A.49})$$

with corresponding absorbed photon flux,

$$\hat{I}_{\text{a}} = \hat{a}_{\text{a,out}}^\dagger \hat{a}_{\text{a,out}}. \quad (\text{A.50})$$

The absorption photon flux is composed of two terms, i.e., a DC term $\bar{I}_{\text{a}} = \kappa_{\text{a}} |\bar{a}|^2$, and a fluctuating term,

$$\delta \hat{I}_{\text{a}} = \kappa_{\text{a}} (\bar{a} \delta \hat{a}^\dagger + \bar{a}^* \delta \hat{a}) - \sqrt{\kappa_{\text{a}}} (\bar{a}^* \delta \hat{a}_{\text{a,in}} + \delta \hat{a}_{\text{a,in}}^\dagger \bar{a}). \quad (\text{A.51})$$

The dynamics of the temperature change due to the optical absorption is simplified by the following diffusion equation, $\delta \dot{T}(t) = -\gamma_{\text{th}} \delta T(t) + g_1 \hat{I}_{\text{a}}$, where $g_1 \hat{I}_{\text{a}}$ is the rate of the temperature change due to the optical absorption, and γ_{th} is the thermal decay rate. The macroscopic apparatus, i.e., δT , is not a quantum operator. Our treatment here is similar to that of the measurement-based feedback of mechanical oscillator in Section B.7, that a quantum description is identical to that of a proper symmetrized formalism. The QLE of the linearized optical field fluctuations can be obtained in the frequency domain,

$$\delta \hat{a} = \chi_{\text{c},0}(\omega) \left(\sigma_d(\omega) \kappa_d (\delta \hat{a} + \delta \hat{a}^\dagger) + \sqrt{\kappa_{\text{a}}} \delta \hat{a}_d + \sqrt{\kappa_{\text{ex}}} \delta \hat{a}_{\text{ex,in}} + \sqrt{\kappa_{\text{s}}} \delta \hat{a}_{\text{s,in}} \right), \quad (\text{A.52})$$

with the intrinsic optical susceptibility,

$$\chi_{\text{c},0}(\omega) = \frac{1}{\kappa/2 - i(\omega + \bar{\Delta})}, \quad (\text{A.53})$$

and $\bar{\Delta} = \Delta - g_1 g_2 \kappa_{\text{a}} \bar{n}_c / \gamma_{\text{th}}$, incorporating the additional static cavity frequency shift. As we

Appendix A. Dissipative dynamics in photonic integrated circuits

defined in the previous section, in the following, we use $g_{\text{th}}(\omega) = g_1 g_2 / (-i\omega + \gamma_{\text{th}})$ to represent a general thermal response of the structure whenever possible. The mean intracavity photon number here is $\bar{n}_c = |\bar{a}|^2 = \kappa_{\text{ex}} |\bar{a}_{\text{in}}|^2 / (\kappa^2/4 + \bar{\Delta}^2)$. We note that the intracavity field is now coupled to an effective dissipative reservoir,

$$\delta \hat{a}_d = (1 - \sigma_d(\omega)) \delta \hat{a}_{\text{a,in}} - \sigma_d(\omega) \delta \hat{a}_{\text{a,in}}^\dagger, \quad (\text{A.54})$$

where we introduce a unitless photon number enhanced dissipation coefficient,

$$\sigma_d(\omega) = -i g_{\text{th}}(\omega) \bar{n}_c, \quad (\text{A.55})$$

with $\sigma_d^*(-\omega) = -\sigma_d(\omega)$. A constant single photon dissipation coefficient is given by $\sigma_0(\omega) = \sigma_d(\omega) / \bar{n}_c$.

Novel dynamics arise in the cavity field (cf. Eq. A.52), which can be interpreted as a closed-loop dissipative feedback to the optical cavity as shown in Fig. A.7. The photon absorption manifests as an in-loop photodetection, resulting in a feedback path to the optical cavity, i.e., by changing the cavity frequency via photothermal effects. The noise spectral density of the in-loop photon flux fluctuation δI_a , when normalized to shot noise, is given by

$$S_{\delta I_a}(\omega) = |1 - \chi_{\text{fb}}(\omega)|^{-2}, \quad (\text{A.56})$$

where

$$\chi_{\text{fb}}(\omega) = \sigma_d(\omega) \kappa_a (\chi_{\text{c},0}(\omega) - \chi_{\text{c},0}^*(-\omega)). \quad (\text{A.57})$$

The dissipative feedback results in a squashed or anti-squashed in-loop optical field. We can obtain the *modified optical susceptibility*

$$\chi_{\text{c,eff}}(\omega) = \chi_{\text{c},0}(\omega) / (1 - \chi_{\text{fb}}(\omega)). \quad (\text{A.58})$$

In the case of $\bar{\Delta} \ll -\kappa$, the PSD of the in-loop photon flux at $\omega \sim |\bar{\Delta}|$ is,

$$S_{\delta I_a}(\omega) \simeq \left| 1 + \frac{2\bar{n}_c \kappa_a}{\text{Im}[g_{\text{th}}(\omega)^{-1}] \kappa} \right|^{-2}, \quad (\text{A.59})$$

and the effective optical susceptibility can be further simplified,

$$\chi_{\text{c,eff}}(\omega) = \frac{1}{\kappa_{\text{eff}}/2 - i(\bar{\Delta}_{\text{eff}} + \omega)}, \quad (\text{A.60})$$

with a modified effective cavity linewidth

$$\kappa_{\text{eff}} = \kappa - 2\kappa_a \text{Re}(\sigma_d(\omega)), \quad (\text{A.61})$$

and a modified effective detuning

$$\bar{\Delta}_{\text{eff}} = \bar{\Delta} + \kappa_a \text{Im}(\sigma_d(\omega)), \quad (\text{A.62})$$

where $\bar{\Delta} = \Delta - \bar{n}_c \kappa_a g_{\text{th}}(0)$. Due to the squashed or anti-squashed absorbed photon fluctuations, the dissipative feedback leads to modified cavity susceptibility for the input probing field. In practice, the photothermal coefficient g_2 can have different signs at room and cryogenic temperatures for different materials, e.g., silicon. For $g_2 < 0$, we have $\kappa_{\text{eff}} > \kappa$ and $\bar{\Delta}_{\text{eff}} > \bar{\Delta}$; while for $g_2 > 0$, we have $\kappa_{\text{eff}} < \kappa$ and $\bar{\Delta}_{\text{eff}} < \bar{\Delta}$.

As shown in Eq. A.52, the intracavity field is coupled to an effective dissipative reservoir $\delta \hat{a}_d$. Different from the vacuum noise, the noise operator for the dissipative reservoir $\delta \hat{a}_d$ satisfies the following correlations,

$$\begin{aligned} \langle \delta \hat{a}_d^\dagger(\omega) \delta \hat{a}_d(\omega') \rangle &= -\sigma_d(\omega) \sigma_d(\omega') \delta(\omega + \omega') 2\pi \\ \langle \delta \hat{a}_d(\omega) \delta \hat{a}_d^\dagger(\omega') \rangle &= (1 - \sigma_d(\omega))(1 + \sigma_d(\omega')) \delta(\omega + \omega') 2\pi, \end{aligned} \quad (\text{A.63})$$

which may result in incoherent excess noise and noise correlation for the intracavity field.

Here, we see that dissipative feedback modifies both the cavity response and the bath noise. These effects have been observed in optomechanical systems using microresonators [2, 330], and manifest as a Kerr-type nonlinearity, where the cavity frequency shift is proportional to the intracavity photon number. Kerr medium has been suggested as a quantum non-demolition (QND) device in a feedback loop to generate optical squeezing [331, 332]. In such QND feedback, the intensity of the in-loop optical field is measured and feedback to the phase. The dissipative feedback is fundamentally different from a QND feedback, e.g., Kerr squeezing [331, 332], as excess noise always arises in the out-of-loop field we detect due to uncorrelated noise from the in-loop field $\hat{a}_{\text{a,in}}$, i.e., photon absorption.

In the following, we consider a cavity with coexisting dissipative feedback via photothermal effects and Kerr nonlinearity to explore the interplay between them. We can obtain the quantum Langevin equations of the field fluctuation in the frequency domain again,

$$\delta \hat{a} = \chi_{c,0}(\omega) \left((\bar{n}_c \sigma_0(\omega) \kappa_a - i \bar{n}_c g_{\text{Kerr}}) (\delta \hat{a} + \delta \hat{a}^\dagger) + \sqrt{\kappa_a} \delta \hat{a}_d + \sqrt{\kappa_{\text{ex}}} \delta \hat{a}_{\text{ex,in}} + \sqrt{\kappa_s} \delta \hat{a}_{\text{s,in}} \right) \quad (\text{A.64})$$

where g_{Kerr} is the single photon nonlinear Kerr coupling rate [333] and $\chi_{c,0}(\omega)$ is given by Eq. A.53 with $\bar{\Delta} = \Delta - (\kappa_a g_{\text{th}}(0) + g_{\text{Kerr}}) \bar{n}_c$. We are concerned with the symmetrized PSD of the out-of-loop field quadrature, $\hat{X}_\theta = \delta \hat{a}_{\text{ex,out}} e^{-i\theta} + \delta \hat{a}_{\text{ex,out}}^\dagger e^{i\theta}$. We focus on the simple case where the laser detuning $\bar{\Delta} = 0$. For Kerr squeezing, i.e. $g_{\text{th}} = 0$, the PSD takes the form,

$$S_{\text{I,Kerr}}(\omega) = 1 - \frac{16 \bar{n}_c \eta_c \kappa \sin(\theta) g_{\text{Kerr}} \left((\kappa^2 + 4\omega^2) \cos(\theta) - 4 \bar{n}_c \kappa \sin(\theta) g_{\text{Kerr}} \right)}{(\kappa^2 + 4\omega^2)^2}. \quad (\text{A.65})$$

where we assume an ideal detection and $\eta_c = \kappa_{\text{ex}}/\kappa$. As expected, Kerr squeezing results in an output field with minimum variance below the vacuum noise at an optimal angle.

Appendix A. Dissipative dynamics in photonic integrated circuits

In contrast, for dissipative dynamics only, i.e., $g_{\text{Kerr}} = 0$, as we derived before in the previous section, the PSD takes the form, $S_{I,a}(\omega) = 1 + S_{I,a}^{\text{ex}}(\omega)$, where the incoherent optical absorption always results in excess noise, i.e., the photothermal noise,

$$S_{I,a}^{\text{ex}}(\omega) = \frac{16\bar{n}_c\kappa_a\kappa_{\text{ex}}\sin^2(\theta)^2|g_{\text{th}}(\omega)|^2}{(\kappa^2 + 4\omega^2)} \geq 0. \quad (\text{A.66})$$

We note that this coincides with earlier experimental and theoretical works in optical systems with intensity feedback, where in-loop photocurrent can be squashed while the out-of-loop photocurrent always becomes anti-squashed [334, 335, 336]. Kerr nonlinearity, on the other hand, demonstrates a QND detection of the in-loop optical field, which enables the Kerr squeezing in the out-of-loop field, as expected [331, 332].

When Kerr nonlinearity and dissipative dynamics coexist, the total PSD is given by $S_I(\omega) = S_{I,\text{Kerr}}(\omega) + S_{I,\text{tot}}^{\text{ex}}(\omega)$, with total excess noise $S_{I,\text{tot}}^{\text{ex}}(\omega) = S_{I,a}^{\text{ex}}(\omega) + S_{I,c}^{\text{ex}}(\omega)$ due to the dissipative dynamics. The coherent dissipative dynamics result in an interference with the Kerr effect

$$S_{I,c}^{\text{ex}}(\omega) = \frac{64\bar{n}_c^2\kappa_a\kappa_{\text{ex}}\sin^2(\theta)}{(\kappa^2 + 4\omega^2)} \text{Re} \left[\frac{g_{\text{th}}(\omega)g_{\text{Kerr}}^*}{\kappa - 2i\omega} \right]. \quad (\text{A.67})$$

We note that when $|g_{\text{th}}(\omega)|^2 + 4\text{Re}[g_{\text{th}}(\omega)g_{\text{Kerr}}^*/(\kappa - 2i\omega)] < 0$, the total excess noise $S_{I,\text{tot}}^{\text{ex}} < 0$, which opens an interesting regime for dissipation improved Kerr squeezing. Such a regime is independent of the intracavity photon number and the squeezing angle.

In Fig. A.9(a), we show the theoretical curves of estimated Kerr squeezing in a state-of-art Si_3N_4 micro-ring resonators at optimal squeezing angles with realistic parameters [3]. Kerr nonlinearity in such micro-ring resonator can lead to frequency comb and dissipative soliton generation at low pumping powers (\sim mW) [337], due to the extremely low optical loss ($\kappa/2\pi < 20\text{MHz}$). The red curve includes only Kerr nonlinearity, while the green curve considers both the Kerr nonlinearity and the photothermal dynamics without other classical noise sources such as TRN. As shown in Fig. A.9(a), the green curve exhibits excess noise at low frequencies due to the incoherent dissipative dynamics while showing slight improvement of Kerr squeezing at frequencies between 2MHz \sim 10MHz due to the coherent interference between the dissipative dynamics and Kerr nonlinearity, in a very similar way of photothermal mechanical instability discussed in Section 2.5. In practice, the Kerr squeezing is limited by the detection efficiency and the thermorefractive noise [1, 311, 338].

A.3.2 Photothermal response simulation

In the earlier sections, we assumed a simplified one-pole thermal response in the theoretical treatment of the temperature dynamics. In practice, the thermal response can be rather complex as dissipative absorption in the microcavities can dissipate via different mechanisms, such as radiation, conduction, and convection.

A.3 Absorption-induced dissipative feedback

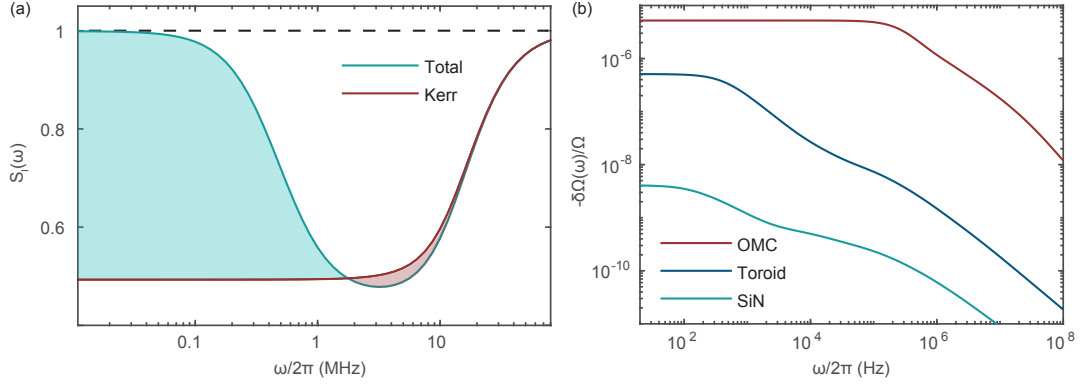


Figure A.9: **(a)** Estimated Kerr squeezing with dissipative dynamics at optimal angles in a Si_3N_4 micro-cavity. The noise spectral density is normalized to the shot noise floor (black dashed line). The red curve corresponds to the case where the dissipative dynamics are absent, while the green curve corresponds to the case where Kerr nonlinearity and dissipative dynamics coexist. The green and red shade areas correspond to the excess noise and improved squeezing due to dissipative feedback. (Parameters: $\kappa/2\pi = 15\text{MHz}$, $\kappa_{\text{ex}}/2\pi = 8\text{MHz}$, $\kappa_a/2\pi = 6\text{MHz}$, $\kappa_s/2\pi = 1\text{MHz}$, $\gamma_{\text{th}}/2\pi = 20\text{kHz}$, $g_1g_2/2\pi = -0.05\text{Hz}$, $g_{\text{Kerr}}/2\pi = -0.5\text{Hz}$, and $\bar{n}_c = 10^7$) **(b)** Simulated cavity frequency response of different micro-cavities from finite element simulations at room temperature, including a silicon OMC [339], silica micro-toroid [340], and SiN ring resonator [3]. The detailed parameters in the FEM simulation are listed in Tab. A.2.

The thermal response can be obtained with finite element methods (FEM) simulations. We first simulate the electric field distribution of the optical mode $\vec{E}(\vec{r})$. The bulk absorption heating

$$P(\vec{r}) = P_{\text{abs}}\epsilon_0\vec{E}(\vec{r}) \times \hat{\epsilon}\vec{E}(\vec{r})/W_E, \quad (\text{A.68})$$

can be added as a heat source in the heat transfer model, with $\hat{\epsilon} = \hat{\epsilon}_0 + \hat{\epsilon}_1$ the permittivity, and $W_E = \int \epsilon_0\vec{E}(\vec{r}) \times \hat{\epsilon}\vec{E}(\vec{r})dV$ the optical mode energy. The frequency component of the temperature distribution $\tilde{T}(\omega, \vec{r})$ can be solved in the Fourier-domain heat equation,

$$i\omega\rho C\tilde{T} + k\Delta\tilde{T} = \tilde{P}, \quad (\text{A.69})$$

where ρ is the density, C the heat capacity, and k the thermal conductivity. The cavity shift frequency takes the form,

$$\frac{\delta\omega_c(\omega)}{\omega_c} = -\frac{1}{W_E} \int \tilde{T}(\omega, \vec{r})\epsilon_0\sqrt{\epsilon(\vec{r})} \frac{dn}{dT}(\vec{r})|\vec{E}(\vec{r})|^2 dV. \quad (\text{A.70})$$

In Fig. A.9(b), we show the cavity frequency responses of three different micro-cavities, i.e., silicon OMC, silica micro-toroid and Si_3N_4 ring resonator, at room temperature with an absorption power $\tilde{P}(\omega) = 1\mu\text{W}$. The cavity frequency responses deviate from the single-pole model that we used earlier. Multiple-pole models are typically required to fit the response [330]. The OMC has a much more significant relative frequency shift at DC than the other two types of cavities due to the small mode volume, resulting in high-frequency poles in the MHz range.

Appendix A. Dissipative dynamics in photonic integrated circuits

Table A.2: **Physical properties used for the FEM simulations of the cavity frequency thermal responses.**

Physical properties	Si ₃ N ₄	Si	SiO ₂
Density ρ (kg m ⁻³)	3290	2329	2203
Refractive index n_0	2.00	3.48	1.50
Thermo-optic dn/dT (10 ⁻⁵ K ⁻¹)	2.45	16.0	1.29
Thermal conductivity k (W m ⁻¹ K ⁻¹)	30	130	1.38
Specific heat capacity C (J kg ⁻¹ K ⁻¹)	800	700	703

Despite the large size of micro-toroids, their thermal bandwidth can be around MHz, e.g., in Ref. [341]. For SiN micro-resonator, the bandwidth is typically in the kHz range, e.g., in Ref. [1]. The relevant material coefficients used in the FEM simulations are shown in Table A.2. In addition to the geometric dependence, the device surroundings sometimes can even have a more significant impact on the cavity frequency thermal response, e.g., gaseous Helium, vacuum or liquid [330, 341].

A.4 Absorption spectroscopy

The framework of the photothermal dissipative feedback we developed can also be useful in some classical applications. In this section, we show that with the framework we developed in Section A.3, we can use the measured cavity nonlinear response function to calibrate the cavity absorption rate κ_{abs} , which was previously hard to retrieve. In Appendix B.11, we also detail the derived fitting function for the measured cavity response in a pump-probe scheme.

We performed this measurement [3] in the Si₃N₄ PIC platform where the nonlinear index n_2 is well known, such that the absorption rate can be easily retrieved. We also developed a measurement technique [4] in the LiNbO₃ (LN) PIC platform where the nonlinear index is not well known, such that absorption rate and the nonlinear index can both be retrieved. We describe the measurement techniques in the following sections and show that this technique offers valuable insights to guide the optimization of PIC fabrication.

A.4.1 Silicon nitride microrings

Quantitative analysis of absorption loss rate

Like in the previous section, we distinguish two loss mechanisms, the intrinsic absorption and scattering losses of our Si₃N₄ waveguides. The optical losses in the telecommunication band have two main contributions: the Rayleigh scattering loss caused mainly by the waveguide sidewall roughness and the absorption loss due to defects, e.g., hydrogen impurities. While the hydrogen absorption loss can be efficiently eliminated via repeated thermal annealing of Si₃N₄ at high temperature $\sim 1200^\circ\text{C}$, efforts on loss reduction have mainly focused on reducing waveguide roughness via optimized dry etching, wet etching, and etchless process. In addition,

A.4 Absorption spectroscopy

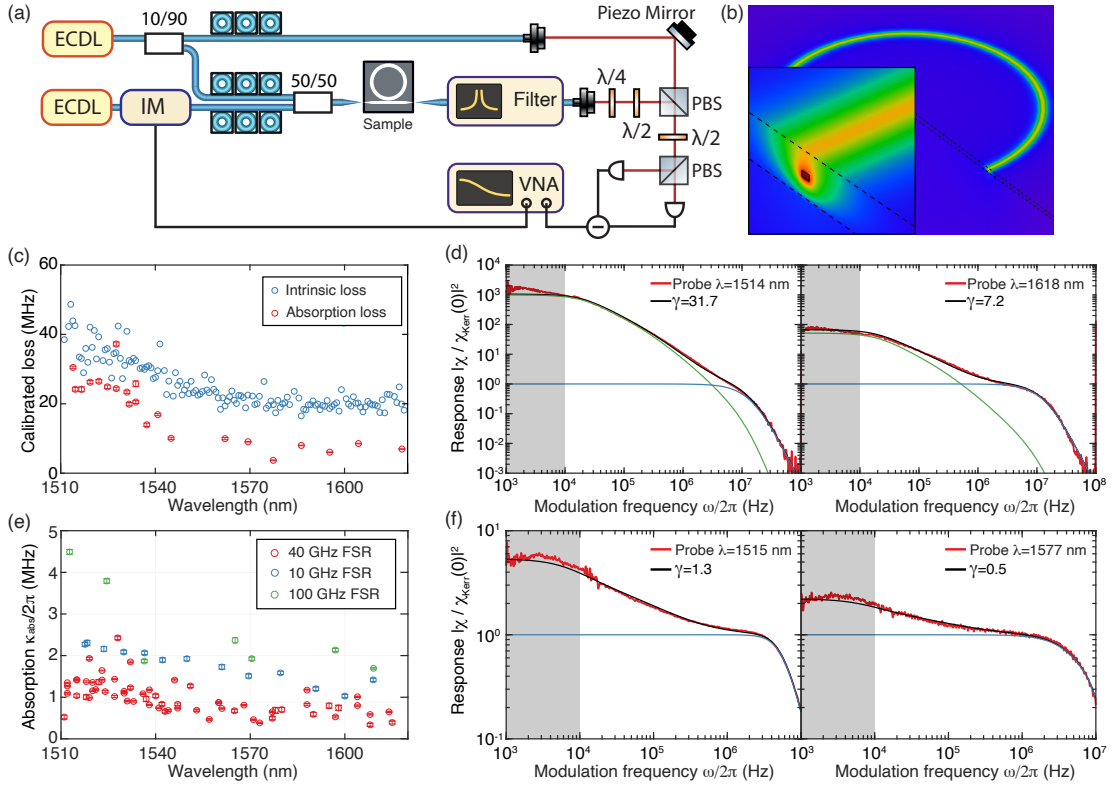


Figure A.10: Probing the absorption loss of Si_3N_4 microresonators via Kerr-nonlinearity-calibrated thermal response measurements. (a) Experiment setup. ECDL: external-cavity diode lasers. IM: intensity modulator. VNA: vector network analyzer. PBS: polarization beam splitter. (b) Thermal simulation of the temperature distribution in the waveguide structures. (c) Comparison of the loss values measured using the response measurement and frequency-comb-assisted diode laser spectroscopy on a partially annealed sample with prominent hydrogen absorption losses. This comparison reveals an approximate, wavelength-independent, 12 MHz loss difference between the two datasets, which is presumed to be due to intrinsic scattering loss. (d) For the two resonances at 1514 nm and 1618 nm shown in (c), the measured (red) and fitted (black) frequency response $\chi(\omega)$ normalized to χ_{Kerr} . The fitted cavity cutoff frequencies are, $\kappa/4\pi = 22.7$ MHz ($\lambda = 1514$ nm), and $\kappa/4\pi = 17.1$ MHz ($\lambda = 1618$). (e) Calibrated absorption loss $\kappa_{\text{abs}}/2\pi$ of different resonances from different samples. (f) For the two resonances at 1515 nm and 1577 nm of the 40-GHz-FSR samples shown in (e), the measured frequency response $\chi(\omega)$ normalized to χ_{Kerr} (red and black). The fitted cavity cutoff frequencies are, $\kappa/4\pi = 7.4$ MHz ($\lambda = 1515$ nm), and $\kappa/4\pi = 10.8$ MHz ($\lambda = 1577$). In (d, f), we show the fitted Kerr (blue) and thermal (green) responses, and the gray areas mark the modulation frequency range from 1 kHz to 10 kHz (the measured response within this range is not included in the response fitting). The fitted values of $\gamma = \frac{\chi_{\text{therm}}(0)}{\chi_{\text{Kerr}}(0)}$ are shown in (d, f). The fitted thermal response $|\frac{\chi_{\text{therm}}(\omega)}{\chi_{\text{Kerr}}(0)}|^2$ is not shown in (f) as it is mostly below 10^{-1} . The error bars in (c, e) account for fitting errors (95% confidence interval).

the large mode area of thin-core Si_3N_4 waveguides results in reduced optical mode interaction

Appendix A. Dissipative dynamics in photonic integrated circuits

with waveguide sidewall roughness, thereby reducing scattering losses.

We perform a modulation response measurement to quantify the photothermal absorption loss of our Si₃N₄ waveguides. The experimental setup is shown in Fig. A.10(a), with two lasers, the pump and the probe. The pump laser is tuned to an optical resonance whose frequency is f_m , and the thermal absorption loss κ_{abs} in this resonance is to be characterized. Meanwhile, the pump laser is intensity-modulated with frequency ω . The probe laser is loosely locked (i.e., low-bandwidth locking) to another optical resonance whose frequency is f'_m .

The principle of the nonlinear microresonator response measurement is to characterize the resonance frequency shift $\delta f_{m'} = \chi(\omega)\delta n_{\text{ph}}$ of the probe mode $f_{m'}$ induced by the intensity modulation δn_{ph} of the pump mode f_m . This intensity modulation changes the resonance frequency of the probe mode $f_{m'}$ via both the Kerr and the photothermal nonlinearities. The frequency response $\delta f_{m'}$ to the pump modulation is transduced into the probe laser's phase modulation, measured using a balanced homodyne detection, with the pump laser being filtered out before detection. The pump power is maintained sufficiently low, such that the steady-state frequency shift of the probe mode is small compared to the resonance linewidth κ , i.e., $\delta f_{m'} \ll \kappa$. In this linear regime, the frequency response to the modulating pump power is given by

$$\chi(\omega) = \frac{\delta f_{m'}}{\delta n_{\text{ph}}} = \chi_{\text{therm}}(\omega) + \chi_{\text{Kerr}}(\omega) \quad (\text{A.71})$$

The total response $\chi(\omega)$ consists of two parts: the Kerr response $\chi_{\text{Kerr}}(\omega)$ with almost infinite bandwidth, and the thermal response $\chi_{\text{therm}}(\omega)$ with a typical bandwidth below 20 kHz. Therefore, by calibrating the response $\chi(\omega)$ as a function of the modulation frequency ω , $\chi_{\text{therm}}(\omega)$ and $\chi_{\text{Kerr}}(\omega)$ can be individually identified by fitting the measurement result. Using the values of $\chi_{\text{therm}}(\omega)$ and $\chi_{\text{Kerr}}(\omega)$ at DC ($\omega = 0$), the absorption rate is calculated as

$$\kappa_{\text{abs}} = \frac{2cn_2}{\overline{n_{\text{eff}}n_g}V_{\text{eff}}}\frac{dP_{\text{abs}}}{dT}\frac{dn_{\text{mat}}}{dT}\frac{\chi_{\text{therm}}(0)}{\chi_{\text{Kerr}}(0)} \quad (\text{A.72})$$

where V_{eff} is the effective optical mode volume, $n_2 = 2.4 \times 10^{-19} \text{m}^2/\text{W}$ is the nonlinear index of Si₃N₄, $\overline{n_{\text{eff}}n_g} = 3.8$ is the mode averaged effective and group index, $n_{\text{mat}} = 2.0$ is the material index and $dn_{\text{mat}}/dT = 2.5 \times 10^{-5}/\text{K}$ is the thermo-optic coefficient, and P_{abs} is the absorbed power.

Finite-element simulations of optical mode profiles and bulk absorption heating (see Figure A.10(b)) are performed to calculate the coefficients V_{eff} and to retrieve the frequency domain thermal response function $\frac{dT}{dP_{\text{abs}}}(\omega)$ used in the fitting. The simulation model we use to extract the thermal response function is validated by our measurement [1] of the thermorefractive noise in these Si₃N₄ devices. Figure A.10(d, f) presents four examples of the measured and the fitted $\chi(\omega)$.

To validate our method, we first benchmark the linear response measurement by characteriz-

ing a partially annealed Si_3N_4 sample whose resonance linewidth data have been published in ref.[306]. We characterize this particular sample using both the response measurement and frequency-comb-assisted diode laser spectroscopy and compare the results using both methods in Fig. A.10(c). Assuming a wavelength-independent scattering loss of 12 MHz, the measured absorption loss using the response measurement agrees with the total loss measured spectroscopically.

Figure A.10(e) shows the calculated absorption rates $\kappa_{\text{abs}}/2\pi$ of different resonances from four 40-GHz-FSR Si_3N_4 samples featuring $Q_0 > 30 \times 10^6$, in comparison with 10-GHz-FSR samples (used in ref.[295], $\kappa_0/2\pi = 8.5$ MHz) and 100-GHz-FSR samples (used in ref.[306], $\kappa_0/2\pi = 13.5$ MHz) fabricated using the same process but from different wafers. All samples show similar trends and present two conclusions. First, the mean absorption loss for 40-GHz-FSR samples is $\kappa_{\text{abs}}/2\pi \sim 1$ MHz, corresponding to an absorption-loss-limited Q factor of approximately 2×10^8 . Therefore, the optical losses of our Si_3N_4 waveguides ($\kappa/2\pi = 6.5$ MHz) are currently dominated by scattering losses. Second, for all the samples studied, $\kappa_{\text{abs}}/2\pi$ is higher around 1520 nm, compared to the value at 1600 nm. This difference is caused by the residual hydrogen impurities in our thermally annealed Si_3N_4 . Note that only standard LPCVD $\text{Si}_3\text{N}_4 / \text{SiO}_2$ films and thermal annealing are used in our fabrication to achieve such low absorption losses.

Thermal simulations

Section A.3.2 discusses the specific steps of simulating a structure's thermal response. We use COMSOL Multiphysics to simulate the thermal response due to bulk absorption heating of our Si_3N_4 waveguides. The leading material property coefficients of interest used in the current simulation are identical to the ones used in ref. [1] for simulating the Si_3N_4 thermorefractive noise. The thermo-optic coefficient of Si_3N_4 , $dn_{\text{mat}}/dT = 2.5 \times 10^{-5} \text{ K}^{-1}$, is used here. We first simulate the waveguide optical mode profile (TE_{00} mode), from which the effective mode volume V_{eff} is calculated. Bulk absorption heating is introduced, whose power distribution is proportional to the intensity distribution of the optical mode v_m . By solving the frequency-domain heat transfer equation, the response of the effective temperature to the modulated absorbed power, $\frac{dT}{dP_{\text{abs}}}(\omega)$, is retrieved from a Fourier frequency sweep. The combined value of $V_{\text{eff}} \cdot dT/dP_{\text{abs}}$ is calculated as $3.60 \times 10^{-13} \text{ K}\cdot\text{m}^3\cdot\text{W}^{-1}$ in the case of full SiO_2 cladding for samples used in Fig. A.10(e, f), and is $4.63 \times 10^{-13} \text{ K}\cdot\text{m}^3\cdot\text{W}^{-1}$ in the case without top SiO_2 cladding for samples used in Fig. A.10(c, d).

Response calibration

To extract the actual microresonator response $\chi(\omega)$ from the experimentally photodetected $\chi'(\omega)$, the frequency response $\chi_{\text{det}}(\omega)$ of our entire experiment setup and detection chain needs to be calibrated first. The calibration is realized by direct detection of the pump power modulation $\delta P(\omega) \propto \chi_{\text{det}}(\omega)$ in the absence of the probe laser and the pump filter. The measured response $\chi'(\omega)$ is normalized to the setup response $\chi_{\text{det}}(\omega)$, and thus the actual microresonator response $\chi(\omega) = \chi'(\omega)/\chi_{\text{det}}(\omega)$ is retrieved, with a constant factor. This constant factor is removed when retrieving $\chi_{\text{therm}}(0)/\chi_{\text{Kerr}}(0)$ from the fitting of $\chi(\omega)$ using a fitting

function

$$\chi(\omega) = \chi_{\text{Kerr}}(0) \cdot \left(1 + \frac{\chi_{\text{therm}}(0)}{\chi_{\text{Kerr}}(0)} \frac{\chi_{\text{therm}}(\omega)}{\chi_{\text{therm}}(0)} \right) \frac{1}{1 + 2i\omega/\kappa_{\text{probe}}} \frac{1}{1 + 2i\omega/\kappa_{\text{pump}}} \quad (\text{A.73})$$

with $\kappa_{\text{probe, pump}}/4\pi$ being the cavity cutoff frequencies for the pump and probe fields, respectively. The normalized thermal response function $\chi_{\text{therm}}(\omega)/\chi_{\text{therm}}(0)$ used in the fitting is retrieved from COMSOL simulation. In Fig. A.10(d, f), only the normalized response $\chi(\omega)/\chi_{\text{Kerr}}(0)$ is shown, with the constant factor removed.

A.4.2 Lithium niobate microrings

In the previous section, we used the well-known Kerr nonlinear coefficients in Si_3N_4 PIC platform to calibrate the absorption rate of the structure. However, the nonlinear index n_2 in other material platforms is not as accurate in the literature. In this section, we show an example of how to calibrate both the n_2 and the absorption rate κ_{abs} in the thin-film lithium niobate platform.

The thin-film lithium niobate (TFLN) platform has enabled many classical and quantum applications [342], many of which crucially rely on low optical loss. For instance, the bandwidth of electro-optic (EO) frequency combs [225] and the efficiency of microwave-to-optical transducers [343, 344] are proportional to the resonator quality factor Q or (loss rate)⁻¹. Currently, the lowest-reported optical loss in ion-sliced TFLN waveguides is ~ 3 dB/m [345], which compares favorably to many photonic platforms. At the same time, a loss of ~ 0.2 dB/m was measured using whispering gallery mode resonators created by polishing bulk congruent LN [346]. It is currently an open question if TFLN can reach this, and ideally even lower, loss rates. For example, it has been speculated that the ion slicing process used to create TFLN from bulk LN [347] may result in implantation damage that could yield higher optical absorption in TFLN than in polished bulk LN.

Here, we first develop a post-fabrication process based on annealing in O_2 atmosphere to reduce material absorption rate κ_{abs} of the TFLN platform. The absorption rate κ_{abs} contributes to the intrinsic loss rate κ_{int} of the resonator, together with the scattering loss rate κ_{sca} . To quantify the reduction of material absorption rate in our samples, we apply the same linear response measurements to the TFLN platform. The method exploits the coexistence of absorption-induced photothermal effect and material Kerr effect and has shown great accuracy in other integrated photonics platforms [3, 5]. The calibration of absorption rate requires parameters such as the nonlinear refractive index n_2 as well as the ratio between the photothermal and Kerr-induced cross-phase modulation (XPM) responses (at bandwidths < 10 MHz) $\gamma = \chi_{\text{therm}}/\chi_{\text{Kerr}}$ of TFLN. These and other parameters are determined by performing laser pump-probe measurements on timescales shorter than the response time of deleterious photorefractive (PR) effects in LN [348]. Using these pump-probe techniques, we determine that the material limited loss in ion-sliced LN is ~ 1.5 dB/m and demonstrate an annealing

A.4 Absorption spectroscopy

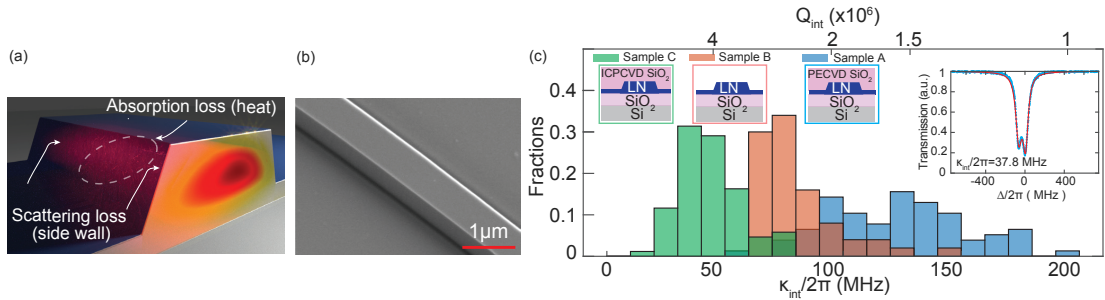


Figure A.11: Low material loss in TFLN micro-ring resonators using thermal annealing. **(a)** Conceptual representation of optical loss in a waveguide at low powers. Energy from an optical mode (profile cross-section shown) is dissipated due to photothermal absorption and sidewall roughness-induced losses, which can generate heat and light scattering, respectively. **(b)** A scanning electron microscope image of a fabricated (bus) waveguide. **(c)** Statistics of intrinsic loss rates (Q -factors) for the three resonators, denoted as Samples A-C, created by different fabrication methods. The vertical axis represents the fraction of the total number of resonances measured for the TE mode in each resonator for wavelengths between 1480 nm and 1680 nm. Left insets: Schematized wafer cross-sections for Samples A-C. Right inset: A split resonance observed from an annealed resonator, with extracted intrinsic loss rate. The horizontal axis denotes laser detuning from resonance.

process that reduces this to ~ 0.2 dB/m that approaches the limit of the bulk LN.

The micro-rings are fabricated on a 600 nm-thick x-cut LN thin-film bonded to a 4.7 μm -thick layer of thermal oxide on a silicon wafer (NanoLN). Electron-beam lithography followed by physical reactive Ar^+ ion etching, with target etch-depth of 300 nm, yields micro-ring resonators of 140 μm radius (Free spectral range of ~ 150 GHz) and a waveguide top-width of 2.4 μm (Fig A.11 (b)). We prepare three sets of resonators from this wafer in the same fabrication run: cladded (Sample-A), annealed (Sample-B), and annealed-cladded-annealed (Sample-C) resonators. All resonators are designed to be undercoupled, with a symmetric point coupling between the bus waveguide and the ring resonator. Sample-A is fabricated with the process reported in Ref. [345]. That is, the resonators are cladded with an 800 nm-thick layer of SiO_2 using plasma-enhanced chemical vapor deposition with substrate temperature of 300°C. For Samples B and C, the resonators are annealed at atmospheric pressures in O_2 at 520°C for two hours. The annealing step is used to improve the crystallinity of TFLN, thereby repairing potential damages [349] caused by ion slicing [350]. We clad Sample C with an 800-nm thick layer of SiO_2 deposited using inductively coupled plasma chemical vapor deposition (ICPCVD) at 80°C, and then re-anneal it under the same conditions. We emphasize the low-temperature nature (80°C) of the ICPCVD process, which we found to be essential to maintain the benefits of the annealing step. We measure a mean Q_{int} of 1.5, 2.5, and 5.0 million in Samples A, B, and C, respectively (Fig. A.11c). All Samples B and C resonances achieve low enough intrinsic loss to exhibit visible asymmetric mode splitting due to Rayleigh back-scattering (Fig. A.11c). We attribute the lower intrinsic quality factors of the current set of devices (compared to results presented in ref. 5) to the possible fabrication variations. We note that Q -factors as high as 12

Appendix A. Dissipative dynamics in photonic integrated circuits

million can be measured using the optimized process.

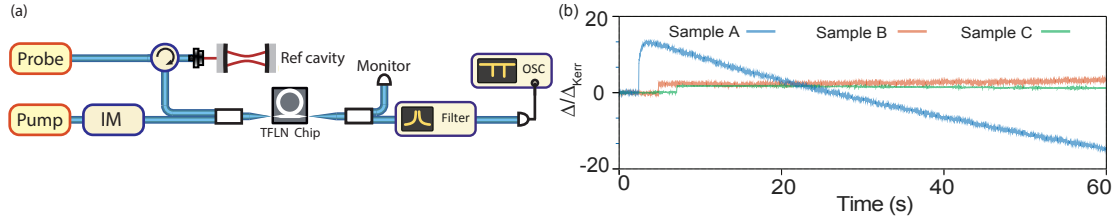


Figure A.12: **(a)** The laser pump-probe setup for a step-response measurement to characterize the timescale of photorefractive effects. **(b)** Dynamics of step excitation-induced cavity resonance shift (normalized to Kerr shift) of the probe after switching off the pump. Measurement is referenced to a thermally stabilized Fabry-Perot cavity. The pump is switched off at slightly different times for Samples A-C. The timing resolution is 1 ms. IM: Intensity Modulator, OSC: Oscilloscope

Before the Kerr-calibrated response measurements, we determine the timescale of photorefractive effects in the micro-rings since PR-induced resonance frequency change could distort the inferred material response at low modulation frequencies. [348]. To do this, we optically pump a micro-ring, then, after extinguishing the pump, we repeatedly measure one of its resonances with a probe, monitoring the time-dependence of the detuning of the resonance (Fig. A.12(a)). The detuning is normalized to the Kerr shift (discussed later) for convenient comparison. For Sample-A, we observe a blue shift with a time constant of ~ 100 s, indicative of photorefractive effects. We did not observe photorefractive behavior for Samples-B and -C over time scales of up to a minute (Fig. A.12(b)). Thus, the photorefractive effect can be ignored for measurements at timescales significantly shorter than 100 s (bandwidths $\gg 0.01$ Hz).

To calibrate the absorption rate of different devices, we need to evaluate

$$\kappa_{\text{abs}} = \frac{2cvn_2\gamma}{n_g n_{\text{eff}} V dv/dP_{\text{abs}}}, \quad (\text{A.74})$$

where V the optical mode volume, n_g the group index, n_{eff} the effective index, and dv/dP_{abs} the photothermal frequency shift gradient at pump frequency ν , mainly determined by the material thermo-optic coefficients [351] and is determined from simulation (See Table A.4). The response ratio γ is the DC offset of the measured response function $\gamma(\omega)$ in the Fourier domain and is obtained through fitting. The material absorption rate also requires a good knowledge of n_2 from TFLN. We did an auxiliary pump-probe measurement to obtain $n_2 = 1.67 \times 10^{-19} \text{ m}^2\text{W}^{-1}$ for our TFLN (see later sections). We did not employ the commonly-used thermal triangle technique[5] to determine n_2 to avoid photorefractive effects.

To separate the photothermal and Kerr effect in our samples and thereby measure γ , we exploit the finite response bandwidth of the photothermal effect. The measurement is accomplished by modulating an optical pump and measuring the resultant side-of-fringe modulation of a probe, as induced by the material response of TFLN (see Fig. A.13a). The pump modulation

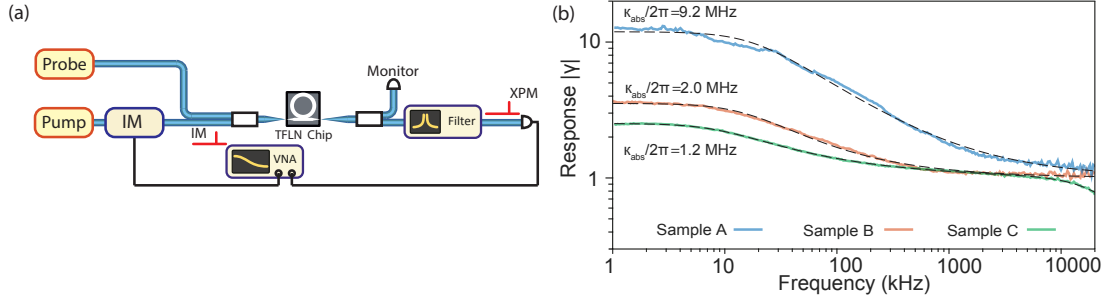


Figure A.13: **(a)** Laser pump-probe setup for measuring the DC offset of the measured response function (γ) with calibrated modulation tones. **(b)** Measured photothermal and XPM responses for Samples A-C. A fit to the curve determines γ . VNA: Vector Network Analyzer, IM: Intensity Modulation.

frequency is varied to elucidate photothermal and Kerr-induced XPM on the probe, which can be distinguished at low (<10 kHz) and high (>1 MHz) modulation frequencies, respectively [3]. The responses of all the devices were measured, and all yielded two plateaus corresponding to either predominantly Kerr-induced (χ_{Kerr}) or photothermal-induced (χ_{therm}) responses. The plateau ratios γ are 11.0, 2.5, and 1.5 for Samples A, B, and C, respectively, indicating that thermal annealing reduces the magnitude of photothermal response. Note that cascaded sum-frequency generation of the pump with the probe will contribute an additional XPM indistinguishable from the Kerr contribution. Given our system parameters, we expect this change to be $\sim 10\%$. For all measurements, the wavelength of the pump is ~ 1550 nm while the probe is at wavelengths detuned several free-spectral ranges of the resonator away, both in TE polarization. The pump power is kept low (<1 mW) to avoid nonlinearity-induced self-feedback.

Finally, using Eq. A.74 we calculate $\kappa_{\text{abs}}/2\pi$ to be 9.2 MHz, 2.0 MHz, and 1.2 MHz for Samples -A, -B, and -C, respectively. The absorption rates corresponding to each sample are calibrated individually. All the measured values for different samples are listed in Table A.3 in the form of quality factors, with Sample-C yielding a material-limited quality factor of 163 million (0.2 dB/m) which is among the highest within integrated photonic platforms, see Table A.4. Our results suggest that the main source of loss in our high-confinement LN waveguides (sample C) is line-edge roughness-induced scattering, which limits the average intrinsic quality factor $Q_{\text{int}}/2\pi$ of resonances around 1550 nm to 34 MHz (Fig. A.11c).

Table A.3: **Comparison of intrinsic quality factors and material limited quality factors of different samples**

Sample	post-processes	$Q_{\text{int}} (10^6)$	$Q_{\text{abs}} (10^6)$
A	PECVD	1.5	21
B	anneal	2.5	97
C	anneal + ICPCVD + anneal	5.0	163

To summarize, using our newly developed absorption calibration method, we find that the

Appendix A. Dissipative dynamics in photonic integrated circuits

Table A.4: **Comparison of material-limited properties among state-of-the-art integrated photonics platforms at 1.5 μm wavelength**[5]

Platform	n	$\chi_2(\text{pm/V})$	$n_2(10^{-20}\text{m}^2/\text{W})$	Q-factor (10^6)
SiO ₂	1.45	0	2.2	3900
SiN	2.0	0	24	290
Ta ₂ O ₅	2.0	0	62	2.4
Al _{0.2} Ga _{0.8} As	3.3	119	2600	2.0
TFLN (this work)	2.2	30	17	163

post-fabrication annealing and low-temperature oxide cladding can significantly reduce optical absorption in TFLN waveguides. Absorption at telecommunication wavelengths is reduced by removing damage potentially caused by ion implantation and reactive-ion etching even at temperatures in which other chemical bonds (e.g., Si-H and O-H) are still present.

Consequently, annealing significantly reduces material absorption loss over a broad frequency range [349]. Our annealing technique yielded absorption-limited loss on par with ~ 0.2 dB/m measured in bulk LN [346], corresponding to a material-limited Q-factor of 163 million. It is speculated that by improving TFLN fabrication strategies, Q-factors approaching the material limit might be achievable, reaching the low-loss regime required for some performance demanding applications, e.g., deterministic room-temperature single-photon source with periodically-poled TFLN micro-ring [352].

In the following subsection, we describe how to calibrate the nonlinear index n_2 .

n_2 calibration method

The material absorption rate requires the evaluation of n_2 . We measure an auxiliary z-cut sample with similar waveguide geometry to determine n_2 . We chose this specific crystal direction to minimize the error of the cascaded χ_2 calculation and mitigate the impact of adiabatic evolution of the modes from TE to TM during propagation in the x-cut sample due to birefringence. Even though anisotropy of $\chi^{(3)}$ nonlinearity was not reported in TFLN, the n_2 might be crystal-orientation dependent. Therefore, we characterized the value for both TE and TM modes in the Z-cut sample, which are aligned to the ordinary and extraordinary axes. The measurement results show little difference of n_2 along these two axes.

Due to the presence of the photorefractive (PR) effect, the commonly-used thermal triangle technique [5] that uses high optical power to determine n_2 is not suitable for thin film lithium niobate (TFLN) platform. Here, we use a pump-probe scheme (setup see Fig. A.14a) similar to the one used in earlier sections (for calibrating the loss) to determine the value of n_2 in TFLN at low optical powers. The main idea of this measurement is to precisely calibrate the impact of the pump intracavity power density modulation $\delta\rho$ on the probe's cavity frequency modulation $\delta\nu$ mediated by the Kerr effect. Our technique allows us to evaluate the value of

Table A.5: Simulated parameters for n_2 measurement and absorption calibration

TE parameters	values
$\overline{n_g \bar{n}}$	4.53
V	$7.47 \times 10^{-16} \text{ m}^3$
TM parameters	values
$\overline{n_g \bar{n}}$	4.14
V	$9.11 \times 10^{-16} \text{ m}^3$
abs parameters	values
cladded $V \frac{dv}{vdP_{\text{abs}}}$	$2.82 \times 10^{-18} \text{ m}^3/\text{W}$
uncladded $V \frac{dv}{vdP_{\text{abs}}}$	$4.05 \times 10^{-18} \text{ m}^3/\text{W}$

n_2 from

$$\delta v = -\frac{2vc\overline{n_2}}{\overline{n_g \bar{n}}} \delta \rho \quad (\text{A.75})$$

where \bar{x} are the mode intensity weighted average of the corresponding physical quantities retrieved from the simulation. Table.A.5 contains the simulated numbers required for the n_2 and absorption calibration (COMSOL).

The intracavity power density modulation $\delta \rho$ is determined by the intensity modulation depth α and the waveguide circulating power P_{WG} ,

$$\delta \rho = \alpha \rho(P_{\text{WG}}). \quad (\text{A.76})$$

We intensity modulate the pump intensity $I(t) = I_0[1 + \alpha \cos(2\pi\Omega_{\text{IM}}t)]$ at $\Omega_{\text{IM}} = 10$ MHz and determine the modulation-depth α using heterodyne measurements (Fig. A.14b red spectrum), frequency offset by 100 MHz using acousto-optic modulators. The intracavity power density $\rho(P_{\text{WG}})$ as a function of waveguide circulating power P_{WG} depends on many parameters. Apart from cavity coupling rates, the power is also affected by the background etalon formed due to the chip facet reflections. Therefore, the measured cavity transmission trace from the laser scan consists of a sinusoidal background modulation and a Fano-shaped cavity resonance dip. We detail the physics of this Fano-type resonance response in Appendix B.12. We express the intracavity power density considering all these effects as

$$\rho(P) = \left| \frac{\chi_{\text{cav}}(\Delta)}{1 - R(1 - \sqrt{\kappa_{\text{ex}}}\chi_{\text{cav}}(\Delta))^2 e^{i\theta_{\text{FP}}(\Delta)}} \right|_{\text{extr}:\Delta}^2 \frac{P}{V}, \quad (\text{A.77})$$

$$\theta_{\text{FP}}(\Delta) = -2\pi \frac{\Delta}{\Delta v_{\text{FP}}} + \Delta\theta_{\text{FP}}, \quad (\text{A.78})$$

$$\chi_{\text{cav}}(\Delta) = \frac{\sqrt{\kappa_{\text{ex}}}}{(\frac{\kappa}{2} + i\Delta)}, \quad (\text{A.79})$$

with κ_{ex} the cavity external coupling rate, κ the cavity linewidth, Δ the laser detuning, Δv_{FP} the waveguide background etalon fringe periodicity, $\Delta\theta_{\text{FP}}$ the etalon phase offset, R the

Appendix A. Dissipative dynamics in photonic integrated circuits

characteristic etalon reflectivity, and V the mode volume of the pump mode. Here, power P is the waveguide circulating power at the quadrature point of the waveguide background etalon fringe. All the parameters used in the power density function are fitted from the pump mode transmission profile shown in Fig.A.14d (TM mode result), using a fitting function,

$$F(\Delta) = \left| \frac{1 - \sqrt{\kappa_{\text{ex}}}\chi_{\text{cav}}(\Delta)}{1 - R(1 - \sqrt{\kappa_{\text{ex}}}\chi_{\text{cav}}(\Delta))^2 e^{i\theta_{\text{FP}}(\Delta)}} \right|^2. \quad (\text{A.80})$$

Laser frequency sidebands at 300 MHz are applied to calibrate the laser detuning. The fitting results are shown in the following table:

mode	$\kappa_{\text{ex}}/2\pi$	$\kappa/2\pi$	R	$\Delta\nu_{\text{FP}}/2\pi$	$\Delta\theta_{\text{FP}}$
TM	14.2 MHz	47.8 MHz	0.152	11.0 GHz	-0.57 rad
TE	87.8 MHz	302 MHz	0.107	9.05 GHz	-1.42 rad

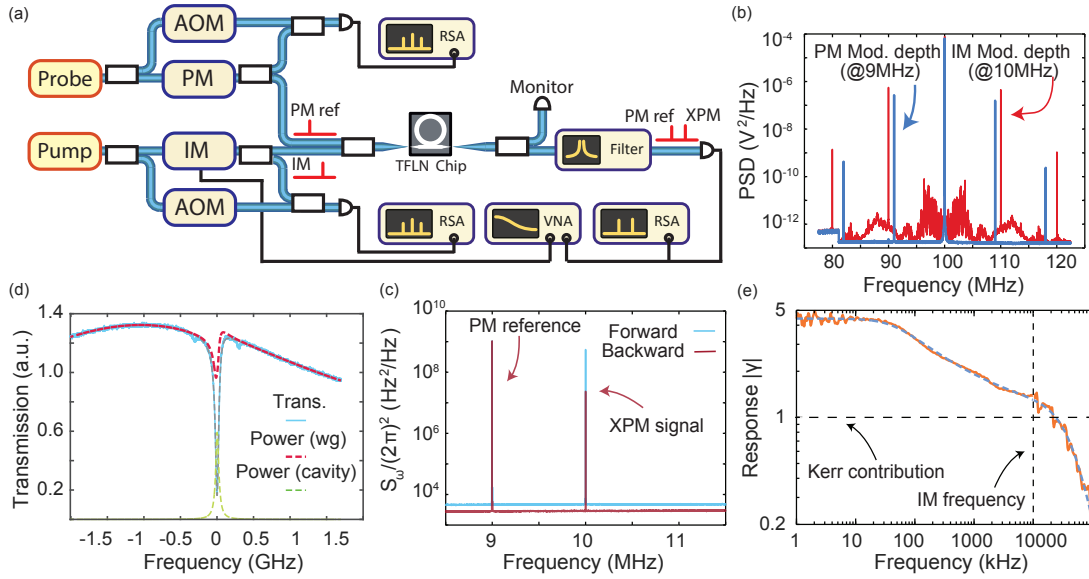


Figure A.14: **(a)** Laser pump-probe setup for measuring n_2 with calibrated intensity modulation and phase reference tones. **(b)** Power spectral density of heterodyne measurement at 100 MHz offset frequency to calibrate pump intensity modulation and probe phase reference for the XPM-induced modulation. **(c)** Measured XPM signals at 10 MHz along with the phase modulation reference tone at 9 MHz. Forward and backward coupling directions are measured to account for facet losses. **(d)** Parameter extraction by fitting a resonance profile of a micro-ring. **(e)** XPM frequency modulation response function. A vertical dashed line shows the intensity modulation frequency used to calculate n_2 . The horizontal dashed line indicates the pure Kerr XPM response. IM: Intensity Modulation, PM: Phase-Modulation, AOM: Acousto-optic Modulation, RSA: real-time spectrum analyzer, VNA: Vector Network Analyzer

After the intracavity power density function is determined by fitting the cavity transmission trace, we need to calibrate how much Kerr frequency modulation $\delta\nu$ on the probe cavity is

induced from a given waveguide circulating power P . To calibrate the cavity frequency modulation depths, we use the method from Ref [47] by comparing the Kerr frequency modulation signal to a reference phase modulation with known depth β (calibrated also using heterodyne measurements, Fig. A.14(b) blue spectrum). The phase modulation $E(t) = E_0 e^{i\beta \cos(2\pi\Omega_{\text{PM}}t)}$ is applied to the probe laser at $\Omega_{\text{PM}} = 9$ MHz, and is visible in Fig. A.14(c) right next to the cavity frequency modulation signal at $\Omega_{\text{IM}} = 10$ MHz. The reference phase modulation acts as a ruler, allowing us to compare and retrieve the cavity frequency modulation depth at different optical powers. To isolate the cavity frequency modulation contributed by the Kerr effect from the one from the thermal effect, we also measured the XPM response at different pump modulation frequencies using a vector network analyzer. We retrieved the fraction of pure Kerr contribution to the total XPM signal $\Gamma(\Omega_{\text{IM}}) = \chi_{\text{Kerr}}(\Omega_{\text{IM}}) / \chi_{\text{XPM}}(\Omega_{\text{IM}}) = 0.60$ for TM mode and 1.00 for TE mode at $\Omega_{\text{IM}} = 10$ MHz by fitting the measured response (TM result shown in Fig. A.14(e)). We also observed the pyroelectric effect on the TE response, discussed in Section A.1.3 [322]. However, this is only a special case for Z-cut TE mode from the extraordinarily low thermo-optic coefficients at the ordinary axes and does not affect the calibration of n_2 and the loss rate calibration of X-cut modes. After that, the Kerr-induced cavity frequency modulation can be expressed as

$$\delta\nu = \beta\Omega_{\text{PM}}\Gamma(\Omega_{\text{IM}})\xi^{1/2} \quad (\text{A.81})$$

where $\xi = S_{\text{XPM}}/S_{\text{ref}}$ is the power spectral density ratio between the XPM total signal S_{XPM} measured on the real-time spectrum analyzer and the reference phase modulation signal S_{ref} .

Since we do not have direct access to the on-chip waveguide circulating power, and the coupling efficiencies at the chip facets can be different, we mitigate the uncertainties by taking the geometry average of the input power P_{in} and output power P_{out} of the chip as the waveguide circulating power $P = \sqrt{P_{\text{in}}P_{\text{out}}}$, measured at the etalon quadrature point. We measure the XPM ratio ξ_F at the given setting and repeat the measurement (measure ratio ξ_R) after reversing the input and output of the micro-ring in order to take into account different coupling efficiencies at the chip facets. The spectrum of TM mode when measuring both ξ_F and ξ_R are shown in Fig. A.14(c), and we take their geometric average as well $\xi = \sqrt{\xi_F\xi_R}$.

For all measurements, the wavelength of the pump is ~ 1550 nm while the probe is at wavelengths detuned several free-spectral ranges of the resonator away. The on-chip pump power is kept low (< 1 mW) to avoid nonlinearity-induced self-feedback. With all relevant parameters measured/fitted, by inverting Eq.A.75, our measurements allow calibrating n_2 using

$$\overline{n_2} = \frac{\beta\Omega_{\text{PM}}\Gamma(\Omega_{\text{IM}})[\xi_F\xi_R]^{1/4}\overline{n_g\overline{n}}}{2c\nu\alpha\rho([P_{\text{in}}P_{\text{out}}]^{1/2})}, \quad (\text{A.82})$$

and we find a material nonlinear refractive index of $n_2 = 1.61 \times 10^{-19} \text{ m}^2\text{W}^{-1}$ for TE mode (aligned to ordinary axis) and $n_2 = 1.74 \times 10^{-19} \text{ m}^2\text{W}^{-1}$ for TM mode (aligned to extraordinary axis). For the TE mode in the X-cut samples we characterized, an averaged value of $n_2 = 1.67 \times 10^{-19} \text{ m}^2\text{W}^{-1}$ is used.

Table A.6: Measured values and derived fitting parameters for n_2 calibration

parameters	TM values	TE values
$\Gamma(\Omega_{\text{IM}})$	0.60	1.00
ξ	44.07	12.44
ξ_R	1.915	6.383
P_{in}	680 μW	2550 μW
P_{out}	6.0 μW	184 μW
$\rho([P_{\text{in}}P_{\text{out}}]^{1/2})$	47.0 J/m^3	91.7 J/m^3
α	0.1619	0.1619
β	0.1245	0.1245

Note that cascaded sum-frequency generation of the pump with the probe will contribute an additional XPM indistinguishable from the Kerr contribution. Given our system parameters, we expect this change to be $\sim 10\%$.

All the physical quantities measured/fitted for the n_2 calibration are shown in Table. A.6

A.5 Unidentified thermal noise in silicon nitride microresonators

In previous sections, we have identified the TRN as the dominant cavity frequency noise source (Section A.1) and analyzed the classical noise contributions to the observation of Kerr squeezing (Section A.2.1), as well as the effect of photothermal dissipative feedback (Section A.3). Even with so many parasitic effects, it is still expected to observe Kerr squeezing near the cavity cut-off frequency. In this section, we describe our attempt to observe Kerr squeezing in silicon nitride microresonators, the emergence of new thermal noise, and our efforts to identify the source by going through the remaining parasitic processes in our system.

We work with a 40-GHz-FSR resonator from [3] using a resonance around 1560 nm with intrinsic loss rate $\kappa_0/2\pi = 8\text{MHz}$, external coupling rate $\kappa_{\text{ex}}/2\pi = 7\text{MHz}$, and characterized $g_{\text{th}}(0)/g_{\text{Kerr}} = 0.5$. Given these system parameters, we expect to observe Kerr squeezing at $\sim 500\mu\text{W}$ of pump power around Fourier frequency 10 MHz. We have characterized our laser amplitude noise in Fig. B.12 and found that at the power level of interest, $C_{qq} \sim 10^{-2}$, which does not pose any limitation. We are aware that laser phase noise might affect our measurement. Therefore, we built a custom optical filter cavity (details in Appendix B.13) with a linewidth of 70 kHz to filter out the laser noise at high Fourier frequencies passively. With this filter cavity, we expect the laser frequency noise at 10-MHz frequency offset to be around $2 \times 10^{-2} \text{ Hz}^2/\text{Hz}$ (3 orders of magnitude reduction), sufficiently low for our need.

In our experiment, we PDH-lock the laser on resonance with the filter cavity and use the transmission light to pump the ring resonator. The filter cavity is actuated with a piezo ring to lock it directly to the ring resonator optical resonance. The setup schematic is shown in Fig. B.22. In this way, we can pump the resonator with an on-chip power of 500 μW (slightly

A.5 Unidentified thermal noise in silicon nitride microresonators

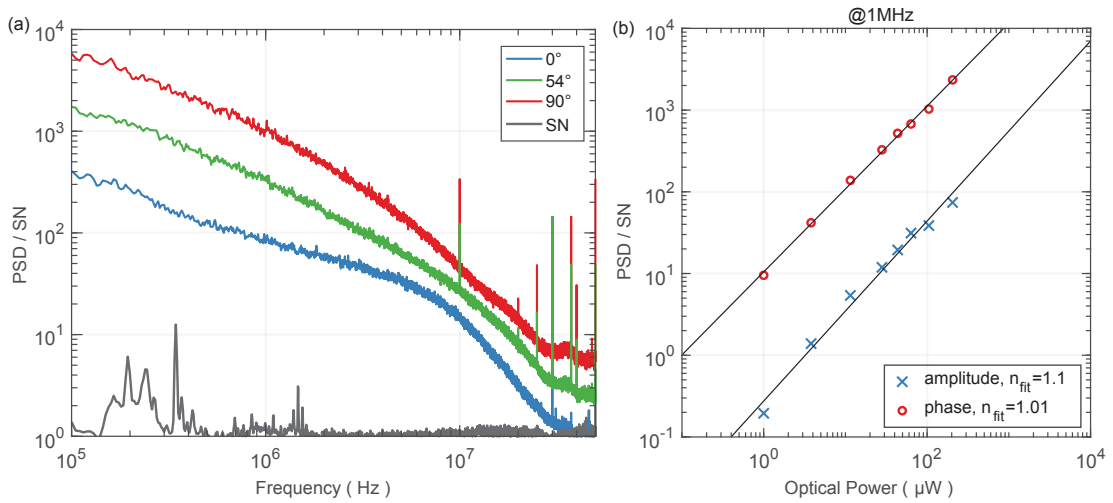


Figure A.15: **(a)** Homodyne photocurrent spectrum at different quadrature angles, normalized to the shot noise of the local oscillator. **(b)** Noise density at 1-MHz offset normalized to the shot noise, recorded at different pump power. A fit to the power scaling shows an unidentified classical noise on the amplitude quadrature that's not associated with Kerr or a photothermal effect.

below the cavity bi-stability threshold) while still able to supply 8 mW of power for the LO.

We measured homodyne photocurrent signal at multiple quadrature angles, with the results shown in Fig. A.15(a). We found that TRN is the dominant noise source at the phase quadrature ($\theta = 90^\circ$). Around the amplitude quadrature ($\theta = 0^\circ$), where we expect to observe Kerr squeezing, we observed an unidentified noise that contaminates the quadrature squeezing. In the following, we refer to this noise as the amplitude noise. To ensure this is not due to the imperfect quadrature angle, we confirmed that this noise is always there using direct detection while continuously tuning the laser detuning across the optical resonance. To understand the property of this noise better in order to identify it, we conducted a power sweep to check the power scaling of this noise, shown in Fig. A.15(b), and found that this noise is simply a classical cavity noise that does not associate with Kerr nor photothermal effect. To this day, we still have not figured out the exact origin of this noise. However, we have ruled out the following candidates: thermodynamical fluctuation of the cavity coupling rate, nonlinear cavity transduction, and cavity mode-splitting. In the following, we analyze each of these individual causes. Even though the origin of the noise has been elusive so far, we can, in principle, check its thermal origin by cooling the resonator to cryogenic temperature, where most of the thermal coefficients of Si_3N_4 go to near zero. In the end, we put this project on hold to leave time for other projects.

Thermodynamical fluctuation of the cavity coupling rate

As we analyzed earlier in Section 2.5.1, some form of dissipative coupling can print the noise directly onto the amplitude quadrature of the light field. For ring resonators, we assume the dominant noise source is the thermodynamical fluctuation of the temperature, which can both dispersively and dissipatively couple to the ring resonator. However, it has been known in cavity optomechanics that it is tough to engineer systems such that the dissipative coupling rate can approach that of the dispersive coupling. The discrepancy between these two mechanisms is because they result in fractional rate fluctuation, i.e., $\delta T \rightarrow \delta f/f$. For high-Q ring resonators we have $\kappa \ll \Omega_{\text{cavity}}$ ($Q \sim 10^7$), such that we expect the dissipative coupling signal $S_{\delta\kappa\delta\kappa}$ to be much smaller than the dispersive coupling signal $S_{\delta\Omega_{\text{cavity}}\delta\Omega_{\text{cavity}}}$, even accounting for the different thermal volume. Therefore, we do not expect the noise to originate from the fluctuation of the cavity coupling rate.

Nonlinear cavity transduction

In Section 2.4, we have discussed the case of nonlinear cavity transduction when the cavity frequency noise variance $\sqrt{\langle\Delta^2\rangle}$ approaches the cavity linewidth κ . The nonlinear cavity transduction is possible with ultra-high-Q microresonators, where thermodynamical fluctuation of the cavity frequency can be relatively large when the mode volume is small. For the 40-GHz-FSR resonator we used in our experiment, we calculated the second-order nonlinear noise, which is the dominant nonlinear noise when pumping on cavity resonance. We compared it with the linear noise in Fig. A.16(a). Even though the nonlinear transduction can be significant, in our experiment, we expect laser shot noise to still dominate at around 10-MHz offset, shown in Fig. A.16(b). Therefore, we do not expect the nonlinear cavity transduction to be the primary source of the unidentified noise we observed.

Note that the detuning dependence we examined in Section 2.4.7 is not possible to check here. As the first-order transduction noise does not exhibit a bandgap, the spectral separation with the second-order noise is not feasible.

Cavity mode splitting

Another complication in the experiment arises from the fact that ring resonators typically host clockwise and counter-clockwise propagating modes at the same eigenfrequency. When there are geometric imperfections, these two degenerate modes couple to each other, which causes mode splitting by the coupling rate γ (can be complex-valued) between the degenerate modes. For the high-Q resonators we use, the frequency splitting can be on the order of cavity decay rate and affect cavity frequency noise's transduction. Here, we analyze this effect at an offset frequency around 1 MHz where we observe classical noise contamination and show that there is still a quiet point where classical noise vanishes, which does not fit our observation of the unidentified noise.

A.5 Unidentified thermal noise in silicon nitride microresonators

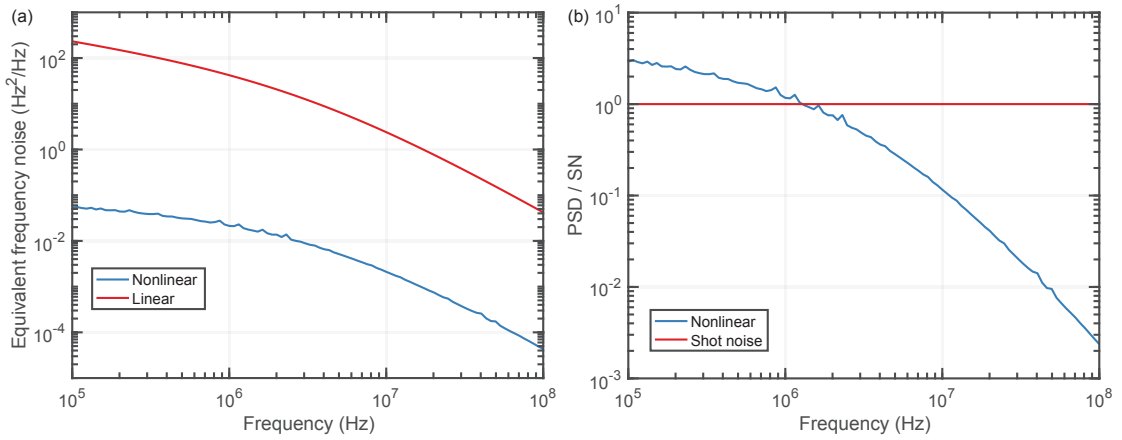


Figure A.16: **(a)** Linear transduction of the cavity frequency noise (TRN) vs. the equivalent cavity frequency noise, but through nonlinear transduction, appears on the amplitude quadrature. **(b)** Expected nonlinear transduction noise on resonance vs. the shot noise level at $500\ \mu\text{W}$.

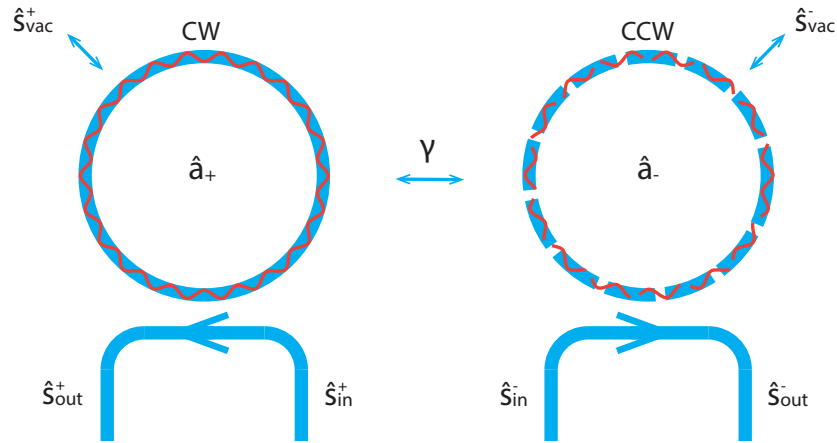


Figure A.17: Physical model describing the coupling γ between the clock-wise a_+ and the counter-clock-wise a_- . In the experiment, we have access to the coupling of the clock-wise mode a_+ , by the input and output bus waveguide channels s_{in}^+ and s_{out}^+ . The noise inputs of s_{vac}^+ , s_{in}^- , s_{out}^- , and s_{vac}^- are not accessible and are assumed to be vacuum noise.

Appendix A. Dissipative dynamics in photonic integrated circuits

Our modeling of the coupled optical modes is illustrated in Fig. A.17, where we couple directly (with efficiency η , linewidth κ) to the clock-wise mode a_+ , which also couples with the counter-clock-wise mode a_- with the coupling rate γ . The corresponding QLEs are

$$\dot{a}_+ = (i\Delta_0 - \frac{\kappa}{2})a_+ + \frac{i\gamma}{2}a_- + \sqrt{\eta\kappa}s_{\text{in}}^+ + \sqrt{(1-\eta)\kappa}s_{\text{vac}}^+ \quad (\text{A.83})$$

$$\dot{a}_- = (i\Delta_0 - \frac{\kappa}{2})a_- + \frac{i\gamma}{2}a_+ + \sqrt{\eta\kappa}s_{\text{in}}^- + \sqrt{(1-\eta)\kappa}s_{\text{vac}}^- \quad (\text{A.84})$$

$$s_{\text{out}}^+ = s_{\text{in}}^+ - \sqrt{\eta\kappa}a_+ \quad (\text{A.85})$$

Note that the splitting coefficient γ could be a complex number, where the real part contributes to the frequency splitting and the imaginary part contributes to the emergence of bright and dark modes with different loss rates. The real part is generally from the direct energy exchange between the two modes. In contrast, the imaginary part comes from a bath mode (e.g., the bus waveguide) that mediates the coupling (with a delay) between the \pm modes. Here Δ_0 is the detuning to the original $+$ mode resonance. From now on, we use $\Delta = \Delta_0$ to simplify the expressions.

We first linearize the equations and obtain the stationary solution

$$\bar{a}_- = \frac{-i\gamma/2}{i\bar{\Delta} - \frac{\kappa}{2}}\bar{a}_+ \quad (\text{A.86})$$

$$\bar{a}_+ = -\sqrt{\eta\kappa} \frac{i\bar{\Delta} - \frac{\kappa}{2}}{(i\bar{\Delta} - \frac{\kappa}{2})^2 + \gamma^2/4} \bar{s}_{\text{in}}^+ \quad (\text{A.87})$$

$$\bar{s}_{\text{out}}^+ = \left[1 + \frac{\eta\kappa(i\bar{\Delta} - \frac{\kappa}{2})}{(i\bar{\Delta} - \frac{\kappa}{2})^2 + \gamma^2/4} \right] \bar{s}_{\text{in}}^+ \quad (\text{A.88})$$

as well as the fluctuation part

$$\delta \dot{a}_+ = i\bar{a}_+ \delta\Delta_+ + (i\bar{\Delta} - \frac{\kappa}{2})\delta a_+ + \frac{i\gamma}{2}\delta a_- + \sqrt{\eta\kappa}\delta s_{\text{in}}^+ + \sqrt{(1-\eta)\kappa}\delta s_{\text{vac}}^+ \quad (\text{A.89})$$

$$\delta \dot{a}_- = i\bar{a}_- \delta\Delta_- + (i\bar{\Delta} - \frac{\kappa}{2})\delta a_- + \frac{i\gamma}{2}\delta a_+ + \sqrt{\eta\kappa}\delta s_{\text{in}}^- + \sqrt{(1-\eta)\kappa}\delta s_{\text{vac}}^- \quad (\text{A.90})$$

Note that there are both $\delta\Delta_+$ and $\delta\Delta_-$ because, in principle, the two modes could have different spatial distributions, such that the cavity frequency noise, e.g., TRN, can be partially uncorrelated. The spatial distribution is identical in our case, but we keep a separate notation such that the result is general. After the FT $\delta a_i \Rightarrow \tilde{a}_i(\omega)$ (denoted by a_i in the following), we obtain the Fourier domain result

$$a_+ = \left(i[i(\omega - \bar{\Delta}) + \frac{\kappa}{2}]\bar{a}_+ \delta\Delta_+ - \frac{\gamma}{2}\bar{a}_- \delta\Delta_- + \frac{i\gamma}{2}(\sqrt{\eta\kappa}s_{\text{in}}^- + \sqrt{(1-\eta)\kappa}s_{\text{vac}}^-) \right. \\ \left. + [i(\omega - \bar{\Delta}) + \frac{\kappa}{2}](\sqrt{\eta\kappa}s_{\text{in}}^+ + \sqrt{(1-\eta)\kappa}s_{\text{vac}}^+) \right) / \left([i(\omega - \bar{\Delta}) + \frac{\kappa}{2}]^2 + \frac{\gamma^2}{4} \right) \quad (\text{A.91})$$

A.5 Unidentified thermal noise in silicon nitride microresonators

Next, we plug in the stationary solutions of Eq. A.86 and Eq. A.87,

$$s_{\Delta} = \frac{i\eta\kappa \left[[i(\omega - \bar{\Delta}) + \frac{\kappa}{2}] \delta\Delta_+ + \frac{\gamma^2/4}{i\bar{\Delta} - \kappa/2} \delta\Delta_- \right]}{[i(\omega - \bar{\Delta}) + \frac{\kappa}{2}]^2 + \frac{\gamma^2}{4}} \frac{i\bar{\Delta} - \kappa/2}{(i\bar{\Delta} - \kappa/2)^2 + \gamma^2/4 + \eta\kappa(i\bar{\Delta} - \kappa/2)} \bar{s}_{\text{out}}^+ \quad (\text{A.92})$$

$$s_{\text{in}} = \left(1 - \frac{[i(\omega - \bar{\Delta}) + \frac{\kappa}{2}]\eta\kappa}{[i(\omega - \bar{\Delta}) + \frac{\kappa}{2}]^2 + \frac{\gamma^2}{4}} \right) s_{\text{in}}^+ \quad (\text{A.93})$$

$$s_{\text{vac}} = -\sqrt{\eta\kappa} \frac{\frac{i\gamma}{2} (\sqrt{\eta\kappa} s_{\text{in}}^- + \sqrt{(1-\eta)\kappa} s_{\text{vac}}^-) + [i(\omega - \bar{\Delta}) + \frac{\kappa}{2}] \sqrt{(1-\eta)\kappa} s_{\text{vac}}^+}{[i(\omega - \bar{\Delta}) + \frac{\kappa}{2}]^2 + \frac{\gamma^2}{4}} \quad (\text{A.94})$$

$$s_{\text{out}}^+ = s_{\Delta} + s_{\text{in}} + s_{\text{vac}} \quad (\text{A.95})$$

Here we define optical quadrature of the output mode as $X_{\theta}^+ = (se^{-i\theta} + s^{\dagger}e^{i\theta})/\sqrt{2}$, where the amplitude quadrature corresponds to $X_{\theta=0}^+$ so that the optical phase of the output mode is 0. The input quadrature is, therefore, $Y_{\theta}^+ = (se^{-i(\theta+\phi)} + s^{\dagger}e^{i(\theta+\phi)})/\sqrt{2}$, where $\phi = \text{angle}[1 + \frac{\eta\kappa(i\bar{\Delta} - \frac{\kappa}{2})}{(i\bar{\Delta} - \frac{\kappa}{2})^2 + \gamma^2/4}]$. Before converting to the quadrature basis, we define some susceptibilities

$$\chi_{\Delta}^+ = \frac{i\eta\kappa [i(\omega - \bar{\Delta}) + \frac{\kappa}{2}]}{[i(\omega - \bar{\Delta}) + \frac{\kappa}{2}]^2 + \frac{\gamma^2}{4}} \frac{(i\bar{\Delta} - \kappa/2) \left| 1 + \frac{\eta\kappa(i\bar{\Delta} - \frac{\kappa}{2})}{(i\bar{\Delta} - \frac{\kappa}{2})^2 + \gamma^2/4} \right| |\bar{s}_{\text{in}}^+|}{(i\bar{\Delta} - \kappa/2)^2 + \gamma^2/4 + \eta\kappa(i\bar{\Delta} - \kappa/2)} \quad (\text{A.96})$$

$$\chi_{\Delta}^- = \frac{i\eta\kappa \left[\frac{\gamma^2/4}{i\bar{\Delta} - \kappa/2} \right]}{[i(\omega - \bar{\Delta}) + \frac{\kappa}{2}]^2 + \frac{\gamma^2}{4}} \frac{(i\bar{\Delta} - \kappa/2) \left| 1 + \frac{\eta\kappa(i\bar{\Delta} - \frac{\kappa}{2})}{(i\bar{\Delta} - \frac{\kappa}{2})^2 + \gamma^2/4} \right| |\bar{s}_{\text{in}}^+|}{(i\bar{\Delta} - \kappa/2)^2 + \gamma^2/4 + \eta\kappa(i\bar{\Delta} - \kappa/2)} \quad (\text{A.97})$$

$$\chi_c = 1 - \frac{[i(\omega - \bar{\Delta}) + \frac{\kappa}{2}]\eta\kappa}{[i(\omega - \bar{\Delta}) + \frac{\kappa}{2}]^2 + \frac{\gamma^2}{4}} \quad (\text{A.98})$$

$$\chi_{i=1,2,3} = -\kappa \frac{\left[\frac{i\gamma}{2}\eta, \frac{i\gamma}{2}\sqrt{\eta(1-\eta)}, [i(\omega - \bar{\Delta}) + \frac{\kappa}{2}]\sqrt{\eta(1-\eta)} \right]}{[i(\omega - \bar{\Delta}) + \frac{\kappa}{2}]^2 + \frac{\gamma^2}{4}} \quad (\text{A.99})$$

$$s_{\Delta} = \chi_{\Delta}^+ \delta\Delta_+ + \chi_{\Delta}^- \delta\Delta_- \quad (\text{A.100})$$

$$s_{\text{in}} = \chi_c s_{\text{in}}^+ \quad (\text{A.101})$$

$$s_{\text{vac}} = \chi_i [s_{\text{in}}^-, s_{\text{vac}}^-, s_{\text{vac}}^+]^T \quad (\text{A.102})$$

$$s_{\text{out}}^+ = s_{\Delta} + s_{\text{in}} + s_{\text{vac}} \quad (\text{A.103})$$

to simplify the expression, where $\bar{s}_{\text{out}}^+ = \left| 1 + \frac{\eta\kappa(i\bar{\Delta} - \frac{\kappa}{2})}{(i\bar{\Delta} - \frac{\kappa}{2})^2 + \gamma^2/4} \right| |\bar{s}_{\text{in}}^+|$ is set to the phase reference $\theta_{\text{out}} = 0$. If we assume s_{in}^+ only consists of vacuum fluctuation, which is indeed our case after

Appendix A. Dissipative dynamics in photonic integrated circuits

passing the laser through the filter cavity, we can simplify the output quadrature to

$$X_{\Delta} = [\chi_{\Delta}^{+}(\omega)e^{-i\theta} + \chi_{\Delta}^{+*}(-\omega)e^{i\theta}]\delta\Delta_{+} + [\chi_{\Delta}^{-}(\omega)e^{-i\theta} + \chi_{\Delta}^{-*}(-\omega)e^{i\theta}]\delta\Delta_{-} \quad (\text{A.104})$$

$$X_{\text{in}} = \frac{\chi_c(\omega) + \chi_c^{*}(-\omega)}{2} Y_{\theta'} + i \frac{\chi_c(\omega) - \chi_c^{*}(-\omega)}{2} Y_{\theta'+\pi/2} \quad (\text{A.105})$$

$$X_{\text{vac}} = \frac{\chi_i(\omega) \pm \chi_i^{*}(-\omega)}{2} [X_{\text{in}}^{-}, X_{\text{vac}}^{-}, X_{\text{vac}}^{+}]_{\theta_i+\pi/2}^T \quad (\text{A.106})$$

$$X_{\theta}^{+} = X_{\Delta} + X_{\text{in}} + X_{\text{vac}} \quad (\text{A.107})$$

From here, we obtain the quadrature PSD (double-sided) as

$$S_{\Delta} = \left| \chi_{\Delta}^{+}(\omega)e^{-i\theta} + \chi_{\Delta}^{+*}(-\omega)e^{i\theta} \right|^2 S_{\Delta_{+}} + \left| \chi_{\Delta}^{-}(\omega)e^{-i\theta} + \chi_{\Delta}^{-*}(-\omega)e^{i\theta} \right|^2 S_{\Delta_{-}} \quad (\text{A.108})$$

$$+ 2\text{Real} \left[(\chi_{\Delta}^{+}(\omega)e^{-i\theta} + \chi_{\Delta}^{+*}(-\omega)e^{i\theta}) * (\chi_{\Delta}^{-}(-\omega)e^{-i\theta} + \chi_{\Delta}^{-*}(\omega)e^{i\theta}) \right] S_{\Delta_{+}\Delta_{-}} \quad (\text{A.109})$$

$$S_{\text{in}} = \left| \frac{\chi_c(-\omega)}{2} \right|^2 \quad (\text{A.110})$$

$$S_{\text{vac}} = \sum_{i=1,2,3} \left| \frac{\chi_i(-\omega)}{2} \right|^2 \quad (\text{A.111})$$

$$S_{\theta}^{+} = S_{\Delta} + S_{\text{in}} + S_{\text{vac}} \quad (\text{A.112})$$

With these results, we investigate the cavity frequency noise transduction (only S_{Δ}) as illustrated in Fig. A.18. We plot both the cavity transmission response and the transduction response at 1-MHz offset with various γ and show that there is always a quiet point where transduction vanishes. We can see from these plots that even with the emergence of bright and dark modes, there is always a detuning with zero transduction. Some of the quiet points do not reach precisely zero because the Δ in the plot is not sampled enough, but they always reach zero with some specific Δ .

During the investigation, we also found that with a proper ratio between γ_{real} and γ_{im} for a given η , there is a critical point at which the transduction dip is so narrow that the Q of such a feature diverges. This effect is illustrated in Fig. A.19. In principle, even though there is always a quiet point at which the transduction vanishes, reaching it is not practical if the feature is too narrow. To rule out this effect, we tested multiple optical resonances with different splitting features. We found no quiet point at the amplitude quadrature on all the tested resonances. Therefore, we can completely rule out mode splitting as the cause of the unidentified noise.

A.5 Unidentified thermal noise in silicon nitride microresonators

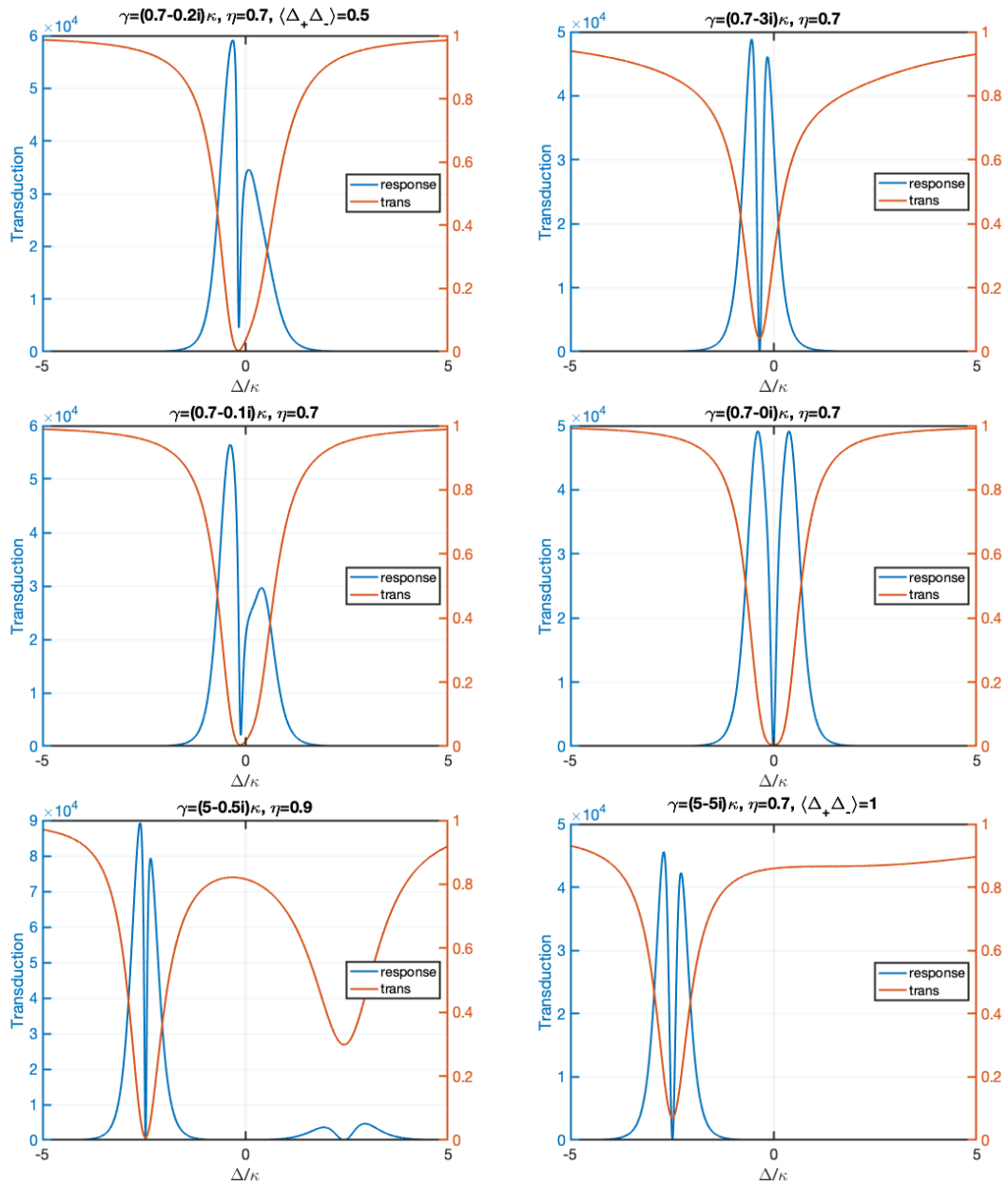


Figure A.18: Cavity frequency noise transduction as well as the transmission response function, of coupled modes with different configurations (γ , η , and noise correlation $\langle\Delta_+\Delta_-\rangle$) at the offset frequency 1 MHz. There is always a detuning (quiet point) that the noise transduction vanishes.

Appendix A. Dissipative dynamics in photonic integrated circuits

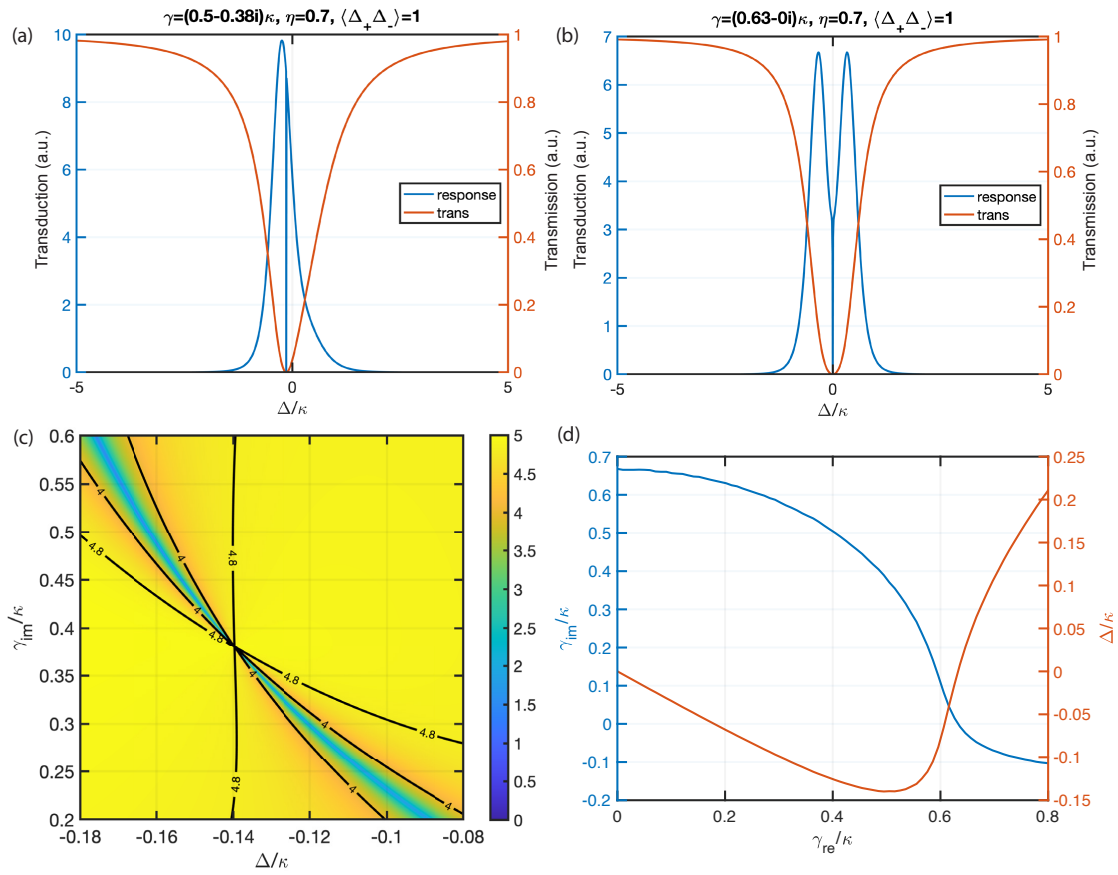


Figure A.19: **(a,b)** Critical feature of cavity frequency transduction. As one can see from these panels, the quiet point is so narrow that the detuning sweep can barely resolve the feature. It turns out that for each γ_{real} there is a γ_{im} that gives rise to this critical feature, visualized as a 2D map in **(c)**, with $\gamma_{\text{real}} = 0.5$. **(d)** For each γ_{real} , we show the γ_{im} and the detuning Δ to achieve this feature, in the bottom right panel.

B Appendix

B.1 Different forms of Langevin equations and interpretations of spectral asymmetry

Much of the derivations here are covered in the book [36]. It is only reproduced here, so the readers do not have to find them in the book, as they are very particular technical details. We aim to distinguish the two forms of the Langevin equations: one that uses the rotating wave approximation (RWA) and the other that does not. In the main body, we use the one with RWA for the optical field and the one without RWA for the mechanical oscillators. These two treatments result in very different equation sets and noise correlations, as well as the physical interpretation of the spectral asymmetry of quantum observables.

B.1.1 General quantum Langevin equation

Here, we derive the quantum Langevin equation without the rotating wave approximation. We consider a quantum system in a potential $\hat{V}(\hat{q})$ that is spring-coupled an ensemble of independent bath oscillators (*independent-oscillator model*). The total Hamiltonian is

$$\hat{H} = \hat{H}_{\text{sys}} + \hat{H}_{\text{sys-bath}} \quad (\text{B.1})$$

$$\hat{H}_{\text{sys}} = \frac{\hat{p}^2}{2m} + \hat{V}(\hat{q}) \quad (\text{B.2})$$

$$\hat{H}_{\text{sys-bath}} = \sum_j \left[\frac{\hat{p}_j^2}{2m_j} + \frac{k_j}{2} (\hat{q}_j - \hat{q})^2 \right] \quad (\text{B.3})$$

where \hat{p} and \hat{q} are the momentum and position of the quantum oscillator, and those indexed by j are the ones of the bath oscillators. The Heisenberg equation of motion for the system

Appendix B. Appendix

and bath position operators are

$$m\ddot{\hat{q}} = -\frac{\partial\hat{V}(\hat{q})}{\partial\hat{q}} + \sum_j k_j(\hat{q}_j - \hat{q}) \quad (\text{B.4})$$

$$m_j\ddot{\hat{q}}_j = -k_j(\hat{q}_j - \hat{q}) \quad (\text{B.5})$$

The Eq.(B.5) is a typical driven oscillator and could be solved easily with Laplace transformation,

$$\hat{q}_j = \hat{q}_j^h(t) + \hat{q}(t) - \int_{-\infty}^t dt' \cos[\Omega_j(t-t')] \dot{\hat{q}}(t') \quad (\text{B.6})$$

$$\hat{q}_k^h(t) = \hat{q}_j(0) \cos(\Omega_j t) + \frac{\hat{p}_j(0)}{\Omega_j m_j} \sin(\Omega_j t) \quad (\text{B.7})$$

Plugging it back to Eq.(B.4), one arrives at the quantum Langevin equation

$$m\ddot{\hat{q}} + \int_{-\infty}^t dt' \mu(t-t') \dot{\hat{q}}(t') + \frac{\partial\hat{V}(\hat{q})}{\partial\hat{q}} = \hat{F}(t) \quad (\text{B.8})$$

$$\hat{F}(t) = \sum_j k_j \hat{q}_k^h(t) \quad (\text{B.9})$$

$$\mu(t) = \sum_j k_j \cos(\Omega_j t) = \int_0^\infty d\Omega \rho(\Omega) k(\Omega) \cos(\Omega t) \quad (\text{B.10})$$

Define a frequency-dependent damping rate $\gamma(\omega) = \frac{\rho(\omega)k(\omega)}{4m}$, and one could find

$$\mu(t) = \int_0^\infty d\Omega 4m\gamma(\Omega) \cos(\Omega t) = \int_0^\infty d\Omega 2m\gamma(\Omega) (e^{i\Omega t} + e^{-i\Omega t}) = 2m\gamma(t), \quad (\text{B.11})$$

and the quantum Langevin equation now reads

$$m\ddot{\hat{q}} + 2m \int_{-\infty}^t dt' \gamma(t-t') \dot{\hat{q}}(t') + \frac{\partial\hat{V}(\hat{q})}{\partial\hat{q}} = \hat{F}(t). \quad (\text{B.12})$$

Applying the *first Markov approximation* so that $\gamma(t) = \gamma\delta(t)$, we arrive at

$$m\ddot{\hat{q}} + m\gamma\dot{\hat{q}} + \frac{\partial\hat{V}(\hat{q})}{\partial\hat{q}} = \hat{F}(t), \quad (\text{B.13})$$

which is the well-known result of the harmonic oscillation equation of motion.

One could also calculate the thermal force $\hat{F} = \hat{f} + \hat{f}^\dagger$ correlation

$$f = \sum_j k_j x_{\text{zp}}^j a_j(0) e^{-i\Omega_j t} \quad (\text{B.14})$$

$$\langle \hat{f}^\dagger(t) \hat{f}(t') \rangle = \int_0^\infty d\Omega \rho(\Omega) k^2(\Omega) x_{\text{zp}}^2(\Omega) \bar{n}(\Omega) e^{i\Omega(t-t')} \quad (\text{B.15})$$

$$\langle \hat{f}(t) \hat{f}^\dagger(t') \rangle = \int_0^\infty d\Omega \rho(\Omega) k^2(\Omega) x_{\text{zp}}^2(\Omega) (\bar{n}(\Omega) + 1) e^{-i\Omega(t-t')} \quad (\text{B.16})$$

$$\langle \hat{F}(t) \hat{F}(t') \rangle = \int_0^\infty d\Omega \rho(\Omega) k^2(\Omega) x_{\text{zp}}^2(\Omega) \left[\bar{n}(\Omega) e^{i\Omega(t-t')} + (\bar{n}(\Omega) + 1) e^{-i\Omega(t-t')} \right] \quad (\text{B.17})$$

B.1 Different forms of Langevin equations and interpretations of spectral asymmetry

The corresponding spectrum is therefore

$$\begin{aligned}
 S_{FF}(\omega) &= \int_{-\infty}^{\infty} \langle \hat{F}(t+\tau) \hat{F}(t) \rangle e^{i\omega\tau} d\tau \\
 &= \rho(\omega) k^2(\omega) x_{zp}^2(\omega) [\Theta(-\omega) \bar{n}(-\omega) + \Theta(\omega) (\bar{n}(\omega) + 1)] \\
 &= 2m\gamma(\omega) \hbar\omega [\Theta(-\omega) \bar{n}(-\omega) + \Theta(\omega) (\bar{n}(\omega) + 1)]
 \end{aligned} \tag{B.18}$$

which is asymmetric in frequency as was shown in Eq.(B.93) and Eq.(B.94). Here, Θ is the heavy step function.

For an arbitrary operator \hat{O} , the Heisenberg equation of motion is

$$\dot{\hat{O}} = \frac{1}{i\hbar} [\hat{O}, \hat{H}_{\text{sys}}] + \frac{1}{i\hbar} [\hat{O}, \hat{H}_{\text{sys-bath}}] \tag{B.19}$$

$$= \frac{1}{i\hbar} [\hat{O}, \hat{H}_{\text{sys}}] - \frac{1}{2i\hbar} \sum_j k_j \{[\hat{O}, \hat{q}], \hat{q}_j - \hat{q}\}_+ \tag{B.20}$$

$$= \frac{1}{i\hbar} [\hat{O}, \hat{H}_{\text{sys}}] - \frac{1}{i\hbar} [\hat{O}, \hat{q}] \hat{F}(t) + \frac{m}{i\hbar} \left\{ [\hat{O}, \hat{q}], \int_{-\infty}^t dt' \gamma(t-t') \dot{\hat{q}}(t') \right\}_+ \tag{B.21}$$

$$= \frac{1}{i\hbar} [\hat{O}, \hat{H}_{\text{sys}}] - \frac{1}{i\hbar} [\hat{O}, \hat{q}] \hat{F}(t) + \frac{m}{2i\hbar} \{[\hat{O}, \hat{q}], \gamma \dot{\hat{q}}(t)\}_+. \tag{B.22}$$

It is generally convenient to re-express the quantum Langevin equation in terms of the dimensionless position operator \hat{Q} and the dimensionless input momentum fluctuations \hat{P}_{in} defined previously. The quantum Langevin equation is then

$$\dot{\hat{O}} = \frac{1}{i\hbar} [\hat{O}, \hat{H}_{\text{sys}}] + i\sqrt{2\gamma} [\hat{O}, \hat{Q}] \hat{P}_{\text{in}} + \frac{\gamma}{2i\Omega} \{[\hat{O}, \hat{Q}], \dot{\hat{Q}}\}_+. \tag{B.23}$$

Applying the QLE to the annihilation operator b yields

$$\dot{b} = i\Omega b + \frac{\gamma}{2}(b^\dagger - b) - \sqrt{\frac{\gamma}{2}}(b_{\text{in}}^\dagger - b_{\text{in}}) \tag{B.24}$$

$$\dot{\hat{Q}} = \Omega \hat{P} \tag{B.25}$$

$$\dot{\hat{P}} = -\Omega \hat{Q} + \sqrt{2\gamma} \hat{P}_{\text{in}} - \gamma \hat{P} \tag{B.26}$$

from which one could find that the mechanical susceptibility $\chi(\omega)$ defined as

$$Q(\omega) = \chi(\omega) \sqrt{2\gamma} \hat{P}_{\text{in}}(\omega) \tag{B.27}$$

$$\chi(\omega) \equiv \frac{\Omega}{\Omega^2 - \omega^2 - i\omega\gamma} \tag{B.28}$$

is symmetric in frequency. Therefore, the result of asymmetry in the mechanical power spectral density is the result of asymmetry in thermal force fluctuations.

B.1.2 Quantum Langevin equation within the rotating wave approximation

The quantum Langevin equation with rotating wave approximation is derived by neglecting all the counter-rotating terms in the coupling (as was generally taught in a quantum optics course) when the coupling rate to the bath g_j is much smaller compared to other relevant rates in the system. The Hamiltonian under the RWA is therefore

$$\hat{H}_{\text{RWA}} = \hat{H}_{\text{sys}} + \sum_j \left[\hbar\Omega_j b_j^\dagger b_j + i\hbar g_j (b_j b^\dagger - b_j^\dagger b) \right] \quad (\text{B.29})$$

The resulting equation of motion for operator \hat{O} is thus

$$\dot{\hat{O}} = \frac{1}{i\hbar} [\hat{O}, \hat{H}_{\text{sys}}] - [\hat{O}, b^\dagger] \left(\frac{\kappa}{2} b - \sqrt{\kappa} b_{\text{in}} \right) + \left(\frac{\kappa}{2} b^\dagger - \sqrt{\kappa} b_{\text{in}}^\dagger \right) [\hat{O}, b] \quad (\text{B.30})$$

with the force term expressed as an input noise operator

$$b_{\text{in}}(t) \equiv \frac{1}{2\pi} \int_{-\infty}^{\infty} d\omega e^{-i\omega(t-t_0)} b_0(\omega). \quad (\text{B.31})$$

with the well-known correlation relations for the annihilation operator and the dimensionless bath position and momentum operators $\hat{Q}_{\text{in}} = (b_{\text{in}}^\dagger + b_{\text{in}})/\sqrt{2}$ and $\hat{P}_{\text{in}} = i(b_{\text{in}}^\dagger - b_{\text{in}})/\sqrt{2}$

$$\langle b_{\text{in}}^\dagger(t) b_{\text{in}}(t') \rangle = \bar{n}_{\text{th}} \delta(t-t') \quad (\text{B.32})$$

$$\langle b_{\text{in}}(t) b_{\text{in}}^\dagger(t') \rangle = (\bar{n}_{\text{th}} + 1) \delta(t-t') \quad (\text{B.33})$$

$$\langle Q_{\text{in}}(t) Q_{\text{in}}(t') \rangle = \langle P_{\text{in}}(t) P_{\text{in}}(t') \rangle = \left(\bar{n}_{\text{th}} + \frac{1}{2} \right) \delta(t-t') \quad (\text{B.34})$$

$$\langle Q_{\text{in}}(t) P_{\text{in}}(t') \rangle = -\langle P_{\text{in}}(t) Q_{\text{in}}(t') \rangle = \frac{i}{2} \delta(t-t'). \quad (\text{B.35})$$

Starting from the RWA QLE, one can easily write down the equation for mechanics annihilation operator b and quadrature operators \hat{Q} and \hat{P} ,

$$\dot{b} = -i\Omega b - \frac{\gamma}{2} b + \sqrt{\gamma} b_{\text{in}} \quad (\text{B.36})$$

$$\dot{\hat{Q}} = \Omega \hat{P} - \frac{\gamma}{2} \hat{Q} + \sqrt{\gamma} \hat{Q}_{\text{in}} \quad (\text{B.37})$$

$$\dot{\hat{P}} = -\Omega \hat{Q} - \frac{\gamma}{2} \hat{P} + \sqrt{\gamma} \hat{P}_{\text{in}} \quad (\text{B.38})$$

From here one could define susceptibility $\chi(\omega) = \frac{1}{i(\Omega - \omega) + \gamma/2}$, such that

$$b(\omega) = \sqrt{\gamma} \chi(\omega) b_{\text{in}} \quad (\text{B.39})$$

$$Q(\omega) = (b + b^\dagger)/\sqrt{2} = \sqrt{\gamma/2} (\chi(\omega) b_{\text{in}} + \chi^*(-\omega) b_{\text{in}}^\dagger) \quad (\text{B.40})$$

B.2 Fabrication process flow of density-modulated PnC membranes

The double-sided displacement noise spectral density is

$$S_{QQ}(\omega) = \int \langle Q(\omega)Q(\omega') \rangle \frac{d\omega'}{2\pi} = \frac{\gamma}{2} (|\chi(\omega)|^2(\bar{n}_{\text{th}} + 1) + |\chi(-\omega)|^2\bar{n}_{\text{th}}), \quad (\text{B.41})$$

where the spectral asymmetry at positive and negative mechanical frequency is the result of the asymmetry of susceptibility $\chi(\omega)$ under the RWA, while the force spectrum $S_{Q_{\text{in}}Q_{\text{in}}}$ and $S_{P_{\text{in}}P_{\text{in}}}$ are symmetric.

B.2 Fabrication process flow of density-modulated PnC membranes

We implement density-modulated PnC membranes by fabricating amorphous silicon (aSi) nanopillars on a high aspect ratio Si_3N_4 membrane. This method has some advantages over the original density-modulated membrane samples [33], where the pillars are made of plasma-enhanced chemical vapor deposition (PECVD) silicon nitride. For example, the dimensional accuracy of the fabricated nanopillars is improved. We also found that density-modulated membranes with PECVD nitride pillars caused significant optical bistability of the MIM cavity [53], probably due to excess optical absorption induced in the Si_3N_4 layer during our particular PECVD process. This experimental obstacle seemingly disappeared, when we adopted new membrane samples with aSi pillars. However, the process becomes more laborious, due to the need to protect the pillars during the membrane undercut. The aSi pillars and the substrate have a very similar chemical composition, and they will be dissolved during the undercut process, if exposed to the etchant (KOH). We devised a PECVD Si_xN_y encapsulation layer for the protection of aSi pillars, that can be removed selectively to the pillars and the membrane as the last step of microfabrication. As previously mentioned, we observed that the optical absorption of the Si_3N_4 membrane layer is significantly increased when the Si_3N_4 is directly exposed to plasma. Therefore, the fabrication process was adapted to prevent this.

In our PnC membranes, we fabricated pillars with diameters between $d_{\text{pil}} = 300 \text{ nm}$ to 800 nm and nearest-neighbor distances between $a_{\text{pil}} = 1.0 \mu\text{m}$ to $2.0 \mu\text{m}$. We chose to use electron beam lithography to pattern the pillars, for the highest versatility of prototyping. Dry etching transfers the mask pattern to the underlying film, while maintaining smooth and vertical sidewalls and keeping the pattern dimensions faithful to the original design. However, there are few dry etching recipes with a good selectivity between Si_3N_4 and Si; as soon as the $\sim 20 \text{ nm}$ Si_3N_4 membrane is uncovered, it would rapidly get consumed by the etching process. One solution is to stop the dry etching step just short of uncovering the Si_3N_4 layer, and finishing with a high-selectivity step such as wet etching [33]. Unfortunately, wet etching is typically isotropic, and would shrink the pillar dimensions from the design values, bringing forth issues in the reproducibility and control of the effective density and pillar damping. We decided to instead employ an etch-stop layer, much more resistant to dry etching than Si_3N_4 , on top of the membrane film, which allows for adequate over-etching and process tolerances. Such an etch-stop material is not difficult to find: for SF_6 -based processes, oxides such as SiO_2 , Al_2O_3 or HfO_2 (hafnium oxide) have been tested and found to provide a suitable selectivity. However,

Appendix B. Appendix

another critical requirement is that subsequent microfabrication steps create no significant undercut in the etch-stop layer. Undercut at the pillar base can dramatically reduce the pillar bending resonance frequency, thus increasing the pillar dissipation at MHz frequencies. HfO_2 proved to satisfy this requirement, as a thin layer with thickness < 5 nm can completely block the dry etching step for a sufficient amount of time, and it is dissolved in many acid and base solutions.

The process starts with (100)-oriented silicon wafers on which a ~ 20 -nm layer of stoichiometric, high stress Si_3N_4 has been grown via low-pressure chemical vapor deposition. After cleaning and dehydrating the wafer with an O_2 plasma, we proceed to grow with atomic layer deposition (ALD) a ~ 6 -nm HfO_2 etch-stop film (step 1 in Fig. 2.13). The growth takes place with a reactor temperature of 200°C , using H_2O and Tetrakis(ethylmethyldamido)hafnium (TEMAHf) as precursors. TEMAHf is pre-heated to 80°C before the deposition begins. We then proceed with the deposition of the aSi pillar layer. We employ a PECVD tool (Oxford PlasmaLabSystem 100), with silane (SiH_4) as the only precursor (step 2 of Fig. 2.13). The chamber temperature is set to 300°C during the deposition, and a 2% $\text{SiH}_4:\text{N}_2$ mixture is flowed in the chamber at 1000 sccm; plasma is generated using 30 W of RF power. The pressure in the chamber is kept around 1500 mtorr during the process. The typical pillar thickness we target is about 600 nm.

We then proceed to define the nanopillar pattern with electron beam lithography. We spin-coat flowable oxide FOx16 resist (a formulation of HSQ) at 2000 RPM, resulting in a mask layer approximately 800-nm thick. FOx is exposed with a dose of about $1400 \mu\text{C}/\text{cm}^2$ and developed with TMAH25% (2 minutes of immersion with agitation). Before the e-beam writing, the pattern is corrected for proximity effects in electron beam exposure that would lead to nonuniformity within the pillar lattice regions. The pattern is transferred to the aSi layer with reactive ion etching (step 3 in Fig. 2.13), using a recipe in which SF_6 and C_4F_8 gases flow simultaneously in the plasma chamber, where the wafer is kept at 20°C . The etch is monitored *in situ* using a 670-nm laser beam reflected from the thin film stack: as the aSi layer is gradually thinned down, fringes are observed, due to thin film interference. When the HfO_2 layer is exposed, the endpoint is visible from the sudden dip of the interference signal slope. We let the dry etching process run for about 30 s after the endpoint to ensure that the pillars are fully defined on the whole wafer, then we stop the process. Finally, we remove the FOx mask and the residual etch-stop layer by dipping the wafer in HF 1% for about 3.5 min.

After patterning the pillars, we encapsulate them in a dielectric layer to protect them during the silicon deep etching step (step 4 in Fig. 2.13). We require a layer that can conformally cover the pillar topography, without defects or pinholes and with tensile deposition strain, so it does not destructively buckle when suspended. Owing to previous experience in other microfabrication projects [353], we employ PECVD Si_xN_y . We first grow a thin (~ 20 nm), protective layer of Al_2O_3 with ALD, to shield the membrane layer from plasma bombardment during PECVD. Then, approximately 125 nm of Si_xN_y is grown in our Oxford PlasmalabSystem100 PECVD with 2% $\text{SiH}_4:\text{N}_2$ and NH_3 as the precursors. The flow rates are set to 975 and 30 sccm. The chamber

B.2 Fabrication process flow of density-modulated PnC membranes

pressure is 800 mtorr, and the reactor temperature is kept to 300 °C during the deposition. 40W of RF power excites the plasma during deposition, and the deposited layer has been characterized to have a tensile stress of around +300 MPa at room temperature. This PECVD layer has perfectly sealed the nanopillars and withstands several hours of immersion in hot KOH without significant consumption.

The process proceeds analogously to conventional stress-modulated PnC membranes, see the Supplementary Material of [42]. A thick ($\sim 3\ \mu\text{m}$) layer of positive tone photoresist is spun on the frontside for protection during the backside lithography process that we perform with an MLA150 laser writer (Heidelberg Instruments), with alignment to 8 frontside markers. Membrane windows must be appropriately resized in order to account for the KOH slow-etching $\langle 111 \rangle$ planes. UV lithography is followed by Si_3N_4 dry etching with a plasma of CHF_3 and SF_6 . After the resist mask and protection layer removal with N-Methyl-2-Pyrrolidone (NMP) and O_2 plasma, we deep-etch with KOH from the membrane windows while keeping the frontside protected, by installing the wafer in a watertight PEEK holder where only the backside is exposed (see [42, 52]). KOH40% at 70 °C is employed, and the etching is interrupted when about 30-40 μm of silicon remain. The wafer is then rinsed and cleaned with hot HCl of the residues formed during KOH etching. Then, the wafer is separated into individual dies before concluding the process: a protective layer of positive-tone resist is coated on the frontside before cutting the wafer with a dicing saw, and the process continues chipwise. Chips are again cleaned with NMP and O_2 plasma, and the deep-etch is concluded with a second immersion in KOH 40% at a lower temperature of 55 °C (step 5 in Fig. 2.13), followed by cleaning in HCl. From the end of the KOH etching step, the composite membranes are suspended, and great care must be adopted in displacing and immersing the samples in liquid; nevertheless, the presence of a relatively thick PECVD nitride layer ensures that the survival yield is quite high after this step ($> 90\%$). We dry the samples by moving them to an ultrapure isopropyl alcohol (IPA) bath after water rinsing. IPA has a low surface tension and a high vapor pressure, therefore, it can be easily dried off the membranes after a few minutes of immersion, with the help of a (cautiously operated) N_2 gun.

Finally, the PECVD nitride and Al_2O_3 layers can be removed selectively with wet etching in buffered HF (BHF; step 6 in Fig. 2.13). The etch rates of the encapsulation layers in BHF are orders of magnitude higher than the etch rate of stoichiometric Si_3N_4 and HfO_2 , therefore even though the membrane backside is exposed, the membrane thinning during this step remains limited (few nanometers). Chips are loaded in a Teflon carrier where they are vertically mounted, and immersed for about 3 min 20 s in BHF 7:1. It is crucial not to over-etch more than necessary to remove the encapsulation films completely: membranes become extremely fragile, and the survival yield drops sharply when their thickness is reduced below $\sim 15\ \text{nm}$. The membranes are then carefully rinsed, transferred in an ethanol bath, and dried in a critical point dryer, where the liquids can be evacuated gently and with little contamination.

B.3 Infinite impulse response filters

In this section, we discuss the implementation of an infinite impulse response (IIR) filter to help suppress the mechanical instabilities from the photothermal effects when pumping at the magic detuning. These digital filters implemented on fast field programmable gate array (FPGA) boards [354] can realize sharp and versatile spectral responses to individually address mechanical modes that have undergone parametric gain in a forest of mechanical signals. In this section, we first discuss the basic theories of IIR, the physical implementations, the filter stability criteria, and a few implementations in the experiments. We use FPGAs from Red Pitaya for their amazingly short delay for digital-analog signal conversions (~ 50 ns each side for the analog-to-digital converter (ADC) and the digital-to-analog converter (DAC)).

IIR filter theory

An infinite impulse response filter is a linear time-invariant system with an infinitely long impulse response function $h(n)$, such that the action of the filter h on the input signal x outputs a signal y given by

$$y(n) = \sum_{i=-\infty}^{\infty} x(i)h(n-i) = x(n) * h(n). \quad (\text{B.42})$$

We are interested in a filter for real-time signal processing, for which causality is required. Therefore, $h(n < 0) = 0$ is required so that the output signal at any given time does not depend on any future input signal that has not yet arrived. Also, for any given input signal, we require a bounded output, which is equivalent to the condition $\sum_{i=-\infty}^{\infty} |h(i)| < \infty$. These causality and stability requirements also have their counterparts for any response functions in a continuous system, which we will discuss in section B.3.

A straightforward way to implement any filter of response $h(n)$ is to store the last n_{FIR} samples of the input signal in a physical memory. This type of digital filter is known as a finite impulse response (FIR) filter because of the finite length of non-zero elements of the impulse response function. The advantages of such filters are the ease of implementation and stability by design. The output will always be bounded since only a finite length of $h(n)$ is nonzero. The disadvantage of FIR filters is the limited frequency resolution $\delta f = f_{\text{sample}}/n_{\text{FIR}}$. This resolution is not ideal for achieving sharp features in the spectral response due to the limited hardware resources on Red Pitaya, given which there is always a trade-off between frequency resolution δf and bandwidth $f_{\text{sample}} = 1/T$, where T is the clock period for the sampling.

An IIR filter, on the other hand, uses the output records stored in the memory in addition to the input records and outputs the following result

$$y(n) = \sum_{i=0}^M b_i x(n-i) - \sum_{j=1}^N a_j y(n-j). \quad (\text{B.43})$$

By inserting the expression of $y(n - j)$ recursively into the right-hand side of the expression, we will find that the system's impulse response indeed has an infinite length for nonzero a_j . Such an implementation is very resource efficient, with excellent frequency resolution, at the expense of design complexity.

To analyze the frequency domain response of this discrete-time system, we use the z-transform (equivalent to the Laplace transform in the continuous time domain) defined below

$$\zeta[x(n)] \equiv X(z) = \sum_{n=-\infty}^{\infty} x(n)z^{-n}, \quad (\text{B.44})$$

where z is the complex-valued discrete frequency and can be converted to the Laplace domain using the bilinear transformation

$$z = e^{sT} \approx \frac{1 + sT/2}{1 - sT/2} \quad s = \frac{2}{T} \frac{z - 1}{z + 1} \quad (\text{B.45})$$

From these definitions, it is straightforward to derive the time-shifted expression $\zeta[x(n + n_0)] = z^{n_0} X(z)$, using which we can easily derive the discrete-frequency domain response function

$$H(z) = \frac{Y(z)}{X(z)} = \frac{\sum_{i=0}^M b_i z^{-i}}{\sum_{j=0}^N a_j z^{-j}} = K \frac{\prod_{i=0}^M (z^{-1} - z_i^{-1})}{\prod_{j=0}^N (z^{-1} - p_j^{-1})} \quad (\text{B.46})$$

where the numerator and the denominator are decomposed into their roots (zeros z_i and poles p_j) of the M th and N th polynomials. Note that the zeros and poles here are not the same as those in the s-domain, which are connected through the bilinear transformation. Because of such differences, the stability criteria of the filter are different for the z and s domains.

When physically implementing the digital filter, we first fix the design with a set of zeros and poles (z_i, p_j), then compute the coefficients (a_j, b_i) of Eq.B.43. However, finite numerical precision from the round-off errors in the physical implementation will lead to arbitrarily large errors for the positions of the implemented poles and zeros. Such errors will grow with more complex filter designs when the orders M and N increase, eventually leading to unstable filters. Therefore, when designing IIR filters, filters up to only the second order are implemented, with which the round-off errors are manageable. Then, several second-order filters are connected in series or parallel to reconstruct the target higher-order IIR filter. The parallel implementation reduces the digital processing time and improves the noise performance, but also leads to drawbacks such as the feasibility problem of realizing the same poles or zeros of multiple orders.

With these design constraints in mind, we show how to convert a target analog transfer function into digital coefficients for physical implementations. We first start in the Laplace domain with a target analog transfer function

$$H_a(s) = K \frac{\prod_{i=0}^M (s - z_i)}{\prod_{j=0}^N (s - p_j)} = D + \sum_{j=1}^N \frac{r_j}{s - p_j} \quad (\text{B.47})$$

Appendix B. Appendix

with designed zeros and poles (z_i, p_j). Note again that the zeros and poles here are in the s-domain and differ from those in the z-domain. In order to implement the partial fraction expansion, it is required not to have any pair of identical poles, as well as poles that are too close to each other, to prevent large numerical errors. Then, to find the correct form in the z-domain, we need to first go to the continuous-time domain through the inverse Laplace transform

$$h_a(t) = D\delta(t) + \sum_{j=1}^N r_j e^{p_j t} u(t) \quad (\text{B.48})$$

where $u(t)$ is again the heavy step function. Discretizing the time variable $t = nT$ leads to the discretized version of the impulse response

$$h(n) = D\delta(nT) + \sum_{j=1}^N r_j e^{p_j nT} u(n), \quad (\text{B.49})$$

from which we arrive at the response in the z-domain as

$$H(z) = D + \sum_{j=1}^N \frac{r_j e^{-p_j T}}{e^{-p_j T} - z^{-1}}. \quad (\text{B.50})$$

In order to cast these parallel sections into physically realizable (real) coefficients (a_j, b_i) in Eq.B.43, we have to pair each section (if p_j or r_j has non-zero imaginary part) with their complex conjugate pairs

$$\frac{r_j}{1 - e^{p_j T} z^{-1}} + \text{conj.} = \frac{2\text{Re}[r_j] + 2\text{Re}[r_j e^{p_j^* T}] z^{-1}}{1 - 2\text{Re}[e^{p_j T}] z^{-1} + |e^{p_j T}|^2 z^{-2}} \quad (\text{B.51})$$

from which one can readily read out the coefficients ($a_0 = 1, a_1 = -2\text{Re}[e^{p_j T}], a_2 = |e^{p_j T}|^2, b_0 = \text{Re}[r_j], b_1 = 2\text{Re}[r_j e^{p_j^* T}]$) for physically implementing the IIR filters. As for D there is one parallel filter with coefficients ($a_0 = 1, b_0 = D$) for the implementation. The conjugate pairing of complex poles is not artificial since real-world systems well modeled by linear differential equations always have poles in conjugate pairs. If conjugate pairs of zeros and poles are already present in the initial design, then we need to pair them, and such a pairing process does not change the positions of the designed (z_i, p_j) up to some numerical errors. Therefore, for physical implementation, any unpaired complex zeros or poles will require additional insertion of their complex conjugate pairs in the continuous time domain design.

Even though different second-order filters of Eq.B.50 are in a parallel form, currently, in the PyRPL package [354] we use, they are realized in series physically. For each clock cycle, the coefficients are updated, and the outputs are computed and added sequentially. Since the delay time is different for sequential second-order filters, the high-frequency ones are implemented last (with newer input data), so the delay time and the overall effect of clock delay on the implemented filter are minimized. The onboard crystal oscillator provides a clock frequency at 125 MHz to match the ADC and DAC speed. One can estimate the delay of the designed filter, e.g., for a filter with five pairs of complex conjugate poles, the maximum delay

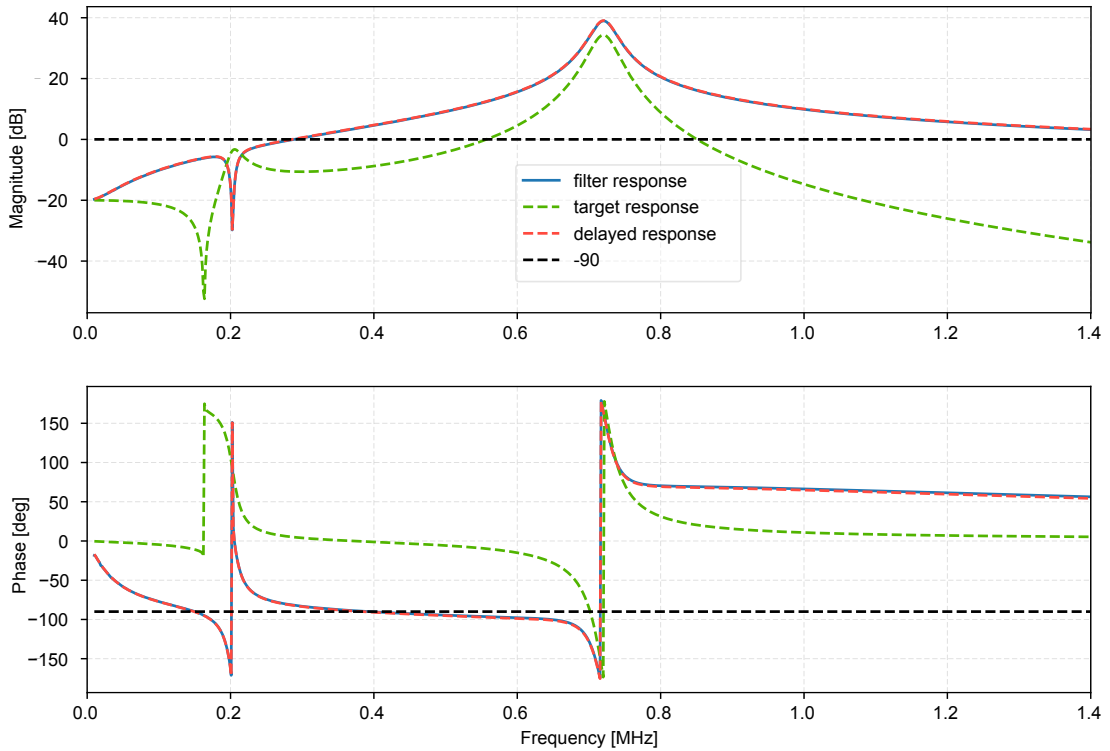


Figure B.1: Spectral response comparison of the designed filter (dashed green) vs. the physically implemented filter (solid blue). There is a large discrepancy between them, explained by the clock delay-induced modification of the filter response, with the theoretical prediction (dashed red) perfectly overlapping the measured response.

for the lowest frequency component is about 40 ns. Therefore, for a more complicated filter designed, depending on specific application bandwidths, it might be worthwhile to implement it in a parallel fashion. The effect of clock delays on different pole sections is illustrated in Fig. B.1, where the analog design function is compared to the physical response measured from the FPGA.

Response stability

Since most systems are usually well-modeled by an ordinary linear differential equation or a set of them, the Laplace transform of the system response can be written as a rational function

$$H(s) = K \frac{\prod_{i=1}^M (s - z_i)}{\prod_{j=1}^N (s - p_j)} \quad (\text{B.52})$$

where K is a constant scaling factor, p_j the complex poles and z_i the complex zeros of the transfer function. Any transfer function is connected to the impulse response of the system

Appendix B. Appendix

through the Laplace transform

$$H(s) = \int_0^{\infty} h(t)e^{-st} dt \quad (\text{B.53})$$

$$h(t) = \frac{1}{2\pi i} \lim_{T \rightarrow \infty} \int_{\gamma-iT}^{\gamma+iT} e^{st} H(s) ds \quad (\text{B.54})$$

where γ is bigger than any real part of all the singularities (poles) of $H(s)$. Stability requires bounded outputs with bounded inputs, which leads to a bounded integral of the impulse response function $\int |h(t)| dt$. This requires the number of zeros to be equal to or less than the number of poles; otherwise, $H(s)$ will blow up at infinity $s \rightarrow \infty$. Somehow, this is also partially connected to the causality of the impulse response function, such that $h(t < 0) = 0$. There is also another requirement on the position of the poles. If there is a pole p_k on the right side of the imaginary axis (positive real part), we can always decompose $H(s)$ like

$$H(s) = \dots + \frac{A_k}{s - p_k} \quad (\text{B.55})$$

$$h(t) = \dots + A_k e^{p_k t} \quad (\text{B.56})$$

which results in unbounded integral of impulse response function $\int |h(t)| dt$ because $|h(t)|$ diverges at large t . Therefore, any stable system requires the transfer function poles to be placed on the left side of the imaginary axis. The z-domain requirement counterpart is easily derived through the bilinear transformation, which transforms the left half of the s-plane into the unit circle in the z-plane, having the imaginary axis in the s-plane transformed into the unit circle in the z-plane. The requirement of $\text{Re}[p_k] < 0$ in the s-plane will thus correspond to $|p'_k| = e^{\text{Re}[p_k]T} < 1$, which means that the z-plane poles need to be inside the unit circle (in unit e^T).

Applications of IIR filters

In this section, we discuss a few applications of IIR filters in our experiment. We typically use these IIR filters when narrow-band addressing of individual mechanical modes is required, e.g., in measurement-based feedback cooling applications. Many filters with valuable functionalities can be implemented with just one pair of zero and pole, with their gain and phase frequency response shown in Fig.B.2. In the following (also in Appendix B.4), we will discuss their applications in a few scenarios with more complex filter functions.

Photothermal effect

One problem that is frequently observed in the MIM system is the photothermal effects of low-frequency modes (< 1 MHz). We discuss it in detail in Section 2.5.2. Due to the interference between photothermal force and radiation pressure force, the sign of the optical backaction feedback can be reversed for modes with low dispersive coupling rates, usually caused by

B.3 Infinite impulse response filters

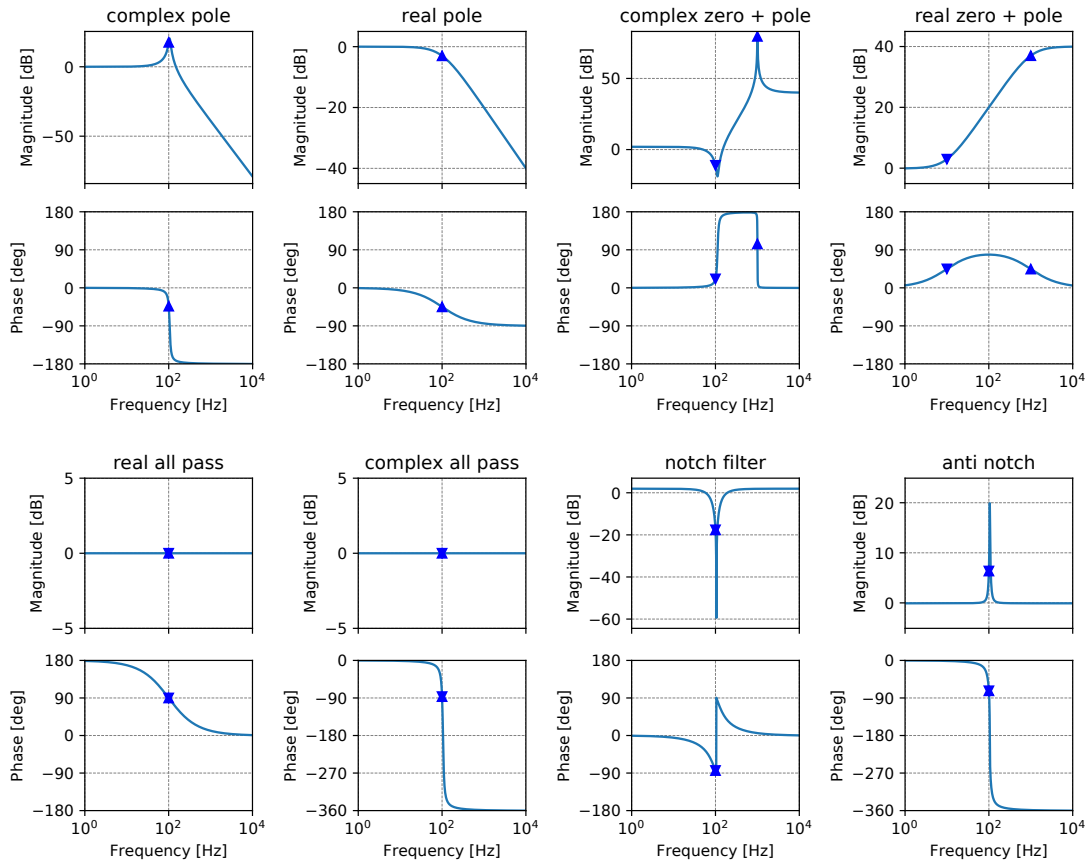


Figure B.2: Transfer functions of basic poles (\blacktriangle) and zeros (\blacktriangledown), and some constructed filter functions from pole-zero pairs. Note that for plots with zeros, there is always at least an equal amount of poles in the design, such that the filter remains causal and stable. The plotted transfer function does not perfectly correspond to the designed pole-zero positions, which is again the effect of clock delays of different pole sections.

little spatial overlap with the optical mode for symmetry reasons. At high optical power, these modes tend to become unstable. They cannot be efficiently cooled from broadband measurement-based feedback cooling for the same reason they can not be optically damped from Doppler cooling. They are typically about 3-10 kHz apart from the nearby modes and can be efficiently addressed with IIR filters.

In the experiment, we use a series of anti-notch filters

$$H(s) = \frac{s - (i\omega_0 + \Gamma)}{s - (i\omega_0 - \Gamma/G)}, \quad (\text{B.57})$$

illustrated in Fig.B.2 as well as Fig.B.2(b), to efficiently damp all the mechanical modes that are unstable. Here ω_0 is the center frequency of the feedback filter, Γ the feedback bandwidth, and G the feedback gain. Such a filter has a sharp phase flip within Γ bandwidth around the

Appendix B. Appendix

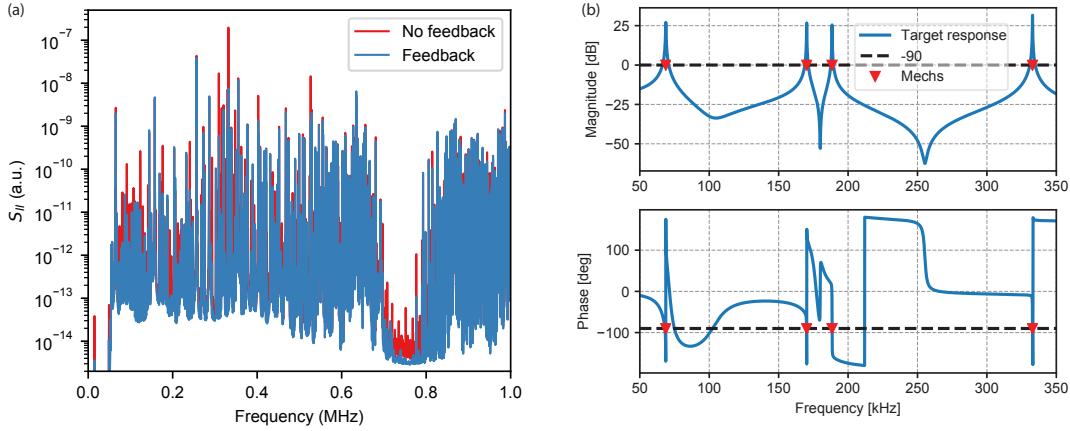


Figure B.3: **(a)** Comparison of the mechanical spectrum with and without the IIR feedback on a mechanical mode at 331 kHz. The instability of the mode is displayed, which also causes an increase in the nonlinear mixing noise inside the mechanical bandgap. **(b)** Applied IIR filter function for simultaneously damping the mechanical modes at 68 kHz, 168 kHz, 187 kHz, and 331 kHz.

mechanical frequency ω_0 for implementing the correct feedback phase for velocity damping and an accompanied peak in gain magnitude to compensate for low optomechanical coupling.

We illustrate one comparison of the mechanical spectra in Fig. B.3(a) to show the effect of the feedback. When the anti-notch filter on mode 331 kHz is turned off, one can see a rising peak at that frequency and the increase of nonlinear noise in the mechanical bandgap. We can reliably implement IIR filters with up to 6 anti-notch filters without significant deviation from the design due to clock delays. This technique improved the C_q from 0.1 to 1.0 with the previous generation device using perforated membranes. We could not improve much further due to the substantially large amount of unstable modes that require individual addressing.

Feedback filter phase correction

In either MIM system or any other multi-mode optomechanical system, feedback damping of an isolated high Q mode to the quantum ground state usually requires very high feedback gain. However, soft-clamped modes enabled by phononic crystal structures usually accompany forests of mechanical modes outside the designed mechanical bandgap. As was reported from earlier MIM ground state cooling experiment [17], even at 10 K temperature and with tailored IQ filter function inside the mechanical bandgap, when the feedback gain ramped up, some modes will become unstable due to the feedback-induced anti-damping. They are usually due to either the flipped phase response of the filter far-off resonance or the delay-induced phase flip at high frequency. In their work, the solution to such a problem was to use many IQ filters physically implemented in parallel to correct the feedback phase of the total filter response at these unstable modes. Their implementation is similar to what we did for the photothermal instabilities, where individual modes must be addressed. For us, we implemented IIR anti-

B.4 Broadband feedback cooling using a digital IIR filter

notch filters such that the physical resources required for addressing the same number of mechanical modes are much less, as these Red Pitaya FPGA boards are only programmed with three IQ filters each.

For other approaches, e.g. [88], IIR notch filters suppress the feedback gain at these modes. The bode plot of such a filter is illustrated in Fig.B.2 next to the anti-notch filter discussed above.

However, as the complexity of the filters grows with more included feedback modes, the accuracy of the implemented spectral response will take a hit. One way to circumvent this issue is to physically implement multiple parallel IIR filters on several FPGA boards to help reduce the on-board gate delays. Therefore, it is more convenient to implement the phase-correcting anti-notch filters with high peak gain, as we implemented for suppressing photothermal gains, with no need to worry about interference between parallel filter functions.

Optimal quantum control of mechanical motions

As discussed in Section 3.2, optimal inference of mechanical motion from the measurement record requires implementing a set of first-order differential equations (quantum master equations) to isolate the mechanical motion from the measurement noise properly. The implementation of this equation set, as well as its update in real time, is the prerequisite for real-time optimal quantum control of mechanical motions.

Even though it is not apparent at first glance, but the quantum master equations represent an infinite impulse response filter, where the present input signal $x(t)$ is combined with the prediction record in the past $y(t' < t)$ to predict the present mechanical motion $y(t)$. Therefore, it has a direct mapping to a set of zeros and poles that can be physically implemented on an FPGA, as long as discretization effects are corrected (details discussed in Section 3.2 as well).

As gate delays happen between the implementation of different sections of individual poles, it is preferred to physically implement the optimal filter in parallel with any other digital filters in the system to help retrieve a faithful implementation of the designed spectral response.

B.4 Broadband feedback cooling using a digital IIR filter

At some point during the thesis study, implementing a broadband digital feedback filter without the limitation of finite damping bandwidth limited by the closed-loop delay is considered. The motivation is to remove the nonlinear mixing noise by simply cooling the mechanical motions. It was observed in the past that broadband analog feedback cooling can reduce the third-order TIN in the bandgap by a factor of 2 but can not improve much further. With analog feedback, see Fig. B.4(a), the cooling is primarily limited to low-frequency modes below 3 MHz, primarily due to the delay in the system. These complications limit the maximum reduction of total thermomechanical noise to around 20 %.

Appendix B. Appendix

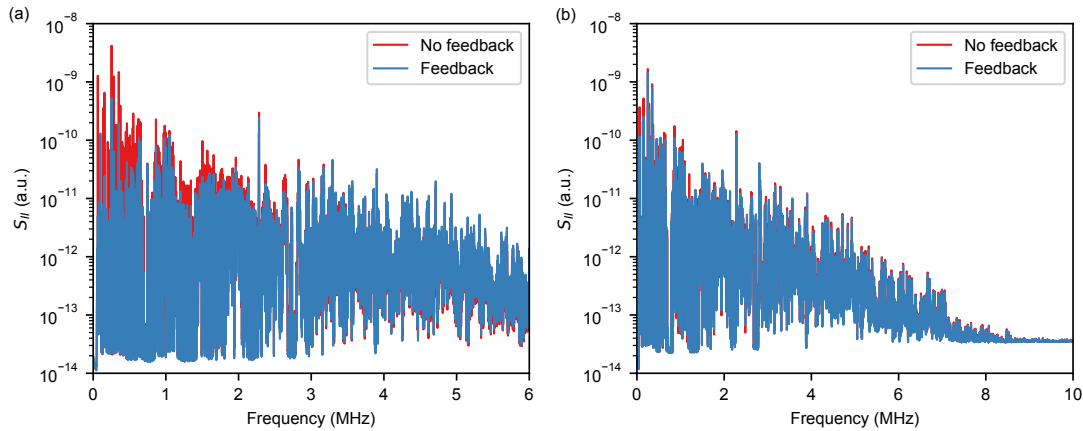


Figure B.4: Broadband feedback cooling comparison between (a) analogue feedback and (b) digital feedback.

The design consideration of a digital filter here is to mitigate the delay-induced linear phase lag with some very sharp poles to make 180° phase flips, such that mechanical modes in a much wider frequency region are being damped ($0 > \theta > -180^\circ$), see Fig. B.5. The pole bandwidths are designed to be narrow enough to avoid overlap with nearby mechanical modes.

However, there is a trade-off between the sharpness of the transition and the cooling rates, which leads to only modest cooling using the digital filter shown in Fig. B.4(b). The problem is that the sharper the phase flip, the higher the gain peak around that frequency. High peak gain will eventually saturate the linear transduction range of the intensity modulator used for modulating the optical force. There is little way around this, which originates from the gain-phase relations. Because of this limitation, the suppression of the total thermomechanical noise is limited to around 10 %.

In the end, we did not find an efficient way to cool the total thermomechanical noise optically in order to reduce nonlinear noise in the mechanical bandgap. We must increase cavity linewidth κ in the experiment using optical resonances with lower finesse.

B.5 Classical measurement noise and suppressions in interferometers

In this section, we discuss various classical measurement noises that we characterized in our MIM setup. These include acousto-optic modulator (AOM) noise, laser noise, mirror noise, interferometer phase noise, and signal cross-talk during feedback. We also discuss the choice of interferometer length balancing to cancel out different types of classical measurement noises.

B.5 Classical measurement noise and suppressions in interferometers

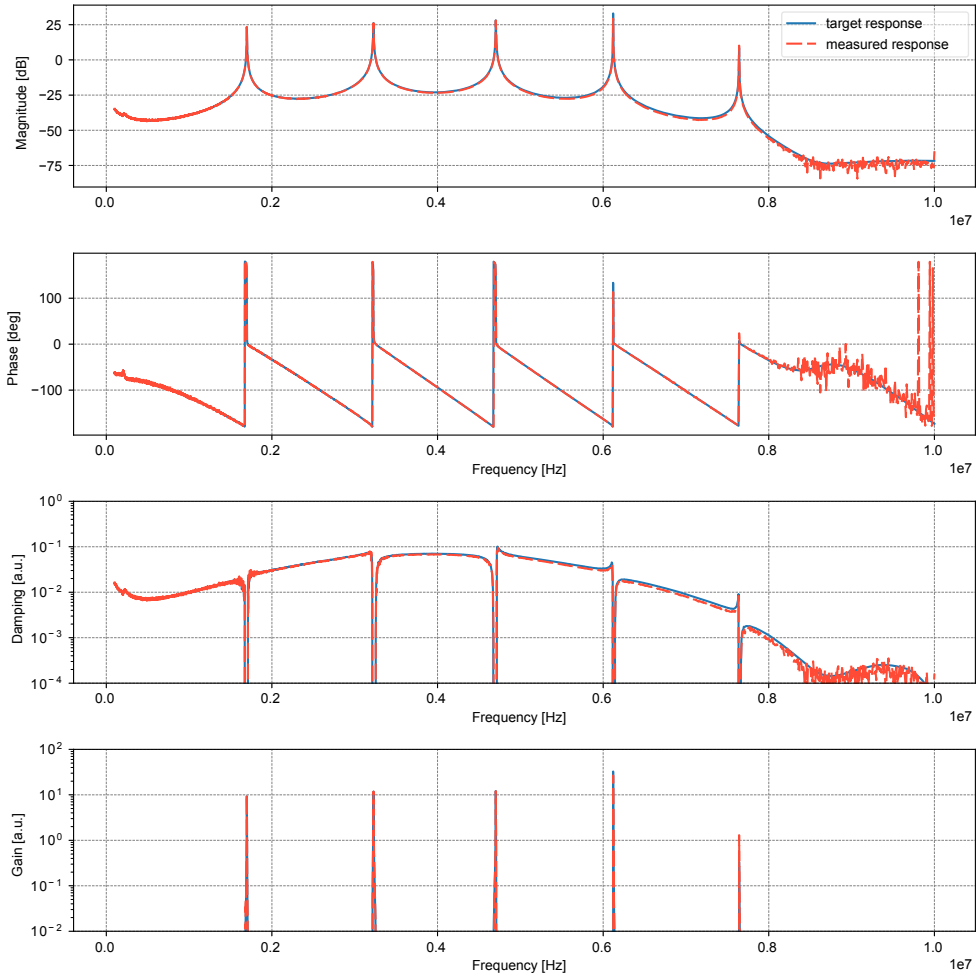


Figure B.5: Designed and measured transfer functions for broadband feedback cooling of mechanical modes spanning from 0.1 MHz to 6 MHz.

Acousto-optic modulator noise

For our previous generation optical setup, we used two sequential AOMs, both driven by voltage-controlled oscillators (VCOs) around ~ 100 MHz. We first pick the $+1$ order sideband after the first AOM and then the -1 order sideband after the second AOM, such that the end frequency of the laser is shifted by a small frequency δf determined by the frequency difference of the two VCOs. This cascaded structure allows us to conveniently actuate the frequency of the local oscillator of the interferometer. For the feedback stabilization of the interferometer phase, the direct actuation of the LO frequency is equivalently a physical integrator lock.

This method is advantageous compared to the conventional LO path length actuation using a piezo mirror, as the piezo has a finite actuation range as far as a few optical wavelengths. Therefore, AOMs significantly improve the long-term stability of the interferometer phase lock.

Appendix B. Appendix

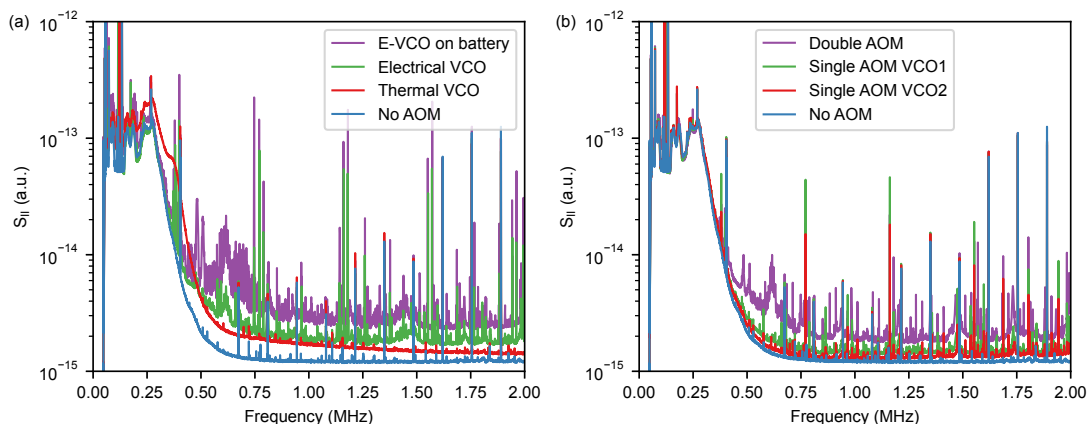


Figure B.6: Laser direct detection photocurrent noise measured at $100\ \mu\text{W}$. **(a)** Noise comparison when the laser is frequency shifted by two AOMs, which are driven by electrically tunable VCOs (socket or battery powered) and thermally tunable VCOs. **(b)** Noise comparison when the laser is frequency-shifted by either one or two AOMs driven by electrically tunable VCOs.

This benefit, however, comes at a price in the form of added phase and amplitude noise on the LO. Here, we quantify just the amplitude noise added to the LO and show that the added noise on the amplitude quadrature of the LO is already beyond the noise budget of our experiment.

We use VCOs to drive the AOMs for their excellent RF phase noise. However, from the measurement shown in Fig. B.6, at the experimentally relevant optical power level of $100\ \mu\text{W}$, the AOMs add a substantial amount of excess noise to the intensity noise of the laser. In Fig. B.6(a), we find that when the laser is frequency-shifted by two electrically tunable VCOs, the laser intensity picks up many noise peaks. We discovered that the noise level also changes when the VCOs are placed at different physical locations in the lab. We expect this noise to originate from the lab's radio-frequency (RF) noise pickup, as the school's electronic workshop assembles the VCO box, and they do not have the perfect electrical isolation. To reduce this noise pickup, we switched to the thermally tunable VCOs, where the frequency of the VCOs is tuned by temperature change and is not expected to pick up noise from the lab. Indeed, we observed that all the noise peaks disappeared; instead, a smooth excess intensity noise remained. As the power of the AOM sidebands is determined by the driving RF power, we expect the intensity noise of the VCOs to be printed onto the light.

We also found that when only one AOM is used, shown in Fig. B.6(b), driven by the electrically tunable VCO, the excess intensity noise is reduced, compared to that of the thermally tunable VCO. However, when we combine two AOMs, the excess noise is much larger than the sum of the two individuals. We found this is due to the cross-talk between the two AOM drives, with which VCO phase noise transduces to laser amplitude noise.

Due to the above reasons, we did not employ this double-AOM interferometer lock in our system and used conventional piezo mirror actuation instead.

B.5 Classical measurement noise and suppressions in interferometers

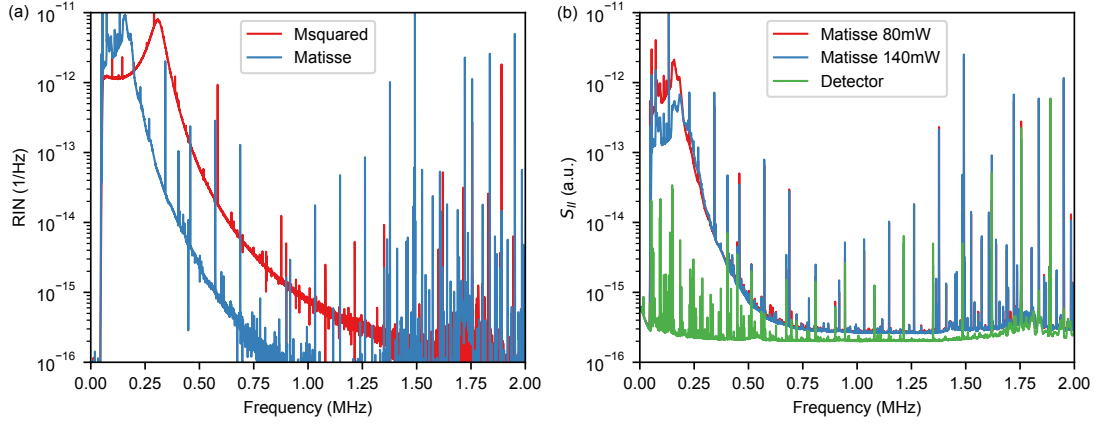


Figure B.7: **(a)** Relative intensity noise (RIN) of the two TiSa lasers used in our experiment. The laser shot noise is calibrated and subtracted from the measured spectra. At 1 MHz, and at optical power $100\mu\text{W}$, the Matisse RIN noise is $\sim 0.5\%$ of the laser shot noise. The large equidistant noise spikes were found to be the electrical noise of the Matisse intra-cavity EOM, which can be removed if the electrical connections are severed. **(b)** RIN noise (2.5 mW on the detector) of Matisse operating at different laser emission powers (shown in the legend). The overlapping relaxation oscillation tails show that RIN is not sensitive to the operating power of TiSa.

Laser noises

The classical noise from the laser is complicated to analyze for two reasons. First, we are employing a specialized single-port homodyne to cancel nonlinear noise. Second, we also have a cavity inside the interferometer loop, as the cavity correlates noises on different quadratures of the light, making the noise property different from that of the local oscillator.

We assume the laser noise of the signal mode (cavity output) is connected to the cavity input mode through a (cavity) response $\delta a_{\text{sig}}(\omega) = \chi(\omega)\delta a_{\text{in}}(\omega)$. We can analyze the laser noise contribution for a single-port homodyne as,

$$\begin{aligned}\delta I(\omega) &= (\overline{a_{\text{LO}}} + i\overline{a_{\text{sig}}}e^{-i\theta})\delta a_{\text{LO}} + h.c. + (\overline{a_{\text{sig}}} - i\overline{a_{\text{LO}}}e^{i\theta})\delta a_{\text{sig}} + h.c. \\ &= (\overline{a_{\text{LO}}} + i\overline{a_{\text{sig}}}e^{-i\theta})(\delta a_{\text{LO}} - ie^{i\theta}\chi(\omega)\delta a_{\text{in}}) + h.c.\end{aligned}\quad (\text{B.58})$$

Note that we have used the notations of the mean fields after they have passed the beam splitter. Now we expand the field fluctuation linearly $\delta a = |a|(\delta A + i\delta\phi)$ into its amplitude δA and phase $\delta\phi$ noise. For the simplification of the expression, we also define the following susceptibilities $\chi_+(\omega) = \frac{\chi(\omega) + \chi^*(-\omega)}{2\chi(0)}$ and $\chi_-(\omega) = \frac{\chi(\omega) - \chi^*(-\omega)}{2i\chi(0)}$. In the case of a cavity response, $\chi_+(\omega) = 1 + i\frac{\omega\kappa/2}{\Delta^2 + (\kappa/2)^2}$ and $\chi_-(\omega) = -i\frac{\omega\Delta}{\Delta^2 + (\kappa/2)^2}(1 + i\frac{\omega\kappa}{\Delta^2 + (\kappa/2)^2})$. Then, we can express the inter-

Appendix B. Appendix

ferometer noise in terms of the amplitude and phase noise of the laser as

$$\begin{aligned}
\delta I(\omega) &= (\overline{a_{\text{LO}}} + i\overline{a_{\text{sig}}}e^{-i\theta})(\overline{a_{\text{LO}}} - ie^{i\theta}\chi(\omega)\overline{a_{\text{in}}})(\delta A + i\delta\phi) + h.c. \\
&= 2[\overline{n_{\text{LO}}} + \overline{n_{\text{sig}}}\chi_+ + \overline{a_{\text{LO}}}\overline{a_{\text{sig}}}(\sin\theta(1 + \chi_+) + \cos\theta\chi_-)]\delta A \\
&\quad - 2[\overline{n_{\text{sig}}}\chi_- + \overline{a_{\text{LO}}}\overline{a_{\text{sig}}}(\cos\theta(1 - \chi_+) + \sin\theta\chi_-)]\delta\phi.
\end{aligned} \tag{B.59}$$

Note that the effective cavity (time) delay effect for the χ_+ and χ_- components are different, with one at $\tau_+ = -\frac{\kappa/2}{\Delta^2 + (\kappa/2)^2}$ and the other at $\tau_- = -\frac{\kappa}{\Delta^2 + (\kappa/2)^2}$.

For our discussion, we are primarily concerned with laser phase noise (characterized in Section 2.3.3) as it is equivalently a cavity displacement noise in the fast-cavity limit. For the laser amplitude noise, illustrated in Fig. B.7, we can easily avoid it by using high-frequency soft-clamped oscillators far away from the laser relaxation oscillation peak, as well as a high-finesse cavity to reduce the photon flux required to reach $C_q \sim 1$.

For the trivial case when the laser is resonant with the cavity $\Delta = 0$, the phase noise does not contribute to the photocurrent since $\chi_- = 0$, except for the delay effect of the cavity $1 - \chi_+ = -2i\omega/\kappa$ appearing on the side of the fringe ($\cos\theta \neq 0$).

Note that our expression now corresponds to a length-balanced interferometer, where the signal and the LO paths are of equal length, excluding the cavity delay. However, it is not evident that length balancing is the optimal setting with the cavity, as it induces an effective length delay on the signal path.

If we apply a response function $\chi^{\text{LO}}(\omega)$ to the LO, which could be a length/time delay $\chi_\tau(\omega) = e^{-i\omega\tau}$, since $\text{FT}_\omega[a(t - \tau)] = e^{-i\omega\tau}\text{FT}_\omega[a(t)]$, we effectively modified the interferometer signal to

$$\begin{aligned}
\delta I(\omega) &= 2[\overline{n_{\text{LO}}}\chi_+^{\text{LO}} + \overline{n_{\text{sig}}}\chi_+ + \overline{a_{\text{LO}}}\overline{a_{\text{sig}}}(\sin\theta(\chi_+ + \chi_+^{\text{LO}}) + \cos\theta(\chi_- - \chi_-^{\text{LO}}))] \delta A \\
&\quad - 2[\overline{n_{\text{LO}}}\chi_-^{\text{LO}} + \overline{n_{\text{sig}}}\chi_- + \overline{a_{\text{LO}}}\overline{a_{\text{sig}}}(\cos\theta(\chi_+^{\text{LO}} - \chi_+) + \sin\theta(\chi_-^{\text{LO}} + \chi_-))] \delta\phi.
\end{aligned} \tag{B.60}$$

At the obvious choice of matching the cavity delay time $\tau = -\frac{\kappa/2}{\Delta^2 + (\kappa/2)^2}$, the phase induced fluctuation reduced to

$$\delta I_\phi = -2[\overline{n_{\text{sig}}} + \overline{a_{\text{LO}}}\overline{a_{\text{sig}}}\sin\theta]\chi_- \delta\phi, \tag{B.61}$$

where one is left with the cavity detuning effect, which can also be canceled at the quadrature angle $\sin\theta = -\sqrt{\frac{\overline{n_{\text{sig}}}}{\overline{n_{\text{LO}}}}}$. Note that by doing this, the thermomechanical signal of the cavity is also canceled, which is not what we want. However, one could imagine that by playing with the delay time τ , one could cancel out the laser phase noise at arbitrary quadrature angles, where the thermomechanical signal of the cavity can, in principle, be maximized.

Feedback signal cancellation

In the case where one is not concerned with laser noises but with feedforward signals δA and $\delta\phi$ only on the signal path (e.g., for mirror noise cancellation or feedback cooling), the result would be

$$\begin{aligned}\delta I_{sig}(\omega) &= (\overline{a_{LO}} + i\overline{a_{sig}}e^{-i\theta})(-ie^{i\theta}\chi(\omega)\overline{a_{in}})(\delta A + i\delta\phi) + h.c. \\ &= 2[\overline{n_{sig}}\chi_+ + \overline{a_{LO}}\overline{a_{sig}}(\sin\theta\chi_+ + \cos\theta\chi_-)]\delta A \\ &\quad - 2[\overline{n_{sig}}\chi_- + \overline{a_{LO}}\overline{a_{sig}}(-\cos\theta\chi_+ + \sin\theta\chi_-)]\delta\phi.\end{aligned}\quad (B.62)$$

In this setting, as the modulation is only on the signal path instead of both, it is possible to cancel out the amplitude modulation (e.g., from feedback cooling) at the local oscillator angle $\sin\theta = -\sqrt{\frac{n_{sig}}{n_{LO}}}$. This angle corresponds to the phase quadrature of the combined field where the thermomechanical signal is maximized, and there is a corresponding LO amplitude to cancel the TIN simultaneously. This arrangement is used in an earlier iteration of the experiment, where an auxiliary laser (M squared) is used to measure the thermomechanical signal and perform feedback cooling to suppress photothermal mechanical instabilities while avoiding cross-talk between measurement and feedback.

Mirror noise cancellation

The mirror motions can be modeled as an effective phase noise $\delta\phi(\omega) = \Delta(\omega)/i\omega$ on the signal path with susceptibilities $\chi_+(\omega) = -i\frac{\omega\kappa/2}{\Delta^2 + (\kappa/2)^2}$ and $\chi_-(\omega) = i\frac{\omega\Delta}{\Delta^2 + (\kappa/2)^2}$. Section 2.3.1 discussed a scheme to cancel the mirror noise by feedforwarding the measurement record from an auxiliary laser to the science laser. We must apply the feedforward signal to the interferometer's signal and the LO arms for mirror noise cancellation. Otherwise, there is no way to cancel the mirror noise in detection.

An easy choice is to cancel out both the cavity delay and transduction on the signal path by picking the laser phase modulation $\delta\phi(\omega) = -\Delta(\omega)/i\omega$, leaving the combined (laser + mirror) susceptibility $\chi_+(\omega) = 1$ and $\chi_-(\omega) = 0$. With this choice of phase modulation, we arrive at the photocurrent expression as

$$\begin{aligned}\delta I(\omega) &= 2[\overline{n_{LO}}\chi_+^{LO} + \overline{n_{sig}} + \overline{a_{LO}}\overline{a_{sig}}(\sin\theta(1 + \chi_+^{LO}) + \cos\theta(-\chi_-^{LO}))]\delta A \\ &\quad - 2[\overline{n_{LO}}\chi_-^{LO} + \overline{a_{LO}}\overline{a_{sig}}(\cos\theta(\chi_+^{LO} - 1) + \sin\theta(\chi_-^{LO}))]\delta\phi,\end{aligned}\quad (B.63)$$

where we are left with the choice of a proper LO delay. The right choice is to balance the LO without considering the cavity delay, i.e., $\chi_+^{LO} = 1$ and $\chi_-^{LO} = 0$. In this case, we can not cancel the intrinsic laser phase noise on the photocurrent, but since the characterized laser noise (Section 2.3.3) is sufficiently low, we do not mind that much.

Now, let us consider what feedback filter function we must apply to cancel out the mirror noise over a large frequency band, e.g., 100 kHz. Taking the loop delay τ into consideration,

Appendix B. Appendix

we can write down the EOM frequency modulation $\delta v(t)$ given the actuation voltage $\delta V(t)$, which is from the measurement data $\delta\Delta$ filtered by the response $g(t)$.

$$\delta v(t) = \delta\dot{\theta}(t) = \frac{d}{dt} \int g_{\text{mod}}(t' - t) \delta V(t) dt' \quad (\text{B.64})$$

$$\delta V(t) = \int g(t' - t) \delta\Delta(t - \tau) \quad (\text{B.65})$$

$$v(\omega) = -i\omega g_{\text{mod}}(\omega) g(\omega) e^{-i\omega\tau} \Delta(\omega), \quad (\text{B.66})$$

where $g(\omega)$ is the feedback frequency response, and $g_{\text{mod}}(\omega)$ the modulator frequency response.

In the hypothetical sense, we can set $v(\omega) = \Delta(\omega)$ to allow a perfect mirror noise cancellation, but would require a non-causal filter response of

$$g(\omega) = \frac{e^{-i\omega\tau}}{i\omega g_{\text{mod}}(\omega)}. \quad (\text{B.67})$$

Nonetheless, we can approach this response using an analog PID controller with the following filter functions

$$g_{\text{lp}}(\omega) = \frac{1}{1 - i\frac{\omega}{\omega_{\text{lp}}}} \quad (\text{B.68})$$

$$g_{\text{hp}}(\omega) = \frac{1}{1 + i\frac{\omega_{\text{hp}}}{\omega}} \quad (\text{B.69})$$

$$g_{\text{PID}}(\omega) = K_p + K_i \frac{1}{-i\omega} + K_d(-i\omega) \quad (\text{B.70})$$

We got the best filter response illustrated in Fig.B.8 through numerical optimization and implemented in Section 2.3.1.

Closed-loop feedback response

In order to effectively cool the mechanical modes or damp unstable modes, we need to engineer the chain response from the mechanical modes, to optical detection, and then to the feedback force. Usually, either an external delay line or analog and digital filters are used such that the feedback damping is efficient,

$$\Gamma_{\text{eff}}(\omega) = \Gamma_m [1 + g_{\text{fb}}(\omega) \cos \delta\phi(\omega)] \quad (\text{B.71})$$

$$\Omega_{\text{eff}}(\omega) = \Omega_m [1 - g_{\text{fb}}(\omega) \frac{\omega\Gamma_m}{\Omega_m^2} \sin \delta\phi(\omega)] \quad (\text{B.72})$$

where $\delta\phi(\omega) = \phi(\omega) + \pi/2$ is the residual phase shift from the ideal feedback phase $-\pi/2$.

The total feedback response $\chi_{\text{fb}} = F/x_m$ consists of many components. The open loop response starts from thermal forces δF_{th} to mechanical response χ_m , then cavity transduction

B.5 Classical measurement noise and suppressions in interferometers

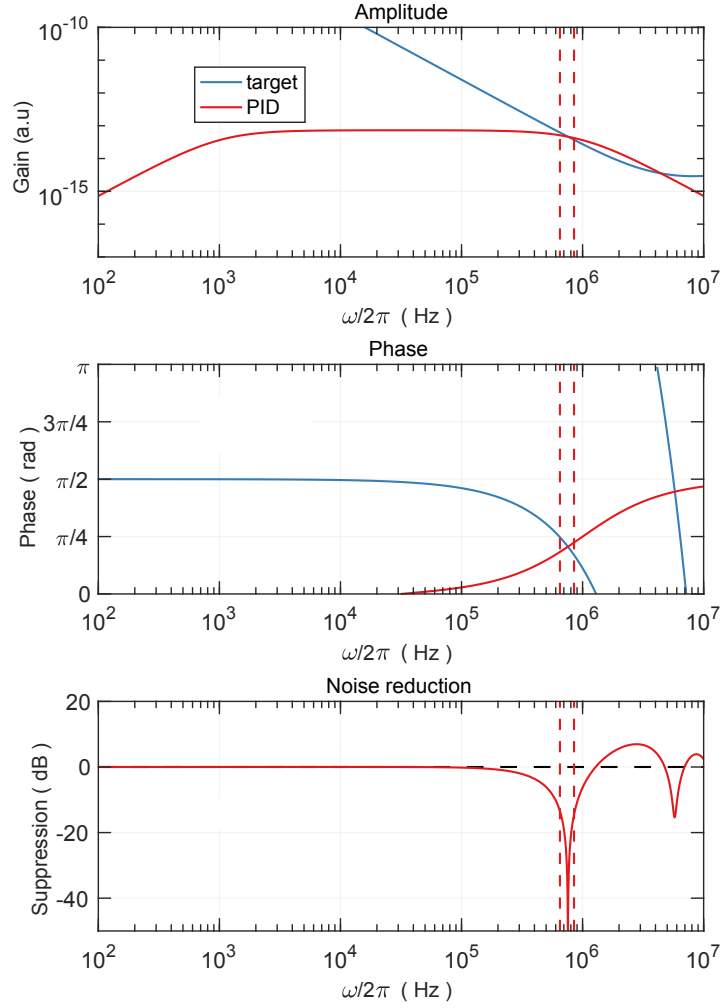


Figure B.8: Optimized mirror noise suppression around 1 MHz. The optimization is done by tuning the feedback delay and the PID gains.

$\chi_{\text{cav},m}$, interferometer detection $\chi_{\text{cav} \rightarrow \text{DET}}$, detection to intensity modulation $\chi_{\text{DET} \rightarrow \text{IM}}$, at which point we arrives at the light intensity signal δA ,

$$\delta A = \frac{x_m \cdot \chi_{\text{cav},m} \chi_{\text{cav} \rightarrow \text{DET}} \chi_{\text{DET} \rightarrow \text{IM}}}{1 - g \chi_{\text{IM} \rightarrow \text{cav}} \chi_{\text{cav},A} \chi_{\text{cav} \rightarrow \text{DET}} \chi_{\text{DET} \rightarrow \text{IM}}} \delta F_{\text{th}} \quad (\text{B.73})$$

where we also considered the finite isolation between the optical feedback signal and the optical measurement, quantified by gain coefficient g . A small g can be detrimental for experiments requiring high feedback gain. In the experiment, we separate these two signals using edge-pass optical filters that can separate two optical wavelengths (of science and auxiliary lasers) with at least 120 dB isolation. In this case, we can safely set $g = 0$. The passive polarization isolation is insufficient as we measured only a maximum of 45 dB isolation over a long time.

Appendix B. Appendix

The force actuated on the mechanical mode needs to go through the cavity input response $\chi_{\text{IM} \rightarrow \text{cav}}$, as well as the optical force response $\chi_{\text{cav},F}$, at which point we finally closed the mechanical actuation feedback loop,

$$F = \chi_{\text{IM} \rightarrow \text{cav}} \chi_{\text{cav},F} \delta A \quad (\text{B.74})$$

$$F = \frac{x_m \cdot \chi_{\text{cav},F} \chi_{\text{cav},m} \chi_{\text{cav} \rightarrow \text{DET}} \chi_{\text{DET} \rightarrow \text{IM}} \chi_{\text{IM} \rightarrow \text{cav}}}{1 - g \chi_{\text{cav},A} \chi_{\text{cav} \rightarrow \text{DET}} \chi_{\text{DET} \rightarrow \text{IM}} \chi_{\text{IM} \rightarrow \text{cav}}} \delta F_{\text{th}} \quad (\text{B.75})$$

We show here the expressions of a few important response functions discussed above

$$\chi_{m \rightarrow \text{DET}} = \frac{I(\omega)}{Q_m(\omega)} \propto -2[\overline{n_{\text{sig}}} \chi_-^m + \overline{a_{\text{LO}} a_{\text{sig}}} (-\cos \theta \chi_+^m + \sin \theta \chi_-^m)] \quad (\text{B.76})$$

$$\chi_{\text{cav},F} = \frac{n(\omega)}{A(\omega)} \propto 1 + i \frac{\omega \kappa / 2}{\Delta^2 + (\kappa / 2)^2} \quad (\text{B.77})$$

$$\chi_{A \rightarrow \text{DET}} = \frac{I(\omega)}{Q_m(\omega)} \propto 2[\overline{n_{\text{sig}}} \chi_+^A + \overline{a_{\text{LO}} a_{\text{sig}}} (\sin \theta \chi_+^A + \cos \theta \chi_-^A)] \quad (\text{B.78})$$

$$\chi_+^m = \frac{\kappa / 2}{\Delta^2 + (\kappa / 2)^2} \left(1 + \frac{i\omega(-\Delta^2 + (\kappa / 2)^2)}{\kappa / 2(\Delta^2 + (\kappa / 2)^2)} \right) \quad (\text{B.79})$$

$$\chi_-^m = \frac{-\Delta}{\Delta^2 + (\kappa / 2)^2} \left(1 + i \frac{\omega \kappa}{\Delta^2 + (\kappa / 2)^2} \right) \quad (\text{B.80})$$

$$\chi_+^A = 1 + i \frac{\omega \kappa / 2}{\Delta^2 + (\kappa / 2)^2} \quad (\text{B.81})$$

$$\chi_-^A = -i \frac{\omega \Delta}{\Delta^2 + (\kappa / 2)^2} \left(1 + i \frac{\omega \kappa}{\Delta^2 + (\kappa / 2)^2} \right) \quad (\text{B.82})$$

Here, we can see that the effective cavity delay on the symmetric and anti-symmetric field components, characterized by χ_+ and χ_- , are different. Therefore, the effective cavity delay will also differ in homodyne detection of different quadrature angles. However, this is not a physical delay length. More accurately, this is cavity-induced linear phase response for Fourier frequency ω in the fast-cavity limit $\omega \ll \kappa$.

In the experiment, we do not have direct access to this feedback response, but we do have the following two chain responses accessible using phase modulation (PM) and intensity modulation (IM) driven by the Red Pitaya (RP) FPGA network analyzer,

$$\chi_{PM} = \frac{\chi_{\text{RP} \rightarrow \text{PM}} \chi_{\text{PM} \rightarrow \text{cav}} \chi_{\text{cav},m} \chi_{\text{cav} \rightarrow \text{DET}} \chi_{\text{DET} \rightarrow \text{RP}}}{1 - g \chi_{\text{IM} \rightarrow \text{cav}} \chi_{\text{cav},A} \chi_{\text{cav} \rightarrow \text{DET}} \chi_{\text{DET} \rightarrow \text{IM}}} \quad (\text{B.83})$$

$$\chi_{IM} = \frac{\chi_{\text{IM} \rightarrow \text{cav}} \chi_{\text{cav},A} \chi_{\text{cav} \rightarrow \text{DET}} \chi_{\text{DET} \rightarrow \text{IM}}}{1 - g \chi_{\text{IM} \rightarrow \text{cav}} \chi_{\text{cav},A} \chi_{\text{cav} \rightarrow \text{DET}} \chi_{\text{DET} \rightarrow \text{IM}}}. \quad (\text{B.84})$$

By comparing them with the chain response of mechanical actuation, the best way to mimic the actual feedback response $\chi_{\text{fb}} = F/x_m$ is to use the phase modulation scheme χ_{PM} and try to match the delay length, either physically or in post-processing, such that $\chi_{\text{RP} \rightarrow \text{PM}} \chi_{\text{PM} \rightarrow \text{cav}} = \chi_{\text{RP} \rightarrow \text{IM}} \chi_{\text{IM} \rightarrow \text{cav}} \chi_{\text{cav},F}$.

We show in Fig. B.9 a few measurements of the system chain responses measured by the VNA without a tailored digital or analog filter. The auxiliary laser intensity is modulated, and the

B.5 Classical measurement noise and suppressions in interferometers

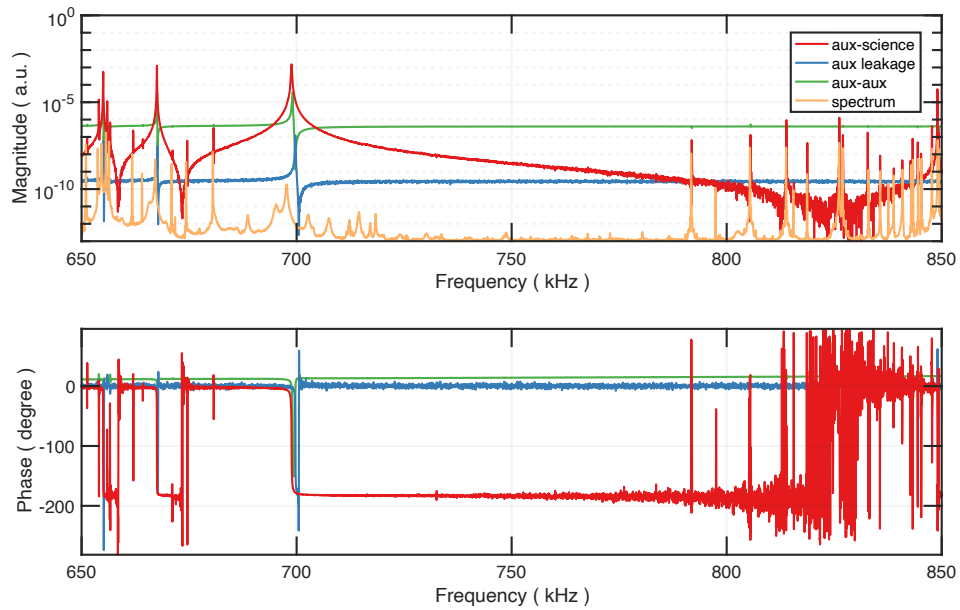


Figure B.9: MIM response measurements using modulation on the auxiliary laser, and detection on both the auxiliary and the science lasers. The open loop feedback response is shown in red, and cross-talk leakage between the two lasers, isolated using polarization isolation, is shown in blue. Compared to the auxiliary laser measurement (green), the isolation achieved is around 40 dB. The mechanical spectrum is also shown as a guide to the eye for comparison to the measured responses.

aux-aux response is measured using direct detection, showing the dispersive features due to mechanical responses. The leakage to the science detection is also measured, showing 40 dB isolation in polarization. In the feedback cooling experiment, the isolation required is much higher than this, and chromatic filters are needed to achieve more isolation of 120 dB. The aux-science response is shown as well. Together with the mechanical spectrum, we can distinguish the soft-clamped mode (700 kHz), other membrane modes with different levels of optomechanical couplings due to spatial symmetries, as well as mirror modes that can not be driven at all.

B.6 Simplified derivation of optomechanical squeezing

Here, we go through the simplified derivation of optomechanical squeezing when the cavity is driven on resonance. In the following, we omit the quantum operator hat on the optical annihilation operator \hat{a} and the mechanical annihilation operator \hat{b} . The optomechanical Hamiltonian is

$$\begin{aligned}\hat{H} &= \hbar(\Delta + G\hat{q})a^\dagger a + \hbar\Omega b^\dagger b \\ &= \hbar\Delta a^\dagger a + \hbar\Omega b^\dagger b + \hbar g_0 a^\dagger a(b^\dagger + b)\end{aligned}\quad (\text{B.85})$$

where the vacuum optomechanical coupling rate is related to the cavity pulling factor by $g_0 \equiv Gx_{\text{zpt}}$, and the position operator can be expressed as $\hat{q} = x_{\text{zpt}}(b^\dagger + b)$, with the zero-point motion $x_{\text{zpt}} = \sqrt{\frac{\hbar}{2m\Omega}}$. Using the RWA Langevin equation

$$\dot{\hat{O}} = \frac{1}{i\hbar} [\hat{O}, \hat{H}_{\text{sys}}] - [\hat{O}, a^\dagger] \left(\frac{\kappa}{2} a - \sqrt{\kappa} a_{\text{in}} \right) + \left(\frac{\kappa}{2} a^\dagger - \sqrt{\kappa} a_{\text{in}}^\dagger \right) [\hat{O}, a^\dagger] \quad (\text{B.86})$$

for the optical field and the general Langevin equation (see section B.1.1 for the general QLE, and section B.1.2 for the QLE with the rotating wave approximation.)

$$\dot{\hat{O}} = \frac{1}{i\hbar} [\hat{O}, \hat{H}_{\text{sys}}] + i\sqrt{2\Gamma} [\hat{O}, \hat{Q}] \hat{P}_{\text{in}} + \frac{\Gamma}{2i\Omega} \{ [\hat{O}, \hat{Q}], \dot{\hat{Q}} \}_+ \quad (\text{B.87})$$

for the mechanical oscillator, we have the following set of coupled equations

$$\dot{a} = - \left[\frac{\kappa}{2} + i(\Delta + \sqrt{2}g_0\hat{Q}) \right] a + \sqrt{\kappa} a_{\text{in}} \quad (\text{B.88})$$

$$\dot{\hat{Q}} = \Omega \hat{P} \quad (\text{B.89})$$

$$\dot{\hat{P}} = -\Omega \hat{Q} + \sqrt{2\Gamma} \hat{P}_{\text{in}} - \Gamma \hat{P} - \sqrt{2}g_0 a^\dagger a \quad (\text{B.90})$$

where we define dimensionless mechanical position operator $\hat{Q} = (b^\dagger + b)/\sqrt{2}$ and momentum operator $\hat{P} = i(b^\dagger - b)/\sqrt{2}$. We could also define the optical quadrature operators $\hat{X} = (a^\dagger + a)/\sqrt{2}$ and $\hat{Y} = i(a^\dagger - a)/\sqrt{2}$. From here, it is also convenient to define the optomechanical

B.6 Simplified derivation of optomechanical squeezing

coupling rate $g = g_0 \bar{a}$. The Mechanical motion obeys

$$\ddot{\hat{Q}} + \Gamma \dot{\hat{Q}} + \Omega^2 \hat{Q} = \sqrt{2\Gamma} \Omega \hat{P}_{\text{in}} - 2g\Omega \hat{X} \quad (\text{B.91})$$

$$\hat{Q}(\omega) = \chi(\omega) \left(\sqrt{2\Gamma} \hat{P}_{\text{in}}(\omega) - 2g \hat{X}(\omega) \right), \quad (\text{B.92})$$

where we introduce the mechanical susceptibility $\chi(\omega) \equiv \Omega / (\Omega^2 - \omega^2 - i\omega\Gamma)$, and the dimensionless input momentum fluctuation $\hat{P}_{\text{in}}(t) = \frac{i}{\sqrt{2}} \left(b_{\text{in}}^\dagger(t) - b_{\text{in}}(t) \right) \equiv \frac{x_{\text{zp}} \hat{P}(t)}{\hbar\sqrt{\Gamma}}$ with correlation

$$S_{FF}(\omega) = 2m\Gamma(\omega)\hbar\omega(\bar{n}(\omega) + 1) \quad (\text{B.93})$$

$$S_{FF}(-\omega) = 2m\Gamma(\omega)\hbar\omega\bar{n}(\omega). \quad (\text{B.94})$$

The asymmetry is the result of operators not generally commuting at different frequencies $[\hat{O}(\omega), \hat{O}(\omega')] \neq 0$, though not measurable in linear quadrature measurements. However, if one starts from the RWA QLE for the mechanics, then the force will be symmetric, and the mechanical susceptibility will be asymmetric instead.

The coupling from the mechanical oscillator to the optical field is modeled in the Fourier domain as

$$\hat{X}(\omega) = \frac{\sqrt{\kappa} \hat{X}_{\text{in}}(\omega)}{\kappa/2 - i\omega} \quad (\text{B.95})$$

$$\hat{Y}(\omega) = \frac{\sqrt{\kappa} \hat{Y}_{\text{in}}(\omega) - 2g\hat{Q}(\omega)}{\kappa/2 - i\omega} \quad (\text{B.96})$$

where we assume zero detuning ($\Delta = 0$) such that the mechanical motion only couples to the optical phase quadrature \hat{Y} . Substituting (B.95) into (B.92), we arrive at the expression for the mechanical position

$$\hat{Q}(\omega) = \sqrt{2\Gamma} \chi(\omega) \left(\hat{P}_{\text{in}}(\omega) - \sqrt{2C_{\text{eff}}} \hat{X}(\omega)_{\text{in}} \right), \quad (\text{B.97})$$

where we introduce the optomechanical cooperativity $C = \frac{4g^2}{\kappa\Gamma}$ and the effective optomechanical cooperativity $C_{\text{eff}} \equiv \frac{C}{(1-2i\omega/\kappa)^2}$. Using the input-output relation, one can arrive at the output field quadrature expressions

$$\hat{X}_{\text{out}}(\omega) = -\frac{\kappa/2 + i\omega}{\kappa/2 - i\omega} \hat{X}_{\text{in}}(\omega) \quad (\text{B.98})$$

$$\begin{aligned} \hat{Y}_{\text{out}}(\omega) &= -\frac{\kappa/2 + i\omega}{\kappa/2 - i\omega} \hat{Y}_{\text{in}}(\omega) - \frac{2\sqrt{\kappa}g\hat{Q}(\omega)}{\kappa/2 - i\omega} \\ &= -\frac{\kappa/2 + i\omega}{\kappa/2 - i\omega} \hat{Y}_{\text{in}}(\omega) - 2\sqrt{\Gamma C_{\text{eff}}} \hat{Q}(\omega) \end{aligned} \quad (\text{B.99})$$

$$\begin{aligned} \hat{X}_{\text{out}}^\theta(\omega) &= \hat{X} \cos\theta + \hat{Y} \sin\theta \\ &= -\left[\frac{\kappa/2 + i\omega}{\kappa/2 - i\omega} \cos\theta + 4\Gamma C_{\text{eff}} \chi(\omega) \sin\theta \right] \hat{X}_{\text{in}}(\omega) \\ &\quad - \frac{\kappa/2 + i\omega}{\kappa/2 - i\omega} \sin\theta \hat{Y}_{\text{in}}(\omega) + 2\Gamma \sqrt{2C_{\text{eff}}} \chi(\omega) \sin\theta \hat{P}_{\text{in}}(\omega) \end{aligned} \quad (\text{B.100})$$

The symmetrized power spectral density that the homodyne detection would measure is then

Appendix B. Appendix

given by

$$\begin{aligned} \bar{S}_{X_{\text{out}}^\theta X_{\text{out}}^\theta}(\omega) &= \frac{1}{2} + 8\Gamma^2 |\chi(\omega)|^2 |C_{\text{eff}}| \left(\bar{n}_{\text{th}} + |C_{\text{eff}}| + \frac{1}{2} \right) \sin^2 \theta \\ &\quad + \Gamma |C_{\text{eff}}| (\chi(\omega) + \chi^*(\omega)) \sin 2\theta \end{aligned} \quad (\text{B.101})$$

From here on could recognize the backaction quanta $n_{\text{ba}} \equiv |C_{\text{eff}}|$. The first term is the original quantum noise on the optical quadrature without any optomechanical interaction. The second term is the mechanical motion, which is always positive in the presence of radiation pressure driving. The third term is the correlation between the optical amplitude quadrature and the driven mechanical motion printed on the optical phase quadrature, which is responsible for ponderomotive squeezing and giving the power spectral density an asymmetric shape. The necessary and sufficient condition for observing squeezing $\bar{S}_{X_{\text{out}}^\theta X_{\text{out}}^\theta}(\omega) < \frac{1}{2}$ is

$$\bar{n}_{\text{th}} + n_{\text{ba}} + \frac{1}{2} < \frac{\Omega^2 - \omega^2}{2\Gamma\Omega \tan \theta}. \quad (\text{B.102})$$

We can see that squeezing can not occur precisely on the mechanical resonance $\omega = \Omega$, but is always present for some range of optical quadrature angles θ , since the right side goes to infinity when $|\theta| \rightarrow 0$. And the Fourier frequency range that one could observe squeezing is roughly $|\Omega - \omega| \sim \Gamma(\bar{n}_{\text{th}} + n_{\text{ba}})$, and the magnitude of the quantum squeezing relative to the optical shot noise is $\sim \frac{n_{\text{ba}}}{\bar{n}_{\text{th}} + n_{\text{ba}}}$.

B.7 Simplified picture of measurement-based feedback cooling

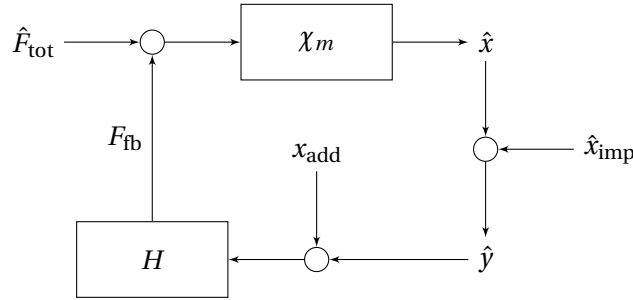


Figure B.10: Measurement-based feedback cooling diagram when the fast optical cavity is driven on resonance.

The complete picture of our system under continuous feedback is illustrated in Fig. 3.7. In this section, we first discuss a simplified picture for measurement-based feedback cooling, shown in Fig. B.10, which corresponds to the limiting case when the cavity is pumped by a laser on resonance $\Delta = 0$. In our experiment, we pump the cavity at the magic detuning Δ_* discussed in Section 2.4.

The feedback loop equations are covered in [17, 86]. Here, we cover the most essential

B.7 Simplified picture of measurement-based feedback cooling

equations for a resonantly driven optical cavity. Note that here we enforce the treatment that the feedback force F_{fb} is quantum, though it is strictly classical. This treatment is also applied in many other sections of this thesis, especially when dissipations are involved (e.g., Section A.3 and Section 2.5). A formal treatment requires symmetrization of the quantum observable in the form of auto/cross-correlations in measurements,

$$2\bar{S}_{\hat{A}\hat{B}}(\omega) = \text{FT}_{\tau}[\langle \hat{A}^{\dagger}(\tau)\hat{B}(0) + \hat{B}(0)\hat{A}^{\dagger}(\tau) \rangle] = S_{\hat{A}\hat{B}}(\omega) + S_{\hat{B}^{\dagger}\hat{A}^{\dagger}}(-\omega). \quad (\text{B.103})$$

In the following, we make a simple argument that there is no difference in the measurement result, whether the feedback force is classical or quantum. We write down the set of equations that describes the simplest feedback problem

$$(F_{\text{fb}} + \hat{F})\chi_m(\omega) + \hat{x}_{\text{imp}} = \hat{y} \quad (\text{B.104})$$

$$F_{\text{fb}} = H(\omega)\bar{\hat{y}} \quad (\text{B.105})$$

where we marked $\bar{\hat{y}}$ such that its auto-correlation function requires symmetrization. We can now calculate the spectral density as in

$$\hat{F}\chi_m(\omega) + \hat{x}_{\text{imp}} = \hat{y} - H(\omega)\chi_m(\omega)\bar{\hat{y}} \quad (\text{B.106})$$

$$\frac{S_{\hat{F}\hat{F}}|\chi_m(\omega)|^2 + S_{\hat{x}_{\text{imp}}\hat{x}_{\text{imp}}}}{|1 - H(\omega)\chi_m(\omega)|^2} = S_{\hat{y}\hat{y}} + \frac{|H(\omega)\chi_m(\omega)|^2}{|1 - H(\omega)\chi_m(\omega)|^2}(\bar{S}_{\hat{y}\hat{y}} - S_{\hat{y}\hat{y}}) - \frac{H(\omega)\chi_m(\omega)(S_{\hat{y}\bar{\hat{y}}} - S_{\hat{y}\hat{y}}) + H(-\omega)\chi_m(-\omega)(S_{\bar{\hat{y}}\hat{y}} - S_{\hat{y}\hat{y}})}{|1 - H(\omega)\chi_m(\omega)|^2} \quad (\text{B.107})$$

$$\frac{\bar{S}_{\hat{F}\hat{F}}|\chi_m(\omega)|^2 + \bar{S}_{\hat{x}_{\text{imp}}\hat{x}_{\text{imp}}}}{|1 - H(\omega)\chi_m(\omega)|^2} = \bar{S}_{\hat{y}\hat{y}} \quad (\text{B.108})$$

where the relation that $S_{\hat{y}\bar{\hat{y}}}(\omega) + S_{\bar{\hat{y}}\hat{y}}(-\omega) = 2\bar{S}_{\hat{y}\hat{y}}(\omega)$ is used. The result is the same as treating the force as quantum. Therefore, in the following, we treat everything as if they are quantum observables ($\hat{}$ omitted).

Following the feedback diagram, we derive the closed-loop results

$$F_{\text{tot}}(\omega) = F_{\text{th}}(\omega) + F_{\text{BA}}(\omega) \quad (\text{B.109})$$

$$F_{\text{fb}}(\omega) = \frac{(F_{\text{tot}}(\omega)\chi_m(\omega) + x_{\text{imp}} + x_{\text{add}})H(\omega)}{1 - \chi_m(\omega)H(\omega)} \quad (\text{B.110})$$

$$y(\omega) = (F_{\text{tot}}(\omega) + F_{\text{fb}}(\omega))\chi_m(\omega) + x_{\text{imp}}(\omega) \quad (\text{B.111})$$

$$\begin{aligned} &= \frac{\chi_m(\omega)}{1 - \chi_m(\omega)H(\omega)}F_{\text{tot}}(\omega) + \frac{1}{1 - \chi_m(\omega)H(\omega)}x_{\text{imp}}(\omega) + \frac{\chi_m(\omega)H(\omega)}{1 - \chi_m(\omega)H(\omega)}x_{\text{add}}(\omega) \\ x(\omega) &= (F_{\text{tot}}(\omega) + F_{\text{fb}}(\omega))\chi_m(\omega) \quad (\text{B.112}) \\ &= \frac{\chi_m(\omega)}{1 - \chi_m(\omega)H(\omega)}F_{\text{tot}}(\omega) + \frac{\chi_m(\omega)H(\omega)}{1 - \chi_m(\omega)H(\omega)}(x_{\text{imp}}(\omega) + x_{\text{add}}(\omega)) \end{aligned}$$

where F_{tot} is the total force fluctuations experienced by the mechanical mode, including the thermal force F_{th} and the quantum backaction force F_{BA} . The mechanical mode also

Appendix B. Appendix

experiences a feedback force F_{fb} , which is determined by the measurement record $y(\omega)$ as well as the feedback filter response $H(\omega)$. The mechanical position $x(\omega)$ describes the mechanical motion to be cooled.

We can derive the corresponding spectral densities of the in-loop measurement record y , as well as the out-of-loop mechanical position x ,

$$S_{yy}(\omega) = \left| \frac{\chi_m(\omega)}{1 - \chi_m(\omega)H(\omega)} \right|^2 S_{FF}^{\text{tot}}(\omega) + \frac{1}{|1 - \chi_m(\omega)H(\omega)|^2} S_{xx}^{\text{imp}}(\omega) + \left| \frac{\chi_m(\omega)H(\omega)}{1 - \chi_m(\omega)H(\omega)} \right|^2 S_{xx}^{\text{add}}(\omega) \quad (\text{B.113})$$

$$S_{xx}(\omega) = \left| \frac{\chi_m(\omega)}{1 - \chi_m(\omega)H(\omega)} \right|^2 S_{FF}^{\text{tot}}(\omega) + \left| \frac{\chi_m(\omega)H(\omega)}{1 - \chi_m(\omega)H(\omega)} \right|^2 (S_{xx}^{\text{imp}}(\omega) + S_{xx}^{\text{add}}(\omega)) \quad (\text{B.114})$$

We can analyze how the feedback filter H selection influences the mechanical phonon occupancy with these expressions.

Note that an approximation is used here, that F_{BA} is uncorrelated with x_{imp} . The approximation is only valid for resonant probing ($\Delta = 0$) and optical phase quadrature detection. In the general case, there is a correlation between the backaction force F_{BA} and the measurement imprecision x_{imp} , which leads to measurement beyond SQL and ponderomotive squeezing. However, we can rotate the measurement quadrature angle so that the force-imprecision correlation will vanish when the mechanical SNR is maximized. However, measurement imprecision other than that of the quantum optical origin, e.g., cavity frequency noise, requires a more delicate treatment, which is covered in Fig. 3.7.

Optimal filter through functional minimization

With the expressions of these spectral density functions in mind, one might think that we can optimize the mechanical phonon occupation $\int S_{xx}(\omega)d\omega$ through functional minimization using the feedback filter response $H(\omega)$. This approach was investigated in the thesis [86]. Here, we show that the feedback filter obtained through functional minimization is not stable and can not be used for real-time feedback cooling experiments, and that the filter covered in Section 3.2.1 is the only correct one.

The optimal filter design can be obtained by functional minimization over the final phonon

B.7 Simplified picture of measurement-based feedback cooling

occupancy by introducing a perturbation function $\epsilon\eta(\omega)$,

$$n \propto \int S_{xx}(\omega) d\omega \quad (\text{B.115})$$

$$\begin{aligned} n(\epsilon \rightarrow 0) &\propto \int d\omega \frac{S_{FF}^{\text{tot}}(\omega) + |H(\omega) + \epsilon\eta(\omega)|^2 S_{xx}^{\text{imp}}(\omega)}{|\chi_m^{-1}(\omega) - (H(\omega) + \epsilon\eta(\omega))|^2} \\ &= \int d\omega \frac{S_{FF}^{\text{tot}}(\omega) + (|H(\omega)|^2 + 2\epsilon\text{Re}[H(\omega)\eta^*(\omega)]) S_{xx}^{\text{imp}}(\omega)}{|\chi_m^{-1}(\omega) - H(\omega)|^2 - 2\epsilon\text{Re}[(\chi_m^{-1}(\omega) - H(\omega))\eta^*(\omega)]} \end{aligned} \quad (\text{B.116})$$

$$\epsilon\partial_\epsilon n = n(\epsilon) - n(0) \propto \int d\omega 2\epsilon\text{Re} \left[\eta^*(\omega) \frac{S_{FF}^{\text{tot}}(\omega) + \chi_m^{*-1}(\omega)H(\omega)S_{xx}^{\text{imp}}(\omega)}{(\chi_m^{-1}(\omega) - H(\omega))^{-1} |\chi_m^{-1}(\omega) - H(\omega)|^4} \right] \quad (\text{B.117})$$

which leads to the "optimal" feedback filter response

$$H_{\text{opt}}(\omega) = -\chi_m^*(\omega) \frac{S_{FF}^{\text{tot}}(\omega)}{S_{xx}^{\text{imp}}(\omega)}. \quad (\text{B.118})$$

We show below that this filter is unstable.

Stability analysis

The stability of the closed-loop system with the filter $H(s)$ analyzed above, is essentially the stability of the following response functions

$$\frac{\chi_m(s)}{1 - \chi_m(s)H(s)} \quad \text{or} \quad \frac{\chi_m(s)H(s)}{1 - \chi_m(s)H(s)}. \quad (\text{B.119})$$

Since it is a closed-loop system, it does not matter whether χ_m or H are stable. The relevant response is actually

$$L(s) = \frac{1}{\chi_m^{-1}(s)H^{-1}(s) - 1} \quad (\text{B.120})$$

which can be stable if either χ_m or H is stable. In the following, we analyze the stability of this response by checking if the time-domain function diverges in the long time limit.

In the case of the derived optimal filter, we have the following responses

$$\chi_m(s) = \frac{\Omega}{s^2 + s\Gamma + \Omega^2} \quad H(s) = -\frac{A > 0}{s^2 - s\Gamma + \Omega^2}. \quad (\text{B.121})$$

We can proceed to factorize the denominator of the closed-loop response to different poles

$$\begin{aligned} L(s) &\propto \frac{1}{(s^2 + s\Gamma + \Omega^2)(s^2 - s\Gamma + \Omega^2) + A} \\ &= (s^4 + (2\Omega^2 - \Gamma^2)s^2 + \Omega^4 + A)^{-1} \end{aligned} \quad (\text{B.122})$$

Appendix B. Appendix

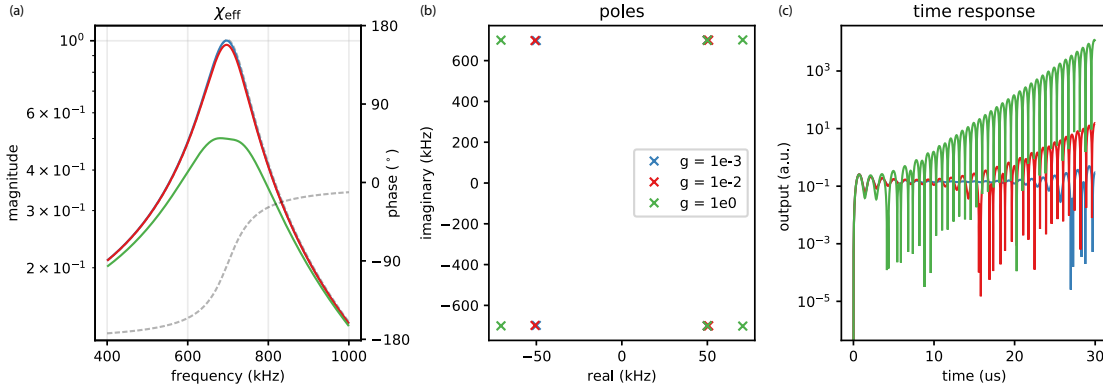


Figure B.11: Stability analysis of the "optimal filter" derived from minimizing integral of spectral density under three different feedback gain settings. **(a)** Effective mechanical susceptibilities (magnitude as the solid lines, phase as the dashed line) under feedback damping using the "optimal filter". **(b)** Poles of the closed-loop response in the complex domain. **(c)** Time domain response of the closed-loop system, showing an exponential increase of the output signal.

with the solutions

$$s^2 = \frac{-2\Omega^2 + \Gamma^2 \pm i\sqrt{(4\Omega^2 - \Gamma^2)\Gamma^2 + 4A}}{2} \approx -\Omega^2 \pm 2iB \quad (\text{B.123})$$

Assume the solution to the poles is separated into real and imaginary parts $s = R + iI$, we can derive the solution of the real part of the filter:

$$\begin{aligned} RI &= \pm B \\ R^2 - I^2 &= -\Omega^2 \\ \Rightarrow R &= \pm \sqrt{\frac{-\Omega^2 + \sqrt{\Omega^4 + 4B^2}}{2}}. \end{aligned} \quad (\text{B.124})$$

The result shows that there is always at least a positive real pole. After Fourier-transform back into the time-domain filter response, the positive real part will lead to an exponentially increasing temporal envelope, which leads to divergence. The divergence means the closed-loop system is unstable. When minimizing the integral of spectral density, the stability criteria of the system response is not considered so it can lead to unphysical results. This effect is also analyzed numerically, shown in Fig. B.11, where we observed the filter's instability in the time-domain response.

B.8 Classical laser noise effects on sideband asymmetry

This section analyzes the case where the system is contaminated by the laser amplitude and phase noise (cavity frequency noise ignored here). This is not the case in our system, as our

B.8 Classical laser noise effects on sideband asymmetry

laser is quantum-limited in both phase and amplitude. Nevertheless, we would like to know the effect of laser noise on the measured sideband asymmetry.

We assume the input field is injected from an auxiliary port that is not the main output port of the cavity and define C_{qq} and C_{pp} (set $C_{pq} = 0$) for the field intensity at the output port. Recall the field correlations in terms of classical noise density,

$$S_{a_{\text{in}}a_{\text{in}}} = \frac{C_{qq} + C_{pp}}{2} \quad (\text{B.125})$$

$$S_{a_{\text{in}}^\dagger a_{\text{in}}^\dagger} = 1 + \frac{C_{qq} + C_{pp}}{2} \quad (\text{B.126})$$

$$S_{a_{\text{in}}a_{\text{in}}^\dagger} = \frac{e^{-2i\phi}C_{qq} - e^{-2i\phi}C_{pp}}{2} - ie^{-i\phi}C_{pq} \quad (\text{B.127})$$

$$\phi = \arg(1 + 2i\bar{\Delta}/\kappa) \quad (\text{B.128})$$

with which we derive again the output field spectral density

$$\begin{aligned} S_{a_{\text{out}}a_{\text{out}}}(\omega) &= 4g^2\Gamma_m|\chi'_m|^2\kappa|\chi_{\text{cav}}|^2 \left(n_{\text{th}} + \frac{C}{1 + (2(\bar{\Delta} + \omega)/\kappa)^2} \right) \\ &+ \kappa^2|\chi_{\text{cav}}|^2 \left| 1 + 4ig^2\chi'_m\chi_{\text{cav}} \left(1 + \frac{i\omega\kappa/2}{(\kappa/2)^2 + \bar{\Delta}^2} \right) \right|^2 \frac{C_{qq}}{2} \\ &+ \kappa^2|\chi_{\text{cav}}|^2 \left| 1 + 4g^2\chi'_m\chi_{\text{cav}} \frac{\bar{\Delta}\omega}{(\kappa/2)^2 + \bar{\Delta}^2} \right|^2 \frac{C_{pp}}{2} \end{aligned} \quad (\text{B.129})$$

where we have the classical-noise-induced heating (taking $\omega \ll \kappa$)

$$\bar{n}_{\text{eff}} = \bar{n}_{\text{ideal}} + \frac{2g^2\kappa|\chi_{\text{cav}}|^2}{\Gamma'_m} \left(C_{qq} + C_{pp} \frac{\bar{\Delta}^2\Omega_m^2}{((\kappa/2)^2 + \bar{\Delta}^2)^2} \right) \quad (\text{B.130})$$

as well as the output field interference with the classical backaction.

To simplify the discussion, we analyze the interference effect at the peak of the mechanical mode and find that the asymmetry quanta and the phonon quanta are modified by

$$\frac{1}{2} \rightarrow \frac{1}{2} \left(1 + \frac{2}{1 + (2\bar{\Delta}/\kappa)^2} C_{qq} \right) \quad (\text{B.131})$$

$$\bar{n}_{\text{eff}} \rightarrow \bar{n}_{\text{eff}} - C_{pp} \frac{2}{1 + (2\bar{\Delta}/\kappa)^2} \frac{(2\bar{\Delta}/\kappa)(2\Omega_m/\kappa)}{1 + (2\bar{\Delta}/\kappa)^2} \quad (\text{B.132})$$

Modifying the sideband asymmetry factor 1/2 is only possible when the classical noise is present on the probe laser. For any noise originating from the cavity, this is not possible.

One thing to remember is that the results derived here assume a noiseless local oscillator. In reality, phase and amplitude noise are present on both the probe and local oscillator beams. When they combine to form a homodyne, noise interferes. Therefore, the result derived here

does not directly apply to experimental realizations and only provides a magnitude estimation of these effects. To account for the noise interference, physical details of the interferometers need to be considered, e.g., whether it is a balanced homodyne and how the interferometer length is balanced. The laser noises measured at higher power, shown in Fig. 2.17 and Fig. 3.2, indicate that at the power level of the asymmetry measurement (50 μ W) $C_{pp} \ll 1$ and $C_{qq} \ll 1$. Therefore, we can safely ignore the classical noise contributions.

B.9 Theory of dissipative Kerr solitons

The physical theory of generating nonlinear optical states in microresonators [224] is rich and we will not be able to cover them in the context of this thesis. In our experiments, we routinely generate nonlinear states, including primary comb, secondary comb, modulation instability, and dissipative solitons. In the following, we list some essential equations, closely following [355], describing the generation of solitons and their optical properties. These results are used to study soliton interaction with free electrons in Section 5.2.

The internal optical field evolution in a microresonator (with only Kerr nonlinearity) can be described by the Lugiato-Lefever equation (LLE),

$$\frac{\partial A}{\partial t} - i \frac{D_2}{2} \frac{\partial^2 A}{\partial \phi^2} - i g |A|^2 A = -\left(\frac{\kappa}{2} + i\Delta\right) A + \sqrt{\frac{\kappa \eta P_{\text{in}}}{\hbar \omega_0}} \quad (\text{B.133})$$

where $A(\phi, t)$ is the slowing varying field amplitude of the carrier, and $\phi \in [0, 2\pi]$ is the angular coordinate inside the ring resonator with a periodic boundary condition. $\eta = \kappa_{\text{ex}}/\kappa$ is the resonator coupling efficiency. $\Delta = \omega_0 - \omega_{\text{laser}}$ is the laser detuning relative to the pump cavity resonance. P_{in} is the optical input power to the resonator. Most importantly, $g = \frac{\hbar \omega^2 c n_2}{n^2 V}$ is the nonlinear coupling constant (self-Kerr resonance frequency shift per photon), and D_2 is the second order dispersion of the cavity resonance frequencies $\omega_\mu \approx \omega_0 + D_1 \mu + D_2 \mu^2/2 + \dots$. The above equation can be further cast into a dimensionless nonlinear Schrödinger equation with a driving and a damping term,

$$i \frac{\partial \psi}{\partial \tau} + \frac{1}{2} \frac{\partial^2 \psi}{\partial \theta^2} + |\psi|^2 \psi = (-i + \xi_0) \psi + i f, \quad (\text{B.134})$$

where ψ is again the dimensionless field envelope, $\theta = \phi/\sqrt{2D_2/\kappa}$ is the dimensionless longitudinal coordinate, $\tau = \kappa t/2$ is the dimensionless slow time, $\xi_0 = 2\Delta/\kappa$ is the normalized detuning, and $f = \sqrt{8g/\kappa^3} \sqrt{\kappa \eta P_{\text{in}}/\hbar \omega_0}$ is the normalized pump power relative to the required power to achieve nonlinear process.

An approximate solution for the dissipative solitons, accounting for a flat continuous-wave (CW) background, is given by

$$\psi = \frac{f}{\xi_0^2} - i \frac{f}{\xi_0} + \sqrt{2\xi_0} e^{i\phi_0} \text{sech}(\sqrt{2\xi_0}\theta) \quad (\text{B.135})$$

B.10 Classical noise contributions in the Kerr squeezing experiment

with the stability requirement $\sqrt{3} < \xi_0 \leq \pi^2 f^2/8$ and a large detuning $f^2 < \frac{2}{27}\xi_0(\xi_0^2 + 9)$. Here, the soliton phase $\cos\phi_0 = \sqrt{8\xi_0}/\pi f$. As we see, the soliton exhibits a sech shape on top of the CW drive field background. At very large detuning ξ_0 , the soliton-CW peak ratio can be greatly enhanced and typically achieves a factor of 10-100. We use these waveforms to study electron-photon interaction with nonlinear optical states in Section 5.2.

B.10 Classical noise contributions in the Kerr squeezing experiment

Here, we discuss a few noise contributions, including the laser phase and amplitude noise and the inclusion of TRN in our model. How homodyne length balancing influences the classical noises is also analyzed.

Laser noise contributions

Modeling the laser phase and amplitude noise correlations as [356]

$$\begin{pmatrix} \langle \delta q(t)\delta q(t') \rangle & \langle \delta q(t)\delta p(t') \rangle \\ \langle \delta p(t)\delta q(t') \rangle & \langle \delta p(t)\delta p(t') \rangle \end{pmatrix} = \frac{1}{2} \begin{pmatrix} 1+2C_{qq} & i+2C_{qp} \\ -i+2C_{qp} & 1+2C_{pp} \end{pmatrix} \delta(t-t') \quad (\text{B.136})$$

$$\begin{pmatrix} S_{qq} & S_{qp} \\ S_{pq} & S_{pp} \end{pmatrix} = \frac{1}{2} \begin{pmatrix} 1 & i \\ -i & 1 \end{pmatrix} + \begin{pmatrix} C_{qq} & C_{qp} \\ C_{qp} & C_{pp} \end{pmatrix} \quad (\text{B.137})$$

The amplitude noise spectrum $S_I(\omega)$ can be measured using direct photodetection. We can characterize the excess amplitude noise C_{qq} by checking the deviation of the noise variance from the shot noise, either by directly comparing noise variance difference or based on their different scaling on power. In the end, we can convert between C_{qq} and S_I using

$$C_{qq} = \frac{1}{2} \left(\frac{S_I}{S_{\text{SN}}} - 1 \right). \quad (\text{B.138})$$

For the phase noise $S_{\phi\phi}$ of the laser, we can measure it by the method described in Section 2.3.3, but here we beat the 1550-nm ECDL with a reference laser with much lower phase noise. For this purpose, we use an ultra-low noise laser stabilized to a filter cavity (Appendix B.13). The excess phase quadrature noise of the laser can be converted from the measured laser phase noise by

$$C_{pp} = 2\langle \dot{n} \rangle S_{\phi\phi}, \quad (\text{B.139})$$

where $\langle \dot{n} \rangle$ is the photon flux rate of the input light. From our measurement, C_{pp} drops as ω increases and is quantum limited at around 10MHz. The measured phase and amplitude laser noise of the ECDL used for our measurements are shown in Fig. B.12.

As for the quadrature cross-correlations, we have the bound $C_{qp} \leq \sqrt{C_{qq}C_{pp}}$ from the Cauchy-Schwarz inequality. And if we consider that the noise arises from a quantum state ρ , we have

Appendix B. Appendix

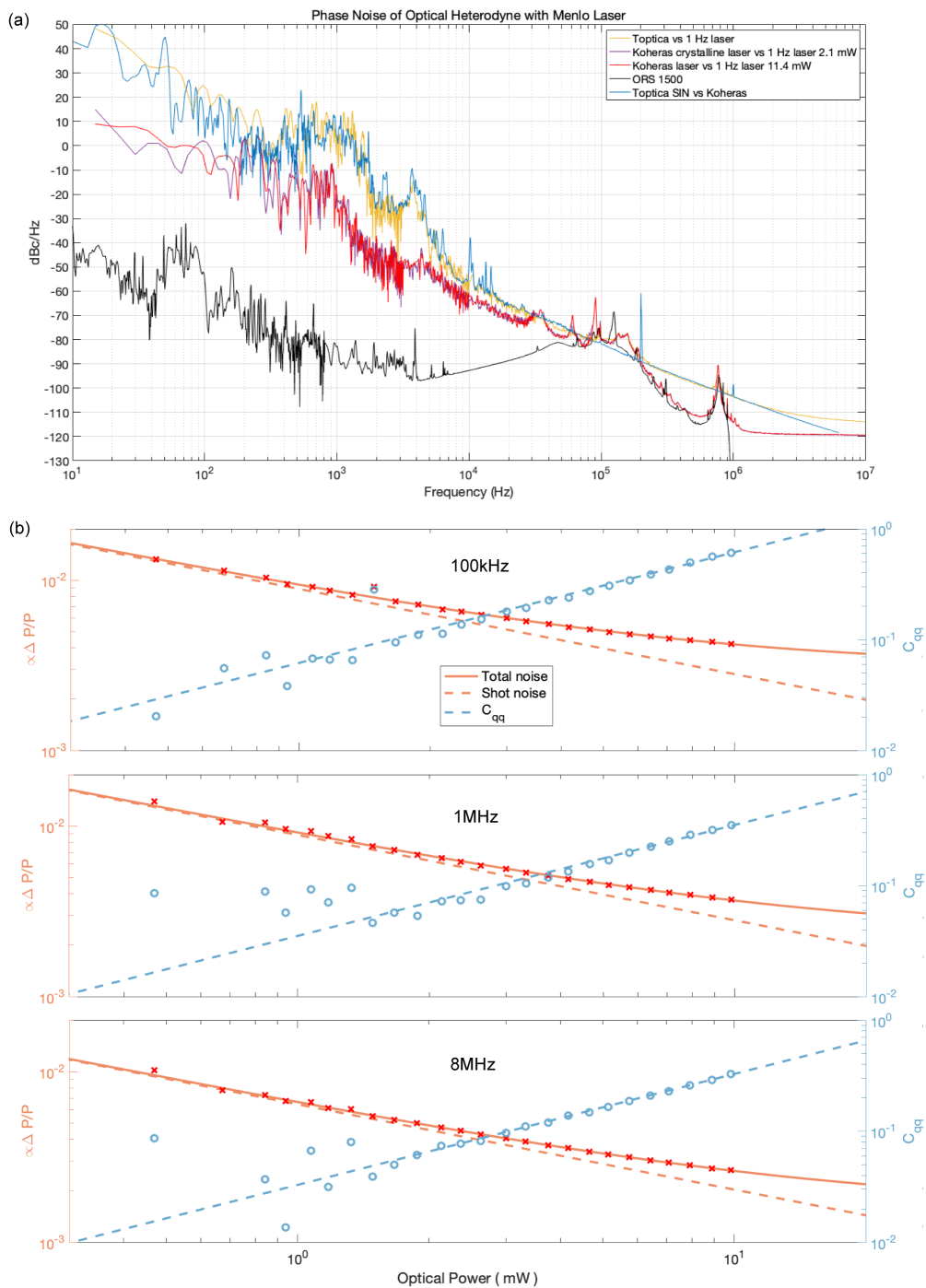


Figure B.12: **(a)** Measured Toptica ECDL laser phase noise by beating with other low noise laser sources [357]. **(b)** Measured ECDL amplitude noise at different Fourier frequency bands by an optical power sweep.

B.10 Classical noise contributions in the Kerr squeezing experiment

the covariance matrix

$$\det \begin{pmatrix} \frac{1}{2} + C_{qq} & C_{qp} \\ C_{qp} & \frac{1}{2} + C_{pp} \end{pmatrix} \geq 0, \quad (\text{B.140})$$

which results in a larger bound

$$C_{qp}^2 \leq C_{qq}C_{pp} \left(1 + \frac{1}{\sqrt{C_{qq}C_{pp}}} \right). \quad (\text{B.141})$$

In most experiments, as long as $C_{qq}C_{pp} \ll 1$, it is safe to ignore C_{qp} . Otherwise, we must use this bond to approximate C_{qp} . We know that the amplitude and laser phase noise have drastically different spectral features, so we are not concerned with their correlations.

Cavity frequency noise

Apart from the laser's classical noise, the cavity's thermo-refractive noise causes classical detuning noise in the measurement. In the case of a balanced homodyne measurement, the laser phase noise and cavity frequency noise contribute to the measurement equivalently when the cavity is pumped on resonance and obeys the following conversion relation

$$S_{\phi\phi} = \left(\frac{4\kappa_{\text{ex}}}{\kappa_{\text{ex}}^2 - \kappa_0^2} \right)^2 S_{\delta f}. \quad (\text{B.142})$$

According to this equation, if we consider the TRN as an input phase quadrature noise from the laser, an over-coupled 1-THz Si₃N₄ ring resonator usually has C_{pp} at the level of 10^4 near the optimized squeezing power.

Generally, there is a difference in the cavity frequency and laser phase noise. Here, we derive the cavity noise transduction by adding a perturbation $\delta\Delta$ term into Eq.A.9 as

$$\frac{da}{dt} = -(\kappa/2 + i(\Delta + \delta\Delta))a - ig a^\dagger a^2 + \sqrt{\kappa_{\text{ex}}}a_{\text{in}} + \sqrt{\kappa_0}b_{\text{in}}. \quad (\text{B.143})$$

This adds an additional term in the linearized equation

$$\frac{d\mathbf{a}}{dt} = [M - \frac{\kappa}{2}I]\mathbf{a} + \sqrt{\kappa_{\text{ex}}}\mathbf{a}_{\text{in}} + \sqrt{\kappa_0}\mathbf{b} + \delta\Delta\mathbf{i}\boldsymbol{\alpha}, \quad (\text{B.144})$$

where $\mathbf{i}\boldsymbol{\alpha} = \begin{pmatrix} i\langle A \rangle \\ -i\langle A^* \rangle \end{pmatrix}$. In the quadrature basis, we have

$$\frac{d}{dt} \begin{pmatrix} \delta Y_1 \\ \delta Y_2 \end{pmatrix} = \begin{pmatrix} G_1 & H_1 \\ H_2 & G_2 \end{pmatrix} \begin{pmatrix} \delta Y_1 \\ \delta Y_2 \end{pmatrix} + \begin{pmatrix} J_1 \\ J_2 \end{pmatrix} + i\delta\Delta \begin{pmatrix} \langle Y_2 \rangle \\ \langle Y_1 \rangle \end{pmatrix}. \quad (\text{B.145})$$

Appendix B. Appendix

The output quadrature equation now obtains a new term,

$$\tilde{Y}_i^{\text{out}} = \frac{[\text{old terms}] - i\sqrt{\kappa_{\text{ex}}}(H_i\langle Y_i \rangle + (i\omega + G_j)\langle Y_j \rangle)\tilde{\Delta}}{(G_i + i\omega)(G_j + i\omega) - H_i H_j}. \quad (\text{B.146})$$

The output spectrum also obtains a new term that comes from cavity frequency noise

$$S_{Y_i Y_i}^{\text{out}} = [\text{old terms}] + \frac{\kappa_{\text{ex}}|H_i\langle Y_i \rangle - (i\omega + G_j)\langle Y_j \rangle|^2 S_{\Delta\Delta}}{|(G_i + i\omega)(G_j + i\omega) - H_i H_j|^2}, \quad (\text{B.147})$$

in which $S_{\Delta\Delta}$ is the TRN spectrum S_{TRN} measured in Section A.1. It is worth noticing that this expression is different from adding the TRN noise as the laser phase noise.

We can easily verify this expression by taking the limit $g \rightarrow 0$ and $\Delta \rightarrow 0$, which results in the expression

$$S_{Y_i}^{\Delta}(g=0, \Delta=0) = \frac{|\kappa_{\text{ex}} - \kappa/2 + i\omega|^2 S_{Y_i}^{\text{in}} + \kappa_{\text{ex}}\kappa_0 S_{Y_i}^b + \kappa_{\text{ex}}|\langle Y_j \rangle|^2 S_{\Delta}}{|-\kappa/2 + i\omega|^2}. \quad (\text{B.148})$$

It consists of the input field, the vacuum field from the loss port, and the TRN transduction of the cavity. Sharp eyes might notice that the TRN term does not have the same ratio as Eq. B.142. However, they are the same if we consider the input-output mean-field solution

$$|\alpha|^2 = \frac{4\kappa_{\text{ex}}}{(\kappa_{\text{ex}} - \kappa_0)^2} |\alpha^{\text{out}}|^2. \quad (\text{B.149})$$

We show one of the simulated Kerr squeezing spectra at the optimal quadrature angle in Fig. A.6. Given the spectral property of the TRN, it dominates at low frequency. The squeezing band is thus restricted to high frequency, penalized by the cavity cut-off effect.

Homodyne detection response

Our experiment uses homodyne detection to measure the quadrature variance at offset frequencies. As homodyne detection requires an interferometer, laser noise interference, i.e., when the signal is combined with the local oscillator, will affect how the laser noise enters the measurement record. For example, a length balancing of the signal and LO arms would partially cancel out the laser phase noise contribution on the measurement record. To correctly account for these effects, we include the interferometer response in the system model derived in previous sections.

We define the homodyne measurement variable as a combination of the signal and the local oscillator added noise

$$\delta H = \delta q_{\text{sig}}^{\theta} + \sqrt{\langle n_{\text{sig}} \rangle / \langle n_{\text{LO}} \rangle} \delta q_{\text{LO}}^{-\theta} \quad (\text{B.150})$$

where we relate the signal flux to the input flux through $\frac{n_{\text{sig}}}{n_{\text{in}}} = \frac{(\kappa_{\text{ex}} - \kappa_0)^2 / 4 + \Delta_{\text{eff}}^2}{(\kappa_{\text{ex}} + \kappa_0)^2 / 4 + \Delta_{\text{eff}}^2}$. When Δ is big,

B.10 Classical noise contributions in the Kerr squeezing experiment

the classical noise in the interferometer gets canceled if it is length balanced.

Recall a few terms we defined earlier when only considering the cavity nonlinearity,

$$\begin{aligned} G_i &= -(\kappa/2 \pm i \frac{g}{2} [\alpha^2 e^{-2i\theta} - \alpha^{*2} e^{2i\theta}]) \\ H_i &= \pm(\Delta + 2g|\alpha|^2) - \frac{g}{2} [\alpha^2 e^{-2i\theta} + \alpha^{*2} e^{2i\theta}] \\ J_i &= \sqrt{\kappa_{\text{ex}}}\delta Y_i^{\text{in}} + \sqrt{\kappa_0}\delta Y_i^b, \end{aligned}$$

on top of which we also define the following terms to help us simplify the final expression when considering the interferometer response,

$$A = [(G_2 + i\omega)(\kappa_{\text{ex}} + G_1 + i\omega) - H_1 H_2] \quad (\text{B.151})$$

$$B = -H_1 \kappa_{\text{ex}} \quad (\text{B.152})$$

$$C = -H_1 \sqrt{\kappa_{\text{ex}}\kappa_0} \quad (\text{B.153})$$

$$D = -\sqrt{\kappa_{\text{ex}}\kappa_0}(G_2 + i\omega) \quad (\text{B.154})$$

$$E = (G_1 + i\omega)(G_2 + i\omega) - H_1 H_2. \quad (\text{B.155})$$

With these terms, we rewrite the homodyne observable δH as

$$\begin{aligned} \delta H &= \left((A \cos \theta' - B \sin \theta') \delta q + (A \sin \theta' + B \cos \theta') \delta p \right. \\ &\left. + E \sqrt{\frac{\langle n_{\text{sig}} \rangle}{\langle n_{\text{LO}} \rangle}} (\cos \theta \delta q_{\text{LO}} - \sin \theta \delta p_{\text{LO}}) + C \delta Y_2^b + D \delta Y_1^b \right) / E. \end{aligned} \quad (\text{B.156})$$

Here, we define $\theta' = \theta - \Delta\theta_{\alpha_{\text{in}}/\alpha_{\text{out}}}$ to account for the signal field phase rotation relative to the input laser field. As for the quadrature noises δp and δq , we have the following relations

$$\delta q = \sqrt{2}\delta\alpha + \delta q_0 \quad (\text{B.157})$$

$$\delta p = \sqrt{2}|\langle a \rangle| \delta\phi + \delta p_0 \quad (\text{B.158})$$

to separate the classical fluctuations $\delta\alpha$ and $\delta\phi$ from the quantum fluctuations. It is possible to separate the homodyne observable also into a quantum term and a classical term $\delta H = \delta H_0 + \delta H_c$, where

$$\begin{aligned} \delta H_0 &= \left((A \cos \theta' - B \sin \theta') \delta q_0 + (A \sin \theta' + B \cos \theta') \delta p_0 + \right. \\ &\left. E \sqrt{\frac{\langle n_{\text{sig}} \rangle}{\langle n_{\text{LO}} \rangle}} (\cos \theta \delta q_0^{\text{LO}} - \sin \theta \delta p_0^{\text{LO}}) + C \delta Y_2^b + D \delta Y_1^b \right) / E \end{aligned} \quad (\text{B.159})$$

Appendix B. Appendix

denotes the vacuum fluctuation and

$$\begin{aligned} \delta H_c = & \left(((A \cos \theta' - B \sin \theta') + E \cos \theta \sqrt{\frac{\langle n_{\text{sig}} \rangle}{\langle n_{\text{in}} \rangle}}) \sqrt{2} \delta \alpha + ((A \sin \theta' + B \cos \theta') \right. \\ & \left. - E \sin \theta \sqrt{\frac{\langle n_{\text{sig}} \rangle}{\langle n_{\text{in}} \rangle}}) \sqrt{2} |a_{\text{in}}| \delta \phi \right) / E \end{aligned} \quad (\text{B.160})$$

denotes the classical fluctuation.

Therefore, we can write out the final expression $S_{\text{HH}}(\theta) = S_{H_0 H_0} + S_{H_c H_c} + S_{\text{TRN}}$, taking into account the vacuum fluctuations $S_{H_0 H_0}$, classical laser noises $S_{H_c H_c}$, as well as the cavity frequency noise S_{TRN} ,

$$\begin{aligned} S_{H_0 H_0} = & (|A \cos \theta' - B \sin \theta'|^2 S_q^0 + |A \sin \theta' + B \cos \theta'|^2 S_p^0 + |C|^2 S_2^b + |D|^2 S_1^b) \\ & + 2\text{Re}[DC^* S_{pq}^b] + 2\text{Re}[(A \cos \theta' - B \sin \theta')(A \sin \theta' + B \cos \theta')^* S_{pq}^0] / |E|^2 + \frac{\langle n_{\text{sig}} \rangle}{\langle n_{\text{LO}} \rangle} S_{\text{LO}}^0 \end{aligned} \quad (\text{B.161})$$

$$\begin{aligned} S_{H_c H_c} = & \left(\left| (A \cos \theta' - B \sin \theta') + E \cos \theta \sqrt{\frac{\langle n_{\text{sig}} \rangle}{\langle n_{\text{in}} \rangle}} \right|^2 C_{qq} + \left| (A \sin \theta' + B \cos \theta') \right. \right. \\ & \left. \left. - E \sin \theta \sqrt{\frac{\langle n_{\text{sig}} \rangle}{\langle n_{\text{in}} \rangle}} \right|^2 C_{pp} + 2\text{Re} \left[\left((A \cos \theta' - B \sin \theta') + E \cos \theta \sqrt{\frac{\langle n_{\text{sig}} \rangle}{\langle n_{\text{in}} \rangle}} \right) \right. \right. \\ & \left. \left. \left((A \sin \theta' + B \cos \theta') - E \sin \theta \sqrt{\frac{\langle n_{\text{sig}} \rangle}{\langle n_{\text{in}} \rangle}} \right)^* \right] C_{pq} \right) / |E|^2 \end{aligned} \quad (\text{B.162})$$

$$S_{\text{TRN}} = \frac{\kappa_{\text{ex}} |H_1 \langle Y_1 \rangle - (i\omega + G_2) \langle Y_2 \rangle|^2 S_{\Delta\Delta}}{|E|^2} \quad (\text{B.163})$$

Again, we must remember that quadrature angles have relative rotation, e.g., between $Y^{\text{out/sig}}$ and Y . Since we define the quadrature angle with respect to $Y_i^{\text{out}}(\theta)$, we need to use $Y_i(\theta - \Delta\theta_{\alpha_{\text{cav}}/\alpha_{\text{out}}})$.

To account for the finite detection efficiency η , we can replace E with $E\eta^{-1/2}$, such that the signal is attenuated. Also, $\frac{\langle n_{\text{sig}} \rangle}{\langle n_{\text{in}} \rangle}$ is replaced by $\eta \frac{\langle n_{\text{sig}} \rangle}{\langle n_{\text{in}} \rangle}$, such that the signal classical noise is also adjusted for the reduced power. Besides the change in classical noise, vacuum noise $\frac{1}{2} - \eta$ must also be added.

We illustrate the result of the classical laser phase noise $\delta\phi(\omega)$ cancellation by the interferometer in Fig. B.13. One important thing to notice about the length balancing is that the laser phase noise is only well canceled when the laser is far off the cavity resonance (Fig. B.13(b)). When the laser is on resonance, only noise within the cavity bandwidth is well canceled (Fig. B.13(a)). If the laser is slightly detuned from the cavity resonance, the carrier frequency noise is not well canceled because of cavity transduction and quadrature rotation (Fig. B.13(c)). As the sideband phase noise $\delta\phi(\omega)$ acquires a phase shift when the Fourier frequency ω approaches the cavity bandwidth, even when the laser is on resonance. Therefore, these noise components

B.11 Cavity nonlinearity-induced pump-probe response

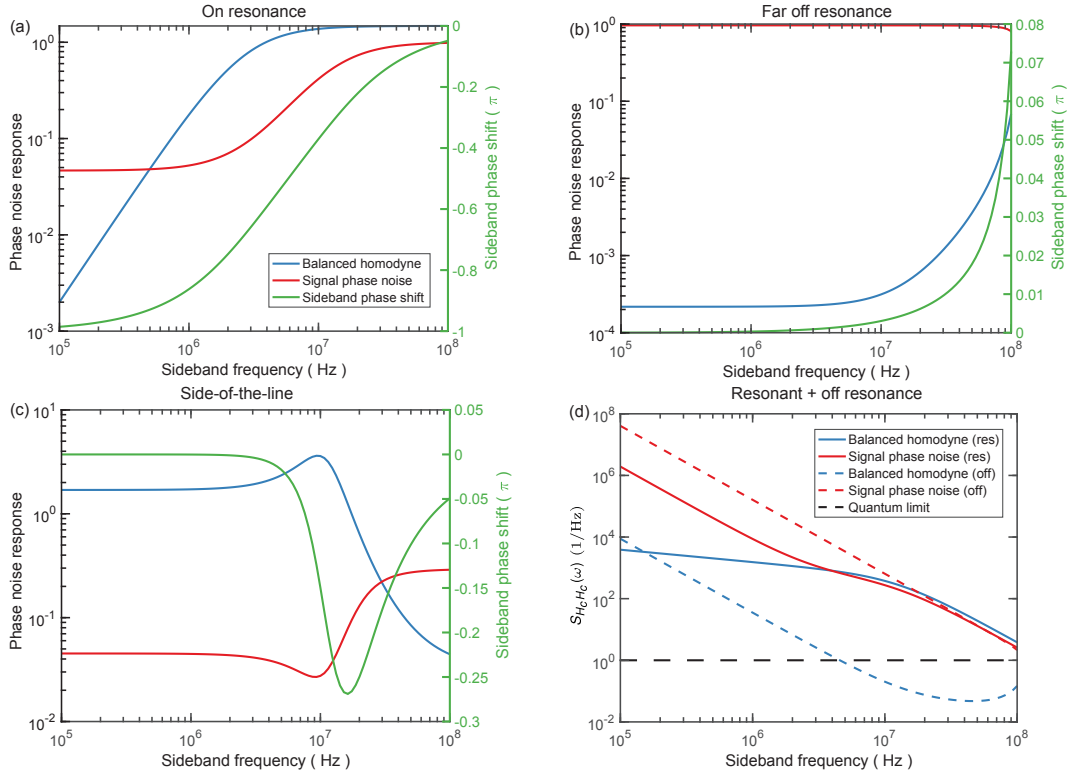


Figure B.13: **Classical laser phase noise cancellation in a length-balanced homodyne.** Classical phase noise spectral response when **(a)** laser is resonant with the cavity, **(b)** laser is far off resonance from the cavity, and **(c)** the laser is side-of-the-line of the cavity resonance. The phase noise is only well canceled in detection when the laser is far off the cavity response **(b)**. When the laser is within the cavity bandwidth **((a,b))**, the phase noise cancellation is impeded by the cavity response of the phase noise Fourier components, which modifies both the phase and the amplitude of the laser phase noise. **(d)** Simulated $S_{H_c H_c}$ with a length-balanced homodyne with a resonantly driven cavity.

get amplified instead. We expect Kerr squeezing near the cavity bandwidth edge $\omega \sim \kappa$, as TRN dominates the low-frequency span $\omega \ll \kappa$. So, it is vital to account for the laser phase noise as the length balancing of the homodyne actually amplifies the phase noise in the frequency span of interest for the Kerr squeezing application. We should in Fig. A.6 the simulated spectrum, considering all the classical noise sources and the homodyne response.

B.11 Cavity nonlinearity-induced pump-probe response

In microresonators, the pump light can cause cross-Kerr, heating, and even charge carrier effects that change the probe resonance frequency. Using a pump-probe scheme, we can probe these responses in both time and frequency domains and separate them using their distinct features. System parameters, e.g., absorption rate κ_{abs} and nonlinear index n_2 can be

Appendix B. Appendix

retrieved by careful calibration.

Here, we have the first equation to define the cavity frequency linear response function

$$\delta\Delta(t) = \int_{-\infty}^t \mu(t-t')n(t')dt', \quad (\text{B.164})$$

where $\delta\Delta(t)$ is the intracavity photon $n(t)$ induced cavity frequency shift and $\mu(t \geq 0)$ is the cavity response function, in which at different time scales, different effects dominate, e.g., the photorefractive effect at sub-Hz frequencies, the thermal effect at kHz frequencies, and the Kerr effect around MHz frequencies. Mathematically, the easiest thing one could do to measure the response function is by setting the intracavity photon number to be a delta function $n(t) = \delta(t)$ and by measuring cavity detuning $\delta\Delta(t) = \int \mu(t-t')\delta(t')dt' = \mu(t)$ one directly gets the response function $\mu(t)$.

In reality, $\delta n(t)$ changes to an external drive, as well as the readout of $\delta\Delta(t)$, is limited by the cavity bandwidth. Therefore, for fast frequency response concerning the thermal and Kerr effects, we use frequency domain response measurement to account for the finite cavity response bandwidth.

Response of probe laser to cavity frequency shifts

The cavity detuning is not directly accessible, and the accessible physical quantity is instead cavity transmission/reflection measured by an auxiliary probe laser a with a very weak intensity so that cavity nonlinear effects can be ignored. In this setting, we have the following Langevin equations (vacuum noise omitted)

$$a_{\text{out}} = a_{\text{in}} - \sqrt{\kappa_{\text{ex}}}a \quad (\text{B.165})$$

$$\dot{a}(t) = \left(-\frac{\kappa}{2} + i\Delta(t)\right)a(t) + \sqrt{\kappa_{\text{ex}}}a_{\text{in}}. \quad (\text{B.166})$$

In the limit of small perturbation, the system can be treated linearly, and the output probe intensity can be expressed as

$$\delta|a_{\text{out}}(t)|^2 = \int_{-\infty}^t \chi(t-t')\delta\Delta(t')dt' \quad (\text{B.167})$$

where $\chi(t) = \text{FT}^{-1}\chi(\omega)$ in frequency domain is

$$\chi(\omega) = \frac{2\bar{\Delta}\kappa_{\text{ex}}[\kappa_0 - i\omega]|a_{\text{in}}|^2}{[\kappa^2/4 + \bar{\Delta}^2][(\kappa/2 - i\omega)^2 + \bar{\Delta}^2]}. \quad (\text{B.168})$$

With these results, we proceed to calculate how cavity nonlinearity transduces pump intensity modulation to probe cavity frequency shift.

Response of cavity to pump intensity modulation

Intracavity photon number under the modulation of the pump mode (b) is tricky to analyze due to the cavity nonlinear effects. In the weak modulation limit, we have the following Langevin equations describing the pump cavity photon number and the detuning,

$$n(\omega) = 2\kappa_{\text{ex}}|b_{\text{in}}|^2 \frac{-\bar{\Delta}\Delta(\omega) + [\kappa^2/4 - i\omega\kappa/2 + \bar{\Delta}^2]A(\omega)}{[\kappa^2/4 + \bar{\Delta}^2][(\kappa/2 - i\omega)^2 + \bar{\Delta}^2]} \quad (\text{B.169})$$

$$\Delta(\omega) = \mu_b(\omega)n(\omega) \quad (\text{B.170})$$

where all the parameters refer to the pump optical mode, and the field amplitude modulation coefficient $A(t)$ is defined as $b_{\text{in}}(t) = b_{\text{in}}(1 + A(t))$. Here, $\mu_b = \dots + \chi_{\text{SPM}}$ consists of the Kerr self-phase-modulation response. One could see that at non-zero detuning $\bar{\Delta} \neq 0$, the two equations are coupled. The resulting response relation is modified to

$$\Delta(\omega) = \frac{2\kappa_{\text{ex}}|b_{\text{in}}|^2[\kappa^2/4 - i\omega\kappa/2 + \bar{\Delta}^2]\mu_b(\omega)}{[\kappa^2/4 + \bar{\Delta}^2][(\kappa/2 - i\omega)^2 + \bar{\Delta}^2] + 2\kappa_{\text{ex}}|b_{\text{in}}|^2\bar{\Delta}\mu_b(\omega)}A(\omega) \quad (\text{B.171})$$

$$n(\omega) = \frac{2\kappa_{\text{ex}}|b_{\text{in}}|^2[\kappa^2/4 - i\omega\kappa/2 + \bar{\Delta}^2]}{[\kappa^2/4 + \bar{\Delta}^2][(\kappa/2 - i\omega)^2 + \bar{\Delta}^2] + 2\kappa_{\text{ex}}|b_{\text{in}}|^2\bar{\Delta}\mu_b(\omega)}A(\omega). \quad (\text{B.172})$$

where cavity induces self-feedback from the term $2\kappa_{\text{ex}}|b_{\text{in}}|^2\bar{\Delta}\mu_b(\omega)$, which should be avoided in the pump-probe scheme.

Pump-probe chain response

Given the results derived above, we can write down the pump-probe chain response as

$$\delta|a_{\text{out}}|(\omega) = \chi_a(\omega)\mu_a(\omega)n_b(\omega) \quad (\text{B.173})$$

$$\chi_a(\omega) = \frac{2\bar{\Delta}_a\kappa_{a,\text{ex}}[\kappa_{a,0} - i\omega]|a_{\text{in}}|^2}{[\kappa_a^2/4 + \bar{\Delta}_a^2][(\kappa_a/2 - i\omega)^2 + \bar{\Delta}_a^2]} \quad (\text{B.174})$$

$$n_b(\omega) = \frac{2\kappa_{b,\text{ex}}|b_{\text{in}}|^2[\kappa_b^2/4 - i\omega\kappa_b/2 + \bar{\Delta}_b^2]}{[\kappa_b^2/4 + \bar{\Delta}_b^2][(\kappa_b/2 - i\omega)^2 + \bar{\Delta}_b^2] + 2\kappa_{b,\text{ex}}|b_{\text{in}}|^2\bar{\Delta}_b\mu_b(\omega)}A(\omega) \quad (\text{B.175})$$

where $\mu_a = \dots + \chi_{\text{XPM}}$ consists of the Kerr cross-phase-modulation response, and is ideally twice the self-phase-modulation response.

When the pump is on resonance $\bar{\Delta} = 0$, we can simplify the above result to

$$\delta|a_{\text{out}}|(\omega) = \frac{8\mu_a(\omega)\bar{\Delta}_a\kappa_{a,\text{ex}}[\kappa_{a,0} - i\omega]|a_{\text{in}}|^2}{[\kappa_a^2/4 + \bar{\Delta}_a^2][(\kappa_a/2 - i\omega)^2 + \bar{\Delta}_a^2]} \frac{\kappa_{b,\text{ex}}|b_{\text{in}}|^2}{\kappa_b[\kappa_b/2 - i\omega]}A(\omega) \quad (\text{B.176})$$

which we use as our fitting function.

B.12 Fano and split resonances in ring resonators

Split resonances are relatively common in microresonators. They are usually the result of inter-mode coupling between two optical modes, sometimes degenerate in frequency (e.g., whispering gallery clockwise and counter-clockwise modes), and sometimes non-degenerate (e.g., a fundamental mode hybridized with a higher order mode). Our experiment primarily concerns the degenerate case, with examples in these references [345, 358, 359]. Some even use the measured splitting as a particle sensor [360].

There are two common mechanisms for degenerate mode splitting. First is the weak mode overlap between the clockwise and counter-clockwise modes due to imperfect resonator geometry. Such a coupling generally results in symmetric splitting, and does not modify the dissipation. The second one can be summarised as bath coupling, that a shared coupled bath mediates the coupling between two modes. The bath in our experiment is mostly the bus waveguide. However, generally, it can be, e.g., a tiny particle and happens mostly at wavelength scale. It is usually characterized by a coupling rate κ and an effective phase ϕ from propagation delay in the bath channel. A heuristic derivation using Langevin equations can illustrate this effect:

$$\dot{a}_1 = \left(-\frac{\kappa}{2} - i\Delta\right)a_1 + \sqrt{\kappa}a_{1,\text{in}} \quad (\text{B.177})$$

$$a_{2,\text{in}} = e^{i\phi} a_{1,\text{out}} = e^{i\phi} (-a_{1,\text{in}} + \sqrt{\kappa}a_1) \quad (\text{B.178})$$

$$\dot{a}_2 = \left(-\frac{\kappa}{2} - i\Delta\right)a_2 + \sqrt{\kappa}a_{2,\text{in}} \quad (\text{B.179})$$

$$= \left(-\frac{\kappa}{2} - i\Delta\right)a_2 + e^{i\phi}\kappa a_1 - e^{i\phi}\sqrt{\kappa}a_{1,\text{in}} \quad (\text{B.180})$$

where the equations describe a common waveguide coupling between two degenerate modes, where the input channel of mode a_2 is connected to the output channel of mode a_1 with some delay. This coupling usually results in a complex coupling coefficient $e^{i\phi}\kappa$ and a correlated bath $a_{1,\text{in}}$, and are generally nonreciprocal. Also, such a coupling generally modifies dissipation in the system. Because of the complex coupling coefficient that's phase dependent, apart from frequency splitting, *dark* and *bright* modes also emerge with asymmetric linewidths.

Fano resonances are another typical feature of microresonators, e.g., *anti-resonances*. They are usually the result of external etalons formed due to some weak reflections back from the waveguide and fiber facets. The mechanism is similar to the bath coupling, as it forms a feedback loop due to back reflection, except the shared bath input $a_{1,\text{in}}$ can be excited by the laser instead of the vacuum. In integrated circuits, back reflection is typically about a few % at the chip facet due to refractive index mismatch. It is typically characterized by the oscillating background of the laser transmission when sweeping the laser frequencies, as it is equivalently a weak etalon. The Fano effect is significant for highly overcoupled resonances due to their significant phase wrapping across the resonance. Thus, correctly modeling the Fano effect is particularly important for calibrations such as retrieving external coupling efficiencies for highly over-coupled resonances.

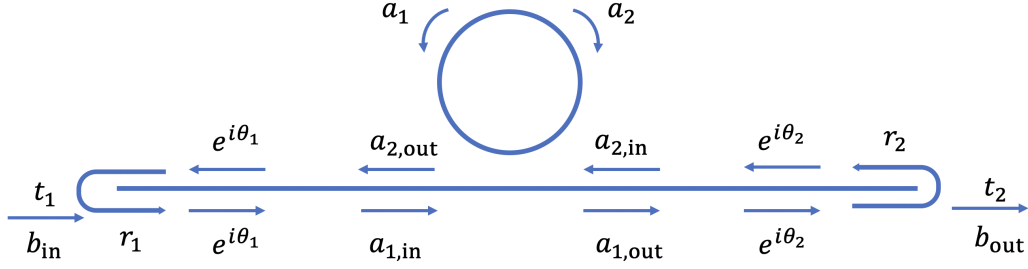


Figure B.14: Illustration of field relations of a ring resonator with chip facet reflections.

The resonance splitting and Fano shape affect the system calibrations with these resonators. One typical case is accurately extracting different resonances' loss and coupling rates. In our most recent characterizations [4, 5], accurate modeling is essential in calibrating the intracavity field strength to accurately retrieve the nonlinear index n_2 . In this section, we are primarily concerned with this task: how to accurately extract the resonators' loss rates and coupling rates from various accessible physical quantities one can measure in the lab.

Theory basics

Fano-shaped microresonator transmissions generally result from the field interference effect with the waveguide etalon due to small chip facet reflectivity. Here, we briefly discuss modeling this effect in microresonator systems and how one can accurately extract the system parameters from fitting a Fano-shaped resonance.

Consider a ring resonator with total linewidth κ coupled to a bus waveguide with coupling rate κ_{ex} . The ring also supports a degenerate pair of clockwise and counter-clockwise modes that couples to each other. The Langevin equations of such a system can be expressed as:

$$a_{1,\text{out}} = a_{1,\text{in}} - \sqrt{\kappa_{\text{ex}}} a_1 \quad (\text{B.181})$$

$$a_{2,\text{out}} = a_{2,\text{in}} - \sqrt{\kappa_{\text{ex}}} a_2 \quad (\text{B.182})$$

$$\dot{a}_1 = \left(-\frac{\kappa}{2} - i\Delta\right) a_1 + g_{21} a_2 + \sqrt{\kappa_{\text{ex}}} a_{1,\text{in}} \quad (\text{B.183})$$

$$\dot{a}_2 = \left(-\frac{\kappa}{2} - i\Delta\right) a_2 + g_{12} a_1 + \sqrt{\kappa_{\text{ex}}} a_{2,\text{in}}, \quad (\text{B.184})$$

where $\Delta = \omega_{\text{cavity}} - \omega_{\text{laser}}$, with complex parameter $g_{ij} = (\gamma_{\text{Re},ij} + i\gamma_{\text{Im},ij})$ quantifying the clockwise counter-clockwise coupling. Here, the coupling between the two optical modes can be non-reciprocal due to the possibility of bath coupling and dissipation. Therefore, we distinguish them at this stage of the calculation.

After the field is coupled out of the resonator and enters the waveguide, the light is partially reflected from the waveguide facets (field reflectivity r_i and transmission t_i) and couples back to the resonator again. This process forms a feedback loop and is visualized in Fig.B.14. The

Appendix B. Appendix

field relations of different input-output fields are

$$a_{1,\text{in}} = t_1 b_{\text{in}} + r_1 a_{2,\text{out}} e^{2i\theta_1} \quad (\text{B.185})$$

$$a_{2,\text{in}} = r_2 a_{1,\text{out}} e^{2i\theta_2} \quad (\text{B.186})$$

$$b_{\text{out}} = t_2 a_{1,\text{out}} e^{i\theta_2}, \quad (\text{B.187})$$

where $\theta_i = -k(\Delta)L_i$ is the optical phase accumulated when light propagates in the bus waveguide. The loss in the waveguide propagation is not considered here but can generally also be included as an effective modification of the facet reflection and transmission.

In most of the experimental settings, we care about the laser transmission response in the steady state limit when scanning the detuning across the optical resonance, i.e., $\chi(\Delta) = \frac{b_{\text{out}}(\Delta)}{b_{\text{in}}}$. One can easily derive the expression of these quantities using the equations we listed above. As an example, the expressions for the facet-to-facet reflection and transmission are

$$b_{\text{out}} = \chi(\Delta) b_{\text{in}} \quad (\text{B.188})$$

$$b_{\text{ref}} = \chi'(\Delta) b_{\text{in}} \quad (\text{B.189})$$

$$\chi(\Delta) = \frac{t_1 t_2 e^{i(\theta_1 + \theta_2)} (\chi_{11} + \frac{r_2 \chi_{11} \chi_{12} e^{2i\theta_2}}{1 - r_2 \chi_{12} e^{2i\theta_2}})}{1 - r_1 (\chi_{12} e^{2i\theta_1} + \frac{r_2 \chi_{11}^2 e^{2i(\theta_1 + \theta_2)}}{1 - r_2 \chi_{12} e^{2i\theta_2}})} \quad (\text{B.190})$$

$$\chi'(\Delta) = \frac{-r_1 + (\chi_{12} e^{2i\theta_1} + \frac{r_2 \chi_{11}^2 e^{2i(\theta_1 + \theta_2)}}{1 - r_2 \chi_{12} e^{2i\theta_2}})}{1 - r_1 (\chi_{12} e^{2i\theta_1} + \frac{r_2 \chi_{11}^2 e^{2i(\theta_1 + \theta_2)}}{1 - r_2 \chi_{12} e^{2i\theta_2}})} \quad (\text{B.191})$$

$$\chi_{11}(\Delta) = \frac{(i\Delta + \frac{\kappa}{2})^2 - g_{12} g_{21} - \kappa_{\text{ex}}(i\Delta + \frac{\kappa}{2})}{(i\Delta + \frac{\kappa}{2})^2 - g_{12} g_{21}} \quad (\text{B.192})$$

$$\chi_{12}(\Delta) = \frac{-g_{12} \kappa_{\text{ex}}}{(i\Delta + \frac{\kappa}{2})^2 - g_{12} g_{21}}. \quad (\text{B.193})$$

The expressions above are for the most general case, where all the system parameters are considered. However, it is generally not easy to fit all the parameters accurately, with only the knowledge of the transmission response of the chip. Some coefficients are only sensitive to other measurement results, e.g., the reflection response, and can yield unphysical results if not fitted properly.

In the most commonly encountered microresonator cases, the optical mode splitting $g/\kappa \sim 0$

B.13 Filter cavity assembly for the Kerr squeezing experiment

is unresolved. In this limit, the fitting can be greatly simplified to

$$b_{\text{out}} = \frac{t_1 t_2 \chi_{\text{cav}} e^{i(\theta_1 + \theta_2)}}{1 - r_1 r_2 \chi_{\text{cav}}^2 e^{2i(\theta_1 + \theta_2)}} b_{\text{in}} \quad (\text{B.194})$$

$$b_{\text{ref}} = \frac{-r_1 + r_2 \chi_{\text{cav}}^2 e^{2i(\theta_1 + \theta_2)}}{1 - r_1 r_2 \chi_{\text{cav}}^2 e^{2i(\theta_1 + \theta_2)}} b_{\text{in}} \quad (\text{B.195})$$

$$\chi_{\text{cav}} = \frac{i\Delta + \frac{\kappa}{2} - \kappa_{\text{ex}}}{i\Delta + \frac{\kappa}{2}} \quad (\text{B.196})$$

where the transmission function only depends on the cavity response, facet reflectivity, and round-trip phase delay. For example, a fitting result of a typical Fano-shaped transmission trace is illustrated in Fig.A.14, together with the inferred cavity power and the waveguide circulating power. This fitting procedure is also used in recent papers [4, 5].

For more complicated fittings involving Fano and split resonances, one usually needs access to both the reflection and transmission traces since the back-reflection is more sensitive to the split coupling. Therefore, we implemented the general fitting function when characterizing optical resonances with resolved splitting by fitting the transmission and reflection together.

B.13 Filter cavity assembly for the Kerr squeezing experiment

The formulation that I adopted in this note is mainly from this textbook called *Quantum Electronics for Atomic Physics* [46] that I used during my Bachelor's study.

By the time this section is written, we were in the process of conducting the Kerr squeezing experiment. After numerous trials, we were convinced that we were primarily limited by the laser noise (Toptica) over the frequency band near the resonator bandwidth. As Nils and Scott Papp advised, we built a narrow-linewidth filtering cavity for passive laser noise filtering.

Wave optics basics

Here I list some of the most useful guidelines for building a narrow linewidth filter cavity.

Wave optics

We first define Rayleigh length $z_R = \frac{n\pi\omega_0^2}{\lambda}$ which is quite useful, and then write down the wave propagation equations:

$$\omega^2 = \omega_0^2 \left[1 + \left(\frac{z}{z_R} \right) \right] \quad (\text{B.197})$$

$$R(z) = z + \frac{z_R^2}{z}. \quad (\text{B.198})$$

Appendix B. Appendix

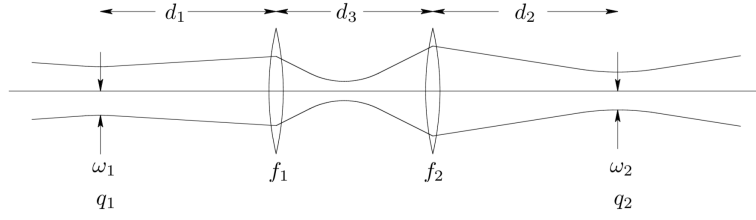


Figure B.15: An example usage of complex beam parameter q updating formula, consisting of two lenses with focal length f_i , and free propagation distances d_i .

where ω is the beam waist and R is the radius of curvature of the Gaussian beam. The complex beam parameter q is then defined as

$$\frac{1}{q} = \frac{1}{R} - i \frac{\lambda}{n\pi\omega^2}. \quad (\text{B.199})$$

which is useful for calculating the beam property evolution over several optical elements. Here, I attach an exemplary usage of the beam parameter q in the setting shown in Fig. B.15 by considering the propagation matrix:

$$\begin{pmatrix} A & B \\ C & D \end{pmatrix} = \begin{pmatrix} 1 & 0 \\ -\frac{1}{f_2} & 1 \end{pmatrix} \begin{pmatrix} 1 & d_3 \\ 0 & 1 \end{pmatrix} \begin{pmatrix} 1 & 0 \\ -\frac{1}{f_1} & 1 \end{pmatrix} \begin{pmatrix} 1 & d_1 \\ 0 & 1 \end{pmatrix} \quad (\text{B.200})$$

with which the complex beam parameter q is updated as

$$q_2 = \frac{Aq_1 + B}{Cq_1 + D} + d_2. \quad (\text{B.201})$$

Using this method, we can derive the beam size at the mirrors and the waist of the cavity. Assuming a symmetric cavity, we can write down the waist of the cavity mode and the spot size at the mirror:

$$\text{At mirror : } \omega^2 = \frac{\lambda R}{n\pi} \sqrt{\frac{d}{2R-d}} \quad (\text{B.202})$$

$$\text{Waist : } \omega_0^2 = \frac{\lambda}{n\pi} \sqrt{\frac{dR}{2} - \frac{d^2}{4}} \quad (\text{B.203})$$

where d is the cavity length, R is the radius of curvature of the mirrors, λ is the wavelength of the light, and n is the refractive index of the medium inside the cavity.

B.13 Filter cavity assembly for the Kerr squeezing experiment

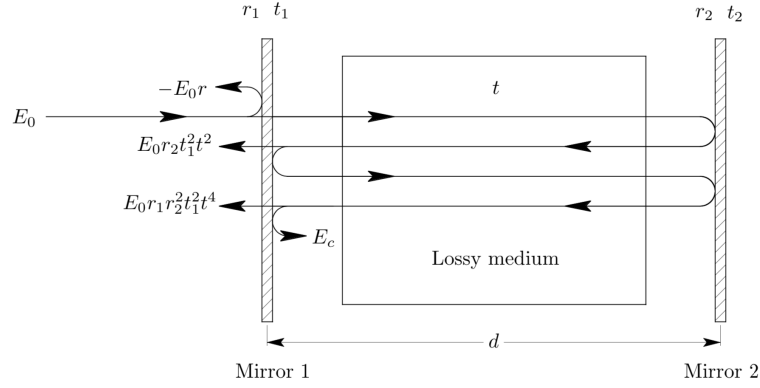


Figure B.16: A simplified model of cavity field relation, consisting of two planar mirrors with field reflectivity r_i and transmission t_i , and a lossy medium with transmission t .

Frequency response

The resonant frequencies of a cavity, including higher-order modes, are:

$$\nu_{nmq} = \left(q + (n + m + 1) \frac{\cos^{-1} \pm \sqrt{g_1 g_2}}{\pi} \right) \frac{c}{2d}, \quad (\text{B.204})$$

where the higher-order factor $\frac{\cos^{-1} \pm \sqrt{g_1 g_2}}{\pi}$ is valued between $0 \sim 1$ and has the following tendency at different cavity geometrical configurations:

0 : near-planar,

1/2 : near-confocal,

1 : near-spherical.

From here, we can define the free spectral range (FSR) for the azimuthal modes (different q) as $\text{FSR} = c/2d$.

To derive the frequency response of these different modes, we use a simplified cavity model shown in Fig. B.16 (from the book [46]), from which we can derive the reflected, circulating, and transmitted light intensity as

$$\text{Reflecting:} \quad I_r = I_0 \frac{(r_2 t^2 - r_1)^2 (F \Delta \nu_{1/2} / \pi)^2 + 4(\nu - \Delta \nu_{1/2})^2}{(\Delta \nu_{1/2})^2 + 4(\nu - \Delta \nu_{1/2})^2} \quad (\text{B.205})$$

$$\text{Circulating:} \quad I_c = I_0 \frac{(t_1 F \Delta \nu_{1/2} / \pi)^2}{(\Delta \nu_{1/2})^2 + 4(\nu - \Delta \nu_{1/2})^2} \quad (\text{B.206})$$

$$\text{Transmission:} \quad I_t = I_0 \frac{(t_1 t_2 F \Delta \nu_{1/2} / \pi)^2}{(\Delta \nu_{1/2})^2 + 4(\nu - \Delta \nu_{1/2})^2} \quad (\text{B.207})$$

where we define the full width at half maximum (FWHM), finesse, and quality factor with their

Appendix B. Appendix

relation:

$$\text{FWHM(phase)} : \quad \Delta\nu_{1/2} = \frac{2(1 - r_1 r_2 t^2)}{\sqrt{r_1 r_2 t^2}} \quad (\text{B.208})$$

$$\text{Finesse} : \quad F = \frac{2\pi}{\Delta\nu_{1/2}} = \frac{\pi\sqrt{r_1 r_2 t^2}}{1 - r_1 r_2 t^2} \quad (\text{B.209})$$

$$\text{Qualityfactor} : \quad Q = \frac{\text{roundtrip} \cdot F}{\lambda} \quad (\text{B.210})$$

where ν is the optical detuning from the cavity resonance, and t_i and r_i are the field transmission and reflectivity of the mirrors and the lossy medium inside the cavity.

To obtain maximum optical transmission through the cavity, we use a symmetric mirror configuration, with which the impedance matching condition is quantified by

$$\frac{I_t}{I_0} = \frac{t_1^2 t_2^2}{(1 - r_1 r_2 t^2)^2} = \left(\frac{t_1 t_2}{(t_1^2 + t_2^2)/2 + (1 - t^2)} \right)^2 \stackrel{\text{sym}}{\approx} \left(\frac{T}{T + L} \right)^2 \stackrel{L \ll T}{\approx} 1 - \frac{2L}{T + L} \quad (\text{B.211})$$

where the total transmission is primarily limited by the cavity loss L .

Cavity design

The design goal is to have a narrow-linewidth, high-transmission cavity at 1550 nm to stabilize the laser frequency and filter the high-frequency noise. The transmitted light should have sufficiently low noise at the frequency band in which Kerr squeezing might be achievable. The cavity resonance is supposed to be tunable to tune the filtered laser into the microresonator resonance to conduct the squeezing experiment. We must also ensure high transmission out of the cavity because we were already power-starving for this experiment. In this case, we design our cavity to be a symmetric, impedance-matched cavity with two identical mirrors with high reflectivity and low loss over transmission ratio.

We purchased the 10CV00SR.70F High-Performance Concave SuperMirrors™ from Newport™ because they offer the quickest delivery service (received in one week). We planned to glue the mirrors to the ZERODUR® ultralow expansion (ULE) glass spacer with the coating at the inner side to form a stable symmetric optical cavity. The ULE glass is used to ensure the thermal stability of the cavity length because the cavity length fluctuation would be printed on the laser. A piezo was also integrated into this assembly to tune the cavity resonance frequency by changing the cavity length.

The mirror specification is shown in Fig. B.17. The reflection is roughly 99.99%, and the transmission is roughly 00.01%, indicating a relatively low loss. These are concave mirrors and the radius of curvature is 1 m, and with the 6 cm ZERODUR spacer we have, they would form a very planar cavity with Finesse roughly at 3×10^4 , FSR 2.5 GHz and linewidth $\Delta\nu_{1/2} = 80$ kHz. The mirror diameter is 25.4 mm, which well matches the ZERODUR ULE's ID=20 mm and

B.13 Filter cavity assembly for the Kerr squeezing experiment

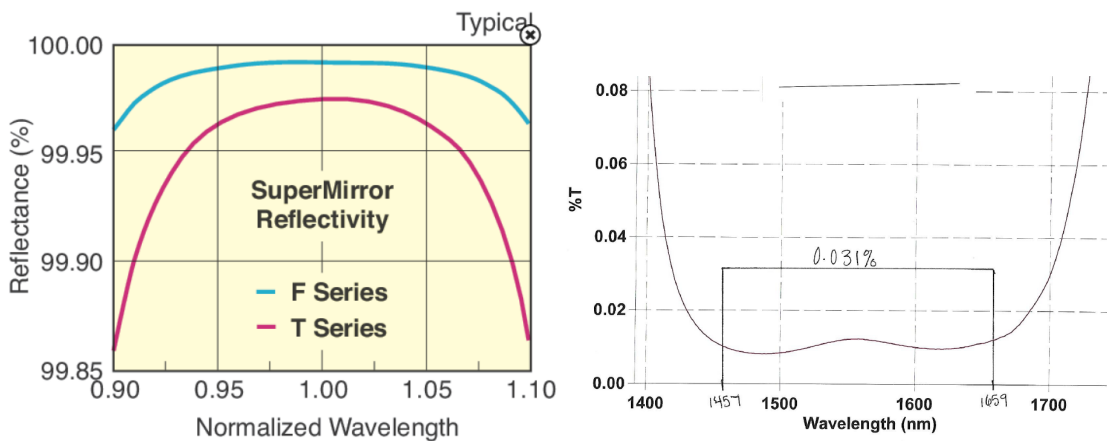


Figure B.17: Reflection and transmission for the 10CV00SR.70F model. The reflection of this model is shown in the legend as the F series.

OD=50 mm.

The piezos actuators HH1-2515-07 are ordered from PiezosystemJena. It is the only type of piezo we found online that matches the geometry of the mirror with OD=25 mm ID=15 mm, and the smallest thickness of 9 mm. This piezo offers about 1.5 μm stroke at a relatively low voltage at 100 V, allowing roughly a 2-FSR tuning range for the cavity optical resonances. However, they needed to make these piezos from scratch, so the delivery time was around four weeks.

With the piezo added, the cavity length would change to 7 cm, with the corresponding free spectral range $\text{FSR}=2.14$ GHz and $\Delta\nu_{1/2} = 71.4$ kHz. The calculated cavity waist is $\omega_0 = 296$ μm , and the beam spot size at the mirror is $\omega = 301$ μm . The Rayleigh length of such cavity is 18.8 cm at which distance the beam size is increased by $\sqrt{2}$ relative to the waist.

The mirror gluing method and cavity holder design take reference from [361] and [362]. We eventually decided to use a V-groove holder with a 120-degree opening. The V-groove is used such that when gravity pulls down the cavity, the mirrors are still parallel to each other. One can also use the Airy points to achieve the same effect and probably better vibration isolation. The design of the cavity holder and the shielding box is shown in Fig. B.18. The cavity is softly clamped to the cavity holder, and the shield box is used to prevent dust from entering the spacer to prevent mirror burning when circulating high optical power.

The mechanical and thermal property of the cavity is also simulated using COMSOL. For the thermal property, we simulated the frequency shift of the cavity resonance frequency caused by laser heating. The simulation result is shown in Fig. B.19. The primary contribution of the thermal expansion is from the piezo, which is expected. With a reasonable power input at 10 mW, assuming a 10% power absorption, the cavity frequency shift will be about 2 MHz, which is acceptable for our experiment with microresonator linewidth around 15 MHz. For the mechanical property shown in Fig. B.20, a piezo is attached to the side of the cavity holder

Appendix B. Appendix

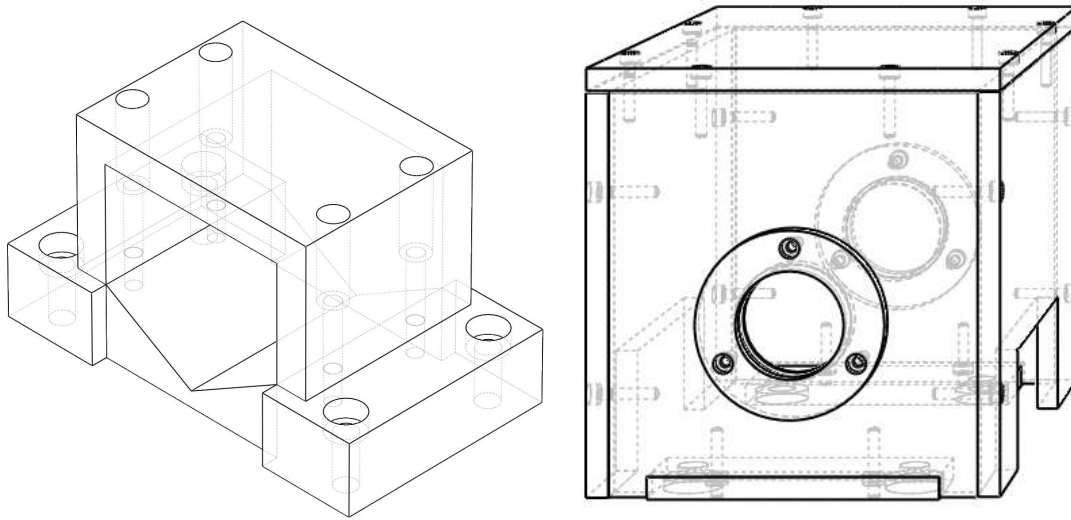


Figure B.18: Holder and shield design for the optical cavity. The holder is designed to prevent gravity-induced bending of the cavity, and the shield is designed to prevent particle contamination.

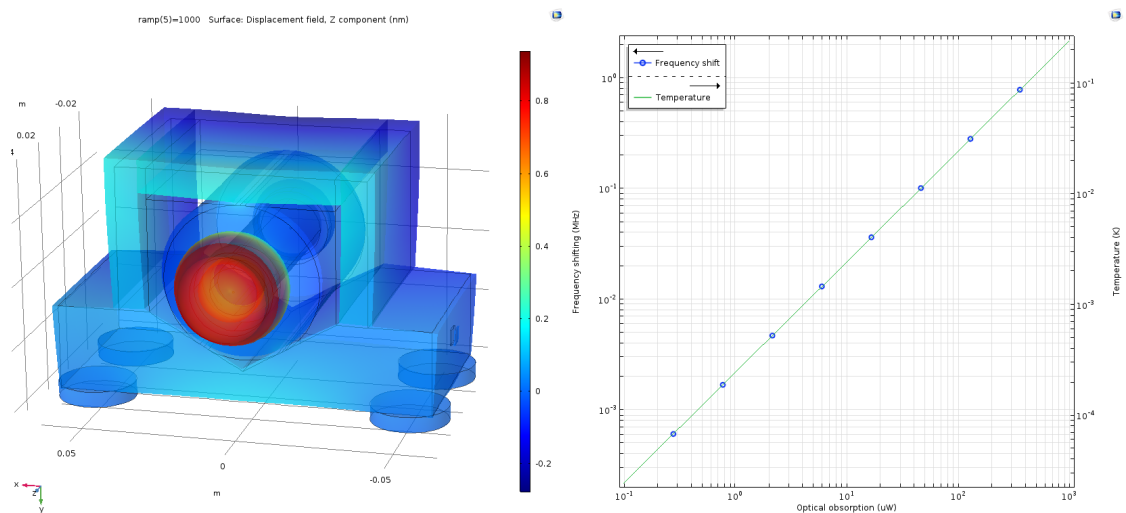


Figure B.19: Thermal property of the cavity simulated in COMSOL. The heat source is located at the presumed beam spot on the mirrors.

B.13 Filter cavity assembly for the Kerr squeezing experiment

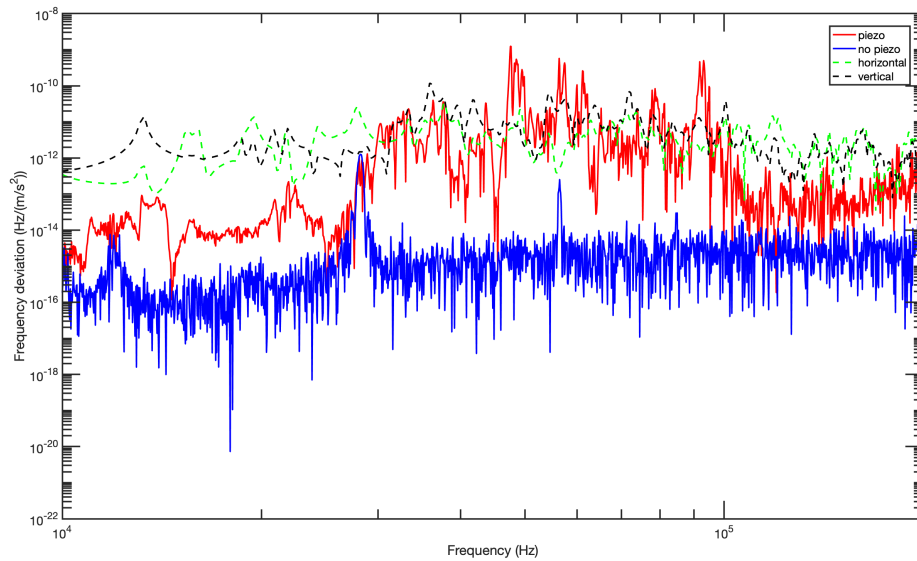


Figure B.20: Mechanical property of the cavity simulated in COMSOL and the experimentally measured response data using a VNA and a vibrometer. The background noise of the vibrometer is also measured. We did not observe a good matching between the mechanical modes but did observe the characteristic mode density distribution in this frequency window.

and drives the cavity. Then, the cavity resonance frequency response relative to the piezo drive is studied in COMSOL simulation and recorded experimentally using a vibrometer. However, very poor correspondence between experimental data and the simulation profile is observed. From the simulation side, we are happy with the different properties of this optical cavity we planned to build, but the simulation was only done after the cavity was assembled.

Cavity assembly procedure

The cavity was first assembled without the integration of piezo nor any gluing element but by fixing the mirror to the spacer through three steel clamps shown in the left panel of Fig. B.21. We first tried this simple configuration with easily removable clamps to test the mirrors and the basic cavity property. When we found that everything was working as expected, we glued the mirrors and integrated a piezo actuator, as shown in the right panel of Fig. B.21.

The piezo integration was successful without changing the optical mode position too much, and no noticeable degradation of the optical linewidth was observed. We orient the ULE cavity stack vertically during the curing process, after aligning the piezo actuator and the mirror horizontally, such that gravity does not displace the components during the curing process. A 200 g post was also put on top of the mirror and piezo stack to apply compressive pressure to keep them in close contact. For gluing, we used the Norland Optical Adhesive 63. It is a type of UV glue that cures pretty hard after a 3s to 2min exposure. As recommended by my

Appendix B. Appendix

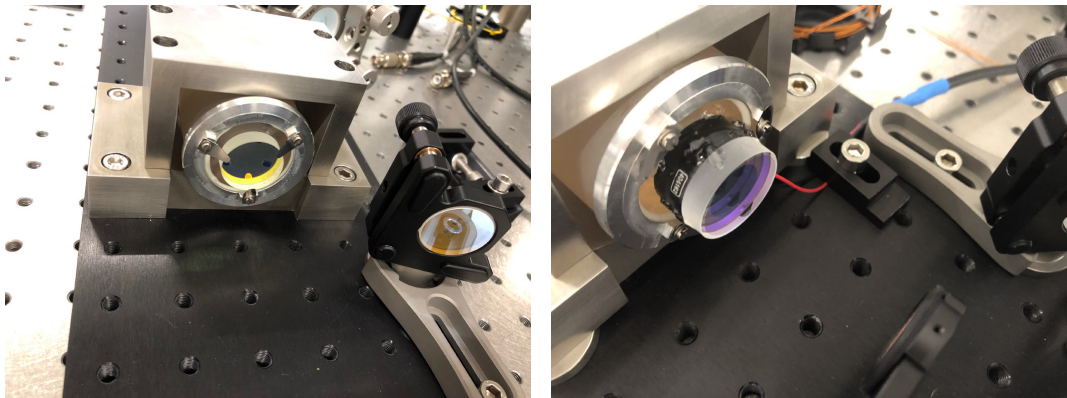


Figure B.21: Assembly of the cavity, showing the cavity without the piezo (left) and the one with the piezo (right). The glues are placed triangularly, after which the clamps are removed.

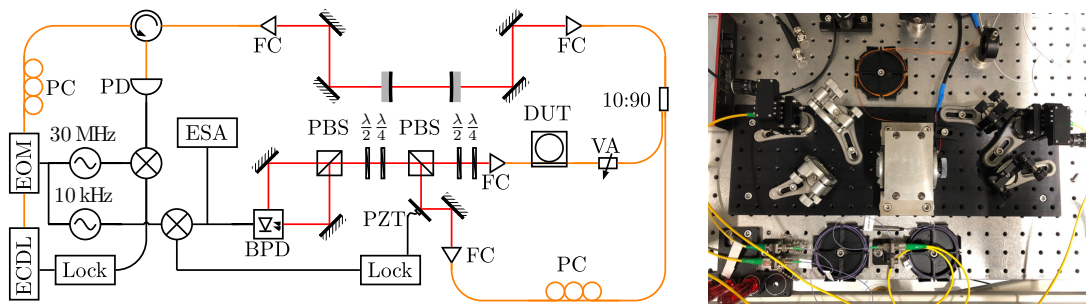


Figure B.22: The experiment setup for the Kerr squeezing experiment (left) and an image of the filtering cavity setup (right), showing two fiber collimators and two sets of alignment mirrors.

colleague Arslan, I used a fiber tip first to get a drop of glue, cure it on the tip, and use it as a transporter of the glue to the mirror edges. As soon as a drop about 1 mm^3 is attached to the connecting edges of between components, quickly use a 3s UV light exposure to pre-cure it, such that it does not flow around. Then, a 1min exposure on each side, and 30s on each side again to uniformly apply pressure to the mirror and piezo so that directional tilting is unlikely to happen. We first glued the side with the piezo and clamped the other mirror without the piezo for a quick test run. As the optical cavity seems to work fine, we glue the remaining side with the clamp.

Before the assembly, we were worried about the mirror tilting due to the imperfection of surface orientation of the piezo because our mirror focus $f = 50 \text{ cm}$ is considerably more significant than the cavity linewidth, so the optical mode position will be susceptible to the mirror orientation. However, everything seems to be working just fine.

B.13 Filter cavity assembly for the Kerr squeezing experiment

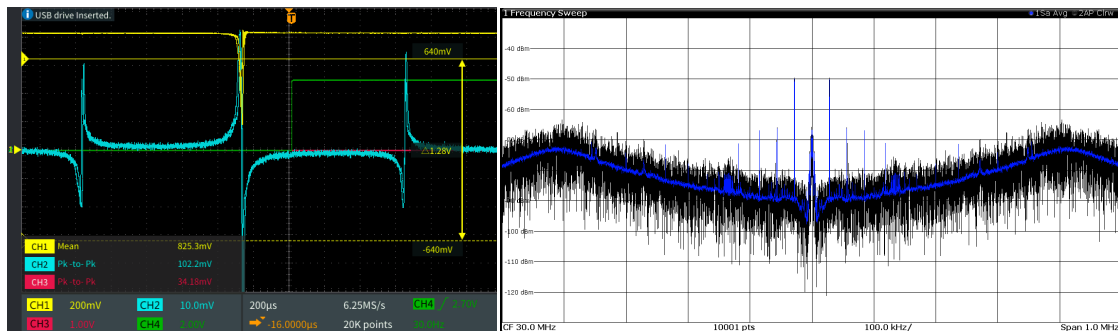


Figure B.23: Toptica laser PDH locking signal to the optical cavity and the transmission signal (left). The in-loop noise near the modulation frequency is also shown on the right.

Cavity characterization

Coupling to the cavity modes

The optical setup used to couple to the optical cavity and receive the transmitted light is illustrated in Fig. B.22. The light is incident onto the cavity mirror facet and coupled to the input fiber collimator. The reflected light is isolated by an optical isolator and monitored using a 125MHz low-noise photo detector. It is expected that the optical mode at the mirror surface should also be perpendicular to the mirror surface so it will overlap with the directly reflected light. In this way, the optical mode search can be realized by keeping a good coupling of the back-reflected light and, simultaneously, scanning the position of the optical beam on the mirror facet. It is expected to see many high-order modes with very weak coupling and small spacing relative to FSR as indicated from Eq. B.204 as we are at the near-planar case. The coupling to the higher-order modes is exhibited as many small dips on the reflection signal when the laser is scanned through a reasonably large frequency span. As the fundamental mode has the lowest optical frequency, we can optimize the coupling to the fundamental mode by improving the coupling to lower and lower frequency modes step by step and eventually find one mode with high coupling and no modes below its frequency.

Locking system

After the fundamental mode is well coupled, we can use the reflected signal to realize the PDH locking of the laser to the optical cavity, of which the signal is illustrated in Fig. B.23. We used a 30 MHz modulation through EOM to create the illustrated PDH signal. A bias-T separated the DC and AC parts of the reflected signal. The DC part was put into the oscilloscope to monitor the cavity reflection (left panel, yellow), and the AC part was fed to the mixer to be demodulated to get the PDH signal we see on the scope (left panel, blue). A directional coupler was also used to get 10% of the AC signal to monitor the noise at modulation frequency on the spectrum analyzer (right panel).

As we can see from the spectrum signal illustrated at the right panel of Fig. B.23, the locking is

Appendix B. Appendix

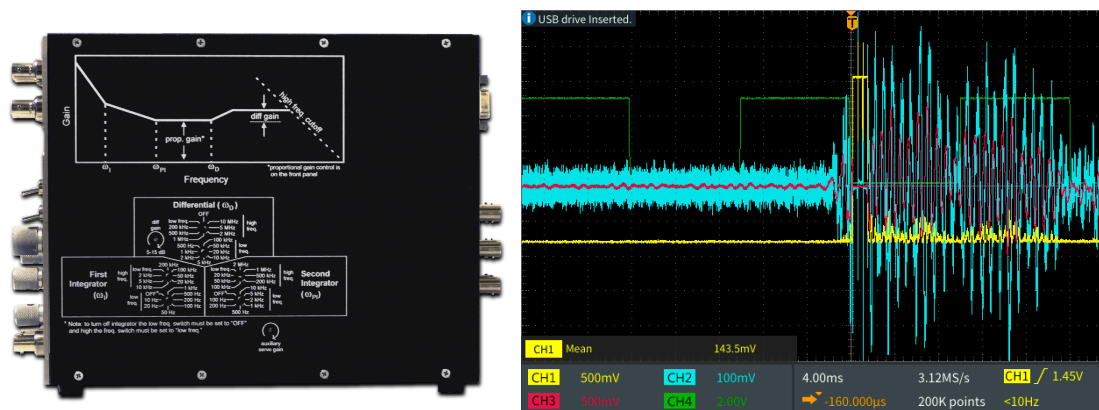


Figure B.24: Vescent lock box (left) and the lock guard functionality (right). After detection of a strong disturbance in the lock signal (blue), the lock disengages for 8 ms (yellow) before reapplying the lock for the vibration to decay.

affected by a strong modulation roughly at 30 kHz. It appears when the mirrors are clamped but not glued and still there after they are glued. We suspected it could be a mechanical motion of the optical cavity that was excited by some external drive. To check such a possibility, a COMSOL simulation of its mechanical response with the setup's actual configuration (including the piezo driving position and two driving directions) was first conducted as shown in Fig. B.20, and we also glued a sheer piezo onto the cavity holder in order to excite the cavity mechanical modes. However, no particular peak was observed at the frequency where the noise appeared. The highest peak is around 47 kHz, near the mirror's vibrational fundamental mode. To rule out the possibility that the noise is just the table violently vibrating, we used a vibra-meter to measure the acoustic noise from the optical table and did not observe any noticeable signal. After the investigation, we are certain it is electronic noise feeding on the laser current. However, we are not able to identify the noise source. We can observe more peaks when the diamond milling machine in the lab is turned on, so we suspect the noise is from one of the high-power transformers.

The lock box that we used is Vescent D2-125, which has up to 10 MHz locking bandwidth, auxiliary feedback output, and lock guard function. We feedback the servo output directly to the laser current for tight laser locking and the auxiliary servo output to the laser controller to do feedback on the piezo. The auxiliary servo output signal is integrated from the servo output so that the laser current does not change during long-term locking.

In order to have the best locking condition, we need to identify the system's phase flip point and ensure that it lands on the proportional gain frequency range with gain < 1. The phase flip point can be identified by having a very high gain on the feedback and looking for the first peak that emerged from the overgain. The old configuration was to set $f_{PI} = 20$ kHz when the phase flip frequency was at 70 kHz, and no derivative module was used. Our current phase flip frequency is actually at 500 kHz, so the f_{PI} can be further increased to achieve better noise suppression at 30 kHz, which is right now the most prominent noise preventing tight locking.

B.13 Filter cavity assembly for the Kerr squeezing experiment

However, it turns out that when f_{PI} increases, the phase flip point frequency also gets lower and lower, such that it does not get better. After a few tests, the best locking condition is still at 20 kHz, with the first integration gain turned off. The overall system gain fixes the second integration gain slope, so if the first integration gain is too high, it could leave the lock unstable against low-frequency environmental noise such as lab-door slamming.

The lock guard function ensures long-term locking stability against spiked environmental noise. It monitors the feedback signal and holds the lock for 8 ms when the feedback signal changes too quickly. After the hold, it will try to relock the system, as illustrated from Fig. B.24, which is usually successful because the spiked noise should already decay significantly by the time. However, if relock is unsuccessful, it will repeat several times with a longer hold time. Using the lock guard, the longest locking record is around 5 hours until I have to leave the lab.

Cavity transmission

The collimator lens is selected with $f = 5$ mm, such that at a relatively long distance ~ 16.5 cm, we can achieve nearly perfect mode matching from cavity mode to fiber mode with $>93\%$ coupling efficiency. Considering the 4% reflection loss from the fiber facet, it is almost perfect mode matching. After the mode matching was realized at the output port, we used it as the input port to check the actual transmission of the cavity mode, which is around 82.3% , from which, together with the cavity ringdown measurement, we derived the 100 ppm transmission and 10 ppm loss of the supermirrors. Then, we use the transmitted light from the cavity mode to optimize the mode matching of the input port until both ports achieved coupling efficiency $>93\%$, with the transmission of the whole setup $>70\%$.

Cavity ring down

As the cavity linewidth is too narrow to be measured using the sideband fitting method, the cavity ring-down measurement was conducted to determine the cavity linewidth. The transmission of the optical cavity was monitored by a 125 MHz low noise photodetector on the oscilloscope, and the input light was periodically switched using an AOM. The RF signal applied to the AOM is switched by a 100 Hz periodic pulse with 50 us pulse duration (shut down), such that the lock is not affected during the switching and the ring down slopes can be averaged many times. The pulse TTL signal is used as the oscilloscope's trigger source, and the ring down slope is averaged 1000 times. The result is illustrated in Fig. B.25(a), from which a linewidth of 68.4 kHz can be obtained with a quality factor around 3 billion, which is more or less consistent with our expectation from the mirror specs.

High optical power operation

A quick trial with over 1.2 mW transmission was tested, and no locking problem was observed. However, we need another reference laser for the cavity frequency thermal shifting. From

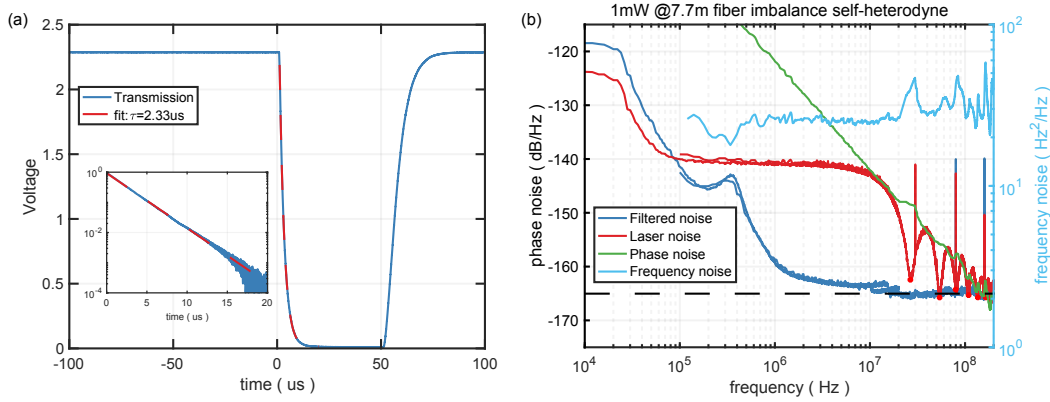


Figure B.25: **(a)** Cavity ring down measurement using an AOM to shutter the input light, showing a cavity linewidth of $\kappa/2\pi = 68.4 \text{ kHz}$ and a quality factor of $Q = 2.82 \times 10^9$. **(b)** Laser phase noise comparison with and without the filter cavity, using unbalanced heterodyne detection. Based on the raw measurement signal in blue and red, the original phase noise is reconstructed in green, and the frequency noise is converted to the right y-axis.

COMSOL simulation, when the cavity is running at 10 mW of input power with 1 mW optical absorption, the resonance frequency will be shifted by about 2 MHz, which is negligible in our experiment setting. However, it still needs experimental verification. The mirror surface’s optical intensity is about ten times higher than the mirror damaging threshold. However, we observed no performance degradation over an extended usage period.

Laser noise filtering

Using a self-heterodyne detection with a 7.7m imbalance, we measured the laser phase noise before and after the filter cavity. One arm is up-shifted by 100MHz using an AOM, and the combined fiber is connected to a 1-GHz photodetector, in which phase noise is exhibited as noises centered around the 100-MHz beating signal. We recorded the laser noise with and without the filtering in Fig. B.25(b), and observed at 1-MHz offset frequency a noise suppression of at least 20dB, and expect 40dB noise reduction at 10-MHz offset frequency, where Kerr squeezing is supposed to be observed.

B.14 Purity and fidelity of heralded optical states by measurements of electron energy

In this section, we derive the heralded optical states by measuring electron energy, and calculate the state fidelity and purity. The optical state generated when there is no higher-order sideband overlap (not a fundamental limit) and when conditioning on a narrow bandwidth

B.14 Purity and fidelity of heralded optical states by measurements of electron energy

around an energy slice $E_c \sim N\hbar\omega$ is

$$|\psi_{\text{ph}}\rangle = \frac{\int \prod_{k=1}^N d\omega_k g_{\omega_k}^* \psi(E + \hbar(\sum_k \omega_k)) \hat{a}_{\omega_k}^\dagger |0\rangle}{\sqrt{\int \prod_{k=1}^N d\omega_k |g_{\omega_k}|^2 |\psi(E + \hbar(\sum_k \omega_k))|^2 (N!)^2}} \quad (\text{B.212})$$

As we can see, the coefficient is a product between the electron wavefunction and the coupling coefficient. This reflects the fact that the electron energy distribution is correlated with the frequency at which the photon is created. We will see later that this is not the case for conditional electron states since in the no-recoil limit, the frequency of the photon does not depend on the electron's energy.

In the first limit, when electron ZLP is much narrower than phase-matching bandwidth, we can simplify the expression to

$$|\psi_{\text{ph}}\rangle = \frac{\int \prod_{k=1}^N d\omega_k \psi(E + \hbar(\sum_k \omega_k)) \hat{a}_{\omega_k}^\dagger |0\rangle}{\sqrt{\int \prod_{k=1}^N d\omega_k |\psi(E + \hbar(\sum_k \omega_k))|^2 (N!)^2}} \quad (\text{B.213})$$

for single-photon states. The frequency components of the generated state are directly linked to $\phi(\omega) \propto \psi(E_c + \hbar\omega)$. Ignoring the waveguide dispersion during propagation, we have the optical waveform

$$\phi(T = t - z_{\parallel}/v) = \tilde{\psi}(T) e^{i\omega_c T} \quad (\text{B.214})$$

where it has a center frequency determined by the conditional electron energy and an envelope profile that is exactly the time domain electron spatial profile $\tilde{\psi}(T)$. Therefore, by shaping electron wavefunctions and conditioning on the selected sideband energy, we can transfer the electron spatial wavefunction to the optical waveform of the photonic state at a desired optical frequency. For readers familiar with optical spontaneous parametric down-conversion, a similar technique is also used in heralded single-photon sources [363] to imprint the waveform of the pump field onto the signal field.

For conditional multi-photon optical states, as we can immediately see from the expression, since the electron wavefunction generally can not be factorized to N components $\psi(E + \hbar(\sum_k \omega_k)) \neq \prod_k \psi_k(E, \omega_k)$, the conditional state can not be addressed into a Fock state of a well defined spatial-temporal mode, but since high phase-matching bandwidth usually comes with low g , we restrict ourselves to single-photon states in this limit. We derive the fidelity of the heralded single-photon state as

$$\mathcal{F} = \left| \langle \psi'_{\text{ph}} | \psi_{\text{ph}} \rangle \right|^2 = \frac{|\int d\omega g_{\omega} |\psi(E + \hbar\omega)|^2|^2}{(\int d\omega |g_{\omega}|^2 |\psi(E + \hbar\omega)|^2) (\int d\omega |\psi(E + \hbar\omega)|^2)}. \quad (\text{B.215})$$

For the case of long propagation, we usually end up with very narrow phase-matching bandwidth and high interaction g . In this case, when conditioning on the N th energy sideband, we

Appendix B. Appendix

can simplify the expression to

$$|\psi_{\text{ph}}\rangle = \frac{\int \prod_{k=1}^N d\omega_k g_{\omega_k}^* \hat{a}_{\omega_k}^\dagger |0\rangle}{\sqrt{\int \prod_{k=1}^N d\omega_k |g_{\omega_k}|^2 (N!)^2}} \quad (\text{B.216})$$

where it is a well-defined N -photon Fock state with mode profile $\phi(t)$ (see Section 6.3.2), which is determined by both the waveguide routing and the material dispersion. To this end, one can adapt the electron positioning and velocity to shape the optical waveform. We derive the fidelity to this state as

$$\mathcal{F} = \left| \langle \psi'_{\text{ph}} | \psi_{\text{ph}} \rangle \right|^2 = \frac{\left| \int \prod_{k=1}^N d\omega_k |g_{\omega_k}|^2 \psi(E + \hbar(\sum_k \omega_k)) \right|^2}{\left(\int \prod_{k=1}^N d\omega_k |g_{\omega_k}|^2 \right) \left(\int \prod_{k=1}^N d\omega_k |g_{\omega_k}|^2 |\psi(E + \hbar(\sum_k \omega_k))|^2 \right)} \quad (\text{B.217})$$

With more electron operation stages, we can select the electron measurement basis. After the pair-state generation, if we pass the electron through, e.g., a PINEM interaction stage characterized by the scattering matrix $\hat{S}(\alpha)$, by conditioning on the energy sideband $|E\rangle$, we are effectively measuring under the basis $\hat{S}^\dagger(\alpha)|E\rangle = \sum_i c_i^* |E_i\rangle$. Formally, we write down the conditional optical state as

$$|\psi_{\text{ph}}\rangle \propto \sum_N \frac{c_N g^N}{\sqrt{N!}} |N\rangle \quad (\text{B.218})$$

$$\hat{\rho}_{\text{ph}} = \langle E | \hat{S}(\alpha) \hat{\rho} \hat{S}^\dagger(\alpha) | E \rangle \quad (\text{B.219})$$

where $|g|^2 = \int d\omega |g_\omega|^2$. This operation effectively projects the optical state into a more general state other than Fock states if we directly measure the electron energy after the pair-state preparation. For these general states, the corresponding heralded state fidelity is an average of all the involved Fock states with a correct weight

$$\mathcal{F} = \left| \langle \psi'_{\text{ph}} | \psi_{\text{ph}} \rangle \right|^2 \quad (\text{B.220})$$

$$= \left| e^{-|g|^2} \sum_N \frac{|c_N|^2 |g|^{2N}}{N!} \frac{\int \prod_{k=1}^N d\omega_k |g_{\omega_k}|^2 \psi(E_N + \hbar(\sum_k \omega_k))}{\sqrt{\left(\int \prod_{k=1}^N d\omega_k |g_{\omega_k}|^2 \right) \left(\int \prod_{k=1}^N d\omega_k |g_{\omega_k}|^2 |\psi(E_N + \hbar(\sum_k \omega_k))|^2 \right)}} \right|^2$$

and the same kind of weighted averaging also needs to be applied to the heralded state purity.

Two main effects can degrade the single-photon state purity. First, the spectral overlap between different sideband orders. Second, the relative bandwidth ratio between ZLP and phase-matching bandwidth. For higher-order Fock states, it is further affected by the spectral distribution of the other optical mode families, e.g., the electron might not be able to distinguish between a two-photon transition of the fundamental optical mode and a single-photon transition of a higher-order mode. Here, we categorize this case into the spectral overlap between electron sidebands.

B.14 Purity and fidelity of heralded optical states by measurements of electron energy

First, let us investigate the purity degradation of the conditional photonic Fock state due to the sideband spectral overlap. In the limit of narrow phase-matching bandwidth, the optical density matrix after detection at electron energy band ΔE electron energy event is

$$\hat{\rho}_{\text{ph}} = \frac{1}{\sum_N \frac{(\int d\omega |g_\omega|^2)^N}{N!} \int_{\Delta E} dE |\psi(E + N\hbar\omega)|^2} \quad (\text{B.221})$$

$$\times \int_{\Delta E} dE \left(\sum_N \frac{(-\int d\omega g_\omega^* \hat{a}_\omega^\dagger)^N}{N!} \prod_\omega |0_\omega\rangle \psi(E + N\hbar\omega) \right) \left(\sum_N \psi^*(E + N\hbar\omega) \prod_\omega \langle 0_\omega | \frac{(-\int d\omega g_\omega \hat{a}_\omega)^N}{N!} \right)$$

The purity of this state is

$$\text{Tr} [\hat{\rho}_{\text{ph}}^2] = \frac{1}{\left(\sum_N \frac{(\int d\omega |g_\omega|^2)^N}{N!} \int_{\Delta E} dE |\psi(E + N\hbar\omega)|^2 \right)^2} \quad (\text{B.222})$$

$$\times \sum_{N, N'} \frac{(\int d\omega |g_\omega|^2)^{N+N'}}{N!N'!} \iint_{\Delta E} dE dE' \psi(E + N\hbar\omega) \psi^*(E + N'\hbar\omega) \psi^*(E' + N\hbar\omega) \psi(E' + N'\hbar\omega)$$

Then, we investigate the effect of finite phase-matching bandwidth, and in the limit where there is no photon sideband overlap, the conditional single-photon Fock state is

$$\hat{\rho}_{\text{ph}} = \frac{1}{\iint_{\Delta E} dE d\omega |g_\omega|^2 |\psi(E + \hbar\omega)|^2} \quad (\text{B.223})$$

$$\times \int_{\Delta E} dE \left(\int d\omega g_\omega^* \psi(E + \hbar\omega) \hat{a}_\omega^\dagger |0\rangle \right) \left(\int d\omega g_\omega \psi^*(E + \hbar\omega) \langle 0 | \hat{a}_\omega \right)$$

with corresponding state purity

$$\text{Tr} [\hat{\rho}_{\text{ph}}^2] = \frac{\iint_{\Delta E} dE dE' d\omega d\omega' |g_\omega|^2 |g_{\omega'}|^2 \psi(E + \hbar\omega) \psi^*(E + \hbar\omega') \psi^*(E' + \hbar\omega) \psi(E' + \hbar\omega')}{\left(\iint_{\Delta E} dE d\omega |g_\omega|^2 |\psi(E + \hbar\omega)|^2 \right)^2} \quad (\text{B.224})$$

In the limit of perfect electron energy resolution $\Delta E \rightarrow 0$, $\text{Tr} [\hat{\rho}_{\text{ph}}^2] \rightarrow 1$. However, experimentally, either the ZLP contains a statistical uncertainty, or the conditioning window ΔE can not be set arbitrarily small due to its effect on the heralding rate. As a result, the purity is limited by both the phase-matching bandwidth and the relative heralding bandwidth.

For a general N -photon Fock state, the density matrix of the heralded state is

$$\hat{\rho}_{\text{ph}} = \frac{1}{\iint_{\Delta E} dE \prod_{k=1}^N d\omega_k |g_{\omega_k}|^2 |\psi(E + \hbar(\sum_k \omega_k))|^2 (N!)^2} \quad (\text{B.225})$$

$$\times \int_{\Delta E} dE \left(\int \prod_{k=1}^N d\omega_k g_{\omega_k}^* \psi \left(E + \hbar(\sum_k \omega_k) \right) \hat{a}_{\omega_k}^\dagger |0\rangle \right) \left(\int \prod_{k=1}^N d\omega_k g_{\omega_k} \psi^* \left(E + \hbar(\sum_k \omega_k) \right) \langle 0 | \hat{a}_{\omega_k} \right)$$

Appendix B. Appendix

with the corresponding state purity

$$\begin{aligned} \text{Tr}[\hat{\rho}_{\text{ph}}^2] &= \left(\iint_{\Delta E} dE \prod_{i=1}^N d\omega_i |g_{\omega_i}|^2 |\psi(E + \hbar(\sum_i \omega_i))|^2 \right)^{-2} \iint_{\Delta E} dE dE' \prod_{i,j=1}^N d\omega_i d\omega'_j \\ &\times |g_{\omega_i}|^2 |g_{\omega'_j}|^2 \psi(E + \hbar(\sum_i \omega_i)) \psi^*(E + \hbar(\sum_j \omega'_j)) \psi^*(E' + \hbar(\sum_i \omega_i)) \psi(E' + \hbar(\sum_j \omega'_j)) \end{aligned} \quad (\text{B.226})$$

To illustrate the impact of relative heralding bandwidth on state purity, we show the overall scaling of $1 - \mathcal{P} \propto \gamma^2$ in the limit of small heralding bandwidth in Fig. 6.12. For a general state $|\psi_{\text{ph}}\rangle = \sum c_N |N\rangle$, which consists of a coherent superposition of different Fock states $|N\rangle$, as discussed before in the state fidelity calculation, the purity is a $|c_N|^2$ weighted average of each Fock state component, shown as

$$\begin{aligned} \text{Tr}[\hat{\rho}_{\text{ph}}^2] &= \sum_N |c_N|^4 \mathcal{P}_N + \sum_{N,N'} |c_N|^2 |c_{N'}|^2 \mathcal{P}_{N,N'} \quad (\text{B.227}) \\ \mathcal{P}_{N,N'} &= \iint_{\Delta E} dE dE' \prod_{i=1}^N \prod_{j=1}^{N'} d\omega_i d\omega'_j |g_{\omega_i}|^2 |g_{\omega'_j}|^2 \\ &\times \psi\left(E + \hbar(\sum_i \omega_i - N\bar{\omega})\right) \psi^*\left(E + \hbar(\sum_j \omega'_j - N'\bar{\omega})\right) \\ &\psi^*\left(E' + \hbar(\sum_i \omega_i - N\bar{\omega})\right) \psi\left(E' + \hbar(\sum_j \omega'_j - N'\bar{\omega})\right) \\ &\times \left(\iint_{\Delta E} dE \prod_{i=1}^N d\omega_i |g_{\omega_i}|^2 |\psi(E + \hbar(\sum_i \omega_i - N\bar{\omega}))|^2 \right)^{-1} \\ &\left(\iint_{\Delta E} dE \prod_{j=1}^{N'} d\omega'_j |g_{\omega'_j}|^2 |\psi(E + \hbar(\sum_j \omega'_j - N'\bar{\omega}))|^2 \right)^{-1}, \end{aligned} \quad (\text{B.228})$$

where \mathcal{P}_N is the purity of the N th Fock state component, $\mathcal{P}_{N,N'}$ is the purity of the off-diagonal terms, and $\bar{\omega}$ is the center frequency of the optical state.

B.15 Purity of heralded electron states by measurements of optical state

In this section, we consider heralding schemes that generate complex electron states, and derive the expression of purity of the heralded electron state by the optical measurement. With multiple single-photon detectors, if one conditions on a N -photon counting event, one projects the electron into a corresponding energy state that loses an equal amount of energy. However, these types of photon counting measurements can not project the electron into a coherent superposition of multiple sideband states. This restriction results from the chosen measurement operator $a^\dagger a$, whose eigenstates are Fock states. However, we can select

B.15 Purity of heralded electron states by measurements of optical state

a measurement basis to project the electron onto a more general state. These operations require high detection efficiencies (no information loss), which must be considered carefully when applying optical elements, e.g., spectral filters. The first simple method to change the measurement basis would be to combine the signal with a strong local oscillator through a high aspect ratio beam splitter. This interference modifies the detection from photon-number detection to field detection in the basis of displaced Fock states. With the ability to mode-match to an optical reference field, homodyne types of detection can also be realized. In the setting where the signal field is split and detected by two homodyne in orthogonal quadratures, the measurement is effectively under the coherent state basis. More sophisticated operations can be done with an atomic system to provide an arbitrary measurement basis.

Now, we consider a general heralded electron state, with the N th sideband density matrix component as

$$\hat{\rho}_e = \frac{1}{\iint_{\Delta\omega} dE \prod_{k=1}^N d\omega_k |g_{\omega_k}|^2 |\psi(E + \hbar(\sum_k \omega_k))|^2} \int_{\Delta\omega} \prod_{k=1}^N d\omega_k |g_{\omega_k}|^2 \left(\int dE \psi(E) |E - \hbar(\sum_k \omega_k)\rangle \right) \left(\int dE \psi^*(E) \langle E - \hbar(\sum_k \omega_k)| \right) \quad (\text{B.229})$$

Note that the corresponding electron wavefunction for each sideband state is not shaped by the optical detection and maintains the original shape. This effect is in sharp contrast to the heralded optical state by measuring electron energies. The difference is that the electron energy loss heavily depends on optical frequency, but the optical frequency does not depend on electron energy under the no-recoil approximation. Therefore, any measurement of the frequency of the created photons translates the original electron energy state down by a corresponding photon energy. Because of that, we do not define the fidelity of the electron wavefunction in the limit of perfect photon frequency resolution.

We proceed to calculate the state purity of the N th electron sideband component as

$$\begin{aligned} \text{Tr}[\hat{\rho}_e^2] &= \left(\iint_{\Delta\omega} dE \prod_{i=1}^N d\omega_i |g_{\omega_i}|^2 |\psi(E + \hbar(\sum_i \omega_i))|^2 \right)^{-2} \\ &\quad \iint_{\Delta\omega} dE dE' \prod_{i,j=1}^N d\omega_i d\omega'_j |g_{\omega_i}|^2 |g_{\omega'_j}|^2 \\ &\quad \psi\left(E + \hbar(\sum_i \omega_i)\right) \psi^*\left(E + \hbar(\sum_j \omega'_j)\right) \psi^*\left(E' + \hbar(\sum_i \omega_i)\right) \psi\left(E' + \hbar(\sum_j \omega'_j)\right) \end{aligned} \quad (\text{B.230})$$

where the same weighted average needs to be applied for a general state with weights $|c_N|^2$, similar to the case of heralded optical states.

B.16 Electron-photon entangled states in the wave-like regime

Starting with the optical cavity modes in their vacuum states $\prod_{\mu} |0_{\mu}\rangle$, and the electron state at initial energy E_0 (ideal energy eigenstate, wave-like regime), the interaction results in

$$|\psi_e, \{\psi_{\mu}\}\rangle = \exp\left(-i \sum_{\mu} g_{\mu} a_{\mu} b_{\mu}^{\dagger} - \text{h.c.}\right) |E_0\rangle \prod_{\mu} |0_{\mu}\rangle. \quad (\text{B.231})$$

To proceed with the calculation, we have to take into account the commutation relations $[a_{\mu}^{\dagger}, a_{\nu}] = -\delta_{\mu,\nu}$ for optical modes, and $[b_{\mu}^{\dagger}, b_{\nu}] = 0$ for electrons. Therefore, using the Baker-Campbell-Hausdorff formula

$$e^{\hat{A}+\hat{B}} = e^{\hat{A}} e^{\hat{B}} e^{-[\hat{A},\hat{B}]/2} e^{2i[\hat{B},[\hat{A},\hat{B}]]+[\hat{A},[\hat{A},\hat{B}]]/6} \dots \quad (\text{B.232})$$

we have

$$\begin{aligned} |\psi_e, \{\psi_{\mu}\}\rangle &= \exp\left(-\frac{1}{2} \sum_{\mu} |g_{\mu}|^2\right) \exp\left(-i \sum_{\mu} g_{\mu}^* a_{\mu}^{\dagger} b_{\mu}\right) \exp\left(-i \sum_{\mu} g_{\mu} a_{\mu} b_{\mu}^{\dagger}\right) |E_0\rangle \prod_{\mu} |0_{\mu}\rangle \\ &= \exp\left(-\frac{1}{2} \sum_{\mu} |g_{\mu}|^2\right) \exp\left(-i \sum_{\mu} g_{\mu}^* a_{\mu}^{\dagger} b_{\mu}\right) |E_0\rangle \prod_{\mu} |0_{\mu}\rangle \\ &= \exp\left(-\frac{1}{2} \sum_{\mu} |g_{\mu}|^2\right) \sum_{\{n_{\mu}\}} \frac{\prod_{\mu} (-i g_{\mu}^*)^{n_{\mu}}}{\sqrt{\prod_{\mu} n_{\mu}!}} |E_0 - \sum_{\mu} n_{\mu} \hbar \omega_{\mu}\rangle \prod_{\mu} |n_{\mu}\rangle. \end{aligned} \quad (\text{B.233})$$

The expression above is a highly entangled state between the electron and the photons from different optical modes with distinguishable frequencies. If one traces out the optical system, the reduced electron density matrix will be a mixed state

$$\rho_e = \exp\left(-\sum_{\mu} |g_{\mu}|^2\right) \sum_{\{n_{\mu}\}} \frac{\prod_{\mu} |g_{\mu}|^{2n_{\mu}}}{\prod_{\mu} n_{\mu}!} |E_0 - \sum_{\mu} n_{\mu} \hbar \omega_{\mu}\rangle \langle E_0 - \sum_{\mu} n_{\mu} \hbar \omega_{\mu}| \quad (\text{B.234})$$

while tracing out the electron system produces the reduced optical density matrix of

$$\rho_o = \exp\left(-\sum_{\mu} |g_{\mu}|^2\right) \sum_{\delta E} \left(\sum_{\sum_{\mu} n_{\mu} \hbar \omega_{\mu} = \delta E} \frac{\prod_{\mu} (-i g_{\mu}^*)^{n_{\mu}}}{\sqrt{\prod_{\mu} n_{\mu}!}} \prod_{\mu} |n_{\mu}\rangle \right) \left(\sum_{\sum_{\mu} n_{\mu} \hbar \omega_{\mu} = \delta E} \frac{\prod_{\mu} (i g_{\mu})^{n_{\mu}}}{\sqrt{\prod_{\mu} n_{\mu}!}} \prod_{\mu} \langle n_{\mu}| \right). \quad (\text{B.235})$$

In this current form, it is not possible to define a single spatial-temporal mode on the optical side, as expected from the wave-like regime.

B.17 Second-order correlation functions of photons generated by electrons

Statistical properties of the continuous-wave electrons and the generated photons

We assume at the timescale of our experiment, i.e. slightly less than a ns, the arrival timing of the electrons (which also behaves as point-particles at this timescale considering their coherence time) follows a Poisson point process. The anti-correlations of the electrons by their fermionic nature can only be resolved with correlation measurements using two electron detectors [364], and preferably using spin-polarized beams. With a flux rate of Γ , the probability of finding N electrons in a time-bin window $\Delta t \sim 200$ ps follows a Poisson distribution

$$P_e(N) = e^{-\Gamma\Delta t} \frac{(\Gamma\Delta t)^N}{N!}, \quad (\text{B.236})$$

and is independent from the records in other time-bin windows. This process results in randomly but also uniformly distributed electron events in time, with the arrival time interval τ between sequential electrons following a distribution

$$P_\tau(t) = \Gamma^2 e^{-\Gamma t} t. \quad (\text{B.237})$$

Each electron also accompanies a photon emission process following a Poisson distribution of photon numbers n , with the probability distribution of

$$P_{\text{ph}}(n) = e^{-g} \frac{g^n}{n!}, \quad (\text{B.238})$$

where g is the expectation of photon number.

Statistics of unheralded photon correlations

In this section, we start with analyzing the probabilities of two-photon events $P_0 = P_{n=0}$ (no correlation or condition on zero-loss) with different delays. In the configuration of an HBT measurement, two-photon correlation $g_2(\tau_1, \tau_2)$ as a function of the two detectors' delays τ_1, τ_2 are analyzed using these probabilities. When $|\tau = \tau_1 - \tau_2|$ is much larger than the temporal duration $\tau_{\text{ph}} \sim 1$ ps of the optical pulse that is associated with a single electron, and also the time-bin width Δt such that $|\tau| \geq \Delta t$, coincidences only consist of two photons each coming from a different and independent electron. Note that our $\Delta t \sim 200$ ps $\gg \tau_{\text{ph}}$, and we neglect the case when two electrons interact with the same spatial-temporal mode of the waveguide (coherence length approximately $10 \mu\text{m}$). We also assume perfect timing uncertainty δ_{pp} between the two photon detectors for now, i.e. $\delta_{\text{pp}} \ll \Delta t$, but later take it into account using a form factor $f(\tau)$. The probability of observing such an event in a time-bin

Appendix B. Appendix

with width Δt , identical to that of conditioning on no electron-energy loss, is

$$\begin{aligned} P_0(|\tau| \gg \Delta t) &= \left(1 - \sum_{k=0}^{\infty} e^{-\Gamma \Delta t} \frac{(\Gamma \Delta t)^k}{k!} e^{-k\eta g} \right)^2 \\ &= \left(1 - e^{-\Gamma \Delta t (1 - e^{-\eta g})} \right)^2 \approx (\Gamma \Delta t \eta g)^2 \end{aligned} \quad (\text{B.239})$$

where η is the optical detection efficiency from the point of interaction to the photon counting at one of the detectors. The approximation \approx is valid when $\Gamma \Delta t \ll 1$ and $\eta g \ll 1$, i.e. in this time-bin there is only a small probability of having one electron and also a small probability of observing one photon.

When $|\tau| \ll \Delta t$, we are looking at the same time-bin window from the two detectors. The photons can be either from the same electron or two different ones. The probability of observing such an event is

$$\begin{aligned} P_0(|\tau| \ll \Delta t) &= \sum_{k=1}^{\infty} e^{-\Gamma \Delta t} \frac{(\Gamma \Delta t)^k}{k!} (1 - e^{-k\eta g})^2 \\ &= (1 - e^{-\Gamma \Delta t}) - 2e^{-\Gamma \Delta t} (e^{\Gamma \Delta t e^{-\eta g}} - 1) + e^{-\Gamma \Delta t} (e^{\Gamma \Delta t e^{-2\eta g}} - 1) \\ &= 1 + e^{-\Gamma \Delta t} (e^{\Gamma \Delta t e^{-2\eta g}} - 2e^{\Gamma \Delta t e^{-\eta g}}) \approx \eta^2 g^2 \Gamma \Delta t (1 + \Gamma \Delta t), \end{aligned} \quad (\text{B.240})$$

using the preservation of Poisson statistics of photons when beam splitters are applied. Also, we used the fact that the summation of Poisson variables is also a Poisson variable. Therefore, the bunching factor should be

$$g_{2,\text{unheralded}}(\tau) = \frac{P_0(\tau_1, \tau_2 = \tau_1 + \tau)}{P_{0,i=1}(\tau_1)P_{0,i=2}(\tau_1 + \tau)} \approx 1 + \frac{\delta(\tau_1, \tau_2)}{\Gamma \Delta t} \quad (\text{B.241})$$

Note that function $\delta(\tau_1, \tau_2)$ can be broadened to a form factor $f(\tau_1 - \tau_2)$ if the timing uncertainty δt_{pp} between the two optical detectors is large, i.e. $\delta t_{\text{pp}} > \Delta t$. The form factor has the property of $\int f(t) dt = 1$.

When the electron states are post-selected with one-photon or multi-photon sidebands, the generated photon statistics are effectively modified and deviate from a Poissonian distribution. Therefore, a lot of the nice tricks that we do here are not possible for the heralded electrons, but still can be applied to the stray electrons.

Statistics of one-photon-loss heralded photon correlations

In this section, we start with analyzing the probability of two-photon events $P_1 = P_{n=1}$ (condition on one-photon-loss on the electron energy) with different delays. In the following, we first assume perfect electron sideband isolation, so when we herald on a single-photon-loss sideband, the heralded electron generates only one photon. However, stray electrons can still arrive at the same time-bin window as they follow a Poisson point process and therefore can

B.17 Second-order correlation functions of photons generated by electrons

generate Poisson-distributed photons. In the following, we analyze the probability of different two-photon events when two detectors are with different delays τ_i .

When two detectors are both delayed differently by $|\tau_i| \gg \Delta t$, such that the photons are unlikely from the heralded electron, we have the probability

$$P_1(|\tau_1|, |\tau_2| \gg \Delta t, \tau_1 \neq \tau_2) = P_0(|\tau| \gg \Delta t) = \left(1 - e^{-\Gamma\Delta t(1-e^{-\eta g})}\right)^2 \approx (\Gamma\Delta t\eta g)^2. \quad (\text{B.242})$$

When the delays are the same, we have the probability

$$P_1(|\tau_1|, |\tau_2| \gg \Delta t, \tau_1 = \tau_2) = P_0(|\tau| \ll \Delta t) = 1 + e^{-\Gamma\Delta t}(e^{\Gamma\Delta t e^{-2\eta g}} - 2e^{\Gamma\Delta t e^{-\eta g}}) \approx \eta^2 g^2 \Gamma\Delta t(1 + \Gamma\Delta t). \quad (\text{B.243})$$

Therefore, we expect to see photon bunching when matching the relative delay τ between the two detectors.

When one of the detectors' delay is close to zero, let's say $\tau_1 = 0$, one of the photons can be from the heralded electron, and also stray electrons, while the other is only from the stray electrons. The probability of such an event is

$$P_1(|\tau_1| = 0, |\tau_2| \gg \Delta t) = \eta P_{\text{corr}}(\tau = 0) e^{-\Gamma\Delta t(1-e^{-\eta g})} (1 - e^{-\Gamma\Delta t(1-e^{-\eta g})}) + P_0(|\tau| \gg \Delta t) \approx \eta P_{\text{corr}}(\tau = 0) \Gamma\Delta t\eta g + (\Gamma\Delta t\eta g)^2 \quad (\text{B.244})$$

where $P_{\text{corr}}(0) \approx \Delta t / \delta t_{\text{ep}}$ is due to the spreading of the correlated photon arrival due to the hardware timing uncertainty $\delta t_{\text{ep}} > \Delta t$ of the electron-photon correlation. It is directly connected to the experimentally measured electron-photon correlation $g_{\text{ep}}(\tau)$ by $P_{\text{corr}}(\tau) = \Gamma\Delta t g(g_{\text{ep}}(\tau) - 1)$. When the uncertainty δt_{ep} is very small, i.e. $\delta t_{\text{ep}} \ll \Delta t$, $P_{\text{corr}}(\tau) = \delta(\tau, 0)$.

When the delays of both detectors are close to zero, i.e. $\tau_i = 0$, the two photons cannot be both from the heralded electron, since there is only one-photon electron-energy loss. The possible cases are one from the heralded electron or both from the stray electrons. We retrieve the probability of this case as

$$P_1(|\tau_1 = \tau_2| \ll \Delta t) = 2 \left(\eta P_{\text{corr}} e^{-\Gamma\Delta t(1-e^{-\eta g})} (1 - e^{-\Gamma\Delta t(1-e^{-\eta g})}) \right) + P_0(|\tau| \ll \Delta t) \approx 2\eta P_{\text{corr}} \Gamma\Delta t\eta g + \eta^2 g^2 \Gamma\Delta t(1 + \Gamma\Delta t) \quad (\text{B.245})$$

To calculate $g_2(n=1, \tau) = \frac{P_1(\tau_1=0, \tau_2=\tau)}{P_{1,i=1}(0)P_{1,i=2}(\tau)}$, we need to know the photon detection probability for each detector at different τ . We have the following results

$$P_{1,i}(\tau = 0) = 1 - (1 - \eta P_{\text{corr}}) e^{-\Gamma\Delta t(1-e^{-\eta g})} \approx \eta P_{\text{corr}} + \Gamma\Delta t\eta g \quad (\text{B.246})$$

$$P_{1,i}(|\tau| \gg \delta t_{\text{ep}}) = 1 - e^{-\Gamma\Delta t(1-e^{-\eta g})} \approx \Gamma\Delta t\eta g \quad (\text{B.247})$$

Appendix B. Appendix

Therefore,

$$g_2(n=1, \tau=0) = \frac{P_1(\tau_1=0, \tau_2=0)}{P_{1,i=1}(0)P_{1,i=2}(0)} \approx \frac{2P_{\text{corr}}\Gamma\Delta t g + g^2\Gamma\Delta t(1+\Gamma\Delta t)}{(P_{\text{corr}} + \Gamma\Delta t g)^2} = \frac{2g_{\text{ep}} - 1 + \frac{1}{\Gamma\Delta t}}{g_{\text{ep}}^2} \quad (\text{B.248})$$

where $g_{\text{ep}}(\tau=0) = \frac{P_{\text{corr}} + \Gamma\Delta t g}{\Gamma\Delta t g} \sim 30$ is the electron-photon correlation SNR in our experiment. Here, the effect of photon bunching $\frac{1}{\Gamma\Delta t}$ from stray electrons is diluted away by the SNR squared.

More generally with finite $\tau \neq 0$, we have

$$\begin{aligned} g_2(n=1, \tau) &= \frac{P_1(\tau_1=0, \tau_2=\tau)}{P_{1,i=1}(0)P_{1,i=2}(\tau)} \approx \frac{(P_{\text{corr}}(0) + P_{\text{corr}}(\tau))\Gamma\Delta t g + g^2\Gamma\Delta t(\delta(\tau, \tau_1) + \Gamma\Delta t)}{(P_{\text{corr}}(0) + \Gamma\Delta t g)(P_{\text{corr}}(\tau) + \Gamma\Delta t g)} \\ &= \frac{g_{\text{ep}}(0) + g_{\text{ep}}(\tau) - 1 + \frac{\delta(\tau, \tau_1)}{\Gamma\Delta t}}{g_{\text{ep}}(0)g_{\text{ep}}(\tau)} \end{aligned} \quad (\text{B.249})$$

Note again that function $\delta(\tau, \tau_1)$ can be broadened to a form factor $f(\tau - \tau_1)$ if the timing uncertainty δt_{pp} between the two optical detectors is large, i.e. $\delta t_{\text{pp}} > \Delta t$.

Statistics of two-photon-loss heralded photon correlations

In this section, we start with analyzing the probability of two-photon events $P_2 = P_{n=2}$ (condition on two-photon-loss on the electron energy) with different delays. Following similar treatment, we have the following probabilities that are the same as that of the one-photon-loss case,

$$P_2(|\tau_1|, |\tau_2| \gg \Delta t, \tau_1 \neq \tau_2) = P_1(|\tau_1|, |\tau_2| \gg \Delta t, \tau_1 \neq \tau_2) \quad (\text{B.250})$$

$$P_2(|\tau_1|, |\tau_2| \gg \Delta t, \tau_1 = \tau_2) = P_1(|\tau_1|, |\tau_2| \gg \Delta t, \tau_1 = \tau_2), \quad (\text{B.251})$$

since they are only associated with stray electrons.

When one of the detectors' delay τ_1 is close to zero, there, one of the photons can be from the heralded electron. Following a similar treatment, we arrive at the probability of

$$\begin{aligned} P_2(|\tau_1|=0, |\tau_2| \gg \Delta t) &= (2\eta - \eta^2)P_{\text{corr}}e^{-\Gamma\Delta t(1-e^{-\eta g})}(1 - e^{-\Gamma\Delta t(1-e^{-\eta g})}) + P_0(|\tau| \gg \Delta t) \\ &\approx (2\eta - \eta^2)P_{\text{corr}}\Gamma\Delta t\eta g + (\Gamma\Delta t\eta g)^2. \end{aligned} \quad (\text{B.252})$$

Then, when two detectors are both of zero delay, in addition to what we analyzed in the one-photon-loss case, we have the situation where the two photons are both from the heralded

B.17 Second-order correlation functions of photons generated by electrons

electron. Because of this, we have the probability of

$$\begin{aligned}
 P_2(|\tau_1 = \tau_2| \ll \Delta t) &= \frac{\eta^2}{2} P_{\text{corr}} e^{-2\Gamma\Delta t(1-e^{-\eta g})} \\
 &+ 2 \left((2\eta - \eta^2) P_{\text{corr}} e^{-\Gamma\Delta t(1-e^{-\eta g})} (1 - e^{-\Gamma\Delta t(1-e^{-\eta g})}) \right) + P_0(|\tau| \ll \Delta t) \\
 &\approx \frac{\eta^2}{2} P_{\text{corr}} + 2(2\eta - \eta^2) P_{\text{corr}} \Gamma \Delta t \eta g + \eta^2 g^2 \Gamma \Delta t (1 + \Gamma \Delta t). \tag{B.253}
 \end{aligned}$$

Again, we calculate the unconditional probabilities of both detectors

$$P_{2,i}(\tau = 0) = 1 - (1 - (2\eta - \eta^2) P_{\text{corr}}) e^{-\Gamma\Delta t(1-e^{-\eta g})} \approx (2\eta - \eta^2) P_{\text{corr}} + \Gamma \Delta t \eta g \tag{B.254}$$

$$P_{2,i}(|\tau| \gg \delta t_{\text{ep}}) = 1 - e^{-\Gamma\Delta t(1-e^{-\eta g})} \approx \Gamma \Delta t \eta g. \tag{B.255}$$

Therefore, the second-order correlation is

$$\begin{aligned}
 g_2(n=2, \tau=0) &= \frac{P_2(\tau_1=0, \tau_2=0)}{P_{2,i=1}(0)P_{2,i=2}(0)} \approx \frac{\frac{1}{2}P_{\text{corr}} + 2(2-\eta)P_{\text{corr}}\Gamma\Delta t g + g^2\Gamma\Delta t(1+\Gamma\Delta t)}{((2-\eta)P_{\text{corr}} + \Gamma\Delta t g)^2} \\
 &= \frac{\frac{(g_{\text{ep}}-1)^2}{2P_{\text{corr}}} + 2(2-\eta)g_{\text{ep}} + 2\eta - 3 + \frac{1}{\Gamma\Delta t}}{(2-\eta)g_{\text{ep}} + \eta - 1)^2} \tag{B.256}
 \end{aligned}$$

In the limit when the electron-photon correlation SNR $g_{\text{ep}}(\tau=0) \gg 1$, we can simplify the second-order correlation to $g_2(n=2, \tau=0) \approx 1/(8P_{\text{corr}}(0))$. When the time-bin width Δt is much smaller than the correlation time uncertainty δt_{ep} , $P_{\text{corr}}(0) \ll 1$ and we would expect photon bunching. Note that this two-photon-loss conditioned photon bunching is from photons of a coincidence electron, whereas the bunching of the unconditional case is from photons of an accident electron.

More generally, P_{corr} and g_{ep} are a function of τ , with the properties of $P_{\text{corr}}(|\tau| \gg \delta t_{\text{ep}}) \rightarrow 0$ and $g_{\text{ep}}(|\tau| \gg \delta t_{\text{ep}}) = P_{\text{corr}}(\tau)/(\Gamma\Delta t g) + 1 \rightarrow 1$. With these in mind, we have a more general second-order correlation function as a function of τ ,

$$\begin{aligned}
 g_2(n=2, \tau) &= \frac{P_2(\tau_1=0, \tau_2=\tau)}{P_{2,i=1}(0)P_{2,i=2}(\tau_2=\tau)} \\
 &\approx \frac{\frac{1}{2}P_{\text{corr}}(\tau)\delta(\tau, \tau_1) + (2-\eta)(P_{\text{corr}}(0) + P_{\text{corr}}(\tau))\Gamma\Delta t g + g^2\Gamma\Delta t(\delta(\tau, \tau_1) + \Gamma\Delta t)}{((2-\eta)P_{\text{corr}}(0) + \Gamma\Delta t g)((2-\eta)P_{\text{corr}}(\tau) + \Gamma\Delta t g)} \\
 &= \frac{\frac{(g_{\text{ep}}(\tau)-1)^2}{2P_{\text{corr}}(\tau)}\delta(\tau, \tau_1) + (2-\eta)(g_{\text{ep}}(0) + g_{\text{ep}}(\tau)) + 2\eta - 3 + \frac{\delta(\tau, \tau_1)}{\Gamma\Delta t}}{((2-\eta)g_{\text{ep}}(0) + \eta - 1)((2-\eta)g_{\text{ep}}(\tau) + \eta - 1)} \tag{B.257}
 \end{aligned}$$

Therefore, g_2 should show bunching $g_2 \approx 1/(8P_{\text{corr}}(0))$ when $\tau_1 = \tau_2 = 0$, and anti-bunching $g_2 \approx (4g_{\text{ep}}(0) - 3)/(2g_{\text{ep}}(0) - 1)^2$ when $\Delta t, \delta t_{\text{pp}} < |\tau_1 - \tau_2| < \delta t_{\text{ep}}$. Note again that function $\delta(\tau, \tau_1)$ can be broadened to a form factor $f(\tau - \tau_1)$ if the timing uncertainty δt_{pp} between the two optical detectors is large, i.e. $\delta t_{\text{pp}} > \Delta t$.

Bibliography

- [1] Guanhao Huang, Erwan Lucas, Junqiu Liu, Arslan S. Raja, Grigory Lihachev, Michael L. Gorodetsky, Nils J. Engelsen, and Tobias J. Kippenberg. Thermorefractive noise in silicon-nitride microresonators. *Physical Review A*, 99(6):061801, June 2019. doi: 10.1103/PhysRevA.99.061801. URL <https://link.aps.org/doi/10.1103/PhysRevA.99.061801>.
- [2] Liu Qiu, Guanhao Huang, Itay Shomroni, Jiahe Pan, Paul Seidler, and Tobias J. Kippenberg. Dissipative quantum feedback in measurements using a parametrically coupled microcavity. *PRX Quantum*, 3:020309, Apr 2022. doi: 10.1103/PRXQuantum.3.020309. URL <https://link.aps.org/doi/10.1103/PRXQuantum.3.020309>.
- [3] Junqiu Liu, Guanhao Huang, Rui Ning Wang, Jijun He, Arslan S. Raja, Tianyi Liu, Nils J. Engelsen, and Tobias J. Kippenberg. High-yield, wafer-scale fabrication of ultralow-loss, dispersion-engineered silicon nitride photonic circuits. *Nature Communications*, 12(1): 2236, 2021. ISSN 2041-1723. doi: 10.1038/s41467-021-21973-z.
- [4] Amirhassan Shams-Ansari, Guanhao Huang, Lingyan He, Zihan Li, Jeffrey Holzgrafe, Marc Jankowski, Mikhail Churaev, Prashanta Kharel, Rebecca Cheng, Di Zhu, Neil Sinclair, Boris Desiatov, Mian Zhang, Tobias J. Kippenberg, and Marko Lončar. Reduced material loss in thin-film lithium niobate waveguides. *APL Photonics*, 7(8):081301, 08 2022. ISSN 2378-0967. doi: 10.1063/5.0095146. URL <https://doi.org/10.1063/5.0095146>.
- [5] Maodong Gao, Qi-Fan Yang, Qing-Xin Ji, Heming Wang, Lue Wu, Boqiang Shen, Junqiu Liu, Guanhao Huang, Lin Chang, Weiqiang Xie, Su-Peng Yu, Scott B. Papp, John E. Bowers, Tobias J. Kippenberg, and Kerry J. Vahala. Probing material absorption and optical nonlinearity of integrated photonic materials. *Nature Communications*, 13(1):3323, Jun 2022. ISSN 2041-1723. doi: 10.1038/s41467-022-30966-5. URL <https://doi.org/10.1038/s41467-022-30966-5>.
- [6] Wentao Chen, Yao Lu, Shuaining Zhang, Kuan Zhang, Guanhao Huang, Mu Qiao, Xiaolu Su, Jialiang Zhang, Jing-Ning Zhang, Leonardo Banchi, M. S. Kim, and Kihwan Kim. Scalable and programmable phononic network with trapped ions. *Nature Physics*, 19(6):877–883, Jun 2023. ISSN 1745-2481. doi: 10.1038/s41567-023-01952-5. URL <https://doi.org/10.1038/s41567-023-01952-5>.

Bibliography

- [7] Jan-Wilke Henke, Arslan Sajid Raja, Armin Feist, Guanhao Huang, Germaine Arend, Yujia Yang, F. Jasmin Kappert, Rui Ning Wang, Marcel Möller, Jiahe Pan, Junqiu Liu, Ofer Kfir, Claus Ropers, and Tobias J. Kippenberg. Integrated photonics enables continuous-beam electron phase modulation. *Nature*, 600(7890):653–658, Dec 2021. ISSN 1476-4687. doi: 10.1038/s41586-021-04197-5. URL <https://doi.org/10.1038/s41586-021-04197-5>.
- [8] Armin Feist, Guanhao Huang, Germaine Arend, Yujia Yang, Jan-Wilke Henke, Arslan Sajid Raja, F. Jasmin Kappert, Rui Ning Wang, Hugo Lourenço-Martins, Zheru Qiu, Junqiu Liu, Ofer Kfir, Tobias J. Kippenberg, and Claus Ropers. Cavity-mediated electron-photon pairs. *Science*, 377(6607):777–780, 2022. doi: 10.1126/science.abo5037. URL <https://www.science.org/doi/abs/10.1126/science.abo5037>.
- [9] Guanhao Huang, Nils J. Engelsen, Ofer Kfir, Claus Ropers, and Tobias J. Kippenberg. Electron-photon quantum state heralding using photonic integrated circuits. *PRX Quantum*, 4:020351, Jun 2023. doi: 10.1103/PRXQuantum.4.020351. URL <https://link.aps.org/doi/10.1103/PRXQuantum.4.020351>.
- [10] Guanhao Huang, Alberto Beccari, Nils J. Engelsen, and Tobias J. Kippenberg. Room-temperature quantum optomechanics using an ultra-low noise cavity, 2023.
- [11] Yujia Yang, Jan-Wilke Henke, Arslan S. Raja, F. Jasmin Kappert, Guanhao Huang, Germaine Arend, Zheru Qiu, Armin Feist, Rui Ning Wang, Aleksandr Tusnin, Alexey Tikan, Claus Ropers, and Tobias J. Kippenberg. Free-electron interaction with nonlinear optical states in microresonators, 2023.
- [12] Serge Haroche and Jean-Michel Raimond. *Exploring the Quantum: Atoms, Cavities, and Photons*. Oxford University Press, 2006.
- [13] Markus Aspelmeyer, Tobias J. Kippenberg, and Florian Marquardt. Cavity optomechanics. *Reviews of Modern Physics*, 86(4):1391–1452, December 2014. ISSN 0034-6861, 1539-0756. doi: 10.1103/RevModPhys.86.1391.
- [14] Yiwen Chu, Prashanta Kharel, William H. Renninger, Luke D. Burkhardt, Luigi Frunzio, Peter T. Rakich, and Robert J. Schoelkopf. Quantum acoustics with superconducting qubits. *Science*, 358(6360):199–202, 2017.
- [15] K. J. Satzinger, Y. P. Zhong, H.-S. Chang, G. A. Peairs, A. Bienfait, Ming-Han Chou, A. Y. Cleland, C. R. Conner, É Dumur, J. Grebel, I. Gutierrez, B. H. November, R. G. Povey, S. J. Whiteley, D. D. Awschalom, D. I. Schuster, and A. N. Cleland. Quantum control of surface acoustic-wave phonons. *Nature*, 563(7733):661–665, November 2018. ISSN 1476-4687. doi: 10.1038/s41586-018-0719-5.
- [16] Jasper Chan, T. P. Mayer Alegre, Amir H. Safavi-Naeini, Jeff T. Hill, Alex Krause, Simon Gröblacher, Markus Aspelmeyer, and Oskar Painter. Laser cooling of a nanomechanical oscillator into its quantum ground state. *Nature*, 478(7367):89–92, October 2011. ISSN 1476-4687. doi: 10.1038/nature10461.

-
- [17] Massimiliano Rossi, David Mason, Junxin Chen, Yeghishe Tsaturyan, and Albert Schliesser. Measurement-based quantum control of mechanical motion. *Nature*, 563 (7729):53–58, November 2018. ISSN 1476-4687. doi: 10.1038/s41586-018-0643-8.
- [18] Amir H. Safavi-Naeini, Simon Gröblacher, Jeff T. Hill, Jasper Chan, Markus Aspelmeyer, and Oskar Painter. Squeezed light from a silicon micromechanical resonator. *Nature*, 500(7461):185–189, August 2013. ISSN 1476-4687. doi: 10.1038/nature12307.
- [19] William Hvidtfelt Padkær Nielsen, Yeghishe Tsaturyan, Christoffer Bo Møller, Eugene S. Polzik, and Albert Schliesser. Multimode optomechanical system in the quantum regime. *Proceedings of the National Academy of Sciences*, 114(1):62–66, January 2017. doi: 10.1073/pnas.1608412114.
- [20] T. P. Purdy, P.-L. Yu, R. W. Peterson, N. S. Kampel, and C. A. Regal. Strong Optomechanical Squeezing of Light. *Physical Review X*, 3(3):031012, September 2013. doi: 10.1103/PhysRevX.3.031012.
- [21] Nancy Aggarwal, Torrey J. Cullen, Jonathan Cripe, Garrett D. Cole, Robert Lanza, Adam Libson, David Follman, Paula Heu, Thomas Corbitt, and Nergis Mavalvala. Room-temperature optomechanical squeezing. *Nature Physics*, 16(7):784–788, July 2020. ISSN 1745-2481. doi: 10.1038/s41567-020-0877-x.
- [22] David Mason, Junxin Chen, Massimiliano Rossi, Yeghishe Tsaturyan, and Albert Schliesser. Continuous force and displacement measurement below the standard quantum limit. *Nature Physics*, 15(8):745–749, August 2019. ISSN 1745-2481. doi: 10.1038/s41567-019-0533-5.
- [23] Ralf Riedinger, Andreas Wallucks, Igor Marinković, Clemens Löschnauer, Markus Aspelmeyer, Sungkun Hong, and Simon Gröblacher. Remote quantum entanglement between two micromechanical oscillators. *Nature*, 556(7702):473–477, Apr 2018. ISSN 1476-4687. doi: 10.1038/s41586-018-0036-z. URL <https://doi.org/10.1038/s41586-018-0036-z>.
- [24] Laure Mercier de Lépinay, Caspar F. Ockeloen-Korppi, Matthew J. Woolley, and Mika A. Sillanpää. Quantum mechanics-free subsystem with mechanical oscillators. *Science*, 372(6542):625–629, May 2021. doi: 10.1126/science.abf5389.
- [25] Shlomi Kotler, Gabriel A. Peterson, Ezad Shojaee, Florent Lecocq, Katarina Cicak, Alex Kwiatkowski, Shawn Geller, Scott Glancy, Emanuel Knill, Raymond W. Simmonds, José Aumentado, and John D. Teufel. Direct observation of deterministic macroscopic entanglement. *Science*, 372(6542):622–625, May 2021. doi: 10.1126/science.abf2998.
- [26] R. D. Delaney, M. D. Urmey, S. Mittal, B. M. Brubaker, J. M. Kindem, P. S. Burns, C. A. Regal, and K. W. Lehnert. Superconducting-qubit readout via low-backaction electro-optic transduction. *Nature*, 606(7914):489–493, June 2022. ISSN 1476-4687. doi: 10.1038/s41586-022-04720-2.

Bibliography

- [27] Björn Schrämski, Yu Yang, Uwe von Lüpke, Marius Bild, Yiwen Chu, Klaus Hornberger, Stefan Nimmrichter, and Matteo Fadel. Macroscopic Quantum Test with Bulk Acoustic Wave Resonators. *Physical Review Letters*, 130(13):133604, March 2023. doi: 10.1103/PhysRevLett.130.133604.
- [28] Zhores I. Alferov. Nobel Lecture: The double heterostructure concept and its applications in physics, electronics, and technology. *Reviews of Modern Physics*, 73(3):767–782, October 2001. ISSN 0034-6861, 1539-0756. doi: 10.1103/RevModPhys.73.767.
- [29] Immanuel Bloch, Jean Dalibard, and Wilhelm Zwerger. Many-body physics with ultracold gases. *Reviews of Modern Physics*, 80(3):885–964, July 2008. doi: 10.1103/RevModPhys.80.885.
- [30] Kai Bongs, Michael Holynski, Jamie Vovrosh, Philippe Bouyer, Gabriel Condon, Ernst Rasel, Christian Schubert, Wolfgang P. Schleich, and Albert Roura. Taking atom interferometric quantum sensors from the laboratory to real-world applications. *Nature Reviews Physics*, 1(12):731–739, December 2019. ISSN 2522-5820. doi: 10.1038/s42254-019-0117-4.
- [31] Christoffer B. Møller, Rodrigo A. Thomas, Georgios Vasilakis, Emil Zeuthen, Yeghishe Tsaturyan, Mikhail Balabas, Kasper Jensen, Albert Schliesser, Klemens Hammerer, and Eugene S. Polzik. Quantum back-action-evading measurement of motion in a negative mass reference frame. *Nature*, 547(7662):191–195, July 2017. ISSN 1476-4687. doi: 10.1038/nature22980.
- [32] David Hälg, Thomas Gisler, Yeghishe Tsaturyan, Letizia Catalini, Urs Grob, Marc-Dominik Krass, Martin Héritier, Hinrich Mattiat, Ann-Katrin Thamm, Romana Schirhagl, Eric C. Langman, Albert Schliesser, Christian L. Degen, and Alexander Eichler. Membrane-Based Scanning Force Microscopy. *Physical Review Applied*, 15(2):L021001, February 2021. doi: 10.1103/PhysRevApplied.15.L021001.
- [33] Dennis Høj, Ulrich Busk Hoff, and Ulrik Lund Andersen. Ultra-coherent nanomechanical resonators based on density phononic crystal engineering, July 2022.
- [34] Marlan O. Scully and Muhammad Suhail Zubairy. *Quantum Optics*. Cambridge University Press, Cambridge ; New York, 1997. ISBN 978-0-521-43458-4 978-0-521-43595-6.
- [35] Roy J. Glauber and M. Lewenstein. Quantum optics of dielectric media. *Phys. Rev. A*, 43:467–491, Jan 1991. doi: 10.1103/PhysRevA.43.467. URL <https://link.aps.org/doi/10.1103/PhysRevA.43.467>.
- [36] Warwick P. Bowen and Gerard J. Milburn. *Quantum Optomechanics*. CRC Press, Boca Raton, December 2015. ISBN 978-0-429-15931-2. doi: 10.1201/b19379.
- [37] Jonathan Cripe, Nancy Aggarwal, Robert Lanza, Adam Libson, Robinjeet Singh, Paula Heu, David Follman, Garrett D. Cole, Nergis Mavalvala, and Thomas Corbitt. Measure-

- ment of quantum back action in the audio band at room temperature. *Nature*, 568 (7752):364–367, April 2019. ISSN 1476-4687. doi: 10.1038/s41586-019-1051-4.
- [38] D. E. Chang, C. A. Regal, S. B. Papp, D. J. Wilson, J. Ye, O. Painter, H. J. Kimble, and P. Zoller. Cavity opto-mechanics using an optically levitated nanosphere. *Proceedings of the National Academy of Sciences*, 107(3):1005–1010, January 2010. doi: 10.1073/pnas.0912969107.
- [39] Thomas Corbitt, Yanbei Chen, Farid Khalili, David Ottaway, Sergey Vyatchanin, Stan Whitcomb, and Nergis Mavalvala. Squeezed-state source using radiation-pressure-induced rigidity. *Physical Review A*, 73(2):023801, February 2006. doi: 10.1103/PhysRevA.73.023801.
- [40] Lorenzo Magrini, Victor A. Camarena-Chávez, Constanze Bach, Aisling Johnson, and Markus Aspelmeyer. Squeezed Light from a Levitated Nanoparticle at Room Temperature. *Physical Review Letters*, 129(5):053601, July 2022. doi: 10.1103/PhysRevLett.129.053601.
- [41] Lorenzo Magrini, Philipp Rosenzweig, Constanze Bach, Andreas Deutschmann-Olek, Sebastian G. Hofer, Sungkun Hong, Nikolai Kiesel, Andreas Kugi, and Markus Aspelmeyer. Real-time optimal quantum control of mechanical motion at room temperature. *Nature*, 595(7867):373–377, July 2021. ISSN 1476-4687. doi: 10.1038/s41586-021-03602-3.
- [42] Sergey A. Fedorov, Alberto Beccari, Amirali Arabmoheghi, Dalziel J. Wilson, Nils J. Engelsens, and Tobias J. Kippenberg. Thermal intermodulation noise in cavity-based measurements. *Optica*, 7(11):1609–1616, November 2020. ISSN 2334-2536. doi: 10.1364/OPTICA.402449.
- [43] Sampo A. Saarinen, Nenad Kralj, Eric C. Langman, Yeghishe Tsaturyan, and Albert Schliesser. Laser cooling a membrane-in-the-middle system close to the quantum ground state from room temperature. *Optica*, 10(3):364–372, March 2023. ISSN 2334-2536. doi: 10.1364/OPTICA.468590.
- [44] Constanze Metzger, Max Ludwig, Clemens Neuenhahn, Alexander Ortlieb, Ivan Favero, Khaled Karrai, and Florian Marquardt. Self-Induced Oscillations in an Optomechanical System Driven by Bolometric Backaction. *Physical Review Letters*, 101(13):133903, September 2008. doi: 10.1103/PhysRevLett.101.133903.
- [45] D. J. Wilson. *Cavity Optomechanics with High-Stress Silicon Nitride Films*. PhD thesis, California Institute of Technology, 2012.
- [46] Warren Nagourney. *Quantum electronics for atomic physics and telecommunication*. OUP Oxford, 2014.
- [47] M. L. Gorodetsky, A. Schliesser, G. Anetsberger, S. Deleglise, and T. J. Kippenberg. Determination of the vacuum optomechanical coupling rate using frequency noise cal-

Bibliography

- ibration. *Optics Express*, 18(22):23236–23246, October 2010. ISSN 1094-4087. doi: 10.1364/OE.18.023236.
- [48] Stefan Weis, Rémi Rivière, Samuel Deléglise, Emanuel Gavartin, Olivier Arcizet, Albert Schliesser, and Tobias J. Kippenberg. Optomechanically Induced Transparency. *Science*, 330(6010):1520–1523, December 2010. doi: 10.1126/science.1195596.
- [49] M. J. Beryyhi, A. Beccari, R. Groth, S. A. Fedorov, A. Arabmoheghi, T. J. Kippenberg, and N. J. Engelsen. Hierarchical tensile structures with ultralow mechanical dissipation. *Nature Communications*, 13(1):3097, June 2022. ISSN 2041-1723. doi: 10.1038/s41467-022-30586-z.
- [50] Dalziel J. Wilson, Cindy A. Regal, Scott B. Papp, and H. J. Kimble. Cavity optomechanics with stoichiometric SiN films. *Physical review letters*, 103(20):207204, 2009.
- [51] Yeghishe Tsaturyan, Andreas Barg, Anders Simonsen, Luis Guillermo Villanueva, Silvan Schmid, Albert Schliesser, and Eugene S. Polzik. Demonstration of suppressed phonon tunneling losses in phononic bandgap shielded membrane resonators for high-q optomechanics. *Opt. Express*, 22(6):6810–6821, Mar 2014. doi: 10.1364/OE.22.006810. URL <https://opg.optica.org/oe/abstract.cfm?URI=oe-22-6-6810>.
- [52] Y. Tsaturyan, A. Barg, E. S. Polzik, and A. Schliesser. Ultra-coherent nanomechanical resonators via soft clamping and dissipation dilution. *Nature Nanotechnology*, 12(8):776–783, August 2017. ISSN 1748-3387. doi: 10.1038/nnano.2017.101.
- [53] K. An, B. A. Sones, C. Fang-Yen, R. R. Dasari, and M. S. Feld. Optical bistability induced by mirror absorption: Measurement of absorption coefficients at the sub-ppm level. *Optics Letters*, 22(18):1433–1435, September 1997. ISSN 1539-4794. doi: 10.1364/OL.22.001433.
- [54] A. H. Ghadimi, S. A. Fedorov, N. J. Engelsen, M. J. Beryyhi, R. Schilling, D. J. Wilson, and T. J. Kippenberg. Elastic strain engineering for ultralow mechanical dissipation. *Science*, 360(6390):764–768, May 2018. ISSN 0036-8075, 1095-9203. doi: 10.1126/science.aar6939.
- [55] Dennis Høj, Fengwen Wang, Wenjun Gao, Ulrich Busk Hoff, Ole Sigmund, and Ulrik Lund Andersen. Ultra-coherent nanomechanical resonators based on inverse design. *Nature Communications*, 12(1):5766, October 2021. ISSN 2041-1723. doi: 10.1038/s41467-021-26102-4.
- [56] Mohammad J. Beryyhi, Amirali Arabmoheghi, Alberto Beccari, Sergey A. Fedorov, Guan-hao Huang, Tobias J. Kippenberg, and Nils J. Engelsen. Perimeter Modes of Nanomechanical Resonators Exhibit Quality Factors Exceeding 10^9 at Room Temperature. *Physical Review X*, 12(2):021036, May 2022. doi: 10.1103/PhysRevX.12.021036.
- [57] Dongil Shin, Andrea Cupertino, Matthijs H. J. de Jong, Peter G. Steeneken, Miguel A. Bessa, and Richard A. Norte. Spiderweb nanomechanical resonators via Bayesian

- optimization: Inspired by nature and guided by machine learning. *Advanced Materials*, 34(3):2106248, January 2022. ISSN 0935-9648, 1521-4095. doi: 10.1002/adma.202106248.
- [58] S. A. Fedorov, N. J. Engelsen, A. H. Ghadimi, M. J. Bereyhi, R. Schilling, D. J. Wilson, and T. J. Kippenberg. Generalized dissipation dilution in strained mechanical resonators. *Physical Review B*, 99(5):054107, February 2019. doi: 10.1103/PhysRevB.99.054107.
- [59] P-L Yu, TP Purdy, and CA Regal. Control of material damping in high-Q membrane microresonators. *Phys. Rev. Lett.*, 108(8):083603, 2012.
- [60] Minhang Bao, Heng Yang, Hao Yin, and Yuancheng Sun. Energy transfer model for squeeze-film air damping in low vacuum. *Journal of Micromechanics and Microengineering*, 12(3):341–346, May 2002. ISSN 09601317. doi: 10.1088/0960-1317/12/3/322.
- [61] Alberto Beccari. Nanomechanical resonators with low dissipation for quantum optomechanics. page 197, 2023. doi: <https://doi.org/10.5075/epfl-thesis-9611>. URL <http://infoscience.epfl.ch/record/305199>.
- [62] J. D. Thompson, B. M. Zwickl, A. M. Jayich, Florian Marquardt, S. M. Girvin, and J. G. E. Harris. Strong dispersive coupling of a high-finesse cavity to a micromechanical membrane. *Nature*, 452(7183):72–75, March 2008. ISSN 0028-0836, 1476-4687. doi: 10.1038/nature06715.
- [63] P. Rabl, C. Genes, K. Hammerer, and M. Aspelmeyer. Phase-noise induced limitations on cooling and coherent evolution in optomechanical systems. *Physical Review A*, 80(6):063819, December 2009. ISSN 1050-2947, 1094-1622. doi: 10.1103/PhysRevA.80.063819.
- [64] Yi Zhao, Dalziel J. Wilson, K.-K. Ni, and H. J. Kimble. Suppression of extraneous thermal noise in cavity optomechanics. *Optics Express*, 20(4):3586–3612, February 2012. ISSN 1094-4087. doi: 10.1364/OE.20.003586.
- [65] Crispin W Gardiner et al. *Handbook of stochastic methods*, volume 3. springer Berlin, 1985.
- [66] RWP Drever, John L Hall, FV Kowalski, J_ Hough, GM Ford, AJ Munley, and H Ward. Laser phase and frequency stabilization using an optical resonator. *Applied Physics B*, 31(2):97–105, 1983. doi: 10.1007/BF00702605.
- [67] Andrew T. Land, Mitul Dey Chowdhury, Aman R. Agrawal, and Dalziel J. Wilson. Sub-ppm nanomechanical absorption spectroscopy of silicon nitride, 2023.
- [68] Alexander K. Tagantsev and Sergey A. Fedorov. Quantum-limited measurements using an optical cavity with modulated intrinsic loss. *Phys. Rev. Lett.*, 123:043602, Jul 2019. doi: 10.1103/PhysRevLett.123.043602. URL <https://link.aps.org/doi/10.1103/PhysRevLett.123.043602>.

Bibliography

- [69] A. J. Weinstein, C. U. Lei, E. E. Wollman, J. Suh, A. Metelmann, A. A. Clerk, and K. C. Schwab. Observation and interpretation of motional sideband asymmetry in a quantum electromechanical device. *Phys. Rev. X*, 4:041003, Oct 2014. doi: 10.1103/PhysRevX.4.041003. URL <https://link.aps.org/doi/10.1103/PhysRevX.4.041003>.
- [70] Ralf Riedinger, Sungkun Hong, Richard A. Norte, Joshua A. Slater, Juying Shang, Alexander G. Krause, Vikas Anant, Markus Aspelmeyer, and Simon Gröblacher. Non-classical correlations between single photons and phonons from a mechanical oscillator. *Nature*, 530(7590):313–316, February 2016. ISSN 1476-4687. doi: 10.1038/nature16536.
- [71] T. P. Purdy, R. W. Peterson, and C. A. Regal. Observation of Radiation Pressure Shot Noise on a Macroscopic Object. *Science*, 339(6121):801–804, February 2013. ISSN 0036-8075, 1095-9203. doi: 10.1126/science.1231282.
- [72] Christian M. Pluchar, Aman R. Agrawal, and Dalziel J. Wilson. Thermal intermodulation backaction in a high-cooperativity optomechanical system, July 2023.
- [73] C. W. Gardiner and M. J. Collett. Input and output in damped quantum systems: Quantum stochastic differential equations and the master equation. *Phys. Rev. A*, 31:3761–3774, Jun 1985. doi: 10.1103/PhysRevA.31.3761. URL <https://link.aps.org/doi/10.1103/PhysRevA.31.3761>.
- [74] Kurt Jacobs and Daniel A Steck. A straightforward introduction to continuous quantum measurement. *Contemporary Physics*, 47(5):279–303, 2006.
- [75] Søren Gammelmark, Brian Julsgaard, and Klaus Mølmer. Past quantum states of a monitored system. *Physical review letters*, 111(16):160401, 2013.
- [76] Jinglei Zhang and Klaus Mølmer. Prediction and retrodiction with continuously monitored Gaussian states. *Physical Review A*, 96(6):062131, December 2017. doi: 10.1103/PhysRevA.96.062131.
- [77] Massimiliano Rossi, David Mason, Junxin Chen, and Albert Schliesser. Observing and Verifying the Quantum Trajectory of a Mechanical Resonator. *Physical Review Letters*, 123(16):163601, October 2019. doi: 10.1103/PhysRevLett.123.163601.
- [78] Chao Meng, George A. Brawley, Soroush Khademi, Elizabeth M. Bridge, James S. Bennett, and Warwick P. Bowen. Measurement-based preparation of multimode mechanical states. *Science Advances*, 8(21):eabm7585, May 2022. doi: 10.1126/sciadv.abm7585.
- [79] Gerardo Adesso, Sammy Ragy, and Antony R. Lee. Continuous variable quantum information: Gaussian states and beyond. *Open Systems & Information Dynamics*, 21(01n02):1440001, 2014. doi: 10.1142/S1230161214400010. URL <https://doi.org/10.1142/S1230161214400010>.
- [80] A. A. Clerk, M. H. Devoret, S. M. Girvin, Florian Marquardt, and R. J. Schoelkopf. Introduction to quantum noise, measurement, and amplification. *Reviews of Modern Physics*, 82(2):1155–1208, April 2010. doi: 10.1103/RevModPhys.82.1155.

- [81] Witlef Wieczorek, Sebastian G. Hofer, Jason Hoelscher-Obermaier, Ralf Riedinger, Klemens Hammerer, and Markus Aspelmeyer. Optimal State Estimation for Cavity Optomechanical Systems. *Physical Review Letters*, 114(22):223601, June 2015. ISSN 0031-9007, 1079-7114. doi: 10.1103/PhysRevLett.114.223601.
- [82] Lu-Ming Duan, G. Giedke, J. I. Cirac, and P. Zoller. Inseparability criterion for continuous variable systems. *Phys. Rev. Lett.*, 84:2722–2725, Mar 2000. doi: 10.1103/PhysRevLett.84.2722. URL <https://link.aps.org/doi/10.1103/PhysRevLett.84.2722>.
- [83] C. F. Ockeloen-Korppi, E. Damskäg, J.-M. Pirkkalainen, M. Asjad, A. A. Clerk, F. Massel, M. J. Woolley, and M. A. Sillanpää. Stabilized entanglement of massive mechanical oscillators. *Nature*, 556(7702):478–482, Apr 2018. ISSN 1476-4687. doi: 10.1038/s41586-018-0038-x. URL <https://doi.org/10.1038/s41586-018-0038-x>.
- [84] Rodrigo A. Thomas, Michał Parniak, Christoffer Østfeldt, Christoffer B. Møller, Christian Bærentsen, Yeghishe Tsaturyan, Albert Schliesser, Jürgen Appel, Emil Zeuthen, and Eugene S. Polzik. Entanglement between distant macroscopic mechanical and spin systems. *Nature Physics*, 17(2):228–233, Feb 2021. ISSN 1745-2481. doi: 10.1038/s41567-020-1031-5. URL <https://doi.org/10.1038/s41567-020-1031-5>.
- [85] Chao Meng, George A. Brawley, James S. Bennett, Michael R. Vanner, and Warwick P. Bowen. Mechanical squeezing via fast continuous measurement. *Phys. Rev. Lett.*, 125:043604, Jul 2020. doi: 10.1103/PhysRevLett.125.043604. URL <https://link.aps.org/doi/10.1103/PhysRevLett.125.043604>.
- [86] Vivishek Sudhir. Quantum limits on measurement and control of a mechanical oscillator. page 183, 2016. doi: <https://doi.org/10.5075/epfl-thesis-7202>. URL <http://infoscience.epfl.ch/record/221295>.
- [87] Francesco Massel, Sung Un Cho, Juha-Matti Pirkkalainen, Pertti J. Hakonen, Tero T. Heikkilä, and Mika A. Sillanpää. Multimode circuit optomechanics near the quantum limit. *Nature Communications*, 3(1):987, August 2012. ISSN 2041-1723. doi: 10.1038/ncomms1993.
- [88] Jingkun Guo, Richard Norte, and Simon Gröblacher. Feedback Cooling of a Room Temperature Mechanical Oscillator close to its Motional Ground State. *Physical Review Letters*, 123(22):223602, November 2019. doi: 10.1103/PhysRevLett.123.223602.
- [89] Matteo Brunelli, Daniel Malz, Albert Schliesser, and Andreas Nunnenkamp. Stroboscopic quantum optomechanics. *Phys. Rev. Res.*, 2:023241, May 2020. doi: 10.1103/PhysRevResearch.2.023241. URL <https://link.aps.org/doi/10.1103/PhysRevResearch.2.023241>.
- [90] Xinghan Guo, Mouzhe Xie, Anchita Addhya, Avery Linder, Uri Zvi, Tanvi D. Deshmukh, Yuzi Liu, Ian N. Hammock, Zixi Li, Clayton T. DeVault, Amy Butcher, Aaron P. Esser-Kahn, David D. Awschalom, Nazar Deegan, Peter C. Maurer, F. Joseph Heremans, and

Bibliography

- Alexander A. High. Direct-bonded diamond membranes for heterogeneous quantum and electronic technologies, 2023.
- [91] Chengli Wang, Zhiwei Fang, Ailun Yi, Bingcheng Yang, Zhe Wang, Liping Zhou, Chen Shen, Yifan Zhu, Yuan Zhou, Rui Bao, Zhongxu Li, Yang Chen, Kai Huang, Jiayang Zhang, Ya Cheng, and Xin Ou. High-q microresonators on 4h-silicon-carbide-on-insulator platform for nonlinear photonics. *Light: Science & Applications*, 10(1):139, Jul 2021. ISSN 2047-7538. doi: 10.1038/s41377-021-00584-9. URL <https://doi.org/10.1038/s41377-021-00584-9>.
- [92] Graham D. Joe, Cleaven Chia, Benjamin Pingault, Michael Haas, Michelle Chalupnik, Eliza Cornell, Kazuhiro Kuruma, Bartholomeus Machielse, Neil Sinclair, Srujan Meesala, and Marko Lončar. High q-factor diamond optomechanical resonators with silicon vacancy centers at millikelvin temperatures, 2023.
- [93] D. Leibfried, R. Blatt, C. Monroe, and D. Wineland. Quantum dynamics of single trapped ions. *Rev. Mod. Phys.*, 75:281–324, Mar 2003. doi: 10.1103/RevModPhys.75.281. URL <https://link.aps.org/doi/10.1103/RevModPhys.75.281>.
- [94] Robert Hooke. *Micrographia: or some physiological descriptions of minute bodies made by magnifying glasses, with observations and inquiries thereupon*. Courier Corporation, 2003.
- [95] M. Knoll and E. Ruska. Beitrag zur geometrischen elektronenoptik. i. *Annalen der Physik*, 404(5):607–640, 1932. doi: <https://doi.org/10.1002/andp.19324040506>. URL <https://onlinelibrary.wiley.com/doi/abs/10.1002/andp.19324040506>.
- [96] Gustav A Kausche, Edgar Pfankuch, and Helmut Ruska. Die sichtbarmachung von pflanzlichem virus im übermikroskop. *Naturwissenschaften*, 27:292–299, 1939.
- [97] R. Henderson, J.M. Baldwin, T.A. Ceska, F. Zemlin, E. Beckmann, and K.H. Downing. Model for the structure of bacteriorhodopsin based on high-resolution electron cryo-microscopy. *Journal of Molecular Biology*, 213(4):899–929, 1990. ISSN 0022-2836. doi: [https://doi.org/10.1016/S0022-2836\(05\)80271-2](https://doi.org/10.1016/S0022-2836(05)80271-2). URL <https://www.sciencedirect.com/science/article/pii/S0022283605802712>.
- [98] Estia J. Eichten, Kenneth D. Lane, and Michael E. Peskin. New tests for quark and lepton substructure. *Phys. Rev. Lett.*, 50:811–814, Mar 1983. doi: 10.1103/PhysRevLett.50.811. URL <https://link.aps.org/doi/10.1103/PhysRevLett.50.811>.
- [99] Osip Schwartz, Jeremy J. Axelrod, Sara L. Campbell, Carter Turnbaugh, Robert M. Glaeser, and Holger Müller. Laser phase plate for transmission electron microscopy. *Nature Methods*, 16(10):1016–1020, 2019. ISSN 1548-7091, 1548-7105. doi: 10.1038/s41592-019-0552-2.

- [100] A. Ryabov, J. W. Thurner, D. Nabben, M. V. Tsarev, and P. Baum. Attosecond metrology in a continuous-beam transmission electron microscope. *Science Advances*, 6(46):eabb1393, 2020. ISSN 2375-2548. doi: 10.1126/sciadv.abb1393.
- [101] Avraham Gover and Amnon Yariv. Free-Electron–Bound-Electron Resonant Interaction. *Physical Review Letters*, 124(6):064801, 2020. ISSN 0031-9007, 1079-7114. doi: 10.1103/PhysRevLett.124.064801.
- [102] Zhexin Zhao, Xiao-Qi Sun, and Shanhui Fan. Quantum entanglement and modulation enhancement of free-electron–bound-electron interaction. *Phys. Rev. Lett.*, 126:233402, Jun 2021. doi: 10.1103/PhysRevLett.126.233402. URL <https://link.aps.org/doi/10.1103/PhysRevLett.126.233402>.
- [103] Sergey V. Yalunin, Armin Feist, and Claus Ropers. Tailored high-contrast attosecond electron pulses for coherent excitation and scattering. *Physical Review Research*, 3(3):L032036, 2021. ISSN 2643-1564. doi: 10.1103/physrevresearch.3.l032036.
- [104] R. Joel England, Robert J. Noble, Karl Bane, David H. Dowell, Cho-Kuen Ng, James E. Spencer, Sami Tantawi, Ziran Wu, Robert L. Byer, Edgar Peralta, Ken Soong, Chia-Ming Chang, Behnam Montazeri, Stephen J. Wolf, Benjamin Cowan, Jay Dawson, Wei Gai, Peter Hommelhoff, Yen-Chieh Huang, Chunguang Jing, Christopher McGuinness, Robert B. Palmer, Brian Naranjo, James Rosenzweig, Gil Travish, Amit Mizrahi, Levi Schachter, Christopher Sears, Gregory R. Werner, and Rodney B. Yoder. Dielectric laser accelerators. *Reviews of Modern Physics*, 86(4):1337–1389, 2014. ISSN 0034-6861, 1539-0756. doi: 10.1103/RevModPhys.86.1337.
- [105] Neil V. Saprà, Ki Youl Yang, Dries Verduyck, Kenneth J. Leedle, Dylan S. Black, R. Joel England, Logan Su, Rahul Trivedi, Yu Miao, Olav Solgaard, Robert L. Byer, and Jelena Vučković. On-chip integrated laser-driven particle accelerator. *Science*, 367(6473):79–83, 2020. doi: 10.1126/science.aay5734. URL <https://www.science.org/doi/abs/10.1126/science.aay5734>.
- [106] R. Shiloh, J. Illmer, T. Chlouba, P. Yousefi, N. Schönenberger, U. Niedermayer, A. Mittelbach, and P. Hommelhoff. Electron phase-space control in photonic chip-based particle acceleration. *Nature*, 597(7877):498–502, Sep 2021. ISSN 1476-4687. doi: 10.1038/s41586-021-03812-9. URL <https://doi.org/10.1038/s41586-021-03812-9>.
- [107] Ofer Kfir. Entanglements of Electrons and Cavity Photons in the Strong-Coupling Regime. *Physical Review Letters*, 123(10):103602, 2019. ISSN 0031-9007, 1079-7114. doi: 10.1103/PhysRevLett.123.103602.
- [108] Valerio Di Giulio, Mathieu Kociak, and F. Javier García de Abajo. Probing quantum optical excitations with fast electrons. *Optica*, 6(12):1524, 2019. ISSN 2334-2536. doi: 10.1364/OPTICA.6.001524.

Bibliography

- [109] Yiming Pan and Avraham Gover. Spontaneous and stimulated emissions of a preformed quantum free-electron wave function. *Phys. Rev. A*, 99(5):052107, 2019. ISSN 2469-9926, 2469-9934. doi: 10.1103/PhysRevA.99.052107.
- [110] A. Ben Hayun, O. Reinhardt, J. Nemirovsky, A. Karnieli, N. Rivera, and I. Kaminer. Shaping quantum photonic states using free electrons. *Science Advances*, 7(11):eabe4270, 2021. ISSN 2375-2548. doi: 10.1126/sciadv.abe4270.
- [111] H. J. Kimble. Strong Interactions of Single Atoms and Photons in CavityQED. *Physica Scripta*, T76(1):127, 1998. ISSN 0031-8949. doi: 10.1238/Physica.Topical.076a00127.
- [112] Nahid Talebi. Electron-light interactions beyond the adiabatic approximation: recoil engineering and spectral interferometry. *Advances in Physics: X*, 3(1):1499438, 2018. doi: 10.1080/23746149.2018.1499438. URL <https://doi.org/10.1080/23746149.2018.1499438>.
- [113] F. J. García de Abajo. Optical excitations in electron microscopy. *Reviews of Modern Physics*, 82(1):209–275, 2010. ISSN 0034-6861. doi: 10.1103/RevModPhys.82.209.
- [114] Ho Trung Dung, Ludwig Knöll, and Dirk-Gunnar Welsch. Three-dimensional quantization of the electromagnetic field in dispersive and absorbing inhomogeneous dielectrics. *Phys. Rev. A*, 57:3931–3942, May 1998. doi: 10.1103/PhysRevA.57.3931. URL <https://link.aps.org/doi/10.1103/PhysRevA.57.3931>.
- [115] Ahmed H. Zewail. Four-Dimensional Electron Microscopy. *Science*, 328(5975):187–193, 2010. ISSN 0036-8075, 1095-9203. doi: 10.1126/science.1166135.
- [116] Katharina E. Priebe, Christopher Rathje, Sergey V. Yalunin, Thorsten Hohage, Armin Feist, Sascha Schäfer, and Claus Ropers. Attosecond electron pulse trains and quantum state reconstruction in ultrafast transmission electron microscopy. *Nature Photonics*, 11(12):793–797, 2017. ISSN 1749-4885, 1749-4893. doi: 10.1038/s41566-017-0045-8.
- [117] P. Bertet, A. Auffeves, P. Maioli, S. Osnaghi, T. Meunier, M. Brune, J. M. Raimond, and S. Haroche. Direct measurement of the wigner function of a one-photon fock state in a cavity. *Phys. Rev. Lett.*, 89:200402, Oct 2002. doi: 10.1103/PhysRevLett.89.200402. URL <https://link.aps.org/doi/10.1103/PhysRevLett.89.200402>.
- [118] U.I. Andersen, G. Leuchs, and C. Silberhorn. Continuous-variable quantum information processing. *Laser & Photonics Reviews*, 4(3):337–354, 2010. ISSN 1863-8899. doi: 10.1002/lpor.200910010.
- [119] John F. Clauser. Experimental distinction between the quantum and classical field-theoretic predictions for the photoelectric effect. *Phys. Rev. D*, 9:853–860, Feb 1974. doi: 10.1103/PhysRevD.9.853. URL <https://link.aps.org/doi/10.1103/PhysRevD.9.853>.
- [120] Armin Feist, Katharina E. Echterkamp, Jakob Schauss, Sergey V. Yalunin, Sascha Schäfer, and Claus Ropers. Quantum coherent optical phase modulation in an ultrafast transmission electron microscope. *Nature*, 521(7551):200–203, 2015. ISSN 0028-0836, 1476-4687. doi: 10.1038/nature14463.

- [121] Raphael Dahan, Saar Nehemia, Michael Shentcis, Ori Reinhardt, Yuval Adiv, Xihang Shi, Orr Be'er, Morgan H. Lynch, Yaniv Kurman, Kangpeng Wang, and Ido Kaminer. Resonant phase-matching between a light wave and a free-electron wavefunction. *Nature Physics*, 16(11):1123–1131, 2020. ISSN 1745-2481. doi: 10.1038/s41567-020-01042-w.
- [122] Herman Batelaan. Colloquium: Illuminating the kapitza-dirac effect with electron matter optics. *Reviews of Modern Physics*, 79(3):929, 2007.
- [123] P.W. Milonni. *The Quantum Vacuum: An Introduction to Quantum Electrodynamics*. Elsevier Science, 1994. ISBN 9780124980808. URL <https://books.google.ch/books?id=P83vAAAAMAAJ>.
- [124] Ofer Kfir, Valerio Di Giulio, F Javier García de Abajo, and Claus Ropers. Optical coherence transfer mediated by free electrons. *Science Advances*, 7(18):eabf6380, 2021. ISSN 2375-2548. doi: 10.1126/sciadv.abf6380.
- [125] Valerio Di Giulio, Ofer Kfir, Claus Ropers, and F Javier García de Abajo. Modulation of Cathodoluminescence Emission by Interference with External Light. *ACS Nano*, page acsnano.1c00549, 2021. ISSN 1936-0851, 1936-086X. doi: 10.1021/acsnano.1c00549.
- [126] T. Gruner and D.-G. Welsch. Green-function approach to the radiation-field quantization for homogeneous and inhomogeneous kramers-kronig dielectrics. *Phys. Rev. A*, 53: 1818–1829, Mar 1996. doi: 10.1103/PhysRevA.53.1818. URL <https://link.aps.org/doi/10.1103/PhysRevA.53.1818>.
- [127] B Barwick and H Batelaan. Aharonov–bohm phase shifts induced by laser pulses. *New Journal of Physics*, 10(8):083036, aug 2008. doi: 10.1088/1367-2630/10/8/083036. URL <https://dx.doi.org/10.1088/1367-2630/10/8/083036>.
- [128] Johannes Feist, Antonio I. Fernández-Domínguez, and Francisco J. García-Vidal. Macroscopic qed for quantum nanophotonics: emitter-centered modes as a minimal basis for multiemitter problems. *Nanophotonics*, 10(1):477–489, 2021. doi: doi:10.1515/nanoph-2020-0451. URL <https://doi.org/10.1515/nanoph-2020-0451>.
- [129] R. H. Ritchie and A. Howie. Inelastic scattering probabilities in scanning transmission electron microscopy. *Philosophical Magazine A*, 58(5):753–767, 1988. doi: 10.1080/01418618808209951. URL <https://doi.org/10.1080/01418618808209951>.
- [130] R. H. Ritchie. Plasma losses by fast electrons in thin films. *Phys. Rev.*, 106:874–881, Jun 1957. doi: 10.1103/PhysRev.106.874. URL <https://link.aps.org/doi/10.1103/PhysRev.106.874>.
- [131] K. J. Blow, Rodney Loudon, Simon J. D. Phoenix, and T. J. Shepherd. Continuum fields in quantum optics. *Phys. Rev. A*, 42:4102–4114, Oct 1990. doi: 10.1103/PhysRevA.42.4102. URL <https://link.aps.org/doi/10.1103/PhysRevA.42.4102>.

Bibliography

- [132] B. Brecht, Dileep V. Reddy, C. Silberhorn, and M. G. Raymer. Photon temporal modes: A complete framework for quantum information science. *Phys. Rev. X*, 5:041017, Oct 2015. doi: 10.1103/PhysRevX.5.041017. URL <https://link.aps.org/doi/10.1103/PhysRevX.5.041017>.
- [133] Michael G Raymer and Ian A Walmsley. Temporal modes in quantum optics: then and now. *Physica Scripta*, 95(6):064002, mar 2020. doi: 10.1088/1402-4896/ab6153. URL <https://doi.org/10.1088/1402-4896/ab6153>.
- [134] J. D. Thompson, T. G. Tiecke, N. P. de Leon, J. Feist, A. V. Akimov, M. Gullans, A. S. Zibrov, V. Vuletić, and M. D. Lukin. Coupling a Single Trapped Atom to a Nanoscale Optical Cavity. *Science*, 340(6137):1202–1205, 2013. ISSN 0036-8075, 1095-9203. doi: 10.1126/science.1237125.
- [135] Karan K. Mehta, Chi Zhang, Maciej Malinowski, Thanh-Long Nguyen, Martin Stadler, and Jonathan P. Home. Integrated optical multi-ion quantum logic. *Nature*, 586(7830): 533–537, 2020. ISSN 1476-4687. doi: 10.1038/s41586-020-2823-6.
- [136] R. J. Niffenegger, J. Stuart, C. Sorace-Agaskar, D. Kharas, S. Bramhavar, C. D. Bruzewicz, W. Loh, R. T. Maxson, R. McConnell, D. Reens, G. N. West, J. M. Sage, and J. Chiaverini. Integrated multi-wavelength control of an ion qubit. *Nature*, 586(7830):538–542, 2020. ISSN 1476-4687. doi: 10.1038/s41586-020-2811-x.
- [137] Peter Lodahl, Sahand Mahmoodian, and Søren Stobbe. Interfacing single photons and single quantum dots with photonic nanostructures. *Reviews of Modern Physics*, 87(2): 347–400, 2015. doi: 10.1103/RevModPhys.87.347.
- [138] A. Sipahigil, R. E. Evans, D. D. Sukachev, M. J. Burek, J. Borregaard, M. K. Bhaskar, C. T. Nguyen, J. L. Pacheco, H. A. Atikian, C. Meuwly, R. M. Camacho, F. Jelezko, E. Bielejec, H. Park, M. Lončar, and M. D. Lukin. An integrated diamond nanophotonics platform for quantum-optical networks. *Science*, 354(6314):847–850, 2016. doi: 10.1126/science.aah6875.
- [139] Brett Barwick, David J. Flannigan, and Ahmed H. Zewail. Photon-induced near-field electron microscopy. *Nature*, 462(7275):902–906, 2009. ISSN 0028-0836, 1476-4687. doi: 10.1038/nature08662.
- [140] Katharina E. Echternkamp, Armin Feist, Sascha Schäfer, and Claus Ropers. Ramsey-type phase control of free-electron beams. *Nature Physics*, 12(11):1000–1004, 2016. ISSN 1745-2473, 1745-2481. doi: 10.1038/nphys3844.
- [141] Raphael Dahan, Alexey Gorlach, Urs Haeusler, Aviv Karnieli, Ori Eyal, Peyman Yousefi, Mordechai Segev, Ady Arie, Gadi Eisenstein, Peter Hommelhoff, and Ido Kaminer. Imprinting the quantum statistics of photons on free electrons. *Science*, 373(6561):eabj7128, 2021. ISSN 0036-8075, 1095-9203. doi: 10.1126/science.abj7128.

- [142] Christopher M. S. Sears, Eric Colby, Rasmus Ischebeck, Christopher McGuinness, Janice Nelson, Robert Noble, Robert H. Siemann, James Spencer, Dieter Walz, Tomas Plettner, and Robert L. Byer. Production and characterization of attosecond electron bunch trains. *Physical Review Special Topics - Accelerators and Beams*, 11(6):061301, 2008. ISSN 1098-4402. doi: 10.1103/PhysRevSTAB.11.061301.
- [143] Yuya Morimoto and Peter Baum. Diffraction and microscopy with attosecond electron pulse trains. *Nature Physics*, 14(3):252–256, Mar 2018. ISSN 1745-2481. doi: 10.1038/s41567-017-0007-6. URL <https://doi.org/10.1038/s41567-017-0007-6>.
- [144] M. Kozák, N. Schönenberger, and P. Hommelhoff. Ponderomotive Generation and Detection of Attosecond Free-Electron Pulse Trains. *Physical Review Letters*, 120(10):103203, 2018. ISSN 0031-9007, 1079-7114. doi: 10.1103/PhysRevLett.120.103203.
- [145] Nadezda Varkentina, Yves Auad, Steffi Y. Woo, Alberto Zobelli, Laura Bocher, Jean-Denis Blazit, Xiaoyan Li, Marcel Tencé, Kenji Watanabe, Takashi Taniguchi, Odile Stéphan, Mathieu Kociak, and Luiz H. G. Tizei. Cathodoluminescence excitation spectroscopy: Nanoscale imaging of excitation pathways. *Science Advances*, 8(40):eabq4947, 2022. doi: 10.1126/sciadv.abq4947. URL <https://www.science.org/doi/abs/10.1126/sciadv.abq4947>.
- [146] P. Das, J.D. Blazit, M. Tencé, L.F. Zagonel, Y. Auad, Y.H. Lee, X.Y. Ling, A. Losquin, C. Colliex, O. Stéphan, F.J. García de Abajo, and M. Kociak. Stimulated electron energy loss and gain in an electron microscope without a pulsed electron gun. *Ultramicroscopy*, 203:44–51, 2019. ISSN 03043991. doi: 10.1016/j.ultramic.2018.12.011.
- [147] Chenze Liu, Yueying Wu, Zhongwei Hu, Jacob A. Busche, Elliot K. Beutler, Nicholas P. Montoni, Thomas M. Moore, Gregory A. Magel, Jon P. Camden, David J. Masiello, Gerd Duscher, and Philip D. Rack. Continuous Wave Resonant Photon Stimulated Electron Energy-Gain and Electron Energy-Loss Spectroscopy of Individual Plasmonic Nanoparticles. *ACS Photonics*, 6(10):2499–2508, 2019. ISSN 2330-4022, 2330-4022. doi: 10.1021/acsp Photonics.9b00830.
- [148] M. Kozák, P. Beck, H. Deng, J. McNeur, N. Schönenberger, C. Gaida, F. Stutzki, M. Gebhardt, J. Limpert, A. Ruehl, I. Hartl, O. Solgaard, J. S. Harris, R. L. Byer, and P. Hommelhoff. Acceleration of sub-relativistic electrons with an evanescent optical wave at a planar interface. *Optics Express*, 25(16):19195, 2017. ISSN 1094-4087. doi: 10.1364/OE.25.019195.
- [149] Ofer Kfir, Hugo Lourenço-Martins, Gero Storeck, Murat Sivis, Tyler R. Harvey, Tobias J. Kippenberg, Armin Feist, and Claus Ropers. Controlling free electrons with optical whispering-gallery modes. *Nature*, 582(7810):46–49, 2020. ISSN 0028-0836, 1476-4687. doi: 10.1038/s41586-020-2320-y.
- [150] F. J. García de Abajo and M. Kociak. Electron energy-gain spectroscopy. *New Journal of Physics*, 10(7):073035, 2008. ISSN 1367-2630. doi: 2008072203130300.

Bibliography

- [151] V. Brasch, M. Geiselmann, T. Herr, G. Lihachev, M. H. P. Pfeiffer, M. L. Gorodetsky, and T. J. Kippenberg. Photonic chip-based optical frequency comb using soliton Cherenkov radiation. *Science*, 351(6271):357–360, 2016. ISSN 0036-8075, 1095-9203. doi: 10.1126/science.aad4811.
- [152] Martin H. P. Pfeiffer, Arne Kordts, Victor Brasch, Michael Zervas, Michael Geiselmann, John D. Jost, and Tobias J. Kippenberg. Photonic Damascene process for integrated high-Q microresonator based nonlinear photonics. *Optica*, 3(1):20–25, 2016. ISSN 2334-2536. doi: 10.1364/OPTICA.3.000020.
- [153] Kenneth J. Leedle, Andrew Ceballos, Huiyang Deng, Olav Solgaard, R. Fabian Pease, Robert L. Byer, and James S. Harris. Dielectric laser acceleration of sub-100 keV electrons with silicon dual-pillar grating structures. *Optics Letters*, 40(18):4344, 2015. ISSN 0146-9592, 1539-4794. doi: 10/gmpfjm.
- [154] T. J. Kippenberg, S. M. Spillane, and K. J. Vahala. Modal coupling in traveling-wave resonators. *Optics Letters*, 27(19):1669–1671, 2002. ISSN 1539-4794. doi: 10.1364/OL.27.001669.
- [155] Enrico Pomarico, Ivan Madan, Gabriele Berruto, Giovanni Maria Vanacore, Kangpeng Wang, Ido Kaminer, F. Javier García de Abajo, and Fabrizio Carbone. meV Resolution in Laser-Assisted Energy-Filtered Transmission Electron Microscopy. *ACS Photonics*, 5(3):759–764, 2018. ISSN 2330-4022, 2330-4022. doi: 10/gdbmk2.
- [156] Michael L. Gorodetsky, Andrew D. Pryamikov, and Vladimir S. Ilchenko. Rayleigh scattering in high-q microspheres. *J. Opt. Soc. Am. B*, 17(6):1051–1057, Jun 2000. doi: 10.1364/JOSAB.17.001051. URL <http://josab.osa.org/abstract.cfm?URI=josab-17-6-1051>.
- [157] D. Foreman-Mackey, D. W. Hogg, D. Lang, and J. Goodman. emcee: The mcmc hammer. *PASP*, 125:306–312, 2013. doi: 10.1086/670067.
- [158] Armin Feist, Nora Bach, Nara Rubiano da Silva, Thomas Danz, Marcel Möller, Katharina E. Priebe, Till Domröse, J. Gregor Gatzmann, Stefan Rost, Jakob Schauss, Stefanie Strauch, Reiner Bormann, Murat Sivis, Sascha Schäfer, and Claus Ropers. Ultrafast transmission electron microscopy using a laser-driven field emitter: Femtosecond resolution with a high coherence electron beam. *Ultramicroscopy*, 176:63–73, 2017. ISSN 0304-3991. doi: <https://doi.org/10.1016/j.ultramic.2016.12.005>. URL <https://www.sciencedirect.com/science/article/pii/S0304399116303709>. 70th Birthday of Robert Sinclair and 65th Birthday of Nestor J. Zaluzec PICO 2017 – Fourth Conference on Frontiers of Aberration Corrected Electron Microscopy.
- [159] Binghai Liu, Zhi Li Dong, Younan Hua, Chao Fu, Xiaomin Li, Pik Kee Tan, and Yuzhe Zhao. Electron-beam radiation induced degradation of silicon nitride and its impact to semiconductor failure analysis by TEM. *AIP Advances*, 8(11):115327, 2018. ISSN 2158-3226. doi: 10.1063/1.5051813.

- [160] Miles H. Anderson, Romain Bouchand, Junqiu Liu, Wenle Weng, Ewelina Obrzud, Tobias Herr, and Tobias J. Kippenberg. Photonic chip-based resonant supercontinuum via pulse-driven kerr microresonator solitons. *Optica*, 8(6):771–779, Jun 2021. doi: 10.1364/OPTICA.403302. URL <https://opg.optica.org/optica/abstract.cfm?URI=optica-8-6-771>.
- [161] H. J. Kimble. The quantum internet. *Nature*, 453(7198):1023–1030, Jun 2008. ISSN 1476-4687. doi: 10.1038/nature07127. URL <https://doi.org/10.1038/nature07127>.
- [162] M Wallquist, K Hammerer, P Rabl, M Lukin, and P Zoller. Hybrid quantum devices and quantum engineering. *Physica Scripta*, 2009(T137):014001, dec 2009. doi: 10.1088/0031-8949/2009/T137/014001. URL <https://dx.doi.org/10.1088/0031-8949/2009/T137/014001>.
- [163] David Awschalom, Karl K. Berggren, Hannes Bernien, Sunil Bhave, Lincoln D. Carr, Paul Davids, Sophia E. Economou, Dirk Englund, Andrei Faraon, Martin Fejer, Saikat Guha, Martin V. Gustafsson, Evelyn Hu, Liang Jiang, Jungsang Kim, Boris Korzh, Prem Kumar, Paul G. Kwiat, Marko Lončar, Mikhail D. Lukin, David A.B. Miller, Christopher Monroe, Sae Woo Nam, Prineha Narang, Jason S. Orcutt, Michael G. Raymer, Amir H. Safavi-Naeini, Maria Spiropulu, Kartik Srinivasan, Shuo Sun, Jelena Vučković, Edo Waks, Ronald Walsworth, Andrew M. Weiner, and Zheshen Zhang. Development of quantum interconnects (quics) for next-generation information technologies. *PRX Quantum*, 2: 017002, Feb 2021. doi: 10.1103/PRXQuantum.2.017002. URL <https://link.aps.org/doi/10.1103/PRXQuantum.2.017002>.
- [164] Mohammad Mirhosseini, Alp Sipahigil, Mahmoud Kalaei, and Oskar Painter. Superconducting qubit to optical photon transduction. *Nature*, 588(7839):599–603, Dec 2020. ISSN 1476-4687. doi: 10.1038/s41586-020-3038-6. URL <https://doi.org/10.1038/s41586-020-3038-6>.
- [165] R. W. Andrews, R. W. Peterson, T. P. Purdy, K. Cicak, R. W. Simmonds, C. A. Regal, and K. W. Lehnert. Bidirectional and efficient conversion between microwave and optical light. *Nature Physics*, 10(4):321–326, April 2014. ISSN 1745-2473. doi: 10.1038/nphys2911.
- [166] Noel H. Wan, Tsung-Ju Lu, Kevin C. Chen, Michael P. Walsh, Matthew E. Trusheim, Lorenzo De Santis, Eric A. Bersin, Isaac B. Harris, Sara L. Mouradian, Ian R. Christen, Edward S. Bielejec, and Dirk Englund. Large-scale integration of artificial atoms in hybrid photonic circuits. *Nature*, 583(7815):226–231, Jul 2020. ISSN 1476-4687. doi: 10.1038/s41586-020-2441-3. URL <https://doi.org/10.1038/s41586-020-2441-3>.
- [167] Gregory S. MacCabe, Hengjiang Ren, Jie Luo, Justin D. Cohen, Hengyun Zhou, Alp Sipahigil, Mohammad Mirhosseini, and Oskar Painter. Nano-acoustic resonator with ultralong phonon lifetime. *Science*, 370(6518):840–843, 2020. doi: 10.1126/science.abc7312. URL <https://www.science.org/doi/abs/10.1126/science.abc7312>.
- [168] C. Monroe, R. Raussendorf, A. Ruthven, K. R. Brown, P. Maunz, L.-M. Duan, and J. Kim. Large-scale modular quantum-computer architecture with atomic memory and pho-

Bibliography

- tonic interconnects. *Phys. Rev. A*, 89:022317, Feb 2014. doi: 10.1103/PhysRevA.89.022317. URL <https://link.aps.org/doi/10.1103/PhysRevA.89.022317>.
- [169] B. Brandstätter, A. McClung, K. Schüppert, B. Casabone, K. Friebe, A. Stute, P. O. Schmidt, C. Deutsch, J. Reichel, R. Blatt, and T. E. Northup. Integrated fiber-mirror ion trap for strong ion-cavity coupling. *Review of Scientific Instruments*, 84(12):123104, 2013. doi: 10.1063/1.4838696. URL <https://doi.org/10.1063/1.4838696>.
- [170] Itay Shomroni, Serge Rosenblum, Yulia Lovsky, Orel Bechler, Gabriel Guendelman, and Barak Dayan. All-optical routing of single photons by a one-atom switch controlled by a single photon. *Science*, 345(6199):903–906, 2014. doi: 10.1126/science.1254699. URL <https://www.science.org/doi/abs/10.1126/science.1254699>.
- [171] T. G. Tiecke, J. D. Thompson, N. P. de Leon, L. R. Liu, V. Vuletić, and M. D. Lukin. Nanophotonic quantum phase switch with a single atom. *Nature*, 508(7495):241–244, Apr 2014. ISSN 1476-4687. doi: 10.1038/nature13188. URL <https://doi.org/10.1038/nature13188>.
- [172] Manuel Brekenfeld, Dominik Niemietz, Joseph Dale Christesen, and Gerhard Rempe. A quantum network node with crossed optical fibre cavities. *Nature Physics*, 16(6): 647–651, Jun 2020. ISSN 1745-2481. doi: 10.1038/s41567-020-0855-3. URL <https://doi.org/10.1038/s41567-020-0855-3>.
- [173] Sang Tae Park, Milo Lin, and Ahmed H Zewail. Photon-induced near-field electron microscopy (pinem): theoretical and experimental. *New Journal of Physics*, 12(12): 123028, dec 2010. doi: 10.1088/1367-2630/12/12/123028. URL <https://dx.doi.org/10.1088/1367-2630/12/12/123028>.
- [174] Ayca Yurtsever, Renske M van der Veen, and Ahmed H Zewail. Subparticle Ultrafast Spectrum Imaging in 4D Electron Microscopy. *Science*, 335(6064):59–64, 2012. ISSN 0036-8075. doi: 10.1126/science.1213504.
- [175] John Breuer and Peter Hommelhoff. Laser-based acceleration of nonrelativistic electrons at a dielectric structure. *Phys. Rev. Lett.*, 111:134803, Sep 2013. doi: 10.1103/PhysRevLett.111.134803. URL <https://link.aps.org/doi/10.1103/PhysRevLett.111.134803>.
- [176] E. A. Peralta, K. Soong, R. J. England, E. R. Colby, Z. Wu, B. Montazeri, C. McGuinness, J. McNeur, K. J. Leedle, D. Walz, E. B. Sozer, B. Cowan, B. Schwartz, G. Travish, and R. L. Byer. Demonstration of electron acceleration in a laser-driven dielectric microstructure. *Nature*, 503(7474):91–94, Nov 2013. ISSN 1476-4687. doi: 10.1038/nature12664. URL <https://doi.org/10.1038/nature12664>.
- [177] L Piazza, T.T.A. Lummen, E Quiñonez, Y Murooka, B.W. Reed, B Barwick, and F Carbone. Simultaneous observation of the quantization and the interference pattern of a plasmonic near-field. *Nature Communications*, 6(1):6407, 2015. ISSN 2041-1723. doi: 10.1038/ncomms7407.

- [178] Kangpeng Wang, Raphael Dahan, Michael Shentcis, Yaron Kauffmann, Adi Ben Hayun, Ori Reinhardt, Shai Tsesses, and Ido Kaminer. Coherent interaction between free electrons and a photonic cavity. *Nature*, 582(7810):50–54, 2020. ISSN 0028-0836, 1476-4687. doi: 10.1038/s41586-020-2321-x.
- [179] Yaniv Kurman, Raphael Dahan, Hanan Herzig Sheinfux, Kangpeng Wang, Michael Yannai, Yuval Adiv, Ori Reinhardt, Luiz H. G. Tizei, Steffi Y. Woo, Jiahua Li, James H. Edgar, Mathieu Kociak, Frank H. L. Koppens, and Ido Kaminer. Spatiotemporal imaging of 2D polariton wave packet dynamics using free electrons. *Science*, 372(6547):1181–1186, 2021. ISSN 0036-8075, 1095-9203. doi: 10.1126/science.abg9015.
- [180] Matthias Liebtrau, Murat Sivis, Armin Feist, Hugo Lourenço-Martins, Nicolas Pazos-Pérez, Ramon A. Alvarez-Puebla, F. Javier García de Abajo, Albert Polman, and Claus Ropers. Spontaneous and stimulated electron–photon interactions in nanoscale plasmonic near fields. *Light: Science & Applications*, 10(1):82, 2021. ISSN 2047-7538. doi: 10.1038/s41377-021-00511-y.
- [181] M. Kociak and L.F. Zagonel. Cathodoluminescence in the scanning transmission electron microscope. *Ultramicroscopy*, 176:112–131, 2017. ISSN 03043991. doi: 10.1016/j.ultramic.2017.03.014.
- [182] Albert Polman, Mathieu Kociak, and F. Javier García de Abajo. Electron-beam spectroscopy for nanophotonics. *Nature Materials*, 18(11):1158–1171, 2019. ISSN 1476-1122, 1476-4660. doi: 10.1038/s41563-019-0409-1.
- [183] F. Javier García de Abajo and Valerio Di Giulio. Optical Excitations with Electron Beams: Challenges and Opportunities. *ACS Photonics*, page acsphotonics.0c01950, 2021. ISSN 2330-4022, 2330-4022. doi: 10.1021/acsphotonics.0c01950.
- [184] Niklas Müller, Vincent Hock, Holger Koch, Nora Bach, Christopher Rathje, and Sascha Schäfer. Broadband Coupling of Fast Electrons to High-Q Whispering-Gallery Mode Resonators. *ACS Photonics*, page acsphotonics.1c00456, 2021. ISSN 2330-4022, 2330-4022. doi: 10.1021/acsphotonics.1c00456.
- [185] Yves Auad, Cyrille Hamon, Marcel Tencé, Hugo Lourenço-Martins, Vahagn Mkhitarian, Odile Stéphan, F. Javier García de Abajo, Luiz H. G. Tizei, and Mathieu Kociak. Unveiling the Coupling of Single Metallic Nanoparticles to Whispering-Gallery Microcavities. *Nano Letters*, 22(1):319–327, 2022. ISSN 1530-6984, 1530-6992. doi: 10.1021/acs.nanolett.1c03826.
- [186] Raphael Dahan, Gefen Baranes, Alexey Gorlach, Ron Ruimy, Nicholas Rivera, and Ido Kaminer. Creation of optical cat and gkp states using shaped free electrons. *Phys. Rev. X*, 13:031001, Jul 2023. doi: 10.1103/PhysRevX.13.031001. URL <https://link.aps.org/doi/10.1103/PhysRevX.13.031001>.

Bibliography

- [187] Dmitri K. Gramotnev and Sergey I. Bozhevolnyi. Plasmonics beyond the diffraction limit. *Nature Photonics*, 4(2):83–91, Feb 2010. ISSN 1749-4893. doi: 10.1038/nphoton.2009.282. URL <https://doi.org/10.1038/nphoton.2009.282>.
- [188] F. J. García de Abajo and A. Howie. Relativistic electron energy loss and electron-induced photon emission in inhomogeneous dielectrics. *Phys. Rev. Lett.*, 80:5180–5183, Jun 1998. doi: 10.1103/PhysRevLett.80.5180. URL <https://link.aps.org/doi/10.1103/PhysRevLett.80.5180>.
- [189] Martin H. P. Pfeiffer, Clemens Herkommer, Junqiu Liu, Hairun Guo, Maxim Karpov, Erwan Lucas, Michael Zervas, and Tobias J. Kippenberg. Octave-spanning dissipative kerr soliton frequency combs in si_3n_4 microresonators. *Optica*, 4(7):684–691, Jul 2017. doi: 10.1364/OPTICA.4.000684. URL <http://opg.optica.org/optica/abstract.cfm?URI=optica-4-7-684>.
- [190] Grégory Moille, Xiyuan Lu, Jordan Stone, Daron Westly, and Kartik Srinivasan. Fourier synthesis dispersion engineering of photonic crystal microrings for broadband frequency combs. *Communications Physics*, 6(1):144, Jun 2023. ISSN 2399-3650. doi: 10.1038/s42005-023-01253-6. URL <https://doi.org/10.1038/s42005-023-01253-6>.
- [191] Vilson R. Almeida, Roberto R. Panepucci, and Michal Lipson. Nanotaper for compact mode conversion. *Opt. Lett.*, 28(15):1302–1304, Aug 2003. doi: 10.1364/OL.28.001302. URL <http://opg.optica.org/ol/abstract.cfm?URI=ol-28-15-1302>.
- [192] Wim Bogaerts, Daniel Pérez, José Capmany, David A. B. Miller, Joyce Poon, Dirk Englund, Francesco Morichetti, and Andrea Melloni. Programmable photonic circuits. *Nature*, 586(7828):207–216, Oct 2020. ISSN 1476-4687. doi: 10.1038/s41586-020-2764-0. URL <https://doi.org/10.1038/s41586-020-2764-0>.
- [193] Ang Li and Yeshiahu Fainman. On-chip spectrometers using stratified waveguide filters. *Nature Communications*, 12(1):2704, May 2021. ISSN 2041-1723. doi: 10.1038/s41467-021-23001-6. URL <https://doi.org/10.1038/s41467-021-23001-6>.
- [194] Faraz Najafi, Jacob Mower, Nicholas C. Harris, Francesco Bellei, Andrew Dane, Catherine Lee, Xiaolong Hu, Prashanta Kharel, Francesco Marsili, Solomon Assefa, Karl K. Berggren, and Dirk Englund. On-chip detection of non-classical light by scalable integration of single-photon detectors. *Nature Communications*, 6(1):5873, Jan 2015. ISSN 2041-1723. doi: 10.1038/ncomms6873. URL <https://doi.org/10.1038/ncomms6873>.
- [195] Alberto Politi, Martin J. Cryan, John G. Rarity, Siyuan Yu, and Jeremy L. O’Brien. Silicon-silicon waveguide quantum circuits. *Science*, 320(5876):646–649, 2008. doi: 10.1126/science.1155441. URL <https://www.science.org/doi/abs/10.1126/science.1155441>.
- [196] Yuval Adiv, Hao Hu, Shai Tseses, Raphael Dahan, Kangpeng Wang, Yaniv Kurman, Alexey Gorlach, Hongsheng Chen, Xiao Lin, Guy Bartal, and Ido Kaminer. Observation of 2d cherenkov radiation. *Phys. Rev. X*, 13:011002, Jan 2023. doi: 10.1103/PhysRevX.13.011002. URL <https://link.aps.org/doi/10.1103/PhysRevX.13.011002>.

- [197] Alfréd Rényi et al. On measures of entropy and information. In *Proceedings of the fourth Berkeley symposium on mathematical statistics and probability*, number 547-561. Berkeley, California, USA, 1961.
- [198] Yiming Pan and Avraham Gover. Beyond fermi's golden rule in free-electron quantum electrodynamics: acceleration/radiation correspondence. *New Journal of Physics*, 23(6):063070, jun 2021. doi: 10.1088/1367-2630/abd35c. URL <https://dx.doi.org/10.1088/1367-2630/abd35c>.
- [199] Aviv Karnieli, Nicholas Rivera, Ady Arie, and Ido Kaminer. The coherence of light is fundamentally tied to the quantum coherence of the emitting particle. *Science Advances*, 7(18):eabf8096, 2021. doi: 10.1126/sciadv.abf8096. URL <https://www.science.org/doi/abs/10.1126/sciadv.abf8096>.
- [200] Norbert Schönerberger, Anna Mittelbach, Peyman Yousefi, Joshua McNeur, Uwe Niedermayer, and Peter Hommelhoff. Generation and characterization of attosecond microbunched electron pulse trains via dielectric laser acceleration. *Phys. Rev. Lett.*, 123:264803, Dec 2019. doi: 10.1103/PhysRevLett.123.264803. URL <https://link.aps.org/doi/10.1103/PhysRevLett.123.264803>.
- [201] O.L. Krivanek, N. Dellby, J.A. Hachtel, J.-C. Idrobo, M.T. Hotz, B. Plotkin-Swing, N.J. Bacon, A.L. Bleloch, G.J. Corbin, M.V. Hoffman, C.E. Meyer, and T.C. Lovejoy. Progress in ultrahigh energy resolution eels. *Ultramicroscopy*, 203:60–67, 2019. ISSN 0304-3991. doi: <https://doi.org/10.1016/j.ultramic.2018.12.006>. URL <https://www.sciencedirect.com/science/article/pii/S0304399118303668>. 75th Birthday of Christian Colliex, 85th Birthday of Archie Howie, and 75th Birthday of Hannes Lichte / PICO 2019 - Fifth Conference on Frontiers of Aberration Corrected Electron Microscopy.
- [202] Rodrigo A. Vicencio, Camilo Cantillano, Luis Morales-Inostroza, Bastián Real, Cristian Mejía-Cortés, Steffen Weimann, Alexander Szameit, and Mario I. Molina. Observation of localized states in lieb photonic lattices. *Phys. Rev. Lett.*, 114:245503, Jun 2015. doi: 10.1103/PhysRevLett.114.245503. URL <https://link.aps.org/doi/10.1103/PhysRevLett.114.245503>.
- [203] Seabrat Mukherjee, Alexander Spracklen, Debaditya Choudhury, Nathan Goldman, Patrik Öhberg, Erika Andersson, and Robert R. Thomson. Observation of a localized flat-band state in a photonic lieb lattice. *Phys. Rev. Lett.*, 114:245504, Jun 2015. doi: 10.1103/PhysRevLett.114.245504. URL <https://link.aps.org/doi/10.1103/PhysRevLett.114.245504>.
- [204] Yi Yang, Charles Roques-Carmes, Steven E. Kooi, Haoning Tang, Justin Beroz, Eric Mazur, Ido Kaminer, John D. Joannopoulos, and Marin Soljačić. Photonic flatband resonances for free-electron radiation. *Nature*, 613(7942):42–47, Jan 2023. ISSN 1476-4687. doi: 10.1038/s41586-022-05387-5. URL <https://doi.org/10.1038/s41586-022-05387-5>.

Bibliography

- [205] Erwan Lucas, Su-Peng Yu, Travis C. Briles, David R. Carlson, and Scott B. Papp. Tailoring microcombs with inverse-designed, meta-dispersion microresonators. *Nature Photonics*, 17(11):943–950, Nov 2023. ISSN 1749-4893. doi: 10.1038/s41566-023-01252-7. URL <https://doi.org/10.1038/s41566-023-01252-7>.
- [206] E. M. Purcell. *Spontaneous Emission Probabilities at Radio Frequencies*, pages 839–839. Springer US, Boston, MA, 1995. ISBN 978-1-4615-1963-8. doi: 10.1007/978-1-4615-1963-8_40. URL https://doi.org/10.1007/978-1-4615-1963-8_40.
- [207] M. W. Mitchell, J. S. Lundeen, and A. M. Steinberg. Super-resolving phase measurements with a multiphoton entangled state. *Nature*, 429(6988):161–164, May 2004. ISSN 1476-4687. doi: 10.1038/nature02493. URL <https://doi.org/10.1038/nature02493>.
- [208] Franz Hasselbach. Progress in electron- and ion-interferometry. *Reports on Progress in Physics*, 73(1):016101, dec 2009. doi: 10.1088/0034-4885/73/1/016101. URL <https://dx.doi.org/10.1088/0034-4885/73/1/016101>.
- [209] Alex O. C. Davis, Valérian Thiel, Michał Karpiński, and Brian J. Smith. Measuring the single-photon temporal-spectral wave function. *Phys. Rev. Lett.*, 121:083602, Aug 2018. doi: 10.1103/PhysRevLett.121.083602. URL <https://link.aps.org/doi/10.1103/PhysRevLett.121.083602>.
- [210] Uwe Niedermayer, Thilo Egenolf, and Oliver Boine-Frankenheim. Three dimensional alternating-phase focusing for dielectric-laser electron accelerators. *Phys. Rev. Lett.*, 125:164801, Oct 2020. doi: 10.1103/PhysRevLett.125.164801. URL <https://link.aps.org/doi/10.1103/PhysRevLett.125.164801>.
- [211] O.L. Krivanek, N. Dellby, and A.R. Lupini. Towards sub-Å electron beams. *Ultramicroscopy*, 78(1):1–11, 1999. ISSN 0304-3991. doi: [https://doi.org/10.1016/S0304-3991\(99\)00013-3](https://doi.org/10.1016/S0304-3991(99)00013-3). URL <https://www.sciencedirect.com/science/article/pii/S0304399199000133>.
- [212] K. J. Resch, K. L. Pregnell, R. Prevedel, A. Gilchrist, G. J. Pryde, J. L. O’Brien, and A. G. White. Time-reversal and super-resolving phase measurements. *Phys. Rev. Lett.*, 98:223601, May 2007. doi: 10.1103/PhysRevLett.98.223601. URL <https://link.aps.org/doi/10.1103/PhysRevLett.98.223601>.
- [213] Ori Reinhardt and Ido Kaminer. Theory of shaping electron wavepackets with light. *ACS Photonics*, 7(10):2859–2870, Oct 2020. doi: 10.1021/acsp Photonics.0c01133. URL <https://doi.org/10.1021/acsp Photonics.0c01133>.
- [214] Peter Baum. On the physics of ultrashort single-electron pulses for time-resolved microscopy and diffraction. *Chemical Physics*, 423:55–61, 2013. ISSN 0301-0104. doi: <https://doi.org/10.1016/j.chemphys.2013.06.012>. URL <https://www.sciencedirect.com/science/article/pii/S0301010413002681>.

- [215] Ulf Leonhardt. Quantum-state tomography and discrete wigner function. *Phys. Rev. Lett.*, 74:4101–4105, May 1995. doi: 10.1103/PhysRevLett.74.4101. URL <https://link.aps.org/doi/10.1103/PhysRevLett.74.4101>.
- [216] Matteo G.A. Paris. Displacement operator by beam splitter. *Physics Letters A*, 217(2): 78–80, 1996. ISSN 0375-9601. doi: [https://doi.org/10.1016/0375-9601\(96\)00339-8](https://doi.org/10.1016/0375-9601(96)00339-8). URL <https://www.sciencedirect.com/science/article/pii/0375960196003398>.
- [217] Miller Eaton, Amr Hossameldin, Richard J. Birrittella, Paul M. Alsing, Christopher C. Gerry, Hai Dong, Chris Cuevas, and Olivier Pfister. Resolution of 100 photons and quantum generation of unbiased random numbers. *Nature Photonics*, Dec 2022. ISSN 1749-4893. doi: 10.1038/s41566-022-01105-9. URL <https://doi.org/10.1038/s41566-022-01105-9>.
- [218] Risheng Cheng, Yiyu Zhou, Sihao Wang, Mohan Shen, Towsif Taher, and Hong X. Tang. A 100-pixel photon-number-resolving detector unveiling photon statistics. *Nature Photonics*, Dec 2022. ISSN 1749-4893. doi: 10.1038/s41566-022-01119-3. URL <https://doi.org/10.1038/s41566-022-01119-3>.
- [219] Severin Daiss, Stephan Welte, Bastian Hacker, Lin Li, and Gerhard Rempe. Single-photon distillation via a photonic parity measurement using cavity qed. *Phys. Rev. Lett.*, 122: 133603, Apr 2019. doi: 10.1103/PhysRevLett.122.133603. URL <https://link.aps.org/doi/10.1103/PhysRevLett.122.133603>.
- [220] Daniel Najer, Immo Söllner, Pavel Sekatski, Vincent Dolique, Matthias C. Löbl, Daniel Riedel, Rüdiger Schott, Sebastian Starosielec, Sascha R. Valentin, Andreas D. Wieck, Nicolas Sangouard, Arne Ludwig, and Richard J. Warburton. A gated quantum dot strongly coupled to an optical microcavity. *Nature*, 575(7784):622–627, Nov 2019. ISSN 1476-4687. doi: 10.1038/s41586-019-1709-y. URL <https://doi.org/10.1038/s41586-019-1709-y>.
- [221] G. S. Thekkadath, B. A. Bell, I. A. Walmsley, and A. I. Lvovsky. Engineering Schrödinger cat states with a photonic even-parity detector. *Quantum*, 4:239, March 2020. ISSN 2521-327X. doi: 10.22331/q-2020-03-02-239. URL <https://doi.org/10.22331/q-2020-03-02-239>.
- [222] Erwan Bimbard, Rajiv Boddeda, Nicolas Vitrant, Andrey Grankin, Valentina Parigi, Jovica Stanojevic, Alexei Ourjoumsev, and Philippe Grangier. Homodyne tomography of a single photon retrieved on demand from a cavity-enhanced cold atom memory. *Phys. Rev. Lett.*, 112:033601, Jan 2014. doi: 10.1103/PhysRevLett.112.033601. URL <https://link.aps.org/doi/10.1103/PhysRevLett.112.033601>.
- [223] A. Tikan, J. Riemensberger, K. Komagata, S. Hönl, M. Churayev, C. Skehan, H. Guo, R. N. Wang, J. Liu, P. Seidler, and T. J. Kippenberg. Emergent nonlinear phenomena in a driven dissipative photonic dimer. *Nature Physics*, 17(5):604–610, May 2021. ISSN 1745-2481. doi: 10.1038/s41567-020-01159-y. URL <https://doi.org/10.1038/s41567-020-01159-y>.

Bibliography

- [224] Tobias J Kippenberg, Alexander L Gaeta, Michal Lipson, and Michael L Gorodetsky. Dissipative kerr solitons in optical microresonators. *Science*, 361(6402):eaa8083, 2018. doi: 10.1126/science.aaa8083.
- [225] Mian Zhang, Brandon Buscaino, Cheng Wang, Amirhassan Shams-Ansari, Christian Reimer, Rongrong Zhu, Joseph M. Kahn, and Marko Lončar. Broadband electro-optic frequency comb generation in a lithium niobate microring resonator. *Nature*, 568(7752):373–377, Apr 2019. ISSN 1476-4687. doi: 10.1038/s41586-019-1008-7. URL <https://doi.org/10.1038/s41586-019-1008-7>.
- [226] A. M. Weiner. Femtosecond pulse shaping using spatial light modulators. *Review of Scientific Instruments*, 71(5):1929–1960, 2000. doi: 10.1063/1.1150614. URL <https://doi.org/10.1063/1.1150614>.
- [227] Matthew W. Puckett, Kaikai Liu, Nitesh Chauhan, Qiancheng Zhao, Naijun Jin, Haotian Cheng, Jianfeng Wu, Ryan O. Behunin, Peter T. Rakich, Karl D. Nelson, and Daniel J. Blumenthal. 422 million intrinsic quality factor planar integrated all-waveguide resonator with sub-mhz linewidth. *Nature Communications*, 12(1):934, Feb 2021. ISSN 2041-1723. doi: 10.1038/s41467-021-21205-4. URL <https://doi.org/10.1038/s41467-021-21205-4>.
- [228] Rishabh Sahu, William Hease, Alfredo Rueda, Georg Arnold, Liu Qiu, and Johannes M. Fink. Quantum-enabled operation of a microwave-optical interface. *Nature Communications*, 13(1):1276, Mar 2022. ISSN 2041-1723. doi: 10.1038/s41467-022-28924-2. URL <https://doi.org/10.1038/s41467-022-28924-2>.
- [229] Linran Fan, Chang-Ling Zou, Risheng Cheng, Xiang Guo, Xu Han, Zheng Gong, Sihao Wang, and Hong X. Tang. Superconducting cavity electro-optics: A platform for coherent photon conversion between superconducting and photonic circuits. *Science Advances*, 4(8):eaar4994, 2018. doi: 10.1126/sciadv.aar4994. URL <https://www.science.org/doi/abs/10.1126/sciadv.aar4994>.
- [230] C. K. Law and J. H. Eberly. Arbitrary control of a quantum electromagnetic field. *Phys. Rev. Lett.*, 76:1055–1058, Feb 1996. doi: 10.1103/PhysRevLett.76.1055. URL <https://link.aps.org/doi/10.1103/PhysRevLett.76.1055>.
- [231] Max Hofheinz, H. Wang, M. Ansmann, Radoslaw C. Bialczak, Erik Lucero, M. Neeley, A. D. O’Connell, D. Sank, J. Wenner, John M. Martinis, and A. N. Cleland. Synthesizing arbitrary quantum states in a superconducting resonator. *Nature*, 459(7246):546–549, May 2009. ISSN 1476-4687. doi: 10.1038/nature08005. URL <https://doi.org/10.1038/nature08005>.
- [232] D. I. Schuster, A. A. Houck, J. A. Schreier, A. Wallraff, J. M. Gambetta, A. Blais, L. Frunzio, J. Majer, B. Johnson, M. H. Devoret, S. M. Girvin, and R. J. Schoelkopf. Resolving photon number states in a superconducting circuit. *Nature*, 445(7127):515–518, Feb 2007. ISSN 1476-4687. doi: 10.1038/nature05461. URL <https://doi.org/10.1038/nature05461>.

- [233] Yoon-Ho Kim, Rong Yu, Sergei P. Kulik, Yanhua Shih, and Marlan O. Scully. Delayed “choice” quantum eraser. *Phys. Rev. Lett.*, 84:1–5, Jan 2000. doi: 10.1103/PhysRevLett.84.1. URL <https://link.aps.org/doi/10.1103/PhysRevLett.84.1>.
- [234] Tomáš Tyc and Barry C Sanders. Operational formulation of homodyne detection. *Journal of Physics A: Mathematical and General*, 37(29):7341, jul 2004. doi: 10.1088/0305-4470/37/29/010. URL <https://dx.doi.org/10.1088/0305-4470/37/29/010>.
- [235] Francisco Soto-Eguibar and Héctor Manuel Moya-Cessa. Harmonic oscillator position eigenstates via application of an operator on the vacuum. *Revista mexicana de física E*, 59(2):122–127, 2013.
- [236] A. P. Higginbotham, P. S. Burns, M. D. Urmey, R. W. Peterson, N. S. Kampel, B. M. Brubaker, G. Smith, K. W. Lehnert, and C. A. Regal. Harnessing electro-optic correlations in an efficient mechanical converter. *Nature Physics*, 14(10):1038–1042, Oct 2018. ISSN 1745-2481. doi: 10.1038/s41567-018-0210-0. URL <https://doi.org/10.1038/s41567-018-0210-0>.
- [237] C. Javerzac-Galy, K. Plekhanov, N. R. Bernier, L. D. Toth, A. K. Feofanov, and T. J. Kippenberg. On-chip microwave-to-optical quantum coherent converter based on a superconducting resonator coupled to an electro-optic microresonator. *Phys. Rev. A*, 94:053815, Nov 2016. doi: 10.1103/PhysRevA.94.053815. URL <https://link.aps.org/doi/10.1103/PhysRevA.94.053815>.
- [238] P. Kruit, R.G. Hobbs, C-S. Kim, Y. Yang, V.R. Manfrinato, J. Hammer, S. Thomas, P. Weber, B. Klopfer, C. Kohstall, T. Juffmann, M.A. Kasevich, P. Hommelhoff, and K.K. Berggren. Designs for a quantum electron microscope. *Ultramicroscopy*, 164:31–45, 2016. ISSN 03043991. doi: 10.1016/j.ultramic.2016.03.004.
- [239] Hiroshi Okamoto. A universal quantum electron microscope for phase objects: Hardware designs and possible applications, 2022. URL <https://arxiv.org/abs/2209.04819>.
- [240] W. J. Tomlinson, R. H. Stolen, and C. V. Shank. Compression of optical pulses chirped by self-phase modulation in fibers. *J. Opt. Soc. Am. B*, 1(2):139–149, Apr 1984. doi: 10.1364/JOSAB.1.000139. URL <https://opg.optica.org/josab/abstract.cfm?URI=josab-1-2-139>.
- [241] Edgars Nitiss, Jianqi Hu, Anton Stroganov, and Camille-Sophie Brès. Optically reconfigurable quasi-phase-matching in silicon nitride microresonators. *Nature Photonics*, 16(2):134–141, Feb 2022. ISSN 1749-4893. doi: 10.1038/s41566-021-00925-5. URL <https://doi.org/10.1038/s41566-021-00925-5>.
- [242] Leiran Wang, Lin Chang, Nicolas Volet, Martin H. P. Pfeiffer, Michael Zervas, Hairun Guo, Tobias J. Kippenberg, and John E. Bowers. Frequency comb generation in the green using silicon nitride microresonators. *Laser & Photonics Reviews*, 10(4):631–638, 2016. doi: <https://doi.org/10.1002/lpor.201600006>. URL <https://onlinelibrary.wiley.com/doi/abs/10.1002/lpor.201600006>.

Bibliography

- [243] Anat Siddharth, Thomas Wunderer, Grigory Lihachev, Andrey S. Voloshin, Camille Haller, Rui Ning Wang, Mark Teepe, Zhihong Yang, Junqiu Liu, Johann Riemensberger, Nicolas Grandjean, Noble Johnson, and Tobias J. Kippenberg. Near ultraviolet photonic integrated lasers based on silicon nitride. *APL Photonics*, 7(4):046108, 2022. doi: 10.1063/5.0081660. URL <https://doi.org/10.1063/5.0081660>.
- [244] Minh A. Tran, Chong Zhang, Theodore J. Morin, Lin Chang, Sabyasachi Barik, Zhiquan Yuan, Woonghee Lee, Glenn Kim, Aditya Malik, Zeyu Zhang, Joel Guo, Heming Wang, Boqiang Shen, Lue Wu, Kerry Vahala, John E. Bowers, Hyundai Park, and Tin Komljenovic. Extending the spectrum of fully integrated photonics to submicrometre wavelengths. *Nature*, 610(7930):54–60, Oct 2022. ISSN 1476-4687. doi: 10.1038/s41586-022-05119-9. URL <https://doi.org/10.1038/s41586-022-05119-9>.
- [245] Avraham Gover and Amnon Yariv. Free-electron–bound-electron resonant interaction. *Phys. Rev. Lett.*, 124:064801, Feb 2020. doi: 10.1103/PhysRevLett.124.064801. URL <https://link.aps.org/doi/10.1103/PhysRevLett.124.064801>.
- [246] Maxim Karpov, Hairun Guo, Arne Kordts, Victor Brasch, Martin H. P. Pfeiffer, Michail Zervas, Michael Geiselmann, and Tobias J. Kippenberg. Raman self-frequency shift of dissipative kerr solitons in an optical microresonator. *Phys. Rev. Lett.*, 116:103902, Mar 2016. doi: 10.1103/PhysRevLett.116.103902. URL <https://link.aps.org/doi/10.1103/PhysRevLett.116.103902>.
- [247] Ondrej L. Krivanek, Tracy C. Lovejoy, Niklas Dellby, Toshihiro Aoki, R. W. Carpenter, Peter Rez, Emmanuel Soignard, Jiangtao Zhu, Philip E. Batson, Maureen J. Lagos, Ray F. Egerton, and Peter A. Crozier. Vibrational spectroscopy in the electron microscope. *Nature*, 514(7521):209–212, Oct 2014. ISSN 1476-4687. doi: 10.1038/nature13870. URL <https://doi.org/10.1038/nature13870>.
- [248] Kartik Venkatraman, Barnaby D. A. Levin, Katia March, Peter Rez, and Peter A. Crozier. Vibrational spectroscopy at atomic resolution with electron impact scattering. *Nature Physics*, 15(12):1237–1241, Dec 2019. ISSN 1745-2481. doi: 10.1038/s41567-019-0675-5. URL <https://doi.org/10.1038/s41567-019-0675-5>.
- [249] F Hofer, F P Schmidt, W Grogger, and G Kothleitner. Fundamentals of electron energy-loss spectroscopy. *IOP Conference Series: Materials Science and Engineering*, 109(1):012007, Jan 2016. doi: 10.1088/1757-899X/109/1/012007. URL <https://dx.doi.org/10.1088/1757-899X/109/1/012007>.
- [250] Paul G. Kwiat, Klaus Mattle, Harald Weinfurter, Anton Zeilinger, Alexander V. Sergienko, and Yanhua Shih. New High-Intensity Source of Polarization-Entangled Photon Pairs. *Phys. Rev. Lett.*, 75(24):4337–4341, 1995. ISSN 0031-9007, 1079-7114. doi: 10.1103/PhysRevLett.75.4337.
- [251] Nicolas Gisin and Rob Thew. Quantum communication. *Nature Photon*, 1(3):165–171, 2007. ISSN 1749-4885, 1749-4893. doi: 10/fp82m2.

- [252] F. Borselli, M. Maiwöger, T. Zhang, P. Haslinger, V. Mukherjee, A. Negretti, S. Montangero, T. Calarco, I. Mazets, M. Bonneau, and J. Schmiedmayer. Two-Particle Interference with Double Twin-Atom Beams. *Phys. Rev. Lett.*, 126(8):083603, 2021. ISSN 0031-9007, 1079-7114. doi: 10.1103/PhysRevLett.126.083603.
- [253] B. Hensen, H. Bernien, A. E. Dréau, A. Reiserer, N. Kalb, M. S. Blok, J. Ruitenberg, R. F. L. Vermeulen, R. N. Schouten, C. Abellán, W. Amaya, V. Pruneri, M. W. Mitchell, M. Markham, D. J. Twitchen, D. Elkouss, S. Wehner, T. H. Taminiau, and R. Hanson. Loophole-free Bell inequality violation using electron spins separated by 1.3 kilometres. *Nature*, 526(7575):682–686, 2015. ISSN 0028-0836, 1476-4687. doi: 10.1038/nature15759.
- [254] Amy E. Turner, Cameron W. Johnson, Pieter Kruit, and Benjamin J. McMorran. Interaction-Free Measurement with Electrons. *Phys. Rev. Lett.*, 127(11):110401, 2021. ISSN 0031-9007, 1079-7114. doi: 10.1103/physrevlett.127.110401.
- [255] E. Rotunno, S. Gargiulo, G. M. Vanacore, C. Mechel, A. Tavabi, R. E. Dunin Borkowski, F. Carbone, I. Maidan, M. Zanfrognini, S. Frabboni, T. Guner, E. Karimi, I. Kaminer, and V. Grillo. One-dimensional ghost imaging with an electron microscope: A route towards ghost imaging with inelastically scattered electrons. *arXiv:2106.08955*, 2021.
- [256] M. Tsarev, A. Ryabov, and P. Baum. Measurement of Temporal Coherence of Free Electrons by Time-Domain Electron Interferometry. *Phys. Rev. Lett.*, 127(16):165501, 2021. ISSN 0031-9007, 1079-7114. doi: 10.1103/physrevlett.127.165501.
- [257] Romain Bourrellier, Sophie Meuret, Anna Tararan, Odile Stéphan, Mathieu Kociak, Luiz H. G. Tizei, and Alberto Zobelli. Bright UV Single Photon Emission at Point Defects in *h*-BN. *Nano Lett.*, 16(7):4317–4321, 2016. ISSN 1530-6984, 1530-6992. doi: 10/f8t95d.
- [258] S. Meuret, L. H. G. Tizei, T. Cazimajou, R. Bourrellier, H. C. Chang, F. Treussart, and M. Kociak. Photon Bunching in Cathodoluminescence. *Phys. Rev. Lett.*, 114(19):197401, 2015. ISSN 0031-9007, 1079-7114. doi: 10.1103/physrevlett.114.197401.
- [259] Magdalena Solà-Garcia, Kelly W. Mauser, Matthias Liebtrau, Toon Coenen, Silke Christiansen, Sophie Meuret, and Albert Polman. Photon Statistics of Incoherent Cathodoluminescence with Continuous and Pulsed Electron Beams. *ACS Photonics*, 8(3):916–925, 2021. ISSN 2330-4022, 2330-4022. doi: 10.1021/acsp Photonics.0c01939.
- [260] Michael Scheucher, Thomas Schachinger, Thomas Spielauer, Michael Stöger-Pollach, and Philipp Haslinger. Discrimination of coherent and incoherent cathodoluminescence using temporal photon correlations. *Ultramicroscopy*, 241:113594, 2022. ISSN 0304-3991. doi: <https://doi.org/10.1016/j.ultramic.2022.113594>. URL <https://www.sciencedirect.com/science/article/pii/S0304399122001127>.
- [261] Valerio Di Giulio and F. Javier García de Abajo. Free-electron shaping using quantum light. *Optica*, 7(12):1820, 2020. ISSN 2334-2536. doi: 10.1364/OPTICA.404598.

Bibliography

- [262] Andrea Konečná, Fadil Iyikanat, and F. Javier García de Abajo. Entangling free electrons and optical excitations. *Science Advances*, 8(47):eabo7853, 2022. doi: 10.1126/sciadv.abo7853. URL <https://www.science.org/doi/abs/10.1126/sciadv.abo7853>.
- [263] W. Dür, G. Vidal, and J. I. Cirac. Three qubits can be entangled in two inequivalent ways. *Phys. Rev. A*, 62(6):062314, 2000. ISSN 1050-2947, 1094-1622. doi: 10.1103/physreva.62.062314.
- [264] H. Häffner, W. Hänsel, C. F. Roos, J. Benhelm, D. Chek-al-kar, M. Chwalla, T. Körber, U. D. Rapol, M. Riebe, P. O. Schmidt, C. Becher, O. Gühne, W. Dür, and R. Blatt. Scalable multiparticle entanglement of trapped ions. *Nature*, 438(7068):643–646, 2005. ISSN 0028-0836, 1476-4687. doi: 10.1038/nature04279.
- [265] Markus Gräfe, René Heilmann, Armando Perez-Leija, Robert Keil, Felix Dreisow, Matthias Heinrich, Hector Moya-Cessa, Stefan Nolte, Demetrios N. Christodoulides, and Alexander Szameit. On-chip generation of high-order single-photon W-states. *Nature Photon*, 8(10):791–795, 2014. ISSN 1749-4885, 1749-4893. doi: 10/f6ksdg.
- [266] Nahid Talebi. A directional, ultrafast and integrated few-photon source utilizing the interaction of electron beams and plasmonic nanoantennas. *New J. Phys.*, 16(5):053021, 2014. ISSN 1367-2630. doi: 10.1088/1367-2630/16/5/053021.
- [267] Natasha Tomm, Alisa Javadi, Nadia Olympia Antoniadis, Daniel Najer, Matthias Christian Löbl, Alexander Rolf Korsch, Rüdiger Schott, Sascha René Valentin, Andreas Dirk Wieck, Arne Ludwig, and Richard John Warburton. A bright and fast source of coherent single photons. *Nat. Nanotechnol.*, 16(4):399–403, 2021. ISSN 1748-3387, 1748-3395. doi: 10.1038/s41565-020-00831-x.
- [268] S. Signorini and L. Pavesi. On-chip heralded single photon sources. *AVS Quantum Sci.*, 2(4):041701, 2020. ISSN 2639-0213. doi: 10/gjsc5b.
- [269] Yoshinori Uemura, Masaru Irita, Yoshikazu Homma, and Mark Sadgrove. Probing the local density of states near the diffraction limit using nanowaveguide-collected cathode luminescence. *Phys. Rev. A*, 104(3):L031504, 2021. ISSN 2469-9926, 2469-9934. doi: 10/gm77kf.
- [270] Magdalena Solà-Garcia, Kelly W. Mauser, Matthias Liebtrau, Toon Coenen, Silke Christiansen, Sophie Meuret, and Albert Polman. Photon statistics of incoherent cathodoluminescence with continuous and pulsed electron beams. *ACS Photonics*, 8(3):916–925, 2021. doi: 10.1021/acsp Photonics.0c01939. URL <https://doi.org/10.1021/acsp Photonics.0c01939>. PMID: 33763505.
- [271] M. D. Reid and D. F. Walls. Violations of classical inequalities in quantum optics. *Phys. Rev. A*, 34:1260–1276, Aug 1986. doi: 10.1103/PhysRevA.34.1260. URL <https://link.aps.org/doi/10.1103/PhysRevA.34.1260>.

- [272] Nicolai B. Grosse, Thomas Symul, Magdalena Stobińska, Timothy C. Ralph, and Ping Koy Lam. Measuring photon antibunching from continuous variable sideband squeezing. *Phys. Rev. Lett.*, 98:153603, Apr 2007. doi: 10.1103/PhysRevLett.98.153603. URL <https://link.aps.org/doi/10.1103/PhysRevLett.98.153603>.
- [273] R. J. Graham, J.C.H. Spence, and H. Alexander. Infrared Cathodoluminescence Studies from Dislocations in Silicon in tem, a Fourier Transform Spectrometer for Cl in Tem and Els/cl Coincidence Measurements of Lifetimes in Semiconductors. *MRS Proc.*, 82:235, 1986. ISSN 0272-9172, 1946-4274. doi: 10.1557/PROC-82-235.
- [274] Daen Jannis, Knut Müller-Caspary, Armand Béché, and Jo Verbeeck. Coincidence Detection of EELS and EDX Spectral Events in the Electron Microscope. *Applied Sciences*, 11(19):9058, 2021. ISSN 2076-3417. doi: 10.3390/app11199058.
- [275] Daen Jannis, Knut Müller-Caspary, Armand Béché, Andreas Oelsner, and Johan Verbeeck. Spectroscopic coincidence experiments in transmission electron microscopy. *Appl. Phys. Lett.*, 114(14):143101, 2019. ISSN 0003-6951, 1077-3118. doi: 10.1063/1.5092945.
- [276] Michel Bosman, Vicki J Keast, Masashi Watanabe, Abbas I Maarroof, and Michael B Cortie. Mapping surface plasmons at the nanometre scale with an electron beam. *Nanotechnology*, 18(16):165505, mar 2007. doi: 10.1088/0957-4484/18/16/165505. URL <https://dx.doi.org/10.1088/0957-4484/18/16/165505>.
- [277] Ori Reinhardt, Chen Mechel, Morgan Lynch, and Ido Kaminer. Free-electron qubits, 2019. URL <https://arxiv.org/abs/1907.10281>.
- [278] M. V. Tsarev, A. Ryabov, and P. Baum. Free-electron qubits and maximum-contrast attosecond pulses via temporal talbot revivals. *Phys. Rev. Res.*, 3:043033, Oct 2021. doi: 10.1103/PhysRevResearch.3.043033. URL <https://link.aps.org/doi/10.1103/PhysRevResearch.3.043033>.
- [279] William B. Case, Mathias Tomandl, Sarayut Deachapunya, and Markus Arndt. Realization of optical carpets in the talbot and talbot-lau configurations. *Opt. Express*, 17(23):20966–20974, Nov 2009. doi: 10.1364/OE.17.020966. URL <https://opg.optica.org/oe/abstract.cfm?URI=oe-17-23-20966>.
- [280] Thomas Wunderer, Anat Siddharth, Noble M. Johnson, Christopher L. Chua, Mark Teepe, Zhihong Yang, Max Batres, Patrick Maeda, Grigory Lihachev, and Tobias J. Kippenberg. Single-frequency violet and blue laser emission from algainn photonic integrated circuit chips. *Opt. Lett.*, 48(11):2781–2784, Jun 2023. doi: 10.1364/OL.486758. URL <https://opg.optica.org/ol/abstract.cfm?URI=ol-48-11-2781>.
- [281] Daniel Collins, Nicolas Gisin, Noah Linden, Serge Massar, and Sandu Popescu. Bell inequalities for arbitrarily high-dimensional systems. *Phys. Rev. Lett.*, 88:040404, Jan 2002. doi: 10.1103/PhysRevLett.88.040404. URL <https://link.aps.org/doi/10.1103/PhysRevLett.88.040404>.

Bibliography

- [282] Jeff Hecht. *City of light: the story of fiber optics*. Sloan Technology, 2004.
- [283] M.K. Smit and C. Van Dam. Phasar-based wdm-devices: Principles, design and applications. *IEEE Journal of Selected Topics in Quantum Electronics*, 2(2):236–250, 1996. doi: 10.1109/2944.577370.
- [284] Di Liang and John E Bowers. Recent progress in lasers on silicon. *Nature Photonics*, 4(8): 511, 2010. doi: 10.1038/nphoton.2010.167.
- [285] Sarat Gundavarapu, Grant M Brodnik, Matthew Puckett, Taran Huffman, Debapam Bose, Ryan Behunin, Jianfeng Wu, Tiequn Qiu, Cátia Pinho, Nitesh Chauhan, et al. Sub-hertz fundamental linewidth photonic integrated brillouin laser. *Nature Photonics*, 13(1):60–+, 2019. doi: 10.1038/s41566-018-0313-2.
- [286] Cheng Wang, Mian Zhang, Xi Chen, Maxime Bertrand, Amirhassan Shams-Ansari, Sethumadhavan Chandrasekhar, Peter Winzer, and Marko Lončar. Integrated lithium niobate electro-optic modulators operating at cmos-compatible voltages. *Nature*, 562(7725):101–104, 2018.
- [287] P. Trocha, M. Karpov, D. Ganin, M. H. P. Pfeiffer, A. Kordts, S. Wolf, J. Krockenberger, P. Marin-Palomo, C. Weimann, S. Randel, W. Freude, T. J. Kippenberg, and C. Koos. Ultrafast optical ranging using microresonator soliton frequency combs. *Science*, 359(6378):887–891, 2018. doi: 10.1126/science.aao3924. URL <https://www.science.org/doi/abs/10.1126/science.aao3924>.
- [288] Yang Liu, Zheru Qiu, Xinru Ji, Anton Lukashchuk, Jijun He, Johann Riemensberger, Martin Hafermann, Rui Ning Wang, Junqiu Liu, Carsten Ronning, and Tobias J. Kippenberg. A photonic integrated circuit-based erbium-doped amplifier. *Science*, 376(6599): 1309–1313, 2022. doi: 10.1126/science.abo2631. URL <https://www.science.org/doi/abs/10.1126/science.abo2631>.
- [289] Jianwei Wang, Fabio Sciarrino, Anthony Laing, and Mark G Thompson. Integrated photonic quantum technologies. *Nature Photonics*, 14(5):273–284, 2020.
- [290] Lars S Madsen, Fabian Laudenbach, Mohsen Falamarzi Askarani, Fabien Rortais, Trevor Vincent, Jacob FF Bulmer, Filippo M Miatto, Leonhard Neuhaus, Lukas G Helt, Matthew J Collins, et al. Quantum computational advantage with a programmable photonic processor. *Nature*, 606(7912):75–81, 2022.
- [291] Avik Dutt, Kevin Luke, Sasikanth Manipatruni, Alexander L Gaeta, Paulo Nussenzveig, and Michal Lipson. On-chip optical squeezing. *Physical Review Applied*, 3(4):044005, 2015.
- [292] Han-Sen Zhong, Hui Wang, Yu-Hao Deng, Ming-Cheng Chen, Li-Chao Peng, Yi-Han Luo, Jian Qin, Dian Wu, Xing Ding, Yi Hu, et al. Quantum computational advantage using photons. *Science*, 370(6523):1460–1463, 2020.

- [293] D. Ganapathy, W. Jia, M. Nakano, V. Xu, N. Aritomi, T. Cullen, N. Kijbunchoo, S. E. Dwyer, A. Mullavey, L. McCuller, R. Abbott, I. Abouelfettouh, R. X. Adhikari, A. Ananyeva, S. Appert, K. Arai, S. M. Aston, M. Ball, S. W. Ballmer, D. Barker, L. Barsotti, B. K. Berger, J. Betzwieser, D. Bhattacharjee, G. Billingsley, S. Biscans, N. Bode, E. Bonilla, V. Bossilkov, A. Branch, A. F. Brooks, D. D. Brown, J. Bryant, C. Cahillane, H. Cao, E. Capote, F. Clara, J. Collins, C. M. Compton, R. Cottingham, D. C. Coyne, R. Crouch, J. Csizmazia, L. P. Dartez, N. Demos, E. Dohmen, J. C. Driggers, A. Effler, A. Ejlli, T. Etzel, M. Evans, J. Feicht, R. Frey, W. Frischhertz, P. Fritschel, V. V. Frolov, P. Fulda, M. Fyffe, B. Gateley, J. A. Giaime, K. D. Giardino, J. Glanzer, E. Goetz, R. Goetz, A. W. Goodwin-Jones, S. Gras, C. Gray, D. Griffith, H. Grote, T. Guidry, E. D. Hall, J. Hanks, J. Hanson, M. C. Heintze, A. F. Helmling-Cornell, N. A. Holland, D. Hoyland, H. Y. Huang, Y. Inoue, A. L. James, A. Jennings, S. Karat, S. Karki, M. Kasprzack, K. Kawabe, P. J. King, J. S. Kissel, K. Komori, A. Kontos, R. Kumar, K. Kuns, M. Landry, B. Lantz, M. Laxen, K. Lee, M. Lesovsky, F. Llamas, M. Lormand, H. A. Loughlin, R. Macas, M. MacInnis, C. N. Makarem, B. Mannix, G. L. Mansell, R. M. Martin, K. Mason, F. Matichard, N. Mavalvala, N. Maxwell, G. McCarrol, R. McCarthy, D. E. McClelland, S. McCormick, T. McRae, F. Mera, E. L. Merilh, F. Meylahn, R. Mittleman, D. Moraru, G. Moreno, T. J. N. Nelson, A. Neunzert, J. Notte, J. Oberling, T. O’Hanlon, C. Osthelder, D. J. Ottaway, H. Overmier, W. Parker, A. Pele, H. Pham, M. Pirello, V. Quetschke, K. E. Ramirez, J. Reyes, J. W. Richardson, M. Robinson, J. G. Rollins, C. L. Romel, J. H. Romie, M. P. Ross, K. Ryan, T. Sadecki, A. Sanchez, E. J. Sanchez, L. E. Sanchez, R. L. Savage, D. Schaetzl, M. G. Schiowski, R. Schnabel, R. M. S. Schofield, E. Schwartz, D. Sellers, T. Shaffer, R. W. Short, D. Sigg, B. J. J. Slagmolen, C. Soike, S. Soni, V. Srivastava, L. Sun, D. B. Tanner, M. Thomas, P. Thomas, K. A. Thorne, C. I. Torrie, G. Traylor, A. S. Ubhi, G. Vajente, J. Vanosky, A. Vecchio, P. J. Veitch, A. M. Vibhute, E. R. G. von Reis, J. Warner, B. Weaver, R. Weiss, C. Whittle, B. Willke, C. C. Wipf, H. Yamamoto, L. Zhang, and M. E. Zucker. Broadband quantum enhancement of the ligo detectors with frequency-dependent squeezing. *Phys. Rev. X*, 13:041021, Oct 2023. doi: 10.1103/PhysRevX.13.041021. URL <https://link.aps.org/doi/10.1103/PhysRevX.13.041021>.
- [294] Wei Liang, Danny Eliyahu, Vladimir S Ilchenko, Anatoliy A Savchenkov, Andrey B Matsko, David Seidel, and Lute Maleki. High spectral purity kerr frequency comb radio frequency photonic oscillator. *Nature communications*, 6:7957, 2015. doi: 10.1038/ncomms8957.
- [295] Junqiu Liu, Erwan Lucas, Arslan S. Raja, Jijun He, Johann Riemensberger, Rui Ning Wang, Maxim Karpov, Hairun Guo, Romain Bouchand, and Tobias J. Kippenberg. Photonic microwave generation in the x- and k-band using integrated soliton microcombs. *Nature Photonics*, 14(8):486–491, Aug 2020. ISSN 1749-4893. doi: 10.1038/s41566-020-0617-x. URL <https://doi.org/10.1038/s41566-020-0617-x>.
- [296] Tara E Drake, Jordan R Stone, Travis C Briles, Daryl T Spencer, and Scott B Papp. Thermal decoherence of the carrier-envelope-offset frequency in a kerr-microresonator comb. In *Frontiers in Optics*, pages JTU2A–62. Optical Society of America, 2018. doi: 10.1364/FIO.2018.JTU2A.62.

Bibliography

- [297] Andrew G White, Ping Koy Lam, David E McClelland, Hans-A Bachor, and William J Munro. Kerr noise reduction and squeezing. *Journal of Optics B: Quantum and Semi-classical Optics*, 2(4):553, 2000.
- [298] Victor Brasch, Qun-Feng Chen, Stephan Schiller, and Tobias J Kippenberg. Radiation hardness of high-q silicon nitride microresonators for space compatible integrated optics. *Optics Express*, 22(25):30786–30794, 2014. doi: 10.1364/OE.22.030786.
- [299] David J Moss, Roberto Morandotti, Alexander L Gaeta, and Michal Lipson. New cmos-compatible platforms based on silicon nitride and hydex for nonlinear optics. *Nature Photonics*, 7(8):597, 2013. doi: 10.1038/nphoton.2013.183.
- [300] Xingchen Ji, Felipe AS Barbosa, Samantha P Roberts, Avik Dutt, Jaime Cardenas, Yoshitomo Okawachi, Alex Bryant, Alexander L Gaeta, and Michal Lipson. Ultra-low-loss on-chip resonators with sub-milliwatt parametric oscillation threshold. *Optica*, 4(6):619–624, 2017. doi: 10.1364/OPTICA.4.000619.
- [301] Jared F Bauters, Martijn JR Heck, Demis D John, Jonathon S Barton, Christiaan M Bruinink, Arne Leinse, René G Heideman, Daniel J Blumenthal, and John E Bowers. Planar waveguides with less than 0.1 db/m propagation loss fabricated with wafer bonding. *Optics Express*, 19(24):24090–24101, 2011. doi: 10.1364/OE.19.024090.
- [302] Tobias J Kippenberg, Ronald Holzwarth, and Scott A Diddams. Microresonator-based optical frequency combs. *Science*, 332(6029):555–559, 2011. doi: 10.1126/science.1193968.
- [303] Qing Li, Travis C Briles, Daron A Westly, Tara E Drake, Jordan R Stone, B Robert Ilic, Scott A Diddams, Scott B Papp, and Kartik Srinivasan. Stably accessing octave-spanning microresonator frequency combs in the soliton regime. *Optica*, 4(2):193–203, 2017. doi: 10.1364/OPTICA.4.000193.
- [304] Travis C Briles, Jordan R Stone, Tara E Drake, Daryl T Spencer, Connor Fredrick, Qing Li, Daron Westly, BR Ilic, Kartik Srinivasan, Scott A Diddams, et al. Interlocking kerr-microresonator frequency combs for microwave to optical synthesis. *Optics Letters*, 43(12):2933–2936, 2018. doi: 10.1364/OL.43.002933.
- [305] Martin Hubert Peter Pfeiffer, Clemens Herkommer, Junqiu Liu, Tiago Morais, Michael Zervas, Michael Geiselmann, and Tobias J Kippenberg. Photonic damascene process for low-loss, high-confinement silicon nitride waveguides. *IEEE Journal of Selected Topics in Quantum Electronics*, 24(4):1–11, 2018. doi: 10.1109/JSTQE.2018.2808258.
- [306] Junqiu Liu, Arslan S. Raja, Maxim Karpov, Bahareh Ghadiani, Martin H. P. Pfeiffer, Botao Du, Nils J. Engelsen, Hairun Guo, Michael Zervas, and Tobias J. Kippenberg. Ultralow-power chip-based soliton microcombs for photonic integration. *Optica*, 5(10):1347–1353, Oct 2018. doi: 10.1364/OPTICA.5.001347. URL <http://www.osapublishing.org/optica/abstract.cfm?URI=optica-5-10-1347>.

- [307] Ulrich B Hoff, Bo M Nielsen, and Ulrik L Andersen. Integrated source of broadband quadrature squeezed light. *Optics Express*, 23(9):12013–12036, 2015. doi: 10.1364/OE.23.012013.
- [308] O. Arcizet, R. Rivière, A. Schliesser, G. Anetsberger, and T. J. Kippenberg. Cryogenic properties of optomechanical silica microcavities. *Phys. Rev. A*, 80:021803, Aug 2009. doi: 10.1103/PhysRevA.80.021803. URL <https://link.aps.org/doi/10.1103/PhysRevA.80.021803>.
- [309] Michael L Gorodetsky and Ivan S Grudinin. Fundamental thermal fluctuations in microspheres. *J. Opt. Soc. Am. B*, 21(4):697–705, 2004. doi: 10.1364/JOSAB.21.000697.
- [310] Akobuije Chijioke, Qun-Feng Chen, Alexander Yu. Nevsky, and Stephan Schiller. Thermal noise of whispering-gallery resonators. *Phys. Rev. A*, 85:053814, May 2012. doi: 10.1103/PhysRevA.85.053814. URL <https://link.aps.org/doi/10.1103/PhysRevA.85.053814>.
- [311] V. B. Braginsky, M. L. Gorodetsky, and S. P. Vyatchanin. Thermo-refractive noise in gravitational wave antennae. *Physics Letters A*, 271(5):303–307, July 2000. ISSN 0375-9601. doi: 10.1016/S0375-9601(00)00389-3. URL <http://www.sciencedirect.com/science/article/pii/S0375960100003893>.
- [312] Matthew R. Foreman, Jon D. Swaim, and Frank Vollmer. Whispering gallery mode sensors. *Adv. Opt. Photon.*, 7(2):168–240, Jun 2015. doi: 10.1364/AOP.7.000168. URL <http://aop.osa.org/abstract.cfm?URI=aop-7-2-168>.
- [313] Georg Anetsberger, Emanuel Gavartin, Olivier Arcizet, Quirin P Unterreithmeier, Eva Maria Weig, Michael L Gorodetsky, Jörg Peter Kotthaus, and Tobias J Kippenberg. Measuring nanomechanical motion with an imprecision below the standard quantum limit. *Physical Review A*, 82(6):061804, 2010. doi: 10.1103/PhysRevA.82.061804.
- [314] N. G. Pavlov, N. M. Kondratyev, and M. L. Gorodetsky. Modeling the whispering gallery microresonator-based optical modulator. *Appl. Opt.*, 54(35):10460–10466, Dec 2015. doi: 10.1364/AO.54.010460. URL <http://ao.osa.org/abstract.cfm?URI=ao-54-35-10460>.
- [315] Lute Maleki. The opto-electronic oscillator (oeo): Review and recent progress. In *2012 European Frequency and Time Forum*, pages 497–500, 2012. doi: 10.1109/EFTF.2012.6502432.
- [316] Andrey B. Matsko, Anatoliy A. Savchenkov, Nan Yu, and Lute Maleki. Whispering-gallery-mode resonators as frequency references. i. fundamental limitations. *J. Opt. Soc. Am. B*, 24(6):1324–1335, Jun 2007. doi: 10.1364/JOSAB.24.001324. URL <http://josab.osa.org/abstract.cfm?URI=josab-24-6-1324>.
- [317] Wenle Weng, Philip S Light, and Andre N Luiten. Ultra-sensitive lithium niobate thermometer based on a dual-resonant whispering-gallery-mode cavity. *Optics Letters*, 43(7):1415–1418, 2018. doi: 10.1364/OL.43.001415.

Bibliography

- [318] NM Kondratiev and ML Gorodetsky. Thermorefractive noise in whispering gallery mode microresonators: Analytical results and numerical simulation. *Physics Letters A*, 382(33): 2265–2268, 2018. doi: 10.1016/j.physleta.2017.04.043.
- [319] Amir Arbabi and Lynford L. Goddard. Measurements of the refractive indices and thermo-optic coefficients of Si_3N_4 and SiO_2 using microring resonances. *Optics Letters*, 38(19):3878–3881, Oct 2013. doi: 10.1364/OL.38.003878. URL <http://ol.osa.org/abstract.cfm?URI=ol-38-19-3878>.
- [320] Jinkang Lim, Anatoliy A. Savchenkov, Elijah Dale, Wei Liang, Danny Eliyahu, Vladimir Ilchenko, Andrey B. Matsko, Lute Maleki, and Chee Wei Wong. Chasing the thermodynamical noise limit in whispering-gallery-mode resonators for ultrastable laser frequency stabilization. *Nature Communications*, 8(1):8, Jan 2017. ISSN 2041-1723. doi: 10.1038/s41467-017-00021-9. URL <http://arxiv.org/abs/1701.05285><http://dx.doi.org/10.1038/s41467-017-00021-9>.
- [321] H. J. Kimble, Benjamin L. Lev, and Jun Ye. Optical interferometers with reduced sensitivity to thermal noise. *Phys. Rev. Lett.*, 101:260602, Dec 2008. doi: 10.1103/PhysRevLett.101.260602. URL <https://link.aps.org/doi/10.1103/PhysRevLett.101.260602>.
- [322] Junyin Zhang, Zihan Li, Johann Riemensberger, Grigory Lihachev, Guan Hao Huang, and Tobias J. Kippenberg. Fundamental charge noise in electro-optic photonic integrated circuits, 2023.
- [323] J Abadie, BP Abbott, R Abbott, TD Abbott, M Abernathy, C Adams, R Adhikari, C Affeldt, B Allen, GS Allen, et al. A gravitational wave observatory operating beyond the quantum shot-noise limit. *Nature Physics*, 7(12):962, 2011.
- [324] Lars S Madsen, Vladyslav C Usenko, Mikael Lassen, Radim Filip, and Ulrik L Andersen. Continuous variable quantum key distribution with modulated entangled states. *Nature communications*, 3:1083, 2012.
- [325] R_E Slusher, LW Hollberg, Bernard Yurke, JC Mertz, and JF Valley. Observation of squeezed states generated by four-wave mixing in an optical cavity. *Physical Review Letters*, 55(22):2409, 1985.
- [326] RM Shelby, MD Levenson, SH Perlmutter, RG DeVoe, and DF Walls. Broad-band parametric deamplification of quantum noise in an optical fiber. *Physical review letters*, 57(6):691, 1986.
- [327] Daniel WC Brooks, Thierry Botter, Sydney Schreppler, Thomas P Purdy, Nathan Brahms, and Dan M Stamper-Kurn. Non-classical light generated by quantum-noise-driven cavity optomechanics. *Nature*, 488(7412):476, 2012.
- [328] Axel Schönbeck, Fabian Thies, and Roman Schnabel. 13 db squeezed vacuum states at 1550 nm from 12 mw external pump power at 775 nm. *Optics letters*, 43(1):110–113, 2018.

- [329] Keren Bergman and HA Haus. Squeezing in fibers with optical pulses. *Optics letters*, 16(9):663–665, 1991.
- [330] Liu Qiu, Itay Shomroni, Marie A. Ioannou, Nicolas Piro, Daniel Malz, Andreas Nunnenkamp, and Tobias J. Kippenberg. Floquet dynamics in the quantum measurement of mechanical motion. *Physical Review A*, 100(5):053852, November 2019. doi: 10.1103/PhysRevA.100.053852. URL <https://link.aps.org/doi/10.1103/PhysRevA.100.053852>.
- [331] J. H. Shapiro, G. Saplakoglu, S.-T. Ho, P. Kumar, B. E. A. Saleh, and M. C. Teich. Theory of light detection in the presence of feedback. *JOSA B*, 4(10):1604–1620, October 1987. ISSN 1520-8540. doi: 10.1364/JOSAB.4.001604. URL <https://www.osapublishing.org/josab/abstract.cfm?uri=josab-4-10-1604>.
- [332] H. A. Haus and Y. Yamamoto. Theory of feedback-generated squeezed states. *Physical Review A*, 34(1):270–292, July 1986. doi: 10.1103/PhysRevA.34.270. URL <https://link.aps.org/doi/10.1103/PhysRevA.34.270>.
- [333] Andrey B. Matsko, Anatoliy A. Savchenkov, Dmitry Strekalov, Vladimir S. Ilchenko, and Lute Maleki. Optical hyperparametric oscillations in a whispering-gallery-mode resonator: Threshold and phase diffusion. *Physical Review A*, 71(3):033804, March 2005. doi: 10.1103/PhysRevA.71.033804. URL <https://link.aps.org/doi/10.1103/PhysRevA.71.033804>.
- [334] Matthew S. Taubman, Howard Wiseman, David E. McClelland, and Hans-A. Bachor. Intensity feedback effects on quantum-limited noise. *Journal of the Optical Society of America B*, 12(10):1792, October 1995. ISSN 0740-3224, 1520-8540. doi: 10.1364/JOSAB.12.001792. URL <https://www.osapublishing.org/abstract.cfm?URI=josab-12-10-1792>.
- [335] H. M. Wiseman. In-Loop Squeezing Is Like Real Squeezing to an In-Loop Atom. *Physical Review Letters*, 81(18):3840–3843, November 1998. doi: 10.1103/PhysRevLett.81.3840. URL <https://link.aps.org/doi/10.1103/PhysRevLett.81.3840>.
- [336] H. M. Wiseman. Squashed states of light: Theory and applications to quantum spectroscopy. *Journal of Optics B: Quantum and Semiclassical Optics*, 1(4):459–463, August 1999. ISSN 1464-4266. doi: 10.1088/1464-4266/1/4/317. URL <https://doi.org/10.1088/1464-4266/1/4/317>.
- [337] Alexander L. Gaeta, Michal Lipson, and Tobias J. Kippenberg. Photonic-chip-based frequency combs. *Nature Photonics*, 13(3):158–169, March 2019. ISSN 1749-4893. doi: 10.1038/s41566-019-0358-x. URL <https://www.nature.com/articles/s41566-019-0358-x>.
- [338] Christopher Panuski, Dirk Englund, and Ryan Hamerly. Fundamental thermal noise limits for optical microcavities. *Phys. Rev. X*, 10:041046, Dec 2020. doi: 10.1103/PhysRevX.10.041046. URL <https://link.aps.org/doi/10.1103/PhysRevX.10.041046>.

Bibliography

- [339] Jasper Chan, Amir H. Safavi-Naeini, Jeff T. Hill, Seán Meenehan, and Oskar Painter. Optimized optomechanical crystal cavity with acoustic radiation shield. *Applied Physics Letters*, 101(8):081115, 2012. ISSN 00036951. doi: 10.1063/1.4747726.
- [340] E. Verhagen, S. Deléglise, S. Weis, A. Schliesser, and T. J. Kippenberg. Quantum-coherent coupling of a mechanical oscillator to an optical cavity mode. *Nature*, 482(7383):63–67, February 2012. ISSN 0028-0836, 1476-4687. doi: 10.1038/nature10787. URL <http://www.nature.com/articles/nature10787>.
- [341] Rémi Rivière. *Cavity Optomechanics with Silica Toroidal Microresonators down to Low Phonon Occupancy*. Phd, Ludwig-Maximilians-Universität, Munchen, 2011.
- [342] Di Zhu, Linbo Shao, Mengjie Yu, Rebecca Cheng, Boris Desiatov, CJ Xin, Yaowen Hu, Jeffrey Holzgrafe, Soumya Ghosh, Amirhassan Shams-Ansari, et al. Integrated photonics on thin-film lithium niobate. *Advances in Optics and Photonics*, 13(2):242–352, 2021.
- [343] Jeffrey Holzgrafe, Neil Sinclair, Di Zhu, Amirhassan Shams-Ansari, Marco Colangelo, Yaowen Hu, Mian Zhang, Karl K. Berggren, and Marko Lončar. Cavity electro-optics in thin-film lithium niobate for efficient microwave-to-optical transduction. *Optica*, 7(12):1714–1720, Dec 2020. doi: 10.1364/OPTICA.397513. URL <http://www.osapublishing.org/optica/abstract.cfm?URI=optica-7-12-1714>.
- [344] Timothy P. McKenna, Jeremy D. Witmer, Rishi N. Patel, Wentao Jiang, Raphaël Van Laer, Patricio Arrangoiz-Arriola, E. Alex Wollack, Jason F. Herrmann, and Amir H. Safavi-Naeini. Cryogenic microwave-to-optical conversion using a triply resonant lithium-niobate-on-sapphire transducer. *Optica*, 7(12):1737–1745, Dec 2020. doi: 10.1364/OPTICA.397235. URL <http://www.osapublishing.org/optica/abstract.cfm?URI=optica-7-12-1737>.
- [345] Mian Zhang, Cheng Wang, Rebecca Cheng, Amirhassan Shams-Ansari, and Marko Lončar. Monolithic ultra-high-q lithium niobate microring resonator. *Optica*, 4(12):1536–1537, 2017.
- [346] Vladimir S Ilchenko, Anatoliy A Savchenkov, Andrey B Matsko, and Lute Maleki. Nonlinear optics and crystalline whispering gallery mode cavities. *Physical review letters*, 92(4):043903, 2004.
- [347] Payam Rabiei and Peter Gunter. Optical and electro-optical properties of submicrometer lithium niobate slab waveguides prepared by crystal ion slicing and wafer bonding. *Applied Physics Letters*, 85(20):4603–4605, 2004.
- [348] Haowei Jiang, Rui Luo, Hanxiao Liang, Xianfeng Chen, Yuping Chen, and Qiang Lin. Fast response of photorefraction in lithium niobate microresonators. *Optics letters*, 42(17):3267–3270, 2017.

- [349] Markus Leidinger, Karsten Buse, and Ingo Breunig. Influence of dry-oxygen-annealing on the residual absorption of lithium niobate crystals in the spectral range from 500 to 2900 nanometers. *Optical Materials Express*, 6(1):264–269, 2016.
- [350] Huangpu Han, Lutong Cai, and Hui Hu. Optical and structural properties of single-crystal lithium niobate thin film. *Optical Materials*, 42:47–51, 2015.
- [351] Luigi Moretti, Mario Iodice, Francesco G. Della Corte, and Ivo Rendina. Temperature dependence of the thermo-optic coefficient of lithium niobate, from 300 to 515 k in the visible and infrared regions. *Journal of Applied Physics*, 98(3):036101, 2005. doi: 10.1063/1.1988987. URL <https://doi.org/10.1063/1.1988987>.
- [352] Juanjuan Lu, Ming Li, Chang-Ling Zou, Ayed Al Sayem, and Hong X Tang. Toward 1% single-photon anharmonicity with periodically poled lithium niobate microring resonators. *Optica*, 7(12):1654–1659, 2020.
- [353] A. Beccari, D. A. Visani, S. A. Fedorov, M. J. Berekhi, V. Boureau, N. J. Engelsens, and T. J. Kippenberg. Strained crystalline nanomechanical resonators with quality factors above 10 billion. *Nature Physics*, 18(4):436–441, April 2022. ISSN 1745-2481. doi: 10.1038/s41567-021-01498-4.
- [354] Leonhard Neuhaus. *Cooling a macroscopic mechanical oscillator close to its quantum ground state*. Theses, Université Pierre et Marie Curie - Paris VI, December 2016. URL <https://theses.hal.science/tel-01467924>.
- [355] Tobias Herr, Michael L. Gorodetsky, and Tobias J. Kippenberg. *Dissipative Kerr Solitons in Optical Microresonators*, chapter 6, pages 129–162. John Wiley & Sons, Ltd, 2016. ISBN 9783527686476. doi: <https://doi.org/10.1002/9783527686476.ch6>. URL <https://onlinelibrary.wiley.com/doi/abs/10.1002/9783527686476.ch6>.
- [356] V. Sudhir, D. J. Wilson, R. Schilling, H. Schütz, S. A. Fedorov, A. H. Ghadimi, A. Nunnenkamp, and T. J. Kippenberg. Appearance and Disappearance of Quantum Correlations in Measurement-Based Feedback Control of a Mechanical Oscillator. *Physical Review X*, 7(1):011001, January 2017. doi: 10.1103/PhysRevX.7.011001.
- [357] Erwan Guillaume Albert Lucas. Physics of dissipative kerr solitons in optical microresonators and application to frequency synthesis. page 248, 2019. doi: <https://doi.org/10.5075/epfl-thesis-9109>. URL <http://infoscience.epfl.ch/record/267490>.
- [358] D. J. Wilson, V. Sudhir, N. Piro, R. Schilling, A. Ghadimi, and T. J. Kippenberg. Measurement-based control of a mechanical oscillator at its thermal decoherence rate. *Nature*, 524(7565):325–329, August 2015. ISSN 1476-4687. doi: 10.1038/nature14672.
- [359] Martin HP Pfeiffer, Junqiu Liu, Arslan S Raja, Tiago Morais, Bahareh Ghadiani, and Tobias J Kippenberg. Ultra-smooth silicon nitride waveguides based on the damascene reflow process: fabrication and loss origins. *Optica*, 5(7):884–892, 2018. doi: 10.1364/OPTICA.5.000884.

Bibliography

- [360] Jiangang Zhu, Sahin Kaya Ozdemir, Yun-Feng Xiao, Lin Li, Lina He, Da-Ren Chen, and Lan Yang. On-chip single nanoparticle detection and sizing by mode splitting in an ultrahigh-q microresonator. *Nature photonics*, 4(1):46–49, 2010.
- [361] Katharina Möhle. Piezoelectrically tunable optical cavities for the gravitational wave detector lisa. 2013.
- [362] Lisheng Chen, John L Hall, Jun Ye, Tao Yang, Erjun Zang, and Tianchu Li. Vibration-induced elastic deformation of fabry-perot cavities. *Physical Review A*, 74(5):053801, 2006.
- [363] A. I. Lvovsky, H. Hansen, T. Aichele, O. Benson, J. Mlynek, and S. Schiller. Quantum state reconstruction of the single-photon fock state. *Phys. Rev. Lett.*, 87:050402, Jul 2001. doi: 10.1103/PhysRevLett.87.050402. URL <https://link.aps.org/doi/10.1103/PhysRevLett.87.050402>.
- [364] Harald Kiesel, Andreas Renz, and Franz Hasselbach. Observation of hanbury brown–twiss anticorrelations for free electrons. *Nature*, 418(6896):392–394, Jul 2002. ISSN 1476-4687. doi: 10.1038/nature00911. URL <https://doi.org/10.1038/nature00911>.

Guanhao Huang

Permanent address: Chemin de Grand-Vennes 19, 1010 Lausanne, Switzerland

Email: huangguanhao14@gmail.com

EDUCATION

Ecole Polytechnique Fédérale de Lausanne

Lausanne, Switzerland

Ph.D. Physics

2018 - 2024

Thesis topic: *Room-temperature quantum optomechanics and free-electron quantum optics*

Supervisor: *Prof. Tobias Kippenberg*

Tsinghua University

Beijing, China

B.A. Physics and Mathematics

2014 - 2018

Thesis topic: *Quantum simulation using spin and motional degrees of freedom of a trapped Yb¹⁷¹ ion*

Academic advisor: *Prof. Kihwan Kim*

RESEARCH AND WORK EXPERIENCE

Ecole Polytechnique Fédérale de Lausanne

Lausanne, Switzerland

Doctoral research assistant

2018-2024

- Investigated dissipative dynamics in photonic integrated devices, including thermodynamical frequency noise, dissipative feedback and absorption spectroscopy.
- Studied and developed a framework for free-electron-photon interaction using photonic integrated circuits in electron microscopes. Demonstrated non-classical electron-photon correlation.
- Developed a cavity optomechanics system with a ultra-low-loss nanomechanical resonator and a ultra-low-noise optical cavity. Demonstrated quantum optomechanical phenomena at room temperature.

Supervisor: *Prof. Tobias Kippenberg*

Ecole Polytechnique Fédérale de Lausanne

Lausanne, Switzerland

Independent Research

2021-2022

- Investigated high-dimensional angular synchronization problems in the context of statistical inferences. Developed approximate message passing and survey propagation algorithms to study the inference phase transitions and the symmetry breaking phenomenon.

Project PI: *Prof. Lenka Zdeborová*

Tsinghua University

Beijing, China

Thesis student

2016-2018

- Explored quantum simulation & computation techniques with trapped ion systems. Developed phase-coherent beam splitter operation of the axial motions, leading to the implementation of scalable trapped ion phononic network for boson samplings.

Academic advisor: *Prof. Kihwan Kim*

ETH Zürich

Zürich, Switzerland

Intern

2017 summer

- Developed automated fiber ablation workbench for fiber-cavity integrated ion traps.

Academic advisor: *Prof. Jonathan Home*

PUBLICATIONS

- [1] **G Huang***, A Beccari*, NJ. Engelsen, TJ Kippenberg. 2024. Room-temperature quantum optomechanics using an ultra-low noise cavity *Nature* 626(7999), 512–516
- [2] Y Yang*, J-W Henke*, AS. Raja*, F.J Kappert*, **G Huang**, G Arend, Z Qiu, A Feist, RN Wang, A Tusnin, A Tikan, C Ropers, TJ. Kippenberg. 2024. Free electron interaction with nonlinear optical states *Science* 383(6679), 168-173.
- [3] J Zhang, Z Li, J Riemensberger, G Lihachev, **G Huang**, TJ. Kippenberg. 2023. Fundamental charge noise in electro-optic photonic integrated circuits arXiv:2308.15404
- [4] **G Huang**, NJ. Engelsen, O Kfir, C Ropers, TJ. Kippenberg. 2023. Electron-photon quantum state heralding using photonic integrated circuits *PRX Quantum* 4, 020351
- [5] V Snigirev*, A Riedhauser*, G Lihachev, J Riemensberger, RN Wang, C Moehl, M Churaev, A Siddharth, **G Huang**, C Möhl, Y Popoff, U Drechsler, D Caimi, S Hönl, J Liu, P Seidler, TJ. Kippenberg. 2023. Ultrafast tunable lasers using lithium niobate integrated photonics *Nature* 615(7952), 411-417
- [6] W Chen, Y Lu, S Zhang, K Zhang, **G Huang**, M Qiao, Xu Su, J Zhang, J-N Zhang, L Banchi, M. S. Kim, K Kim. 2023. Scalable and Programmable Phononic Network with Trapped Ions *Nature Physics* 1745-2481
- [7] S Chen*, **G Huang***, G Piccioli*, L Zdeborová. 2022. The planted XY model: thermodynamics and inference *Phys. Rev. E* 106, 054115
- [8] A Feist*, **G Huang***, G Arend*, Y Yang*, J-W. Henke, A S. Raja, F.J. Kappert, R N Wang, H Lourenço-Martins, Z Qiu, J Liu, O Kfir, TJ. Kippenberg, C Ropers. 2022. Cavity-mediated electron-photon pairs *Science* 377(6607), 777-780
- [9] A Shams-Ansari*, **G Huang***, L He, Z Li, J Holzgrafe, M Jankowski, M Churaev, P Kharel, R Cheng, D Zhu, N Sinclair, B Desiatov, M Zhang, TJ. Kippenberg, M Loncar. 2022. Reduced Material Loss in Thin-film Lithium Niobate Waveguides *APL Photonics* 7, 081301
- [10] M Gao*, QF Yang*, QX Ji*, H Wang, L Wu, B Shen, J Liu, **G Huang**, L Chang, W Xie, S-P Yu, SB. Papp, JE. Bowers, TJ. Kippenberg, KJ. Vahala. 2022. Probing material absorption and optical nonlinearity of integrated photonic materials *Nature Communications* 13 (1), 1-8
- [11] MJ Beryhi*, A Arabmoheghi*, A Beccari, SA Fedorov, **G Huang**, TJ. Kippenberg, NJ. Engelsen. 2022. Perimeter Modes of Nanomechanical Resonators Exhibit Quality Factors Exceeding at Room Temperature *Physical Review X* 12 (2), 021036
- [12] L Qiu, **G Huang**, I Shomroni, J Pan, P Seidler, TJ. Kippenberg. 2022. Dissipative Quantum Feedback in Measurements Using a Parametrically Coupled Microcavity *PRX Quantum* 3 (2), 020309
- [13] JW Henke*, AS Raja*, A Feist, **G Huang**, G Arend, Y Yang, F. J Kappert, RN Wang, M Möller, J Pan, J Liu, O Kfir, C Ropers, TJ. Kippenberg. 2021. Integrated photonics enables continuous-beam electron phase modulation *Nature* 600 (7890), 653-658

* equal contribution

[14] J Liu, **G Huang**, RN Wang, J He, AS. Raja, T Liu, NJ. Engelsen, TJ. Kippenberg. 2021. High-yield, wafer-scale fabrication of ultralow-loss, dispersion-engineered silicon nitride photonic circuits *Nature communications* 12 (1), 1-9

[15] **G Huang**, E Lucas, J Liu, AS. Raja, G Lihachev, ML. Gorodetsky, NJ. Engelsen, TJ. Kippenberg. 2019. Thermorefractive noise in silicon-nitride microresonators *Physical Review A* 99 (6), 061801

Seminars	
Massachusetts Institute of Technology, Optics and Quantum Electronics Seminar "Room-temperature quantum optomechanics using engineered mechanical resonators"	11/10/2023
Institute of Science and Technology Austria "Free-electron interaction with photonic integrated circuits"	11/01/2024
Chalmers University of Technology "Interfacing free electrons and light using photonic integrated circuits"	26/02/2024
ETH Zurich, Quantum Center Seminar "Interfacing free electrons and light using photonic integrated circuits"	27/02/2024

PROFESSIONAL SERVICE

Reviewer for *PRX Quantum* (2), *Physical Review Letters* (1), *Physical Review A* (5).

TEACHING EXPERIENCE

Teaching Assistant

Ecole Polytechnique Fédérale de Lausanne Lausanne, Switzerland
Statistical Physics IV Spring of 2020, 2021, 2022

Covers stochastic calculus, classical statistical physics and non-equilibrium thermal dynamics, open quantum systems, quantum trajectories & stochastic calculus, and applications to quantum engineering problems, continuous measurement, feedback, and quantum information processing devices.

Quantum electrodynamics and quantum optics Fall of 2019, 2020, 2022

Develops the quantum theory of electromagnetic radiation. Covers basis historic developments and moreover modern developments, e.g. superconducting circuits and quantum measurement theory.

Statistical physics for optimization & learning Fall of 2021

Covers the statistical physics approach to computer science problems ranging from graph theory and constraint satisfaction to inference and machine learning. In particular the replica and cavity methods, message passing algorithms, and analysis of the related phase transitions.

TECHNICAL

Scientific Programming
 Python, Matlab, Mathematica

Research Software

COMSOL Multiphysics, Lumerical

Lab Skills

Design and implementation of feedback control, Instrument control, Lasers, Free-space and fiber optics

Language Skills

Chinese (Native), English (Fluent), French (A2)